



Advances in wind turbine blade design and materials

Edited by Povl Brøndsted and Rogier P. L. Nijssen

Advances in wind turbine blade design
and materials

Related titles:

Electrical drives for direct drive renewable energy systems
(ISBN 978-1-84569-783-9)

Wind energy systems: Optimising design and construction for safe and reliable operation
(ISBN 978-1-84569-580-4)

Stand-alone and hybrid wind energy systems: Technology, energy storage and applications
(ISBN 978-1-84569-527-9)

Fatigue Life Prediction of Composites and Composite Structures
(ISBN 978-1-84569-525-5)

Failure Analysis and Fractography of Polymer Composites
(ISBN 978-1-84569-217-9)

Details of these books and a complete list of titles from Woodhead Publishing can be obtained by:

- visiting our web site at www.woodheadpublishing.com
- contacting Customer Services (e-mail: sales@woodheadpublishing.com; fax: +44 (0) 1223 832819; tel.: +44 (0) 1223 499140 ext. 130; address: Woodhead Publishing Limited, 80 High Street, Sawston, Cambridge CB22 3HJ UK)
- in North America, contacting our US office (e-mail: usmarketing@woodheadpublishing.com; tel.: (215) 928 9112; address: Woodhead Publishing, 1518 Walnut Street, Suite 1100, Philadelphia, PA 19102-3406, USA)

If you would like e-versions of our content, please visit our online platform: www.woodheadpublishingonline.com. Please recommend it to your librarian so that everyone in your institution can benefit from the wealth of content on the site.

We are always happy to receive suggestions for new books from potential editors. To enquire about contributing to our Energy series, please send your name, contact address and details of the topic/s you are interested in to sarah.hughes@woodheadpublishing.com. We look forward to hearing from you.

The team responsible for publishing this book:

Commissioning Editor: Sarah Hughes

Publications Coordinator: Steven Mathews

Project Editor: Kate Hardcastle

Editorial and Production Manager: Mary Campbell

Production Editor: Richard Fairclough

Project Manager: Newgen Knowledge Works Pvt Ltd

Copyeditor: Newgen Knowledge Works Pvt Ltd

Proofreader: Newgen Knowledge Works Pvt Ltd

Cover Designer: Terry Callanan

Woodhead Publishing Series in Energy: Number 47

Advances in wind turbine blade design and materials

Edited by
Povl Brøndsted and
Rogier P. L. Nijssen



Oxford Cambridge Philadelphia New Delhi

Published by Woodhead Publishing Limited,
80 High Street, Sawston, Cambridge CB22 3HJ, UK
www.woodheadpublishing.com
www.woodheadpublishingonline.com

Woodhead Publishing, 1518 Walnut Street, Suite 1100, Philadelphia,
PA 19102-3406, USA

Woodhead Publishing India Private Limited, 303 Vardaan House, 7/28 Ansari Road,
Daryaganj, New Delhi – 110002, India
www.woodheadpublishingindia.com

First published 2013, Woodhead Publishing Limited

© Woodhead Publishing Limited, 2013. Note: the publisher has made every effort to ensure that permission for copyright material has been obtained by authors wishing to use such material. The authors and the publisher will be glad to hear from any copyright holder it has not been possible to contact.

The authors have asserted their moral rights.

This book contains information obtained from authentic and highly regarded sources. Reprinted material is quoted with permission, and sources are indicated. Reasonable efforts have been made to publish reliable data and information, but the authors and the publisher cannot assume responsibility for the validity of all materials. Neither the authors nor the publisher, nor anyone else associated with this publication, shall be liable for any loss, damage or liability directly or indirectly caused or alleged to be caused by this book.

Neither this book nor any part may be reproduced or transmitted in any form or by any means, electronic or mechanical, including photocopying, microfilming and recording, or by any information storage or retrieval system, without permission in writing from Woodhead Publishing Limited.

The consent of Woodhead Publishing Limited does not extend to copying for general distribution, for promotion, for creating new works, or for resale. Specific permission must be obtained in writing from Woodhead Publishing Limited for such copying.

Trademark notice: Product or corporate names may be trademarks or registered trademarks, and are used only for identification and explanation, without intent to infringe.

British Library Cataloguing in Publication Data
A catalogue record for this book is available from the British Library.

Library of Congress Control Number: 2013948042

ISBN 978-0-85709-426-1 (print)

ISBN 978-0-85709-728-6 (online)

ISSN: 2044-9364 Woodhead Publishing Series in Energy (print)

ISSN: 2044-9372 Woodhead Publishing Series in Energy (online)

The publisher's policy is to use permanent paper from mills that operate a sustainable forestry policy, and which has been manufactured from pulp which is processed using acid-free and elemental chlorine-free practices. Furthermore, the publisher ensures that the text paper and cover board used have met acceptable environmental accreditation standards.

Typeset by Newgen Knowledge Works Pvt Ltd, India
Printed by Lightning Source

Contents

<i>Contributor contact details</i>	<i>xi</i>
<i>Woodhead Publishing Series in Energy</i>	<i>xiv</i>
<i>Introduction</i>	<i>xix</i>
Part I Wind turbine blade design: challenges and developments	1
1 Introduction to wind turbine blade design	3
F. MØLHOLT JENSEN, Bladena, Denmark and K. BRANNER, Technical University of Denmark, Denmark	
1.1 Introduction	3
1.2 Design principles and failure mechanisms	6
1.3 Challenges and future trends	18
1.4 References	25
2 Loads on wind turbine blades	29
H. SÖKER, Deutsches Windenergie-Institut GmbH, Germany	
2.1 Introduction	29
2.2 Types of load	30
2.3 Generation of loads	35
2.4 Fatigue and extreme loads	46
2.5 Design verification testing	50
2.6 Challenges and future trends	54
2.7 Sources of further information and advice	57
2.8 References	57

3	Aerodynamic design of wind turbine rotors C. BAK, Technical University of Denmark, Denmark	59
3.1	Introduction	59
3.2	The blade element momentum (BEM) method	63
3.3	Important parameters in aerodynamic rotor design	72
3.4	Particular design parameters	78
3.5	An example of the rotor design process	86
3.6	Future trends	102
3.7	Sources of further information and advice	103
3.8	Acknowledgements	104
3.9	References	104
3.10	Appendix: Nomenclature	107
4	Aerodynamic characteristics of wind turbine blade airfoils W. A. TIMMER, Delft University of Technology, the Netherlands and C. BAK, Technical University of Denmark, Denmark	109
4.1	Introduction	109
4.2	Computational methods	110
4.3	Desired characteristics	116
4.4	The effect of leading edge contamination (roughness) and Reynolds number	120
4.5	Airfoil testing	124
4.6	Airfoil characteristics at high angles of attack	128
4.7	Correction for centrifugal and Coriolis forces	133
4.8	Establishing data for blade design	140
4.9	Future trends	145
4.10	References	146
4.11	Appendix: Nomenclature	149
5	Aeroelastic design of wind turbine blades J. G. HOLIERHOEK, Energy research Centre of the Netherlands, The Netherlands	150
5.1	Introduction	150
5.2	Wind turbine blade aeroelasticity	155
5.3	Blade design	162
5.4	Complete turbine design	167
5.5	Challenges and future trends	170
5.6	Sources of further information and advice	171
5.7	References	171

Part II	Fatigue behaviour of composite wind turbine blades	173
6	Fatigue as a design driver for composite wind turbine blades	175
	R. P. L. NIJSSEN, Knowledge Centre Wind turbine Materials and Constructions, The Netherlands and P. BRØNDSTED, Technical University of Denmark, Denmark	
6.1	Introduction	175
6.2	Materials in blades	176
6.3	Blade structure and components	177
6.4	Fundamentals of wind turbine blade fatigue	183
6.5	Research into wind turbine blade fatigue and its modelling	191
6.6	Future trends	201
6.7	Conclusion	206
6.8	Sources of further information and advice	206
6.9	References	207
7	Effects of resin and reinforcement variations on fatigue resistance of wind turbine blades	210
	J. F. MANDELL, D. D. SAMBORSKY and D. A. MILLER, Montana State University, USA	
7.1	Introduction	210
7.2	Effects of loading conditions for glass and carbon laminates	211
7.3	Tensile fatigue trends with laminate construction and fiber content for glass fiber laminates	217
7.4	Effects of resin and fabric structure on tensile fatigue resistance	226
7.5	Delamination and material transitions	236
7.6	Comparison of fatigue trends for blade materials	243
7.7	Conclusion	246
7.8	Future trends	247
7.9	Sources of further information and advice	248
7.10	Acknowledgments	248
7.11	References	249
8	Fatigue life prediction of wind turbine blade composite materials	251
	A. P. VASSILOPOULOS, École Polytechnique Fédérale de Lausanne (EPFL), Switzerland	
8.1	Introduction	251
8.2	Macroscopic failure theories	255

8.3	Strength and stiffness degradation fatigue theories	268
8.4	Fracture mechanics fatigue theories	273
8.5	Case study: Phenomenological fatigue life prediction	284
8.6	Future trends	289
8.7	References	291
9	Micromechanical modelling of wind turbine blade materials	298
	L. MISHNAEVSKY JR., Technical University of Denmark, Denmark	
9.1	Introduction	298
9.2	Analytical models of the mechanical behaviour, strength and damage of fibre-reinforced composites: an overview	300
9.3	Unit cell modelling of fibre-reinforced composites	304
9.4	Three-dimensional modelling of composite degradation under tensile loading	306
9.5	Carbon fibre-reinforced composites: statistical and compressive loading effects	311
9.6	Hierarchical composites with nanoengineered matrix	316
9.7	Conclusions and future trends	317
9.8	Sources of further information and advice	319
9.9	Acknowledgements	320
9.10	References	320
10	Probabilistic design of wind turbine blades	325
	D. J. LEKOU, Centre for Renewable Energy Sources and Saving (CRES), Greece	
10.1	Introduction	325
10.2	Structural analysis models	329
10.3	Failure definition	333
10.4	Random variables	338
10.5	Probabilistic methods and models	342
10.6	Application examples and discussion of techniques	348
10.7	Challenges and future trends	351
10.8	Sources of further information and advice	353
10.9	References	354

Part III Advances in wind turbine blade materials, development and testing	361
11 Biobased composites: materials, properties and potential applications as wind turbine blade materials	363
B. MADSEN, P. BRØNDSTED and T. LØGSTRUP ANDERSEN, Technical University of Denmark, Denmark	
11.1 Introduction	363
11.2 Biobased fibres and matrix materials	366
11.3 Biobased composites	371
11.4 Case study: Comparison between cellulose and glass fibre composites	374
11.5 Special considerations in the development and application of biobased composites	377
11.6 Sources of further information and advice	382
11.7 References	383
12 Surface protection and coatings for wind turbine rotor blades	387
B. KJÆRSIDE STORM, Aalborg University, Denmark	
12.1 Introduction	387
12.2 Fundamentals of surface protection for wind turbine blades	389
12.3 Protection from blade icing, lightning and air traffic	398
12.4 Performance testing of protection layers: an introduction	400
12.5 Accelerated testing of the surface coatings of wind turbine blades in practice	406
12.6 Conclusions, challenges and future trends	409
12.7 References	411
13 Design, manufacture and testing of small wind turbine blades	413
P. D. CLAUSEN and F. REYNAL, University of Newcastle, Australia and D. H. WOOD, University of Calgary, Canada	
13.1 Introduction	413
13.2 Requirements for small wind turbine blades	416
13.3 Materials and manufacture	418
13.4 Blade testing	421

x Contents

13.5	Installation and operation	426
13.6	Challenges and future trends	428
13.7	Acknowledgements	429
13.8	References	430
14	Wind turbine blade structural performance testing	432
	J. J. HEIJDRA, M. S. BORST and D. R. V. VAN DELFT, Knowledge Centre WMC, The Netherlands	
14.1	Introduction	432
14.2	Test program	433
14.3	Types of tests	434
14.4	Test loads	437
14.5	Test details	441
14.6	Conclusion	445
14.7	References	445
	<i>Index</i>	<i>446</i>

Contributor contact details

(* = main contact)

Editors and Chapter 6

P. Brøndsted
DTU Wind Energy
Technical University of Denmark
Building 228
P.O. Box 49
Frederiksborgvej 399
4000 Roskilde, Denmark
E-mail: pobr@dtu.dk

R. P. L. Nijssen
Knowledge Centre Wind turbine
Materials and Constructions
(WMC)
P.O. Box 43, 1770 AA
Wieringerwerf, the Netherlands
E-mail: r.p.l.nijssen@wmc.eu

Chapter 1

F. Mølholt Jensen*
Bladena
Sct. Hansgade 9²
DK – 4100 Ringsted, Denmark
E-mail: fmj@bladena.com

K. Branner
DTU Wind Energy
Technical University of Denmark
Building 118
P.O. Box 49
Frederiksborgvej 399
4000 Roskilde, Denmark
E-mail: kibr@dtu.dk

Chapter 2

H. Söker
Technical Director
Head of Mechanical Loads
DEWI
GmbH
Ebertstrasse 96
26382
Wilhelmshaven, Germany
E-mail: h.soeker@dewi.de

Chapter 3

C. Bak
DTU Wind Energy
Technical University of Denmark
Building 118
P.O. Box 49
Frederiksborgvej 399
4000 Roskilde, Denmark
E-mail: chba@dtu.dk

Chapter 4

W. A. Timmer*

Delft University of Technology
Faculty of Aerospace Engineering
Wind Energy Section
Kluyverweg 1
2629 HS Delft, the Netherlands

E-mail: W.A.Timmer@tudelft.nl

C. Bak

DTU Wind Energy
Technical University of Denmark
Building 118
P.O. Box 49
Frederiksborvej 399
4000 Roskilde, Denmark

E-mail: chba@dtu.dk

Chapter 5

J. G. Holierhoek

ECN Wind Energy
Energy research Centre of the
Netherlands
P.O. Box 1
1755 ZG Petten, the Netherlands

E-mail: holierhoek@ecn.nl

Chapter 7

J. F. Mandell* and

D. D. Samborsky

Department of Chemical and
Biological Engineering
Montana State University
306 Cobleigh Hall
Bozeman, MT 59717, USA

E-mail: JohnM@coe.montana.edu;
Daniels@coe.montana.edu

D. A. Miller

Department of Mechanical and
Industrial Engineering
Montana State University
220 Roberts Hall
Bozeman, MT 59717, USA
E-mail: dmiller@me.montana.edu

Chapter 8

A. P. Vassilopoulos

École Polytechnique Fédérale de
Lausanne (EPFL)
School of Architecture, Civil and
Environmental Engineering
(ENAC)
Composite Construction
Laboratory (CCLab)
BP 2122 (Bat. BP), Station 16
CH – 1015 Lausanne, Switzerland

E-mail:

anastasios.vasilopoulos@epfl.ch

Chapter 9

L. Mishnaevsky Jr.

DTU Wind Energy
Technical University of Denmark
Building 228
P.O. Box 49
Frederiksborvej 399
4000 Roskilde, Denmark
E-mail: lemi@dtu.dk

Chapter 10

D. J. Lekou

Wind Energy Section
Centre for Renewable Energy
Sources and Saving (CRES)
19th km Marathonos Avenue
GR-190 09, Pikermi, Greece

E-mail: dlekou@cres.gr

Chapter 11

B. Madsen,* P. Brøndsted and
T. Løgstrup Andersen
DTU Wind Energy
Technical University of Denmark
Building 228
P.O. Box 49
Frederiksborgvej 399
4000 Roskilde, Denmark
E-mail: boma@dtu.dk

Chapter 12

B. Kjærside Storm
Institute for Chemistry and
Biotechnology
Aalborg University
Niels Bohrsvej 8
6700 Esbjerg, Denmark

E-mail: bkstorm@bbsyd.dk

Chapter 13

P. D. Clausen* and F. Reynal
School of Engineering
University of Newcastle
NSW 2308, Australia

E-mail: Philip.Clausen@newcastle.edu.au

D. H. Wood

Department of Mechanical and
Manufacturing Engineering
University of Calgary
AB T2N 1N4, Canada

E-mail: dhwood@ucalgary.ca

Chapter 14

J. J. Heijdra,* M. S. Borst and
D. R. V. van Delft
Knowledge Centre Wind Turbine
Materials and Constructions
(WMC)
P.O. Box 43, 1770 AA
Wieringerwerf, the Netherlands

E-mail: j.j.heijdra@wmc.eu;
m.s.borst@wmc.eu;
d.r.v.vandelft@wmc.eu

Woodhead Publishing Series in Energy

- 1 **Generating power at high efficiency: Combined cycle technology for sustainable energy production**
Edited by Eric Jeffs
- 2 **Advanced separation techniques for nuclear fuel reprocessing and radioactive waste treatment**
Edited by Kenneth L. Nash and Gregg J. Lumetta
- 3 **Bioalcohol production: Biochemical conversion of lignocellulosic biomass**
Edited by K. W. Waldron
- 4 **Understanding and mitigating ageing in nuclear power plants: Materials and operational aspects of plant life management (PLiM)**
Edited by Philip G. Tipping
- 5 **Advanced power plant materials, design and technologies**
Edited by Dermot Roddy
- 6 **Stand-alone and hybrid wind energy systems: Technology, energy storage and applications**
Edited by J. K. Kaldellis
- 7 **Biodiesel science and technology: From soil to oil**
Edited by Jan C. J. Bart, Natale Palmeri and Stefano Cavallaro
- 8 **Developments and innovation in carbon dioxide (CO₂) capture and storage technology Volume 1: Carbon dioxide (CO₂) capture, transport and industrial applications**
Edited by M. Mercedes Maroto-Valer
- 9 **Geological repository systems for safe disposal of spent nuclear fuels and radioactive waste**
Edited by Joonhong Ahn and Michael J. Apted
- 10 **Wind energy systems: Optimising design and construction for safe and reliable operation**
Edited by John D. Sørensen and Jens N. Sørensen
- 11 **Solid oxide fuel cell technology: Principles, performance and operations**
Edited by Kevin Huang and John Bannister Goodenough
- 12 **Handbook of advanced radioactive waste conditioning technologies**
Edited by Michael I. Ojovan

- 13 **Membranes for clean and renewable power applications**
Edited by Annarosa Gugliuzza and Angelo Basile
- 14 **Materials for energy efficiency and thermal comfort in buildings**
Edited by Matthew R. Hall
- 15 **Handbook of biofuels production: Processes and technologies**
Edited by Rafael Luque, Juan Campelo and James Clark
- 16 **Developments and innovation in carbon dioxide (CO₂) capture and storage technology Volume 2: Carbon dioxide (CO₂) storage and utilisation**
Edited by M. Mercedes Maroto-Valer
- 17 **Oxy-fuel combustion for power generation and carbon dioxide (CO₂) capture**
Edited by Ligang Zheng
- 18 **Small and micro combined heat and power (CHP) systems: Advanced design, performance, materials and applications**
Edited by Robert Beith
- 19 **Advances in clean hydrocarbon fuel processing: Science and technology**
Edited by M. Rashid Khan
- 20 **Modern gas turbine systems: High efficiency, low emission, fuel flexible power generation**
Edited by Peter Jansohn
- 21 **Concentrating solar power technology: Principles, developments and applications**
Edited by Keith Lovegrove and Wes Stein
- 22 **Nuclear corrosion science and engineering**
Edited by Damien Féron
- 23 **Power plant life management and performance improvement**
Edited by John E. Oakey
- 24 **Electrical drives for direct drive renewable energy systems**
Edited by Markus Mueller and Henk Polinder
- 25 **Advanced membrane science and technology for sustainable energy and environmental applications**
Edited by Angelo Basile and Suzana Pereira Nunes
- 26 **Irradiation embrittlement of reactor pressure vessels (RPVs) in nuclear power plants**
Edited by Naoki Soneda
- 27 **High temperature superconductors (HTS) for energy applications**
Edited by Ziad Melhem
- 28 **Infrastructure and methodologies for the justification of nuclear power programmes**
Edited by Agustín Alonso
- 29 **Waste to energy conversion technology**
Edited by Naomi B. Klinghoffer and Marco J. Castaldi

- 30 **Polymer electrolyte membrane and direct methanol fuel cell technology**
Volume 1: Fundamentals and performance of low temperature fuel cells
Edited by Christoph Hartnig and Christina Roth
- 31 **Polymer electrolyte membrane and direct methanol fuel cell technology**
Volume 2: In situ characterization techniques for low temperature fuel cells
Edited by Christoph Hartnig and Christina Roth
- 32 **Combined cycle systems for near-zero emission power generation**
Edited by Ashok D. Rao
- 33 **Modern earth buildings: Materials, engineering, construction and applications**
Edited by Matthew R. Hall, Rick Lindsay and Meror Krayenhoff
- 34 **Metropolitan sustainability: Understanding and improving the urban environment**
Edited by Frank Zeman
- 35 **Functional materials for sustainable energy applications**
Edited by John A. Kilner, Stephen J. Skinner, Stuart J. C. Irvine and Peter P. Edwards
- 36 **Nuclear decommissioning: Planning, execution and international experience**
Edited by Michele Laraia
- 37 **Nuclear fuel cycle science and engineering**
Edited by Ian Crossland
- 38 **Electricity transmission, distribution and storage systems**
Edited by Ziad Melhem
- 39 **Advances in biodiesel production: Processes and technologies**
Edited by Rafael Luque and Juan A. Melero
- 40 **Biomass combustion science, technology and engineering**
Edited by Lasse Rosendahl
- 41 **Ultra-supercritical coal power plants: Materials, technologies and optimisation**
Edited by Dongke Zhang
- 42 **Radionuclide behaviour in the natural environment: Science, implications and lessons for the nuclear industry**
Edited by Christophe Poinsot and Horst Geckeis
- 43 **Calcium and chemical looping technology for power generation and carbon dioxide (CO₂) capture: Solid oxygen- and CO₂-carriers**
P. Fennell and E. J. Anthony
- 44 **Materials' ageing and degradation in light water reactors: Mechanisms, and management**
Edited by K. L. Murty
- 45 **Structural alloys for power plants: Operational challenges and high-temperature materials**
Edited by Amir Shirzadi, Rob Wallach and Susan Jackson

- 46 **Biolubricants: Science and technology**
Jan C. J. Bart, Emanuele Gucciardi and Stefano Cavallaro
- 47 **Advances in wind turbine blade design and materials**
Edited by Povl Brøndsted and Rogier P. L. Nijssen
- 48 **Radioactive waste management and contaminated site clean-up: Processes, technologies and international experience**
Edited by William E. Lee, Michael I. Ojovan, Carol M. Jantzen
- 49 **Probabilistic safety assessment for optimum nuclear power plant life management (PLiM): Theory and application of reliability analysis methods for major power plant components**
Gennadij V. Arkadov, Alexander F. Getman and Andrei N. Rodionov
- 50 **The coal handbook Volume 1: Towards cleaner production**
Edited by D. G. Osborne
- 51 **The coal handbook Volume 2: Coal utilisation**
Edited by D. G. Osborne
- 52 **The biogas handbook: Science, production and applications**
Edited by Arthur Wellinger, Jerry Murphy and David Baxter
- 53 **Advances in biorefineries: Biomass and waste supply chain exploitation**
Edited by K. W. Waldron
- 54 **Geological storage of carbon dioxide (CO₂): Geoscience, technologies, environmental aspects and legal frameworks**
Edited by Jon Gluyas and Simon Mathias
- 55 **Handbook of membrane reactors Volume 1: Fundamental materials science, design and optimisation**
Edited by Angelo Basile
- 56 **Handbook of membrane reactors Volume 2: Reactor types and industrial applications**
Edited by Angelo Basile
- 57 **Alternative fuels and advanced vehicle technologies: Towards zero carbon transportation**
Edited by Richard Folkson
- 58 **Handbook of microalgal bioprocess engineering**
Christopher Lan and Bei Wang
- 59 **Fluidized bed technologies for near-zero emission combustion and gasification**
Edited by Fabrizio Scala
- 60 **Managing nuclear projects: A comprehensive management resource**
Edited by Jas Devgun
- 61 **Handbook of process integration: Minimisation of energy and water use, waste and emissions**
Edited by Jiří Klemeš

Introduction

Global demand for energy has increased concern about greenhouse effects caused by fossil incineration and fuel consumption. This has resulted in global heating and melting of the ice caps and has necessitated the increasing use of the sustainable energy resources provided by biomass, sun, wave and wind. Over the last 35 years, wind energy has become a prominent part of the solution to these problems, and the development, manufacture and operation of wind energy harvesters is no longer carried out on a small-scale, experimental basis but has grown into a fully modern and mature industrial sector.

Wind energy power generation is expected to continue the enormous growth it has enjoyed during recent decades, see Fig. 1.¹ It is expected that wind power will deliver 2.5% of the world's electricity in 2013. Predictions indicate that wind power will be able to meet 8% of the world's consumption of electricity by 2021, only eight years from now. The average annual growth rate for new installations seems to have slowed down due to the economic recession, and it is expected that for 2013 it will be only 10%, although economic and political predictions indicate that the growth rate will increase and once again reach the rates seen 5–8 years ago.

The business driver for wind energy developments and the main challenge is to make the cost of wind energy comparable with that of competing energy sources. The cost of producing kWhs over the lifetime of the wind turbine, the Cost of Energy (CoE), is roughly estimated from²:

$$\text{CoE} = \frac{\text{CoT} + \text{CoI} + \text{CoM}}{\text{PP}}$$

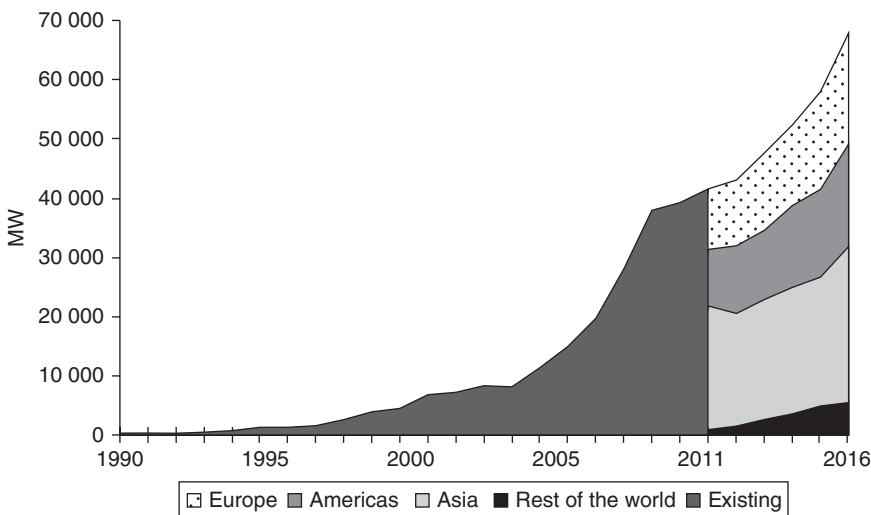
where:

CoT = Cost of the Turbine,

CoI = Cost of the Installation and Transportation,

CoM = Cost of the Operation and Maintenance during the lifetime of the turbine,

PP = Power Produced.



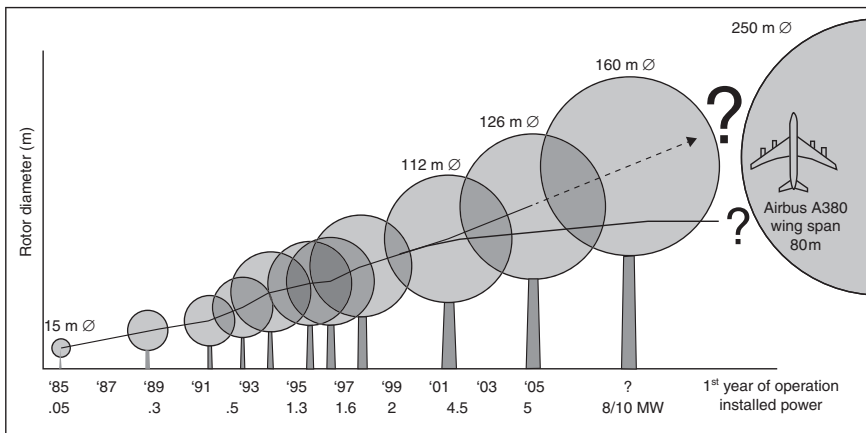
1 Development of installed wind power in the world 1990–2011 and forecast 2012–2016.

Wind turbines are available with power ratings that range from a few kilowatts to 8 MW, currently the largest that have been installed. Manufacturers are working on the designs of turbines of around 10 MW for offshore wind farms and are reducing the CoE by increasing turbine size, thereby reducing the number of turbines in a farm (lowering the CoI), and also by reducing the total CoM. In addition, the PP is being maximized through improved control, integrated design, and site evaluations.^{2,3}

A wind turbine contains many dedicated components all playing their part in the conversion of the wind's kinetic energy to electrical energy. Each of these components has experienced tremendous development, improvement and increase in scale in the past decade (Fig. 2)⁴ to meet the requirements posed by the drive for CoE reduction, resulting in tower top masses reaching 100–450 tonnes.

This book describes how these development trends have led to advances in the engineering of rotor blades, which are the main components of a wind turbine. The objective of the book is to evaluate the challenges in rotor blade design and to discuss the requirements and challenges for the composite materials to be used in the wind turbine blades of the future. This is achieved by presenting current scientific and engineering concepts, and the intention is not only to focus on blades for larger wind turbines, but also to present methodologies which can be applied to the full size-range of wind turbine blades planned for the future market.

The fundamental and the advanced knowledge which influence rotor blade design are both described, by various experts from industry, R&D



2 Upscaling history for the size of wind turbines.⁴

institutes and universities, in the three parts of the book. The first part gives an overview of wind turbine design and an introduction to how external loads affect the blades, followed by essential background knowledge in the fields of aerodynamics and aeroelasticity. The loads, the blade aerodynamics, and the rotor stability can be seen to form a design envelope within which the structural engineer is required to interact.

The second part focuses on one of the main drivers affecting blade design, namely the fatigue evaluation of materials and of structural details, and the associated lifetime prediction and damage modeling. This is followed by chapters linking materials and design in a description of state-of-the-art micromechanical modeling and modern probabilistic design methods.

Part III demonstrates popular current topics and future possibilities in material sustainability, surface durability and the design and manufacture of small (micro) wind mills, with the final chapter describing the methodologies encountered in the challenging field of full-scale blade testing.

It is the hope of the editors that the book will inspire researchers and innovators to contribute to meeting the materials and design methods challenges of the wind turbine blades of the future.

References

1. World Market Update 2011. BTM consult, 2012.
2. T.K. Jacobsen. Materials technology for large wind turbine rotor blades – limits and challenges. in: Composite materials for structural performance: towards higher limits. Proceedings of the 32nd Risø International Symposium on Materials Science. Ed S. Fæster *et al.*, Roskilde 2011.

3. Strategic Energy Technology Plan. Scientific Assessment in support of the Materials Roadmap enabling Low Carbon Energy Technologies Wind Energy. L.G.J. Janssen (rapporteur), R. Lacal Arántegui, P. Brøndsted, P. Gimondo, A.Klimpel, B.B. Johansen, P.Thibaux. EUR 25197 EN – 2012. European Union, 2012.
4. J. Beurskens. Developing Offshore Wind Energy now and in the future. Third We@Sea Conference, IJmuiden, 25 November 2010. <http://www.we-at-sea.org/leden/docs/conference2010/1.pdf>.

Introduction to wind turbine blade design

F. MØLHOLT JENSEN, Bladena, Denmark and
K. BRANNER, Technical University of Denmark, Denmark

DOI: 10.1533/9780857097286.1.3

Abstract: An overview of the current and future trends in wind turbine blade structural design process is presented. The main design principles and failure mechanisms of blades in operation are assessed and explained through an industry point of view, in a realistic manner. A number of failure modes which are not addressed sufficiently in the certificate guidelines are presented. An example on how to use the new design philosophy is presented. The manufactured prototype is a 44m long load carrying spar and the weight is reduced by 40%.

Key words: structural blade design, failure modes, cross-sectional shear distortion, bond line failure, buckling.

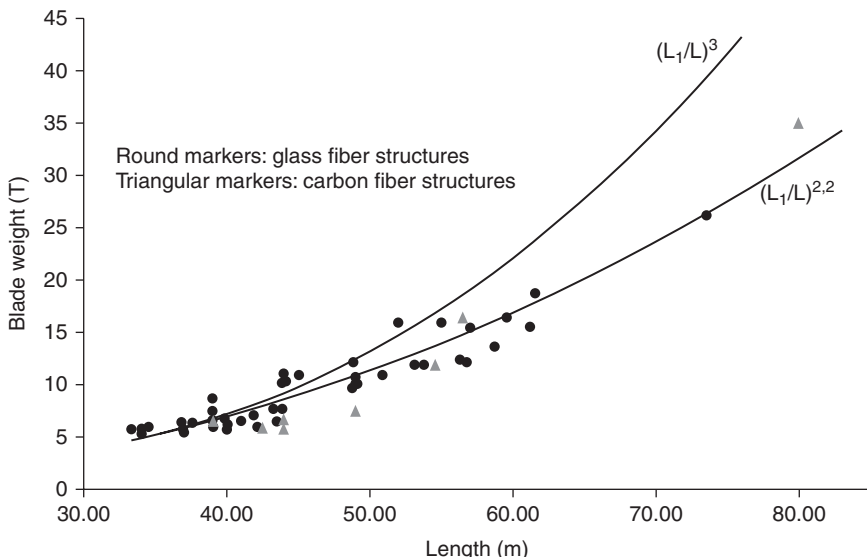
1.1 Introduction

Wind turbines have grown substantially in size over the years since commercial wind turbines were introduced around 1980. After a few years during which the focus was on increased reliability, we once again (2011) see growth in the size of wind turbines, see Fig. 1.1.

Using normal scaling laws, the weight of wind turbine blades should increase with length to the power of three. However, historically, according to Fig. 1.1, blade weights have only increased to the power of 2.3 as blade manufacturers have successfully improved the aerodynamic performance and control of wind turbines, as well as their structural design, and have optimized the use of materials and process technology.

Wind turbine blades are now so large that gravity and inertia loads have started to dominate more than aerodynamic loads. It is therefore of increasing importance to reduce weight.

Research carried out at the Department of Wind Energy at the Technical University of Denmark (DTU Wind Energy) on wind turbine blades has shown that the classical failure mechanisms such as buckling, material failure, etc., are not enough to determine the design of the blades. Other failure mechanisms need to be taken into account. One mechanism which may lead to failure is cross-sectional shear distortion. This mechanism has been demonstrated in full-scale tests and is not covered by type certification tests.



1.1 Blade weight vs blade length (L).

Another mechanism is the non-linear out-of-plane deformation of the load-carrying cap laminate, which could be the reason for some adhesive joint failures experienced in wind turbine blades today.

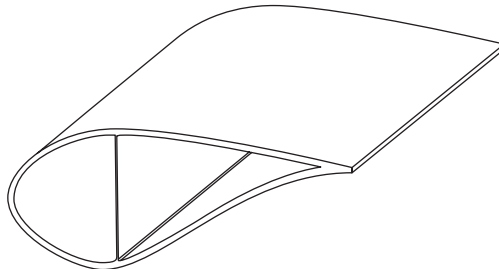
1.1.1 Typical blade designs

The design of a wind turbine blade is a compromise between aerodynamic and structural considerations. Aerodynamic considerations usually dominate the design of the outer two-thirds of the blade while structural considerations are more important for the design of the inner one-third of the blade.

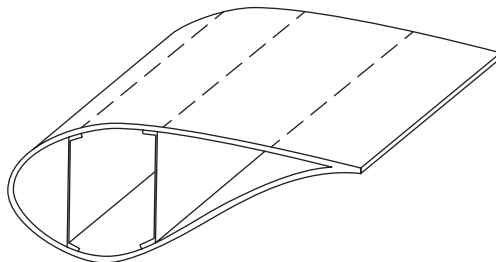
Structurally the blade is typically hollow with the outer geometry formed by two shells: one on the suction side and one on the pressure side. One or more structural webs are fitted to join the two shells together and to transfer shear loads, see Figs 1.2 and 1.3.

A load-carrying box girder is used in some blade designs, see Fig. 1.4, usually for blades with two webs including spar caps.

In Fig. 1.5, three older blade designs from different manufacturers (LM Wind Power, SSP Technology and Vestas Wind Systems) are shown. In the blade from LM Wind Power, an upper shell, a lower shell and two webs are bonded together to form the blade structure as shown in Fig. 1.5a. In the blade from SSP Technology, a box girder is created from two half-parts bonded together, as depicted in Fig. 1.5b, while Vestas Wind Systems uses exemplarily a box girder which is manufactured on a mandrel, see Fig. 1.5c.



1.2 Sketches of different blade concepts. Blade design with one shear web.

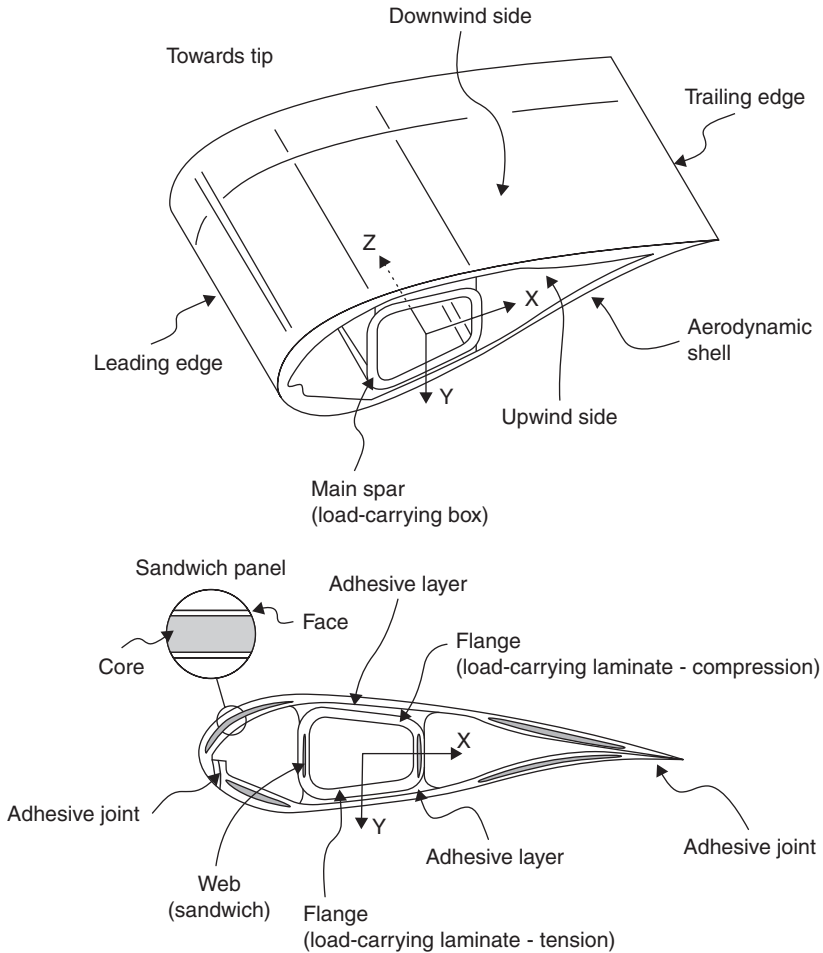


1.3 Blade design with two shear webs.

In Fig. 1.6, rib/bulkhead solutions from two different blade manufacturers are shown.

The blade design from 1948, shown in Fig. 1.6, was used in a 200-foot diameter wind turbine which was the first to implement ribs in a wind turbine blade. The blade was manufactured from plywood with ribs of stainless steel and reveals quite a few similarities to an aircraft wing design. Current blade-manufacturing technology based on thermosetting composites is not suitable for producing rib-reinforced blades in an economically sound manner, see References [2] and [3]. However, rib/bulkhead blade design using a reactively processed thermoplastic together with vacuum infusion is currently under development, see References [2] and [3]. Today, there are limitations in melt processing and consequently the size and the thickness is limited. However, if current research in materials technology is successful, rib/bulkhead design could be reintroduced in wind turbine blades, see Reference [4].

Other types of internal structures are also being considered. DTU Wind Energy has designed a load-carrying box using different structural members inside the box girder. By means of these additional members the thickness of the load-carrying laminates was decreased by 40% and the box was prevented from distorting in the transverse direction, see Fig. 1.27 and Section 1.3 of this chapter.



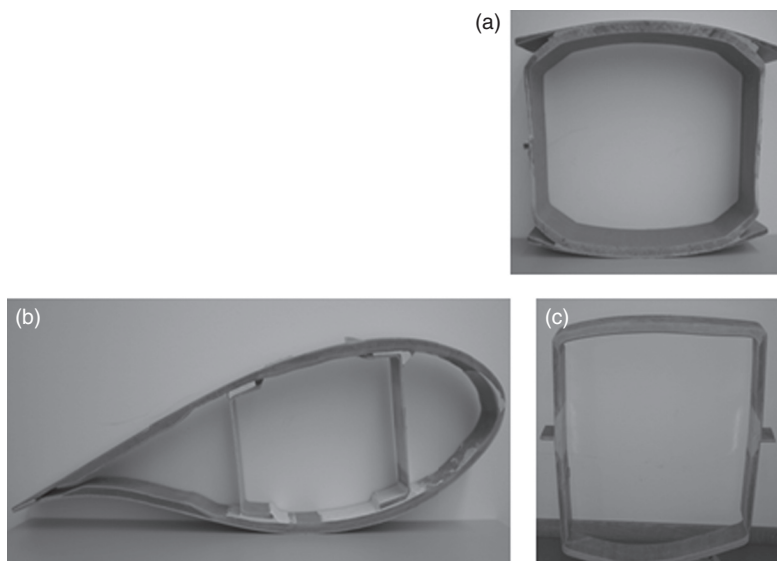
1.4 Blade design with a load-carrying box girder. (Source: From Reference [1].)

1.2 Design principles and failure mechanisms

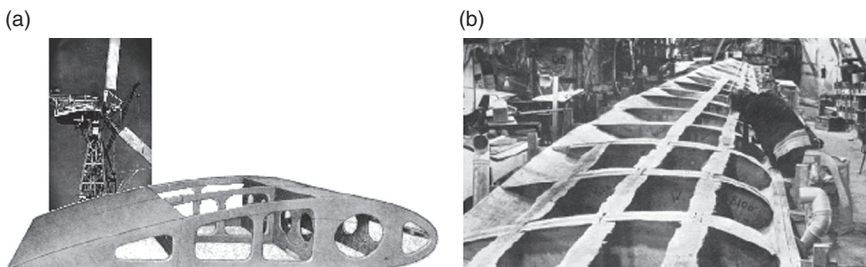
In the following section a number of failure mechanism will be presented.

1.2.1 Design principles

Current wind turbine blades are generally not fully optimized with regards to structural strength. Therefore, large differences can be expected in the safety analysis of various types of failure modes. The safety margins of different failure modes in current blade design, including material, structural and buckling



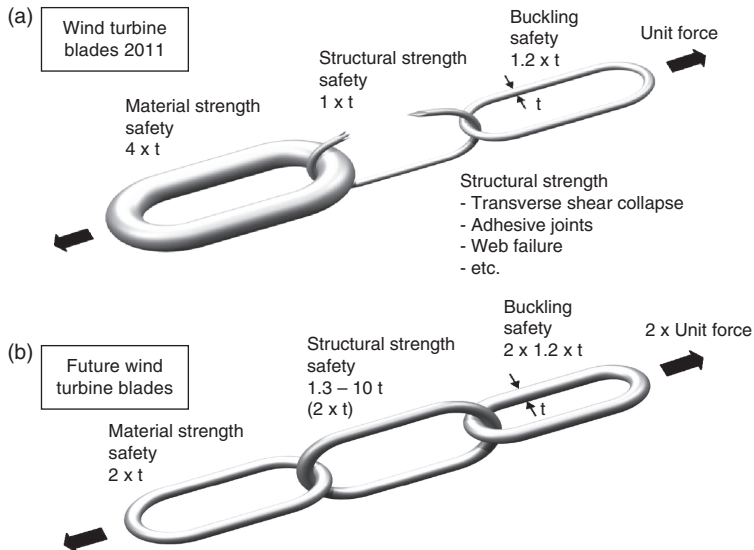
1.5 Different wind turbine blade designs. (a) LM Wind Power design.
(b) SSP Technology design. (c) Vestas box girder.



1.6 Ribs/Bulkheads used in wind turbine blades. (a) Photo of a 200-foot diameter wind turbine from United States Plywood Corporation.
(b) Photo of a Tvind wind turbine blade.

failure, is schematically illustrated in Fig. 1.7. Buckling and structural strength have been separated even though both relate to the structural aspect. This is in order to illustrate the difference in unused capacity.

Figure 1.7 illustrates that material strength enjoys a very large safety margin in modern wind turbine blades. This postulate is based on experimental work^{5–10} in which panels from three blade manufacturers were tested in compression. Even though the test specimens were made similar to the load-carrying laminate in a typical wind turbine blade, the material properties are not fully representative of those in real wind turbine blades as

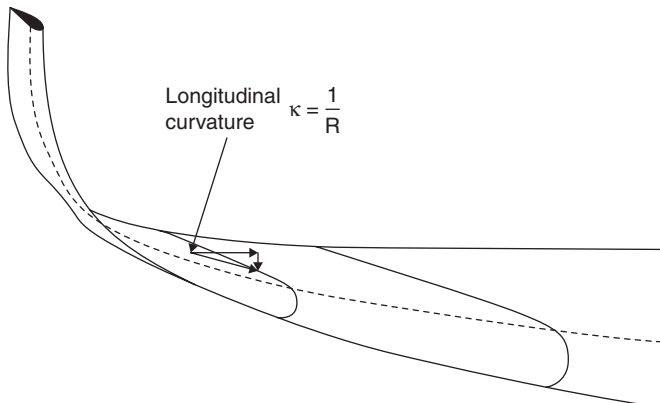


1.7 Illustration of the safety margins for current wind turbine blades.
The parameter 't' representing the thickness of the chain links illustrates the safety margin against ultimate failure. The figures are estimated based on experience in the PhD project¹⁴ and panel tests prepared by colleagues at various institutes at DTU, see References [5], [6], [9] and [10]. The arrows represent the safety of the chain illustrated by unit forces.

the specimens were produced in a laboratory under different conditions. Strains measured in the panel tests, with small defects, were in the range of 20 000–25 000 $\mu\epsilon$, which is a factor of 4–5 times higher than those measured in full-scale tests, see References [11–15]. For panels with large embedded defects the strain levels were in the range of 10–15 000 $\mu\epsilon$, which is a factor of 2–3 times higher than those obtained in the full-scale tests.

Figure 1.7 illustrates schematically that the safety margin (or reliability) of the optimized blade (chain in Fig. 1.7b) can carry double the load of current wind turbine blades (chain in Fig. 1.7a).

In order to use the full potential it is important to take non-linear geometric effects into account. Large deformations of a cross-sectional blade subjected to bending must be considered. The longitudinal compressive and tensile stresses caused by bending result in transverse stresses towards the neutral plane of the blade, see Fig. 1.8. These transverse stresses cause flattening of a hollow cylinder or hollow box. This then results in reduction of the bending stiffness of the section. This is known as the Brazier Effect¹⁶ and these transverse stresses are hereinafter referred to as the 'crushing pressure'. This crushing pressure increases with the square of the longitudinal curvature, so if blades are designed to be more flexible than current practice,

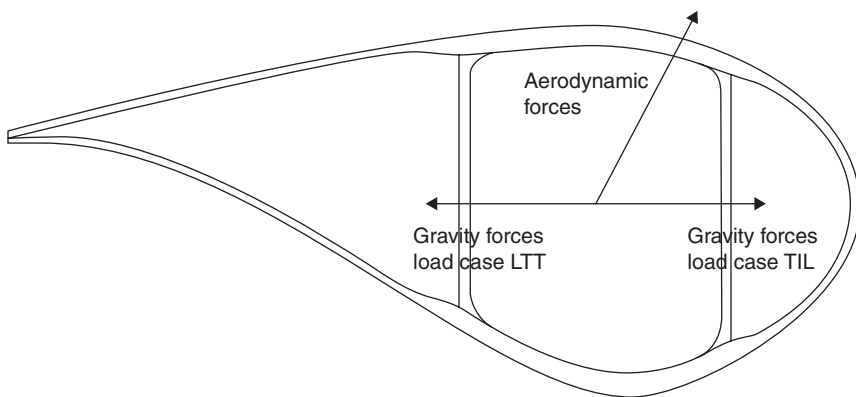


1.8 Crushing pressure on a wind turbine blade section. (Source: Figures from Reference [14].)

this force component becomes more dominant. To take this into account a non-linear Finite Element (FE) model is required, but since other failure mechanisms (e.g. buckling) are dominated by non-linear effects, non-linear FE is strongly recommended. This is explained in detail later in this chapter.

The main purpose of blade testing (which is treated in more detail in Chapter 14) is to verify the blade's structural strength for static and fatigue loading. The main advantage of full-scale testing, compared with numerical FE simulation, is that it gives a 'true' picture of the blade's capacity (fatigue and ultimate strength), including defects caused during production. This, however, only holds for the specific blade selected (typically only one with a characteristic manufacturing deviation – not necessarily identical to those caused during serial production) and the load case tested (and unfortunately only a few simple load cases are tested).

Typically, two flapwise and two edgewise load cases are tested. The combination of these loads is not always considered, but this is recommended for the future, since it is a realistic load scenario, see Fig. 1.9. FE studies, discussed later in this chapter, show why this combination of loads needs more consideration. Failure mechanisms and stress distributions under combined loading differ from those tested under traditional load cases. Also, the way in which loads are applied in the full-scale test should be reconsidered since the fixation from the typical clamps used for load application prevents the blade from distorting in a realistic manner, see Fig. 1.10. New clamps, called anchor plates, have been developed at DTU Wind Energy, see Fig. 1.11. This way of applying loads will allow cross-sectional shear distortion and could be used in future full-scale tests.



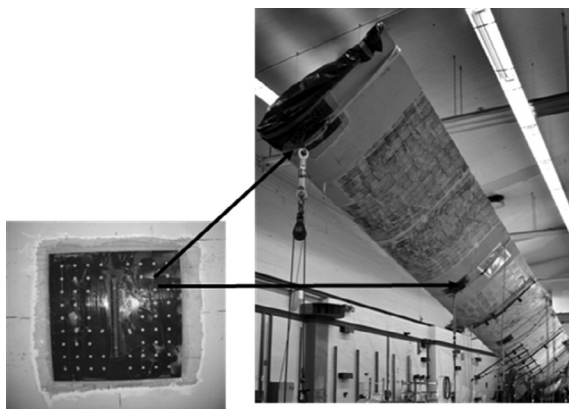
1.9 Aerodynamic and gravity loads applied to the FE model.
Aerodynamic and gravity loads represented by single force vectors. LTT, leading towards trailing edge; TTL: trailing towards leading edge.



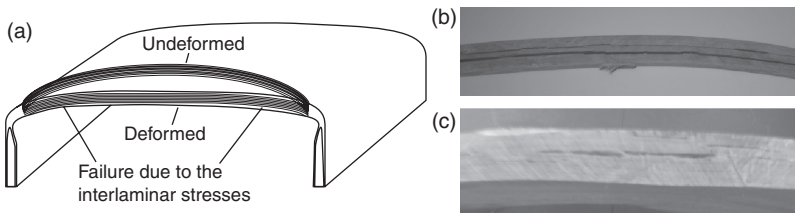
1.10 Different ways to apply load to the blade structure. Loading clamp used at Blaest test centre.

1.2.2 Failure mechanisms

The ultimate failure of a wind turbine blade often starts in the elastic regime and then develops to material failure which can be analysed using fracture mechanics. The failures can be stable or unstable, and in case of unstable failure mechanisms, extra safety margins should be considered.



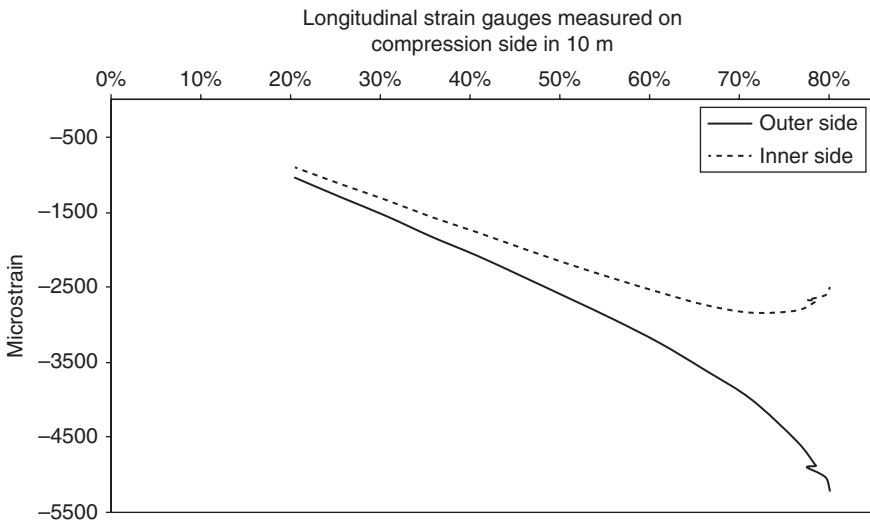
1.11 Anchor plates are used in the full-scale tests at Risø DTU. The load direction is vertical to the floor, simulating a combined load.



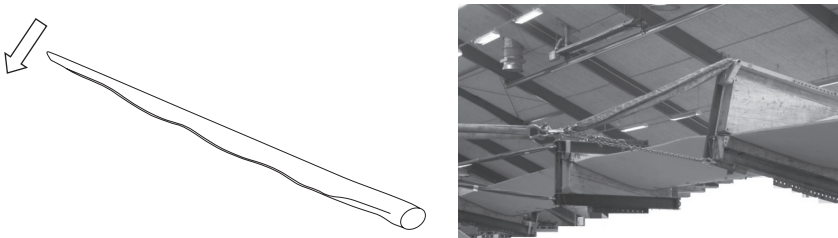
1.12 Interlaminar shear failure of the load-carrying cap laminate:
 (a) sketch of cap deformation and failure between layers, (b) photo of a cap with delamination and (c) photo of a cap with a manufacturing defect.

Failure in the cap(s) caused by Brazier loads

The out-of-plane deformation (flattening) of the caps, caused by the Brazier loads, may cause failure in the caps. The failure can be either a transverse tension failure in the unidirectional layers closest to the neutral axis or an interlaminar shear failure between the layers, see Fig. 1.12. A typical lay-up is not particularly well suited to the reduction of cap deflections since the fibres are mainly placed in the longitudinal direction of the blade. The lack of fibres in the transverse direction causes the cap to be relatively flexible in the lateral direction. When the cap deflects there is a risk of transverse tension failure in the unidirectional laminates. Furthermore, it is common that manufacturing imperfections inside the laminate further reduce the fatigue and ultimate strength of the laminate. More details about this failure mode can be found in References [17] and [18].



1.13 ‘Back to back’ strain measurements from a full-scale test from Reference [14] showing buckling behaviour at 70% load.

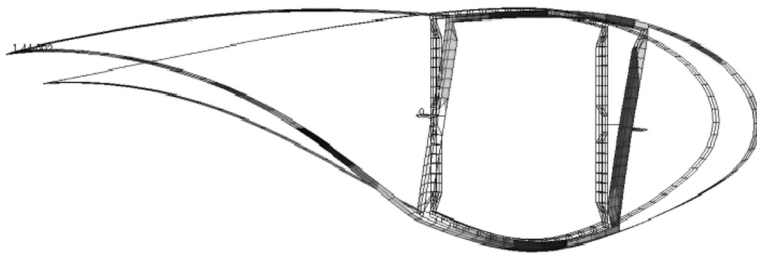


1.14 Buckling of the trailing edge. (Source: Photo from Reference[14].)

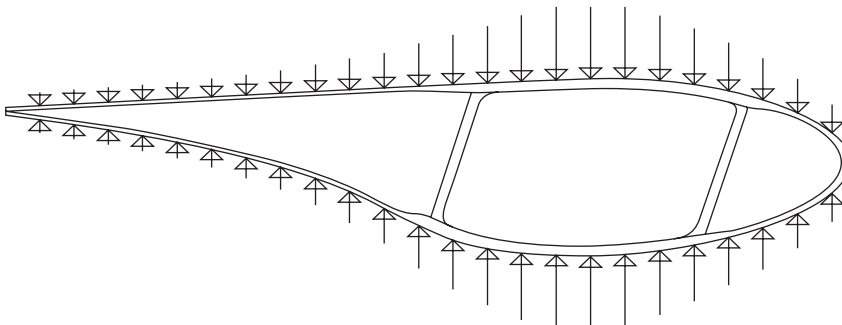
Buckling

Buckling is a structural non-linear instability phenomenon which is important for the design of wind turbine blades, see References [19–21]. The buckling capacity can either be addressed by a non-linear geometric FE analysis or a linear eigenvalue buckling analysis. Accordingly, linear buckling analysis is a guideline for the design load to which a suitable reduction factor is applied. However, this approach is not always on the conservative side, and therefore the non-linear approach is recommended.

During a full-scale test, buckling can be detected by measuring the ‘back to back’ longitudinal strains, see Fig. 1.13. In Fig. 1.13, buckling of the load-carrying cap, loaded in a flapwise direction is shown. The load scale refers to a failure load in a full-scale test of a 34 m box girder, see Reference [14]. In



1.15 Flapwise Numerical simulation shows transverse shear distortion of a cross-section loaded in a combined edge- and flap-wise direction.



1.16 Crushing pressure from the longitudinal bending (Brazier loads) at a distorted profile.

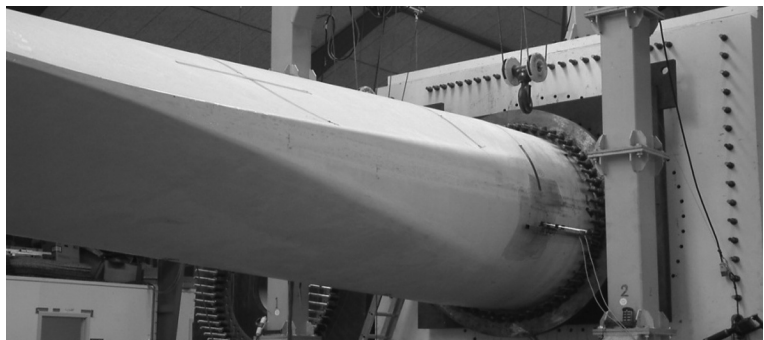
Fig. 1.13, buckling can be observed at approximately 70% of the certification load where the strains starts to become non-linear.

In addition, the trailing edge must be checked for buckling, see Fig. 1.14, especially as the edgewise loads increase when the blades increase in size, owing to the edgewise gravity that is induced.

Cross-sectional shear distortion

An important elastic mechanism, which may lead to failure and should therefore be considered, is cross-sectional shear distortion, see Fig. 1.15 and Reference [22]. This mechanism becomes more critical with size (and weight) of the blade since the large increase in edgewise loads changes the angle of the resultant to a more critical angle e.g. 30° to the flapwise load direction.

Furthermore, if future wind turbine blades become more flexible due to further structural optimization, the longitudinal curvature will increase, raising the crushing pressure, which could be even more critical for a shear distorted blade section, see Fig. 1.16 from Reference [14].



1.17 Photo showing a classical fatigue failure in the transition area from max. chord to the root. The failure is caused by the out-of-plane deformations of the large trailing edge panels, which is sometimes called 'pumping'.

Fatigue problem at the root transition area

In the transition zone from maximum chord to the cylindric and stiff root region problems are often seen, see Fig. 1.17. The reason is that large edge-wise forces have to be 'carried' through large curved panels, which results in 'pumping' out-of-plane deformations and then causes peeling in bond-lines where the trailing edge panels are connected to the cylindrical root.

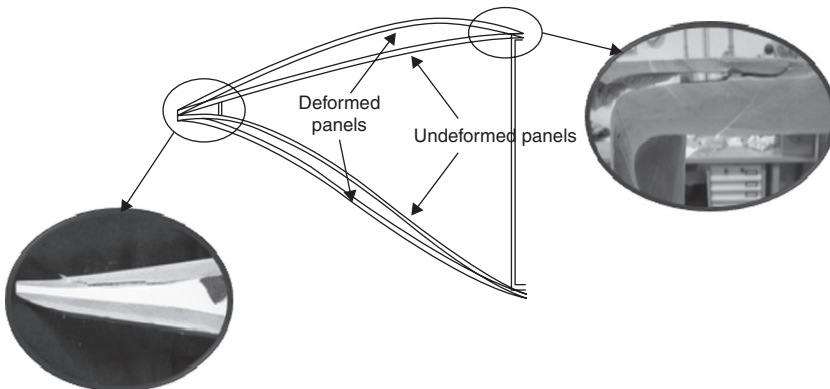
Since the root bending moments are proportional to the length to the power of 4, this fatigue failure will be extremely critical for future wind turbine blades. Special design-specific considerations and modifications need to be taken into account during the upscaling process.

Failure in the adhesive bondlines

Out-of-plane deformations of the trailing edge panels are important since they cause peeling stresses in the bondlines, which may be the main reason for fatigue failure in trailing edge adhesive joints, see Fig. 1.18 and Reference [23]. According to Reference [24] the bondlines have a low strength when exposed to peeling stresses compared with the other loading modes, e.g. the fracture energy is approximately a factor 8–10 higher for mode 2 (shearing) than for mode 1 (peeling).

Buckling-driven delamination

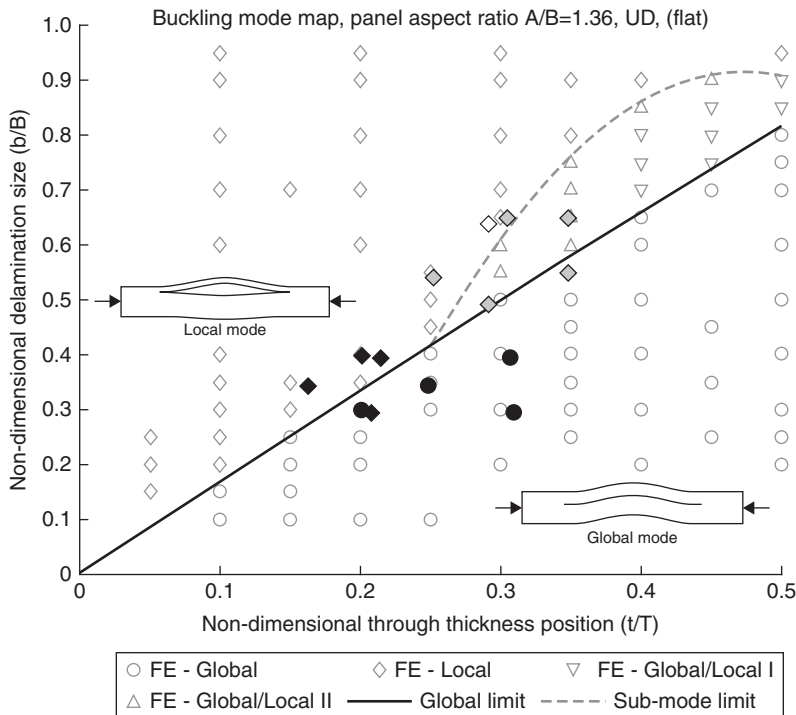
Buckling-driven delamination is a progressive failure mechanism for composite panels in compression. It requires that a delamination (a type of imperfection) is already present in the structure.



1.18 Sketch of the trailing edge shells with out-of-plane deformations. The close ups show failure at the trailing edge as well as debonding of the outer skin on the box girder.

Of all imperfections delamination is probably the most critical, see References [25] and [26]. Delaminations can be defined as areas with poor or no bonding between adjacent layers. They are typical in layered composite structures and can be considered as a type of interlaminar crack that reduces the strength of the structure. Delaminations usually originate from either the manufacturing process or from impact damage during production, transport or service. A panel with a delamination subjected to compressive loading may buckle and fail in two different ways. The panel may buckle in a local buckling mode, where the sub-laminate on mainly one side of the delamination buckles, which typically occurs when the delamination is large in size and positioned close to one of the surfaces. The other buckling mode is global buckling where both the sub-laminate and the remaining panel buckle towards the same side of the panel, which typically occurs when the delamination is small and deep in the laminate. In the local buckling mode the buckling may drive a growth of the delamination leading to panel failure (buckling-driven delamination).

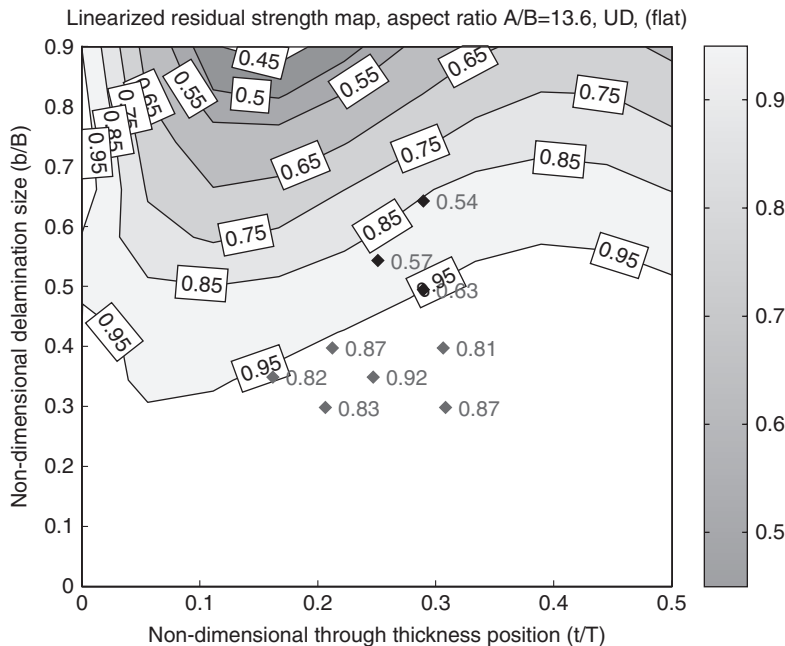
A large numerical parameter study was performed in References [27] and [28] to investigate the buckling response and reduction of strength due to different sizes of delaminations and different locations through the thickness of the panels. Results obtained from numerical analyses were compared with an experimental test campaign performed on flat composite panels with and without delaminations, see References [27] and [29]. In Fig. 1.19 the buckling behaviour is shown for flat UD (uni-directional fiber layup) panels and compared with the experimental results for the panels tested. The numerical



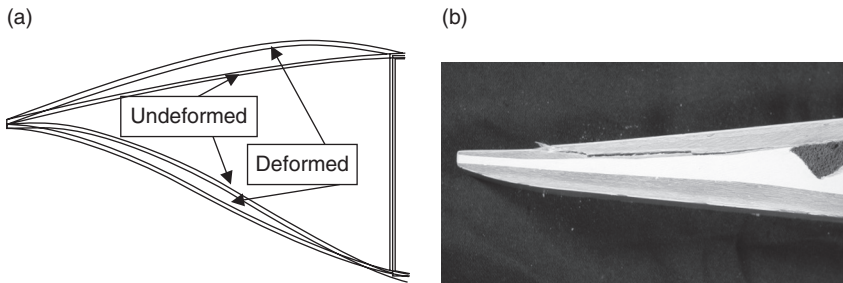
1.19 Buckling mode map for flat UD panels with experimental results included.²⁹ Pre-preg panels are solid black and vacuum infusion panels black outlined. Circles mean global buckling while diamonds mean local buckling. The light gray coloured diamonds mean that the local buckling behaviour is uncertain or the panels sometime show global behaviour.

analyses show quite a sharp borderline between the local and global buckling modes. However, the experimental data show that this borderline is not sharp since there is a band along the borderline where both local and global buckling behaviour is indicated. This band seems to be wider as the delaminations get bigger and deeper in the panels.

The reduced compressive strength caused by delaminations in the flat UD panels is shown in Fig. 1.20 where the results from the solid element models are compared with the experimental data. The tests also show that large and deep delaminations cause local buckling and instant failure while smaller delaminations closer to the surface in some cases are found to give stable delamination growth. When large and deep delaminations open, much elastic energy is released, driving a rapid growth of the delamination. These deep delaminations are therefore found to be more dangerous than delaminations closer to the surface where the released elastic energy may not be high enough to drive a growth of the



1.20 Reduced compressive strength for flat UD solid element panels with experimental data included.²⁹ Pre-preg panels are black diamonds and vacuum infusion panels gray diamonds. The labels indicate the average reduced buckling load factor from the experiments.

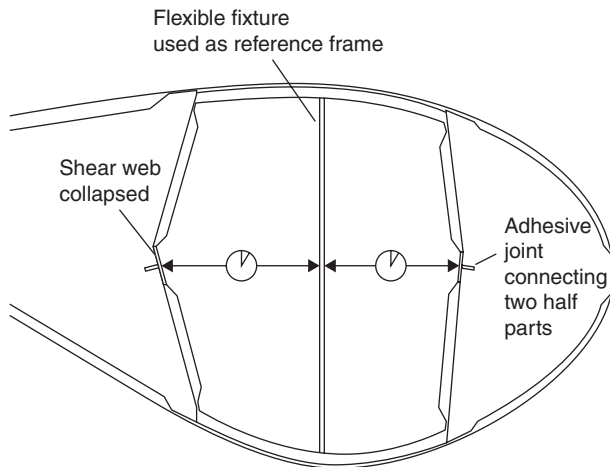


1.21 Trailing edge failure. (a) Sketch of the trailing edge shells with 'out-of-plane' deformations. (b) Fatigue failure in the trailing edge.

delamination. Figure 1.21 depicts one of the most common failure modes, which is peeling failures in adhesive bond lines caused by out-of-plane deformation of the trailing edge panels.

Web failure

Web failures have sometimes been observed to be the main reason for collapse, see Figs 1.22 and 1.23 from Reference [14].



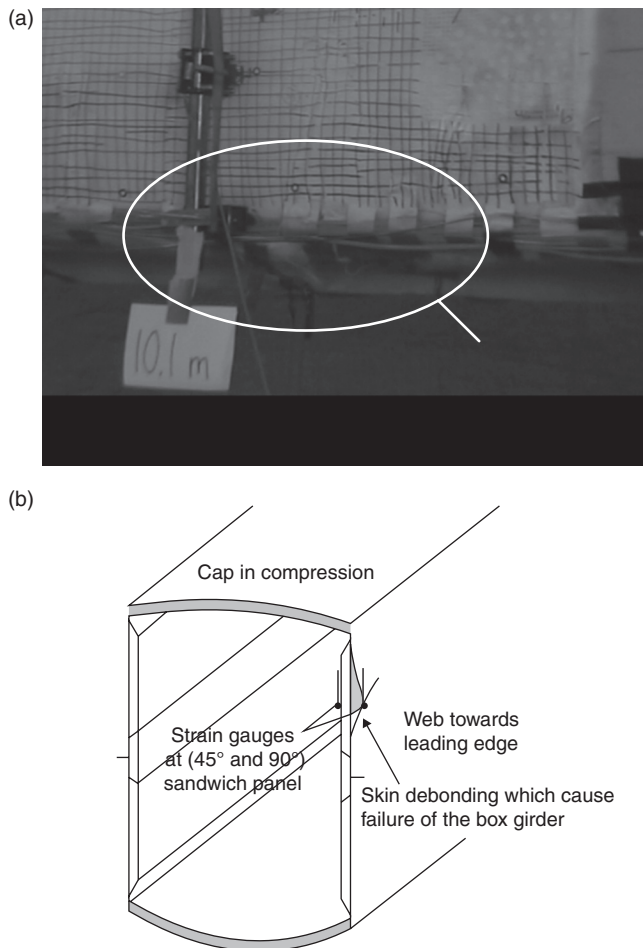
1.22 Sketch of two different web failure modes observed in a full-scale tests from Reference [14]. Shear webs collapse at the first full-scale test, which had no additional reinforcement where the two half-parts were connected.

1.3 Challenges and future trends

Dealing with failure fiber composite, testing is requested due to the limitation in the failure criteria. Ideally, a number of full-scale tests should be performed at an earlier stage, but is obvious not possible since the blade first has to be manufactured and therefore always have to be the last part of the design and certification process. Furthermore full-scale testing is costly, so a set-up with smaller test specimens need to be developed and not only the coupon test which is required today.

1.3.1 Testing approach

Full-scale testing as shown in Fig. 1.24 is mandatory for certification of large wind turbine blades. The basic purpose of these blade tests is to demonstrate that the blade type has the prescribed reliability with reference to specific limit states with a reasonable level of certainty. According to Det Norske Veritas (DNV)³¹ a limit state is defined as a state beyond which the structure no longer satisfies the requirements. The following categories of limit states are of relevance for structures: ultimate limit state (ULS), fatigue limit state (FLS) and serviceability limit state (SLS). The blade should be manufactured according to a certain set of specifications in order to ensure that the test blade is representative of the whole series of blades. In other words, the purpose of the blade tests is to verify that the specified limit states are



1.23 Sketch showing skin debonding failure of the sandwich shear webs, which was observed in a full-scale test of a 34 m load-carrying box girder. (Source: Figures from References [14] and [30].)

not reached and that the type of blade in question possesses the projected strength and lifetime.

Normally, the full-scale tests used for certification are performed on only one or two blades of a given design, so no statistical distribution of production blade strength can be obtained. Therefore, although the tests do give information valid for the blade type, they cannot replace either a rigorous design process or the use of a quality control system for blade production.

Additionally, tests can be used to determine blade properties in order to validate some vital design assumptions used as inputs for the design



1.24 Full-scale testing: A 61.5 m long wind turbine blade subjected to static test (flapwise direction). (*Source:* Courtesy of LM Glasfiber A/S.)

load calculations. Finally, full-scale tests give valuable information to the designers on how the structure behaves in the test situation, and which structural details are important and should be included in the structural models for design; valuable information is obtained if the blade is tested to failure.

According to DNV, see Reference [31], the test programme for a blade type should be composed of at least the following tests in this order:

- Mass, centre of gravity, stiffness distribution and natural frequencies;
- Static tests;
- Fatigue load tests;
- Post fatigue static tests.

All tests should be done in a flapwise direction towards both the downwind (suction) and upwind (pressure) sides and in an edgewise directions towards both the leading and trailing edges. If it is important for the design, a torsion test is also needed in order to determine the torsional stiffness distribution. The tests are undertaken to obtain two separate types of information. One set of information relates to the blade's ability to resist the loads for which the blade has been designed. The second set of information relates to blade properties, strains and deflections arising from the applied loads.

All tests in a given direction and in a given area of a blade should be performed on the same blade part. The flap- and edge-wise sequence of testing may be performed on two separate blades. However, if an area of the blade is critical due to the combination of flap- and edge-wise loading, then the entire test sequence should be performed on one blade.

The current practice of using static and fatigue testing of one or two blades is not a particularly efficient way of assessing the reliability of the design. The question is whether it is better to combine a larger number of subcomponent tests with numerical simulation than to perform a few time-consuming full-scale tests.

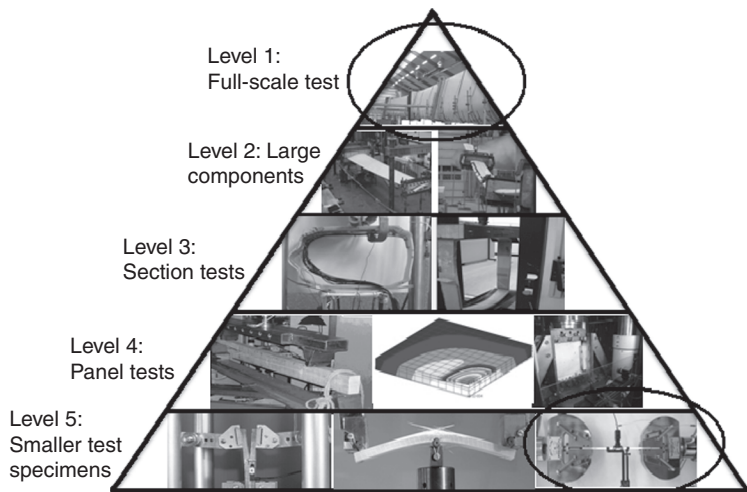
Extensive use of subcomponent tests will probably speed up the design-to-market period and increase the reliability of the design at the same time. The reliability of the design can be increased by combining subcomponent tests with numerical models and tests at other scales, such as full-scale blade tests and smaller subcomponent tests. A framework for reliability analysis with a special focus on the testing of larger subcomponents currently forms part of research projects underway at DTU Wind Energy.

In order to be able to test larger subcomponents as realistically as possible, methods are being developed so that representative boundary conditions can be applied to the subcomponents. The vision is that, with the use of a numerical model of the full blade, the behaviour of the subcomponent boundaries can be calculated and then applied during testing so that the subcomponent behaves as it would do if it were part of the full blade.

In Fig. 1.25 a pyramid representing a multi-scale approach to testing is shown. The pyramid in Fig. 1.25 is a collection of tests which have been performed at DTU during the last decade. Only full-scale tests (Level 1) and the small specimen tests (Level 5, right) are required by the certifying agencies when preparing the documentation forming the basis for type certification, see References [32–35].

Researchers are currently trying to create a consistent system for subcomponent testing (Levels 2–5) so that such testing can be used in the design and certification process. This approach has also been used in recent years by wind turbine manufacturers, see Reference [36]. The approach is expected to be adopted in the certification process in the future. In the ‘DNV-Risø Guideline for design of wind turbines’ published in 2008³² a description of this approach, called ‘Building block approach’, can be found. Load application in Level 1 testing is traditionally quite simplistic as described earlier. Examples of more sophisticated load applications can be found in References [37] and [38].

Subcomponent testing (Levels 2 and 3 in Fig. 1.25) will be of increasing importance in tomorrow’s wind turbines as the size of the blades, the number of blades manufactured and the general costs increase. Full-scale testing is a very costly and time-consuming final verification of the design, and all



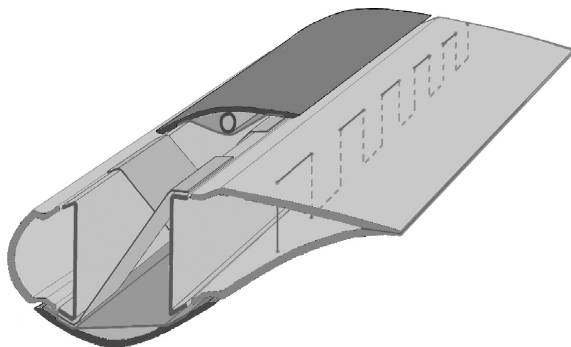
1.25 Multi-scale approach for testing and analysis of wind turbine blades used at Risø DTU. The experiments are performed either at Risø DTU or at DTU Campus.

technical risks associated with it are sought to be minimized through testing at coupon and component level as well as non-linear finite element analysis. Blade testing is treated in more detail in Chapter 14.

Finite element approach

Finite Element Analysis (FEA) is a powerful tool to understand structural behaviour. However, it has certain limitations. FEA usually does not take defects from the manufacturing process into account, and failure criteria of composites are inaccurate particularly under non in-plane loading conditions. Failure criteria may be improved by taking fracture mechanical failure into account, but today it is unrealistic to include all types of interlaminar crack growth in an FEA of an entire wind turbine blade or a larger section, mainly due to computational limitations. Furthermore, the inputs to fracture mechanics models, e.g. the cohesive opening laws (References [24], [39] and [40]) still need further development before they are reliable at all load conditions. Mixed mode opening problems, in particular, are not fully understood, see References [1], [24], [40] and [42].

As already mentioned, more systematized experimental testing should be used in connection with large numerical non-linear FE models, which do not necessarily take all potential kinds of failure into account, but which do take more combinations into consideration. The increasing complexity of FE models, including the non-linearity and the complex load cases, will



1.26 New design philosophy using internal members. (*Source:* Drawing from Reference [42].)

enable designers to predict new elastic failure mechanisms, which at present do not receive much attention.

Novel structural design approach may be the future

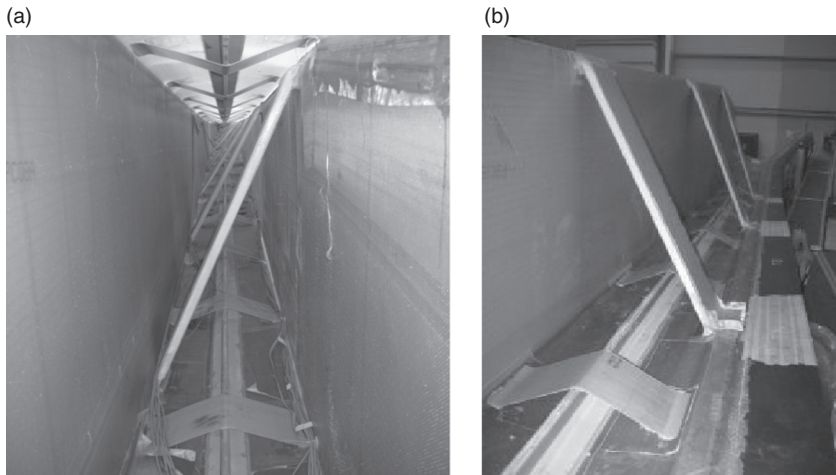
New findings in failure modes lead to the consideration of new design philosophies, see, e.g. Fig. 1.26 from Reference [42].

One failure mode, not covered by commercial certification tests, is cross-sectional shear distortion. Another failure mechanism is the non-linear out-of-plane deformation of the load-carrying cap laminate which could be the reason for the failure of some of today's wind turbine blades. These two potential failure mechanisms are taken into account in the design of a new innovative 44 m load-carrying box girder at DTU Wind Energy. Further details can be found in Reference [43] and in the following section.

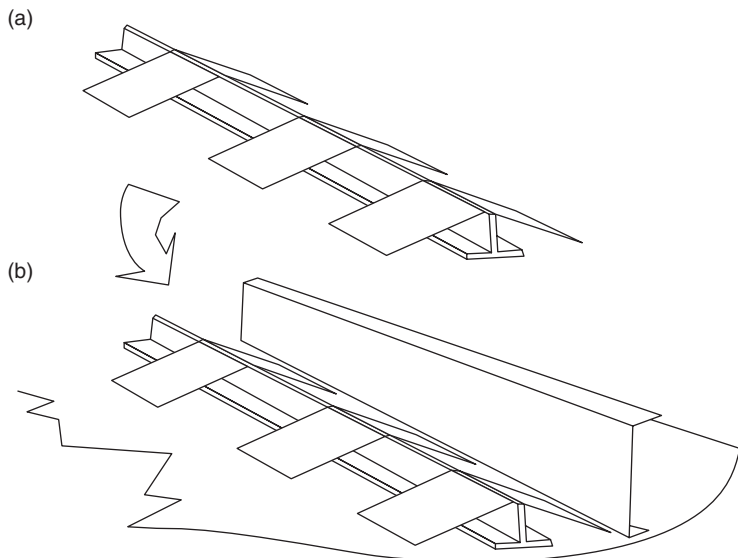
The box girder includes three patented structural solutions: two cap reinforcements and one diagonal reinforcement, see References [44–46]. By means of these inventions the thickness of the load-carrying laminates was decreased by 40% and the box was prevented from distorting in the transverse direction.

1.3.2 Manufacturing

The cap reinforcements and the diagonal stiffener were introduced in the concept blade designed and manufactured as part of a research-demonstration project performed at DTU Wind Energy. The box girder was manufactured by SSP Technology A/S who have developed a patented spar solution which uses resin infusion in female moulds. The female mould technique employed has the advantage of a defined outer geometry, which is beneficial



1.27 The assembled box girder with cap reinforcement in both upper and lower parts and cross reinforcement between the corners. (*Source:* Photo from a load-carrying box girder designed by Risø DTU and manufactured by SSP Technology A/S. Photo from Reference [42].)



1.28 Box girder manufacturing using technology from SSP Technology A/S. Sketch show a technique which is expected to be used for serial production. The idea is to 'collect' the subcomponents (longitudinal and transverse stiffener) at a table in order to reduce mould time for the box girder.

when the box girder is going to be assembled with the aerodynamic shells. A female mould also makes it easier to incorporate the reinforcements into the box girder because of better access to the inside of the girder, see Fig. 1.27.

The reinforcements to the blade were implemented using pre-manufactured parts which were ready to install in the box girder as soon as the curing was completed and before the box girder was assembled. Some of the parts were manufactured using the pultrusion process, which is very efficient and delivers specimens of high quality. The project demonstrated only one technique for implementing the reinforcements, but the experience gained has already resulted in new suggestions to reduce production time and costs, see Fig. 1.28. Also, the decrease in the material thickness obtained by the new design is beneficial for the manufacturing process because it is less time-consuming and prevents defects in the finished laminate. Moreover, the curing process is easier to control since thin laminates reach lower temperatures during the exotherm.

The primary conclusion drawn from this study confirms significant improvement in the structural response of the blade obtained by utilization of the structural solutions that have been invented.

1.4 References

1. Sørensen, B.F. *Improved design of large wind turbine blade of fibre composites based on studies of scale effects (Phase 1) – Summary Report*. Risø-R-1390(EN). (2004).
2. Rijswijk, K. v. *Thermoplastic Composite Wind Turbine Blades*. PhD Thesis, Delft University of Technology, Netherlands. (April 2007).
3. Rijswijk, K. v., Joncas, S., Malek, O.J.A., Bersee, H.E.N., Beukers, A. *Vacuum infused thermoplastic composites for wind turbines blades*. 27th Risø International Symposium on Material Science: Polymer Composite Materials for Wind Turbine Power: Roskilde, Denmark. (May 2006).
4. Joncas, S., Jan de Ruiter, M., van Keulen, F. Delf. *Preliminary Design of Large Wind Turbine Blades Using Layout Optimization Techniques*. University of Technology, Delft, the Netherlands.
5. Berggreen, C., Tsouvalis, N., Hayman, B., Branner, K. ‘Buckling Strength of Thick Composite Panels in Wind Turbine Blades – Part I: Effect of Geometrical Imperfections’ 4th International conference on composites testing and model identification, 20–22 October 2008, Dayton, Ohio, USA.
6. Branner, K., Berring, P., Berggreen, C. ‘Buckling Strength of Thick Composite Panels in Wind Turbine Blades – Part II: Effect of Delamination’, 4th International Conference on Composites Testing and Model Identification, 20–22 October 2008, Dayton, Ohio, USA.
7. Branner, K., Jensen, F. M., Berring, P., Puri, A., Morris, A., Dear, J. P. ‘Effect of sandwich core properties on ultimate strength of a wind turbine blade’, in: Proc. of 8th International Conference on Sandwich Structures, 6–8 May 2008, University of Porto, Portugal.

8. Geiger, T. *Buck Blade*. Report about buckling tests. (1998).
9. Jensen, C. *Defects in FRP Panels and their Influence on Compressive Strength*. Master's Thesis. Technical University of Denmark and Risø National Laboratory. (February 2006).
10. Moslemian, R., Berggreen, C., Branner, K., Carlsson, L.A. *On the Effect of Curvature in Debonded Sandwich Panels Subjected to Compressive Loading*, in: Proc. of 8th International Conference on Sandwich Structures, 6–8 May 2008, University of Porto, Portugal.
11. Jensen, F. M., Branner, K., Nielsen, P. H., Berring, P., Antvorskov, T. S., Lund, B., Jensen, C., Reffs, J. H., Nielsen, R. F., Jensen, P. H., McGugan, M., Borum, K., Hansen, R. S., Skamris, C., Sørensen, F., Nielsen, R. S., Laursen, J. H., Klein, M., Morris, A., Gwayne, A., Stang, H., Wedel-Heinen, J., Dear, J. P., Puri, A., Fergusson, A. *Full-scale Test of a SSP34m box girder 1 – Data Report*. Risø-R-1588(EN), Risø National Laboratory, Denmark, 2008.
12. Jensen, F.M., Branner, K., Nielsen., P. H, Berring, P., Antvorskov, T. S., Nielsen, M., Lindahl, M., Reffs, J.H., Jensen, P.H, McGugan, M., Skamris, C., Sørensen, F., Nielsen, R.S., Laursen, J.H., Klein, M., Stang, H., Morris, A., Dear, J.P., Puri, A., Fergusson, A., Wedel-Heinen J. *Full-scale Test of a SSP34m box girder 2 – Data Report*. Risø-R-1622(EN), Risø National Laboratory, Denmark, 2008.
13. Jensen, F.M., Falzon, B.G., Ankersen, J., Stang, H. 'Structural testing and numerical simulation of a 34 m composite wind turbine blade'. *Composite Structures* **76**, pp. 52–61 (August 2005).
14. Jensen. F. M. *Ultimate strength of a large wind turbine blade*, PhD Thesis. ISBN 978-87-550-3634-5. Risø National Laboratory, Technical University of Denmark. May 2008.
15. Thomsen C. L., Jørgensen E. R., Borum K. K., McGugan M., Debel C. P., Sørensen B., Jensen F. M. *V52 Statisk Styrke*. Risø-I-Report. (April 2003).
16. Brazier, L. G. On the flexure of thin cylindrical shells & other thin sections. *Proceedings of the Royal Society London, A* **116**, pp. 104–114, 1927.
17. Jensen F.M., Puri A.S., Dear J.P., Branner K., Morris A., *Investigating the impact of non-linear geometrical effects on wind turbine blades Part 1: Current design status and future challenges in design optimization*, Wind Energy, Volume **14** Issue 2, March 2011, pp. 239–254, DOI: 10.1002/we.415.
18. Puri, A. *Researching methods for monitoring strain in wind turbine blades as part of an operation and maintenance programme*, PhD Thesis Imperial College London, Department of Mechanical Engineering, June 2010.
19. Kühlmeier, L. *Buckling of wind turbine rotor blades. Analysis, design and experimental validation*. PhD Thesis. Special Report No. 58 (November 2007).
20. Lindenburg, C. *Buck Blade. Buckling Load Design Methods for Rotor Blades*. (May 1999).
21. Lindenburg, C., Geiger, T., Joosse, P.A., Weisser, B. *Buck Blade Finite Element Buckling Analysis of Wind Turbine Blades*.
22. Roczek-Sieradzan A., Nielsen M., Branner K., Jensen F.M., Bitsche R.D. *Wind turbine blade testing under combined loading*, in: Proc. of 32nd Risø International Symposium on Materials Science, 5–9 September 2011, Roskilde, Denmark.
23. Jensen, F.M., Sørensen, J. D., Nielsen, P.H., Berring, P., Flores, S. *Failures in Trailing Edge Bondlines of Wind Turbine Blades*. (Risø DTU Symposium September 2011).

24. Sørensen, B. F., Jacobsen, T. K. Delamination of fibre composites: Determination of mixed mode cohesive laws. *Journal of the Mechanics and Physics of Solids*.
25. Abrate, S. Impact on laminated composite materials. *Applied Mechanical Review* **44**, pp. 155–190, 1991.
26. Pavier, M. J., Clarke, M. P. Experimental techniques for the investigation of the effects of impact damage on carbon fibre composites. *Composites Science and Technology* **55**, pp. 157–169, 1995.
27. Branner, K., Berring, P., Gaiotti, M., Rizzo, C. M. *Comparison of Two Finite Element Methods with Experiments of Delaminated Composite Panels*, in: Proc. of 18th International Conference of Composite Materials (ICCM), 21–26 August 2011, Jeju Island, Korea.
28. Gaiotti, M., Rizzo, C. M., Branner, K., Berring, P. *Finite Elements Modeling of Delaminations in Composite Laminates*, in: Proc. of 3rd International Conference on Marine Structures (MARSTRUCT), 28–30 March 2011, Hamburg, Germany.
29. Branner, K., Berring, P. *Compressive Strength of Thick Composite Panels*, in: Proc. of 32nd Risø International Symposium on Materials Science, 5–9 September 2011, Roskilde, Denmark.
30. Jensen F. M., Weaver P. M., Cecchini L. S., Stang H., Nielsen R.F. 'The Braziers effect in wind turbine blades and its influence on design.' *Wind Energy Journal* 2011. DOI: 10.1002/we.473
31. Det Norske Veritas, *Design and Manufacture of Wind Turbine Blades, Offshore and Onshore Wind Turbines*, Offshore Standard DNV-OS-J102m, 2006.
32. DNV/Risø publication, *Guidelines for Design of Wind Turbines*, 3rd edition. Denmark. (2008).
33. International Electrotechnical Commission. *IEC 61400-1: Wind Turbine Generator Systems – Part 1: Safety Requirements*. 2nd edition, International standard 1400-1, (1999).
34. International Electrotechnical Commission. *IEC 61400-23 TS. Wind Turbine Generator Systems – Part 23. Full-scale Structural Testing of Rotor Blades for WTGSs*. 1st edition, International standard.
35. Tadich J.K., Wedel-Heinen. Full-scale testing of blades. Now, and for the future. *J. EWEC*. (May 2007).
36. Korsgaard, J., Jacobsen, T. K. *Integrated Testing in Reliable Design of Large Wind Turbine Blades*. LM Glassfiber A/S, Denmark.
37. Berring, P., Branner, K., Berggreen, C., Knudsen, H. W. Torsional Performance of Wind Turbine Blades – Part I: Experimental Investigation', in: Proc. of 16th International Conference of Composite Materials, 8–13 July 2007, Kyoto, Japan.
38. Branner, K., Berring, P., Berggreen, C. and Knudsen, H. W. Torsional Performance of Wind Turbine Blades – Part II: Numerical Verification, in: Proc. of 16th International Conference of Composite Materials, 8–13 July 2007, Kyoto, Japan.
39. Höglberg, J. L., Sørensen, B. F., Stigh, U. *Constitutive Behaviour of Mixed Mode Loaded Adhesive Layer*. International Journal of Solids and Structures. (2007).
40. Østergaard, Rasmus C. *Interface Fracture in Composite Materials and Structures*. PhD Thesis, Technical University of Denmark, Department of Mechanical Engineering. DCAMM Special report No. S102. (November 2007).

41. Sørensen, B.F., Branner, K., Stang, H., Jensen, H.M., Lund, E., Jacobsen, T.K., Halling, K.M. *Improved design of large wind turbine blades of fibre composites (Phase2) – Summary Report*, Risø-R-1526(EN), Risø National Laboratory, Denmark, 2005.
42. Riva, I., Tesauro, A. *Feasibility Study of a New Structural Blade*, Master Thesis. Risø National Laboratory, Technical University of Denmark, (August 2010).
43. Jensen, F.M., Nielsen, P.H., Roczek-Sieradzan, A., Sieradzan, T., Banner, K., Bitsche, R.D. *On Innovative Concepts of Wind Turbine Blade Design*, in: Proc. of European Wind Energy Conference and Exhibition (EWEA), 14–17 March 2011, Brussels, Belgium.
44. Jensen, F. M. *Reinforced blade for wind turbine (shear cross – patent C)*. PCT WO 2008/089765 (January 2007). www.bladena.com
45. Jensen, F. M. *Reinforced aerodynamic profile – Cap reinforcement*. PCT WO 2008/071195. (December 2006). www.bladena.com
46. Jensen, F. M. *Reinforced blade for wind turbine cross*. PCT/ EP2010/068521. (June 2008). www.bladena.com
47. Brøndsted, P., Lilholt, H., Lystrup, Aa. *Composite materials for wind power turbine blades*. Materials Research Department, Risø National Laboratory (4 April 2005).
48. BTM Consultaps ApS. *International Wind Energy Development – World Market Update 2010*. Ringkøbing, Denmark. (2010).
49. DNV-OS-J102, Design and manufacture of wind turbine blades, offshore and onshore wind turbines. October 2006.
50. Jensen, F. M., Morris, A. *Full-scale Testing and Finite Element Simulation of a 34 Metre Long Wind Turbine Blade*. NAFEMS World Congress – Vancouver. (April 2007).
51. Puri A., Dear J.P., Morris A., Jensen M. F. *Analysis of Wind Turbine Material using Digital Image Correlation*. EWEC Conference. (2008).
52. Tadich J.K., Wedel-Heinen, J., Petersen, P. *New guidance for the development of wind turbine blades*. Det Norske Veritas – Global Wind Energy conference, Copenhagen, Denmark. (2005).

Loads on wind turbine blades

H. SÖKER, Deutsches Windenergie-Institut GmbH, Germany

DOI: 10.1533/9780857097286.1.29

Abstract: This chapter deals with loads on wind turbine blades. It describes the load generating process, wind fields, and the concepts of stresses and strains. Aerodynamic loads, loads introduced by inertia, gravitation and gyroscopic effects, and actuation loads are discussed. The loading effects on the rotor blades and how they are interconnected with the dynamics of the turbine structure are highlighted. There is a discussion on how stochastic loads can be analysed and an outline of cycle counting methodology. The method of design verification testing is briefly described.

Key words: wind turbine loads, wind field, global loads, local strains and stresses, deflection and deformation, aerodynamic loads, inertia loads, gravitational loads, gyroscopic loads, actuation loads, fatigue loads, extreme loads, design verification testing, calibration of global bending moment measurements, aeroelastic tailoring, vortex generators, load mitigation, individual pitch control.

2.1 Introduction

Wind turbines are among those industrial structures that undergo the most intense loading throughout their service life. Exposed to nature's forces and depending on their site of deployment they not only have to withstand winds of various characteristics but also extreme heat or cold, solar radiation, erosion or even earthquakes. They have to operate or at least survive in any external conditions that may come upon them. To enable wind turbine structures to achieve their expected service lifespan, each component has to be designed adequately, manufactured with suitable quality, installed accurately and tuned to harmonize perfectly with the rest of the structure during operation. The existing state-of-the-art concerning the design requirements of wind turbines and their key components is comprehensively captured in a number of guidelines, such as the IEC 61400-Series.¹

The rotor blades of a wind turbine are key structural components that are decisive for the efficient conversion of the kinetic energy of the inflowing wind into mechanical torque that is finally converted into electrical energy in the generator. But as nothing comes for free, the aerodynamic process taking place at the rotor blades is the origin of the mechanical loads that the

wind turbine as a structure has to digest and withstand. While part of the aerodynamic energy is converted into the desired generator driving torque, the larger part is converted into the rotor thrust, the source of various loads throughout the turbine structure.

The following sections will illustrate the loading effects in the rotor blades and how they are interconnected with the dynamics of the turbine structure.

2.2 Types of load

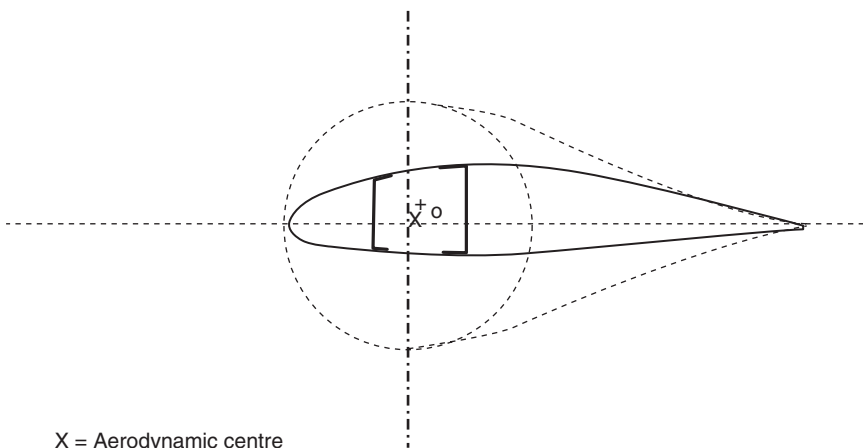
Typically loads are understood as global forces and moments acting on a rotor blade or wind turbine. However, such global forces and moments load the structure, creating stresses, strains, deflections and even deformations. All of these phenomena are referred to as loads.

2.2.1 Global loads

When discussing blade loads, most of the time the so-called global loads are of primary interest. The global loads are the loads that are transferred from the blade into the hub/main shaft assembly, being the next main component along the load path from the rotor to the foundation of a wind turbine.

To describe the global loads acting on a rotor blade during operation it is convenient to imagine the blade to consist of a discrete number of elements with specific cross sections, specific structural properties and specific masses lined up on the longitudinal axis of the blade.² Each of these elements' cross sections along the blade span is an aerodynamic aerofoil creating aerodynamic lift and drag forces that act in the aerodynamic centre of the aerofoil. The lift and drag forces are oriented perpendicular to and along the direction of the inflow, respectively. At the same time each blade element has a discrete mass that, by being moved in the gravitation field of the earth and by being accelerated or decelerated in and out of the rotor plane, creates inertia forces and moments. The structural properties of the blade element, such as location of the centre of gravity, location of the centre of shear and location of the aerodynamic centre with respect to the pitch axis of the blade, can cause a particular blade element to develop a torsion moment in operation. This twist moment will appear when at least one of the given centres does not coincide with the intersection point of the blade pitch axis with the cross-sectional plane of the blade element (Fig. 2.1).

Each blade element along the blade span contributes fractional loads at its specific radial position: in-plane driving force, out-of-plane thrust force and a torsion moment. Hence, these sectional loads can be modelled by line forces or moment distributions along the blade axis. Integration of these fractional loads along the blade span results in the global bending and torsion loads in the blade root section.



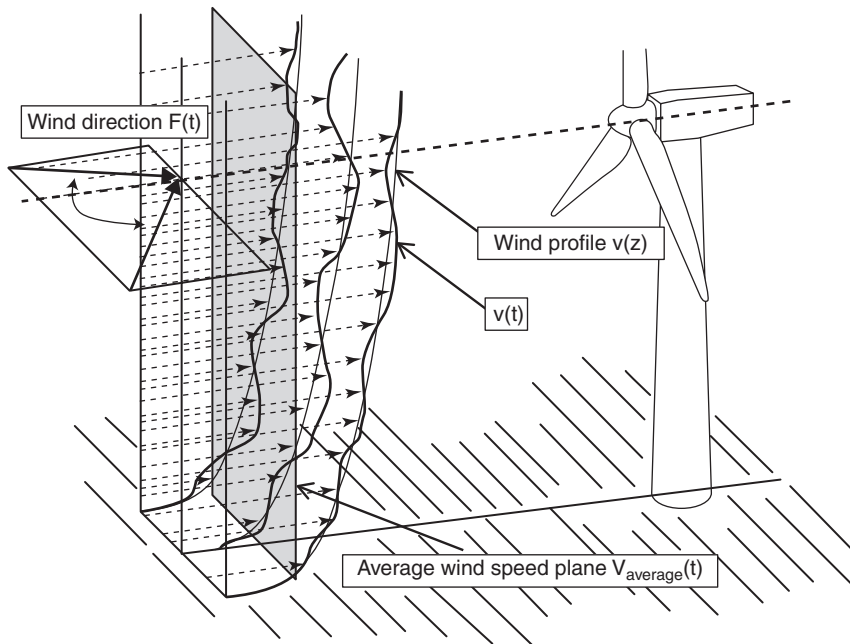
X = Aerodynamic centre
O = Centre of gravity
+ = Centre of shear

2.1 Centre of gravity, centre of shear, aerodynamic centre, pitch axis of the blade. (*Source:* DEWI.)

Typically the rotor thrust force does not apply in the centre of the rotor but at some distance above due to the wind speed being typically larger at greater height above ground. This generates a tilt moment on the rotor plane about the horizontal axis perpendicular to the wind turbine's main shaft longitudinal axis. As the rotor represents a gyroscope, any tilt moment will be accompanied by a corresponding yaw moment. The driving torque, the thrust force, and the gyroscopic tilt and yaw moments are transferred to the main shaft. Following the load path, the torque is transmitted through the torque arms of the gearbox and the generator mounts to the machine frame. The rotor bearings must absorb the thrust force and rotor tilt and yaw moments. The nacelle bearing transmits the rotor moments and the thrust force from the machine frame into the tower. And at the bottom of the tower all loads are introduced into the foundation as overturning, lateral and torsion moments.

To have a good understanding of the nature of the loading of rotor blades, it is helpful to look at the wind field that the rotor of a wind turbine will see during operation or even at idling or standstill condition. The wind field can be imagined as a plane characterized by differing wind speed vectors approaching the rotor (Fig. 2.2).

Depending on meteorology and site (topography), this wind field will have specific characteristics, such as increasing wind speed when crossing the rotor plane from lower blade tip level to upper blade tip level (wind shear), slow and coherent variability of wind speed (trended wind speed), rather sudden coherent change in wind speed (gust) and quick variation of wind speed vectors (turbulence). The complete plane can even have an inclination with respect to the rotor plane in a horizontal or vertical direction,



2.2 Upscaling history for the size of wind turbines.¹

resulting in oblique inflow conditions. Such a situation may be caused by slow or sudden changes in wind direction (trended or gust) or by wind flow over inclined terrain. It becomes immediately clear that external operating conditions are extremely variable and hence will create extreme, stationary and variable global loads at times.

2.2.2 Local strains and stresses

Typically, loads are understood as external forces and moments acting on a rotor blade as explained in the previous section. However, along the load path through the blade structure the material will be stressed as cross-sections with given properties must carry that load. The measurable reaction of the load-carrying component will be that the surfaces will show strains proportional to the force being transmitted. Obviously, the magnitude and orientation of such internal loads must be of interest to the designer as the blade's structure has to be designed in a way that controls these loads and keeps them below the limits that are permissible for the material used in a specific component. In this regard, the foremost advantage of the fibre reinforced plastics (FRP) used in modern

rotor blade design is that the orientation of the load-carrying fibres can be aligned with the direction of forces that are to be transmitted. This way two of the main requirements in blade design can be achieved: maximum stiffness and minimum weight.

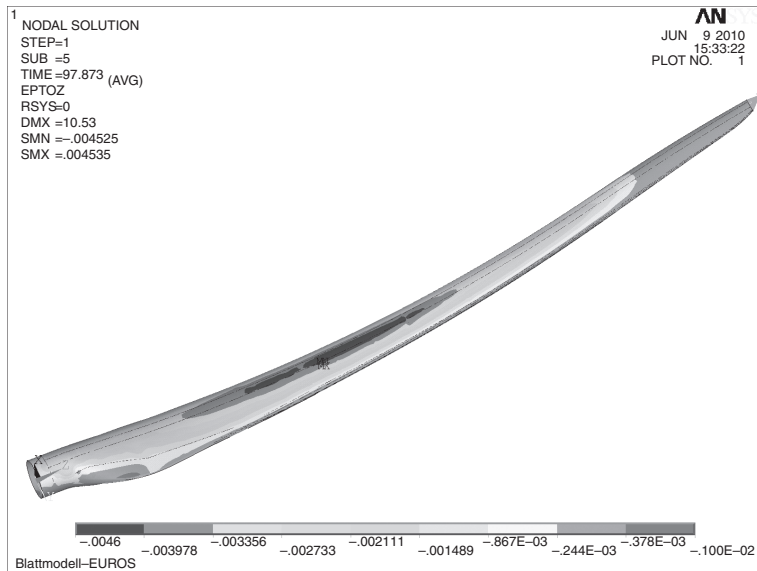
Taking this concept one step further, specific blade components are employed to take care of specific loads; for example, the blade spar acts like a cantilevered beam, taking up the main lateral bending loads. The blade spar may be realized in many different ways; however there are always the upper/lower girders (spar caps) to take the normal strain in blade longitudinal direction and the spar webs to take up the shear loads. Spar webs keep the suction-side and pressure-side surfaces apart during deflection. The shell is needed to create the actual aerodynamic shape. The upper and lower blade halves must be glued together and hence there are a number of bonding joints.

Depending on the specific load and the component, and assuming elastic deflection and limited deformation, only normal stresses and shear stresses are of interest in a proper design.

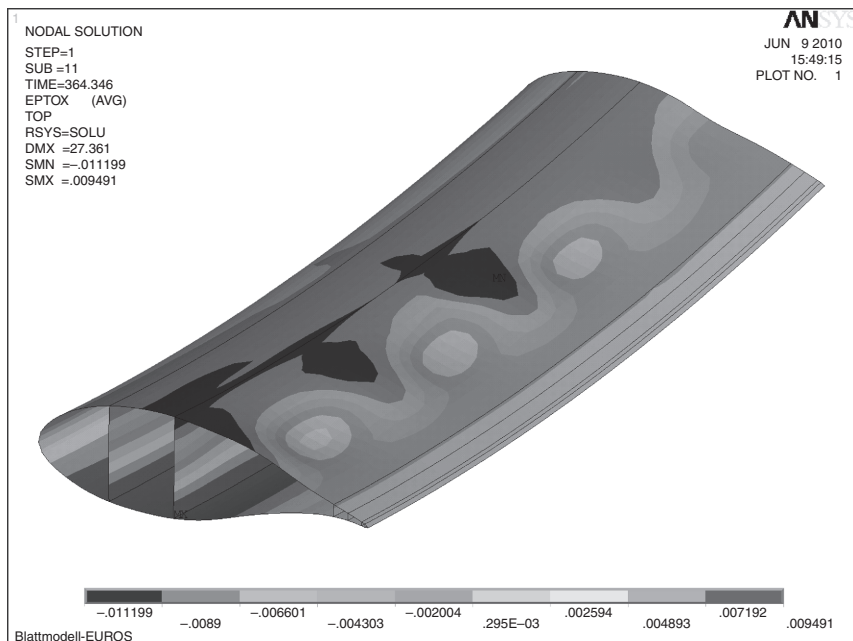
2.2.3 Deflection and deformation

The external loads acting on the rotor blades described above do not only create internal loads in terms of stresses and strains. They can also cause the blade's shape to change noticeably: at specific sections or areas the whole blade and/or the surface of the blade sometimes deflect, even changing cross-section shape. An example of such changes is the very obvious deflection of the blade tip that can be observed on many operating wind turbines. In fact, maximum blade tip deflection is an important design parameter as the blade must be kept at a safe distance from the tower. Another problem with large blade deflection may arise as blade elements are translated out of the rotor plane or in lead-lag direction. In this situation the aerodynamic forces apply at a point that is not in the rotor plane or off the radial direction and hence they create additional moments.

However, less obvious phenomena, such as buckling of panels in the blade's surface, can also be detected. Such deformations are typically observed in the blade's shell panels, beside the spar towards both trailing edge and leading edge. The blade shell is not designed to carry the main loads, but its primary task is to establish the aerodynamic aerofoil shape and to convert aerodynamic pressure to a force that is transmitted to the main load-carrying spar. To allow predictable and effective performance of the blade it is of paramount importance that the aerofoil shape is maintained in any loading situation. That is why sandwich structures are used to provide sufficient stiffness at low weight.



2.3 Deflection of blade under extreme load.⁵



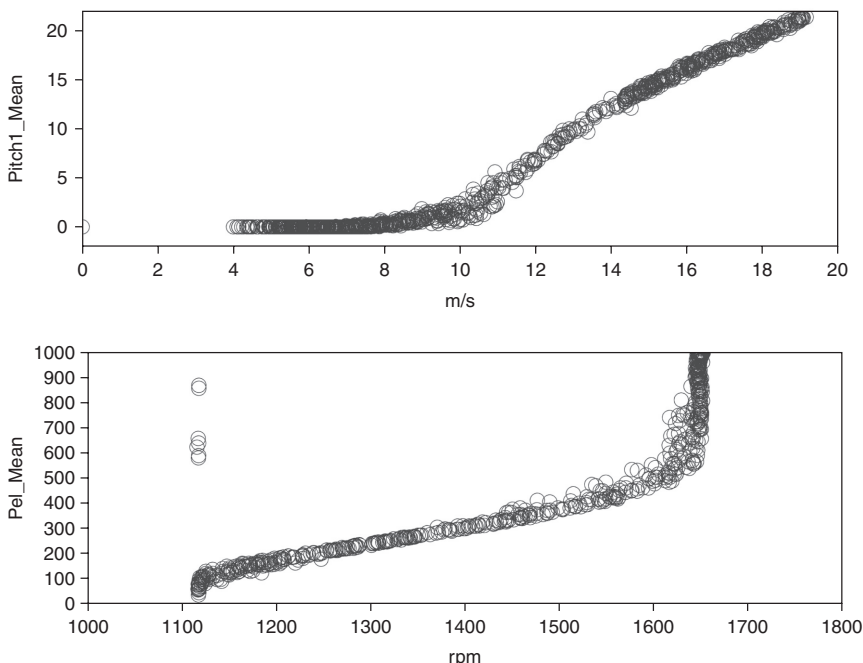
2.4 Buckling of blade surface under extreme load.⁵

Buckling of the blade's surface under extreme flapwise loading is particularly dangerous as the shape of the buckled cross-section will change dramatically, accompanied by an equally dramatic loss in the cross-section's resistance against bending. Extreme buckling may even cause complete failure of the blade (Figs 2.3 and 2.4).

2.3 Generation of loads

As explained in Section 2.2, aerofoil shape and blade mass create aerodynamic and inertia loads on the rotor blade. These are balanced by corresponding structural loads governed by the blades' structural properties, such as structural stiffness and damping. The dynamic characteristics of the complete structure feed back into the blades, which are a part of the flexible and deforming structure of the wind turbine as a whole.

More than that, the wind turbine operation is a controlled process using a specific concept and corresponding actuators to control rotor speed and power output (Fig. 2.5). In modern large scale wind turbines it is standard to control rotor speed in partial load operation through torque actuation



2.5 Wind turbine control: pitch vs wind speed and power output vs generator speed trajectories. Pel = electrical Power.

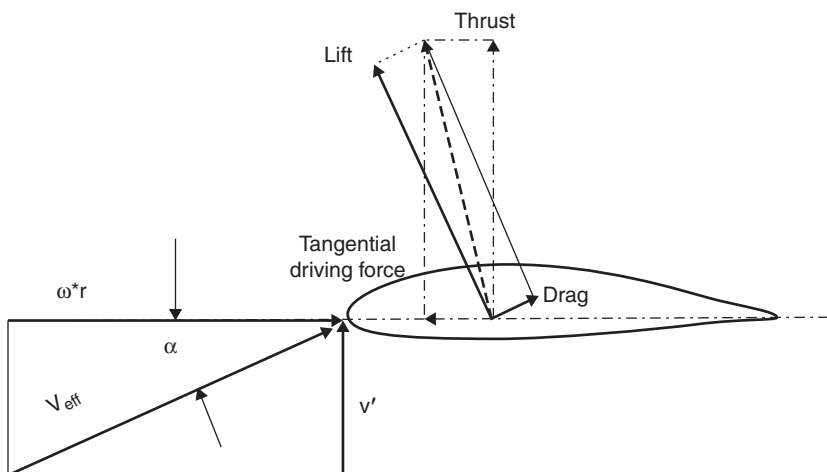
in the generator and to control power output in full load operation by blade pitch angle adjustment. Both controlling speed and controlling pitch angle adjust the inflow angle to the blade elements, causing more or less kinetic wind energy to be converted into driving torque and thrust.

Aerodynamic characteristics of the aerofoils in use, mechanical properties of the blade structure and turbine controller characteristics make modelling of a rotor blade in operation a complex task. While the discussion on modelling of wind turbines must be left to dedicated literature, the following sections will outline the most important mechanisms for load generation on rotor blades.

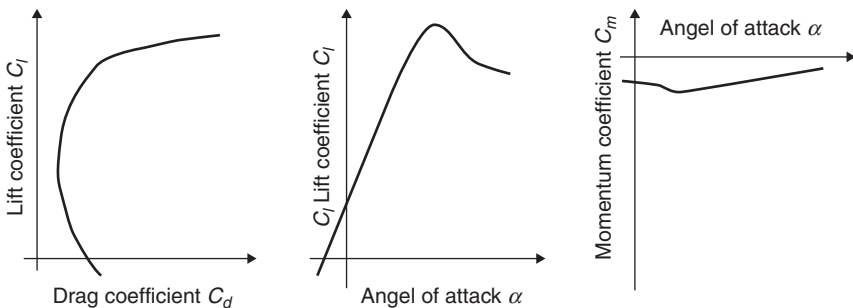
2.3.1 Aerodynamic loads in operation and at idling or standstill

The aerodynamic conversion process happening at the blade elements creates substantial aerodynamic lift and drag forces that are transformed into driving force (in-plane) and thrust force (out-of-plane) (Fig. 2.6). In modern aerofoils the lift force is approximately 10–100 times larger than the drag force and hence it is the overwhelming source of thrust and driving force.

While wind speed and, for most modern large scale wind turbines, rotor speed vary, effective inflow speed and inflow angle (angle of attack) to the rotor blade element and associated aerodynamic forces change in magnitude and orientation. The changes are due to the variation of inflow speed



2.6 Blade cross-section and aerodynamic forces.



2.7 Lift/drag/momentum coefficients of an aerofoil.

and angle of attack, but are also governed by the aerofoil characteristics as expressed by the lift coefficient C_l , the drag coefficient C_d and the coefficient of momentum C_m vs angle of attack (Fig. 2.7). In modern wind turbine design, specially designed aerofoils are in use and the research for ever better solutions continues.

As discussed in Section 2.2, it is crucial to understand that the aerodynamic loads created by and acting on a rotor blade are highly variable in intensity due to the stochastic nature of the wind field:

- Variation of inflowing wind speed with time (fast variation = turbulent winds, slower variation: inflowing gust, weather front, diurnal rise or descent of wind speed).
- Variation of inflowing wind speed with height (wind shear).
- Variation of wind speed due to vortex-shedding obstacles or wake-shedding upwind wind turbines.
- Variation of local wind speed at the blade elements during one rotation due to oblique inflow to the rotor plane (horizontal or vertical inclination of the wind vector with respect to the rotor plane, wind direction change).

Combining variations of the wind field as listed above with a so-called design situation, a set of load cases representing the turbine life is defined.³ Design situations represent the most important conditions that a wind turbine may experience in its service life, for example normal power production, power production while a fault occurs, transitions such as start up or shut down, emergency shutdown, idling state or standstill. In any of these design situations the external conditions, namely wind conditions, are described with normal or extreme models or descriptions. The models and descriptions defined in IEC61400-1: Wind turbines – Part 1: Design Requirements are normal turbulence model (NTM), normal wind profile model (NWP), extreme operating gust (EOG), extreme direction change (EDC), extreme coherent gust with direction change (ECD), extreme wind speed model (EWM), extreme wind

Table 2.1 Load cases according to IEC 61400-1 [3] – excerpt

Design situation	DLC	Wind condition	Other conditions	Type of analysis	Partial safety factors
1. Power production			For extrapolation of extreme events	Ultimate	Normal
	1.1	NTM $V_{in} < V_{hub} < V_{out}$			
	1.2	NTM $V_{in} < V_{hub} < V_{out}$	F	*	
	1.3	ETM $V_{in} < V_{hub} < V_{out}$	U	N	
	1.4	ECD $V_{hub} = V_r - 2 \text{ m/s}$	U	N	
	...	$V_r + 2 \text{ m/s}$			
2. Power production plus occurrence of fault	2.1	NTM $V_{in} < V_{hub} < V_{out}$	Control system fault or loss of electrical network	U	N
	2.2	...			
3. Start up	3.1	... NWP $V_{in} < V_{hub} < V_{out}$	F	*	
	3.2	... EOG $V_{hub} = V_r \pm 2 \text{ m/s}$ and V_{out}	U	N	
	...				
4. Normal shut down	4.1	... NWP $V_{in} < V_{hub} < V_{out}$	U	N	
	...		F	*	
5. Emergency shut down	5.1	... NTM $V_{hub} = V_r \pm 2 \text{ m/s}$ and V_{out}	U	N	
6. Parked (standing still or idling)	6.1	... EWM 50-year recurrence period	U	N	
	...				
7. Parked and fault conditions	7.1	... EWM 1-year recurrence period	U	N	
8. Transport assembly, maintenance and repair	8.1	NTM V_{main} to be stated by the manufacturer	U	T	
	...				

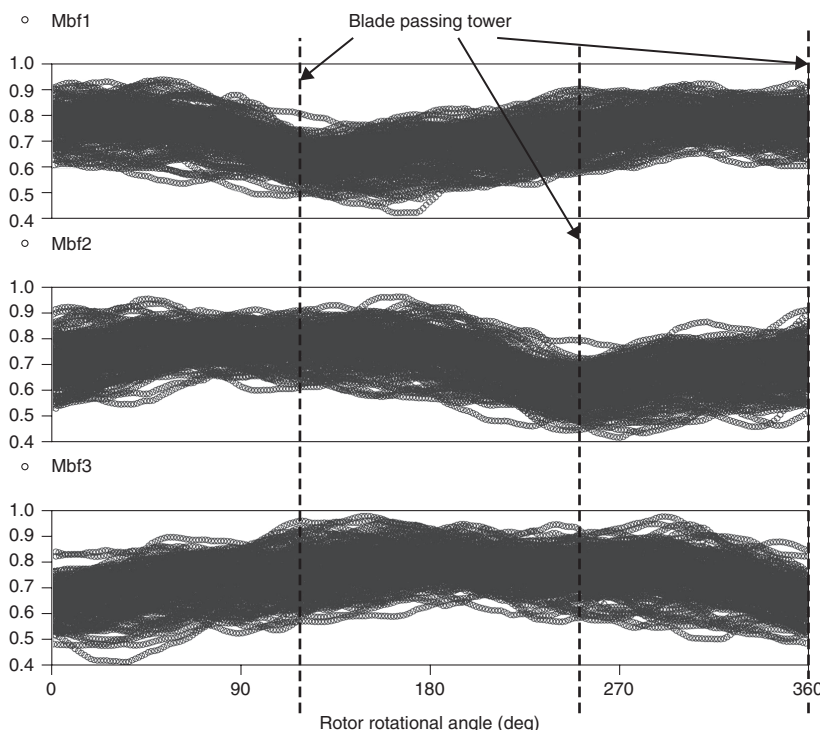
* Partial safety factor for fatigue; DLC = design load case; F = fatigue; U = ultimate; N = normal; T = transport and erection.

Source: IEC: International Standard IEC61400-1: Wind turbines – Part 1: Design Requirements, Ed. 3, Geneva: IEC, 2005.

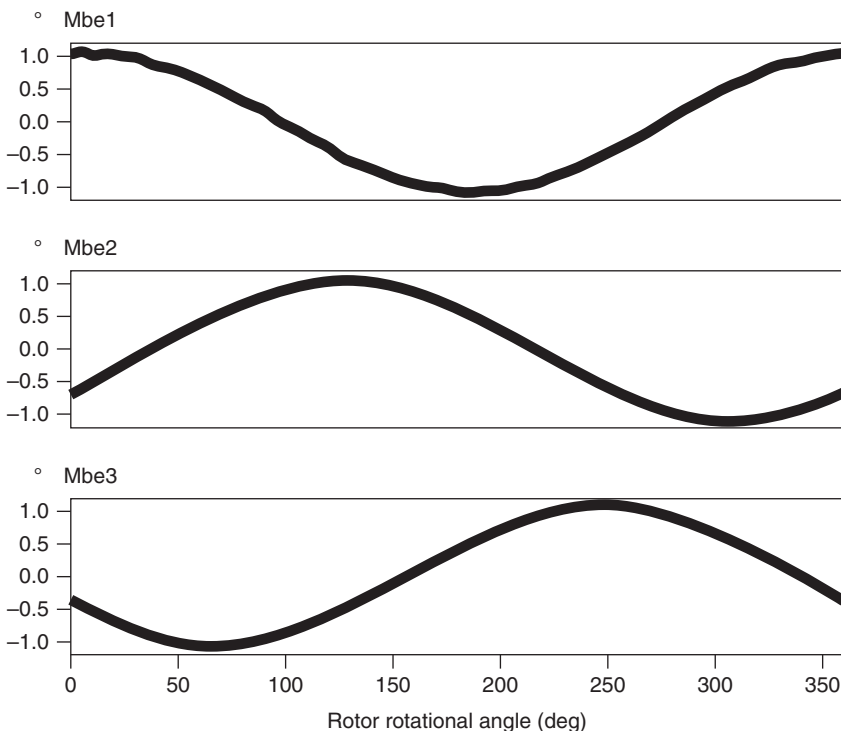
shear (EWS) and, finally, extreme turbulence model (ETM). Table 2.1 summarizes the main design load cases as covered in IEC61400-1. It must be noted that this list is by no means exhaustive and must be complemented depending on the actual design of the blade or wind turbine.

2.3.2 Inertia, gravitational and gyroscopic loads

Whatever the load case, inertia, gravity and gyro effects can make a significant contribution to the blade loads. This is even more important with modern wind turbines, which have become increasingly flexible structures due to mass reduction needs. The turbine is exposed to cyclic excitations causing the entire structure to oscillate constantly. Predominant and strong cyclic excitations arise from cyclic gravity and aerodynamic load variations caused, for example, by the rotating blade masses, by the blade aerofoil passing through an unsteady wind field or even by dynamic stall effects. This effect is sometimes called rotational sampling of a load variation once per



2.8 Tower effect: variation of blade root bending in out-of-rotor plane direction vs rotor rotational angle. Mbif1,2,3 = blade root bending moment in flapwise direction in blade 1,2,3, (normalized); Flapwise = out of rotor plane for non-pitched blade position. (Source: DEWI.)

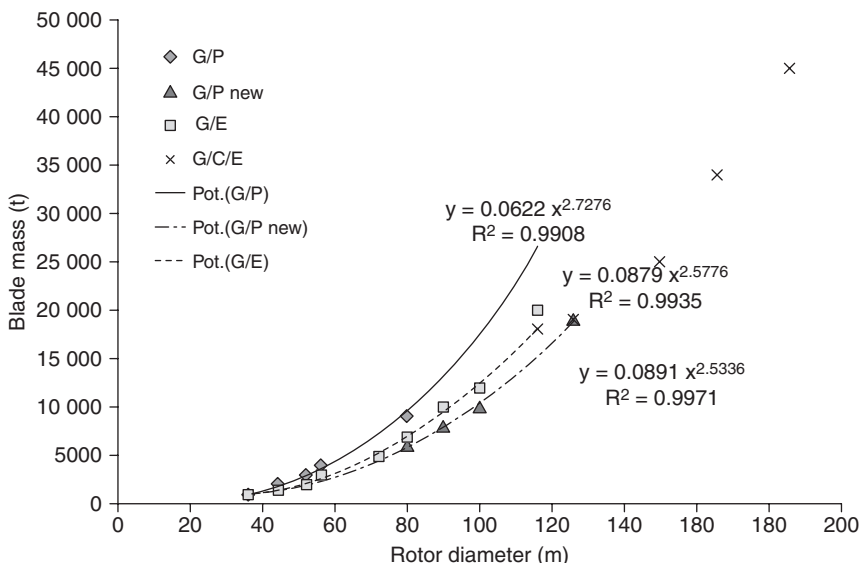


2.9 Sinusoidal in-rotor plane blade root bending moments M_{be} vs rotor rotational angle. $M_{be1,2,3}$ = blade root bending moment in edgewise direction in blade 1,2,3 (normalized); Edgewise = in rotor plane for non-pitched blade position. (Source: DEWI.)

rotation. An obvious example (Fig. 2.8) is the sudden drop in the blade aerodynamic force when passing through the area of lower flow velocity near the tower's stagnation point or in the tower's wake.

Another example of cyclic loading is the deterministic gravity loading caused by the blade mass rotating in the earth's gravity field. As gravity knows only one direction, the weight forces on the blade masses change their direction with respect to a rotor fixed-coordinate system throughout one rotation of the wind turbine rotor. In the rotor fixed-coordinate system, the in-plane blade root bending moment of an idling blade (i.e. no power generation) appears as a sinusoidal load oscillating around zero (Fig. 2.9).

The gravitational oscillating load is not transferred into the non-rotating part of the turbine structure provided that the rotor is mass balanced. Nevertheless, for large turbines this deterministic cyclic load on the rotor blade has become quite dominant, since blade masses and associated weight forces grow with the cube of the rotor radius (Fig. 2.10) if rules of similarity

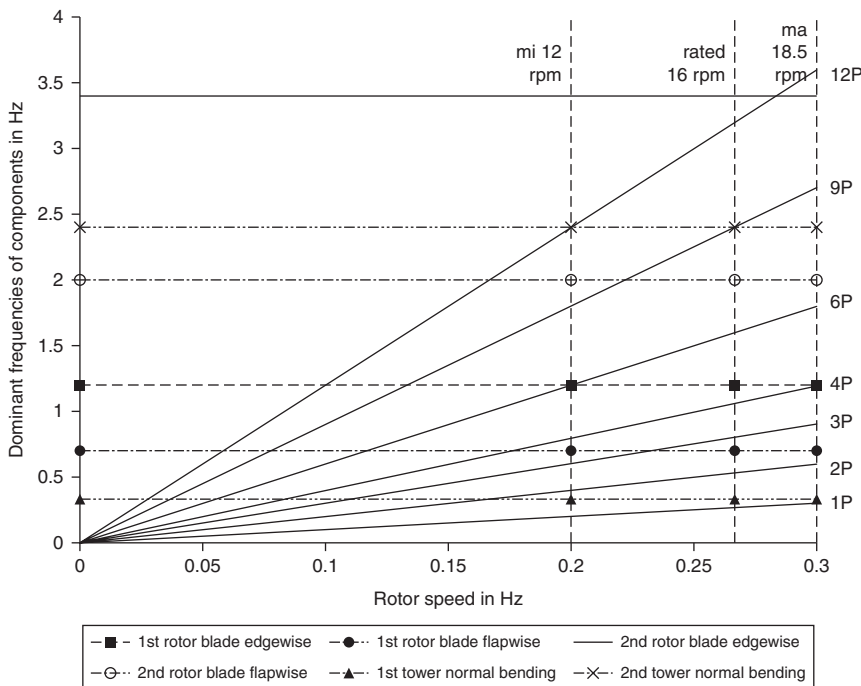


2.10 Blade mass versus rotor diameter.⁵ G/P, Glass fiber/Polyester; G/E, Glass fiber/Epoxy; G/C/E, Glass fiber/Carbon fiber/Epoxy.

for airflow are applied for upscaling.⁵ It is worth noting that, as a consequence, new blade concepts implement designs with reduced specific blade mass (i.e. blade mass per rotor diameter).

Generally, any design must ensure that component natural frequencies cannot be excited by eigenmodes of the overall structural oscillation. To check the relation of relevant excitation frequencies and component natural frequencies the Campbell plot (Fig. 2.11) is used. It depicts an oscillating system's (i.e. a wind turbine's) eigenmode frequencies and component natural frequencies together with the system's excitation regime. In the Campbell plot, the eigenmode and component natural frequencies that are typically invariant with respect to the rotor speed are given as horizontal lines over the operating rotor speed range. The exciting frequencies are found on lines that are defined by the rotor revolution frequency and its multiples. Potentially dangerous situations are indicated by intersections of the exciting frequencies and the component eigenfrequencies or eigenmode frequencies. At these intersections, resonance phenomena may occur if damping (structural or other) is insufficient.

Important excitation frequencies are at once per rotor revolution, often referred to as 1P, and at blade passing frequency, i.e. 2-P for a two-blade rotor, 3-P for a three bladed rotor. Although less energetic, excitations at higher multiples of the rotor frequency, such as 4-P, 6-P, 8-P, 9-P and 12-P, can still be significant if they are close to a component or system natural

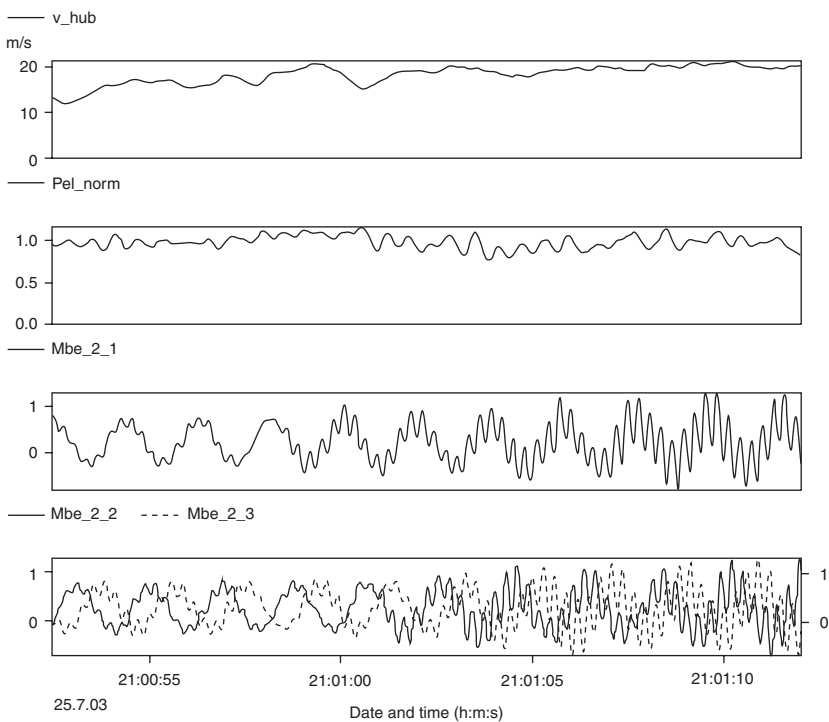


2.11 Campbell plot. (Source: DEWI.)

frequency (mode) and if this oscillation (mode) is not well damped. In such cases, resonance can cause the rotor blade to oscillate at significant amplitudes due to the transfer of energy between the kinetic motion energy and the potential deformation energy of the blade.

A good example of resonance phenomena was seen in the late 1990s when stall-induced edgewise (lead-lag) blade oscillations created a serious threat to the wind turbine industry (Fig. 2.12).

Such stall-induced vibrations were driven by aerodynamic forces in dynamic stall operation that excited the fundamental edgewise blade natural frequency.⁴ In this blade vibration mode the aerodynamic forces actually provided negative damping, i.e. they enhanced the vibration in the edgewise direction creating load cycles with ranges of multiples of the blade gravity load cycle. This was possible because, for the specific vibration mode shape, the direction of the aerodynamic forces coincided with the direction of the blade motion. At times, such vibrations were so violent that blades were destroyed within days of operation. In some cases the problem was unleashed by supposedly insignificant changes to the design, for instance an introduction of extenders at the blade root to increase the rotor diameter:



**2.12 Example of edgewise vibration, v_{hub} = wind speed (m/s),
 Pel_norm = normalized electrical power, Mbe = normalized edgewise
 in-rotor plane blade root bending moments of blades 1 to 3.
 (Source: DEWI.)**

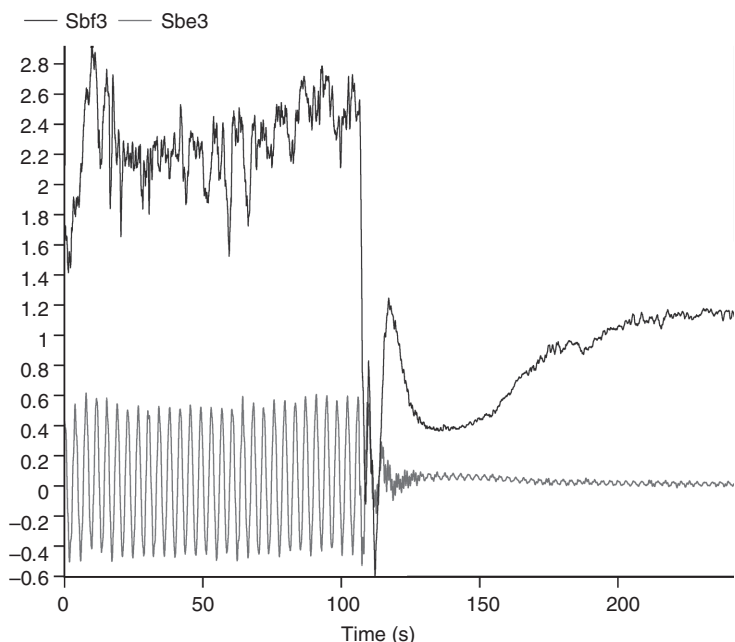
the extension moved the centre of mass outboard, causing the natural frequencies of the blade/extender assembly to change and to come close to one of the fundamental rotor whirl mode frequencies. Rotor whirl modes are modes with coupled yaw and tilt motions of the rotor, with the rotor centre moving in elliptical orbits. This coincidence of the blade edgewise natural frequency with one of the rotor whirl modes in this case triggered the edgewise stall-induced vibrations. This shows that even the repercussions of changes in the supporting structure can cause significant and detrimental blade loads.

In contrast to the example of edgewise stall-induced vibrations, in the case of flapwise oscillations of the rotor blades, deflection and the associated aerodynamic forces are typically in opposite directions. Hence a flapwise oscillation is usually well damped, making it sometimes very difficult to find the blade's flapwise natural frequency in measured (blade root bending) data taken during blade operation.

It can be concluded that, overall, turbine dynamic characteristics on the one hand and blade natural frequencies on the other hand are very important for the benign dynamic behaviour of the complete structure.

2.3.3 Actuation loads

Further loading events are generated by the activity of the turbine controllers. Depending on the operating conditions and the situation, the controller's actuators will be used to keep the wind turbine within safe operating limits. For example, in a stop sequence the controller will actuate the pitch angle of the rotor blade to reduce power input to the rotor by rotating the blade around the pitch axis with the leading edge towards inflow direction. This actuation causes the angle of attack to become smaller, and hence the aerodynamic lift force generated will also decrease. Pitching the blade far enough will cause the angle of attack to become negative, which is associated with the appearance of aerodynamic lift force on the pressure side of the blade. In this situation the blade generates a braking moment, causing the rotor to decelerate quickly: at the end of this sequence the controller will apply the mechanical brake to stop the turbine and park it. As previously described,

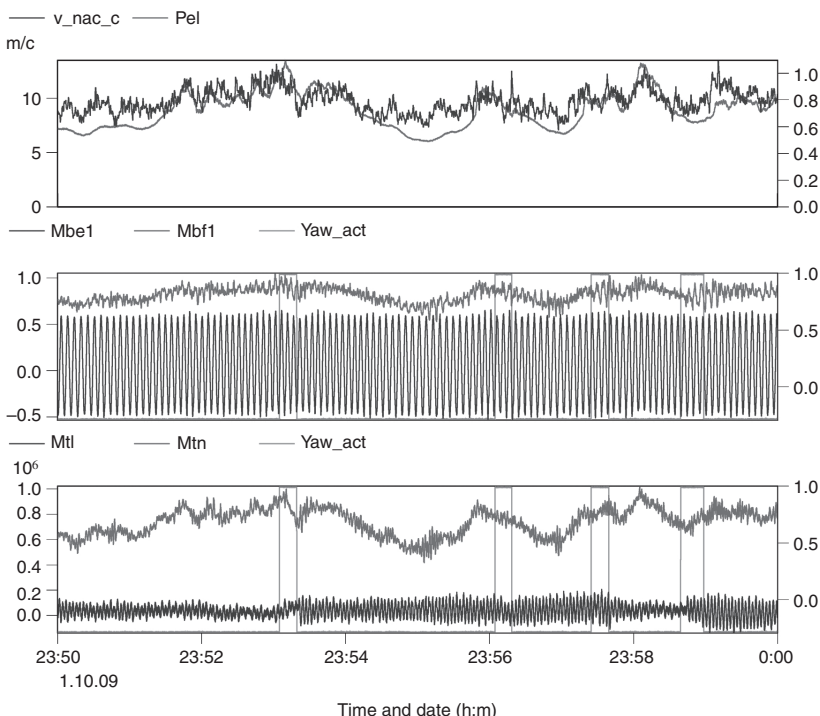


2.13 Example for actuation loads 1, flatwise and edgewise blade root bending moments Sbf and Sbe of blade 3 during emergency stop. Sbe = normalized edgewise in-rotor plane blade root bending moments of blade 3; Sbf = normalized flapwise in-rotor plane blade root bending moments of blade 3. (Source: DEWI.)

the external forces acting on the blade will change amplitude and direction giving rise to loading and unloading events. Depending on the remaining rotor speed just before the mechanical brake is applied, an abrupt engagement of the brake causes another step input to flapwise inertia loading.

There are many manoeuvres that will generate actuation loads in the blades and hence they must be identified and considered as load cases. The manner in which the actuations are performed may be decisive for the size of the loads generated, e.g. pitching the blade from full load operation towards feathered position at too high a speed may cause the blade to develop a large flap load in upwind direction (Fig. 2.13). Such loading is completely opposite to the expected bending load in normal operation and therefore, if not considered in load calculations, may cause the ultimate limit state, i.e. the permissible load limit, to be reached unexpectedly.

In another example (Fig. 2.14), actuation of the nacelle's yaw position represents a step input to the rotor yaw moment. Such step input to the yaw



2.14 Example for actuation loads 2, v_{nac_c} = corrected wind speed at nacelle (m/s), Pel = normalized electrical power, Yaw_act = status signal for yaw activity, Mbe = normalized edgewise in-rotor plane blade root bending moments, Mbf = normalized edgewise in-rotor plane blade root bending moment, Mtl , Mtn = normalized tower base lateral and downwind bending moment. (Source: DEWI.)

moment of the rotating rotor causes a gyroscopic tilt moment to appear. In unfavourably tuned turbine structures, such step input can give rise to a coupled gyroscopic yaw and tilt motion of the rotor (rotor whirl mode) with corresponding feedback of inertia forces on the blade (in out-of-plane direction). In most cases the resulting fore-aft motion of the rotor blades will be well damped as the corresponding changes in aerodynamic forces counteract the motion. This aerodynamic damping helps control turbine dynamic behaviour by suppressing blade flapwise oscillations effectively. For tower side-to-side oscillation the aerodynamic damping does not apply and the gyroscopic excitation input can cause considerable amplitude of the tower head oscillation with associated in-plane inertia loads on the rotor blades.

2.4 Fatigue and extreme loads

Load cases can be ultimate in nature, which means that the actual load applied in the specific load case has a potential to reach the limit state, i.e. the load in question may become as large as its permissible value. In such cases the blade can be destroyed in one loading and unloading event.

Other load cases characteristically damage the structure through many small loading and unloading events that are cascaded in the time history of the loads in question. In such cases the partial damage of the individual load cycle (i.e. single loading and unloading event from a start level to another load level back to the start level) is very small, and it is only because of the large number of these load cycles that considerable damage can be accumulated in the blade's material.

It is important to understand that both types of loading always occur at the same time and without pause throughout the turbine's service life. It is up to the designer and her/his understanding of the particular load case to indicate which load components are to be analysed and which type of analysis, ultimate or fatigue, is appropriate.

2.4.1 Assessment of ultimate loading

In ultimate loading analysis a single loading and unloading event is assumed that may cause the limit state to be reached. The analysis seeks to demonstrate that the actual load to which an additional safety factor is applied does not surpass the permissible load level. Obviously such a load will generate rather large partial damage of the rotor blade material with one load cycle. The following load case can be used as an example: a pitch controlled turbine in parked/idling condition with blades in feathered position is hit by an extreme coherent gust with direction change (ECD). Assuming that the ECD is too quick for the yaw system of the

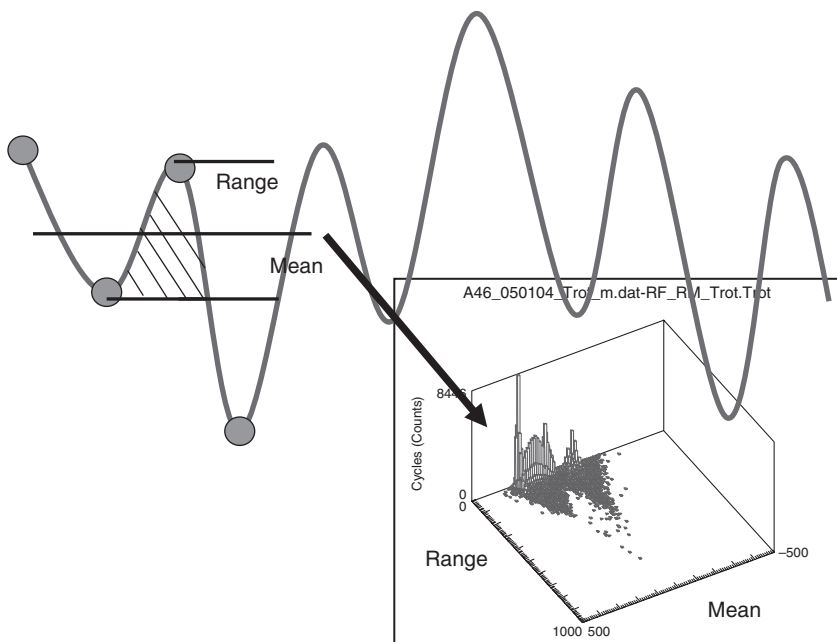
turbine to react, or that the yaw system is inactive due to grid failure, the rotor cannot be yawed to face the wind and hence the gust may hit the blade in maximum lift direction. The gust applies over the complete rotor span (coherent) and causes inflow to the blade elements at the angle of attack with maximum lift coefficient creating maximum aerodynamic forces.

2.4.2 Assessment of fatigue loads

Fatigue loading describes load cycles created in the normal operating process. The individual load cycles are rather small and do not significantly contribute to material damage. However, a large number of such load cycles is able to cause cumulative damage to the material.

To analyse this phenomenon a cycle counting method is applied that decomposes the load time history into a number of load cycles. There is a variety of such cycle counting methods in use, but for use in variable amplitude fatigue analysis the so-called rainflow counting method has become the prevailing method.⁷ If the operation of a rotor blade is thought of as a sequence of cascaded smaller and larger load cycles, a specific 4-point-check, which is able to extract smaller load cycles that occur during a larger scale loading and unloading event, can be applied on the time series of the load. The method mimics the behaviour of water flowing down a pagoda roof during heavy rainfall: the water will drop from one roof level to the next lowest roof enclosing the recess to the building's main structure. This recess represents the load cycle and its depth is synonymous with the load range. The algorithm identifies such smaller load cycles, keeping in mind the starting point of the larger scale rise in load in which they are engulfed. The same algorithm works for descending load, and as a consequence the algorithm delivers a number of full 'rainflow' load cycles (i.e. the load varies from one level to another and back to the start level) and a sequence of alternate loading and unloading events called residuals. The residuals have monotonously increasing ranges until the maximum load range of the analysed time series is reached. Subsequently the residual half cycles decrease in range. The result of such a rainflow counting analysis is a comprehensive and cumulative range-pair spectrum (Fig. 2.15).

State-of-the-art assessment of wind turbine fatigue loads concentrates on load cycles that are found within simulated or measured 10-min realizations of the investigated load, the 10-min time series being used because minimal cyclic variation in wind speed is found within periods of 10-min to 1 h. The philosophy is based on the assumption that the loading, throughout the service life of the wind turbine, can be described by means of capture matrices that are expanded by the two parameters of inflow turbulence intensity and



2.15 Rainflow method. (Source: DEWI.)

average wind speed.⁶ In this data base shown in Table 2.2, time series of 10-min duration for any possible combination of these two parameters are captured. There are capture matrices for normal power production operation, but also for other fatigue relevant load cases, for example regular transients of the turbine such as idling, standstill, start up, shut down or other rotor speed changes (Table 2.2).

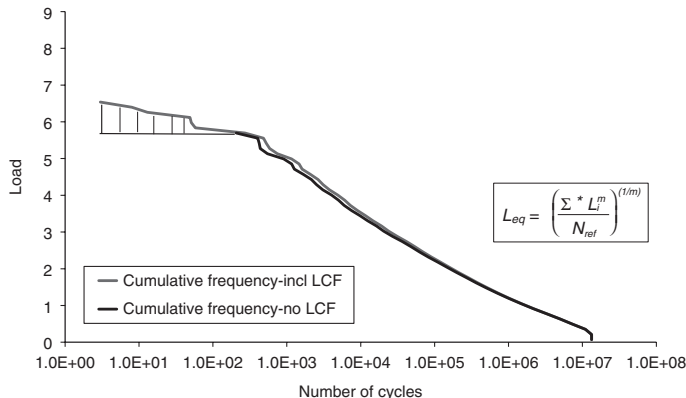
The range-pair load spectra as used in fatigue life calculations are found by superposition and extrapolation of the rainflow counted load cycles that can be found within each of the time series used. It is worth noting that in this procedure the loading effect of variation in the wind speed between one 10-min average and the next is neglected. Especially with respect to the blade's fatigue, such 'low cycle fatigue' loading (LCF) may become more important as modern blade design tries to make better, more efficient use of the available materials.

A method for taking such low cycle fatigue loads into consideration was suggested by Larsen and Thomsen from RISØ⁸ as early as 1996 and applied by the author⁹ in 2004 (Fig. 2.16). The conclusion of this work was that LCF may contribute significantly to structural damage in components made of materials that are sensitive to load cycles with large ranges, such as fibre reinforced plastics and nodular cast iron components.

Table 2.2 Example capture matrix for normal power production:x-axis: wind speed, y-axis: turbulence intensity. The numbers in the matrix cells indicate the number of data sets available for the combination of wind speed and turbulence intensity

V (m/s)	0	3.5	4.5	5.5	6.5	7.5	8.5	9.5	10.5	11.5	12.5	13.5	14.5	15.5	16.5	17.5	18.5	19.5	20.5	> 21.5	V _{out}
I (%)	3.5	4.5	5.5	6.5	7.5	8.5	9.5	10.5	11.5	12.5	13.5	14.5	15.5	16.5	17.5	18.5	19.5	20.5	21.5		
0-<3	3	2	1	1	6	6	6	6	1	2	1	1	2	1	2	1	2	1	2	3	
3-5	6	4	1	10	11	8	11	11	2	2	22	19	14	14	25	8	1	2	1	2	
5-7	13	26	21	53	95	61	48	20	20	22	19	14	14	31	25	8	1	2	3		
7-9	15	62	98	145	159	128	83	65	34	34	31	25	25	25	20	10	4	10	4	2	
9-11	1	42	74	74	83	74	55	18	17	17	20	10	10	10	6	3	3	2	1	2	
11-13	7	21	27	21	27	12	14	10	10	10	10	6	6	6	4	4	4	1	1	1	
13-15		12	14	10	8	6	5	4	4	4	3	1	1	1	1	1	1	1	1		
15-17	2	3	10	4	6	4	4	4	4	4	1	1	1	1	1	1	1	1	1		
17-19	2	3	1	1	1	1	1	1	1	1	1	1	1	1	1	1	1	1	1		
19-21		1	1	1	1	1	1	1	1	1	1	1	1	1	1	1	1	1	1		
21-23		1	1	1	1	1	1	1	1	1	1	1	1	1	1	1	1	1	1		
23-25																					
25-27																					
27-29																					
>29																					

Source: DEWI



2.16 Normalized cumulative flapwise blade load spectra w./w.o. LCF, the hatched area indicates the load cycles added by considering LCF.⁹

2.5 Design verification testing

Every design needs verification in order to make sure the expectation of the designer are met in reality. With today's capabilities to model complex structures in the computer and the extensive use of such advanced models in turbine design, the task to verify the used computational model is key to successful design development.

2.5.1 Design verification process

In the last decade the wind energy industry has recognized the importance of design verification by means of prototype testing. This insight was triggered by experiences such as the stall-induced vibration phenomenon described above in Section 2.3.2 and due to the increasing financial risk associated with the development of ever-larger wind turbines. It is clear that the need for testing equally applies to the individual components such as blades, giving rise to ever more extensive campaigns. While in the late 1990s test campaigns were carried out even for empirical design verification, today's test campaigns serve foremost the aim of validating the aeroelastic and structural computer models used in the design of wind turbines. The idea is to make sure the computational models have the ability to describe all relevant load cases sufficiently to enable computation and synthesis of the design life load-spectrum using these models. The paper 'A Guide to Design Load Validation'¹⁰ published at DEWEK 2006 highlights a possible approach to performing model/design load validation (Table 2.3).

Table 2.3 Use of load measurements in the design verification process¹⁰

Step	Quantity to check	Example for methods	Objective of validation step
1	<ul style="list-style-type: none"> • Documentation • Selected time series 	<ul style="list-style-type: none"> • Comparison of model data against weighing log • Spectral analysis of selected time series for various operational states (e.g. in partial and full load) 	<ul style="list-style-type: none"> • Main structural properties like masses, stiffnesses, eigenfrequencies and coupled modes
2	Characteristics curves	<p>Visual comparison of curves of operational parameters (e.g. speed, power) and loading for several environmental conditions</p>	<ul style="list-style-type: none"> • Validation of basic control characteristics and rotor aerodynamics as well as mechanical and electrical parameters (e.g. losses)
3	Time series of various operational states, like <ul style="list-style-type: none"> • Power production • Start • Stop • Emergency stop 	<ul style="list-style-type: none"> • Visual comparison of data in time and frequency domain • Check of statistical properties of data • Analysis of decay rates oscillations during stopping procedures 	<ul style="list-style-type: none"> • Dynamic behaviour all important and assessable operational states with focus on aerodynamic mode, controller model and actuator models • Structural and aerodynamic damping
4	Post-processed data	<p>Comparison of loading spectra like</p> <ul style="list-style-type: none"> • Rain flow distribution • Load duration distributions • Damage equivalent loads 	<ul style="list-style-type: none"> • Final check of turbine behaviour and dynamic properties • Check of all previously performed validation steps

For the structural verification of the rotor blade, at least two stages are required:

1. Verification of the global turbine model used for calculating the operational loads at the blade elements and at the blade root and verification of the extreme loads found by analytic calculations.
2. Finite Element Analysis (FEA) to refine the results of step 1 and to follow up on specific problems like buckling of blade areas.

In advanced blade design increasingly comprehensive simulation tools are used combining advanced aerodynamic Computational Fluid Dynamics (CFD) modelling and FEA or multi-body structural simulations.

The purpose of testing is to provide ‘real world’ data for the sectional loads at the joint of the rotor blade and the hub for use in global turbine model verification. Applying the same logic, detailed models such as FEA can be verified using measured data for internal loads at points of special interest, for instance areas with increased strain/stress levels or with a potential to develop deformations.

The verification testing is done in three tests:

1. Static blade test,
2. Dynamic blade test,
3. In-field type testing.

In all of these tests the reaction of the blades and the blade’s materials is measured in terms of strains, accelerations, deformations and displacements. The sensors used in this task are typically strain gages, accelerometers and displacement sensors.

2.5.2 Instrumentation

Conventional strain gages are used in experimental blade-load validation. In recent years optical strain gages have also been used with success; however, the high cost of these gages and their signal conditioning hardware limits the attractiveness of this advanced technique mainly to measurements in extreme (external) conditions, such as very long monitoring periods or where there is lightning risk.

In addition to the appropriate electrical set up in full-, half- and quarter-bridge assemblies exact positioning of the strain gages is of paramount importance. This statement holds true for both measurement setups for global moment measurements and measurement setups for local strain measurements.

Besides global blade-bending moment verification the strain gage measurement technique is applied to experimentally verify local strain phenomena such as

- buckling strain,
- maximum strain at trailing edge,
- shear strain in the blade's web,
- shear strain in bonded joints.

Accelerometers can be attached to the blade structure at specific positions along its radial span. The idea for acceleration measurements is to identify the mode shapes of the blade's oscillations during turbine operation. The reason for this is that the quality of a computational model is defined, among other things, by the accuracy of frequency and shape with which higher oscillation modes are simulated.

Displacements are normally measured in static or dynamic blade testing in a dedicated testing facility. Measuring displacements typically requires availability of a fixed reference, a condition that is hard to meet in measurements taken during the blade's operation at the turbine. For displacement measurements a variety of sensors may be used, including draw-wire sensors (static testing) and optical sensors (dynamic measurements).

2.5.3 Calibration of global bending moment measurements

The calibration of the blade-load strain gage sensors to provide root bending moment data is effected by using the blade's weight force as an external calibration load. The range of the measurement signal during several full revolutions of the rotor is recorded and compared to the theoretic gravity-induced bending moment of the blade. This method is applied for calibrating edge- and flap-wise bending in pitch controlled wind turbines as the rotor blade can be pitched to align either the edgewise or the flapwise direction of the blade's coordinate system with the plane of rotation. For stall controlled turbines that cannot pitch their blades the flapwise direction must be calibrated by applying an external calibration load. This is put into practice by pulling the blade towards the tower while simultaneously measuring the pulling force and the strain gage sensor output. When conducting a blade-pulling test, special attention must be given to the maximum transversal load that may be applied: because of the blade's structure, transversal loads are quite limited to avoid local damage of the structure.

When using the blade's gravitational bending load for calibration typically 20–40% of the expected operational loads can be achieved for the flapwise direction. In edgewise direction as much as 40–60% of the edge-wise bending load during operation can be covered. This is in contrast to the values that can be obtained when pulling at the blade: here 6–15% of the operational load range may be achieved for a multi-megawatt turbine and a sub-megawatt turbine, respectively. This indicates that blade-pulling calibration is less effective for large blades and therefore not likely to be an attractive alternative for the future.

2.6 Challenges and future trends

Recent development trends show that modern wind turbines are designed with lower specific capacities using larger rotors at lower rated power output.¹¹ This trend is pushed by the wish to produce wind energy at a higher capacity factor, i.e. rated power is provided over a longer period throughout the year. Rating turbines in this way allows for improved predictability of power contribution into the grid and better utilization of infrastructure such as transmission lines. Both are key issues for the operation of large offshore wind farms whose energy is transmitted over large distances to the consumer centres. Because of the expected large contribution of offshore wind power to the electric energy supply and electric power demand it will be absolutely necessary to reliably forecast the short term power production in order to ensure stability of the grid.

As turbines continue to get bigger, with every new generation blade loads will increase accordingly. Blades that must grow in length while at the same time keeping mass at the lowest possible level will most probably feature reduced chord length. The resulting slender blade structure needs to maintain performance and, of course, must equally be able to carry the loads generated in the aerodynamic energy conversion process. At first glance, this sounds like attempting to square the circle; however, there are a number of research and development approaches for design options and operation strategies for load mitigation. In this respect, the reports of Scott J. Johnson, C.P. 'Case' van Dam and Dale E. Berg,¹² Thanasis Barlas¹³ and G.A.M. van Kuik¹⁴ give a comprehensive overview of advanced passive and active load control techniques for wind turbines. The options discussed in the above-mentioned reports are too many to be discussed here and the reader is referred to the original sources for a detailed study. Just two possible design options and one operation strategy will be highlighted in the following sections as being representative of the wealth of ideas and concepts. The examples have been chosen for the fact that they have been seen implemented in commercially operating turbines.

2.6.1 Design options

Aeroelastic tailoring

As described in Section 2.3, non-coincidence of the aerodynamic and the shear centre of an aerofoil leads to a blade twist moment when the aerodynamic thrust force is applied. With increasing thrust the blade will be bent and at the same time twisted towards the inflow. This coupled motion reduces the angle of attack at the blade element and the aerodynamic force is alleviated. This effect can be amplified and utilized by aeroelastic tailoring of the rotor blade structure, i.e. using appropriate fibre orientations to generate the desired twist deformation under bending loads. The idea is appealing as it does not require extra sensors, aerodynamic surfaces or actuators in the blade. However, it holds the intrinsic risk of exciting a dangerous aerodynamic instability phenomenon called ‘flutter’. In ‘flutter’ condition, the aerodynamic forces (here flapwise and twist moment) interact with the structure’s natural mode of vibration to produce a potentially destructive vibration. As in any vibration problem, stiffness, damping, eigen-mode frequency and excitation frequency play decisive roles in the analysis. To design a robust and well-behaved aeroelastic tailored blade, modern simulation tools joining complex aerodynamic and structural models are indispensable.

Vortex generators

Tabs mounted on the suction-side aerofoil surface are able to re-energize the boundary layer of the airflow around the aerofoil, avoiding premature flow separation, or to increase the lift coefficient of the profile. Increasing the lift coefficient and keeping the flow attached to the aerofoil surface allows the use of blades with reduced chord length, and so uses less material (mass). At the same time the lift characteristics are tuned in such a way that increase in lift force, for any given increase in angle of attack ($\delta L/\delta\alpha$), is smaller as compared to a blade with longer chord and no vortex generators. This leads to reduced load variation caused by wind speed variation through turbulence or gust phenomena.¹²

2.6.2 Operation strategies to mitigate loading

As can be learned from many prototype-testing campaigns, thorough tuning of the drive train and pitch controller is always a good strategy for avoiding extra loads caused by resonances or other oscillation phenomena. It is also a good idea to verify maximum acceptable lag time, pitch

speed and stiffness of the pitch actuation system. Failure to implement fully specific features of the design, coupled with sensitive aerodynamic airfoils and turbulent wind conditions, can lead to unexpected power trips. Therefore, a valid strategy is to avoid unexpected loads by ensuring that the standard control strategy as designed in theory is working in the real turbine.

Individual pitch control

There are methods to achieve load alleviation through active flow control employing the turbines full-span pitch system. As most modern turbines feature three mechanically independent, electrically driven pitch systems it is possible to control individual pitch angles to each of the rotor blades. Such infrastructure is available in many wind turbines and can be employed to mitigate the aerodynamic loads caused by wind speed variations individually experienced by each blade.^{12,15} In order to have sufficient good quality input for such advanced control strategies, information about the flow/loading conditions at the individual blades is required. Bossanyi showed that separation of the general collective pitch control action based on rotor speed from the individual pitch control action based on load measurements at the blade roots led to the best results. Simulations showed that reductions of up to 30% in both fatigue and extreme loads on blade root, main shaft and yaw bearing could be possible. Alternative load measurements at the hub or low speed shaft or bearing were also eligible for use as satisfactory controller input.¹⁵ A note that must be made here is that robust and reliable sensors must be available in order to implement the described technique.

2.6.3 Materials issues

Another complementary direction that will be followed is the development of optimized materials. As loads cannot be avoided it must be a consideration to make more efficient use of the material, i.e. to fully exploit the properties of a given material. Taking the stresses in the critical cross-sections to the limits, however, requires exact, reliable knowledge of the materials used. To establish such a database for state-of-the-art and new glass fibre reinforced plastic (GFRP) materials in turn demands agreed and validated testing and qualification procedures. In this respect, the interested reader is referred to the appropriate chapters of this book and to the final report of the OPTIMAT BLADES: Reliable Optimal Use of Materials for Wind Turbine Rotor Blades project.¹⁶

2.7 Sources of further information and advice

- <http://www.actiflow.com>: active boundary layer control
<http://smart-blade.com/research>: flexible flap, Gurney flap, micro flap, leading edge auxiliary aerofoil
<http://www.cortenergy.eu/>: vortex generators

2.8 References

1. International Electrotechnical Commission: IEC61400-x Series.
2. Manwell, J.F., McGowan, J.G., Rogers, A.L.: Wind Energy Explained, Chapter 3: Aerodynamics of Wind Turbines. West-Sussex, England: John Wiley and Sons, Ltd; 2002.
3. IEC: International Standard IEC61400–1: Wind turbines – Part 1: Design Requirements, Ed. 3, Genever: IEC, 2005.
4. Petersen, J.T. *et al.*: Prediction of Dynamic Loads and Induced Vibrations in Stall. RISO-R-1045(EN).
5. Graue H., EUROS: Structural design of wind turbine blades. Presentation held at ‘Wind Turbine Rotor Blades’, 3rd Technical Conference organized by Haus der Technik, Essen, June 2011.
6. IEC: International Standard IEC61400–13: Wind turbines – Part 1: Mechanical load measurements, Ed. 1, Genever: IEC, 2001.
7. ASTM E1049 – 85(2011)e1: Standard Practices for Cycle Counting in Fatigue Analysis, ASTM International, West Conshohocken, PA, 2006, DOI: 10.1520/E1049–85R11E01, www.astm.org.
8. Larsen, G., Thomsen, K.: A simple approximative procedure for taking into account low cycle fatigue loads. Paper presented at IEA-Symposium on Wind Turbine Fatigue, Stuttgart, 1–2 February 1996.
9. Söker, H., Kensche, C. *et al.*: Introducing Low Cycle Fatigue in IEC Standard Range Pair Spectra. Proceedings of the 7th German Wind Energy Conference DEWEK 2004. DEWI GmbH: Wilhelmshaven, 2004.
10. Söker, H. *et al.*: A Guide to Design Load Validation. Proceedings of the 8th German Wind Energy Conference DEWEK 2006. DEWI GmbH: Wilhelmshaven, 2006.
11. Molly, J.P.: Rated Power of Wind Turbines: What Is Best? DEWI Magazine 38. DEWI GmbH: Wilhelmshaven, February 2011.
12. Johnson, S.J., van Dam, C.P., Berg, D.E.: Active Load Control Techniques for Wind Turbines, SANDIA REPORT SAND 2008–4809. Sandia National Laboratories: Albuquerque, New Mexico 87185 and Livermore, California 94550, 2008.
13. Barlas, T. *et al.*: Upwind – Smart Rotor Blades and Rotor Control for Wind Turbines-State of the Art-Knowledge Base Report for UpWind WP 1B3. Delft University Wind Energy Research Institute (DUWIND). Delft, The Netherlands: DUWIND, 2007.
14. van Kuik, G.A.M. (Editor): UPWIND – Final Report, showing the potential of smart rotor blades and rotor control, Final Report for UpWind WP 1B3.

- Delft University Wind Energy Research Institute (DUWIND). Delft, The Netherlands: DUWIND, 2011.
- 15. Bossanyi, E.A.: Individual Blade Pitch Control for Load Reduction. *Wind Energ.* 2003; 6:119–128 (DOI: 10.1002/we.76). West Sussex, England; John Wiley & Sons, 2002.
 - 16. Janssen, L.G.J., van Wingerde, A.M., Kensche, Ch.W., Philippidis, T.P., Brøndsted, P., Dutton, A.G., Nijssen, R.P.L., Krause, O.: OPTIMAT BLADES final report OB_OC_R17rev001, ECN-C—06023. Bergen, The Netherlands: ECN, 2006.

Aerodynamic design of wind turbine rotors

C. BAK, Technical University of Denmark, Denmark

DOI: 10.1533/9780857097286.1.59

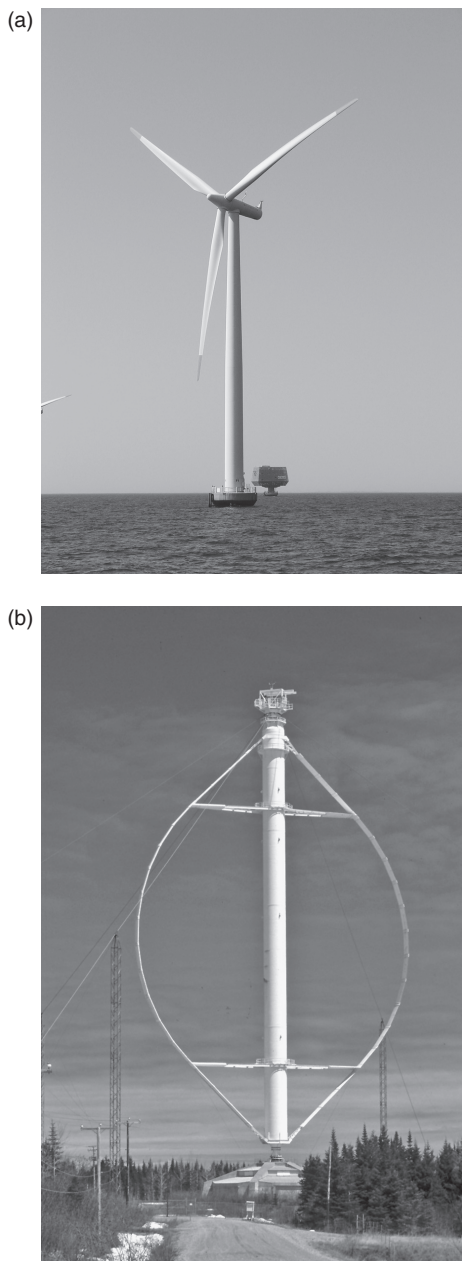
Abstract: This chapter describes the process of aerodynamic rotor design for horizontal axis wind turbines. Apart from describing the state-of-the-art, it presents the mathematical models used, explains how airfoil and rotor control choice are decided and lists common design constraints. An example is used to illustrate the rotor design process, covering all the main aspects from choice of rotor size, airfoil types and number of blades to the exact aerodynamic shape of the blades. At the end of the chapter there is a summary of future trends and sources of further information.

Key words: rotor design, wind turbine rotor, wind turbine airfoils, aerodynamic design, wind turbine power performance.

Note: This chapter is a revised and updated version of Chapter 6 ‘Aerodynamic design of wind turbine rotors’ by C. Bak in *Wind energy systems*, edited by J. D. Sørensen and J. N. Sørensen, Woodhead Publishing Limited, 2010, ISBN: 978-1-84569-580-4.

3.1 Introduction

The wind turbine rotor with its blades is the part of the wind turbine that extracts kinetic energy from the wind and converts it into mechanical power and further into electricity, which can be used for water heating, pumping, etc. A result of extracting energy is that the speed of airflow through the area swept by the rotor is reduced in the rotor plane and behind the rotor. There are therefore many different ways to extract energy from the wind. Wind turbine rotors can be divided into those which are driven by the lift on the airfoils and those which are driven by the drag on the blades. In addition, rotors can be divided into those with low rotational speed, causing a high torque, and those with high rotational speed, which are common in electricity production. Furthermore, wind turbines can be divided into horizontal axis wind turbines (HAWTs) and vertical axis wind turbines (VAWTs). The most common today is the HAWT, see Fig. 3.1 (a), with varying numbers of blades, driven by the lift on the airfoils, and with high rotational speed. A VAWT is also shown, see Fig. 3.1 (b), driven by the lift on the airfoils and with high rotational speed. The three-bladed HAWT with the rotor upstream



3.1 (a) Horizontal axis wind turbine (HAWT), Siemens 2.3 MW wind turbine, 69 m hub height, situated at Rødsand, Denmark. (*Source:* Photo by Christian Bak, DTU Wind Energy.) (b) Vertical axis wind turbine (VAWT), Éole 4 MW wind turbine, height of 110 m, situated at Cap Chat, Quebec, Canada. (*Source:* Photo by Paul Gipe, wind-works.org.)

of the tower is the dominating concept of today, and the ten biggest suppliers of wind energy, installing around 78% of the capacity in 2011,¹ and the majority of remaining suppliers, use this concept. Because of the significant domination of the HAWT concept, this chapter will limit the description of aerodynamic design to HAWT rotors driven by the lift on the airfoils and with high rotational speed.

This chapter describes briefly the state-of-the-art within aerodynamic design of rotors and explains the principles of an aerodynamic design process that uses simple but common methods. The introduction to rotor design focusses on the Blade Element Momentum (BEM) method, and this is followed by an explanation of how decisions are reached concerning rotational speed, rotor size, rotor control and number of blades, what the design constraints are, and how the rotor design is evaluated. Based on this introduction, an example of a rotor design process, covering the design of the first draft of a rotor for a 1 MW wind turbine, is described. The methods for carrying out an aerodynamic rotor design are thus described, but that part of the process from the first draft design, as presented in this chapter, to the final rotor, including aeroelastic computations, structural considerations such as buckling and tip deflection, and the performance of the rotor in the wind turbine system, is not shown. At the end of the chapter, future trends and sources of further information can be found.

Although the scope of this chapter is restricted to aerodynamic rotor design it should be emphasized that the rotor design process should be considered as part of the wind turbine design process as a whole, which includes the aeroelastic response of the entire wind turbine and the structural design of the blades. Further, aerodynamic rotor design is closely connected to the process of structural lay-up of the blade and choice of material. This chapter's description of the aerodynamic rotor design process will therefore include occasional reminders to the reader of the importance of these connections.

3.1.1 State-of-the-art rotor design

Many simulation tools have been developed for prediction of wind turbine rotor flow. They range from the very simple models, such as the Blade Element Momentum (BEM) method, requiring low computational means, to the very advanced models, such as three-dimensional Computational Fluid Dynamics (CFD) which resolves the boundary layers on the rotor and the domain several rotor diameters upstream and downstream of the rotor plane, thus requiring high computational means. However, despite the fast development of computer power, using the very advanced models to produce predictions to inform the optimization process is, even now in 2013,

still rather time-consuming; these methods should therefore be considered as tools for evaluating the rotor design, rather than as part of the inherently iterative rotor design process.

That is the reason for the extensive use of the BEM method in tools designed to predict rotor aerodynamics, but also in tools for predicting the aeroelastic response of the entire wind turbine. A common way of designing rotors in 2013 is to produce a draft rotor design using a simple method such as the BEM method, and then evaluate it using a so-called aeroelastic code. If the rotor design turns out to be efficient, it can be evaluated using advanced tools, such as CFD, if they are available.

The rotor design approach described above is a manual process based on trial-and-error, and works with great success if the designer is experienced. However, the design can also be carried out using numerical optimization, where an object function is minimized or maximized. The object function could be the power coefficient or the annual energy production subject to constraints, such as maximum loads below a certain level, and absolute thickness distribution of the blades above a certain level to ensure a certain minimum stiffness. In such a tool, coupling to an aeroelastic code is possible, which can automate the rotor and wind turbine design to some degree. However, the output of such a design study is dependent on the object function and the constraints, so carrying out such a design process requires an experienced user. Furthermore, such a design method is time-consuming, especially if the design is based on aeroelastic calculations, and therefore certain simplifications are often needed to reduce the computational time. Despite being time-consuming, such a tool can be profitable, because trends in the rotor design, which are not part of the analysis, can be revealed. At least one tool can create designs based on both aerodynamic and aeroelastic calculations using numerical optimization.² If aerodynamic optimizations are sufficient, a few other tools can be used.³

Because the simple BEM method is often used in the rotor design process, the design could benefit from being evaluated using more advanced methods. The most time-consuming simulation method is based on an exact modeling of the surface geometry of the blade and rotor, where the boundary layer of the flow over the surface is resolved. Here, a significant part of the operator time is spent on generating a computational mesh that satisfies the conditions necessary for creating reliable solutions. Apart from commercially available CFD codes,^{4–6} significant work has also been carried out since the start of the 1990s to develop this technique specifically for wind turbines.^{7–10} Reduced models exist as well, where the rotor is modeled by introducing volume forces into the flow, either by lines simulating each blade (Actuator Line method),^{11, 12} or by a disc simulating the entire rotor, where the blade forces are smeared out on the entire rotor plane (Actuator Disc method).¹³ The results from these methods compare quite well with

the full model, as described above, where power curves and force distributions along the blades, for example, are very similar. However, details such as airfoil characteristics and tip flow cannot be extracted. Finally, techniques using discrete vortices have been developed and are fairly fast as well; this depends, however, on whether the wake behind the turbine is free to move or frozen.¹⁴

3.1.2 Models and elements used in the rotor design process

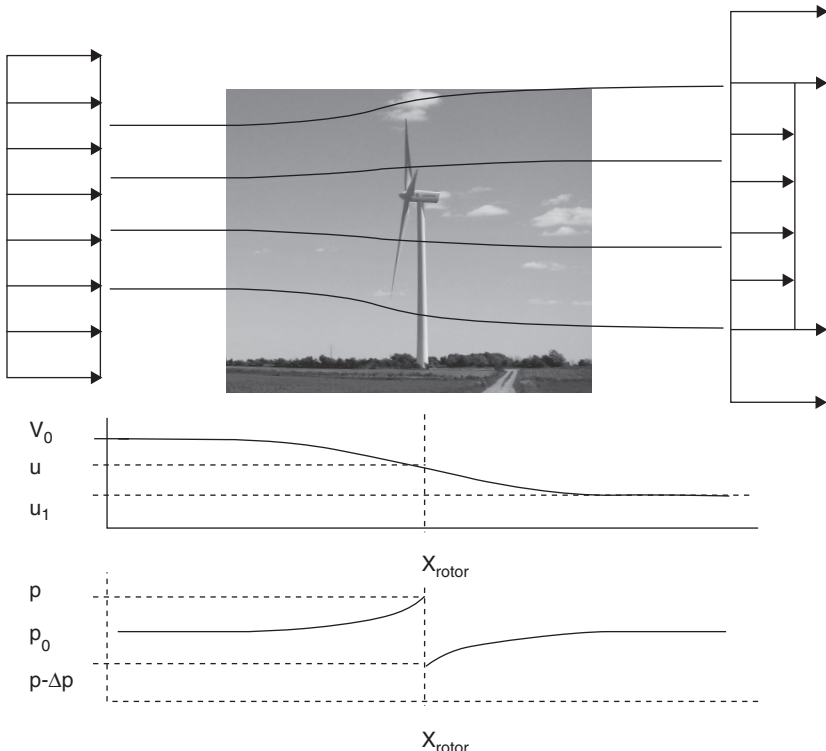
In the previous section it was stated that the most common method for prediction of rotor performance in the aerodynamic design of rotors was the Blade Element Momentum (BEM) method and that it required low computational means. In the sections that follow, the various elements required for the aerodynamic design of rotors using BEM are described. Because the aerodynamic rotor design should be considered as integrated in the design of the entire wind turbine, aspects such as constraints relating to the aerodynamic rotor design process, are described. Furthermore, a few rules of thumb required to make the rotor design process operational are described, but these rules are based on the experience of existing rotor designs and are not necessarily applicable for all designs.

3.2 The blade element momentum (BEM) method

The BEM method was developed in the 1930s,¹⁵ and since then other, but not very different, formulations have been developed.^{16–18} In what follows, the BEM method will be described, starting with a simplified model which assumes that the flow through the rotor behaves the same way at all points making the problem one-dimensional. Furthermore, the assumption in the one-dimensional problem is that the rotor has no losses such as friction caused by the air viscosity and no losses caused by the flow at the tips. The description of the simplified one-dimensional model is followed by a description of the more advanced BEM model, which uses the one-dimensional model in each annular element and also takes these types of losses into account.

3.2.1 One-dimensional momentum theory

In this first analysis of the rotor flow, it is assumed that the rotor is a disc and that it is ideal, i.e. the flow is inviscid (no air viscosity) and there are no losses at the tips. The disc has the characteristic that it reduces the flow speed and extracts all the energy resulting from the reduction of the flow speed.



3.2 Sketch of flow around the ideal wind turbine rotor. (Source: Photo: Vestas V80 at Tjæreborg Enge, Denmark, by Christian Bak, DTU Wind Energy.).

In Fig. 3.2, a sketch of the flow around an ideal wind turbine rotor is shown, where the development of the velocity and pressure from far upstream of the rotor to far downstream of the rotor is shown.

From Bernoulli's equation, it is possible to make a connection between pressure and velocity both upstream and downstream of the rotor. Bernoulli's equation states that along a stream line the dynamic pressure, determined by the flow speed, added to the static pressure equals the total pressure, Equation [3.1]:

$$\frac{1}{2} \rho u^2 + p = H \quad [3.1]$$

From the equation, it can be seen that when the velocity decreases, the pressure will increase and vice versa. However, this equation is not valid

through the rotor plane, though the flow upstream and downstream of the rotor plane can be analyzed. Upstream, the connection is as described in Equation [3.2]:

$$p_0 + \frac{1}{2} \rho V_0^2 = p + \frac{1}{2} \rho u^2 \quad [3.2]$$

Downstream of the rotor, the connection is as described in Equation [3.3]:

$$P_0 + \frac{1}{2} \rho u_1^2 = p - \Delta p + \frac{1}{2} \rho u^2 \quad [3.3]$$

By subtracting Equations [3.2] and [3.3] from each other, an expression of the pressure drop through the rotor plane is obtained, Equation [3.4]:

$$\Delta p = \frac{1}{2} \rho (V_0^2 - u_1^2) \quad [3.4]$$

The pressure drop can also be expressed as the change in momentum of the air passing through a unit area of the rotor per second,⁸ Equation [3.5]:

$$\Delta p = \rho u (V_0 - u_1) \quad [3.5]$$

Coupling Equations [3.4] and [3.5] gives the following result, Equation [3.6]:

$$u = \frac{1}{2} (V_0 + u_1) \quad [3.6]$$

Equation [3.6] tells us that the air speed in the rotor plane has been decelerated to exactly half of the total velocity deficit that it will experience from far upstream to far downstream in the rotor wake. Thus, the other half of the deceleration of the wind takes place in the wake, downstream of the rotor.

In this context, a convenient entity to be defined is the axial induction factor, a , defined as in Equation [3.7]:

$$u = (1 - a) V_0 \quad [3.7]$$

Therefore, from Equation [3.6] we get $u_1 = (1 - 2a)V_0$ and the following expression for the extracted power, P , and the corresponding thrust, T , are, Equations [3.8] and [3.9]⁸:

$$P = \frac{1}{2} \rho u (V_0^2 - u_1^2) A = 2\rho a(1-a)^2 V_0^3 A \quad [3.8]$$

$$T = \Delta p A = 2\rho a(1-a)V_0^2 A \quad [3.9]$$

The rate of the kinetic energy through the rotor disc, P_{wind} , and the stagnation pressure on the rotor disc, T_{wind} , are, Equations [3.10] and [3.11]:

$$P_{\text{wind}} = \frac{1}{2} \rho V_0^3 A \quad [3.10]$$

$$T_{\text{wind}} = \frac{1}{2} \rho V_0^2 A \quad [3.11]$$

Nondimensional coefficients for the power and the thrust are convenient to use and can be defined using Equations [3.10] and [3.11] as follows, Equations [3.12] and [3.13]:

$$C_P = \frac{P}{P_{\text{wind}}} = \frac{P}{(1/2)\rho V_0^3 A} \quad [3.12]$$

$$C_T = \frac{T}{T_{\text{wind}}} = \frac{T}{(1/2)\rho V_0^2 A} \quad [3.13]$$

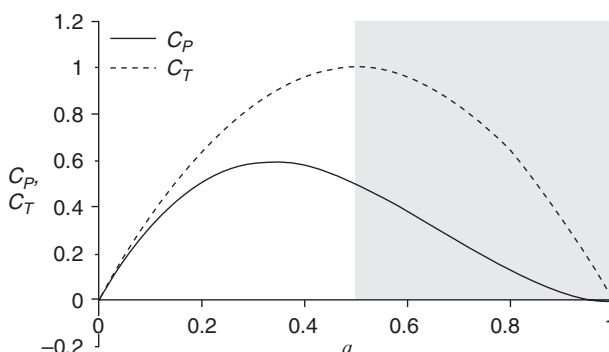
Using this definition, Equations [3.8] and [3.9] can be written as Equations [3.14] and [3.15]:

$$C_p = 4a(1-a)^2 \quad [3.14]$$

$$C_T = 4a(1-a) \quad [3.15]$$

Equation [3.14] is very important for understanding wind power extraction, because it tells us that the maximum obtainable power from the wind is $C_p = 16/27$ (approximately 0.593) and that this maximum value is obtained for an axial induction factor of $a = 1/3$. This means that not all of the existing wind power can be extracted but only 0.593 at the very maximum. This maximum limit is usually called the Betz limit.¹⁹ This means that the maximum power is extracted when the wind speed is decreased by 1/3 of the free wind speed in the rotor plane and by 2/3 of the free wind speed in the far wake. An explanation as to why not all power can be extracted is the need to transport the air away from the rotor after the power has been extracted. If the air were completely stopped and all existing power extracted, the air would have to be accumulated somewhere. Thus the remaining power in the wind is required to transport the air downstream and away from the rotor disc. From Equation [3.15] it is seen that the corresponding thrust coefficient, C_T , is 8/9 (approximately 0.89).

As shown in Fig. 3.3, both C_p and C_T are increasing for increasing axial induction a for small values of a . However, for $a > 1/3$, C_p decreases while C_T still increases. For $a > 1/3$, the theory is increasingly uncertain compared to real rotor aerodynamics. For $a = 0.5$, the far wake has reached a standstill and for $a > 0.5$ reversed flow in the far wake is the result. Thus, for $a \geq 0.5$ the theory breaks down. According to the theory $C_T = 1$ for $a = 0.5$ and the rotor is said to be highly loaded. However, in reality the rotor may be even more loaded, because the assumptions used in the derivation of the theory no longer hold for $a > 1/3$. Corrections for $a > 1/3$ will be given in the next section.



3.3 The power coefficient (C_p) and thrust coefficient (C_T) for one-dimensional momentum theory as a function of axial induction (a).

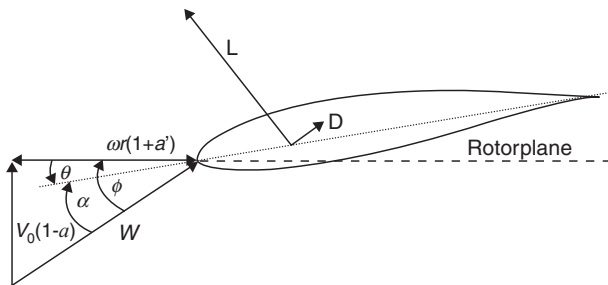
3.2.2 Blade element momentum theory

Even though the flow through a wind turbine is very complex due to the tip and root vortices and the mutual interaction of the wind flows among the rotor blades, it is possible to simplify the mechanisms in a very efficient way. As shown in Fig. 3.4, the rotor can be divided into annular elements of span width, dr . Because the theory that will be developed in this section is based on the one-dimensional momentum theory, it must be assumed that there is no interaction between neighboring elements, something which one-dimensional momentum theory can show to be a good assumption.⁸ Also, it must be assumed that the axial and tangential velocity are uniformly distributed all over the annular element. This means that the forces are not concentrated on the blades, but are smeared out over the annular element.

Figure 3.5 shows a section on the rotor blade illustrating the symbols used in the Blade Element Momentum formulation. The blade section is exposed to the axial velocity (wind speed) V_0 and the tangential velocity (eigen



3.4 Sketch of the division of a wind turbine rotor into annular elements.
(Source: Photo: NM80 at Tjæreborg Enge, Denmark by Christian Bak, DTU Wind Energy.)



3.5 Sketch of a section on the rotor blade illustrating the symbols used in the Blade Element Momentum formulation. The arrows show the direction of positive values.

velocity) $r\omega$. Because of the forces from the rotor on the wind, where the total induced velocity is parallel to the lift force but in the opposite direction, the axial velocity is reduced to $(1 - a)V_0$, and the tangential velocity is increased to $(1 + a')r\omega$. The resulting velocity that the blade section experiences, the relative velocity, W , is the vector sum of the axial and tangential velocity. The angle from W to the rotor plane is called the inflow angle, ϕ . The blade section is in general twisted, θ , positive in an anticlockwise direction. The twist is defined as the angle from the rotor plane to the airfoil chord line, which is from the very leading edge of the airfoil to the very trailing edge of the airfoil. The angle from the relative velocity, W , to the chord line is called the angle of attack, α .

Based on the sketch in Fig. 3.5, the following relations can be derived, Equations [3.16] and [3.17]:

$$\alpha = \phi - \theta \quad [3.16]$$

$$\tan \phi = \frac{1-a}{1+a'} \frac{V_0}{r\omega} \Leftrightarrow \phi = \arctan \left(\frac{1-a}{1+a'} \frac{V_0}{r\omega} \right) \quad [3.17]$$

From the principles of wing section theory, see, e.g. Abbot and Doenhoff,²⁰ the lift and drag forces per length on each blade section, respectively, can be expressed in terms of respectively lift and drag coefficients as, Equations [3.18] and [3.19]:

$$l = \frac{1}{2} \rho W^2 c c_l \quad [3.18]$$

$$d = \frac{1}{2} \rho W^2 c c_d \quad [3.19]$$

Here, c is the chord length and c_l and c_d are the lift and drag coefficients per meter, respectively. These coefficients are described further in Section 3.3.1 and in Chapter 4. For each annular element, the thrust and torque, respectively, are

$$dT = \frac{1}{2} \rho W^2 c B c_y dr \quad [3.20]$$

$$dQ = \frac{1}{2} \rho W^2 c B c_x r dr \quad [3.21]$$

Here, the force coefficients normal to the rotor plane, c_y , and parallel to the rotor plane, c_x , have been used

$$c_y = c_l \cos \phi + c_d \sin \phi \quad [3.22]$$

and

$$c_x = c_l \sin \phi - c_d \cos \phi. \quad [3.23]$$

To combine the forces from the blade elements with the results from the momentum theory, the response from the tangential forces must be taken into account. Therefore, the one-dimensional theory, described in the previous section, where the wake rotation is not part of the theory, must be extended with a rotational part reflecting the momentum in tangential direction. Furthermore, a correction for a finite number of blades will be included as shown in Equations [3.24] and [3.25]:

$$dT = \rho u (V_0 - u_1) F dA \Leftrightarrow dT = \frac{1}{2} \rho V_0^2 4Fa(1-a)2\pi r dr \quad [3.24]$$

$$dQ = \rho u u_t r F dA \Leftrightarrow dQ = \frac{1}{2} \rho V_0^2 4F(1-a)a' \frac{\alpha r}{V_0} r 2\pi r dr \quad [3.25]$$

Here u_t is the tangential velocity caused by the wake rotation in the far wake, a' is the tangential induction factor and F is the Prandtl correction for a finite number of blades described by Glauert:¹⁵

$$F = \frac{2}{\pi} \arccos(e^{-f}) \quad \text{with} \quad f = \frac{B}{2} \frac{R-r}{r \sin \phi} \quad [3.26]$$

The above formulation of thrust and torque for an annular blade element, Equations [3.20] and [3.21], can now be used in combination with the extended momentum theory, Equations [3.24] and [3.25]. The result can be written as:

$$\frac{a}{1-a} = \frac{1}{4} \frac{1}{F \sin^2 \phi} \frac{cB}{2\pi r} c_y \quad [3.27]$$

$$\frac{a'}{1+a'} = \frac{1}{4} \frac{1}{F \sin \phi \cos \phi} \frac{cB}{2\pi r} c_x, \quad [3.28]$$

With the solidity of the rotor defined as

$$\sigma = \frac{cB}{2\pi r} \quad [3.29]$$

the axial and tangential induction, respectively, can be written as:

$$a = \frac{1}{(4F \sin^2 \phi / \sigma c_y) + 1} \quad [3.30]$$

$$a' = \frac{1}{(4F \sin \phi \cos \phi / \sigma c_x) - 1} \quad [3.31]$$

These equations have to be solved iteratively because F , θ , c_y and c_x are all dependent on the induction factors, a and a' . Moreover, the equations are not in agreement with real rotor flow when an axial induction value, a , greater than approximately 1/3 is obtained. The BEM theory assumes no, or small, expansion of the wake. Therefore, the thrust coefficient must be corrected for $a > 1/3$ to be in agreement with real rotor flows. Glauert¹⁵ showed

how such a correction and different empirical relations between the axial induction, a , and the thrust coefficient, C_T , can be made so as to fit measurements, such as the one described by Hansen¹⁸:

$$C_T = \begin{cases} 4a(1-a)F & a \leq 1/3 \\ 4a\left(1-\frac{1}{4}(5-3a)a\right)F & a > 1/3 \end{cases} \quad [3.32]$$

Thus, using the above equations, Equations [3.16]–[3.21], [3.26], [3.30]–[3.32], the rotor aerodynamics can be predicted for all wind speeds. However, before doing this, it is necessary to consider important parameters in rotor design and airfoil characteristics, as outlined in the following sections.

3.3 Important parameters in aerodynamic rotor design

The momentum theory described in the previous section provides the basis for the aerodynamic design of wind turbine rotors. As described earlier, the main driver in the wind turbine design is to minimize the cost of energy. This is done by obtaining the correct ratio between capital cost (e.g. cost of materials and rental of workshop) and energy production. However, irrespective of the constraints that operate to reduce the wind turbine cost, it is important to maximize power production while taking account of the constraints.

The power coefficient in an annular element of the rotor disc can be expressed as, Equation [3.33], where $F_{\text{tangential}}$ describes the force per length unit in tangential direction on an airfoil section and in the rotor plane

$$\begin{aligned} C_p &= \frac{r\omega F_{\text{tangential}} dr}{(1/2)\rho V_0^3 dA} \Leftrightarrow \\ C_p &= \frac{r\omega \frac{1}{2}\rho ((1-a)V_0)^2 + ((1+a')r\omega)^2 c_x c B dr}{\frac{1}{2}\rho V_0^3 2\pi r dr} \Leftrightarrow \\ C_p &= \frac{(((1-a)V_0)^2 + ((1+a')r\omega)^2)}{V_0^2} \frac{r\omega}{2\pi r} \frac{cB}{c_x} \end{aligned} \quad [3.33]$$

Defining

$$\lambda = \frac{\omega R}{V_0} \quad [3.34]$$

as the tip speed ratio between the eigen speed of the blade tip and the free wind speed and

$$\lambda_{\text{loc}} = \lambda \frac{r}{R} \quad [3.35]$$

as the local speed ratio between the eigen speed of the blade at a certain radius and the free wind speed, and using Equation [3.29], results in the following expression for the power coefficient, Equation [3.36]:

$$C_p = \left((1-a)^2 + \left(\lambda \frac{r}{R} \right)^2 (1+a')^2 \right) \lambda \frac{r}{R} \sigma c_x = f \left(\lambda \frac{r}{R}, \sigma c_x, a, a' \right) \quad [3.36]$$

This equation is important in aerodynamic blade design because it tells us that the power coefficient at a certain rotor radius is dependent on the tip speed ratio, λ , the position relative to the tip, r/R , the solidity of the rotor, σ , the force coefficient in the rotor plane, c_x , and induction factors in axial and tangential direction, a and a' , respectively. Deriving the thrust coefficient the same way results in the following expression, Equation [3.37]:

$$C_T = \left((1-a)^2 + \left(\lambda \frac{r}{R} \right)^2 (1+a')^2 \right) \sigma c_y = f \left(\lambda \frac{r}{R}, \sigma c_y, a, a' \right) \quad [3.37]$$

Even though this relation for the thrust coefficient is somewhat different from the relation for the power coefficient, it tells us that the thrust coefficient is dependent on the same parameters as the power coefficient except that the force coefficient normal to the rotor plane, c_y , and not in the rotor plane, c_x , contributes to the thrust. Because the forces and the induction factors are unambiguously connected, and σ and c_x (and c_y) are always used together as in, e.g. Equations [3.30], [3.31], [3.36] and [3.37], C_p and C_T in an annular element can briefly be described by the functions $f(\lambda r/R, \sigma c_x)$ and $f(\lambda r/R, \sigma c_y)$, respectively, meaning that only two parameters in each function control the rotor design. Since c_x and c_y are strongly correlated to c_l (see Equations [3.23] and [3.22], respectively), the rotor design can with very good approximation be described by the function $f(\lambda r/R, \sigma c_l)$. Thus, keeping the local speed ratio, $\lambda r/R$, constant, the term σc_l needs to be kept constant to maintain power production. Therefore, if a blade designer wants to design slender blades the solidity, σ , needs to be reduced, but the lift coefficient, c_l , then needs to be increased to keep σc_l constant. If the designers wants wider blades, σ needs to be increased, but then c_l needs to be decreased.

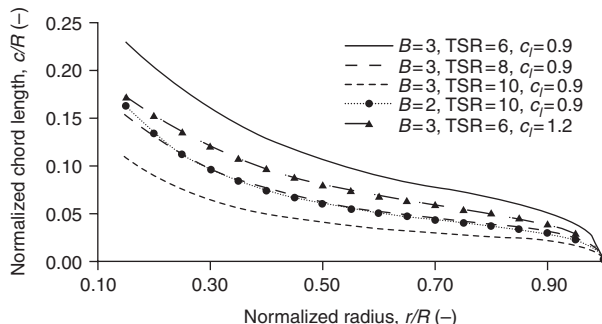
The following shows how the blade chord can be computed if the rotor is designed for maximum power. Based on Equation [3.14], it follows that maximum C_p is ideally 16/27 and that this value is obtained for $a = 1/3$. Using Equation [3.29], and isolating σ while putting $a = 1/3$ in Equation [3.30], gives the following expression, Equation [3.38]:

$$\begin{aligned} \frac{2 \sin^2 \phi F}{c_y} &= \frac{Bc}{2\pi r} \\ c &= 4\pi r \sin^2 \phi F \frac{1}{c_y} \frac{1}{B} \\ \frac{c}{R} &= 4\pi \frac{r}{R} \sin^2 \phi F \arctan \left(\frac{(2/3)}{(1+a')} \frac{1}{\lambda r/R} \right) \frac{1}{c_y} \frac{1}{B} = f(a', \lambda \frac{r}{R}, F, c_y, B) \quad [3.38] \end{aligned}$$

Here, Equations [3.17] and [3.35] are also used for expressing the chord of the blade using the same parameters as in Equations [3.36] and [3.37]. Thus, as stated in Equation [3.38], the normalized chord, c/R , is dependent on the normalized radius, r/R , the tangential induction factor, a' (the axial induction factor, a , is locked to 1/3), the tip speed ratio, λ , the correction for number of blades, F , the force coefficient normal to the rotor disc, c_y , and the number of blades, B .

The equations need to be solved iteratively and some results are shown in Fig. 3.6, assuming that the chosen c_l (closely correlated to c_y) and α is constant for the whole blade. Apart from Equations [3.16] and [3.38], Equation [3.31] must also be solved. Note that increasing c_l (and thereby c_y), B and λ (also called tip speed ratio, TSR) leads to a reduction in the chord distribution.

In addition to predicting the aerodynamic design, the twist angle of the blade must also be calculated. This can be derived from Equation [3.16],



3.6 Example of the chord distribution with different number of blades, different force coefficients normal to the rotor plane and different tip speed ratios, TSRs.

which shows the relation between the inflow angle, the angle of attack and the twist. The inflow angle is known when predicting the induction factor, a' , and the angle of attack is determined from the airfoil characteristics: good airfoil performance, in combination with robust operation, is a factor to be considered when the angle of attack is chosen.

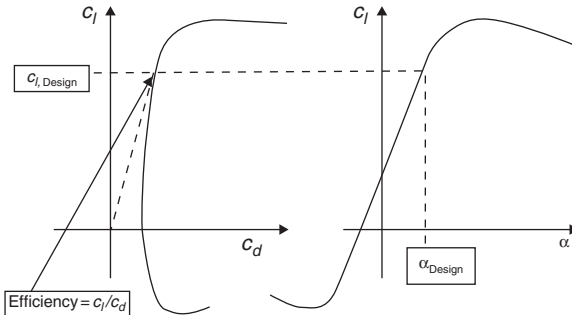
Even though it is very important to design a rotor with high efficiency, it can sometimes be an advantage to decrease the load slightly to save costs on other components in the wind turbine, e.g. the tower. Loads can be reduced by operating the rotor at a lower rotational speed than it has been designed for, but the rotor can also be designed to have an axial induction lower than $a = 1/3$. To do so, Equation [3.38] can be generalized as shown in Equation [3.39].

$$\begin{aligned} c &= 4\pi r \sin^2 \phi F \frac{1}{c_y} \frac{1}{B} \frac{2a}{(1-a)} \\ \frac{c}{R} &= 4\pi \frac{r}{R} \sin^2 \left(\arctan \left(\frac{1-a}{(1+a')} \frac{1}{\lambda} \frac{1}{r/R} \right) \right) F \frac{1}{c_y} \frac{1}{B} \frac{2a}{(1-a)} = f(a, a', \lambda \frac{r}{R}, F, c_y, B) \end{aligned} \quad [3.39]$$

3.3.1 Airfoil performance

As seen in the previous section, important parameters in aerodynamic blade design are the force coefficients in the rotor plane, c_x , and out of the rotor plane, c_y . It is seen from Equations [3.22] and [3.23] that these coefficients are derived from the coefficients c_l and c_d , the lift and drag coefficients, respectively. In Fig. 3.5 the directions of lift and drag are shown. The lift is always normal to the incoming flow whereas the drag is always in the direction of the flow. Thus, the angle of attack, α , gives these directions relative to the airfoil chord. In Fig. 3.7 a sketch of the airfoil characteristics is seen.

To the right is seen the lift coefficient, c_l , vs angle of attack, α , and to the left is seen c_l vs the drag coefficient, c_d , where the coefficients are normalized according to Equations [3.18] and [3.19]. For low α and low c_l , c_d is rather constant and corresponds to a flow around the airfoil which is mainly attached to the surface. For higher α and c_l and approaching maximum c_l , c_d is increasing, which reflects the start of separation typically from the trailing edge. Increasing α will increase the amount of separation, which at the end will cause the airfoil to stall from the leading edge with massively separated flow. Because c_l can be interpreted as a production term and c_d as a loss term, a measure for the airfoil efficiency is the lift-drag ratio, c_l/c_d . The fine dashed line in the left plot illustrates this. The steeper the slope of this line



3.7 Sketch of the airfoil characteristics measured by c_l , c_d and α .

starting in origin, the more efficient the airfoil is. According to Equations [3.22] and [3.23], the normal and tangential force coefficients can be written as, Equations [3.40] and [3.41]:

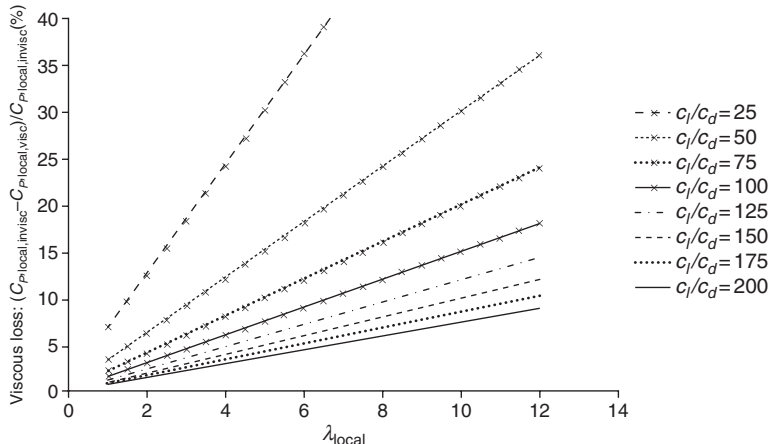
$$c_x = c_l \sin \phi - c_d \cos \phi \Leftrightarrow c_x = c_l \left(\sin \phi - \frac{1}{c_l / c_d} \cos \phi \right) \quad [3.40]$$

$$c_y = c_l \cos \phi + c_d \sin \phi \Leftrightarrow c_y = c_l \left(\cos \phi + \frac{1}{c_l / c_d} \sin \phi \right) \quad [3.41]$$

Equations [3.40] and [3.41] reflect that the in-plane force coefficient contributing to the power is dependent on the lift coefficient, c_l , the inverse lift-drag ratio, c_l/c_d and the inflow angle ϕ . Thus, an airfoil for use on a wind turbine should operate at a point with high c_l/c_d . Commonly, the point at which we find maximum c_l/c_d is called the design point, with the corresponding design lift, $c_{l,\text{design}}$, and design angle of attack, α_{design} . How the c_l/c_d influences the performance of a rotor is shown in Fig. 3.8.

The figure shows the viscous loss in the local power coefficient on a rotor in percent as a function of the local speed ratio and how the loss in the local power coefficient depends on c_l/c_d , where the blade element momentum theory has been used in the analysis assuming that the axial induction factor is $a = 1/3$ and that there is no tip loss. The viscous loss in the local power coefficient is defined as, Equation [3.42]:

$$\text{Power-loss}_{\text{local,viscous}} = \frac{C_{P,\text{local,inviscid}} - C_{P,\text{local,viscous}}}{C_{P,\text{local,inviscid}}} \quad [3.42]$$



3.8 Local power loss as a function of the local speed ratio for different lift–drag ratios.

where C_P (both $C_{P,\text{local,inviscid}}$ and $C_{P,\text{local,viscous}}$) is computed from Equation [3.36]. In the case of inviscid flow, $c_l/c_d \rightarrow \infty$ and in the case of viscous flow c_l/c_d is a finite number. For a common value of c_l/c_d of 100 and for a rotor with a common tip speed ratio of $\lambda = 8$, it can be seen from Fig. 3.8 that such a rotor has at the tip a viscous loss in the local power coefficient of approximately 12% ($\lambda_{\text{loc}} = 8$), but at 25% radius (corresponding to $\lambda_{\text{loc}} = 2$) the viscous loss is only 3%. In relation to this it is important to note that for a rotor, λ_{loc} is proportional to the radius as stated in Equation [3.35]. To analyze Fig. 3.8 further, in addition to the above assumptions ($a = 1/3$ and no tip loss), it can be assumed that the tangential induction is small, $a' \ll 1$, which is a good approximation except at very low values of $\lambda_{\text{loc}} < 1$. With these assumptions Equation [3.42] reduces to a very simple expression, Equation [3.43]:

$$\text{Power-loss}_{\text{local,viscous,simplified}} = \frac{3}{2} \frac{\lambda_{\text{loc}}}{c_l / c_d} \quad [3.43]$$

Equation [3.43] shows that the viscous loss in the local power coefficient increases directly proportional to λ_{loc} and inversely proportional to c_l/c_d . The variation in viscous losses, depending on λ_{loc} , illustrates that it is more important to increase c_l/c_d on the outer part of the rotor than on the inner part. This conclusion is very important, because the viscous loss in the local power coefficient should be weighted with the corresponding area of the annular element of the rotor to predict the absolute viscous power loss in

the annular element measured in Watts. Thus, the absolute viscous power loss in an annular element is proportional to $r \times \text{Power} - \text{loss}_{\text{viscous}}$. According to Equations [3.43] and [3.35] this is proportional to $r^2 \lambda / R(c_l / c_d)$, which means that a high c_l/c_d on the outer part of rotors is even more important. The above considerations are important in the choice of airfoils, but can also be used in the choice of the design tip speed ratio. However, some considerations about the design tip speed ratio are described in Section 3.5.7.

In addition to focusing on the c_l/c_d when selecting airfoils, it is important also to focus on the lift coefficient according to Equation [3.40]. If airfoils are selected to create maximum power it is important that they can generate sufficient lift to obtain maximum power, i.e. to obtain an induction of $a = 1/3$ according to the blade element momentum method. This is also the case for thick airfoils that commonly are mounted on the inner parts of rotors even though they often show rather low lift coefficients. However, it should be emphasized that rotors should be designed to achieve a trade off between power and loads in order to minimize the cost of energy and thus the entire rotor should not necessarily show maximum local power coefficients at all radial positions.

Since c_l and c_l/c_d are created by the airfoil in the flow field, it is important to be aware that the airfoil characteristics, c_l and c_d , as sketched in Fig. 3.7 are not a fixed set of data, but depend on several parameters. Among these the most important parameters that influence the aerodynamic performance are:

- the Reynolds number,
- the relative thickness of the airfoil,
- the airfoil shape, and
- whether the airfoil surface is clean or contaminated.

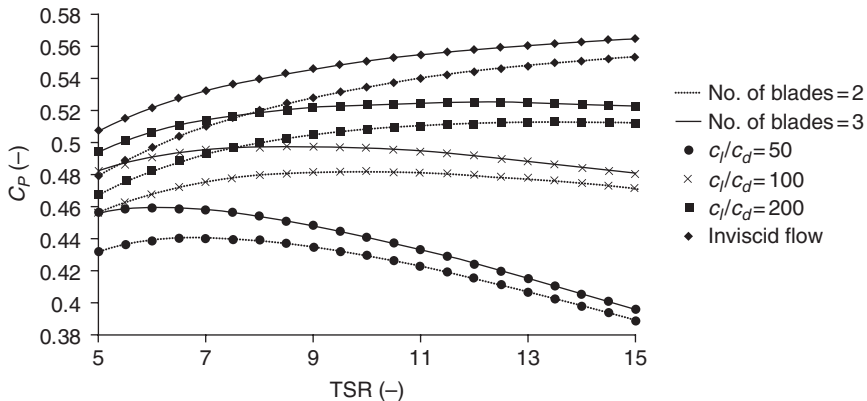
Further information about airfoil performance is described in Chapter 4.

3.4 Particular design parameters

The design of blades requires more than aerodynamic models and knowledge of airfoil performance. The choice of the generator, the tip speed and other constraints need to be selected. In this section these subjects will be addressed.

3.4.1 Tip speed ratio

As seen in Section 3.3 the tip speed ratio, λ , is an important parameter when designing a rotor. When analyzing the influence of λ on the power



3.9 Power coefficient C_p vs tip speed ratio (TSR), λ .

performance, it turns out that λ should be increased to reduce the tip loss. For ideal rotors in inviscid flow, λ should be increased as much as possible, and in theory to infinity, if the target is to maximize power production. However, for real viscous flows the lift–drag ratio of the airfoils counteracts this and λ is limited to between 5 and 12 for rotors between 1 kW and 5 MW depending on the lift–drag ratio and the number of blades.²¹ Figure 3.9 shows the relation between the power coefficient, C_p , and λ assuming that the lift–drag ratio is constant for the entire blade. Thus, knowing the approximate lift–drag ratio of the airfoils used on the blades (Fig. 3.9) indicates which λ to choose with respect to C_p . However, aspects other than power production can be important such as the need to reduce the load, considerations concerning the blade structure, generator torque (which can be reduced by increasing the rotational speed) and noise caused by high tip speed.

3.4.2 Size of rotor/generator

As described above, the design of a rotor is an integral part of the design process for the wind turbine as a whole. The overall goal is to manufacture a wind turbine at lowest cost per energy unit. Therefore, the target when designing a wind turbine rotor is not necessarily to capture the maximum energy at a certain site or the maximum power at a certain (typical) wind speed, but rather to capture as much energy as possible while keeping the cost of all components, from generator and tower to foundation and grid connection, as low as possible.

The size of the rotor is of primary importance when considering the total cost of the wind turbine. With a bigger rotor, more energy can be captured; however this is likely to mean higher loads and a larger generator. At the

very least it is important to determine the ‘rated power’, which is the maximum of the mean power output averaged in a period of 10 min. In general, the rated power correlates with the maximum loads in the normal operation of the wind turbine. The ‘rated wind speed’ is the wind speed at which the rated power is obtained. This wind speed depends on the rotor size, which again depends on the wind climate at a certain site. Therefore a decision on where the wind turbine is likely to be erected is needed. In traditional rotor designs, the rated wind speed is often deemed to be the mean wind speed at a site plus approximately 6 m/s. Thus, if the mean wind speed is 8 m/s, the rated wind speed will be around 14 m/s. This, however, is a rule of thumb, and therefore the choice of rotor size should be based on the specific wind climate, corresponding loads and cost estimations. Recently especially, there has been a trend towards decreasing the range between mean wind speed and rated wind speed, resulting in designs with rather big rotors when compared to the generator size.

A simple way to produce a rough estimate of the rotor size is to decide on the rated power and rated wind speed and use the following procedure. Based on analysis of existing rotor designs, the mechanical power coefficient (which is the efficiency without the loss in generator and gearbox), $C_{P,\text{rated}}$ (see Equation [3.13]), is often between 0.25 and 0.30 at rated wind speed. The radius of the rotor will then be, Equation [3.44]:

$$R = \sqrt{\frac{P_{\text{rated}}}{(1/2)\rho V_{\text{rated}}^3 C_{P,\text{rated}} \pi}} \quad [3.44]$$

Here the rotor area or the area through which the blades sweep, known as the swept area, A , from Equation [3.12] is $A = \pi r^2$. Choosing P_{rated} to 1 MW and $V_{\text{rated}} = 14$ m/s, which corresponds to a site with medium to high wind speed, and assuming air density at standard conditions, $\rho = 1.225$ kg/m³, we get $R = 27.5$ m and a rotor diameter of 55.0 m if $C_{P,\text{rated}}$ is chosen to 0.25.

3.4.3 Rotor control

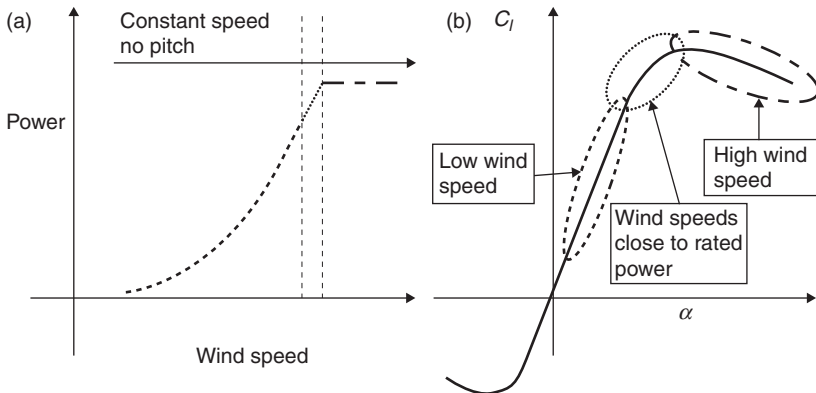
As shown in Sections 3.3 and 3.5.7, the rotor design is dependent, among other parameters, on the tip speed ratio. Therefore, a certain tip speed ratio, λ , must be chosen. To operate the rotor so as to extract maximum power, the ratio between the tip speed and the wind speed must be constant. This means that for increasing wind speed, the tip speed should be increased correspondingly if this is possible according to the choice of generator. However, because of, e.g. noise and erosion of the leading edge, the tip speed should not increase too much. For large modern wind turbines, maximum tip speeds

of 70–90 m/s are common. Therefore, for several reasons it is desirable to limit the tip speed and thereby the rotational speed. Which maximum rotational speed to choose should also depend on an analysis of the total wind turbine cost as described in Section 3.4.2.

As well as λ , the type of rotor control to be used to limit the turbine's power needs to be chosen. The size of the generator and the allowable loads on the turbine determines at which level output should be limited. This limitation is carried out by increasing the drag or decreasing the lift on the airfoil sections. In modern wind turbines this can be done actively by pitching the blades, to decrease the lift on the outboard part of the blade, or passively by letting the blades stall, to increase the drag.

It is now accepted that making an aerodynamic design of a wind turbine rotor requires knowledge of the methods and principles of rotor control, so that such things as whether the turbine should operate with or without stalled condition, and whether the airfoils have the required reserve from design lift to maximum lift, can be known. Several different types of rotor control are possible, the most common of which are described below.

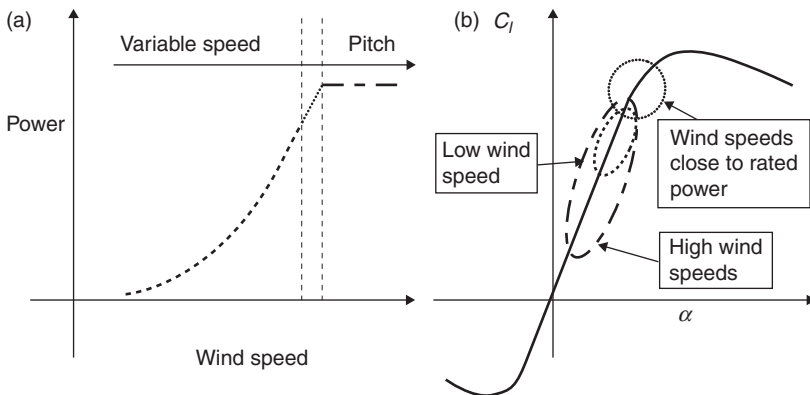
- **Constant/variable rotational rotor speed.** This degree of freedom in the control depends on the characteristics of the generator. If a constant rotor speed is chosen, a simpler and less costly generator can be chosen. However, choosing a variable speed rotor makes it possible to optimize the power for a large range of wind speeds. Also, using this kind of generator creates more flexibility in the connection to the power grid.
- **Pitchable/fixed blades.** Pitchable blades allow the freedom to limit and optimize the power very precisely and also make it possible to stop the turbine, e.g. in emergency situations. When limiting the power, the pitchable blades can be used to reduce the lift or increase the drag by either decreasing or increasing the angle of attack, respectively. Decreasing the angle of attack ensures that the flow is attached to the airfoils so that the operation of the airfoils will be in the linear part of the lift curve; this is called 'pitch control'. Increasing the angle of attack to stall/deep stall ensures a nearly passive limitation of the power because only minor changes to the pitch setting are generally needed; this is called 'active stall control'.
- **Pitch/stall control.** Turbines limit the power by reducing the lift coefficient or increasing the drag coefficient for increasing wind speeds, either in the linear part of the lift curve by reducing the angle of attack (pitch control), or in the stall part of the lift curve by increasing the angle of attack (stall control), respectively. Using fixed blades and constant rotational rotor speed, one is forced to use stall control. This is illustrated in Fig. 3.10, where the power curve is shown to the left with the corresponding airfoil operation in terms of a lift curve to the right.



3.10 Sketch of the principle behind Stall Regulation shown on the power curve (power vs wind speed), (a), and the lift curve (lift coefficient vs angle of attack), (b).

At low wind speeds the angle of attack is low and the lift is thereby also low (dashed lines), operating around maximum lift–drag ratio. The dotted line shows operation at wind speeds close to rated power and at corresponding lift values close to and at maximum lift. The dot-and-dash line shows the operation at high wind speeds where rated power is obtained, and the corresponding operation at high angles of attack in stall, resulting in a (nearly) passive limitation of the power. The stall regulation was a common concept for wind turbines of up to around 2 MW.

Using pitchable blades, both pitch and stall control are possible. However, the (active) stall controlled rotors have, in the case of the bigger rotors of between 500 kW and 2 MW, sometimes exhibited negative aerodynamic damping, which causes undesirable vibrations. Also, the (active) stall controlled rotors experience relatively high loads at high wind speeds compared to the pitch controlled rotors. Using pitch control requires much higher pitch activity, but because stall is avoided, the flow is more reliable and predictable. The pitch control concept is illustrated in Fig. 3.11, where, additionally, variable rotor speed is used at low wind speeds. This kind of control is pitch control in combination with variable rotor speed and is called pitch regulation variable speed (PRVS). Apart from variable rotor speed at low wind speeds, which is used to obtain constant tip speed ratio (λ or TSR), the blades will be pitched to limit output at high wind speeds. However, the blades can in some cases also be pitched for wind speeds between the region of variable rotor speed and the region with power limitation. In Fig. 3.11, it



3.11 Sketch of the principle behind pitch regulated variable speed (PRVS) showed on (a) the power curve (power vs wind speed) and (b) the lift curve (lift coefficient vs angle of attack).

can be seen that the angle of attack is low at high wind (dotted-and-dashed lines) and high (but not entering stall) close to rated power (dotted lines). Furthermore, the rotor load decreases at high wind speeds. Therefore, the loads for a pitch controlled wind turbine will in general be less than for a(n) (active) stall controlled wind turbine. In Fig. 3.11 the dashed line shows operation at low wind speeds at the power curve where the rotor operates at constant tip speed ratio, and corresponding operation at a lift value with high lift–drag ratio.

The common way of controlling today's Mega Watt (MW) turbines is through use of PRVS. However, in the 1970s, 1980s and 1990s, when the rated power of most turbines was below 2 MW, the turbines did not operate as a significant part of the power grid and there were fewer requirements as power quality. Also, the structural dynamics were less sensitive to the aerodynamic damping of the blades. Therefore, a very common control method was stall regulation, with constant rotational speed combined with fixed blades.

Thus, the correct choice of rotor control is necessary in order to:

- select airfoils that have proper design lift, maximum lift and stall characteristics;
- design the rotor in such a way that it can start up at a fairly low wind speed;
- design the rotor in such a way that rated power can be kept fairly constant in all high wind speeds;
- design the rotor at the correct tip speed ratio.

3.4.4 Design constraints

Previous sections have pointed out that rotor design should not focus only on maximizing power production, but also on other aspects relevant to the main objective of reducing the cost of energy. Many constraints affect the ability to achieve this ideal, and these are dependent on, e.g. the rotor size and the selected materials. Examples of such constraints are:

- The maximum chord has to be lower than a certain value so that the blade can be transported, e.g. by truck on roads and below bridges. This is not necessarily an issue, however, if the rotor is going to be installed offshore and therefore transported by ship.
- The maximum chord should be such that the extreme loads, e.g. at standstill, do not cause high loads on other components, such as the tower.
- For structural reasons, the inner part of the blade has to be designed with thicker airfoils than on the outer part of the blade in order to withstand the loads.
- The rotor should be able to cut-in at a fairly low wind speed.
- In order to reduce noise emission the outer part of the blade can be twisted towards lower lift coefficients; this is because, according to current knowledge, noise emission increases for increasing angle of attack.²²
- The rotor speed has to be limited to prevent excessive loads on the whole wind turbine. However, for a given power, the loads on the shaft and the generator reduce with increasing rotor speed. Therefore the maximum rotor speed should be selected appropriately.
- As illustrated in Fig. 3.3, the thrust coefficient, which in general relates to the loads on many component parts of the wind turbine, can be reduced somewhat by reducing a slightly below $a = 1/3$ with only a small reduction in C_p . In this way, loads on the turbine can be reduced significantly without losing too much energy production.
- Pre-bend and/or pre-twist of the blade are options that allow blades to increase their clearance from the tower and obtain the desired twist irrespective of the torsional deformation, respectively. However, these options do not affect the aerodynamic design because the pre-bend ensures the intended maximum rotor area and the pre-twist ensures the intended twist distribution.

There are many other design constraints, depending on the manufacturing process, the particular rotor control concept and the particular wind turbine concept, and so the above is not an exhaustive list of issues, but only indi-

cates some of the most important aspects to be considered as part of the rotor design process.

3.4.5 Choice of number of blades

When choosing the number of blades, several considerations have to be taken into account, such as esthetics, tip loss, structural constraints and Reynolds numbers. Even though the rotor designer will often find that the number of blades is decided by other decision makers, there follows a summary of the relevant design considerations in order to draw a complete picture of the rotor design process.

- **Esthetics.** The design of the complete turbine, including the shape of the nacelle, the spinner and the tower, is important. Likewise the visual impact of the rotating blades is important. These issues pose the question: do two, three or four rotating blades (or even more) look nice?
- **Tip loss.** The rotor becomes more aerodynamically efficient when the number of blades is increased. This is because the distance between the vortex sheets in the wake of the rotor becomes smaller for an increasing number of blades, and therefore flow outside the wake does not flow in between the vortex sheets creating a more diffuse wake and thereby introducing loss. The loss of power efficiency when the number of blades is reduced from three to two is illustrated in Fig. 3.9.
- **Structural considerations.** Increasing the number of blades, for fixed design lift along the blade, reduces the chord length of each blade so as to keep the solidity of the rotor constant. With decreasing chord length, the relative thickness may need to be either increased or maintained, requiring more material to be used in the rotor. The increasing relative thickness generally makes the blade less aerodynamically efficient and the increased amount of material makes it heavier.
- **Reynolds number.** The Reynolds number is proportional to the chord length of the blade and the rotational speed. Therefore, an increase in the number of blades with fixed solidity of the rotor, σ , will result in a decrease of the chord length and thereby a decrease of the Reynolds number. Thus, in terms of Reynolds number, it is desirable to minimize the number of blades.
- **Transportation of blades.** Increasing the number of blades increases the need for transportation. For this reason, too, it is desirable to minimize the number of blades.
- **Manufacturing costs.** Increasing the number of blades increases the need for manpower and space in the manufacturing facility. Thus, reducing the number of blades saves on the costs of rotor manufacture.

3.4.6 Evaluation of the rotor design

When a rotor is aerodynamically designed, it needs to be evaluated to assess the response in terms of power and loads. For this purpose, aerodynamic or aeroelastic codes should be used. Several aerodynamic codes exist, but if an aerodynamic or aeroelastic code is not available, the background for creating an aerodynamic code can be found in Reference 18. Commonly used aeroelastic codes in the wind turbine industry in 2013 are, e.g. FLEX,²³ Bladed,²⁴ Phatas,²⁵ FAST²⁶ and HAWC2.²⁷ Running full aeroelastic computations also requires knowledge of the structural characteristics of the blades and the entire wind turbine.

An aerodynamic code requires the blade planform in terms of chord and twist as function of radius, rotational speed and pitch as function of wind speed, airfoil characteristics in terms of c_l , c_d and c_m as function of α for the different relative thicknesses along the blade, and possibly also losses in the drive train (gear box and generator) in order to predict the electrical power. This information should be provided as a part of the aerodynamic rotor design process.

3.5 An example of the rotor design process

In this section, a rotor for a 1 MW pitch regulated variable speed (PRVS) wind turbine will be aerodynamically designed. The design process has been simplified so that the power is maximized with no considerations of load reduction, even though it is very important to reduce loads on all the components on the turbine. Thus, the rotor is designed for an axial induction of $a = 1/3$ even though a slightly lower value might be more appropriate for load reduction. The process is divided into steps, but in reality each step can appear more than once because it is an iterative process, with knowledge gained there from sometimes proving to have been relevant for an earlier step. The process described for designing the blade does not require any tools other than a spread sheet or access to a programming language, such as Matlab, FORTRAN or C. However, in the evaluation process an aerodynamic or aeroelastic computer code would greatly facilitate a detailed evaluation of the rotor and the wind turbine. The resulting rotor is not meant as an example of an optimal rotor, but should be viewed only as an illustration of the method.

It should be noted that several steps in the design process are probably irrelevant for many rotor designers, as many parameters will have been specified by other decisions makers. The specified parameters could be for example, wind climate, rotor diameter, rated power and hub height and within these constraints the optimum rotor should be designed. However, for the sake of completeness all steps in the design process are considered.

3.5.1 Step 1: Wind climate

Even though the wind turbine under consideration here could be erected at many different sites, a representative wind climate needs to be agreed upon. Standards exist,²⁸ in which turbines are classified by site characteristics such as low/high wind speeds and low/high turbulence. However, in this example, for demonstration purposes, it has been decided to erect the turbine on an inland site at Værløse in Denmark, as listed in Reference 29, p. 146, where the Weibull distribution in 10 m height is given as:

$$F\{V_{10\text{min}} \leq V\} = 1 - \exp(-(V/A)^k)$$

with $A_{h,\text{measured}} = 4.7 \text{ m/s}$, $k_{h,\text{measured}} = 1.55$ and $h_{\text{measured}} = 10 \text{ m}$. The roughness length in Værløse is estimated to $z_0 = 0.01 \text{ m}$, which corresponds to airport runway areas and terrain surface characteristics ranging from very smooth surfaces, e.g. water areas to smooth surfaces, e.g. farmland. The hub height of the wind turbine is set to 60 m and therefore Weibull parameters for this height should be predicted. However, this hub height is based on a rule of thumb which states that the hub height is approximately equal to the rotor diameter. The rotor diameter is set at approximately 60 m, based on experience of other 1 MW turbine projects. It should be emphasized, however, that the hub height is a decision that is part of the overall design of the wind turbine and depends, among other parameters, on the wind climate, because the increase in wind speed as a function of height varies from site to site. Assuming that the wind shear is logarithmic and there are no changes in roughness close to the site, the wind climate parameters will be:

$$A_h = A_{h,\text{measured}} \frac{\ln(h/z_0)}{\ln(h_{\text{measured}} / z_0)} = 5.9 \text{ m/s}$$

$$k_h = k_{h,\text{measured}} = 1.55$$

3.5.2 Step 2: Size of rotor/generator

The choice of the size of the rotor and generator should be made so that the cost of energy is minimized. In other words, the ratio between the wind turbine cost and the predicted energy production in the lifetime of the wind turbine should be minimized. Therefore, a thorough study should be carried out based either on experience of wind turbine costs or based on cost

models. However, in this case the problem is simplified and, based on the knowledge of factor A_h , which is fairly low, it is decided to choose 12 m/s as the rated wind speed, which is approximately 6 m/s higher than the average wind speed on the site. Maximum C_p at rated wind speed is set to $C_p = 0.25$, which will be used to estimate the rotor diameter. The rotor size can be predicted using Equation [3.44]. With $P_{\text{rated}} = 1.0 \text{ MW}$, $V_{\text{rated}} = 12 \text{ m/s}$, $\rho = 1.225 \text{ kg/m}^3$ and $C_p = 0.25$ the rotor must be designed with a diameter of approximately 70 m or a radius of 35.0 m. It should be noted that the trend in recent years has been towards rather big rotors, when compared to the generator size, so some manufacturers might choose an even bigger rotor diameter and therefore a lower rated wind speed.

3.5.3 Step 3: Rotor control

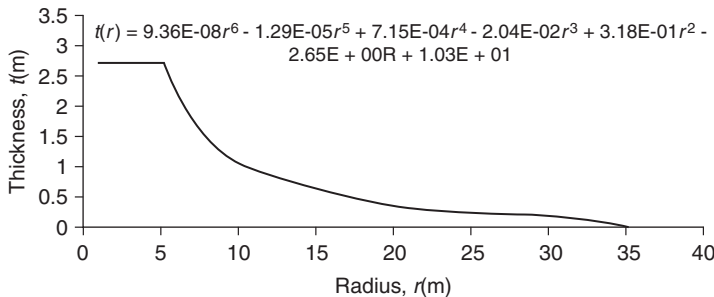
Even though it has been decided that the rotor control in this case is to be of the pitch regulated variable rotor speed (PRVS) type, it is important at this stage to consider the process for choosing the type of control, as set out in Section 3.4.3. The choice of rotor control will be dependent on the size of the rotor and the wind turbine and on the philosophy of the design. In addition, the components forming part of the rotor control, such as the pitch bearings and the variable speed generator, should be considered in order to take the total cost of the turbine, including operation and maintenance costs, into account.

If it were decided to design a stall controlled rotor the same procedure as sketched in the following Steps 4 to 8 could be used. However, if such a rotor were to operate with constant rotational speed, this speed should be selected and considered in relation to the wind speeds which supply the majority of the annual energy. In addition, account should be taken of the fact that the blade design can result in an excess of power at high winds so that the predicted power from the rotor exceeds the desired rated power. The power at high wind can be reduced by maintaining the twist at the outboard part of the blade and twisting the inner part of the blade so that it enters stall at lower wind speeds.

3.5.4 Step 4: Design constraints

There are a number of constraints which the rotor design should fulfill:

- The maximum chord should be limited. In this case it is set to 3.0 m for transportation reason. However, this limit depends on the capacity of the blade manufacturer to transport the blade.
- The maximum tip speed is set to 75 m/s. This is to reduce the maximum noise emission. The tip speed of 75 m/s corresponds to a maximum rotational speed of 20.46 RPM.



3.12 Initial estimate of the thickness distribution of the blade.

- The initial guess for the thickness of the blade is based on structural considerations. Often the aerodynamic rotor design will be based on a distribution based on experience from an earlier design. The structural design should fulfill different requirements, such as a maximum tip deflection and minimizing the weight (i.e. increasing the thickness) without losing too much aerodynamic efficiency. An example of such a thickness distribution is shown in Fig. 3.12. In this example the thickness distribution should simply be considered as an input to the aerodynamic design process. However, when evaluating the rotor design after the aerodynamic rotor design process is carried out, the weighting between the structural and the aerodynamic performance could possibly change the thickness distribution. In Fig. 3.12, a polynomium is shown to describe the thickness distribution from 5.14 m and outwards. For radii less than 5.14 m, the thickness is constantly 2.70 m.

3.5.5 Step 5: Choice of number of blades

For this size of turbine, the number of blades significantly influences transportation, maintenance and rotor costs. Therefore, the number of blades should be reduced as far as possible without compromising the energy production, loads, noise emission and esthetics. This analysis should be based on thorough cost and market estimations. However, since the cost estimation is outside the scope of this chapter, a traditional three-bladed rotor is assumed in this case.

3.5.6 Step 6: Choice of design lift and airfoils

As stated in Chapter 4, several different airfoils exist which can be used for wind turbine rotors. For this rotor, airfoils common in rotor design will be used: the NACA 63–4xx from relative thicknesses $t/c = 15\text{--}21\%$ and FFA-W3-xxx from relative thicknesses $t/c = 24\text{--}36\%$. The airfoil characteristics are shown in Figs 3.13–3.16. When evaluating possible airfoils it is important

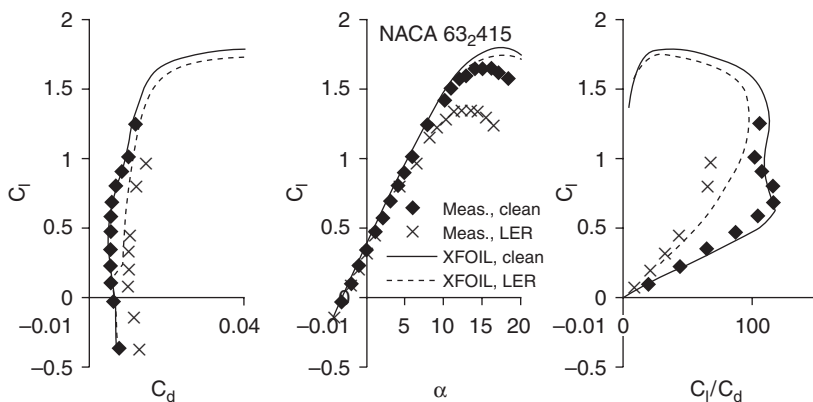
to know at which Reynolds numbers the blade will operate. As a rule of thumb, the Reynolds number will be between $Re = 75\,000R$ and $150\,000R$, which in this case, with $R = 35$ m, is between 2.6×10^6 and 5.3×10^6 .

Wind tunnel measurements exist for most of the chosen airfoils. Measurements on the NACA 63-4xx airfoils are described by Abbott and Doenhoff.²⁰ They are measured at $Re = 3 \times 10^6$ and 6×10^6 . For this purpose $Re = 6 \times 10^6$ has been chosen, because measurements with leading edge roughness (LER) also exist and because most of the energy will be produced for the airfoils operating at the higher end of the Reynolds number interval.

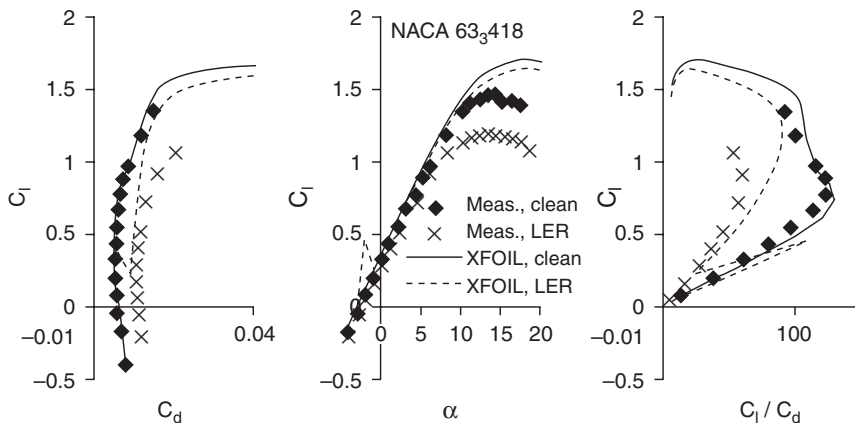
The FFA-W3-xxx airfoils are wind tunnel tested for only the 24% and 30% relative thickness. In addition, the existing wind tunnel tests have been carried out at $Re = 1.6 \times 10^6$, so the design has to rely on measurements based on Reynolds numbers that are too low. Furthermore, data for leading edge roughness for the 30% airfoil is not available.

When analyzing the airfoil characteristics, much emphasis should be put on performance with leading edge roughness (LER), because the rotor will most probably frequently operate with dust and debris on the blade leading edge, which will reduce the airfoil efficiency.

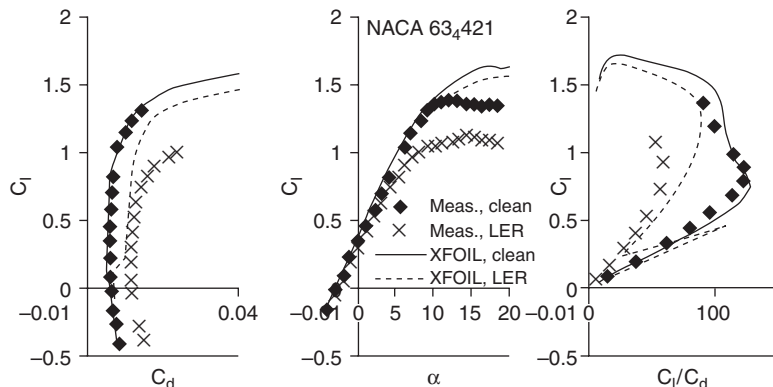
It is obvious from Figs 3.13–3.17 that the computations by XFOIL do not predict the airfoil characteristics very well for the thick airfoils, whereas the predictions are quite good for the thinner airfoils. Even though uncertainties exist for wind tunnel data, considerable emphasis should be put on



3.13 2D airfoil characteristics for NACA 63₂415 at $Re = 6 \times 10^6$. (*Source:* Measurements from References 20 and 30). Computations using XFOIL. XFOIL,clean is free transition and XFOIL,LER is forced transition and computed according to the description in Chapter 4.

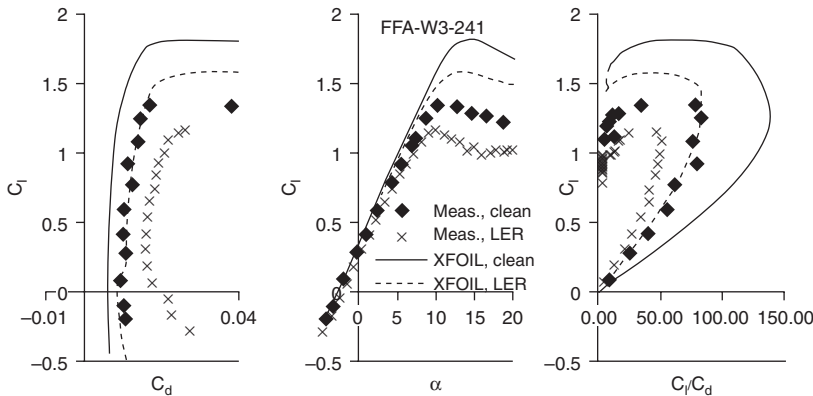


3.14 2D airfoil characteristics for NACA 63₃418 at $Re = 6 \times 10^6$. (Source: Measurements from References 20 and 30). Computations using XFOIL. XFOIL,clean is free transition and XFOIL,LER is forced transition and computed according to the description in Chapter 4.

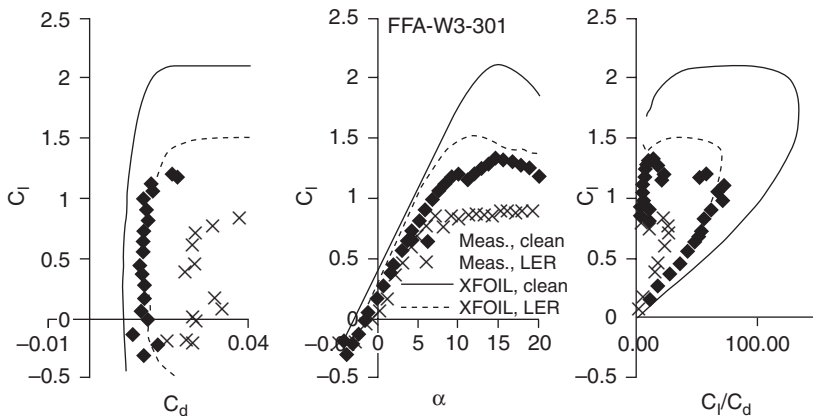


3.15 2D airfoil characteristics for NACA 63₄421 at $Re = 6 \times 10^6$. (Source: Measurements from References 20 and 30). Computations using XFOIL. XFOIL,clean is free transition and XFOIL,LER is forced transition and computed according to the description in Chapter 4.

these data, because XFOIL and other flow simulation tools do not generally predict separated flows very accurately. However, if data are missing for airfoils, a rule of thumb is to simulate the airfoil performance assuming full turbulent flow, i.e. ‘XFOIL, LER’, to introduce a measure of conservatism and then use these data as a basis for the blade design.



3.16 2D airfoil characteristics for FFA-W3-241 at $Re = 1.6 \times 10^6$ for the measurements and $Re = 6 \times 10^6$ for the computations. (Source: Measurements from References 30 and 31.) Computations using XFOIL. XFOIL,clean is free transition and XFOIL,LER is forced transition and computed according to the description in Chapter 4.

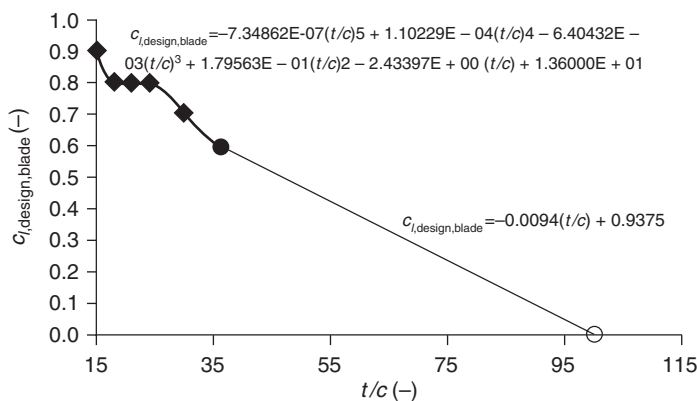


3.17 2D airfoil characteristics for FFA-W3-301 at $Re = 1.6 \times 10^6$ for the measurements and $Re = 6 \times 10^6$ for the computations. (Source: Measurements from References 30 and 31). Computations using XFOIL. XFOIL,clean is free transition and XFOIL,LER is forced transition and computed according to the description in Chapter 4.

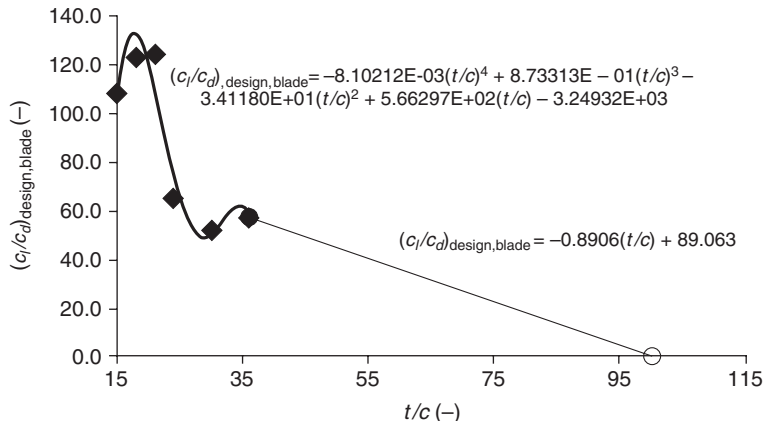
The airfoil characteristics for the rotor should be used when the wind turbine performance is to be simulated at higher wind speeds. However, for the blade design process, the airfoil characteristics should be analyzed to find the lift coefficient used in the blade design, $c_{l,\text{design,blade}}$, and the

corresponding lift–drag ratio, $(c_l/c_d)_{\text{design,blade}}$, and angle of attack, $\alpha_{\text{design,blade}}$. Figures 3.18–3.20 show the distribution of these entities as a function of relative airfoil thickness, which will be used in the blade design process. These values are mainly based on the maximum lift from leading edge roughness measurements and reduced with Δc_l of approximately 0.4 to include a reserve in the operation, so that gusts or further reduction in maximum lift caused by even more severe leading edge roughness will not cause premature separation or stall. Thus, it should be noted that the lift coefficient used in the blade design, $c_{l,\text{design,blade}}$, ought to be equal to the lift coefficient for each airfoil for which the maximum lift–drag ratio exists, $c_{l,\text{design}}$. However, this is generally not possible because of the requirements of attached flow at all wind speeds. Since the data with leading edge roughness is based on severe contamination, the chosen design lift value is somewhat conservative and some designers would choose a higher design lift because this will result in a more slender blade, which again will result in reduced extreme and fatigue loads for the entire wind turbine. Another comment on the choice of $c_{l,\text{design,blade}}$ is, that it should be chosen so that the value is somewhere between the value measured or computed with clean surface and leading edge roughness, respectively, with the weight of, e.g. 70% clean surface and 30% leading edge roughness. This is to take into account the variations in blade surface quality over time.

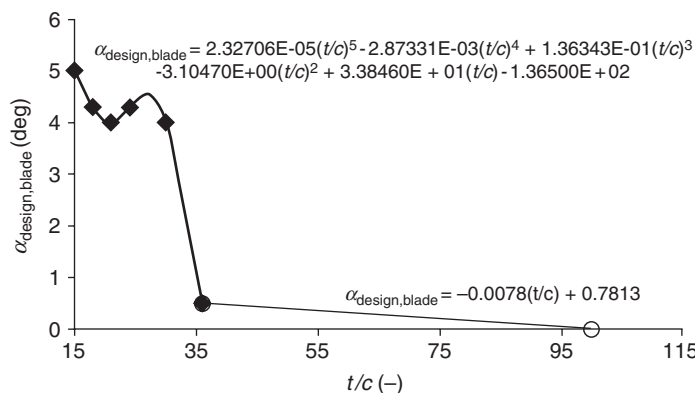
As shown in Figs 3.18–3.20, it has been decided to describe the distribution of the entities using polynomial functions as trend lines because these are relatively smooth and easy to use. The smoothness of the functions will result in a smooth shaped blade. Other trend line functions exist and can



3.18 Distribution of $c_{l,\text{design,blade}}$ as a function of the relative thickness of the airfoil. A 5th order polynomial describes $c_{l,\text{design,blade}}$ from $t/c = 15\text{--}36\%$ and for t/c between 36% and 100% a linear relation is used as shown on the plot.



3.19 Distribution of $(c_l/c_d)_{\text{design,blade}}$ as a function of the relative thickness of the airfoil. A 4th order polynomial describes $(c_l/c_d)_{\text{design,blade}}$ from $t/c = 15-36\%$ and for t/c between 36% and 100% a linear relation is used as shown on the plot.



3.20 Distribution of $\alpha_{\text{design,blade}}$ as a function of the relative thickness of the airfoil. A 5th order polynomial describes $\alpha_{\text{design,blade}}$ from $t/c = 15-36\%$ and for t/c between 36% and 100% a linear relation is used as shown on the plot.

be used as well. Despite the relative smoothness of the functions they show abrupt changes between the 21% and 24% airfoil for the blade design lift-drag ratio distribution and between the 30% and 36% airfoil for the blade design angle-of-attack distribution. It should be noted that care should be taken to ensure that the smooth function is close to the actual values and that no under- or over-shoots of the function appear.

3.5.7 Step 7: Choice of design tip speed ratio

The choice of design tip speed ratio will in this case be simplified and, as previously mentioned, will be based only on maximizing the power coefficient C_P . No considerations concerning load reduction are to be taken into account. As a result of Step 6 it is known that the rotor operates with a lift–drag ratio for the thin airfoil sections of around 120. According to Fig. 3.9, a design TSR of 9 is appropriate for this lift–drag ratio to obtain maximum power efficiency.

3.5.8 Step 8: One point design of blade

In the previous steps, the basis of the blade design has been worked out. To summarize, we are now working on:

- a radius of 35 m,
- three blades,
- a maximum chord length of 3.0 m,
- a tip speed ratio of 9,
- a description of the blade design lift and the corresponding blade design angle of attack and blade design lift–drag ratio, and
- an estimated thickness distribution.

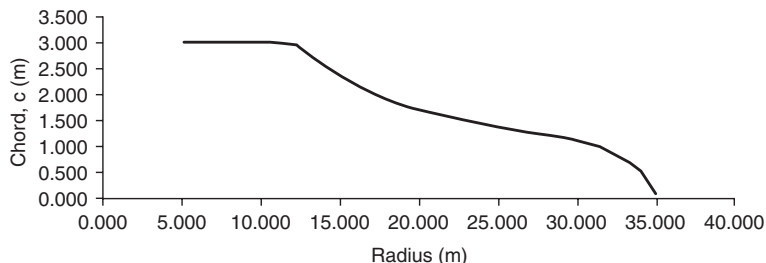
Based on this information, it is possible to design a blade in one point, i.e. at one tip speed ratio. Because the rotor is to operate with PRVS control this one point design will work well at low wind speeds, as long as the variable speed control is active. The planform is shown in Table 3.1 within the bolded lines, and the corresponding quantities are shown on the right of the table. In each column of the table a reference is found to the corresponding equation needed to describe the entity. The planform is plotted in Figs 3.21–3.23. In Fig. 3.21 it is noted that the root part, from around $r = 8$ m and inboards, has an uncommon shape. Often a transition area is needed from the airfoil part to a cylindrical part which will connect the blade to the hub and the pitch bearings. This is not taken into account in this design, where only the aerodynamic performance is in focus. However, this transition area should be corrected for in the final blade design.

3.5.9 Step 9: Evaluation of the blade design

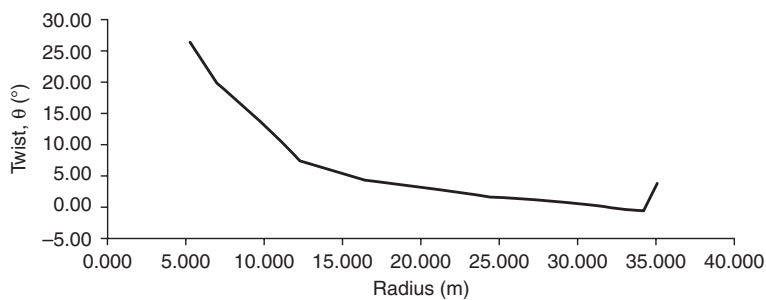
The blade as designed in Step 8 should now be evaluated to reveal the aerodynamic performance, with power performance and load performance also being investigated, as well as the annual energy production. The aerodynamic

Table 3.1 Entities used in the blade design process. In each column there is a reference to an equation that describes the entity

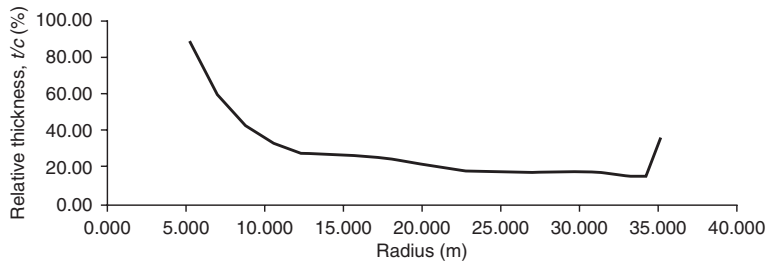
R	c	θ	t/c	ϕ	$a_{\text{design,blade}}$	f	F	a'	σ	c_x	c_y	c_{blade}	$(c/c_d)_{\text{design,blade}}$	λ_{loc}	t
5.250	3.000	26.03	87.77	26.12	0.10	19.304	1.000	0.007	0.273	0.040	0.105	0.112	10.891	1.35	2.633
7.000	3.000	19.65	59.26	19.97	0.32	17.566	1.000	0.005	0.205	0.120	0.361	0.380	36.283	1.80	1.778
8.750	3.000	15.73	43.04	16.18	0.45	16.149	1.000	0.021	0.164	0.138	0.515	0.533	50.728	2.25	1.291
10.500	3.000	11.77	33.75	13.60	1.83	14.881	1.000	0.020	0.136	0.137	0.607	0.622	61.550	2.70	1.012
12.250	2.963	7.35	28.31	11.73	4.38	13.703	1.000	0.019	0.115	0.133	0.716	0.728	48.769	3.15	0.839
14.000	2.583	5.86	27.52	10.34	4.48	12.533	1.000	0.015	0.088	0.118	0.732	0.741	49.197	3.60	0.711
15.750	2.244	4.67	26.76	9.24	4.57	11.415	1.000	0.012	0.068	0.109	0.758	0.766	52.839	4.05	0.600
17.500	1.974	3.88	25.26	8.35	4.47	10.331	1.000	0.010	0.054	0.102	0.783	0.789	62.801	4.50	0.499
19.250	1.774	3.44	23.00	7.61	4.16	9.268	1.000	0.008	0.044	0.097	0.797	0.803	85.370	4.95	0.408
21.000	1.644	2.98	20.31	6.99	4.01	8.218	1.000	0.007	0.037	0.090	0.792	0.797	116.427	5.40	0.334
22.750	1.523	2.25	18.47	6.46	4.21	7.175	1.000	0.006	0.032	0.084	0.792	0.797	130.888	5.85	0.281
24.500	1.407	1.66	17.77	6.01	4.35	6.140	0.999	0.005	0.027	0.078	0.798	0.802	132.764	6.30	0.250
26.250	1.314	1.28	17.84	5.62	4.34	5.110	0.996	0.004	0.024	0.072	0.798	0.801	132.693	6.75	0.234
28.000	1.230	1.01	18.19	5.27	4.26	4.083	0.989	0.004	0.021	0.067	0.795	0.798	131.929	7.20	0.224
29.750	1.136	0.67	18.05	4.96	4.29	3.059	0.970	0.003	0.018	0.063	0.797	0.799	132.306	7.65	0.205
31.500	0.992	0.12	16.86	4.69	4.57	2.038	0.917	0.003	0.015	0.061	0.816	0.818	130.863	8.10	0.167
33.250	0.720	-0.53	15.00	4.45	4.98	1.018	0.765	0.003	0.010	0.061	0.889	0.891	108.681	8.55	0.108
34.125	0.536	-0.67	15.00	4.33	5.00	0.509	0.589	0.003	0.007	0.060	0.898	0.900	105.847	8.78	0.074
34.983	0.1120	3.49	35.50	4.23	0.74	0.010	0.091	0.002	0.034	0.601	0.602	0.601	60.019	9.00	0.043



3.21 Chord distribution.

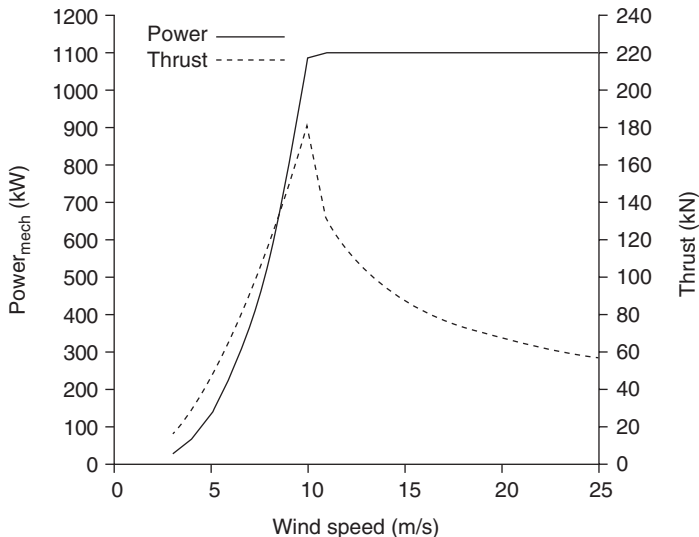


3.22 Twist distribution.



3.23 Relative thickness distribution.

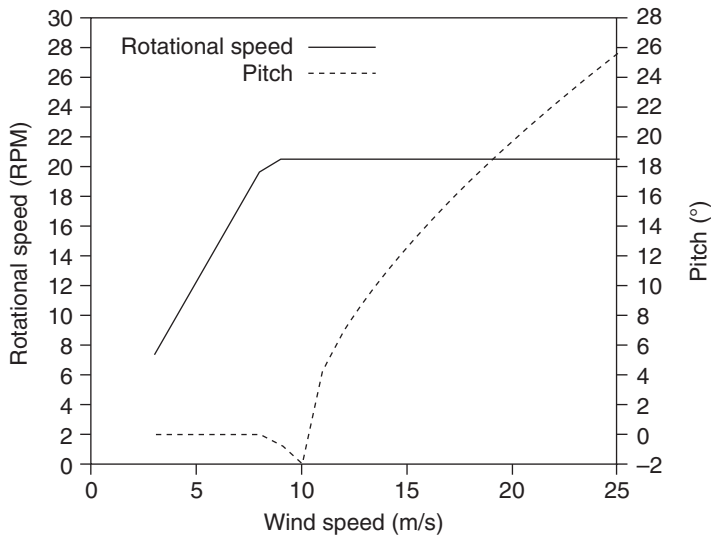
tool HAWTOPT,² developed at DTU Wind Energy, Denmark, will be used. However, before commencing the evaluation, the airfoil characteristics should be corrected for three-dimensional flow effects such as centrifugal and Coriolis forces, which appear when the flow starts to separate. For this purpose, the models mentioned in Chapter 4 can be used. In general, these corrections will increase the maximum lift the closer the airfoil sections are to the hub. The corrections are important for precise estimation of the rotor performance for the PRVS concept, but because most of the rotor experiences attached flow in normal operation the influence of the 3D effects are



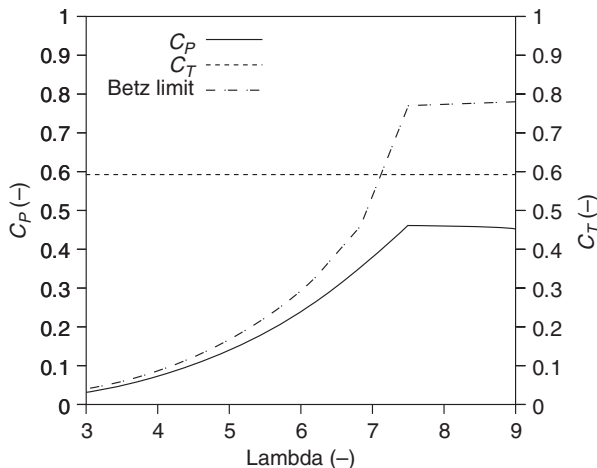
3.24 Mechanical power and thrust as a function of wind speed – so-called power and thrust curves.

fairly small. However, if a rotor for a stall regulated turbine were designed, the rotor would experience, for high wind speeds, separated flow on the entire rotor, and the 3D corrections would be crucial for making fair predictions of power and loads. In this example the 3D correction model by Bak *et al.*³² is used.

The power without drivetrain losses and the thrust are shown in Fig. 3.24 assuming a drivetrain loss of approximately 10%. In addition, Fig. 3.25 shows the corresponding rotational speed and pitch. It can be seen that the rated power obtained is slightly above a wind speed of 10 m/s and not 12 m/s as estimated. This might be due to a relatively optimistic power curve, where the power at the ‘knee’ of the power curve is not obtainable in a real turbine because of the fast changes in the pitch curve at these wind speeds. However, consideration should be given to whether the rotor is the right size in relation to the generator to obtain minimum cost of energy. For this purpose, it is important to predict the annual energy production (*AEP*). With the given control settings and on the given site $AEP = 2270$ MWh. Relating *AEP* to the number of hours in a year, the mean mechanical power for the rotor in this wind climate is 259 kW. This is 25.9% of the rated power, which agrees well with the rule of thumb of 25% for traditional wind turbine rotors. However, the trend for the newest rotor designs is that this value is increasing up to 30% and even 40%, which corresponds to the trend of increasing rotor diameters for fixed generator size.

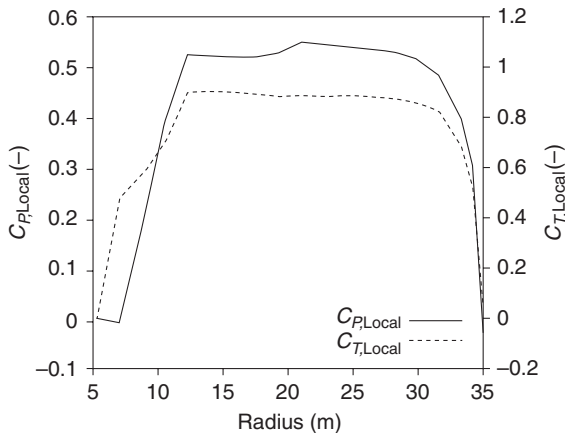


3.25 Rotational speed and pitch as a function of wind speed.

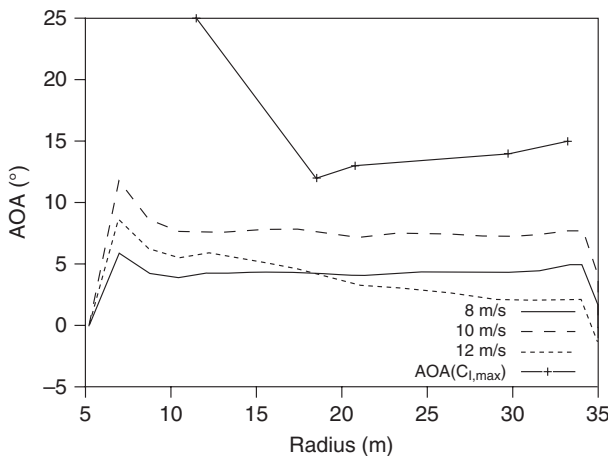


3.26 Power and thrust coefficient as a function of tip speed ratio λ .
Also, the Betz limit is shown.

Figure 3.26 shows the power coefficient and the thrust coefficient. It is noted that the power coefficient is somewhat below the Betz limit. Analyzing this, Fig. 3.27 shows the local power and thrust coefficient, reflecting how the efficiency is distributed along the blade at a wind speed of 8 m/s. In terms of the power coefficient, the blade is rather inefficient on the inner part of the blade, especially from $r = 12$ m and inboards. This is partly due to



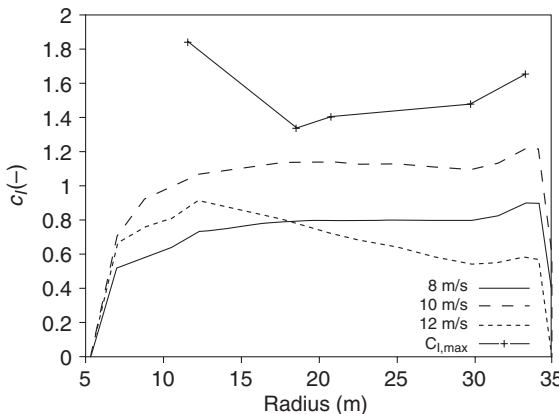
3.27 Local mechanical power and thrust coefficient as a function of rotor radius at a wind speed of 8 m/s corresponding to $\lambda = 9.0$.



3.28 Angle of attack as a function of radius.

the conservatism in the airfoil characteristics for the FFA-W3-xxx airfoils (which were measured at a lower Reynolds number than the number at which the rotor actually operates). In addition, a negative power coefficient is seen at the tip and at the root, which is due to the thick airfoil section of 35.5% relative thickness at the tip and the relative thickness of approximately 60% close to the root.

To ensure that the rotor will not produce too much noise and possibly lose power, the angle of attack during operation should be investigated. This is shown in Fig. 3.28 for the case of mean wind speeds. The corresponding

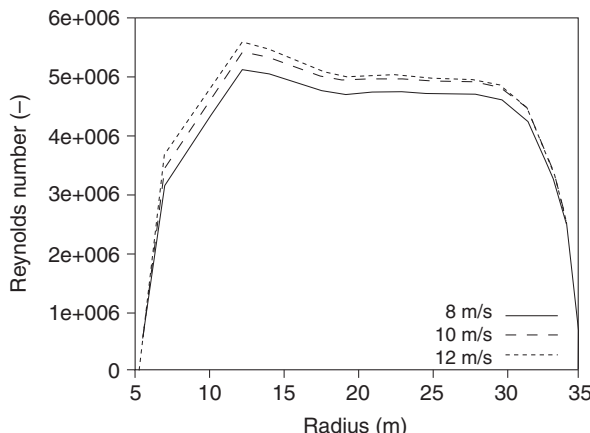


3.29 Lift coefficient as a function of radius.

lift coefficient, c_l , is shown in Fig. 3.29. However, gusts entering the rotor will result in a sudden increase in the angle of attack, potentially causing separation and corresponding noise and loss of power. Thus, even though Figs 3.28 and 3.29 show that the operation at a wind speed of 10 m/s is closest to maximum lift and that the rotor, even at this wind speed, will be free of separation and far from maximum lift, the performance, i.e. load, power and risk of separation, should be investigated using an aeroelastic code which uses the relevant wind climate parameters in terms of turbulence intensity and the Weibull distribution for which it is designed.

Figure 3.30 shows the Reynolds numbers as a function of radius at wind speeds from 8 to 12 m/s. At 8 m/s the rotor is still operating in the variable speed range, but at 10 and 12 m/s maximum rotational speed is obtained. It shows that the Reynolds numbers used from the wind tunnel tests correspond fairly well for the 18% and 21% relative thickness, with a maximum $Re = 5 \times 10^6$ on the blade compared to $Re = 6 \times 10^6$ in the tunnel. However, for the thicker airfoils, $Re = 1.6 \times 10^6$ as measured in the tunnel, is too low compared to the $Re = 5 \times 10^6$ on the blade. For the 15% airfoil the blade seems to operate at $Re = 3 \times 10^6$ on the blade, whereas $Re = 6 \times 10^6$, was used in the design process.

Analyzing the geometry of the blade planform, the chord distribution is relatively smooth and should cause no significant problems when creating the structure. However, the twist and the distribution in relative thickness are not as smooth, and so some adjustments might be necessary to allow the distribution of the different parameters to be smooth and to allow them to change continuously. Finally, the structural design should be analyzed for potential improvements concerning, e.g. strength, stress, strain and manufacturing process.



3.30 Reynolds number as a function of radius.

Using this (Step 9) evaluation of the design, a new iteration in the blade design process is carried out starting from the step at which the findings in the evaluation influence the design for the first time in the process. For the above design, new airfoil characteristics for $t/c = 15\%$ and for $t/c \geq 24\%$ should be obtained because they seem to affect the design too much. Therefore a new iteration in the rotor design process should be carried out starting at Step 6. However, if an aeroelastic code were used to show the load response from the entire wind turbine and if a proper cost function were set up, a new iteration in the rotor design process could start at an even earlier step, possibly beginning at Step 2, scaling the rotor diameter.

3.6 Future trends

With the increasing volume of wind turbines on the world market and the increasing interest in wind energy that is in evidence in 2013, it seems that several development lines in rotor design will be followed. One line is a new market for small wind turbines in the kW range. Many different concepts are being tested, as was the case at the end of the 1970s and in the early 1980s, and so for this size of rotor, the trend is not yet clear. Another line of development is the large MW wind turbine, which is based on experience gained in the early 1980s and up-scaling of concepts from that time.

As far as blade design for MW wind turbines is concerned, different shapes exist at the moment. The differences in shape relate to the degree of load reduction that is required. Some blades are designed with rather thin relative thickness of the airfoil sections from tip to root, and quite large chord lengths are allowed. Other blades are designed with large relative

thickness of the airfoil sections close to the root, with a transition area from the airfoil sections to a cylinder part and a correspondingly small allowable maximum chord length. This difference is due to the load predictions for the entire wind turbine in certain conditions, e.g. with the rotor idling in extreme wind. During recent years, there has been a trend towards slender blades to reduce the loads on the entire turbine. This type of design is often combined with quite a large rotor compared to the generator size in order to increase the swept area and thereby the power. Another way to reduce loads is to equip the blades with trailing edge flaps, so that they can actively reduce fluctuating loads. This technique is being developed and has been investigated for use on wind turbines since 2003.^{33–37} Increased use of sensors will probably also affect blade design with strain gauges and accelerometers being embedded in the blade for control or condition monitoring or laser measurements upstream of the rotor, e.g. the Wind Scanner³⁸ which is used for control of the rotor.

With the increasing volume of wind turbines on the market it seems increasingly cost-effective to design wind turbines and rotors for specific wind climates. Various aspects therefore need to be considered, such as whether the turbine is to be erected offshore or in complex terrain and whether it is to be erected on low wind sites or high wind sites. There is a trend towards designing turbines and rotors which are specialized for particular sites.

Irrespective of whether they are designed with large or small maximum chord lengths close to the root, there is a trend towards making blades more aerodynamically efficient. Especially as regards the inner part of the blade, where thick airfoils are used, much effort is put into the understanding and correct modeling of this part of the rotor, where high thrust close to the root has been observed to result in suction of the flow through the rotor because of swirl in the wake close to the hub.³⁹ Thus, more focus on thicker airfoils, and new concepts relating to the rotor aerodynamics of the inner part of the rotor, will probably be seen.⁴⁰

3.7 Sources of further information and advice

The design of rotors requires the use of different tools. In particular, the mechanisms that cannot be described by the Blade Element Momentum (BEM) method have been the subject of research since the 1980s, and, more recently, advanced tools such as Computational Fluid Dynamics have proved very useful. Wind tunnel tests on rotors have been carried out^{41,42} and rotor tests in atmospheric flow have also been carried out.^{43–46} Recently an experiment on a rotor for a 2.3 MW modern wind turbine was carried out, measuring both pressure distributions on the blade surface and fast pressure fluctuations up to 10 kHz in order to investigate the smallest eddies in the

turbulence characteristics around wind turbine blades in operation.^{47,48} Also, Siemens have carried out full scale experiments on a 2.3 MW wind turbine, measuring the aerodynamic performance.⁴⁹ In addition to these recent full scale tests, details of the aerodynamic rotor design have been investigated at different research institutions such as NREL (USA), UC Davis (USA), ECN (The Netherlands), Delft (The Netherlands), Stuttgart (Germany), FOI (Sweden) and finally DTU MEK and Risø National Laboratory (Denmark) (now merged and called DTU Wind Energy). Overviews of aerodynamic rotor design have been given by Tangler⁵⁰ and Snel.⁵¹

3.8 Acknowledgements

I wish to thank my colleagues at DTU Wind Energy, Denmark, particularly the Aeroelastic Design Section, which is a continuous source of inspiration. I especially wish to thank Mac Gaunaa, Flemming Rasmussen and Frederik Zahle from the Aeroelastic Design Program for fruitful discussion.

3.9 References

1. BTM Consult ApS, 'International Wind Energy Development. World Market Update 2011. Forecast 2012–2016'; BTM Consult, March 2012.
2. Fuglsang, P., Thomsen, K., Site-specific design optimization of 1.5–2.0 MW wind turbines. *J. Solar Energy Eng.*, **123**, 296–303, 2001.
3. Xudong, W., Shen W.Z., Zhu, W.J., Sørensen, J.N., Jin, C., Shape optimization of wind turbine blades. *Wind Energy*, **12**(8), 781–803, 2009.
4. ANSYS Fluent, www.ansys.com
5. ANSYS CFX, www.ansys.com
6. STAR-CD, www.cd-adapco.com
7. Michelsen J.A. Basis3d – a platform for development of multiblock pde solvers. Technical report afm 92–05, Technical University of Denmark, 1992.
8. Michelsen J.A. Block structured multigrid solution of 2d and 3d elliptic pde's. Technical report afm 94–06, Technical University of Denmark, 1994.
9. Sørensen N.N. General purpose flow solver applied to flow over hills. Risø-r-827(en), Risø National Laboratory, Denmark, June 1995.
10. Johansen, J., Madsen, H.Aa., Gauna, M., Bak, C., Sørensen, N.N., Design of a wind turbine rotor for maximum aerodynamic efficiency. *Wind Energy*, **12**(3), 261–273, 2009.
11. Sørensen, J.N., Shen, W.Z., Numerical modelling of Wind Turbine Wakes. *Journal of Fluids Engineering*, **124**(2), 393–399, 2002.
12. Mikkelsen, R., Actuator Disc Methods Applied to Wind Turbines, MEK-FM-PHD 2003–02, Technical University of Denmark, 2003.
13. Madsen, H.A., 'A CFD analysis of the actuator disc flow compared with momentum theory results', 10th IEA meeting on Aerodynamics, University of Edinburgh, 16–17 December 1996.
14. Voutsinas, S.G., Riziotis, V.A., Vortex particle modeling of stall on rotors. Application to wind turbines. Proceedings of the Fluids Engineering Division Summer Meeting, ASME, San Diego, 1996.

15. Glauert, H., Airplane Propellers. *Aerodynamic Theory Volume IV* edited by William Frederick Durand. The Dover edition 1963.
16. Wilson, R.E., Lissaman, P.B.S., Applied aerodynamics of wind power machines. Oregon State University. May 1974.
17. Andersen, P.S., Krabbe, U., Lundsager, P., Petersen, H., ‘Basismateriale for Beregning af Propellervindmølle’, Risø-M-2153(rev.), Risø, Januar, 1980 (in Danish).
18. Hansen., M.O.L., *Aerodynamics of Wind Turbines*, 2nd edition, Earthscan, 2008.
19. Prandtl, L., Betz, A., ‘Schraubenpropeller mit geringstem Energieverlust’, Göttinger Nachrichten, 1919.
20. Abbott, I.H., Doenhoff, A.E.von, *Theory of Wing Sections*, Dover Publications, 1959.
21. Bak, C., ‘Sensitivity of key parameters in aerodynamic wind turbine rotor design on power and energy performance’, Proc. The Science of Making Torque from Wind, *Journal of Physics: Conference Series*, **75**, 012008, 2007.
22. Brooks, T.F., Pope, D.S., Marcolini, M.A., *Airfoil Self-Noise and Prediction*, NASA Reference Publication 1218, USA, 1989.
23. Øye, S., ‘FLEX 4 – Simulation of Wind Turbine Dynamics’, Proceedings of the 28th IEA Meeting of Experts ‘State of the Art of Aeroelastic Codes for Wind Turbine Calculations’, pp. 71–76, Technical University of Denmark, Lyngby, Denmark, 11–12 April 1996.
24. Bossanyi, E.A., *GH-Bladed User Manual*, Issue 14, Garrad Hassan and Partners Limited, Bristol, UK, 2004.
25. Lindenburg, C., Schepers, J.G., ‘Phatas-IV Aero-elastic Modelling, Release’ DEC-1999 and NOV-2000, ECN-CX – 00–027, 2000.
26. Jonkman, J.M., Buhl, Jr., M.L., *FAST User’s Guide*, NREL/EL-500-29798, Golden, CO: National Renewable Energy Laboratory, 2005.
27. Larsen, T.J., Madsen, H.A., Hansen, A.M., Thomsen, K. Investigations of stability effects of an offshore wind turbine using the new aeroelastic code HAWC2. Proceedings of the conference, ‘Copenhagen Offshore Wind 2005’, 2005.
28. International Standard, IEC 61400-1 Edition 3.0, Wind turbines – Part 1: Design requirements, www.iec.ch
29. Troen, I., Lundtang, E.L., *European Wind Atlas*, Risø National Laboratory, Roskilde, Denmark.
30. Bertagnolio, F., Sørensen, N.N., Johansen, J., Fuglsang, P., Wind turbine airfoil catalogue. Risø-R-1280(EN), 151 p, 2001.
31. Fuglsang, P., Antoniou, I., Dahl, K.S., Madsen, H.A., ‘Wind Tunnel Tests of the FFA-W3-241, FFA-W3-301 and NACA 63-430 Airfoils’, Risø-R-1041(EN), Risø National Laboratory, Roskilde, Denmark, December 1998.
32. Bak, C., Johansen, J., Andersen, P.B., Three-Dimensional Corrections of Airfoil Characteristics Based on Pressure Distributions, Proc. European Wind Energy Conference & Exhibition (EWEC), 27 February–2 March 2006, Athens, Greece.
33. Buhl, T., Gaunaa, M., Bak, C., ‘Potential load reduction using airfoils with variable trailing edge geometry’, *Journal of Solar Energy Engineering*, **127**, 503–516, November 2005.
34. Andersen, P.B., Henriksen, L., Gaunaa, M., Bak, C., Buhl, T., Deformable trailing edge flaps for modern megawatt wind turbine controllers using strain gauge sensors, *Wind Energy*, **13**(2–3), 193–206, 2009.

35. Barlas, A., Kuik, G.A.M. van, 'State of the art and prospectives of smart rotor control for wind turbines', In the Proceedings of The Science of Making Torque from Wind, Lyngby, Denmark, August 28–31, 2007.
36. Yen Nakafuji, D., van Dam, C., Smith, R., Collins, S., 'Active load control for airfoils using microtabs', *J. Sol. Energy Eng.*, **123**, 282–289, 2001.
37. Castaignet, D., 'Model predictive control of trailing edge flaps on a wind turbine blade', PhD thesis, Technical University of Denmark, National Laboratory for Sustainable Energy, Wind Energy Department Roskilde, November 2011.
38. Mikkelsen, T., Mann, J., Courtney, M., Sjöholm, M., 'Windscanner: 3-D wind and turbulence measurements from three steerable doppler lidars', 14th International Symposium for the Advancement of Boundary Layer Remote Sensing, Earth and Environmental Science, **1**, 2008.
39. Johansen, J., Madsen, H.Aa., Gaunaa, M., Bak, C., Sørensen, N., 'Design of a wind turbine rotor for maximum aerodynamic efficiency', *Wind Energy*, **12**(3), s. 261–273, 2009.
40. Zahle, F., Gaunaa, M., Sørensen, N.N., Bak,C., 'Design and wind tunnel testing of a thick, multi-element high-lift airfoil', Proc. EWEA 2012 – European Wind Energy Conference & Exhibition, Copenhagen, Denmark, 16–19 April 2012.
41. Hand, M.M., Simms, D.A., Fingersh, L.J., Jager, D.W., Cotrell, J.R., Schreck, S., Larwood, S.M., 'Unsteady Aerodynamics Experiment Phase VI: Wind Tunnel Test Configurations and Available Data Campaigns', NREL/TP-500-29955, National Renewable Energy Laboratory, Golden, Colorado, USA, December 2001.
42. Snel, H., Schepers, J.G., Montgomerie, B., The MEXICO project (Model Experiments in Controlled Conditions): The database and first results of data processing and interpretation, Proc. The Science of Making Torque from Wind, *Journal of Physics: Conference Series*, **75**, 012014, 2007.
43. Madsen, H.A., Petersen, S.M. 'Wind turbine test Tellus T-1995, 95 kW', *Risø-M-2761*, Risø National Laboratory, Roskilde, 1989.
44. Brand, A.J., Dekker, J.W.M., de Groot, C.M., Spath, M., 'Field rotor aerodynamics: the rotating case', ECN-RX – 96-067, ECN, 1996.
45. Simms, D.A., Fingersh, L.J., Butterfield, C.P., 'NREL Unsteady Aerodynamics Experiment Phase III Test Objectives and Preliminary Results', Wind Energy 1995: Proceedings of the Energy and Environmental Expo '95, the Energy-Sources Technology Conference and Exhibition, 29 January–1 February 1995, Houston, Texas. SED-Vol. **16**, pp. 273–275.
46. Schepers, J.G., Brand, A.J., Bruining, A., Graham, J.M.R., Hand, M.M., Infield, D.G., Madsen, H.A., Paynter, R.J.H., Simms, D.A., Final report of IEA Annex XIV: Field Rotor Aerodynamics, ECN-C-97-027, Netherlands Energy Research Foundation, May 1997.
47. Madsen, H.A., Bak, C., Paulsen, U.S., Gaunaa, M., Fuglsang, P., Romblad, J., Olesen, N.A., Enevoldsen, P., Laursen, J., Jensen, L., 'The DAN-AERO MW Experiments. Final report', Risø-R-1726(EN), ISSN 0106-2840, ISBN 978-87-550-3809-7, Risø National Laboratory for Sustainable Energy, Technical University of Denmark, Roskilde, Denmark, September 2010.
48. Bak, C., Madsen, H.A., Paulsen, U.S., Gaunaa, M., Fuglsang, P., Romblad, J., Olesen, N.A., Enevoldsen, P., Laursen, J., Jensen, L., 'DAN-AERO MW: Detailed aerodynamic measurements on a full scale MW wind turbine', Proc. 2010 European Wind Energy Conference and Exhibition, Warsaw, Poland, 20–23 April 2010.

49. Medina, P., Singh, M., Johansen, J., Jove, A.R., Machefaux, E., Fingersh, L.J., Schreck, S., 'Aerodynamic and Performance Measurements on a SWT-2.3-101 Wind Turbine', WINDPOWER 2011 Anaheim, California, 22–25 May 2011.
50. Tangler, 'The Evolution of Rotor and Blade Design', Presented at the American Wind Energy Association WindPower 2000, Palm Springs, California, 30 April–4 May 2000.
51. Snel, H., 'Review of aerodynamics for wind turbines', *Wind Energy*, **6**, 203–211, 2003.

3.10 Appendix: Nomenclature

Symbol	Unit	Description
a	-	Induced axial velocity in rotor plane
a'	-	Induced tangential velocity in rotor plane
A	m^2	Area of rotor plane
A_h	m/s	Parameter in Weibull distribution relating to the mean wind speed
B	-	Number of blades on rotor
c	m	Chord length or distance from very leading edge to very trailing edge of airfoil
c_d	-	Drag coefficient
c_l	-	Lift coefficient
$c_{l,\text{design}}$	-	Lift coefficient at which $(c/c_d)_{\text{design}}$ is obtained (design lift)
$c_{l,\text{design,blade}}$	-	Lift coefficient used to design the blade (blade design lift)
$c_{l,\text{max}}$	-	Maximum lift coefficient
c_l/c_d	-	Lift–drag ratio
$(c_l/c_d)_{\text{design}}$	-	Maximum lift–drag ratio for airfoil section
$(c_l/c_d)_{\text{design,blade}}$	-	Lift–drag ratio at which $c_{l,\text{design,blade}}$ is obtained
c_x	-	Force coefficient on airfoil driving the rotor – parallel to rotor plane
c_y	-	Force coefficient on airfoil contributing to rotor thrust – orthogonal to rotor plane
C_p	-	Rotor power coefficient
C_T	-	Rotor thrust coefficient
D	N	Drag on airfoil
f	-	Exponent in the Prandtl tip correction formula
F	-	Prandtl tip correction
$F_{\text{tangential}}$	N/m	Force per length unit in tangential direction on an airfoil section
h	m	Height above ground at which the wind speed will be modeled
h_{measured}	m	Height above ground at which the wind speed is measured (commonly 10 m)
H	Pa	Stagnation pressure
k_h	-	Parameter in the Weibull distribution
$k_{h,\text{measured}}$	-	Parameter in the Weibull distribution determined from measurements
L	N	Lift on airfoil
p	Pa	Pressure in the rotor plane on the upstream side

Symbol	Unit	Description
p_0	Pa	Pressure far upstream and downstream of the rotor
P	W	Mechanical power from the rotor
P_{wind}	W	Power available from the wind
Q	Nm	Torque from the rotor
r	m	Radius locally on the blade
R	m	Tip radius
Re	-	Reynolds number
t	m	Maximum thickness of airfoil measured orthogonal to the chord
T	N	Thrust on rotor
T_{wind}	N	Thrust from the wind
TSR	-	Tip Speed Ratio = λ
u	m/s	Wind speed in the rotor plane
u_1	m/s	Wind speed far downstream in the rotor wake
V_0	m/s	Wind speed far upstream of the rotor
W	m/s	Relative velocity on the airfoil which is the combination of the axial and the tangential inflow
z_0	m	Terrain roughness length
α	°	Angle of attack
α_{design}	°	Angle of attack at which $c_{l,\text{design}}$ is obtained
$\alpha_{\text{design,blade}}$	°	Angle of attack at which $c_{l,\text{design,blade}}$ is obtained
Δp	Pa	Pressure jump over the rotor disc
ϕ	°	Angle between the relative inflow and the rotor plane
λ_{loc}	-	Ratio between the local tangential velocity of the rotor and the wind speed far upstream
λ	-	Ratio between the tangential velocity at the tip of the rotor and the wind speed far upstream (tip speed ratio)
ν	m^2/s	Air dynamic viscosity
ω	rad/s	Rotational speed of the rotor
ρ	kg/m^3	Air density
σ	-	Solidity of the rotor
θ	°	Pitch angle

Aerodynamic characteristics of wind turbine blade airfoils

W. A. TIMMER, Delft University of Technology,
the Netherlands and C. BAK, Technical University
of Denmark, Denmark

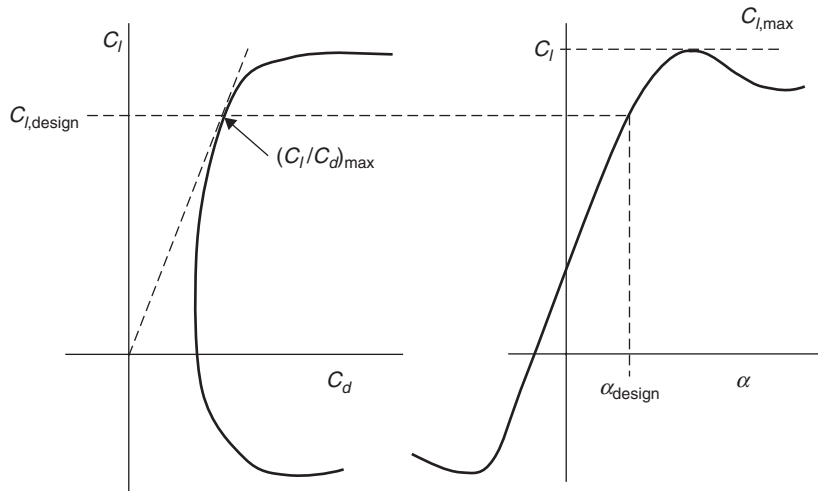
DOI: 10.1533/9780857097286.1.109

Abstract: This chapter focuses on airfoils for wind turbine blades and their characteristics. The use of panel codes such as XFOIL and RFOIL and CFD codes for the prediction of airfoil characteristics is briefly described. The chapter then discusses the requirements for wind turbine blade airfoils and the effect of leading edge roughness and Reynolds number. After a description of how airfoils can be tested the chapter discusses methods to represent airfoil characteristics at high angles of attack. A number of methods for correcting characteristics for the effect of three-dimensional flow on the blade are presented. The chapter then discusses ways to establish a data set for blade design and concludes with a view on future research in the field of wind turbine blade airfoils.

Key words: wind turbine airfoil characteristics, high angles of attack, leading edge roughness, stall delay.

4.1 Introduction

The layout of rotor blades, in terms of twist and chord distribution, depends on the choice of airfoils and consequently, to achieve high performance with acceptable loads, it is important to apply airfoils that are suitable for each specific spanwise part of the blade. Rotor designs until the mid 1980s primarily relied on aviation airfoils, mostly originating from the NACA 4 digit (e.g. NACA 44 series) and 6 digit (e.g. NACA 63 and 64 series) airfoil families.¹ The required thickness towards the blade root was generally achieved by linearly scaling up the coordinates of airfoils with smaller thickness. An exception was the FX 77 airfoil series by F. X. Wortmann at Stuttgart University, Germany, in the late 1970s. These airfoils were specifically developed for the Growian, a first generation 100 m diameter 3 MW turbine, which unfortunately was not very successful. It appeared that the thicker members especially of all these airfoil families suffered from an unacceptable degradation of their performance due to leading edge contamination. Between 1977 and 1984 Wortmann produced a number of airfoils for smaller wind turbines.



4.1 Key design parameters in the airfoil lift and drag characteristics.

The development of a new generation of dedicated wind turbine airfoils started in the mid-1980s with the designs of the S8xx airfoils by Somers and Tangler.² These researchers were followed by Björck,³ Timmer and van Rooij⁴ and Fuglsang and Bak.^{5,6} More recently, van Dam⁷ and other researchers in the USA presented so-called flatback airfoils for the inner part of the blade, characterized by trailing edge thicknesses of 10% chord or more. At present, some of the main wind turbine and blade manufacturers develop their own airfoils using optimization techniques. Others use the wind turbine dedicated airfoils designed by the researchers mentioned above, often in combination with the older aviation airfoils.

This chapter will focus on airfoils for wind turbine blades and their desired characteristics. The authors assume that the reader has a basic knowledge of aerodynamic concepts such as Reynolds number, pressure distributions, laminar and turbulent boundary layers, boundary layer transition and separation, and airfoil camber and thickness distributions. For an overview of general airfoil aerodynamics the reader is referred to text books, e.g. Anderson.⁸

Figure 4.1 presents some key design parameters pertinent to airfoil design, which will frequently be addressed in the following sections.

4.2 Computational methods

The design of new airfoils for wind turbine blades requires codes that have the capability to accurately predict the airfoil performance both in the clean and rough surface condition. At present most new airfoils are being designed

with panel codes, but with the ever increasing computational power, CFD codes are rapidly developing as a valuable tool for the design as well. In this chapter the use of both types of code will be briefly discussed.

4.2.1 Panel codes, XFOIL and RFOIL

For the design and analysis of airfoils, two panel codes are mainly used at present. Somers has used the Eppler code to design the SERI/NREL S8xx-series of airfoils.² However, the most popular code used as a tool for the design of wind turbine airfoils is XFOIL, developed by M. Drela at the Massachusetts Institute of Technology (MIT).⁹ XFOIL is a panel code with a strong viscid–inviscid interaction scheme, giving realistic boundary layer properties. The code uses the ‘e-to-the-nth’ method to predict transition. At present XFOIL forms the heart of many optimization codes for airfoil design, since it is fast and relatively easy to use. Moreover, apart from those for the stalled region and the very thick airfoils, XFOIL predictions are generally in fair agreement with measurements.

A derivative of XFOIL, RFOIL, was developed by the TU Delft, the National Aerospace Laboratory (NLR) and the Netherlands Energy Research Foundation (ECN).¹⁰ This code features a better convergence around the maximum lift due to the use of different velocity profiles for the turbulent boundary layer and due to modifications in the calculation of the turbulent boundary layer shape factor. This gives an amelioration of the predicted maximum lift coefficient.

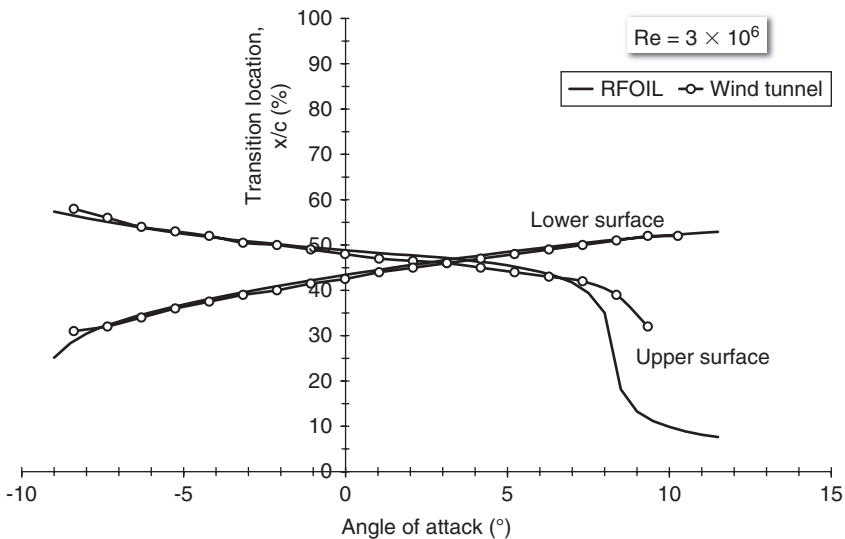
In general the prediction of the transition location is good, as demonstrated by Fig. 4.2. The figure shows very good agreement between the XFOIL/RFOIL predicted transition point and the one measured with a stethoscope in the Delft University wind tunnel.

In the main, the predicted airfoil performance with free transition is in fair to good agreement with measurements. Figure 4.3 shows the measured and RFOIL predicted characteristics for airfoil NACA 64₃–618 at a Reynolds number of 6×10^6 .

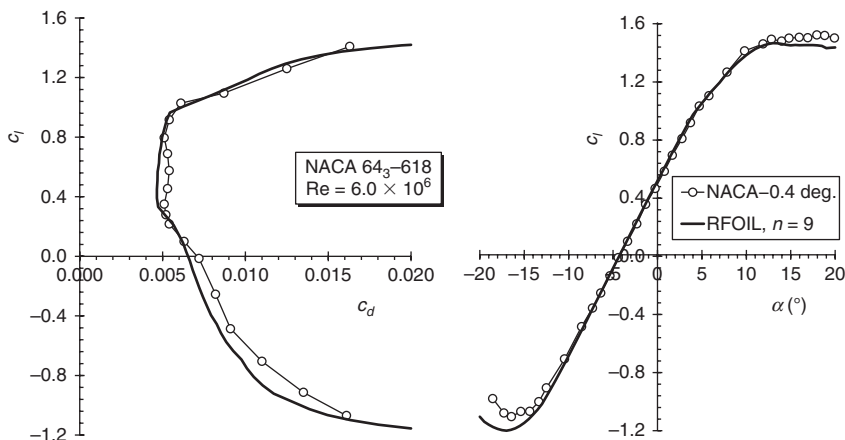
The general trend with RFOIL predictions is that for airfoil relative thicknesses of 18–21% the drag coefficient is underpredicted by about 8–10%. For thicker sections this difference increases. The lift curve for Reynolds numbers up to 6×10^6 is predicted quite well. At higher Reynolds numbers RFOIL tends to underpredict the $C_{l,\max}$.¹¹

4.2.2 Computational fluid dynamics

An alternative to panel codes like XFOIL and RFOIL is the use of computational fluid dynamics (CFD), also called Navier–Stokes codes. This type of



4.2 Comparison of the predicted transition location with RFOIL and the one measured with a stethoscope in the Delft University wind tunnel.



4.3 Comparison of the RFOIL predicted and measured characteristics for airfoil NACA 64₃-618¹ after modification of the angle of attack by -0.4° due to an assumed model zero-lift misalignment. The amplification factor n had the default value of 9.

method solves the non-linear and, in general, time-varying Navier–Stokes equations numerically. In this section, this method will only be briefly described. For further knowledge about CFD see, e.g. Ferziger.¹²

Many different codes exist, both commercial^{13–15} and research based.^{16–19} To use CFD computations to predict the aerodynamic performance of

airfoils several steps are needed. Each of these steps is briefly described below.

Investigation of airfoil contour

When it is decided to predict the aerodynamic performance of a 2-D airfoil contour the coordinates for this airfoil should be provided in terms of x and y coordinates. Often the coordinates are normalized with the chord length, so that the resulting coordinates are x/c and y/c , with the leading edge in $(x/c, y/c) = (0, 0)$ and the trailing edge in $(x/c, y/c) = (1, 0)$. With these coordinates as the basis the contour should be inspected for smoothness in shape, derivatives and curvature of the surface. Very small deviations in airfoil shape, introduced by for example erroneous splining of the surface, can cause small changes in the pressure distribution around the airfoil. This may lead to premature movement of the location of transition from laminar to turbulent flow towards the leading edge, and may ultimately result in an earlier stall.

Mesh generation

Generation of a mesh around the airfoil is necessary to resolve the changes in pressure, velocity and turbulent entities. In each mesh point, values are stored for the pressure, for the velocities in x and y direction, and for variables describing the turbulent quantities – which could, for example, be the turbulent kinetic energy and the specific dissipation. Several types of meshes can be generated, typically consisting of quadrilaterals or triangles, and referred to as structured or unstructured meshes. In a structured 2-D mesh for an airfoil a typical number of mesh points is 256 along the airfoil surface (starting at the trailing edge and ending at the same point via the leading edge) and 128 normal to the airfoil surface, resulting in 32 768 mesh points. When creating a mesh it is important to resolve the boundary layer in normal direction to the surface, to resolve the flow patterns in the direction of the surface contour and also to resolve the wake behind the airfoil. Specific requirements for the cell sizes in the boundary layer depend on the turbulence model used in the CFD solver.

Inspection of mesh

When the mesh has been generated, several geometrical checks have to be carried out. Without giving an exhaustive checklist, it is important to check for

1. orthogonality between the cells, to avoid too much skewness of cells,
2. change of cell size from one cell to its neighbor,

3. height of first cell from airfoil surface, so that the viscous sub-layer of the boundary layer at the airfoil is resolved,
4. the aspect ratio of each cell, and
5. the distance from the airfoil to the outer boundary/inlet/outlet, so that the solution is not unintentionally influenced by the boundary conditions, to avoid erroneous solutions. All checks can be automated and will to some extent be based on experience of the degree of deviation that is allowed.

Boundary conditions

When setting up the boundary conditions, the flow speed and direction at the inlet and outlet conditions are important. The inlet flow speed, together with the dynamic viscosity, the fluid density and the airfoil chord, determines at which Reynolds number the aerodynamic performance is predicted. Furthermore, the inlet flow direction determines at which angle of attack the computations are carried out. A constant pressure gradient is typically chosen as the value for an outlet boundary condition.

Turbulence model

Wind turbines operate in a Reynolds number regime and in such a way that turbulence is generated at some parts of the airfoil. Therefore pure laminar computations are insufficient, and either computations assuming fully turbulent flow from the leading edge or computations including the modeling of transition from laminar to turbulent flow are necessary. The turbulence created as a consequence of the boundary layer can be modeled by turbulence models, of which many exist. A commonly used model is the $k-\omega$ SST model,²⁰ which works very well for flows with adverse pressure gradients, which is the case for airfoil flow.

Computing

Even though CFD has a reputation for being time-consuming, the modern computers of 2013 can obtain a solution for a 2-D airfoil in around 10 seconds for one angle of attack provided that not too much separation/unsteadiness appears and that a fairly efficient CFD code is used. A polar consisting of e.g. 20 angles of attack, including angles of attack where separation appears, will take approximately 5 minutes. Therefore computational time is not a critical issue these days, when CFD is used in the evaluation of aerodynamic airfoil performance.

Inspection of results

Inspection of results from CFD computations can be carried out at several levels. The first step is to integrate pressure and friction distributions to the airfoil's lift, drag and moment, and analyze these values as a function of angle of attack. These values should be plausible according to the existing knowledge and experience of the user. The second step is to analyze the pressure and friction distributions to reveal unexpected performance. The third and final step is to analyze the flow field in terms of velocity vectors and velocity/pressure/turbulence contours. If all these checks seem to produce plausible values, the solution can be trusted. However, even though a plausible solution to the problem exists, an analysis of the grid resolution should be carried out by increasing the number of cells until the solution (e.g. the lift and drag coefficients) converges monotonically to a unique solution. If the solution is time dependent, a study of time step dependence is also necessary, where the time step is reduced until the solution converges.

4.2.3 Panel codes vs Navier–Stokes codes

In the evaluation of 2-D airfoil performance one can choose between a panel code and a Navier–Stokes code. However, each method has its advantages and drawbacks. A few key issues are listed below.

Computational speed

Predicting a lift–drag polar using a panel code takes a matter of seconds, whereas for the CFD code it takes minutes. Thus the CFD code runs approximately 50 times slower, depending on its computational efficiency. Even though the CFD code is more costly in terms of computational time, this is not necessarily critical or a barrier for using the codes. However, if numerous lift–drag polars are to be predicted, meaning that computational time is a critical factor, consideration should be given to options such as parallel computing.

Time for preparation

Comparing preparation time for the two types of codes, the CFD code needs more time than the panel code. Both types of codes need parameter sets, including which airfoil to predict, Reynolds number and angles of attack. In addition, the CFD code requires generation of a mesh. The amount of extra time needed for this to be done depends on the degree to which the processes are automated. Thus, mesh generation can be very time-consuming if

this is being done for the first time, whereas only seconds are needed if the user is experienced and the processes are automated.

Computational details

There is much more detail in CFD computations, from which many different kinds of entities can be extracted such as the pressure field, separation patterns and turbulent kinetic energy. The panel code does not have the same level of capabilities.

Comparisons to measurements

When it comes to comparing the computations to measurements, the CFD code will in general show better agreement than the panel code. Often the panel code will show steeper slopes of the linear part of the lift curve, and maximum lift assuming free transition may be overpredicted. However, in general, the linear part of the lift curve is rather well predicted by both codes, whereas the drag is somewhat underpredicted by the panel code. When separation occurs the CFD code will in general show better agreement with measurements than the panel code.

Summary

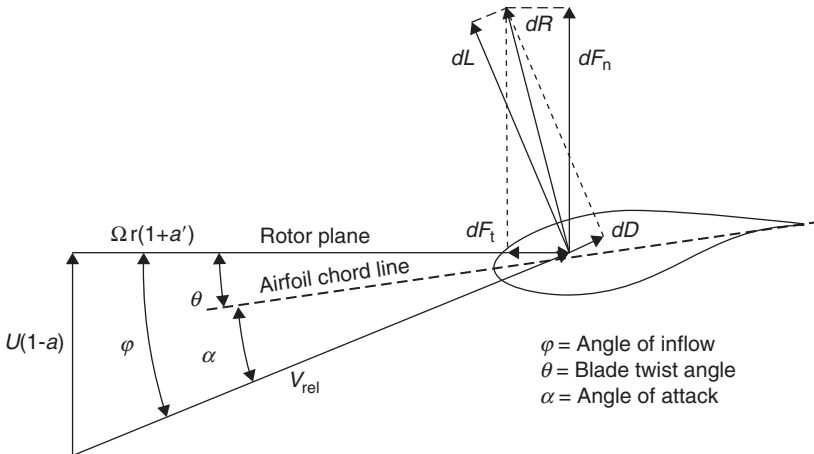
To summarize advantages and drawbacks for the two methods, the CFD code is superior to the panel code as regards agreement with measurements and computational details. However, both types of codes produce reasonable results, especially for the linear part of the lift curve. Concerning computational speed and preparation time the panel code is superior to the CFD code. Thus, whether a panel code or a CFD code should be chosen will depend on the problem that is to be solved, the level of accuracy required and whether computation time is a factor or not.

4.3 Desired characteristics

Wind turbine dedicated airfoils need distinctive characteristics generally not found in aerospace applications. In a blade, going from the root to the tip, the sections change significantly in maximum thickness and shape. This chapter addresses the required airfoil characteristics for various parts of the blade.

4.3.1 The velocity and forces on a blade element

In Fig. 4.4 the force and velocity vectors on a small spanwise element dr of the blade as a result of the rotational velocity and the wind speed are



4.4 Velocities and forces diagram on a blade segment.

displayed. The local chord on a radial distance r from the rotor axis is c and the velocity relative to the blade element is V_{rel} .

The lift force on the element is defined as:

$$dL = C_l \frac{1}{2} \rho V_{\text{rel}}^2 c dr \quad [4.1]$$

And for the drag force we have:

$$dD = C_d \frac{1}{2} \rho V_{\text{rel}}^2 c dr \quad [4.2]$$

Together they form the resultant force dR .

If we decompose the force dR in a component in the rotor plane and one perpendicular to the rotor plane (dF_t and dF_n respectively) we find for dF_t :

$$dF_t = dL \sin \varphi - dD \cos \varphi \quad [4.3]$$

Combining Equations [4.1], [4.2] and [4.3], and after some rearranging, we find for the torque force:

$$dF_t = \frac{1}{2} \rho V_{\text{rel}}^2 C_l c \left(\sin \varphi - \frac{\cos \varphi}{C_l / C_d} \right) dr \quad [4.4]$$

And for the bending force:

$$dF_n = \frac{1}{2} \rho V_{\text{rel}}^2 C_l c \left(\cos \varphi + \frac{\sin \varphi}{C_l/C_d} \right) dr \quad [4.5]$$

We see that for a given rotational speed and given wind speed both the force that gives the rotor torque, F_t , and the blade bending force F_n are governed by the term $C_l c$ and the lift–drag ratio of the airfoil C_l/C_d . A high value for the lift–drag ratio of the airfoil is desirable, since it increases the rotor torque and also reduces the bending moments on the blade for a specific lift value.

Designing wind turbine blades involves finding a balance between several sometimes conflicting requirements, as emphasized by the following examples:

- $C_l c$ needs to be at a certain level to obtain an optimum deceleration of the wind speed. Maximum power will be obtained when the flow is decelerated by approximately 1/3. Thus, high lift coefficients require low chord lengths and vice versa.
- In case of storm loads on a parked rotor, the blade area, and consequently the chord of the blade, should be kept small. Slender blades require high design lift coefficients of the airfoils to keep the term $C_l c$ at a sufficient level. However, using the same airfoils with slender blades reduces the absolute thickness of the blade sections, which – for sufficient stiffness and strength – may mean more material is required, thus increasing the weight.
- To reduce blade weight, airfoils with a high relative thickness can be used. However, compared to thinner airfoils thick airfoils have a higher drag. For a small part this comes from a higher friction drag due to the increased wetted surface. Thick airfoils also have higher upper surface velocities. The associated adverse pressure gradients cause additional growth of the boundary layer thickness, resulting in increased pressure drag. In case of leading edge soiling also premature flow separation will occur, which increases the pressure drag even further. Consequently, with respect to high lift–drag ratios over a sufficient range of angles of attack, they cannot compete with thinner airfoils.

Due to strength and stiffness considerations, the maximum airfoil thickness will increase from tip to root. Traditionally wind turbine blades have airfoil relative thicknesses of about 18% at the tip going to about 25% thickness halfway along the blade span. Airfoil thickness at the root can go up to 40% of the chord, then from the root there is a transition to a cylinder close to the

nacelle. However, manufacturers tend to increase this relative thickness for the very big multi-megawatt wind turbine rotors, with a view to decreasing blade mass while keeping tip deflection within limits.

According to Equations [4.4] and [4.5], for any part of the blade a high lift-to-drag ratio is desired and a choice must be made as to the value of the design lift coefficient, which, for the outer 50% of many modern blades, often lies between 1.1 and 1.25.

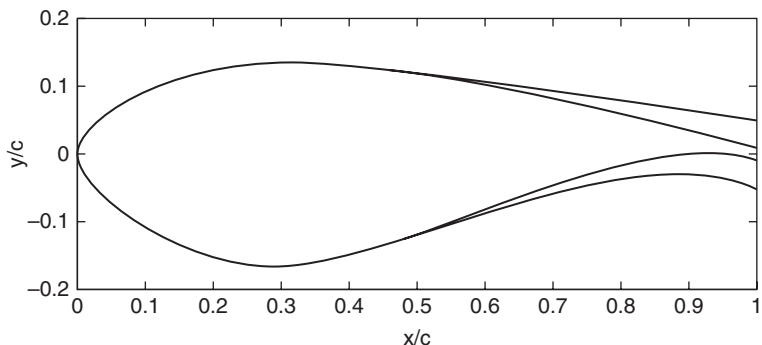
4.3.2 Outboard airfoils

For the outboard airfoils of a variable speed pitch-controlled wind turbine, the difference between the $C_{l,\text{design}}$ and the $C_{l,\text{max}}$ must not be too large, to prevent excessive loads in the case of gusts, and not too small, to prevent the rotor from stalling as a result of turbulence in the incoming flow. A difference between the $C_{l,\text{design}}$ and the $C_{l,\text{max}}$ of about 0.4, or in terms of the angle of attack about 4° or more, is considered to be sufficient. In a turbine using stall control, a high $C_{l,\text{max}}$ is advantageous since this leads to smaller chords and to lower storm loads. However, airfoils with a high $C_{l,\text{max}}$ tend to have a more abrupt stall and larger losses in post-stall lift, increasing blade dynamic excitations (see Chapter 5). Furthermore, the associated angle of attack in the case of roughness may be reduced by several degrees, giving large differences in lift at post-stall angles between the contaminated and the clean airfoil. The loss in rated power due to roughness of a fixed pitch turbine is proportional to these differences in lift.

Above rated wind speed, the fixed pitch stall-controlled turbine will have increasingly more separation on the blades, and so, to reduce fatigue loads, the post-stall performance of the blade airfoils must be benign in character. Where this is the case, no sudden large lift-loss due to stalling should occur.

4.3.3 Inboard airfoils

For structural reasons, significant section thickness is required in the root of the blade. Small root chords and restricted blade weight help to overcome problems of transportation of large blades and to keep down structural loads on the shaft and bearings. This calls for airfoils with a high relative thickness, typically 30–40% chord. The inboard segment of the blade requires a high maximum lift coefficient to deliver sufficient torque at the lower wind speeds. To achieve high lift, the inner 50% span of the blades of stall-controlled wind turbines is often fitted with vortex generators (VGs) and numerous wind tunnel tests have revealed that VGs can easily boost the maximum lift coefficient to over 1.9.



4.5 A flatback airfoil derived from an existing base airfoil, in this case DU 97-W-300.²¹

In a nutshell, desired airfoil characteristics are:

- A high lift-to-drag ratio to optimize aerodynamic performance;
- Benign stall characteristics to reduce fatigue loads;
- A high relative thickness to reduce blade weight;
- A high design lift coefficient giving small chords to reduce parking loads;
- Low susceptibility to leading edge contamination.

A flatback airfoil is an airfoil with a very thick trailing edge. The inclusion of a thick trailing edge gives increased lift and decreased sensitivity of the airfoil to blade soiling compared to the base airfoil, thus satisfying the latter two requirements at best. However, the drag is also increased, and unsteadiness in the wake is created due to bluff body vortices. Since the flatback airfoil will be in the inboard region of the blade the net result on the torque of the rotor may – despite the higher drag – be positive. Figure 4.5 shows a flatback airfoil derived from the DU 97-W-300.²¹

4.4 The effect of leading edge contamination (roughness) and Reynolds number

Contamination by insects and leading edge erosion create changes in the characteristics of the airfoils in a blade. This fact and the effect of the increasing Reynolds number with turbine diameter need to be carefully addressed for a successful blade operation in all conditions.



4.6 Contamination by insect debris on the leading edge of a wind turbine blade in Magallón 26 wind farm in Zaragoza, Spain.²²

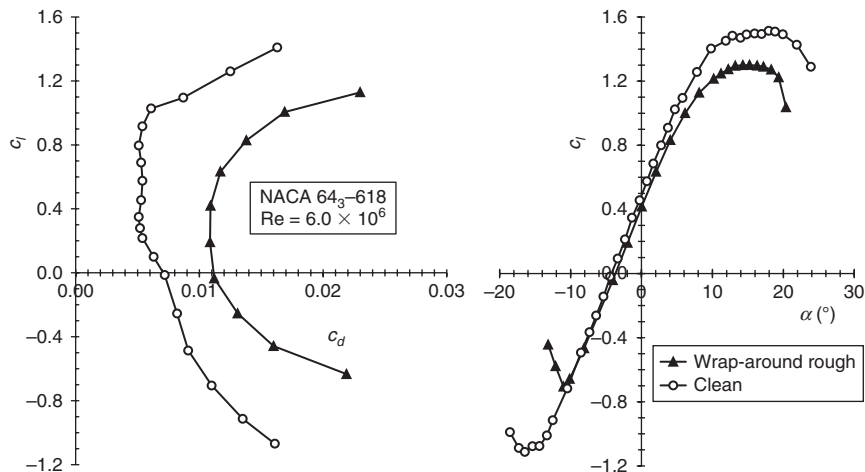
4.4.1 Effects of roughness

Since wind turbine blades, during their lifetime of approximately 20 years, will suffer some degree of soiling (predominantly from insect collisions, but in offshore machines also from salt crystals) and degradation of the material (caused by, e.g. delamination), the choice of airfoil will be influenced by the airfoil performance with a contaminated (or rough) leading edge.

The disappointing performance of existing aviation airfoils with rough leading edges was the reason that new airfoil designs were introduced in the late 1980s. The severity of contamination of the blades that is possible is depicted in Fig. 4.6. It shows the condition of the blade of a turbine in the Magallón 26 wind farm in Zaragoza, Spain after heavy soiling by insect debris.

Unfortunately, generally it is not known *a priori* how rough the blade will be and for how long. (In the case illustrated by Fig. 4.6 the insects fly only for a few weeks; however, without cleaning the blades or without rainfall, the roughness will be present for quite some time.) This obscures the direct choice of a set of airfoils, and hence blade design involves some guesstimating of how to incorporate the effect of roughness in the design.

In addition, the roughness on the blade is difficult to replicate during the verification of airfoil performance in the wind tunnel. Basically there are two ways to evaluate the effect of blade soiling in the wind tunnel: the application of wrap-around roughness, as was done during the design and testing campaign for the NACA airfoils, and the use of a tripping device, such as a wire, or a strip of roughness or zigzag tape on both sides of the model. Figure 4.7 shows the measured effect of grit roughness wrapped around the leading edge of airfoil NACA 64₃-618, the so-called NACA standard roughness.¹



4.7 The effect of NACA standard wrap-around roughness on the performance of airfoil NACA 64₃-618 at a Reynolds number of 6×10^6 . Zero-lift angle adjusted by -0.4° for an assumed model misalignment.

This type of roughness for the 0.61 m chord models consisted of 0.28 mm carborundum grains (no. 60 grit) applied to the airfoil surface at the leading edge over a surface length of 0.08c measured from the leading edge on both surfaces. The grains are thinly spread to cover 5–10% of this area. Figure 4.7 shows that the maximum lift–drag ratio is reduced from 170 to 60, a severe reduction of performance indeed.

There is a significant difference between wrap-around roughness and roughness at discrete chord locations (i.e. the NASA standard roughness), as is shown in Fig. 4.8 for the LS(1)-0417 airfoil.²³

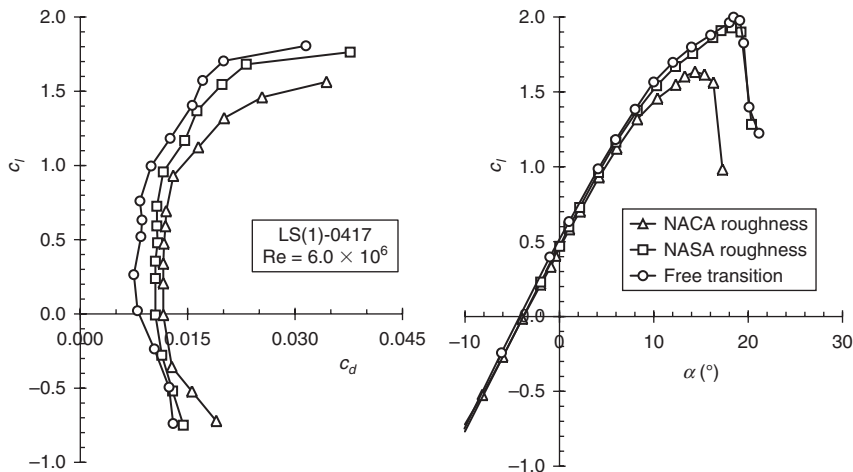
NASA standard roughness consisted of 2.5 mm wide strips with no. 80 grit at $x/c = 0.08$ both on the upper and lower surface.

The wrap-around roughness condition is mostly treated as a worst-case scenario.

4.4.2 The effect of the Reynolds number

The Reynolds number is a scaling parameter and basically gives the ratio of the mechanical forces in the flow (associated with velocity and mass or density of the fluid) and the viscous forces (viscosity). It is defined as

$$\text{Re} = \frac{\rho V c}{\mu} \quad [4.6]$$



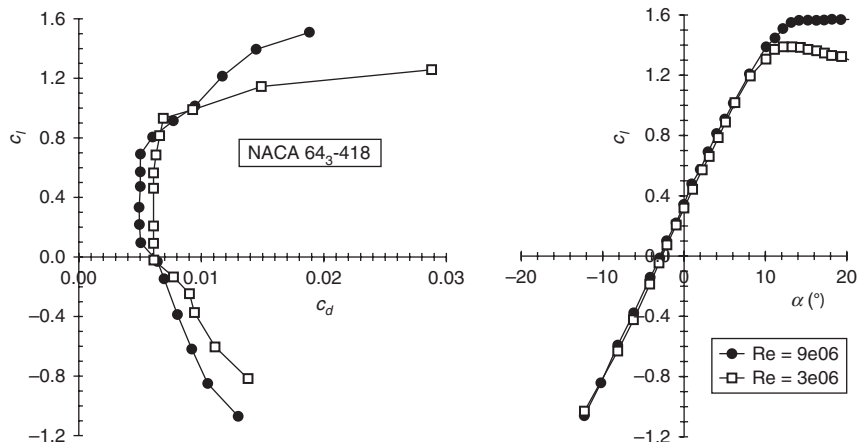
4.8 The effect of NACA standard roughness and NASA standard roughness on the performance of airfoil LS(1)-0417.²³

V is the test section velocity, c is the model chord, ρ is the density of the fluid and μ is the dynamic viscosity of the fluid. The ratio μ/ρ is called ν , the kinematic viscosity, also depending on the fluid density and temperature. For dry air at standard sea level conditions the value of ν is 14.6×10^{-6} . The higher the Reynolds number, the lesser the viscosity plays a role in the flow around the airfoil.

With increasing Reynolds number the boundary layer gets thinner, which results in a lower drag. Increasing the Reynolds number also has a destabilizing effect on the boundary layer flow, which results in the transition location moving towards the leading edge, leading to a turbulent boundary layer over a longer part of the airfoil surface. The net effect is a lower drag but a smaller low-drag range of angles of attack. This implies that the maximum lift–drag ratio will increase, but that the design lift coefficient will have a lower value.

This is demonstrated in Fig. 4.9 for airfoil NACA 64₃-418. At a Reynolds number of 3×10^6 the maximum lift–drag ratio is 131 at a lift coefficient of 0.93. At the higher Reynolds number of 9×10^6 the maximum lift–drag ratio has increased to 138 at a reduced lift coefficient of 0.69.

The example demonstrates that for a good design the characteristics at the right Reynolds number should be derived. Since most data are available at a lower Reynolds number it may be tempting to use these data for the blade design without translation to a higher Reynolds number. This will create uncertainty in the rotor efficiency.



4.9 The aerodynamic performance of airfoil NACA 64₃-418 for $Re = 3 \times 10^6$ and 9×10^6 .

4.5 Airfoil testing

To verify the calculated two-dimensional characteristics of airfoil designs, wind tunnel measurements can be performed. Although this might seem a simple task, in practice it is rather difficult to create the right testing environment to be able to really compare the calculated and measured properties of an airfoil design. Reynolds number, model accuracy, test section velocity, uniformity and turbulence intensity, model blockage, test section longitudinal pressure gradient, test setup and testing apparatus all have to be accurate to give a good result. These ingredients of a successful test do not stand on their own.

As an example, let us look at the Reynolds number. Equation [4.6] gives, with μ/ρ replaced by ν ,

$$Re = \frac{v \cdot c}{\nu} \quad [4.7]$$

In atmospheric tunnels, the maximum attainable Reynolds number is set by the maximum test section velocity (max. installed power) and by the maximum allowable model chord (acceptable blockage of the test section at the higher angles of attack). In most wind tunnels the turbulence intensity also goes up while approaching the maximum velocity. The blockage of a test section is expressed in terms of the blockage parameter c/h , with h being the test section height (or width when the model is in the vertical position). Acceptable values of c/h for a test around the maximum

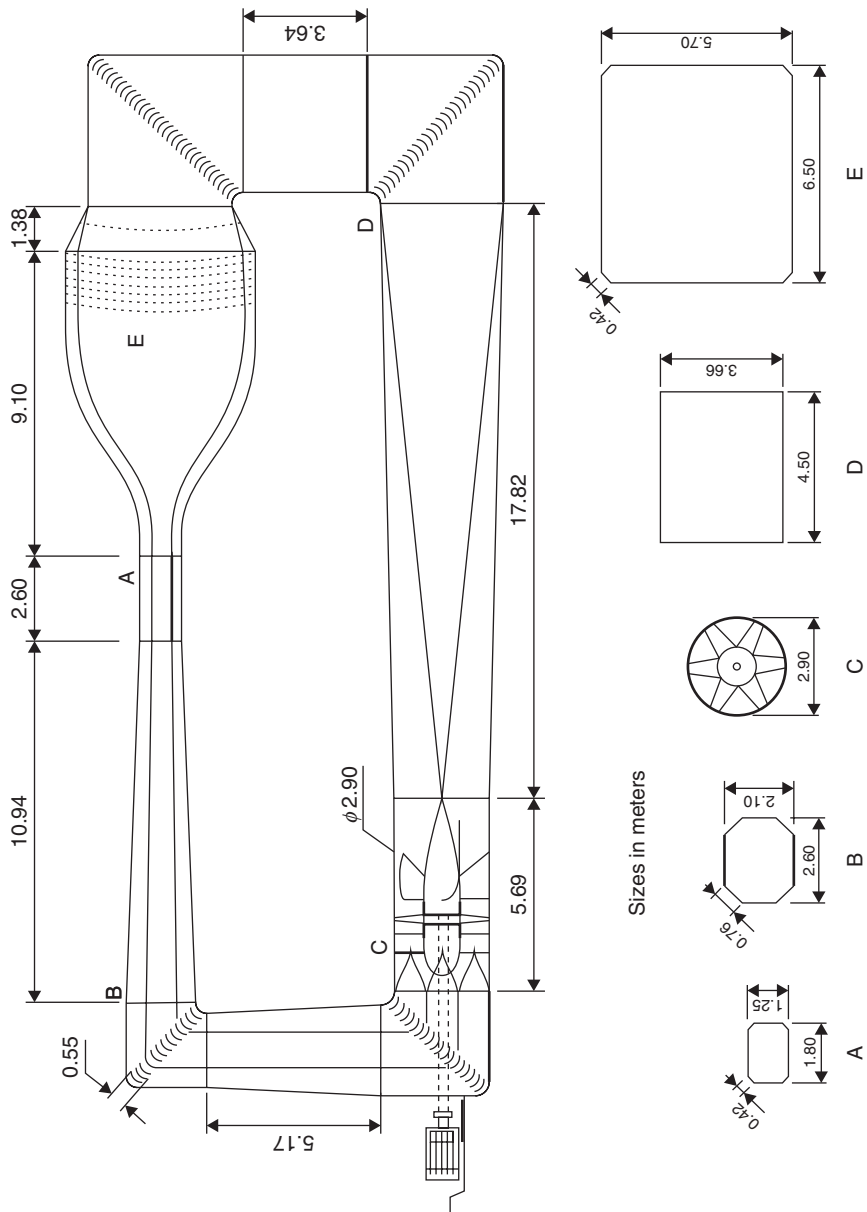
lift coefficient are in the order of 0.3–0.35. Modern turbines easily reach Reynolds numbers of 6×10^6 or higher. To get to this Reynolds number, according to Equation [4.7], we need a model chord of about 1 m with a test section velocity of 90 m/s at standard sea level conditions. The resulting test section dimensions are about 3×2 m, which brings the physical aspect ratio of the model to an acceptable value of 2. For the proper flow quality in terms of velocity uniformity and turbulence intensity a tunnel contraction ratio of at least 9 is desired, giving plenum chamber dimensions of 6×9 m. This already shows the size of the facility. For the combination of a test section area of 6 m^2 and a velocity of 90 m/s an installed power of close to 1 MW is needed. It is not difficult to see that, since facilities of this size are not widespread, doing the proper test is often simply a matter of budget.

In an atmospheric wind tunnel of the size sketched above, Reynolds numbers above 6×10^6 can be obtained by increasing either the velocity or the chord length. Increasing the velocity, however, results in inflow Mach numbers of close to 0.3 and may lead to compressibility effects locally on the airfoil. Increasing the chord length may compromise targets for tunnel blockage and model aspect ratio.

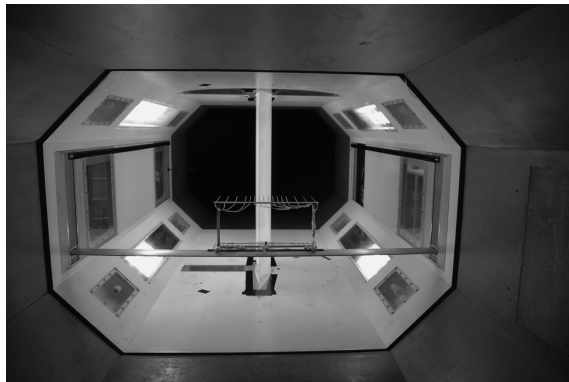
Another way of increasing the Reynolds number is to lower v in Equation [4.7]. This can either be done in a tunnel with pressurized air (a pressure tunnel) or in a tunnel with an arrangement to lower the temperature of the tunnel gas drastically (a cryogenic tunnel). These are expensive facilities, and in both cases the costs may increase to more than ten times the cost of a test in an atmospheric tunnel.

Most two-dimensional testing is performed in closed circuit tunnels, although open jet tunnels are being utilized as well. In the latter case a test stand is fully submerged in the jet and the two-dimensionality of the flow is ensured by end plates at both sides of the model. Depending on the correction scheme and the size of the end plates this might give some anomalies in the airfoil's post-stall angle of attack range. Due to the higher power needed for open jet facilities, the achievable Reynolds number is generally much lower compared to closed test section tunnels.

An example of a closed circuit atmospheric tunnel in which many wind turbine airfoils have been tested is the TU Delft low-speed low-turbulence wind tunnel. A schematic of the tunnel layout is given in Fig. 4.10. The tunnel is built in the vertical plane, and apart from a small part of the contraction and the test section diffuser the entire circuit is of concrete. The installed power is 580 kW. The contraction ratio is 17.8:1, which helps to give the very low-turbulence intensity of 0.02%. The latter is important for the comparison of measurements with calculated characteristics, since increased turbulence adversely affects the boundary layer stability and may lead to early transition.



4.10 A schematic of the Delft University low-speed wind tunnel.



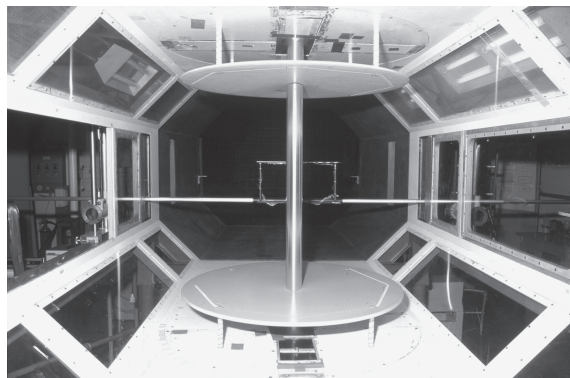
4.11 A model with pressure orifices installed in the test section.

4.5.1 Setup and testing equipment

Figure 4.11 shows a model in the TU Delft wind tunnel, looking upstream from behind the model. The model has pressure orifices to measure the surface pressure distribution. At both ends the model is attached to round plates flush with the tunnel walls to set the angle of attack.

In the foreground a wake rake is present at some distance behind the model trailing edge to measure the static and total pressures in the wake, from which the drag coefficient can be derived. The wake rake can move along the span (to check the two-dimensionality of the flow) as well as perpendicular to the model chord (so that it is positioned in the middle of the wake at all angles of attack). The pressures in most wind tunnels are measured with a system consisting of fast electronic pressure transducers with various ranges. Early separation of the model boundary layer at the tunnel wall–model junctions due to interference with the wall boundary layer may influence the flow over the entire model span. Some wind tunnels have a special system to avoid this flow interference either by blowing small air jets in a chord-wise direction at specific chord stations in the comers, or by suction of (part of) the wall boundary layers around the model leading edge.

Forces on a model can be measured if one or both ends of the model are attached to a balance system. If both model ends are not attached to small discs that are flush with (but free from) the tunnel walls then usually a small gap is present between the model and the tunnel walls. In Fig. 4.12 a test setup using the balance system of the Delft tunnel is depicted. To reduce the forces, inserts are present. This is also a way to avoid interference between the relatively thick boundary layer of the tunnel walls and the model boundary layer. The presence of the gaps transforms the model into a high-aspect-ratio-wing instead of a two-dimensional model. Depending on the width



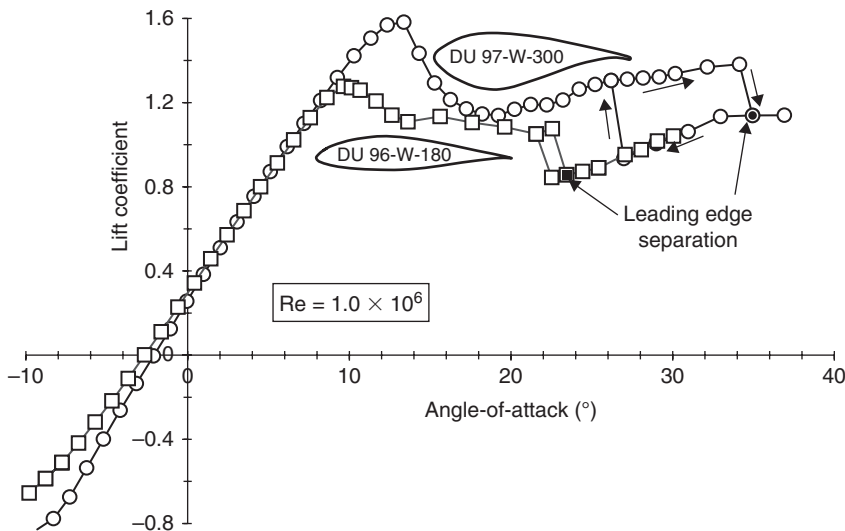
4.12 A test setup using a balance system. Tables are used to avoid interference between boundary layers of the tunnel walls and the model.

of the gaps and the aspect ratio of the model the test results need further treatment to remove induced effects on drag and angle of attack. The model is continued between the tables and the walls with separate parts that rotate with the model to ensure a uniform blockage over the entire test section passage.

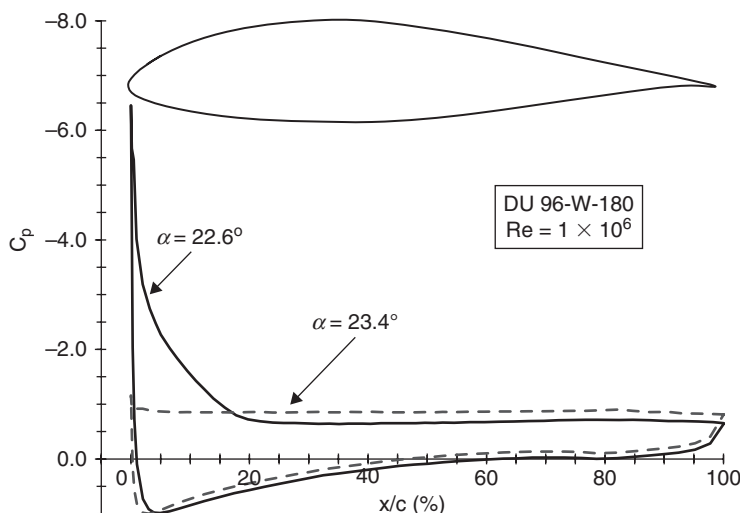
4.6 Airfoil characteristics at high angles of attack

When the angle of attack is increased beyond the static stall angle, the suction peak, and consequently the adverse pressure gradient, on the upper surface leading edge grows, while the separation point on the upper surface moves forward. At a specific angle of attack this adverse pressure gradient reaches such a high value that the boundary layer instantly detaches from the leading edge. The airfoil then enters what is called the ‘deep stall’ region, characterized by highly unsteady flow with vortices being shed from the airfoil with a certain frequency. Due to this periodic flow unsteadiness, the representation of airfoil performance in the deep stall region requires time averaging of the forces and pressures.

Since the value of the suction peak on the leading edge depends on the nose radius, the deep stall angle varies with airfoil shape. An example is given in Fig. 4.13. Figure 4.14 shows the associated pressure distributions for airfoil DU 96-W-180 just before and in deep stall. Timmer²⁴ derived a relation between the leading edge shape and the deep stall angle by correlating the measurements on a number of airfoils in the TU Delft low-speed low-turbulence wind tunnel: $\alpha_{\text{deep-stall}} = 0.1114(y/c)$, where y is the upper surface ordinate at the 1.25% chord station. The relation is graphically presented in Fig. 4.15. It must be noted that the onset of deep stall of an airfoil varies with Reynolds number,

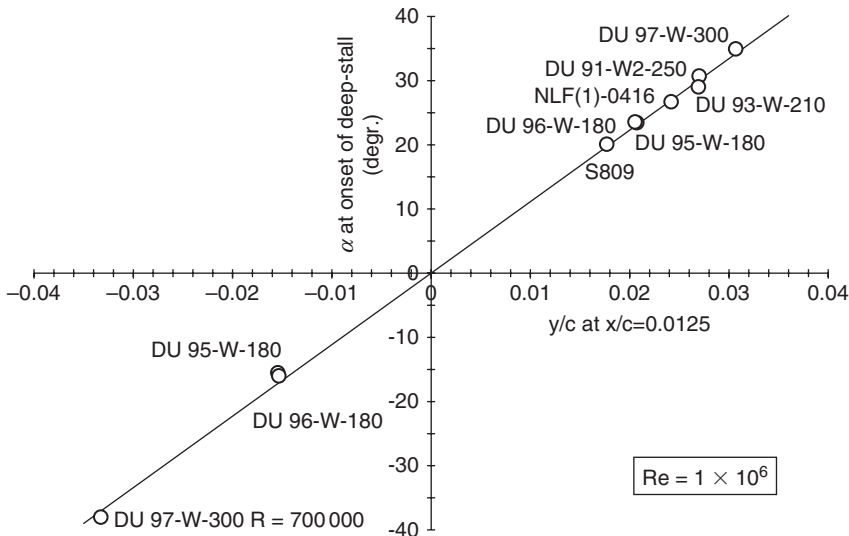


4.13 The measured lift curve for an 18% and a 25% thick wind turbine airfoil at a Reynolds number of 1.0×10^6 , showing the deep stall angle.²⁴



4.14 Measured pressure distributions for airfoil DU 96-W-180 at the boundary of the deep stall region.²⁴

turbulence intensity and general flow conditions on the leading edge (e.g. contamination). Figure 4.15 was constructed using wind tunnel tests in low-turbulence intensity flow for clean models at a Reynolds number of 1×10^6 . The deep stall angle may be notably different in other flow conditions.



4.15 Variation of deep stall angle with upper surface leading edge thickness for a number of wind turbine airfoils.²⁴

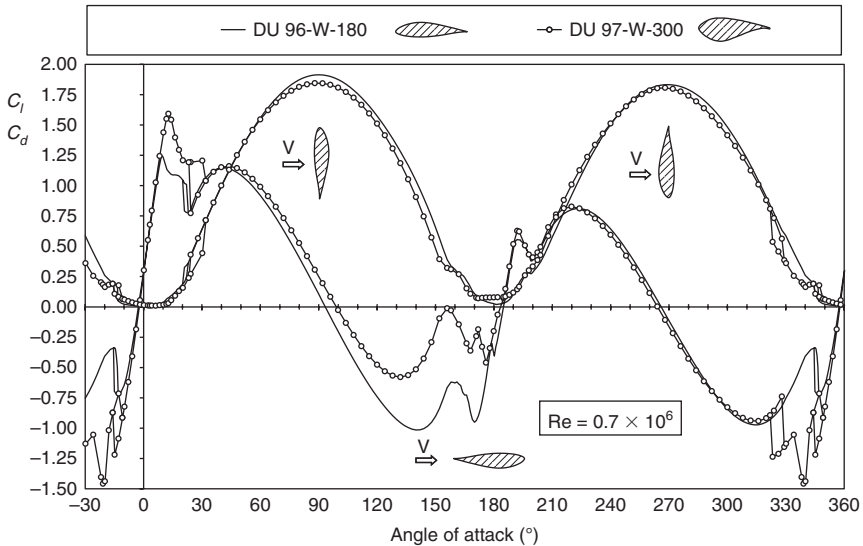
During starts and stops of a rotor and under parked conditions the blades see very high angles of attack and for the purpose of loads calculations it is necessary to establish the performance of the blade in these conditions. Generally this starts with an evaluation of the quasi-steady two-dimensional characteristics of the airfoils incorporated in the blade. Figure 4.16 gives an example of the characteristics at high angles of attack for two wind turbine airfoils measured in a wind tunnel.

Since these measurements have not been performed for all wind turbine airfoils, and the deep stall characteristics cannot be derived without using lengthy CFD calculations, a number of methods for modeling the lift and drag curves on the basis of existing information have been presented.

Viterna and Corrigan²⁵ proposed an empirical model following from derivation of the post-stall airfoil performance, assuming constant rated power for three rotor configurations, of a 100 kW and a 200 kW stall-controlled wind turbine, using strip theory. The method is widely used and returns values for the lift and drag coefficient at high angles of attack starting from the stall point of the airfoil lift curve.

The equations are partly based on the variation of the maximum flat plate drag coefficient with aspect ratio as proposed by Hoerner,²⁶ given in Equation [4.8]:

$$C_{D,\max} = 1.111 + 0.018AR \quad \text{for } AR < 50 \quad [4.8]$$



4.16 The measured aerodynamic performance of two airfoils at high angles of attack.²⁴

$$C_{D,\max} = 2.01 \text{ for } AR \geq 50$$

Here the aspect ratio is defined as the blade radius divided by the chord length at 75% of the span: $AR = R / c_{0.75R}$.

The lift and drag coefficients follow from:

$$C_D = C_{D,\max} \sin^2 \alpha + K_1 \cos \alpha \quad [4.9]$$

with

$$K_1 = \frac{C_{D,s} - C_{D,\max} \sin^2 \alpha_s}{\cos \alpha_s} \quad [4.10]$$

and

$$C_L = \frac{1}{2} C_{D,\max} \sin 2\alpha + K_2 \frac{\cos^2 \alpha}{\sin \alpha} \quad [4.11]$$

where

$$K_2 = (C_{L,s} - C_{D,max} \sin \alpha_s \cos \alpha_s) \frac{\sin \alpha_s}{\cos^2 \alpha_s} \quad [4.12]$$

The index s in these equations indicates the point of maximum lift in the airfoil lift curve, matching the pre-stall characteristics with the calculated post-stall performance of the airfoil.

Despite the fact that the use of the method is widespread and seems to have worked for the two machines under investigation, one should realize that the method is a global one; i.e. the equations are based on matching the total maximum power of the rotor, which means that all (three-dimensional) effects are included. This specifically covers the rotational effects that are dominant at the inboard part of the blade. As the next chapter will show, these effects are dependent on the local value of the rotor solidity, c/r , which makes them also dependent on the blade layout.

Additionally, the authors mention that they have switched off the (Prandtl–Glauert) tip-loss correction in their blade element momentum (BEM) calculations, as they have already accounted for the aspect ratio of the blade in Equation [4.8]. However, the tip-loss correction in BEM theory is not a correction for the *non-infinity of the blade*, but rather a correction for the fact that instead of an actuator disc a *finite number of blades* is used to extract the power. This has an entirely different physical meaning and should not interfere with the blade aerodynamics.

Tangler and Kocurek²⁷ investigated the resulting predicted power for the NREL 10 m diameter Unsteady Aerodynamics Experiment turbine using different input parameters in the Viterna and Corrigan method. They concluded that good results were obtained when the matching point is the deep stall angle of the airfoil instead of the angle for maximum lift.

Lindenburg²⁸ and Spera²⁹ each present their own set of equations, partly based on the drag coefficient at 90° angle of attack, $C_{d,max}$, and also including the effect of aspect ratio. Lindenburg constructed a relation for $C_{d,max}$ using the leading edge radius in combination with the airfoil trailing edge angle. His analysis mainly includes NACA 4-digit airfoils and other shapes found in the literature, such as ellipses, cylinders and wedges. Spera uses the same collection of airfoil maximum drag coefficients and adds the drag coefficient at the onset of deep stall to construct his drag curve. The majority of the $C_{d,max}$ data being used by Lindenburg and consequently also by Spera have a value higher than the flat plate maximum drag coefficient of 1.98. This seems a bit strange. Airfoils have one rounded and one sharp end and a trailing edge angle not deviating much from 0°. One would expect a value of the

maximum drag coefficient below 2. Timmer²⁴ suggested the simple relation given in Equation [4.13]:

$$C_{d,\max} = 1.994 - 5.4375 \left(\frac{y}{c} \right)_{x/c=0.0125} \quad [4.13]$$

where y/c is the upwind (lower surface for 90° and upper surface for 270°) relative y coordinate of the leading edge at 1.25% of the chord station. The line is based on a correlation of the maximum C_d of 7 airfoils with maximum relative thickness ranging from 12% to 30% at angles of 90° and 270° , and it includes the flat plate value of 1.98 for which the y/c value is set to 0. The equation shows that the highest C_d is achieved by having two sharp edges (flat plate) and that the $C_{d,\max}$ reduces with increasing leading edge thickness. According to Equation [4.13] a typical 25% thick mid-span airfoil like the DU 91-W2-250 ($y/c = 0.031$) would have a $C_{d,\max}$ at 90° of 1.83.

Due to the unsteady nature of the flow at high angles of attack there is a great deal of uncertainty in the performance of airfoils and consequently also in the performance of blades, where, in addition, the aspect ratio has an important contribution. The frequency of the vortex shedding, characterized by the Strouhal number, might affect the aeroelastic behavior of the wind turbine.

In view of this unsteadiness and its consequences for the blade aeroelastic behavior, the modeling of wind turbines in standstill has been extensively investigated and discussed.^{30,39} The 3-D CFD computations in Reference 39 show blade section $C_{d,\max}$ values of 1.3 (already known from experience) to 1.5 towards the tip of the blade, leading to a mean blade $C_{D,\max}$ of around 1.3.

Despite the development of these models describing high angle of attack aerodynamics the level of uncertainties that remain justifies more research on this subject.

4.7 Correction for centrifugal and Coriolis forces

To predict the performance of wind turbines, calculations of power and loads are carried out using aeroelastic codes, where the rotor aerodynamics essentially are modeled by the BEM theory, because this model is fast and robust. Using this model the operational conditions, the blade geometry and the airfoil characteristics are required to describe the forces on the blade in terms of lift and drag coefficients as a function of angle of attack. Airfoil characteristics used in BEM calculations are typically based on 2-D wind

tunnel tests on airfoils as described previously in this chapter. However, a direct application of the 2-D characteristics shows poor agreement between measured and calculated loads and power especially for rotors with significant flow separation. Therefore, there is a need for correction of the airfoil characteristics to include centrifugal and Coriolis effects that occur for separated flows. In the following sections, several existing correction models are described. If pitch regulated variable speed (PRVS) wind turbines are considered, the centrifugal and Coriolis effects will not be as significant as for the stall regulated wind turbines, because a significant part of a PRVS rotor operates in attached flow for most of the time. However, all rotors will experience separated flow to some extent during operation and therefore correction for centrifugal and Coriolis forces is necessary.

4.7.1 Existing 3-D correction models

The need to correct for centrifugal and Coriolis forces, which combined effect in the following will be called ‘3-D correction’ of airfoil characteristics, has resulted in several models in which the lift coefficient, and for some models also the drag coefficient and even the moment coefficient, are corrected in the case of flow separation from the airfoil sections. Models have been developed by Snel *et al.*,³¹ Du and Selig,³² Chaviaropoulos and Hansen,³³ Lindenburg³⁴ and Bak *et al.*³⁵ Using these models, 2-D airfoil characteristics are corrected with a limited input. The first four models are expressed as shown in Equation [4.14]:

$$\begin{aligned} c_{l,3D} &= c_{l,2D} + f\left(\frac{c}{r}, \dots\right) \Delta c_l \\ c_{d,3D} &= c_{d,2D} + f\left(\frac{c}{r}, \dots\right) \Delta c_d \end{aligned} \quad [4.14]$$

where 2-D refers to the two-dimensional characteristics of the airfoil established from calculations or wind tunnel measurements and c/r is the ratio between the local chord length and the radius at a certain blade spanwise position (local blade solidity). The expression $f(c/r, \dots)$ means that all models are a function of c/r , but that they also can be a function of other parameters. Δc_l and Δc_d denote the difference between the c_l and c_d that would exist if the flow did not separate. The terms c_l and c_d are the measured or computed lift and drag coefficients including separation. The function $f(c/r, \dots)$ varies from model to model and can shortly be described as:

Snel *et al.*:

$$f_{c_l} = 3 \left(\frac{c}{r} \right)^2$$

Lindenburg:

$$f_{c_l} = 3.1 \left(\frac{\omega r}{V_{\text{rel}}} \right)^2 \left(\frac{c}{r} \right)^2$$

Du and Selig:

$$f_{c_l} = \frac{1}{2\pi} \left[\frac{1.6(c/r)}{0.1267} \frac{a - (c/r)^{\frac{dR}{\Lambda r}}}{b + (c/r)^{\frac{dR}{\Lambda r}}} - 1 \right]$$

$$f_{c_d} = \frac{1}{2\pi} \left[\frac{1.6(c/r)}{0.1267} \frac{a - (c/r)^{\frac{dR}{2\Lambda r}}}{b + (c/r)^{\frac{dR}{2\Lambda r}}} - 1 \right]$$

$$\Lambda = \frac{\omega R}{\sqrt{U_{\text{wind}}^2 + (\omega r)^2}}$$

where $a = b = d = 1$.

Chaviaropoulos and Hansen:

$$f_{c_l, c_d} = a \left(\frac{c}{r} \right)^h \cos^n(\theta), \text{ where } a=2.2, h=1 \text{ and } n=4$$

The models by Snel *et al.* and Lindenburg solely contain a correction for c_l and not for c_d . Furthermore, Lindenburg has also proposed a model based on c_n , which is the force coefficient normal to the chord direction.

The model by Bak *et al.* is somewhat different from the above-described methods because it models the differences between 3-D and 2-D on the level of the pressure distributions and not on the level of the force coefficients. The model consists of four steps. First the difference in pressure

distribution along the chord at a certain radial station is predicted as shown in Equation [4.15]:

$$\Delta Cp = \frac{5}{2} \left(1 - \frac{x}{c}\right)^2 \left(\frac{\alpha - \alpha_{f=1}}{\alpha_{f=0} - \alpha_{f=1}}\right)^2 \sqrt{1 + \left(\frac{R}{r}\right)^2} \frac{(c/r)}{1 + \tan^2(\alpha + \theta)} \quad [4.15]$$

$$\max(\Delta Cp) = \frac{5}{2} \sqrt{1 + \left(\frac{R}{r}\right)^2} \frac{(c/r)}{1 + \tan^2(\alpha + \theta)}$$

Then the differences between 3-D and 2-D in normal and tangential force coefficients and the moment coefficients are computed as shown in Equation [4.16]:

$$\Delta c_x = \int_{x/c=0}^{x/c=1} \Delta Cp d\left(\frac{x}{c}\right)$$

$$\Delta c_t = \int_{y/c=y/c(\text{leading_edge})}^{y/c=y/c(\text{trailing_edge})} \Delta Cp d\left(\frac{y}{c}\right)$$

$$\Delta c_m = - \int_{x/c=0}^{x/c=1} \Delta Cp \left(\frac{x}{c} - 0.25\right) d\left(\frac{x}{c}\right) - \int_{y/c=y/c(\text{leading_edge})}^{y/c=y/c(\text{trailing_edge})} \Delta Cp \left(\frac{y}{c}\right) d\left(\frac{y}{c}\right) \quad [4.16]$$

where Δc_n , Δc_t and Δc_m are extra contributions to the 2-D coefficients.

Then the normal and tangential force coefficients and the moment coefficients are computed according to Equation [4.17]:

$$c_{n,3D} = c_{n,2D} + \Delta c_n$$

$$c_{t,3D} = c_{t,2D} + \Delta c_t$$

$$c_{m,3D} = c_{m,2D} + \Delta c_m \quad [4.17]$$

where $c_{n,3D}$, $c_{t,3D}$ and $c_{m,3D}$ are the 3-D corrected coefficients.

Finally, the lift and drag coefficients are derived according to Equation [4.18]:

$$c_{l,3D} = c_{n,3D} \cos(\alpha) + c_{t,3D} \sin(\alpha)$$

$$c_{d,3D} = c_{n,3D} \sin(\alpha) - c_{t,3D} \cos(\alpha) \quad [4.18]$$

4.7.2 An example of the application of 3-D models to a wind turbine rotor with stall control

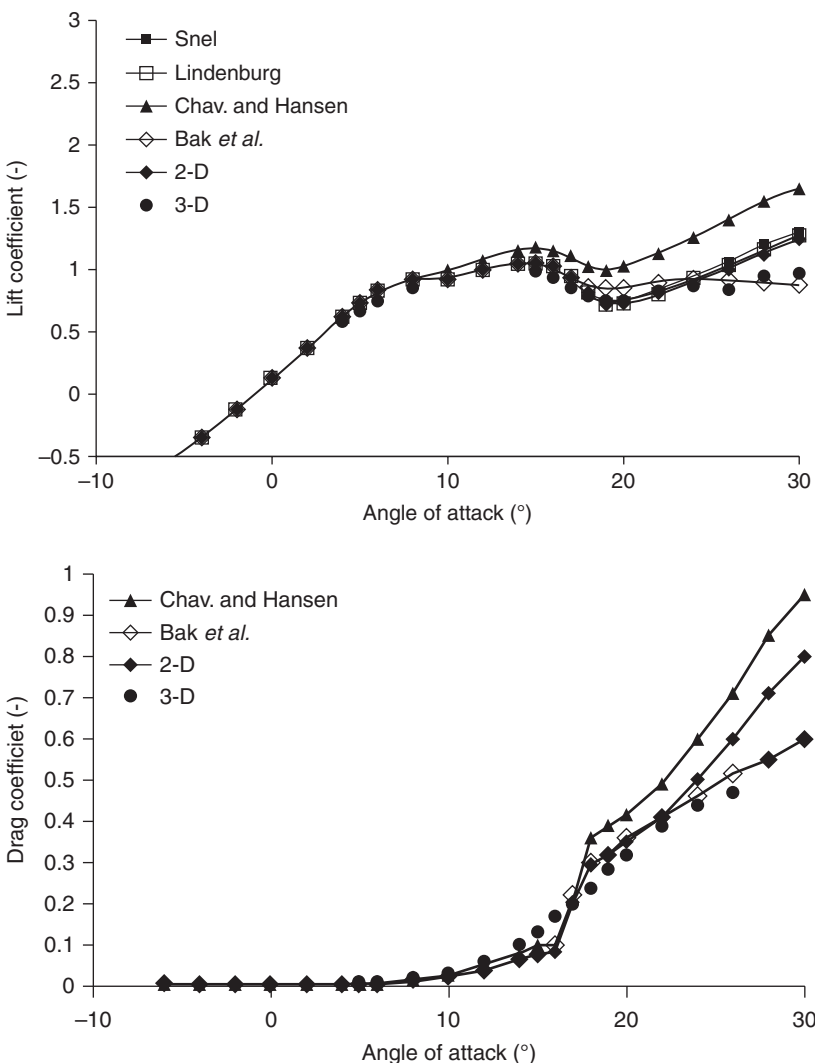
In this example some of the 3-D correction models are applied to the NREL 10 m diameter stall regulated rotor tested in the NASA Ames 24 × 36 m wind tunnel.³⁶ The predictions of overall rotor power and thrust and local blade airfoil characteristics are compared to measurements. These comparisons illustrate strengths and weaknesses of the different models, but also the capability of correction methods in general. Key parameters for the rotor are shown in Table 4.1.

Before a 3-D correction is carried out, it is important to review the 2-D airfoil data. In this process it should be ensured that (1) there is correspondence between the Reynolds number in the wind tunnel test/computations and in the rotor operation and (2) maximum lift and maximum lift–drag ratio are not too optimistic, because the airfoil surface as measured in the wind tunnel could be very smooth and clean and therefore not representative of a typical wind turbine blade surface. When trustworthy 2-D airfoil data is established, a 3-D correction can be carried out. In Figs 4.17 and 4.18 the airfoil characteristics for the rotor at two radial sections are presented. In addition to 2-D wind tunnel data, and the data extracted from the NREL/NASA Ames test, four 3-D correction models are also shown: Snel *et al.*, Chav iaropoulos and Hansen, Lindenburg and Bak *et al.* It can be seen that the models by Snel *et al.* and Bak *et al.* predict the airfoil characteristics quite well at the inner section at radius 30%. However, it should be noted that the model by Snel *et al.* does not include a 3-D correction for the drag. Furthermore, the model by Bak *et al.* is the only model in Fig. 4.18, where c_l shows a negative slope for angles of attack above 25°–30°, something which has been observed in several measurement campaigns.^{37,38}

In Fig. 4.19 the mechanical power and the thrust are depicted. It shows that the models by Chav iaropoulos and Hansen overpredict and the

Table 4.1 Data for the NREL/NASA Ames rotor

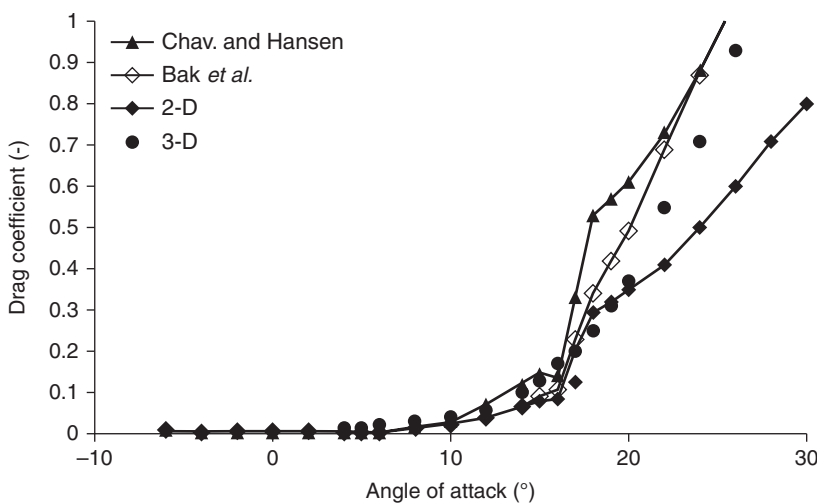
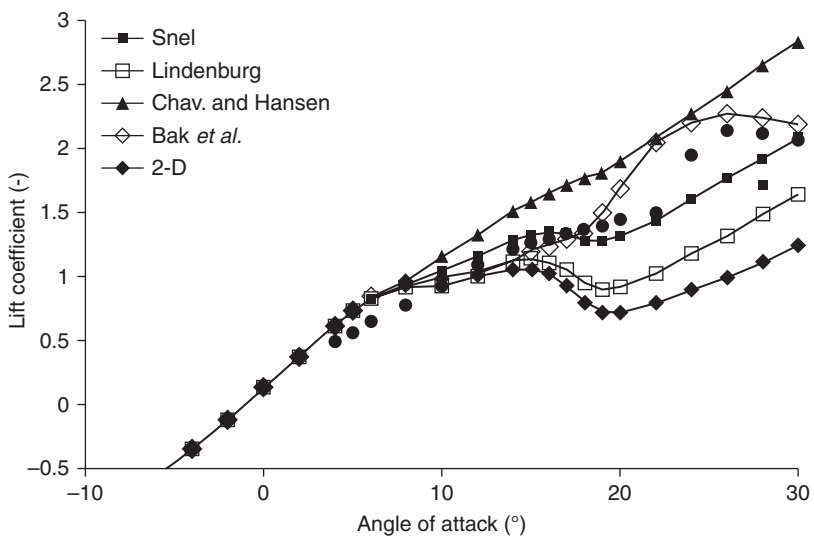
Number of blades	2
Rotor diameter (m)	10.058
Rotational speed (RPM)	72.0
Design tip–speed ratio, Λ (-)	6.3
Tip speed (m/s)	37.9
Airfoil series	S809
Power control	Stall



4.17 3-D corrected airfoil lift (top) and drag (bottom) characteristics for $r/R = 80\%$ compared to 2-D measurements and measured 3-D data.

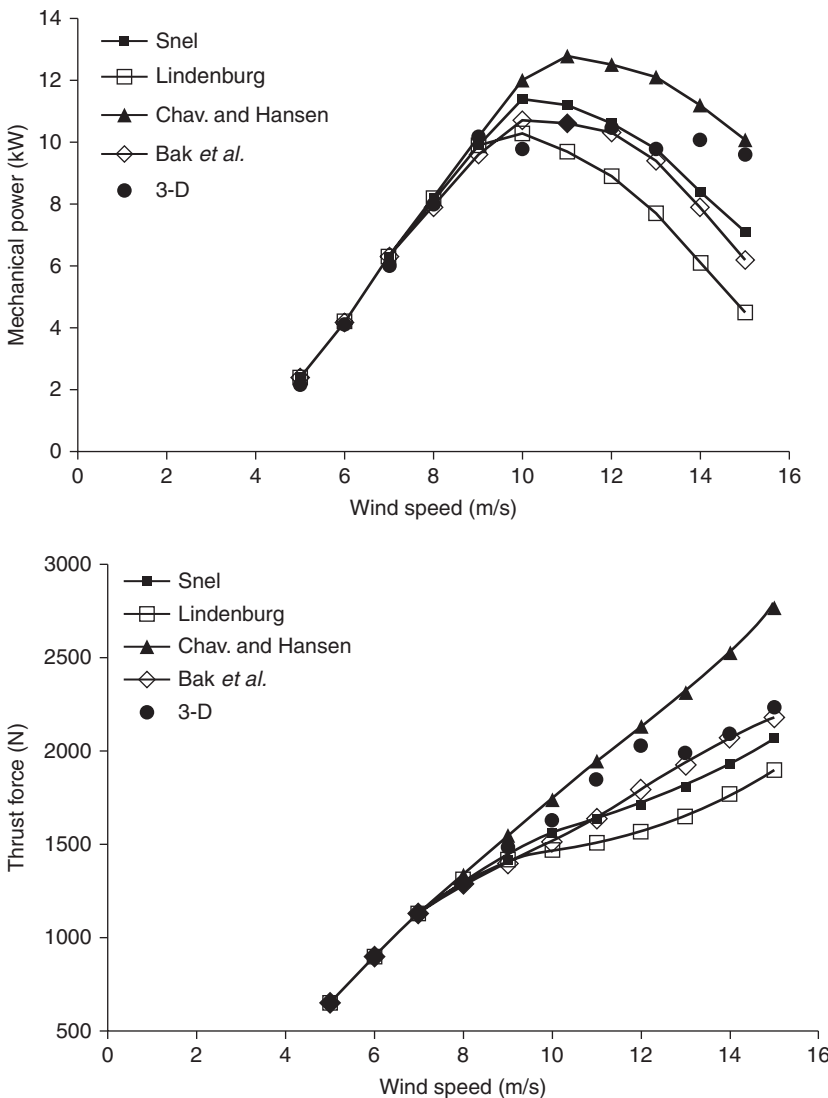
model by Lindenburg underpredicts both power and thrust. However, the models by Snel *et al.* and Bak *et al.* predict both the power and thrust fairly well. At wind speeds above 13 m/s all models show a significant drop in power.

The conclusion from this example is that the predicted power and loads agree better with measurements when the airfoil characteristics are



4.18 3-D corrected airfoil lift (top) and drag (bottom) characteristics for $r/R = 30\%$ compared to 2-D measurements and measured 3-D data.

corrected for 3-D using the existing models. However, even though a fair agreement in power and loads is reached, there are still shortcomings in the 3-D correction models. These are related to both the ability of the tools to predict the onset of stall in 2-D and the understanding of the impact of centrifugal and Coriolis forces on the separated flow.



4.19 Measured 3-D data and computed mechanical power and thrust force for the NREL rotor.

4.8 Establishing data for blade design

The first step in aerodynamic blade design is to find suitable airfoils and their characteristics. Even at this point, choices need to be made regarding the value of the design lift coefficient and associated lift–drag ratio in relation to the maximum relative thickness of the section in the light of the

required strength and stiffness of the blade. Based on the in-plane force dF_t , referred to previously in this chapter, the torque of the rotor follows from

$$Q = \int_0^R B \frac{1}{2} \rho V_{\text{rel}}^2 C_l c \left(\sin \varphi - \frac{\cos \varphi}{C_l / C_d} \right) r dr \quad [4.19]$$

Equation [4.19] shows that, to deliver sufficient torque, slender blades (low value of the chord c) require a high value of the combination V_{rel}^2 (a high design tip-speed ratio) and C_l (a high design lift). Potentially, slender blades can ensure both low extreme and low fatigue loads, but due to the limited absolute thickness more blade mass may be needed to satisfy all structural requirements.

In addition to the airfoil shape and the required design lift coefficient, the local Reynolds number and the expected degree of blade leading edge contamination also need to be addressed, since failure to establish a trustworthy set of data reflecting blade operating conditions may result in failure to predict both rotor power and rotor loads with sufficient accuracy. As explained earlier, the Reynolds number and the maximum lift-drag ratio for a specific airfoil are closely linked. A first estimate of the Reynolds number for a specific data set can be made by taking the product of the local rotational speed $((r/R)V_{\text{tip}})$ and the approximate local chord length c divided by 15×10^{-6} . If the chord length is not known a rule of thumb is that the Reynolds number will be between $75R \times 10^3$ and $150R \times 10^3$.

Since generally the aim of the design is to achieve low-cost energy, no doubt a number of iterations will be needed in order to find the right balance between aerodynamic efficiency, structural integrity and sufficiently low blade mass.

4.8.1 Available airfoils

Unfortunately there is not much information publicly available when searching for dedicated airfoil designs and their measured performance. Airfoils and their characteristics have been collected by Bartognioli *et al.* in a wind turbine airfoil catalogue.⁴⁵ However, the catalogue is not complete and basically contains characteristics measured at Reynolds numbers below 3×10^6 . When it is a question of the bigger machines, with Reynolds numbers of 3×10^6 or higher and design lift coefficients above unity, Tables 4.2–4.5 summarize what information can be found.

Due to the combination of test Reynolds number and design lift coefficient a number of airfoils do not appear in the tables. Since 1984 an appreciable number of S8xx airfoils have been designed under the auspices of

Table 4.2 Airfoils suited for wind turbines with a design lift coefficient higher than 1 and publicly available measured characteristics at about $Re = 3 \times 10^6$. Maximum relative thickness of 18%

Airfoil	t/c	Measured Re	$C_{l,design}$	$C_{l,max}$	$(C_l/C_d)_{max}$	Reference
NACA 63 ₃ -618	0.18	3×10^6	1.1	1.39	138	1
NACA 64 ₃ -618	0.18	3×10^6	1.09	1.37	156	1
DU 96-W-180	0.18	3×10^6	1.06	1.25	143	4
FX S03-182	0.182	3×10^6	1.04	1.48	157	40
NACA 4418	0.18	3×10^6	1.16	1.43	110	1

Table 4.3 Airfoils suited for wind turbines with a design lift coefficient higher than 1 and publicly available measured characteristics at about $Re = 3 \times 10^6$. Maximum relative thickness of 21%

Airfoil	t/c	Measured Re	$C_{l,design}$	$C_{l,max}$	$(C_l/C_d)_{max}$	Reference
NACA 63 ₄ -421	0.21	3×10^6	1.04	1.33	127	1
NACA 64 ₄ -421	0.21	3×10^6	1.04	1.34	142	1
DU 93-W-210	0.21	3×10^6	1.22	1.35	141	4

Table 4.4 Airfoils suited for wind turbines with a design lift coefficient higher than 1 and publicly available measured characteristics at about $Re = 3 \times 10^6$. Maximum relative thickness of approximately 25%

Airfoil	t/c	Measured Re	$C_{l,design}$	$C_{l,max}$	$(C_l/C_d)_{max}$	Reference
DU 91-W2-250	0.25	3×10^6	1.21	1.37	128	4
AH 93-W-257	0.257	3×10^6	1.2	1.41	121	41
NACA 63 ₄₂₁ -425*	0.25	3×10^6	1.07	1.28	120	4
S814	0.241	3×10^6	1.11	1.41	116	42

*This airfoil has an unsatisfactory rough behavior.

Table 4.5 Airfoils suited for wind turbines with a design lift coefficient higher than 1 and publicly available measured characteristics at about $Re = 3 \times 10^6$. Maximum relative thickness of more than 25%

Airfoil	t/c	Measured Re	$C_{l,design}$	$C_{l,max}$	$(C_l/C_d)_{max}$	Reference
DU 97-W-300	0.30	3×10^6	1.39	1.57	98	4
DU 97-W-300Mod	0.30	2.9×10^6	1.34	1.47	108	43
AH 93-W-300	0.30	2.5×10^6	1.02	1.16	66	41
AH 94-W-301	0.301	2.5×10^6	1.33	1.43	100	41
FX 77-W-270 S**	0.27	3×10^6	1.54	1.94	118	41
FX 77-W-343**	0.343	3×10^6	1.72	2.01	96	41
DU 00-W-350	0.35	3×10^6	1.21	1.40	81	44
DU 00-W-401	0.401	3×10^6	0.89	1.25	55	44

** These airfoils have an unsatisfactory rough behavior.

the National Renewable Energy Laboratory (NREL) in the USA, for wind turbines with various control mechanisms. Information about all of these airfoils can be found via the information portal of NREL's National Wind Technology Center. Many designs were verified in the Ohio and Penn State University wind tunnels but, since the designs mainly focused on small to medium size machines (2–50 m diameter), generally containing airfoils with low maximum lift coefficients, here measurements also concentrated on lower Reynolds numbers and airfoil models with design lift coefficients of appreciably below one. Of the more recent airfoils that would apply to the bigger machines on the basis of their design lift coefficient, only performance predictions are available.

The development of Risø's A1, B1, C2 and P airfoil families was supported by full-scale tests and extensive measurement campaigns in the Velux wind tunnel in Denmark.⁴⁶ Since the maximum attainable Reynolds number in this wind tunnel is 1.6×10^6 they do not appear in the tables. The coordinates of the Risø airfoils and measurements at higher Reynolds numbers are not available. Moreover, the FFA-W3 series of airfoils,³ although worth considering, are not included in the tables as no measurements of these airfoils at Reynolds numbers higher than 1.6×10^6 (24% and 30% thick in the Velux tunnel) exist in the public domain. It must be noted that the NREL S8xx and the Risø airfoils are subject to license agreements and the use of the airfoils is generally not free of costs.

The appearance of airfoil FX S03–182 in Table 4.2 is to show that occasionally glider airfoils may also come under consideration for this thickness.

Though many rotor designs put more weight on the structural efficiency at the inner part of the rotor, the aerodynamic efficiency of this part of the rotor must not be ignored. Paying special attention to the aerodynamics of the thickest airfoils may increase the total rotor power by a few percent. Although the DU 00-W-401 airfoil has a design lift coefficient of below 1.0 it appears in Table 4.5 because it is in fact the only recent airfoil of this thickness with publicly available measured performance.

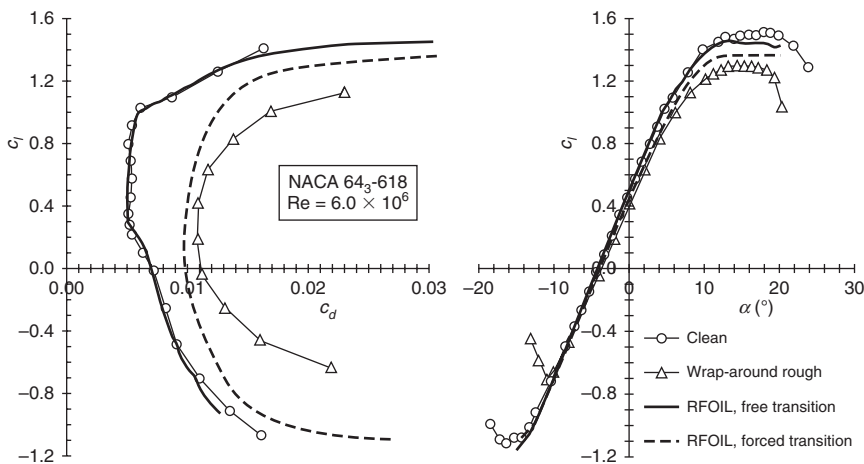
4.8.2 Establishing the data

If, in the search for available measured characteristics, the Reynolds number were increased from 3×10^6 to 6×10^6 , a common value for present day machines, from the airfoils listed in Table 4.3 only the 18% NACA airfoils (with design lift coefficients of about 1.0 at this Reynolds number) and the modified DU airfoil would remain. This makes it clear that measurements of airfoil sections projected for blade design often do not exist in the public domain at the required Reynolds number or even do not exist at all. It is therefore necessary to predict the airfoil performance by computations,

using either panel codes or CFD codes. The measured performance of the airfoil at a lower Reynolds number or the performance of an aviation airfoil at the required Reynolds number can be used as a check on the validity of the predictions, provided that the measured data come from a trustworthy source.

As an outcome of the simulations, two sets of airfoil characteristics should be established: one set assuming a clean airfoil surface (free transition computations) and one set assuming a contaminated airfoil leading edge. Using XFOIL or RFOIL in the evaluation process the model for free transition, the ‘*e*-to-the-*n*th’ method, requires the factor *n* as an input. For very low turbulent flow *n* = 9 or 10 is required, but for many high quality wind tunnels *n* should have values of 6 or 7.

As described in Section 4.4.1 the degree of blade soiling is generally not known and even if it were known there is a limit to what can be simulated with prediction codes. In XFOIL/RFOIL, transition can be fixed on the leading edge so that the entire surface is turbulent. This, however, is not the same as tripping the boundary layer in an experiment, where the tripping device, in addition to making the boundary layer turbulent, by its own thickness adds to the boundary layer thickness and momentum loss thickness. This is demonstrated in Fig. 4.20, which shows the measured and calculated performance of airfoil NACA 64₃-618 in both the clean and the rough condition. In the predictions, transition was fixed at $x/c = 0.1\%$ on the suction side and



4.20 The measured and predicted performance of airfoil NACA 64₃-618 in the clean and rough condition. RFOIL free transition with $n = 10$. Forced transition at $x/c = 0.1\%$ on the suction side and 10% at the pressure side. In contrast to Fig. 4.3 the predicted drag here is multiplied by a factor of 1.08 to show the good match in the low drag region.

$x/c = 10\%$ at the pressure side. The graph clearly shows that the effect of the wrap-around roughness on drag and lift is much more severe than can be calculated by the panel code.

If measurements for a specific airfoil do not exist at the required Reynolds number they should be corrected for this prior to being used in the design. This can be done by determining the changes in c_l , c_d and c_m in the computations while going from the Reynolds number of the experiment to the required value for the design. These changes can then be added to the measurements so that two sets of data exist: one set assuming a clean airfoil surface and one set assuming a contaminated airfoil surface, where both sets reflect the correct Reynolds number.

Airfoil characteristics for wind turbine rotor aerodynamic design should to some extent reflect the existence of soiled blades, but on the other hand the rotor design should not be too conservative resulting in the power being too low or loads being too high. The challenge in the blade design process is to ensure that one set of airfoil characteristics represents the state of the blade surface during a longer period of time. One way of handling this is to blend clean surface airfoil characteristics with characteristics representing a contaminated leading edge, while adding weight factors to the clean and rough airfoil c_l , c_d and c_m curves, e.g. 70% for the clean condition and 30% for the soiled blade.

The result of blending data that are based on different surface configurations is inherently two-dimensional because the computations and measurements assume two-dimensionality. However, on a rotating blade the flow is exposed to, e.g. centrifugal forces, Coriolis forces, tip effects and root effects, resulting in a high degree of three-dimensional flow, especially when separation occurs. As explained earlier in this chapter, models exist to correct for these effects, so the established 2-D data set should be corrected accordingly. Even though some control strategies for wind turbine rotors ensure that separation is not a major factor, it is still important to correct for three-dimensional flow because it is very likely that the flow, especially on the inner part of the rotor, will separate.

4.9 Future trends

The ongoing upscaling of wind turbine blades results in blade section Reynolds numbers of 10×10^6 and more. These high Reynolds numbers are beyond current experience, and panel codes like XFOIL/RFOIL are not sufficiently calibrated for these conditions, which creates additional uncertainty in the simulations.

Until a few years ago the aerodynamic performance of thin to medium thick airfoils ($t/c < 30\%$) received the most attention. With the upscaling of blades to 90 m and more, thicker airfoils ($t/c > 40\%$) are needed to create

the required stiffness. The accuracy of performance prediction of thick airfoils is still not very high. Hence, both the design of thicker airfoils and the ability to predict airfoil performance at these thicknesses at high Reynolds numbers will be the subject of future research.

The fact that the degree of contamination of wind turbine rotor blades is not known in detail hinders the design of new airfoils. Roughness sensitivity plays an important role, especially when thicker airfoils are required for the more outboard sections of the blade. To better map the design space for wind turbine airfoils, blade contamination needs to receive more attention.

As concluded previously in this chapter, few verification possibilities exist for predictions with measured two-dimensional wind turbine airfoil performance characteristics at high Reynolds numbers. As a result, wind tunnel testing campaigns will likely focus on the measurements for thick airfoils with and without leading edge roughness at Reynolds number between 6×10^6 and 12×10^6 .

New concepts are also likely to be introduced, including static add-ons such as slats and flaps, which generally enhance the lift performance and are particularly good at stabilizing the flow over thick airfoils. Specialized tools are needed to model the performance of such add-ons. Moreover, the use of active devices, such as adaptive trailing edge flaps, micro tabs and synthetic jets, creates challenges for experiments and predictions because the inherent unsteadiness is not something which can be ignored in the measuring and simulation process.

4.10 References

1. Abbott IH and von Doenhoff AE, *Theory of Wing Sections*. New York, Dover Publications Inc., 1959.
2. Tangler JL and Somers DM, ‘NREL airfoil families for hawt’s’ *Proc. WINDPOWER’95*, Washington D.C., pages 117–123, 1995.
3. Björk A, Coordinates and calculations for the FFA-W1-xxx, FFA-W2-xxx and FFA-W3-xxx series of airfoils for horizontal axis wind turbines. FFA TN 1990-15, FFA, Stockholm, Sweden, 1990.
4. Timmer WA and van Rooij RPJOM, ‘Summary of the Delft University wind turbine dedicated airfoils’. *41st Aerospace Sciences Meeting, Paper no. AIAA-2003-0352*, January 2003, Reno, USA.
5. Fuglsang P and Bak C, ‘Development of the Risø wind turbine airfoils’. *Wind Energy*, 7:145–162, 2004.
6. Bak C, Andersen PB, Madsen HA, Gaunaa M, Fuglsang P and Bove S, ‘Design and verification of airfoils resistant to surface contamination and turbulence intensity’. *AIAA 2008-7050; 26th AIAA Applied Aerodynamics Conference*, 18–21 August 2008, Honolulu, Hawaii.
7. van Dam C, Mayda E, Chao D, Jackson K, Zuteck M and Berry D, ‘Innovative structural and aerodynamic design approaches for large wind turbine blades’. *AIAA paper 2005-0973*, 2005.

8. Anderson JD, *Fundamentals of Aerodynamics*, 5th edition. New York, McGraw-Hill, 2011.
9. Drela M, 'XFOIL: An analysis and design system for low Reynolds number airfoils'. *Conference on Low Reynolds Number Airfoil Aerodynamics*, University of Notre Dame, June 1989.
10. van Rooij RPJOM, 'Modification of the boundary layer in XFOIL for improved airfoil stall prediction'. Report IW-96087R, Delft University of Technology, September 1996. Delft, The Netherlands.
11. Timmer WA, 'An overview of NACA 6-digit airfoil series characteristics with reference to airfoils for large wind turbine blades'. *AIAA-2009-0268, 47th AIAA Aerospace Sciences Meeting Including The New Horizons Forum and Aerospace Exposition 5–8 January 2009*, Orlando, Florida, USA.
12. Ferziger JH and Peric M, *Computational Methods for Fluid Dynamics*, 3rd Revised Edition, ISBN:3540420746, Springer, December 2001.
13. ANSYS Fluent, www.ansys.com
14. ANSYS CFX, www.ansys.com
15. STAR-CD, www.cd-adapco.com
16. Michelsen JA, 'Basis3d – a platform for development of multiblock PDE Solvers'. Technical Report afm 92-05, Technical University of Denmark, 1992.
17. Michelsen JA, 'Block structured multigrid solution of 2D and 3D elliptic PDE's'. Technical report afm 94-06, Technical University of Denmark, 1994.
18. Sørensen NN, 'General purpose flow solver applied to flow over hills'. Risø-r-827(en), Risø National Laboratory, Denmark, June 1995.
19. OpenFOAM, www.openfoam.com
20. Menter, FR, 'Two-equation eddy-viscosity turbulence models for engineering Applications'. *AIAA Journal*, **32**(8):1598–1605, August 1994.
21. Barone MF and Berg D, 'Aerodynamic and aero-acoustic properties of a flat-back airfoil: An update'. *AIAA 2009-271*, January 2009.
22. <http://bladeCleaning.com/problemsEN.htm>. Accessed 8 August 2012
23. McGhee RJ and Beasley WD, 'Low-speed aerodynamic characteristics of a 17-percent-thick airfoil section designed for general aviation applications'. NASA TN D-7428, 1973.
24. Timmer WA, 'Aerodynamic characteristics of wind turbine blade airfoils at high angles of attack'. *Conference Proceedings Torque 2010, The Science of Making Torque from Wind*. Heraklion, Greece, 28–30 June 2010, pp. 71–97.
25. Viterna LA and Corrigan RD, 'Fixed pitch rotor performance of large horizontal axis wind turbines'. *DOE/NASA Workshop on Large Horizontal Axis Wind Turbines*, Cleveland, Ohio, July 1981.
26. Hoerner SF, *Fluid-dynamic Drag*. Published by the author, 1965.
27. Tangler J and Kocurek JD, 'Wind turbine post-stall airfoil performance characteristics guidelines for blade-element momentum methods'. *43rd AIAA Aerospace Sciences Meeting and Exhibit*. Reno, Nevada, 10–13 January 2005.
28. Lindenburg C, 'Investigation into rotor blade aerodynamics'. Report ECN–03–25, July 2003.
29. Spera AD, 'Models of lift and drag coefficients of stalled and unstalled airfoils in wind turbines and wind tunnels'. NASA/CR–2008–215434, June 2010.
30. Skrzypinski W, 'Analysis and modeling of unsteady aerodynamics with application to wind turbine blade vibration at standstill conditions'. Ph.D. Thesis, DTU Wind Energy, February 2012.

31. Snel H, Houwink R, van Bussel GJW and Bruining A, 'Sectional prediction of 3D effects for stalled flow on rotating blades and comparison with measurements', *Proc. European Community Wind Energy Conference*, Lübeck-Travemünde, Germany, 8–12 March, 1993, pp. 395–399, H.S. Stephens & Associates.
32. Du Z and Selig MS, 'A 3-D stall-delay model for horizontal axis wind turbine performance prediction' *AIAA-98-0021, 36th AIAA Aerospace Sciences Meeting and Exhibit, 1998 ASME Wind Energy Symposium*, Reno, NV, USA, 12–15 January 1998.
33. Chaviaropoulos PK and Hansen MOL, 'Investigating three-dimensional and rotational effects on wind turbine blades by means of a quasi-3D Navier Stokes solver', *J. Fluids Engineering*, **122**:330–336, June 2000.
34. Lindenburg C, 'Modelling of rotational augmentation based on engineering considerations and measurements', *Proc. European Wind Energy Conference*, London, 22–25 November 2004.
35. Bak C, Johansen J and Andersen PB, 'Three-dimensional corrections of airfoil characteristics based on pressure distributions', *Proc. European Wind Energy Conference & Exhibition (EWEC)*, 2006, Athens, Greece.
36. Hand MM, Simms DA, Fingersh LJ, Jager DW, Cotrell JR, Schreck S and Larwood SM, 'Unsteady aerodynamics experiment phase VI: wind tunnel test configurations and available data campaigns'. NREL/TP-500-29955, National Renewable Energy Laboratory, Golden, Colorado, USA, December 2001.
37. Madsen HA and Rasmussen F, 'Derivation of three-dimensional airfoil data on the basis of experiment and theory' *AWEA 1988, Proceedings of the AWEA Windpower Conference*, Vol. **88**, Honolulu, HI, USA.
38. Bak C, 'Udledning af profildata' (in Danish), in Risø-R-1434(DA), *Research in Aero-elasticity*, ed. C. Bak, Risø National Laboratory, Roskilde, Denmark, 2004.
39. Johansen J, Sørensen NN and Mikkelsen R, 'Rotoraerodynamic' (in Danish), in Risø-R-1434(DA), *Research in Aeroelasticity*, ed. C. Bak, Risø National Laboratory, Roskilde, Denmark, 2004.
40. Althaus D, *Stuttgarter Profilkatalog I*. Stuttgart University, Germany, 1972.
41. Althaus D, *Niedriggeschwindigkeitsprofile – Airfoils and experimental Results from the Laminar Wind Tunnel of the Institute for Aerodynamics and Gas Dynamics of the Stuttgart University*, ISBN 3-528-03820-9 Stuttgart, Germany 1984.
42. Somers DM, 'Design and experimental results for the S814 airfoil'. Report NREL/SR-440-6919. 1997.
43. Timmer WA and Schaffarczyk AP, 'The effect of roughness at high Reynolds numbers on the performance of DU 97-W-300Mod' *Proceedings of the conference The Science of making Torque from Wind*, April 2004, Delft, The Netherlands, pp. 71–77.
44. van Rooij RPJOM and Timmer WA, 'Roughness sensitivity considerations for thick rotor blade airfoils', *41st Aerospace Sciences Meeting, Paper no. AIAA-2003-0350*, January 2003, Reno, USA.
45. Bertagnolio F, Sørensen N, Johansen J and Fuglsang P, *Wind Turbine Airfoil Catalogue*, Risø-R-1280(EN), Risø National Laboratory, Roskilde, Denmark, August 2001, ISBN 87-550-2910-8.

46. Bak C, Fuglsang P, Gaunaa M and Antoniou I, 'Design and verification of the Risø-P airfoil family for wind turbines'. *Proceedings of the Conference the Science of Making Torque from Wind*, April 2004, Delft, the Netherlands, pp. 16–24.

4.11 Appendix: Nomenclature

Symbol	Unit	Description
a	-	Induced axial velocity normal to rotor plane
a'	-	Induced tangential velocity in rotor plane
B	-	Number of blades on rotor
c	m	Chord length, distance from leading edge to trailing edge of airfoil
c_d	-	Drag coefficient
$c_{d,max}$	-	Drag coefficient at 90° or 270° angle of attack
c_l	-	Lift coefficient
$c_{l,design}$	-	Lift coefficient at which $(c_l/c_d)_{max}$ is obtained (design lift)
$c_{l,max}$	-	Maximum lift coefficient
c_l/c_d	-	Lift-drag ratio of airfoil section
$(c_l/c_d)_{max}$	-	Maximum lift-drag ratio for airfoil section
D	N	Drag on airfoil
F_n	N	Force on airfoil normal to the rotor plane
F_t	N	Tangential force on airfoil in the rotor plane
L	N	Lift on airfoil
r	m	Radial position on rotor blade
Re	-	Reynolds number
U	m/s	Wind speed
V_{rel}	m/s	Relative flow velocity on the airfoil, which is the combination of the axial and the tangential inflow
α	°	Angle of attack
α_{design}	°	Angle of attack at which $c_{l,design}$ is obtained
ϕ	°	Angle between the relative inflow and the rotor plane
Ω	rad/s	Rotational speed of the rotor
μ	kg/ms	Air dynamic viscosity
ν	m ² /s	Air kinematic viscosity
ρ	kg/m ³	Air density
θ	°	Pitch angle

Aeroelastic design of wind turbine blades

J. G. HOLIERHOEK, Energy research Centre of the Netherlands, The Netherlands

DOI: 10.1533/9780857097286.1.150

Abstract: Aeroelasticity concerns the interaction between aerodynamics, dynamics and elasticity. This interaction can result in negatively or badly damped wind turbine blade modes, which can have a significant effect on the turbine lifetime. The first aeroelastic problem that occurred on commercial wind turbines concerned a negatively damped edgewise mode. It is important to ensure that there is some out-of-plane deformation in this mode shape to prevent the instability. For larger turbine blades with lower torsional stiffness and the possibility of higher tip speeds for the offshore designs, classical flutter could also become relevant. When designing a wind turbine blade, it is therefore crucial that there is enough damping for the different modes and that there is no coincidence of natural frequencies with excitation frequencies (resonance). An effective aeroelastic analysis is also important, and the tools used for such an analysis must include the necessary detail in the structural model.

Key words: aeroelasticity, resonance, eigenmodes, natural frequencies, flutter, aeroelastic analysis.

5.1 Introduction

Wind turbines are structures for which aeroelasticity is an important field of expertise. In addition to the danger that aeroelastic mistakes in the design could result in destruction of the turbine, the more likely risk of fatigue loads being too high due to a lack of damping caused by an instability cannot be ignored.

In this chapter the basics of aeroelasticity will be discussed and aeroelastic issues that are relevant in the design of wind turbine blades are explained. This chapter can be seen as an introduction to the aeroelasticity of wind turbine blades and is intended to provide ample background for those who are not very familiar with aeroelasticity. Readers with a basic knowledge of aeroelasticity can skip the first section which discusses aeroelasticity in general and start with the second section which deals with wind turbine blade aeroelasticity.

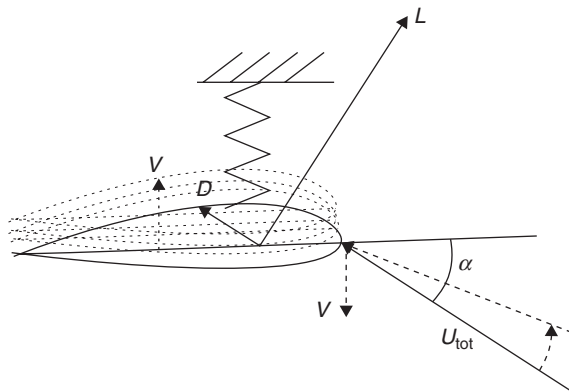
5.1.1 Aeroelasticity

Aeroelasticity is traditionally concerned with the combination of aerodynamic forces, elastic forces and dynamic forces where there is significant mutual interaction between these forces (Dowell, 1995). The interaction of the elastic, dynamic and aerodynamic forces is strong in, e.g., wind turbines, helicopters and aeroplanes, making aeroelasticity a relevant discipline for these fields. The aerodynamic forces on these structures depend on the relative velocities of the air flowing past the structure. If the structure is deforming, the change in shape due to the elastic bending will affect the aerodynamic forces, e.g. a changed angle of twist will alter the angle of attack and therefore the aerodynamic force. The time derivatives of the deformations, i.e. the speed at which the blade is deforming, will result in a change in the relative velocity of the air passing the structure, which also changes the aerodynamic forces. In turn the aerodynamic forces influence the deformation and the acceleration of the structure, so there is a clear two-way interaction. Inertia forces play an important role in the correlation between the aerodynamic and elastic forces and the resulting accelerations.

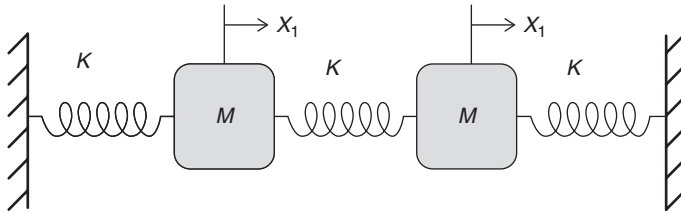
A structure can start to oscillate due to the changing forces. For example, take an aerofoil that is attached to a translational spring, as illustrated in Fig. 5.1. If the blade moves upwards, the local relative velocity of the air will change, and the aerofoil will sense an additional downward wind velocity which decreases the angle of attack. Depending on the size of the angle of attack, this results in a decrease in the lift (operating below stall) or an increase (operating above stall). An increase in lift, i.e. when operating above stall, can result in an additional upward motion, while a decrease in lift will in effect counteract the upward motion. The spring will also provide a force counteracting the upward motion. The combination results in oscillations with an increasing or a decreasing amplitude, depending on the different properties.

The aerofoil in Fig. 5.1 can be seen as a model for the upward bending of an aeroplane wing, or the flapwise deformation of a wind turbine blade – a deformation perpendicular to the rotor plane. When the described vibration has an increasing amplitude, the structure is aeroelastically unstable. This is a simple example of a possible aeroelastic problem showing the different disciplines involved: aerodynamics, elasticity and dynamics.

If a structure is elastic, it will respond to periodic forcing functions by vibrating in discrete geometric patterns (Spera, 1994). These geometric patterns are called the mode shapes or eigenmodes of the structure. Each mode will have a corresponding mode frequency, a natural frequency of the structure. The vibration in the mode shape will occur at this natural frequency. Wind turbines are flexible structures that will vibrate when forces act on the structure. Their responses will be in the mode shapes and at the natural frequencies of the structures.



5.1 An aerofoil that can move up and down. If it has an upward velocity V , the angle of attack (α , the angle between the total velocity (U_{tot}) and the chord) is reduced. This will reduce the lift (L) and the drag (D) forces.



5.2 System with two masses and three springs. This system has two eigenmodes.

The system depicted in Fig. 5.2 is a good example to explain eigenmodes. This system consists of two masses that are connected to each other and to the basement through three translational springs. Both the bodies have a mass M and the stiffness of each spring is K . The horizontal translation of the left mass is represented using coordinate x_1 and for the right mass the coordinate x_2 is used, as shown in the figure. The eigenmodes for this system can easily be derived. The equations of motion, using Newton, are:

$$\begin{aligned} M\ddot{x}_1 &= -Kx_1 + K(x_2 - x_1) \\ M\ddot{x}_2 &= -Kx_2 + K(x_1 - x_2) \end{aligned} \quad [5.1]$$

This system will show oscillations, therefore the solutions

$$\begin{aligned} x_1(t) &= A_1 e^{i\omega t} \\ x_2(t) &= A_2 e^{i\omega t} \end{aligned} \quad [5.2]$$

can be used. Substituting these two expressions in the equations of motion gives:

$$\begin{aligned}-\omega^2 M A_1 e^{i \omega t} &= -2 K A_1 e^{i \omega t} + K A_2 e^{i \omega t} \\ -\omega^2 M A_2 e^{i \omega t} &= K A_1 e^{i \omega t} - 2 K A_2 e^{i \omega t}\end{aligned}\quad [5.3]$$

These equations must be satisfied at every time step t , therefore

$$\begin{aligned}(\omega^2 M - 2K) A_1 + K A_2 &= 0 \\ K A_1 + (\omega^2 M - 2K) A_2 &= 0\end{aligned}\quad [5.4]$$

For this set of equations to have valid solutions, the determinant must be equal to zero:

$$(\omega^2 M - 2K)^2 - K^2 = 0 \quad [5.5]$$

This equation has two solutions for ω ; these are the two natural frequencies:

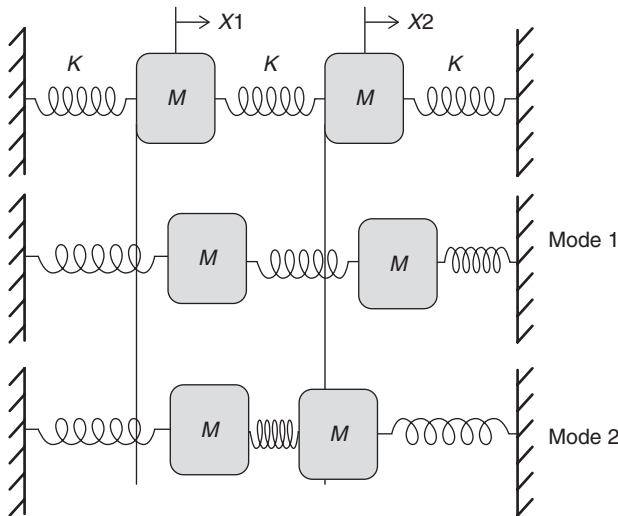
$$\omega_1 = \sqrt{\frac{K}{M}}; \omega_2 = \sqrt{\frac{3K}{M}} \quad [5.6]$$

Substituting these two frequencies in Equation [5.3] gives: A_1 and A_2 . Substituting everything in the original solutions in Equation [5.2] gives:

$$\begin{aligned}\begin{pmatrix} x_1(t) \\ x_2(t) \end{pmatrix} &= c_1 \begin{pmatrix} 1 \\ 1 \end{pmatrix} \cos(\omega_1 t + \phi_1) \\ \begin{pmatrix} x_1(t) \\ x_2(t) \end{pmatrix} &= c_1 \begin{pmatrix} 1 \\ -1 \end{pmatrix} \cos(\omega_2 t + \phi_2)\end{aligned}\quad [5.7]$$

These two equations give the two eigenmodes. An eigenmode only gives the relation between the different coordinates, not actual sizes, and so usually the eigenmodes will be normalized: the largest deformation will be set equal to 1. The eigenmodes for the system used in this example are illustrated in Fig. 5.3.

The first eigenmode shows the two masses moving in the same direction for an equal distance. The second mode shows the two masses moving in opposite direction of each other, again for equal distances. This example shows that every motion of this system can be presented as a combination of these



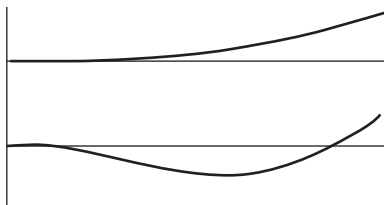
5.3 Illustration of a system with two masses and three springs and the two eigenmodes of this system.

two eigenmodes. For any combination of x_1 and x_2 , there is one and only one combination of the two eigenmodes that exactly represents that case.

If the system is given some initial excitation and no external force acts on it, it will vibrate at a given combination of the two eigenmodes and corresponding natural frequencies. If the excitation includes a velocity, it is possible that there will be a phase difference, given by ϕ in Equation [5.7].

For a continuous beam, such as a wind turbine blade, there will be infinitely many natural frequencies and eigenmodes. For a uniform beam clamped at one side and free at the other end, the first two modes in one direction are illustrated in Fig. 5.4. The beam will have similar modes in the other direction, perpendicular to the length and will have torsion modes with a similar distribution. For aeroelastic analysis of a wind turbine blade, only the lower modes are relevant, as will be explained in Section 5.3.3, though an infinite number of eigenmodes will be present in the blade.

If aerodynamics play an important role in the system, as an external force, the system could become unstable: a vibration could have an increasing amplitude or divergence could occur. For example, the initial design of the Fokker D-8 during the First World War suffered wing failures during high-speed dives. Testing of the cantilever monoplane showed that an increase in load resulted in an increased angle of incidence at the wing tips. This resulted in an increase in load at the tips and the failure of the wings. As more and more cantilever monoplanes were developed, aeroelasticity started to become a serious research subject indeed (Bisplinghoff *et al.*, 1996).



5.4 Sketch of the first two eigenmodes of a uniform beam, clamped at one end.

One must distinguish between aeroelastic instabilities (see, e.g. Hansen, 2007) and resonance (see, e.g. Sullivan, 1981). Resonance is the case where there is an excitation force introduced having a frequency that is close or equal to one of the natural frequencies of the system and where energy can be added to the vibration. This is not the case for aeroelastic instabilities, where the aerodynamic forces also add energy to the system, but not due to some frequency coincidence. If the aerodynamic damping of a mode is negative (aeroelastic instability), this can result in an oscillation with increasing amplitude if the absolute value of the negative aerodynamic damping is higher than the structural damping (or other sources of damping) of the mode. Therefore avoiding the coincidence of natural frequencies with excitation frequencies does not suffice to create an aeroelastically stable design.

For a designer, it is important to avoid both resonance and aeroelastic instabilities, and therefore both will be discussed in the following section.

5.2 Wind turbine blade aeroelasticity

In the previous section some of the basics concerning eigenmodes were discussed. The eigenmodes of wind turbine *blades* will be discussed here, followed by a discussion of the different possible blade instabilities that need to be taken into account.

5.2.1 Wind turbine blade modes

The mode shapes of a wind turbine blade depend mainly on the distribution of mass, the distribution of stiffness and the boundary conditions such as clamped or hinged connections. The rotational motion of the blades also has an effect on the modal shapes and frequencies, because the centrifugal and Coriolis forces cause some changes in the effective stiffnesses of the blades. The aerodynamic damping forces can also have a significant effect on the mode shapes and frequencies.

The first two modes in one direction of a uniform beam were illustrated in the previous section, in Fig. 5.4. A wind turbine blade is somewhat similar to a beam and will have similar eigenmodes, modes with mainly out-of-plane deformation (with respect to the plane described by the rotor blades during rotation), modes with mainly in-plane deformation and modes with mainly torsional deformation.

The modes on a wind turbine blade with mainly out-of-plane motion are called the flap modes, and so there will be a first flap mode similar to the shape illustrated in Fig. 5.4, and a second flap mode similar to the second mode illustrated in the figure. The modes with mainly in-plane deformation are called the edgewise modes. So again, there will be a first edgewise mode, a second edgewise mode, etc. similar to the modes in Fig. 5.4, but now in-plane.

However, in contrast to a simple uniform beam, a wind turbine blade will not have a mode which is purely in-plane, and neither will it have one which is purely out-of-plane, nor one which is purely in torsion. A flap mode (i.e. a mode with mainly out-of-plane deformation) will include some edgewise deformation due to the coupling of the stiffnesses that is a result of the blade twist. An edgewise mode will include some flapwise motion.

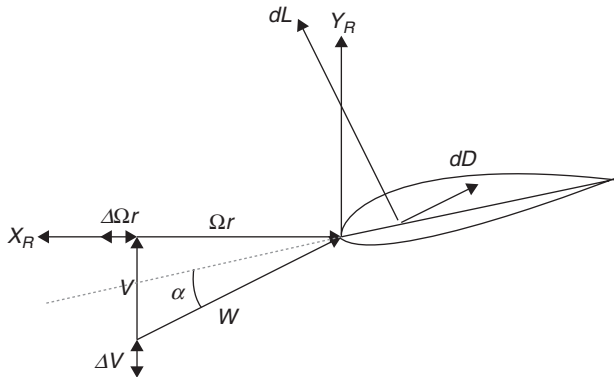
The blade mode with the lowest natural frequency is the mode in the out-of-plane direction, or the first flap mode, as the out-of-plane direction is the least stiff direction of the blade. The mode shape will be rather similar to the first mode shown in Fig. 5.4: mostly out-of-plane, but with some in-plane deformation.

The first edgewise frequency is usually the second blade frequency (going from the lowest to the highest frequency values), due to the significantly higher stiffness in this direction when compared to the out-of-plane direction. The first edgewise mode is also similar to the first mode shown in Fig. 5.4, but now mainly in-plane, with some out-of-plane deformation.

The second flap mode is usually the third blade mode and looks similar to the second mode shown in Fig. 5.4, though again it will not be a purely out-of-plane mode. The second edgewise mode and the third flapwise mode will often be the fourth and fifth blade mode, though which is which can differ. The first torsion mode will be higher, but can be very important, as discussed below. These six modes are probably the most relevant wind turbine blade modes that should be considered in an aeroelastic stability analysis.

5.2.2 Wind turbine blade instabilities

For each mode shape the damping can be determined, and will depend on operating conditions such as rpm, wind speed, pitch angle, yaw error, etc. The first flap mode is usually well damped, except near or in stall. This can be



5.5 Model to determine the aerodynamic damping of an aerofoil, in-plane and out-of-plane.

simply illustrated by modelling a 2-D aerofoil and a relative speed that undergoes small changes in velocity in the rotor plane and perpendicular to the rotor plane (Fig. 5.5). Rasmussen *et al.* (1999) derived the linearized equations for the aerodynamic damping of motions in-plane (xx) and out-of-plane (yy):

$$c_{xx}^R(r\Omega, V) = \frac{1}{2} c \rho \frac{r\Omega}{W} \left[\left(\frac{2r^2\Omega^2 + V^2}{r\Omega} \right) C_d - VCd_\alpha - VC_l + \frac{V^2}{r\Omega} C_{l\alpha} \right] \quad [5.8]$$

$$c_{yy}^R(r\Omega, V) = \frac{1}{2} c \rho \frac{r\Omega}{W} \left[\left(\frac{r^2\Omega^2 + 2V^2}{r\Omega} \right) C_d + VC_{d\alpha} + VC_l + r\Omega C_{l\alpha} \right] \quad [5.9]$$

In these equations c_{xx}^R and c_{yy}^R are the aerodynamic damping of motions in-plane and out-of-plane respectively, c is the chord of the blade section, ρ the air density, r the radial distance of the blade section from the rotor centre, Ω the rotational speed of the blade, W the total relative velocity ($W = \sqrt{V^2 + (r\Omega)^2}$), V the local out-of-plane velocity, C_d the drag coefficient, $C_{d\alpha}$ the derivative of the drag coefficient with respect to the angle of attack, C_l the lift coefficient and $C_{l\alpha}$ the derivative of the lift coefficient w.r.t. the angle of attack.

The equations are derived by considering the change in the aerodynamic forces due to a change in the relative total velocity, both in-plane and out-of-plane. These equations are the result of a simple, but very illustrative, derivation showing the possible problems with regards to damping.

Equations [5.8] and [5.9] show that the damping of the purely out-of-plane motion (yy) will be positive if $C_{l\alpha}$ is positive (under normal operating conditions all other terms cannot become negative). The first flap mode will be

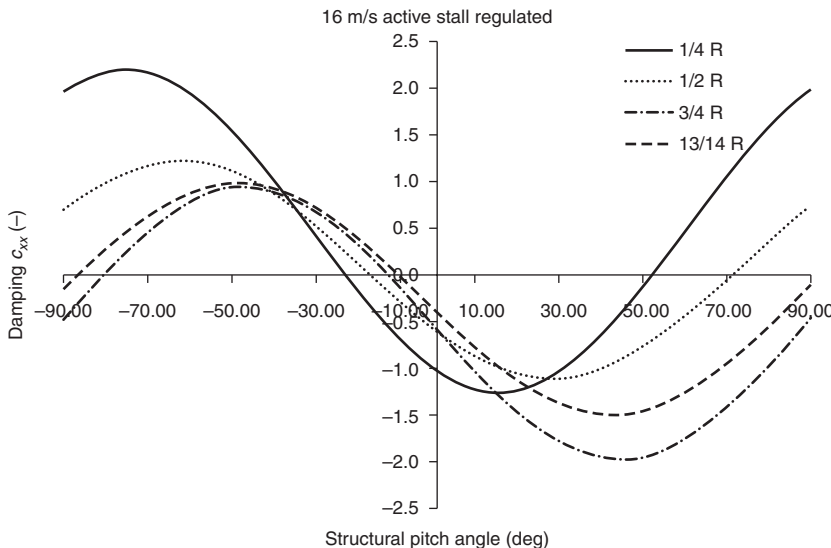
mostly an out-of-plane mode, so the damping will mainly be determined by the out-of-plane damping; therefore the value for c_{yy}^R will closely represent the damping of the flapwise mode. The equation shows that the out-of-plane motion is in general very well damped, but if the blade is operating in stall, there is a risk of reduced damping, as C_{l_α} then becomes negative beyond stall. If this damping were to become negative, it would be an example of a stall-induced vibration which can result in significant reduction of the blade life. This was reported to have occurred on the Nibe turbines (Lundsager *et al.*, 1981).

The first edgewise mode is mainly the in-plane mode. The equations given above (Equations [5.8] and [5.9]) for the damping of the in-plane and out-of-plane motions show that it is possible for the damping of the in-plane motion (Equation [5.8]) to be negative. For this reason it is very important for the first edgewise mode not to be a purely in-plane mode. The first edgewise mode has to include enough out-of-plane motion so that the positive damping from this motion is enough to enable the edgewise mode to be positively damped. Of course this does come at the cost of reducing the damping of the first flapwise mode.

It is possible to calculate the aerodynamic damping of a blade element in a direction other than purely in-plane or out-of-plane using the equations given above. By transforming these to a reference frame that is at an angle θ_{RB} relative to the in-plane direction, the damping coefficient c_{xx}^B can be determined, representing the damping in the actual direction of the mode shape at the specific radial position. An example can be seen in Fig. 5.6, where the damping coefficient for different directions is given. The values for $\theta_{RB} = 0$ are the damping values for a purely in-plane motion. By adding some out-of-plane motion (usually due to the aerodynamically required twist a negative value for this structural pitch angle is present), the damping of the main in-plane mode (i.e. the first edgewise mode) is increased. This is illustrated by the lines in the figure that are going up when moving to the left from the zero line.

Lack of damping of the first edgewise mode, another so-called stall-induced vibration, has been a known problem for wind turbine blades (Stiesdal, 1994; Møller, 1997). A case of negative damping of the edgewise mode also occurred on APX40T blades (Anderson *et al.*, 1999).

The model used so far is an oversimplification of reality. The mechanism behind a negatively damped edgewise mode can also be more complex, especially for larger wind turbine blades. As discussed by Kallesøe *et al.*, for large blades there can be a coupling between bending and torsion due to large deformations (Kallesøe and Hansen, 2008). In Kallesøe (2011), an example is shown that illustrates that the first edgewise mode is strongly influenced by these nonlinear effects. The damping of this mode is reduced and as a result the stall-induced vibrations become a possible instability.

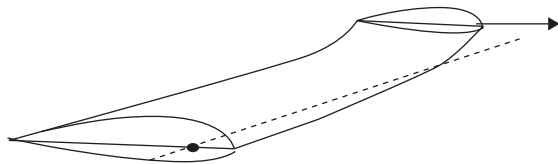


5.6 Non-dimensional values for the damping $c_{xx}^B / 0.5 \rho c r \Omega$ as functions of the structural pitch angle at four different radial distances along the blade for a wind speed of 16 m/s. The pitch setting of a stall regulated turbine has been used.

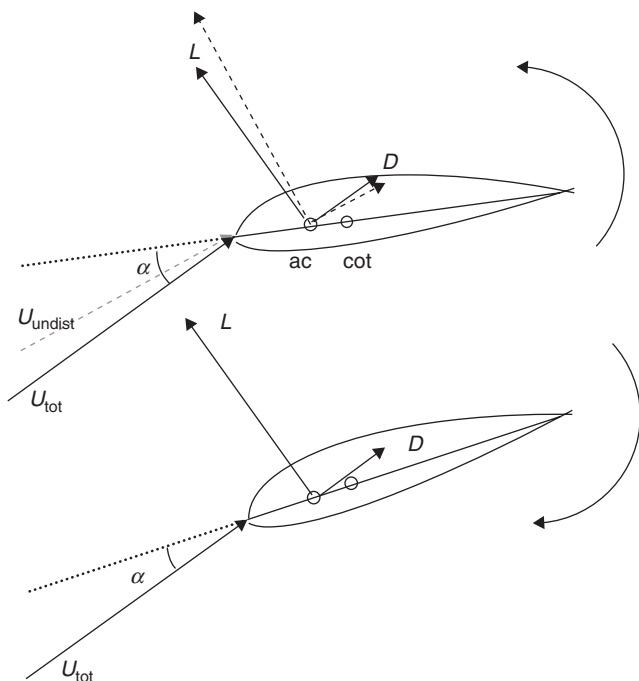
In this example, the torsional deformation present in the edgewise modes did not result in an instability in the attached flow regime. However, in Rasmussen *et al.* (1999) it was shown that the influence of torsion–bending coupling on the damping of the edgewise mode can also be negative in the attached flow regime. The coupling creates a more complex mode with a damping that cannot be explained by considering the aerodynamic forces only; a detailed dynamic model of the deformed blade needs to be considered. The cause of the coupling is illustrated in Fig. 5.7: a large deformation in either flapwise (pre-bend or deformation due to loads) or edgewise direction (e.g. swept blades) will result in a moment about the pitch axis for accelerations in the other direction (edgewise and flapwise respectively), so that twisting becomes apparent in those mode shapes.

In addition to the two aforementioned stall-induced vibrations, other blade instabilities that should be avoided are classical stall flutter and classical flutter.

The classical form of stall flutter is a third type of stall-induced vibration. This instability involves the first torsional mode and the mechanism behind it can be easily explained. Assume that a gust occurs that suddenly increases the angle of attack at the blade elements, while the blade is already in stall, operating in the range where C_{l_α} has negative values. This means that the lift force will decrease with an increasing angle of attack. If the aerodynamic



5.7 A blade with significant flapwise deformation, which causes the edgewise motions (illustrated by the force arrow) to induce some torsional deformation due to the moment that exists about the pitch axis.



5.8 Stall flutter on an aerofoil. A disturbance changes the wind speed and angle of attack, the blade is already in stall and the increase in angle of attack results in a reduction of the lift. The centre of twist (cot) is behind the aerodynamic centre (ac), therefore the aerofoil will twist such that the angle of attack is reduced (lower figure). Here the lift will increase again resulting in a torque to restore the aerofoil to its original position or beyond.

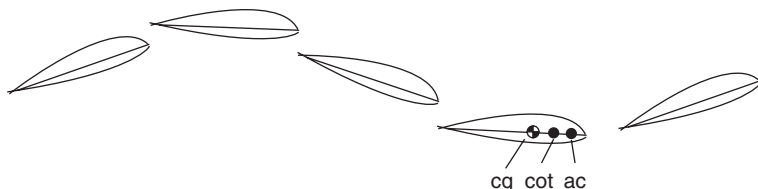
centre is in front of the centre of twist, the reduced lift results in a decrease of the torsional deformation, as illustrated in the top part of Fig. 5.8. This in turn reduces the angle of attack (see the lower part of the figure). For a smaller angle of attack in stall the lift will again increase, resulting in a cycle that can become unstable.

This instability is not likely to occur in wind turbines during normal operating conditions due to their high stiffness in torsion, but it is something to take into account when there is a flexible pitch control system or a pitch-link failure (Eggleston and Stoddard, 1987). For example, an experimental wind turbine called the FLEXTEETER contained a flexible pitch system which resulted in stall flutter (van Kuik and Dekker, 1992). The instability was solved by stiffening the torsional connection of the tip and by adding a damper.

Classical flutter and divergence also need to be avoided. Classical flutter is a destructive combination of a torsional oscillation with a flapping oscillation. In the case of divergence, it can result in twisting off of the blade. The mechanism can be easily explained. If the blade flaps, the changes in aerodynamic force act in the aerodynamic centre but the inertial forces act in the centre of gravity. If the aerodynamic centre does not coincide with the centre of gravity, the flapping motion will result in a moment about the pitch axis. This can change the aerodynamic forces and therefore the flap deformation completing the cycle, as illustrated in Fig. 5.9. As stated by Hansen (2007), classical flutter can occur when the flow is attached, the tip speed is high, the torsional stiffness is rather low and the centre of gravity is positioned behind the aerodynamic centre.

Divergence is only possible when the torsional stiffness is very low, such that the centrifugal twisting moment in flapping is sufficient to drive the blade through stall in a single cycle. For a wind turbine this could be the case when there is a pitch-link failure whereby the stiffness in pitch direction almost completely disappears and divergence could occur. Under the influence of gravity, this could become a limit cycle behaviour.

As pointed out in Hansen (2007), classical flutter has so far not occurred on wind turbines. However, it cannot be ruled out for future (larger) designs,



5.9 Classical flutter of an aerofoil. If the centre of gravity (cg) is behind the aerodynamic centre, a flapping motion will result in a twisting moment due to inertia as well as due to the change in the aerodynamic forces. Twisting of the blade will result in a change in flap deformation due to the change in aerodynamics and inertia. The coupling can result in a cycle of twisting and flapping as illustrated, which under certain circumstances can increase in amplitude.

especially as the offshore turbines might operate at higher tip speed ratios (the ratio between tip speed and undisturbed wind speed).

When a wind turbine is designed, it is important to look at the damping of all relevant modes (e.g. first blade flap mode, first blade edgewise mode, etc., as discussed above). However one should also look at possible frequency coincidence, such as is the case for classical flutter. In this way, any of the above-discussed instabilities can be avoided.

5.3 Blade design

When designing a wind turbine blade there are several aspects that can be taken into account to reduce the risk of the aeroelastic stability of the designed blade being poor. Four of these aspects will be discussed in this section: the avoidance of resonance, the use of the structural pitch angle, the aeroelastic analysis and, briefly, the choice of aerofoils.

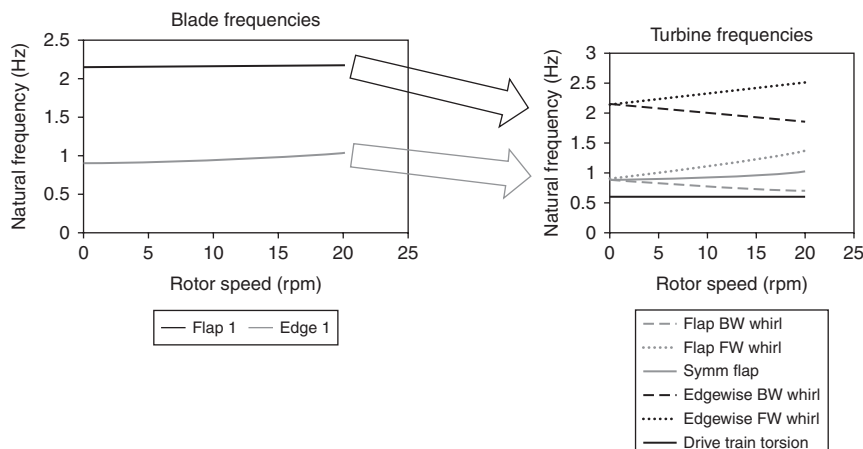
5.3.1 Avoidance of resonance

When designing a wind turbine blade, one has to make sure that the possible resonance frequencies differ sufficiently from the blade's natural frequencies. The main excitation frequencies to be avoided are the rotor speed ($1P$) and its multiples ($2P, 3P, \dots$). As well as the excitation frequencies, coincidence of the natural frequencies should also be avoided; coincidence of the second or third flap frequency with the first torsion frequency, for example, has been shown to be the cause of classical flutter.

The blades are excited at the nP frequencies due to rotational sampling: the turbulence that the blades experience contains significant contributions at the nP frequencies due to the translation of the turbulence from the fixed frame to the rotating frame. The presence of the tower (tower shadow), wind shear, yawed flow and gravity forces also result in significant blade excitations.

The blade passing frequency is especially critical: the natural frequencies of the blade should not be close to this frequency. That said, it must be remembered that the mode shapes and the frequencies of the isolated blade modes are influenced by the rotation and will change to different turbine modes when the blades form part of a complete turbine. The rotation of a blade will affect the frequency due to centrifugal stiffening. The centrifugal force will increase the flap stiffness as it will contribute to the restoring forces on the blade if it bends, similar to the elastic forces. The effect of centrifugal stiffening is clearly visible in the plot on the left in Fig. 5.10: the first flap frequency of the blade increases with the rotor speed. The effect on edgewise modes is much smaller.

Next to centrifugal stiffening, the presence of other components in the turbine will affect the frequencies too. For example, the main shaft torsion stiffness will influence the frequency of some of the edgewise modes on a complete turbine. But a much more relevant effect is the difference that can be seen when the frequencies are looked at in the rotating reference frame compared with the non-rotating frame. As will be explained in the following section when the complete turbine will be addressed, an eigenmode vibration of the rotor can lead to a rather different excitation of the tower. The tower will ‘feel’ a different frequency that can be sensed on the blades. For example, a flap mode in an isolated blade will result in different flap modes on the complete rotor with all two or all three blades becoming part of the eigenmode. The first flap mode will therefore correlate with a backward (BW) whirling flap mode, a forward (FW) whirling flap mode and a symmetric flap mode on a complete turbine. And these modes will have frequencies that are different from the blade frequency. For the edgewise modes there is a similar correlation: a wind turbine will show a backward whirling edge mode, a forward whirling edge mode and a collective edge/drive train mode. The frequencies of the whirling modes are strongly related to the rotational speed: forward whirling modes will have a frequency that is close to the isolated blade frequency increased by the rpm (Ω), while backward whirling modes will have a frequency that is close to the isolated blade frequency reduced by the rpm (Ω). Figure 5.10 shows how the blade frequencies analysed could show up in the Campbell diagram of a complete turbine.



5.10 Campbell diagram of an isolated blade and the corresponding complete wind turbine (with asynchronous generator).

5.3.2 Structural pitch angle

The structural pitch angle is the angle between the stiffest and the most flexible direction; it defines the principal axes. This angle has significant influence on the mode shapes of the flap- and edge-wise modes. As discussed in Section 5.2.2, the stall-induced vibration that results in a negative damping of the first edgewise mode is best counteracted in a design by including enough out-of-plane motion in the edgewise mode. To do this, the structural pitch angle is important. By not putting the stiffest direction exactly in-plane, but having it at a certain angle, the resultant out-of-plane motion will be included in the edgewise mode shape.

Due to the way that a wind turbine blade is built up, the structural pitch angle often closely follows the aerodynamic twist. However, it does not always do so, and the above technique can be actively used in the design to provide additional damping to the edgewise mode if required. To allow effective use of the possibilities that come from adjusting the structural pitch angle in the design, it is clear that the modelling of the turbine blade must be done with enough detail in the model to enable the effect of the structural pitch angle to be represented correctly in the calculation.

5.3.3 Analysis

As discussed in Section 5.1.1, aeroelasticity concerns the response of a structure under the influence of aerodynamics, elasticity and dynamics. However for wind turbines, pitch control and, more essentially, generator control have substantial influence on the aeroelastic stability of the structure and should be included in the aeroelastic analysis of the complete turbine. An aeroelastic analysis will provide the different mode shapes and corresponding frequencies as well as the corresponding damping values. A load analysis will provide the loads on the turbine for a specific load case; and here, too, all aeroelastic effects should be included. Some guidelines as to the minimum requirements for the performance of both these analyses will now be set out.

For a reliable aeroelastic analysis, it is not necessary to include all eigenmodes. This would not be practical nor possible, as theoretically a blade will have an infinite number of eigenmodes. However, at the very least one needs to include the first two flap modes and the first edgewise mode in any aeroelastic analysis in order to get any useful results. But it is strongly recommended that at least the first torsion and an additional flap and edgewise mode should be included in the analysis. For the smaller turbines (<500 kW) the torsional flexibility is not relevant, but for larger turbines the torsional deformations should not be neglected. In the steady state condition the

torsion deformation can result in a difference of a few degrees in the angle of attack near the blade tip, which is well above negligible. With the increase in size of wind turbines and the possibility of higher tip speeds for offshore turbines, it can also be observed that the flutter speed (the rpm above which a negatively damped torsion/flap mode occurs) has drawn closer to the actual operational conditions.

This is a further illustration that torsional flexibility can no longer be neglected in aeroelastic analysis and that the tools used for an aeroelastic analysis must include the necessary detail in the structural model. The modelling of the structural pitch angle, which has already been discussed, is therefore important. Any analysis requires a representative presentation of the mode shapes, as this has a large influence on the damping of the modes. This means that the structural pitch angle values along the radius of the blade should be included in the model.

The discussion in Section 5.2.2 concerning the negative damping of the edgewise mode, and the more complex case of this instability that can occur in large wind turbines due to bending–torsion coupling, illustrates that the analysis should at least take into account a correctly calculated deformed state. When using a linear tool, sometimes the linearization is about the undeformed state, but for current wind turbine sizes the accuracy in such calculations will be limited. As has been explained, the coupling between bending and torsion that is present in the mode shapes has significant influence on the damping of the modes, and is caused by the deformations of the blade in the steady state. If a linearized calculation is performed with a linearization about the deformed steady state it can provide good insight, but it should preferably be complemented by a fully nonlinear calculation to include all of the nonlinearities.

In addition to aerodynamic damping, there are other possible sources of damping, e.g. generator damping and structural damping. If a blade is given an initial deformation while in vacuum, the blade vibration will be damped. This is due to structural damping: some of the energy is changed into heat during the deformation changes. For poorly damped modes, the structural damping can be the most relevant source for damping. Looking at the shapes of higher modes, it is not difficult to see that the structural damping of higher modes will be higher. For higher modes the structural damping can be so high that the total aeroelastic damping will always be positive. Therefore these higher modes are usually not included in the aeroelastic analysis.

For the aerodynamic forces, most codes apply the Blade Element Momentum (BEM) theory. This does require some additional correction models for unsteady aerodynamics (e.g. aerodynamic stall, dynamic inflow) and specific flow cases (yawed flow, turbulent wake state). The dynamic stall model in particular can influence the damping value of some

of the modes as well as the loads. Various dynamic stall models exist, whose results differ from each other quite significantly (Holierhoek *et al.*, 2012); however, including any of the commonly used dynamic stall models will improve the results. As dynamic stall usually increases the damping, leaving it out of an aeroelastic analysis will result in an underestimation of the damping. BEM, used in conjunction with the available correction models, suffices for most calculations and has the great benefit that it is simple and quick. The aerodynamic model could also be improved by using, e.g., a free vortex approach or computational fluid dynamics (CFD), but the benefits of this do not yet outweigh the drawbacks of the lengthy calculation time and the complexity in modelling.

Conclusion

For a reliable aeroelastic analysis the following requirements are the absolute minimum:

Structural blade model: This has to include flexibilities in flapwise, edgewise and torsional direction; at least the first two flapwise modes, the first edge-wise mode and the first torsional mode must be represented with enough accuracy. The effect of the structural pitch angle (using different values along the radius) should be included in the mode shapes. The effect of coupling between bending and torsion must be taken into account in the calculation. Using a linearized model is in most cases a possibility, but the linearization needs to be done about a correctly calculated steady state.

Aerodynamic model: BEM will suffice in all regular cases if the correction models for dynamic stall are included.

5.3.4 Aerofoils

For aeroelastic stability the choice of aerofoils is important. The aerodynamic design of a blade should not be based solely on aerodynamic power: the aeroelastic stability should be taken into account.

From an aeroelastic point of view, the stall characteristics in particular of an aerofoil should be carefully looked at. If the aerofoil shows abrupt stall occurrence, then it would be preferable not to use this aerofoil, or to use it only operating significantly below stall. The negative lift slope after stall can result in negative damping of the flap and edgewise modes. The more negative the slope, the more negative the effect on the damping. Aerofoils that have lower (absolute) values for the negative slope in the lift curve after stall are to be preferred. These show a more gentle stall behaviour and have a less negative effect on the damping. This is especially important for the blade sections close to the tip, as these will have the largest influence

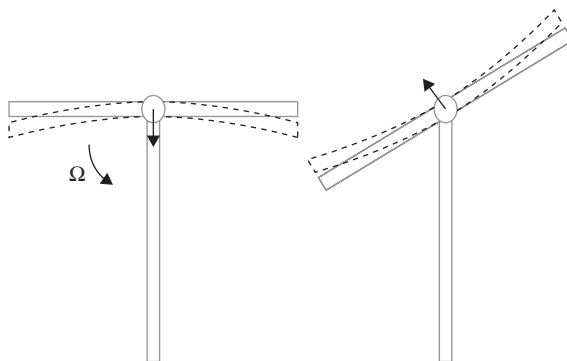
on the total damping of the first flapwise and first edgewise modes. Using aerofoils with abrupt stall behaviour for the inner sections of the blade is less problematic.

Operating close to stall can have a negative effect on other modes as well: the stall-induced vibrations have become a well-known problem for wind turbines of approximately 500 kW and above. Therefore, for aerofoils with milder stall characteristics, it is also preferable to avoid operating close to stall.

5.4 Complete turbine design

The mode shapes of isolated blades were discussed in Section 5.2.1. On a complete wind turbine, there will be two or three blades. Therefore one blade mode will be related to two or three modes respectively on the complete turbine. The isolated blade modes will couple with identical modes on the other blades. For example, on a two-bladed turbine, blades will all flap collectively in one mode and flap in the opposite direction in the second mode; this way the first flap mode of the isolated blade is related to two different modes on the complete turbine. In addition to the multiple blades, other components of a complete wind turbine can also interact with the modes, especially the tower and the main shaft. This will influence the natural mode shapes, the natural frequencies and the corresponding damping values of the complete turbine.

It has already been mentioned in Section 5.3.1 that some of the frequencies on a complete turbine change significantly. To get a better understanding of this shift in frequencies in a complete turbine, first consider the excitations that are felt by the tower if the blades vibrate. For example, consider blades vibrating in the first edgewise mode. The frequencies that are felt by the tower are in some cases not the same as the rotating edgewise frequencies. If multiple blades vibrate at a certain frequency and these blades rotate, the tower can sense other frequencies if these modes have a resulting reaction force or moment on the tower that has a component in the plane of rotation. This can be explained using Fig. 5.11. Here a two-bladed turbine is depicted, whose blades vibrate with the edgewise frequency. When two blades are combined on one tower, this will result in two different multi-blade modes: one as shown in the picture and one where the blades vibrate collectively in the same direction as the rotor rotation (and of course back in the opposite direction). For the case illustrated in Fig. 5.11, the combined vibration results in a reaction force on the remainder of the turbine structure that has a component in the plane of rotation. With the rotation of the rotor and the vibration of the blades, this is felt as an excitation force on the tower at the edgewise frequency ω increased with the rotor rpm ($\omega + \Omega$), and one at the



5.11 A two-bladed turbine with blades vibrating in edgewise direction, illustrating the reaction force on the tower due to this vibration. The rotation of the blades will translate this vibration to the tower as a vibration at two different frequencies: $\omega + \Omega$ and $\omega - \Omega$.

edgewise frequency reduced by the rpm ($\omega - \Omega$). The reaction force in the rotating reference frame will be equal to:

$$F_{xR} = A \sin \omega t; F_{yR} = 0 \quad [5.10]$$

with A the amplitude of the reaction force and ω the edgewise blade frequency. Transforming this to the non-rotating frame will result in the following expression for the force:

$$F_{xNR} = A \sin \omega t \cos \Omega t; F_{yNR} = A \sin \omega t \sin \Omega t \quad [5.11]$$

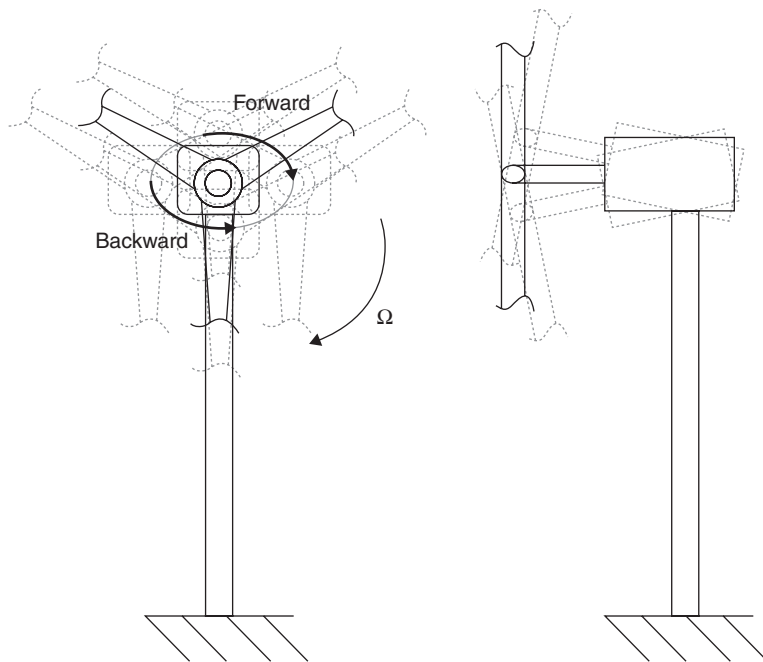
This can be written as:

$$F_{xNR} = \frac{1}{2} A \sin((\omega - \Omega)t) + \frac{1}{2} A \sin((\omega + \Omega)t)$$

$$F_{yNR} = \frac{1}{2} A \cos((\omega - \Omega)t) - \frac{1}{2} A \cos((\omega + \Omega)t) \quad [5.12]$$

This clearly illustrates where the shift in frequencies to $\omega + \Omega$ and $\omega - \Omega$, as illustrated in Fig. 5.10, originates from.

As the different components of the turbine will be flexible, they will interact in the final complete turbine modes, and this excitation in the rotor plane results in the forward whirling modes and backward whirling modes,



5.12 A backward and a forward whirling mode on a complete turbine (left: front view, right: side view). Corresponding blade and tower deformations are not illustrated, these will differ for the different whirling modes.

as illustrated in Fig. 5.12. This produces more complex mode shapes, and at different frequencies than for the isolated blades, and therefore other possible instabilities and resonances.

As was shown for an isolated blade, the mode shape is important for the damping, therefore a change in the mode shape will have a significant effect on the damping of this mode. For example, the backward whirling edgewise mode can become negatively damped due to stall, which is similar to the possibility of negative damping of the first edgewise blade mode. However, the motion of the vibration in the natural mode of the complete turbine is more complex. As analysed by Hansen (2003) and measured by Thomsen *et al.* (2000), the backward edgewise whirling mode has less damping than the forward edgewise whirling mode due to the difference in the amount of out-of-plane motion between the two mode shapes, while both concern the same isolated blade mode.

Edgewise whirling modes will be excited by turbulence and tower shadow at 3P, 6P and 9P. For current wind turbine sizes, it would be realistic to expect that the edgewise whirling modes would be in the region of the 6P excitation. The backward edgewise mode would be close to the 6P excitation

if the standstill edgewise mode were close to 7P. The forward edgewise mode would be close to 6P if the stand still edgewise mode were close to 5P. Therefore, from a resonance point of view, both 5P and 7P standstill rotor frequencies need to be avoided. The most likely frequency for the design would therefore be between 5.5P and 6.5P. Yet, for variable speed wind turbines, one has to ensure that the below rated lower rpms do not result in the whirling modes getting close to an excitation, especially the least-damped backward edgewise mode. Of course, this operating rpm will occur less often and have less impact on the total fatigue loads than the rated rpm.

This discussion illustrates that analysis of an isolated blade is insufficient to ensure a stable wind turbine, though it does provide important insights and knowledge that can help alter designs in order to prevent and remove instabilities.

5.5 Challenges and future trends

The main trend in wind turbine blades is the increase in size. Sometimes, but not always, this goes hand in hand with an increase in power: recently we have seen designs that are simply a longer blade for the same rated power, but lighter and more cost effective.

As discussed in Section 5.2.2, this increase in size has a significant effect. First of all, torsion can no longer be neglected. For offshore wind turbines, which have the potential to operate at higher tip speeds as noise limitations are less relevant offshore, torsion will clearly affect the possible instabilities. As the size of turbines increases further and operating conditions change, new instabilities, such as classical flutter, need to be taken into account. Therefore a flutter analysis to determine the flutter speed of the turbine should be included in the aeroelastic analysis.

Another trend that will have a significant effect on the design of larger blades is the pre-bending of blades. Pre-bending can be in both the flapwise and the edgewise directions. Performing a ‘pre-bend’ on the blades enables the designer to design a blade that will be close to the optimal straight blade when forces are acting on the blade. However, it also complicates the design.

Adding an aft-sweep to a blade can enhance its performance by reducing the loads: the blade will deform in the torsional direction due to the sweep, which then reduces the angle of attack and therefore the loads. However, for both the aft-sweep pre-bending as the out-of-plane pre-bending, effects such as bend-twist coupling can no longer simply be neglected. Therefore, for the larger blades, some of the current analysis methods no longer suffice. In many cases the analysis should be a fully nonlinear analysis in order to include the nonlinear coupling effects of different modes. Not only the pre-bend is responsible for significant coupling between bending and twisting

of the blade, it is also caused by large deformations. For the current size of blades, and larger, the nonlinear effects become more and more relevant due to, among other things, this coupling. At the same time it is not hard to imagine that elastic couplings, which use different layers of fibres at different angles, can be effectively used to increase the stability of the blades or reduce the fatigue loads. One of the main challenges at the moment, therefore, is: how can we achieve the optimal design and be sure that the loads are predicted accurately?

5.6 Sources of further information and advice

Literature concerning the aeroelastic stability of wind turbines can be found mainly in wind energy specific journals, but, for a basic background to aeroelasticity in general, the reader is referred to several good books included in the references list in Section 5.7 below, e.g. Dowell (1995). Articles in the various journals, several of which are listed in the references, provide deeper insight into the possible instabilities of both wind turbine blades and complete wind turbines, the possible solutions, and the nature of the aeroelastic analysis that is required. Finally, it is also worth noting that many publications that concern the aeroelastic stability of helicopter blades can also be very informative when studying the aeroelasticity of wind turbine blades.

5.7 References

- Anderson, C, Heerkes, H and Yemm, R (1999), 'The use of blade-mounted dampers to eliminate edgewise stall vibration', *EWEA 1999*, Nice, France.
- Bisplinghoff, RL, Ashley, H and Halfman, RL (1996), *Aeroelasticity*, Dover Publications Inc., Mineola, New York, USA.
- Dowell, EH (ed.) (1995), *A Modern Course in Aeroelasticity, Third Revised and Enlarged Edition*, Kluwer Academic Publishers, Dordrecht.
- Eggleson, DM and Stoddard, FS (1987), *Wind Turbine Engineering Design*, Van Nostrand Reinhold Company, New York, USA.
- Hansen, MH (2003), 'Improved modal dynamics of wind turbines to avoid stall-induced vibrations', *Wind Energy*, **6**, pp. 179–195.
- Hansen, MH (2007), 'Aeroelastic instability problems for wind turbines', *Wind Energy*, **10**, pp. 551–577.
- Holierhoek, JG, de Vaal, JB, van Zuijlen, AH and Bijl, H (2012), 'Comparing different dynamic stall models', *Wind Energy*, **16**, pp. 139–158, DOI: 10.1002/we.548.
- Kallesøe, BS (2011), 'Effect of steady deflections on the aeroelastic stability of a turbine blade', *Wind Energy*, **14**, pp. 209–224.
- Kallesøe, BS and Hansen, MH (2008), *Effects of Large Bending Deflections on Blade Flutter Limits, UpWind Deliverable D2.3*, Risø National Laboratory, Roskilde, Denmark, Technical Report Risø-R-1642(EN).
- van Kuik, G and Dekker, J (1992), The flexhat program, technology development and testing of flexible rotor systems with fast passive pitch control, *Journal of Wind Engineering and Industrial Aerodynamics*, **39**(1–3), pp. 435–448.

- Lundsager, P, Petersen, H and Frandsen, S (1981), *The Dynamic Behavior of the Stall-Regulated Nibe A Wind Turbine Measurements and a Model for Stall-Induced Vibrations*, Risø National Laboratory, Roskilde, Denmark, Technical Report Risø-M-2253.
- Møller, T (1997), 'Blade cracks signal new stress problem', *WindPower Monthly*, May 1997.
- Rasmussen, F, Petersen, JT and Madsen, HA (1999), 'Dynamic stall and aerodynamic damping', *ASME, Journal of Solar Energy Engineering*, **121**(3), pp. 150–155, <<http://link.aip.org/link/?SLE/121/150/1>> doi 10.1115/1.2888426
- Spera, DA (1994), *Wind Turbine Technology, Fundamental Concepts of Wind Turbine Engineering*, ASME, New York, USA.
- Stiesdal, H (1994), 'Extreme wind loads on stall regulated wind turbines', *BWEA 16*, Stirling, UK, Mechanical Engineering Publications Ltd., June 1994.
- Sullivan, TL (1981), 'A review of resonance response in large, horizontal-axis wind turbines', *Proceedings Wind Turbine Dynamics Workshop*, editor R.W. Thresher, CONF – 810226, NASA Conference Publication 2185, Cleveland Ohio, NASA Lewis Research Center, DOE Publication, pp. 237–244.
- Thomsen, K, Petersen, JT, Nim, E, Øye, S and Petersen, B (2000), 'A method for determination of damping for edgewise blade vibrations', *Wind Energy*, **3**, pp. 233–246.

Fatigue as a design driver for composite wind turbine blades

R. P. L. NIJSSEN, Knowledge Centre Wind turbine Materials and Constructions, The Netherlands and P. BRØNDSTED, Technical University of Denmark, Denmark

DOI: 10.1533/9780857097286.2.175

Abstract: Composites have been the material of choice for wind turbine blade construction for several decades. This chapter explains why. It also shows how wind turbine blade materials and our understanding of their fatigue behaviour have developed recently, and the gaps that still exist in the knowledge. The chapter discusses why fatigue is a predominant design driver for wind turbine blades. The main structural elements of the blade (load bearing components and aerodynamic shell) are considered in terms of material and design requirements, and fundamental research questions are addressed. Finally, there is a comment on current and future trends, as well as a list of recommended reading.

Key words: fatigue, wind turbine rotor blades, life prediction methods, blade design.

6.1 Introduction

Composites have been the material of choice for wind turbine blade construction for several decades, partly due to their superior fatigue performance compared to other materials. Various materials may be found in a blade structure, ranging from the unidirectional reinforcement in the spar caps, to foams, balsa and multiaxial laminates in the aerodynamic ‘shells’. In many designs, structural components are integrated using adhesive bondlines.

All these materials are affected in some manner by fatigue loads. This chapter discusses several reasons why fatigue is a predominant design driver for wind turbine blades. It looks at different research perspectives that should ultimately lead to improved knowledge about the fatigue performance of the materials, and hence improved design guidelines.

Various avenues for tackling fatigue in rotor blades exist. The empirical or phenomenological approaches, in which large amounts of constant

amplitude data are collected and used with relatively simple design rules to conduct a fatigue analysis, are currently prevalent. Micromechanical numerical modelling of damage processes inside the material on a small geometrical scale promises to provide improved insights into how and why fatigue is affected by, e.g. fabric architecture. For very thick laminates (multiple centimetres), it is suspected that various mechanisms (residual stresses caused during manufacturing, self-heating in tests) come into play that distort the relationship between test results on small coupons and the actual fatigue behaviour of thick laminates. A blade may also be regarded as a collection of structural elements connected by adhesives or mechanically. These critical joints suffer from fatigue, which should be well described through experiments and observations.

The chapter is organised as follows. First, the blade's main structural materials and components are discussed in terms of material and design requirements. Fatigue and related fundamental research questions are then addressed. Finally, there is a comment on current and future trends, as well as a list of recommended reading.

6.2 Materials in blades

The main reasons for using composites are their geometrical freedom and their resilience against fatigue failure. The majority of blades are produced from polymer composite materials reinforced with mainly glass fibres, and to some extent carbon fibres and carbon fibres in hybrid combination with glass fibres. Especially for smaller blades, bio-based fibre materials made from hemp, flax or other celluloses based fibres are potential candidate materials. Wood and bamboo are also used.

The single-fibre properties are primarily diameter, stiffness and strength. These properties are controlled in the manufacturing process, in the glass composition and the processing parameters. Due to cost considerations, E-glass, with stiffness of 72–74 GPa, and strength of 1500–2500 MPa, has been the dominant material. Glass diameters are in the range from 10 to 35 microns. However, in recent years a higher stiffness (82–86 GPa), more cost-competitive type, H-glass, has been introduced.

The resins are mainly thermoset polymers such as epoxy, polyester and vinyl ester. Resins such as polyurethane and thermoplastic polymers are being introduced, with sustainability being enhanced through the introduction of bio-based resins in the components.

Resins are used with processing requirements such as viscosity (<500 cps) (for infusion purposes) and processability (gel time > 20 min), which aim to control the solidification process. Shrinkage introduces residual stresses, and therefore ductility and toughness are important properties

to have under control. Compatibility of fibres, sizing and adhesives is required. At both processing and application stages, low moisture absorption is important.

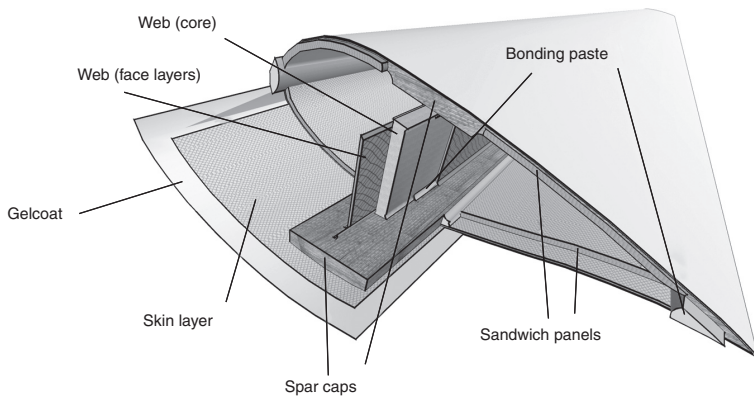
Sizing is an organic based material which is coated onto the individual glass fibre. It has several functions, namely, to ensure processability, to protect the individual fibres and to close surface flaws and defects on the fibre surfaces in order to maintain strength. Most importantly, the sizing forms the interphase between the fibre and the resin and enhances the bonding between the fibre and the resin, the interface strength. The formulation of the sizing is one of the most challenging tasks in fibre production. One challenge is the compatibility of resin and sizing; another, the fact that the processability and lubrication conflicts with the requirement for strong bonding. For this reason, different sizings are sometimes applied at a later stage in the fibre and fabric manufacturing processes.

Hand lay-up of the laminate in early blades resulted in considerable variation in laminate quality as well as serious working-environment problems because of the need to handle both epoxy and polyester. Modern manufacturing methods are dry lay-up followed by vacuum infusion.

The increasing demand for both fibres and resins generates and develops markets for new suppliers and calls for additional quality assurance for the raw materials deliverables. Quality assurance is important to ensure uniformity in the manufacturing processes and thereby maintain product quality. Manufacturers of blades and blade materials must ensure the consistent quality of their fibres, sizings and resins: these are the basic constituents in a composite and the basis for performance. The composite properties are very dependent on consistency between fibre surface treatments (sizings), resin quality and manufacturing parameters. Research disciplines which focus on laminate and sandwich architectures, processing, microstructure characterisation (microscopy), modelling (micromechanical and materials modelling) and mechanical characterisation therefore provide a strong foundation for high-quality performance in the application. The long-term behaviour and the endurance of the complete blade can be controlled by damage detection, non-destructive evaluation and structural health monitoring, and damage mechanics can be used for evaluating the reliability of the blade components.

6.3 Blade structure and components

The next sections look at the composite materials present in the main structural parts of the blade, the characterisation of these materials and design models. The structural requirements of the rotor blade follow directly from the loads acting on it; although a wind turbine rotor blade is an integral



6.1 Rotor blade structural components.

structure, several load bearing components may be identified. Figure 6.1 identifies the blade's structural components.

The aerodynamic loads may be schematised by a flap load that has a roughly triangular distribution along the blade span, with maximum section loads near the tip, and a similar in-plane load representing the aerodynamic profile thrust load which is responsible for the energy generation. The aerodynamic loads vary due to changes in wind speed, wind shear and gusts.

In addition, the gravity load acts roughly in the rotor plane. The gravity load reverses twice every blade rotation, and is a significant source of fatigue damage for larger blades.

Most rotor blades are, essentially, thin-walled, multi-celled, non-prismatic cantilever beam structures. Most of the larger blades are produced in two halves, the upper and the lower part, and are joined using adhesive bonding. Adhesives used are epoxy, vinylester, polyurethane (PUR), methyl methacrylate (MMA) among others. Other production features include fully integrated injection moulding and mould-cast smaller blades. Micro blades can be cut from wood, or cast as pure polymers. Chapter 13 deals with the manufacturing technologies for small wind turbine blades.

In any case, although the rotor blade is an integral structure in which most components work together, separate components can be identified:

- Load carrying spar (for flap loads or lead-lag load):
 - spar caps carrying most of the normal load
 - shear webs carrying most of the shear load
- Aerodynamic shell:
 - outer skin layer for application of gel coat and for carrying torsion and shear loads caused by aerodynamic and gravitational lead-lag actions on the blade

- sandwich panels for maintaining aerodynamic profile and buckling resistance
- Bondlines
- Blade root (or mid-span) connection
 - embedded studs
 - T-bolt connection.

This chapter is limited to the structural blade parts, but of course blades do incorporate lightning protection systems, typically consisting of a copper mesh laminated close to the outer skin, several lightning receptors at spanwise intervals, and copper wire to guide the collected lightning energy to the ground.

In the remaining parts of this section, these structural blade parts are categorised and discussed separately in terms of the material types present, the loads acting on them and the characterisation required for design.

6.3.1 Load bearing components

All of the blade parts can be considered as load bearing parts, but the spar structure is typically responsible for the largest part of the resistance to aerodynamic loads. The rest of the blade can be considered as an aerodynamic shell. The load bearing structure is divided into shear web, spar caps, connections and trailing-edge reinforcement, which will be discussed in this section. The skin and the other aerodynamic parts are then discussed.

As for the spar construction, various classifications of blade structural concepts exist. Joncas¹ classified cross-sectional concepts according to blade length and production method, and proposed the incorporation of ribs as a new concept after a topological optimisation exercise. In his review, the D-shaped spar structure that includes the leading edge (D-nose) was not included.

The spar caps in a rotor blade are among the most heavily loaded parts of the blade. Whether incorporated in a box spar or in a less integrated structure, they consist of a large portion of unidirectional (UD) material in spanwise direction. They are thickest near the root, with laminate thicknesses of up to ~150 mm, and are thickness tapered towards the tip, following the aerodynamic bending moment distribution. The pressure side spar cap material is subjected to predominantly tensile loads, with a fatigue component caused by the varying wind speed, wind shear and gusts. The suction side spar cap is subjected to predominantly compression loads.

Because it is the heaviest loaded material in the blade, spar cap material is the main focus of (fatigue) material research. Recent efforts have focussed on phenomenological fatigue modelling, micromechanical fatigue descriptions, effect of thick laminates and the effects of extreme conditions; these will be discussed in the next section.

Spar cap material is typically a combination of glass and polyester (up to now, mainly LM Windpower have used this material, although the option is being (re-)explored by other blade manufacturers interested in cost reduction) or glass and epoxy. The use of carbon fibre composites was recently estimated, by an independent rotor blade manufacturer, to lead to ca. 20% reduction in blade root bending moment and hence blade mass.² In another recent independent study, the effects of carbon and glass–carbon hybrids were investigated,³ showing the advantages of the hybrid material.

Root and blade joint connections

The rotor blade needs to be connected to the pitch bearing and the hub, neither of which are, typically, composite structures. In addition, split blade concepts have been extensively investigated as solutions to the limitations imposed by road transportation of blades. Connector concepts for the blade root and the blade joint are broadly similar.

Two main types of root and blade joint connections exist:

1. the T-bolt, more popularly referred to as the ‘IKEA’ bolt connection (Fig. 6.2);
2. the embedded ‘stud’, ‘carrot’, or ‘bushing’.

The first type of connection relies on normal stresses to transfer the bolt load to the laminate, whereas the second type mostly relies on shear stresses. The test in Fig. 6.2 shows a specimen with three T-bolts on either side. The central bolt is loaded; the outer T-bolts are present in the specimen to enable



6.2 IKEA bolt connection test specimen.

realistic reproduction of the boundary conditions for the central bolt. The main advantages of the T-bolt connection are its design and manufacturing simplicity (after the blade is completed, two perpendicular holes need to be drilled per bolt), but a disadvantage is that the laminate must be locally damaged to house the cylindrical nuts, so that for a given root circumference, ca. 25% more bolts can be included using embedded studs than using T-bolts. One area of concern with the T-bolt connection is whether the bolts will retain their pre-load during operation (pre-load may be released due to compression creep in the root area laminate). A concern with the embedded stud connection is the wear of the bond between the studs and the surrounding laminate, caused by mechanical or thermal fatigue.

A comparison of bolt connection methods was carried out as part of the Bladeco project.⁴

6.3.2 Aerodynamic shell

The aerodynamic shells and the webs are manufactured from sandwich materials with composite skin layers in $\pm 45^\circ$ or $0/\pm 45^\circ$ laminate lay-up separated with cores made from balsa wood and polyvinyl chloride (PVC). Other materials used as core materials are honeycomb structures or foams, such as polyethylene terephthalate (PET), styrene acrylonitrile (SAN), polyurethane (PU), polystyrene (PS), polyetherimide (PEI), polymethacrylimide (PMI) and polypropylene (PP).

Skin

One of the main functions of the blade skin is not to directly provide structural resistance, as much as to protect from external influences such as UV light and erosion; in that regard the outer gel coat can be considered as the skin. Underneath the gel coat there is typically a $\pm 45^\circ$ layer that does provide some torsional stiffness.

There are two distinct types of sandwich panels in rotor blades: the shear web sandwich and the aerodynamic panels. The former is typically a flat sandwich panel, with $\pm 45^\circ$ layers as skin, and loaded predominantly in in-plane shear. The aerodynamic panels in a blade are curved – often in two directions – and essentially are loaded in tension and/or compression in in-plane direction. In a blade structure, compression loads associated with blade bending result in considerable out-of-plane movement of the panels, and buckling may be critical.

Testing of sandwich panels for rotor blades has only recently become of interest and is still not commonplace. Tests are typically not aimed at the shear web sandwich variants, but at the other panels, since, for the shear web, the critical shear buckling is better verified by means of component



6.3 Sandwich test set-up in three-point bending (after reversed loading).

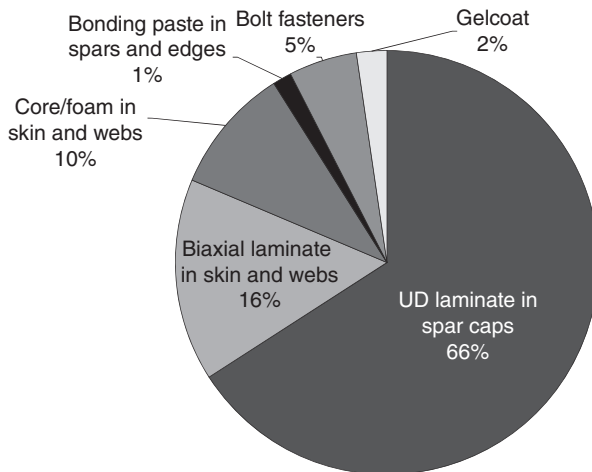
tests. Core materials for sandwich used in aerodynamic panels typically have grooves in one or two directions, to enable sandwich panel curvature. These grooves (achieved by cuts made part-way through the foam, or by application of foam or balsa blocks on a fibrous substrate) tend to consume some resin during infusion to modify the average shear modulus (which is composed of the modulus of core and resin). They therefore have the potential to function as starter notches for damage initiation and growth in the sandwich.

Experimental characterisation of the sandwich is aimed at obtaining basic (shear) stiffness and strength data. For material comparison purposes, a bending fatigue test, an example of which is depicted in Fig. 6.3, is performed to compare resistance to fatigue load, but actual fatigue loading and damage progression in a blade sandwich structure may differ considerably. To analyse performance in a blade structure, component testing is a more promising avenue.

6.3.3 Cost

For a composite blade, costs are in the order of 5–10 €/kg. This consists of materials and manufacturing costs (man-hours, energy, consumables and mould depreciation). For the UPWIND reference blade (a research lay-out blade),⁵ an estimated material cost breakdown is shown in Fig. 6.4.

This breakdown shows that a large part of the cost of the blade's load bearing components is in the spar and skin laminates. Optimisation of materials usage in that area can facilitate cost reductions. The cost of core materials (balsa or foam) is also noteworthy, as these are expensive relative to their mass in a blade. A trend towards better understanding of the structural properties of the core materials and the investigation of low-cost core solutions (such as polystyrene variants) is driven by this observation.



6.4 Estimated blade material cost breakdown, based on a 61 m blade as in Reference 5.

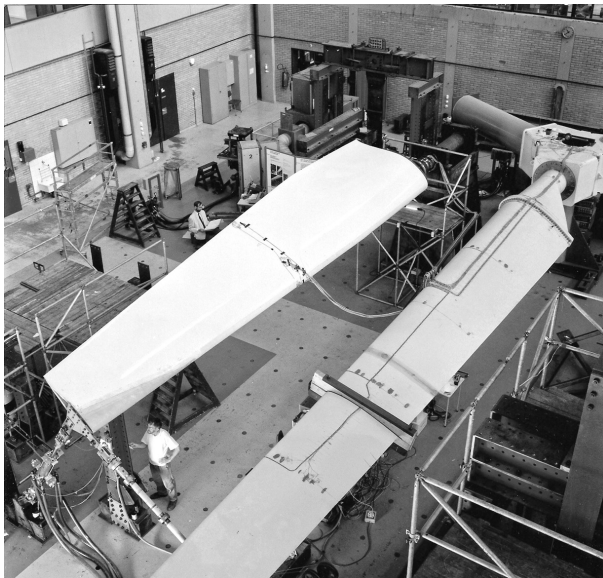
The following section deals in more detail with fatigue research, after a general introduction (see also Reference 6, or more detailed observations in Chapter 8).

6.4 Fundamentals of wind turbine blade fatigue

Wind turbine blades are structures heavily subjected to fatigue loadings and must therefore necessarily be designed against long time high cycle fatigue. Hence in the selection of materials and material systems, these aspects are to be considered and challenge the traditional material selection in advanced engineering components.

6.4.1 Significance of fatigue loading on blades

The first wind turbine blades were often manufactured from steel or aluminium, using experience from the field of aerospace engineering. Fatigue issues soon occurred, however, and solutions for these problems were found in composite materials. The first composite blades were relatively expensive, partly because extensive investigations were carried out into manufacturing techniques that are still considered up-to-date today, such as pre-preg tape winding. Apart from the costs issue, other problems were encountered with the composite blades, including fatigue damage and failure.¹ Partly due to the expanded geometrical freedom, the experience with sailplanes and the availability of relatively cheap production methods that were developed in boat building, blades progressively came to be manufactured of glass fibre and polyester or epoxy, using hand lay-up techniques.



6.5 Rotor blade tests at Delft University of Technology in 1984.⁷

An illustration of this shift from steel to fibre-reinforced plastics is given in Fig. 6.5. The blade on the right is a steel blade from the WPS30 wind turbine; the blade on the left is a laminated wood composite blade. The rotor blade test activity at Delft has moved to an autonomous foundation, WMC, in 2003.

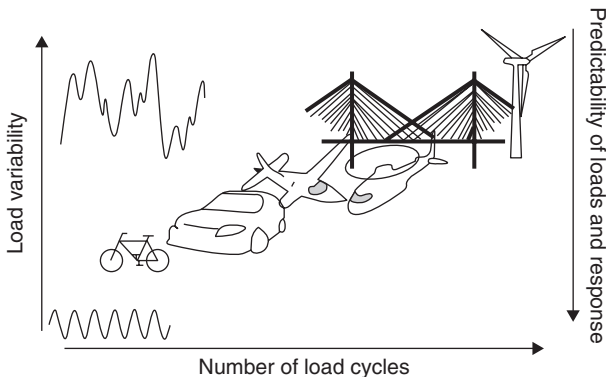
Figure 6.6 shows that wind turbine rotor blades occupy a definite niche in the field of structural composites. Rotor blades experience a very large number of strongly varying load cycles. Prediction of stochastic loads and response is an interesting subject which is considered in Chapter 10.

6.4.2 Number of load cycles

Although Fig. 6.6 is schematic and does not show explicitly the number of cycles encountered by some of the engineering applications of composites drawn in the figure, the number of cycles for a wind turbine during its lifetime can be estimated by the number of revolutions,

$$n = (\text{RPM at rated wind speed}) \times (\text{minutes in design lifetime}) = (\text{RPM}) \times (20 \cdot 365 \cdot 24 \cdot 60)$$

where RPM (Revolutions Per Minute) are set to 20 and design lifetime is normally 20 years. This leads to an estimated number of revolutions of ca. 200 million. The number of fatigue cycles is a multiple of that, since tower passage and gusts generate significant fatigue cycles. For larger, offshore turbines (lower



6.6 Fatigue loading in applications of structural composites.⁸

wind shear and RPM), and for the future ‘smart’ rotor blades (rotor blades with active load alleviation leading to lower fatigue loads) the number and significance of load cycles will decrease. Currently, however, there is no significant experience in this respect with either offshore wind turbines or smart blades.

Bearing in mind the number of load cycles of a wind turbine as estimated above it is worth noting that the industry standard in fatigue life experimental validation is limited to 2–5 million cycles for blades, and 10 million cycles for coupons; this is a small fraction of the actual number of fatigue cycles sustained by the turbine.

6.4.3 Variability of cycles

Although the number of cycles during the lifetime of a blade can be simply estimated, the load magnitude and relative frequency of individual cycles is strongly dependent on the local wind climate. The predictability of the gust loads is highly limited and depends on the prediction accuracy for wind speeds and turbulence intensity.

The variability of load magnitudes is significant for life prediction methods, and counting methods for load sequence characterisation need to be implemented, as well as fatigue models that allow for inclusion of variable amplitude. The term variable amplitude is used to designate the opposite of constant amplitude, and also applies to variable mean or R-value. Whether the order of the load cycles is of great importance for the accuracy of the life prediction remains to be seen. For composites, to date, the scatter in fatigue life data and the associated resolution of fatigue models hinders accurate determination of effect of cyclic order in a representative load sequence.⁸

Experimental validation of the effect of load cycle variability requires sufficient constant amplitude fatigue data as well as variable amplitude load sequences. Although for specific research goals many dedicated variable

amplitude sequences have been devised, standardised load sequences exist. For wind turbine blades, only a limited number of standardised load sequences are available, namely the WISPER, WISPERX, NEW WISPER and Randomised NEW WISPER load sequences. Relevant works on variable amplitude testing and modelling can be found in References 9–11, and in Chapter 8.

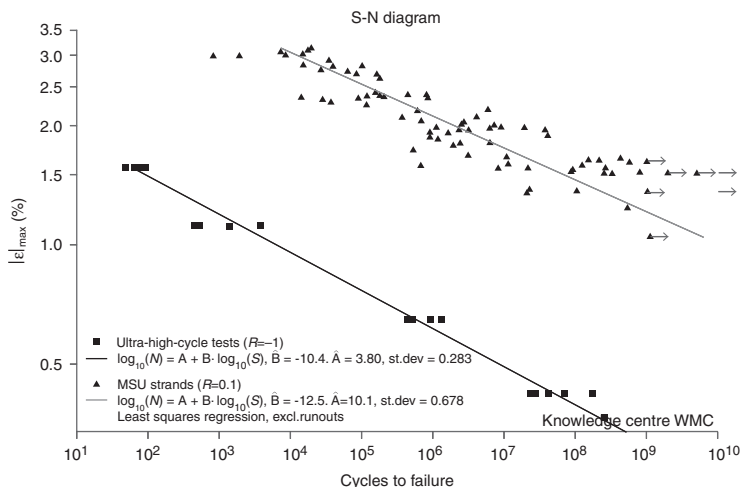
6.4.4 Contribution of each load cycle to fatigue damage

In constant amplitude fatigue, it has become evident from the Ultra High Cycle project (fatigue tests on multi-directional laminate coupons in tension-tension or tension-compression fatigue¹³), from the DOE/MSU database (for impregnated glass-polyester strands in tensile fatigue¹⁴), and from the more recent tests on single-fibre specimens,¹⁵ that even load cycles with a small magnitude will eventually lead to failure; at least, no fatigue limit was encountered in tests up to the giga-cycle range.

Figure 6.7 presents high cycle data from the first two above-mentioned projects, demonstrating the absence of a fatigue limit (at least down to a maximum tensile strain of ca. 0.2%), and, incidentally, the goodness-of-fit of a double-logarithmic expression to describe this S-N curve.

6.4.5 Need for design optimisation

Fatigue damage in rotor blades leading to serious loss of availability of wind turbines is not evident from the scant statistics available. Occurrences of



6.7 Strain based ultra-high cycle fatigue data from a laminate¹³ and from strands.¹⁴

secondary failure modes that could be classified as fatigue failure are found in the form of delamination after blade splitting by lightning strike or by water ingress after hail or rain erosion of the outer layers or gel coat.

One conclusion might be that the fatigue models used in state-of-the-art designs are sufficient in terms of design for fatigue. Another may be that the blades are probably over-dimensioned since they do not appear to be approaching the limits of the materials' possibilities. Hence, lighter and more optimal designs are possible. This is one of the premises of the OPTIMAT BLADES project,¹⁶ from which it became apparent that, although non-conservative fatigue formulations were used in the design guidelines, additional materials added via partial material factors still helped blades last their lifetime. As the usage of materials is reduced by the adaptation of some quasi-static material factors, it is to be expected that the fatigue reliability may come under pressure and more sophisticated fatigue evaluation, which better reflects the actual material behaviour of the materials, will be necessary.

For lighter, more economical, stiffer, and even more sustainable blades, current design rules may not suffice to prevent all possible (fatigue) failure modes, and research into the description of representative failure must coincide with the next design steps.

6.4.6 Fundamentals of fatigue modelling

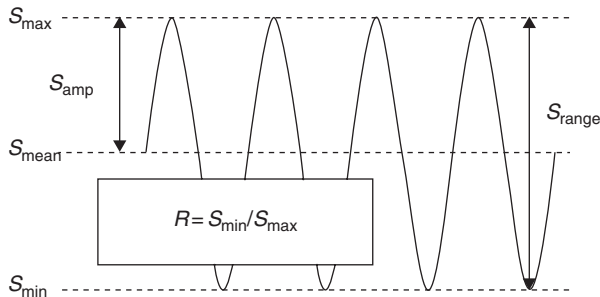
It is assumed here, that at any location in the blade, for any part of the rotor blade's operational life, the loads are known as a time series of stress or strain. Such data are the outcome of a wind turbine dynamic simulation.

Three main steps exist in the fatigue model:

1. cycle counting, resulting in a classification per cycle type;
2. estimating allowable numbers of cycles for each cycle type (this follows from a description of constant amplitude fatigue behaviour through a Constant Life Diagram);
3. damage calculation, combining the results from step 2 with a damage criterion.

The above steps are, often, strongly interdependent. For instance, the damage calculation method (step 3) requires input from step 1 and the order of the loading cycles may or may not be discarded, putting constraints on the counting method followed.

The most commonly used methods for the above steps are: Rainflow counting in step 1 (discarding the order of the cycles), a Constant Life Diagram (CLD) in step 2 and Miner's sum in step 3. For an explanation of Rainflow counting, various sources are available in the literature (see e.g. Reference 17).



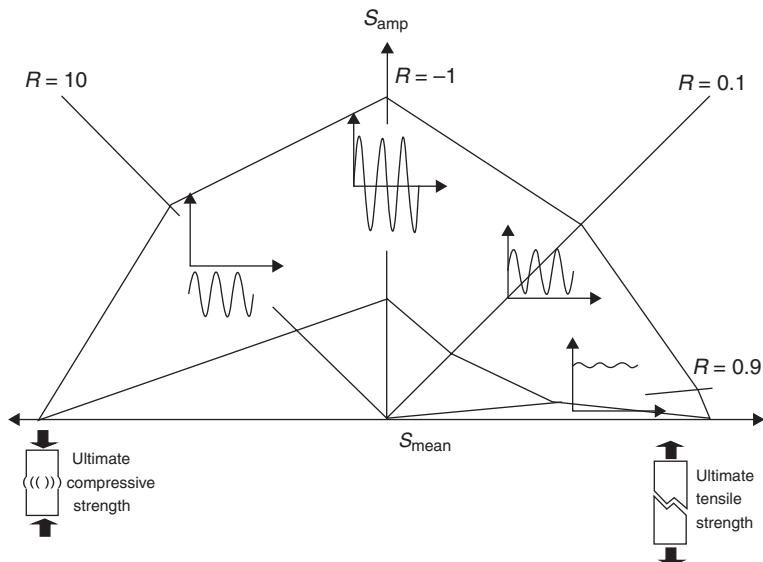
6.8 Fatigue cycle – definitions.

A few definitions are given for a fatigue cycle (Fig. 6.8). For each cycle type in the loading sequence or histogram, it is necessary to quantify the number of cycles that would lead to the fulfilment of the failure criterion. Before elaborating on this, it is necessary to define ‘cycle type’ and ‘failure criterion’. Most commonly, breakage (loss of ability to carry the applied load) is used as a failure criterion. But the definition of failure should be revised for each particular application, for it may well be that a certain decrease of stiffness, or increase in permeability of a composite layer for a fluid, may constitute failure for a certain application.

For the description of a fatigue cycle, one could choose any combination of two of the parameters shown in Fig. 6.8. Since fatigue behaviour in composites is thought to depend both on the cyclic mean and amplitude, cycle type is usually formulated as R-value, i.e. S_{\min}/S_{\max} . This has the advantage of keeping the ratio of tensile and compressive components in the cycle constant.

A CLD is used to estimate the number of cycles to failure. Essentially, this is a diagram spanning all possible combinations of cyclic mean and amplitude, showing lines that connect points with equal (expected) fatigue life. Since it is virtually impossible to determine the complete constant amplitude fatigue behaviour experimentally, the CLD is usually an interpolation of experimental S-N curves, which are typically obtained by doing constant amplitude fatigue tests on specimens, to failure and grouping experimental results by R-value. The CLD is then constructed from these S-N curves. In the CLD, the S-N curves are projected onto the $S_{\text{amp}} - S_{\text{mean}}$ plane, as straight lines from the origin. In the CLD, there are distinct sections where the loading is pure compression, pure tension, or a mix (Fig. 6.9).

On the abscissa (which represents static loading of the material), the constant life lines typically converge to the Ultimate Tensile/Compressive Strength, but this is an artefact. Recent results suggest that constant life lines may continue to run parallel for R-values close to 1.

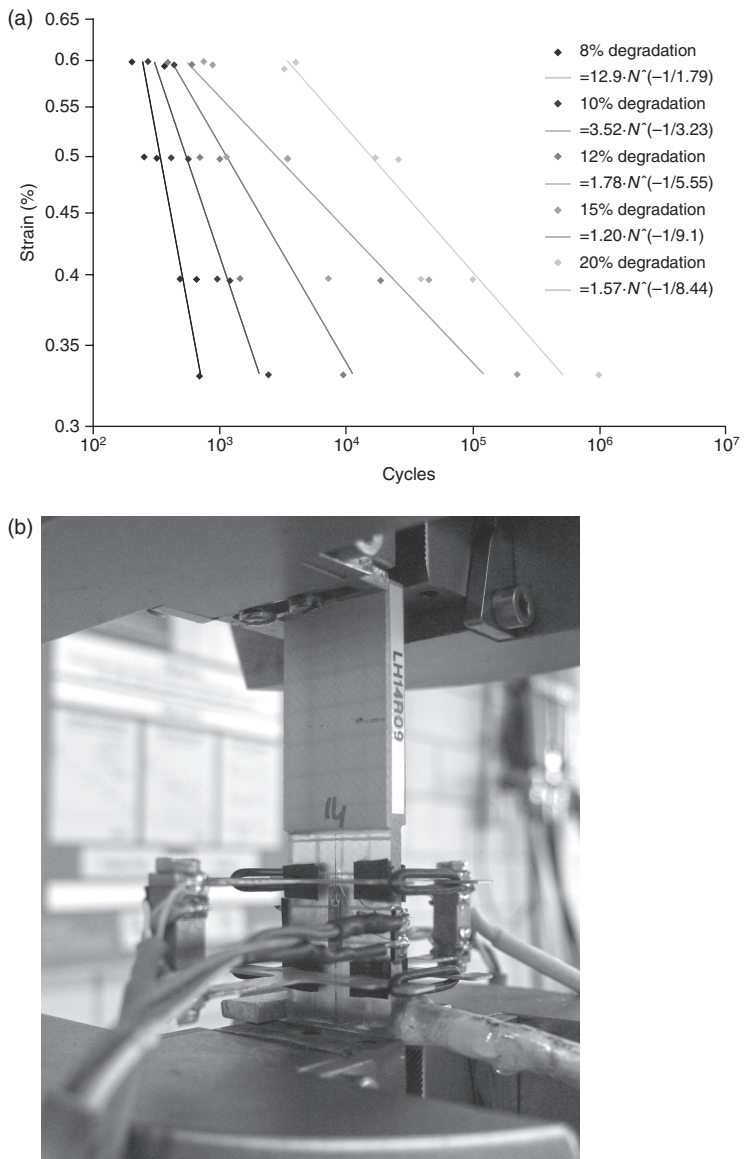


6.9 Schematic of a Constant Life Diagram (CLD).

In the above, fatigue test results, obtained in ‘load control’ mode, are typically used. This means that the test machine applied a constant cyclic load to the specimen. The results are often plotted as stress (load divided by a stressed cross-sectional area) versus cycles. As load cycles are applied to the specimen, a load controlled test results in specimen elongation, and progressive damage growth.

Depending on the hardware and software, other options are possible, such as strain control or displacement control (applying a constant cyclic strain or displacement, respectively). In that case, the fatigue results should be plotted as strain or displacement versus cycles. The behaviour of the specimen in terms of failure mode will be different in these two cases. In strain control, for instance, the damage growth is likely to decrease in rate as the stiffness decreases and stresses decrease accordingly (the load would be continually lowered). Such a test might last for an indefinite number of cycles, and ‘failure’ should not be defined as fracture of the specimen, but as a pre-defined stiffness decrease.

Care should be taken when interpreting S-N curves. Often, ‘strain’ is plotted on the ordinate. In most cases, this refers to e.g. initial strain, i.e. stress divided by initial stiffness, while the data would have been obtained by a load controlled test. So not all S-N curves with ‘strain’ on the ordinate are strain controlled tests (in practice, most of these are actually load controlled tests).



6.10 (a) Curves connecting applied strain-life data for a specific stiffness degradation, from tests on skin materials, shown in Fig. 6.10b.
 (b) Strain-controlled S-N curves for skin material.

The choice of test mode is usually partly pragmatic. Load controlled and displacement controlled tests are easier because generally no strain sensor is necessary to control the test. The sensors (usually extensometers) are monitoring locally on the test samples and therefore sensitive to local

damage through the test and might fail in the measurement or fall off, rendering the test results being invalid. Another main selection criterion is the type of loading the test is aimed to represent. For unidirectional spar cap materials, it is logical to test them in load control, as the actual spar cap is loaded by the wind and this external load is not influenced by the damage state of the spar cap. On the other hand, skin material will often follow the strains of the underlying, longitudinally stiffer, laminates, even if the skin material becomes more flexible as fatigue damage progresses. Thus, a strain controlled test is more realistic for skin material if the longitudinal behaviour is of interest.

Strain controlled test data, where ‘failure’ is constituted by a pre-defined stiffness degradation, are shown in Fig. 6.10.

6.5 Research into wind turbine blade fatigue and its modelling

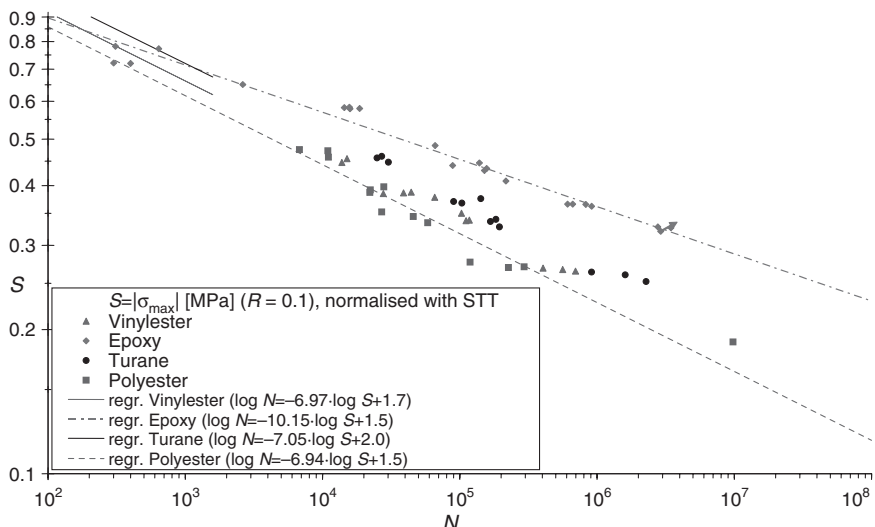
Modelling of the fatigue performance of the composites is a complex and challenging task. The damage mechanisms are complex and the failure criteria and damage rules are still not well established and are mainly based on empirical and phenomenological observations. Hence strong efforts are put into the research in this field.

6.5.1 Empirical and phenomenological fatigue modelling

At the basis of fatigue modelling is the collection of experimental data. These data are used for empirical and phenomenological modelling, which give a description rather than a thoroughly theoretical explanation of fatigue behaviour (see e.g. Reference 18). Data for spar cap materials are mostly collected at constant amplitude, and in load control mode. An example of $R = 0.1$ data collected in load control mode is shown in Fig. 6.11.

Although the spar caps are loaded in tension (pressure side) and compression (suction side) predominantly, reversed loading material characterisation data are widely available since the resulting $R = -1$ test data are very useful in fatigue models such as the Goodman diagram (a special case of the CLD) and, since this can also be considered the most discriminatory R-value, also useful for material selection, which contains both tension and compression.

The focus in fatigue life modelling has shifted over the years from cyclic counting methods, to definition of the S-N curve and damage quantification. Currently, the research theme from which the most relevant results can be expected in the short term is the development of robust, accurate and efficient Constant Life Diagrams (CLDs). These are not complete, however, without



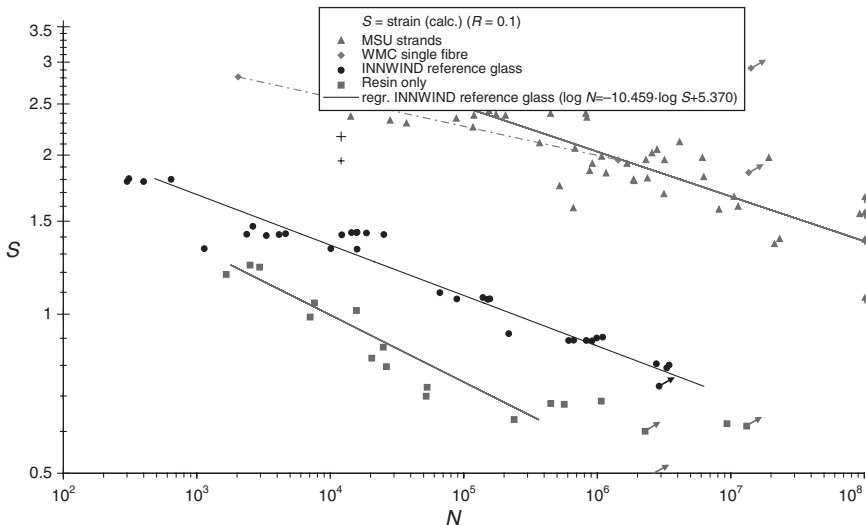
6.11 Constant amplitude tensile fatigue data of spar cap material manufactured with different resins.

ways to account for the effects of e.g. temperature, scatter, defects and creep. An integral material model, taking into account all such effects in all loading conditions, is still some way off for spar cap materials, let alone for all materials in a rotor blade. One of the most recent research efforts focusses on better understanding of damage mechanisms in order to provide a broader basis for such integral material models: micromechanical modelling.

6.5.2 Micromechanical modelling

Micromechanical modelling predominantly involves numerical modelling of restricted volumes of material. In the case of wind turbine composites, attempts are made to link the macroscopic laminate fatigue behaviour to the behaviour of a limited amount of fibres and resin interacting in a microscopically small structure. The explicitly fatigue dominated loading regime and the prevalence of non-woven materials distinguishes the work described here from micromechanical modelling in aerospace. Micromechanical modelling does rely on experimental research, though, in the sense that the input parameters are the constituent properties, such as fatigue behaviour of the resin and fibres. An example of fatigue behaviour of resin, fibres and a composite is shown in Fig. 6.12.

In this figure, which is plotted on strain basis (initial strain in load controlled test, see Section 6.4.6), the high performance of impregnated strands compared with the laminate is obvious. The resin and fibre (fatigue)



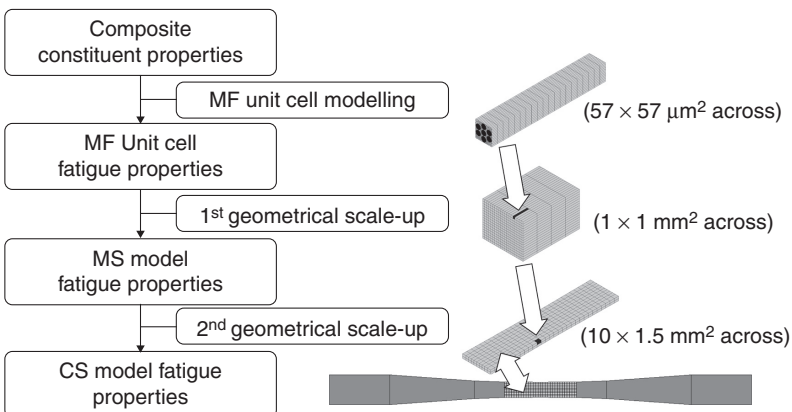
6.12 Fatigue behaviour of fibre bundles, neat resin and composite.

behaviour are input into the micromechanical model and the resulting ‘composite’ behaviour is validated with the composite experimental data.

A widely used tool for micromechanical numerical observations is the ‘unit cell’, or ‘representative volume element’, which is defined as the smallest possible volume element that can be used to model the representative micromechanical failure mechanisms inside a lamina. In practice, the size of the cell is defined as the maximum size which can be handled numerically within a certain time limit (partly dependent on the mechanics that are included in the model). The idea is to investigate the material inside this representative volume element (RVE) and summarise its behaviour in terms of strength development, stiffness degradation and fatigue life. These condensed properties are then projected on FEM-like elements for which a larger construction is modelled. Typical micromechanical models can be built up in a hierarchical manner (Fig. 6.13).

The state-of-the-art in micromechanical modelling is that a full-scale structure cannot yet be predicted, especially in fatigue. Currently, the objective of micromechanical modelling is to fill the gap between layer-scale (meso-scale) laminate modelling and the micromechanical phenomena that occur within the layer. The main difficulties are computing power, which hampers upscaling of the numerical models from micro- to meso-scale; and there is a lack of experimental validation, especially in the micro- and meso-scales of the multi-scale approach described above. The expectation is that micromechanical modelling will find broader application than merely spar cap materials.

One of the difficulties is characterisation and modelling of the bond between the fibre and the resin, through the interface. Important properties



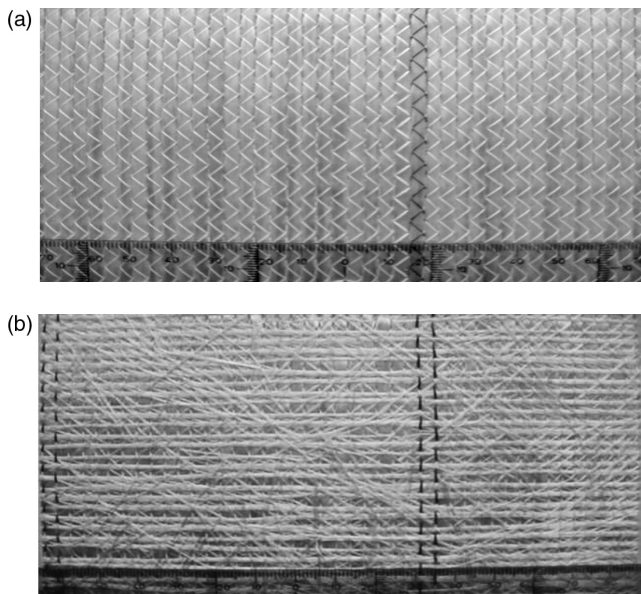
6.13 Hierarchical approach to micromechanical modelling.¹⁹ MS: meso structure, MF: multi-fibre, CS: coupon scale.



6.14 Single-fibre fragmentation test (DTU Wind 2012).

are shear strength and fracture toughness. It is a challenge to measure the interface properties. They can be concluded from tests on impregnated fibre bundles or from tests on laminates with specific architecture and lay-up, or they can be estimated from single-fibre tests on micro-scale, such as a pull- or push-out test or a single-fibre fragmentation test (Fig. 6.14). When the fibre strength and the length of the fibre fragments are known, the interface shear strength can be estimated.

On a higher scale in the scaling hierarchy the fibre lay-up and fibre architecture play an important role in the resulting properties of the laminates. A typical UD composite, used in the main beams of blades, is built up of



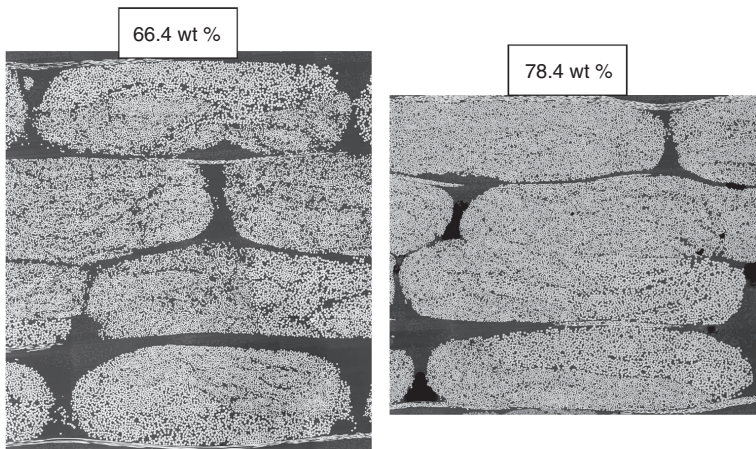
6.15 UD non-woven fabric (a) 0° 2400 Tex. (b) 90°(198 Tex), Mat (24 Tex).

non-woven UD fabrics. The fabrics are made from stitched UD rovings (tow bundles).

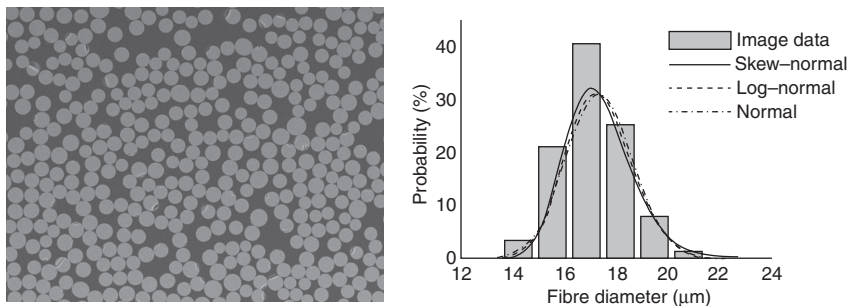
The architecture of the UD fabric influences the fatigue performance. In Chapter 7, Mandell *et al.* show that the fatigue properties of a laminate made from fabrics where the backing layer has been removed shows a significant fatigue life increase.

The planar architecture of a UD fabric is shown in Fig. 6.15. A UD composite is made of stacked UD fabrics and the lay-up and the fibre content (fibre volume fraction or fibre weight fraction) is an important basic parameter in controlling the stiffness and the fatigue performance of the laminate. On this scale, it must also be taken into consideration that the fibres are unevenly distributed in the laminate (Fig. 6.16), causing a strongly varying fibre content in a laminate cross-section. And scaling down further, we find a distribution in fibre diameter, which also influences the behaviour of the fibre bundles (Fig. 6.17).

Static and fatigue behaviour depends on many of the architectural parameters of the fabric, and many different architectures exist. Micromechanical modelling can provide a tool for virtual testing, where the influence of a single parameter can be investigated with minimal physical experimental effort.



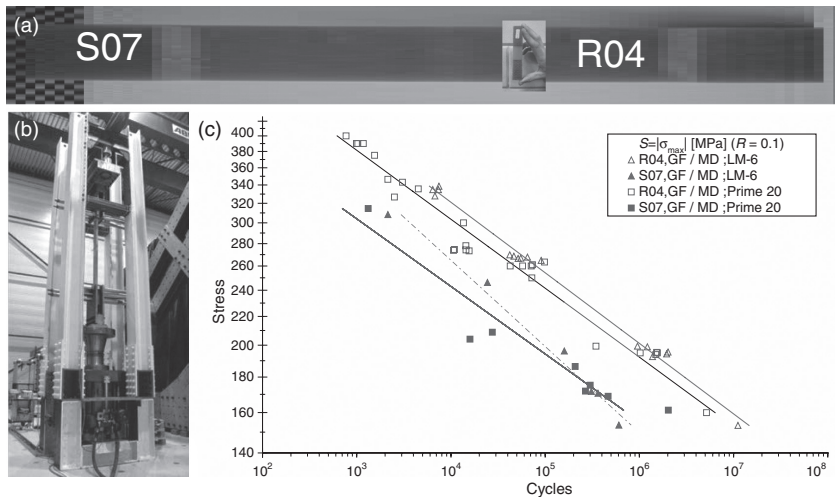
6.16 UD Composites, tow bundles (rovings). Variation in fibre content. (DTU Wind Energy, 2012).



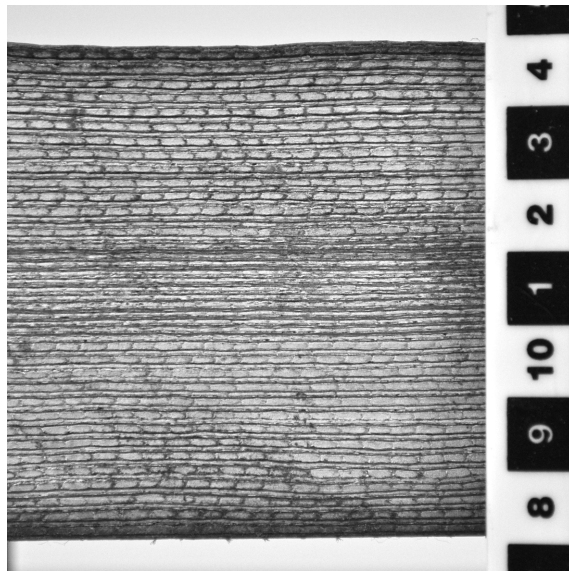
6.17 Fibre tows, variation in fibre diameter.

6.5.3 Thick laminates

Near the blade root, the spar cap materials for large blades reach thicknesses of up to ~ 150 mm. Traditionally, thickness effects are not taken into account in the design, i.e. the laminates are expected to behave in the same manner as the thin laminates used for experimental design data collection. Recent experiments have demonstrated that this expectation might be too optimistic. In Fig. 6.18, specimens S07, with cross-sectional areas 25 times larger than those of specimens R04, clearly show lower fatigue lives because of upscaling effects. In earlier studies, this phenomenon was often related to statistics: thicker laminates have a larger chance of containing imperfections. What is more likely is that multiple potential causes exist, such as material waviness

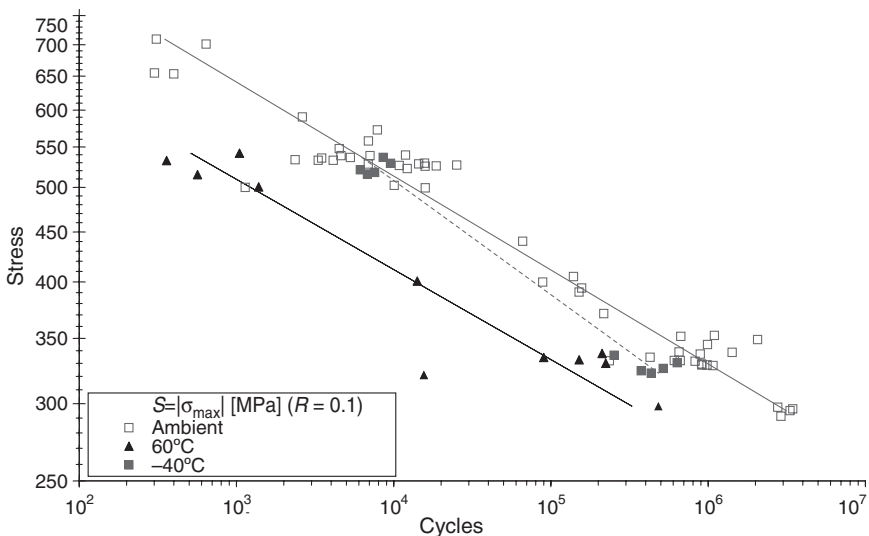


6.18 (a) Relative size between test specimens; (b) test set-up for large specimens and (c) S-N curves showing fatigue levels for small test coupons, R04 compared to the fatigue levels for the large test samples, S07.²⁰



6.19 Waviness in cross-section of a thick laminate.

(Fig. 6.19), or an effect caused by the number of layers; but in the case of coupon tests one should also consider internal temperature and frequency effects, including time-at-load (creep). These effects are further investigated in Section 6.5.4.



6.20 Comparison of specimens tested at room temperature, -40°C and $+60^{\circ}\text{C}$ (tension fatigue).

6.5.4 Extreme conditions

Recent experiments at high and low temperatures have revealed a significant effect of temperature on fatigue behaviour of both UD and $\pm 45^{\circ}$ materials (e.g. Reference 21). At different R-values as well as different load levels, low temperatures have a small or even beneficial effect on strength, stiffness and fatigue life. At higher temperatures, however, the effect is strongly negative. Tests performed at 60°C (i.e. only ca. 37°C above standard laboratory temperature) showed a fatigue life decrease of up to several orders of magnitude at $R = 0.1$ (Fig. 6.20).

Although typical operating temperatures are well below 60°C most of the time, the effects are significant and, with reduced magnitude, also exist at lower temperatures.

In actual blades, frequencies are typically below the frequency required for visco-elastic heating. Thus, internal heating of a rotor blade might be limited to well below the region where it has an effect on life. These results support further investigations into accelerated testing at low temperatures. Especially for tests that run to 10 million cycles (to limit the machine time, this load level is typically tested as run-out, complicating useful statistical treatment of the data), the test time could be easily shortened by 50%, allowing more valuable data to be obtained by e.g. testing less run-outs.

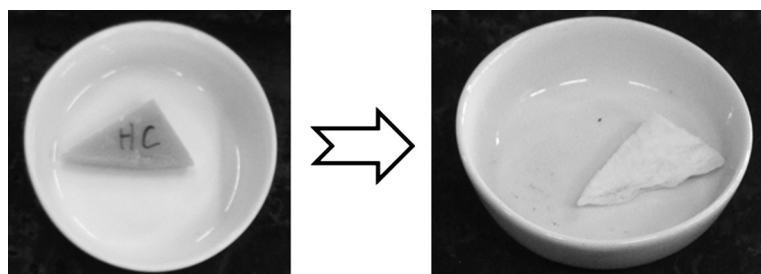
6.5.5 Bondlines

Bondlines are frequently present in rotor blades, although some manufacturers have successfully implemented the principle of ‘one-shot’ resin injection (no bondlines). Often there are bondlines between the spar caps and shear webs of the main spar, and between the aerodynamic pressure and suction shell (Fig. 6.1). These face various challenges. Most importantly, during operation, they need to transfer shear loads from the web to the spar caps, or between shell halves. In practice, this is combined with significant axial strains, since the blade deforms in flapwise and lead–lag direction. For manufacturing, the ‘raw’ material often should be a paste, with sufficient viscosity and tack to stay in place during application and closing of the mould. The high viscosity and tack should be combined with the somewhat opposing demand of low void content. Typically, a bonding paste is a glass-filled epoxy (Fig. 6.21).

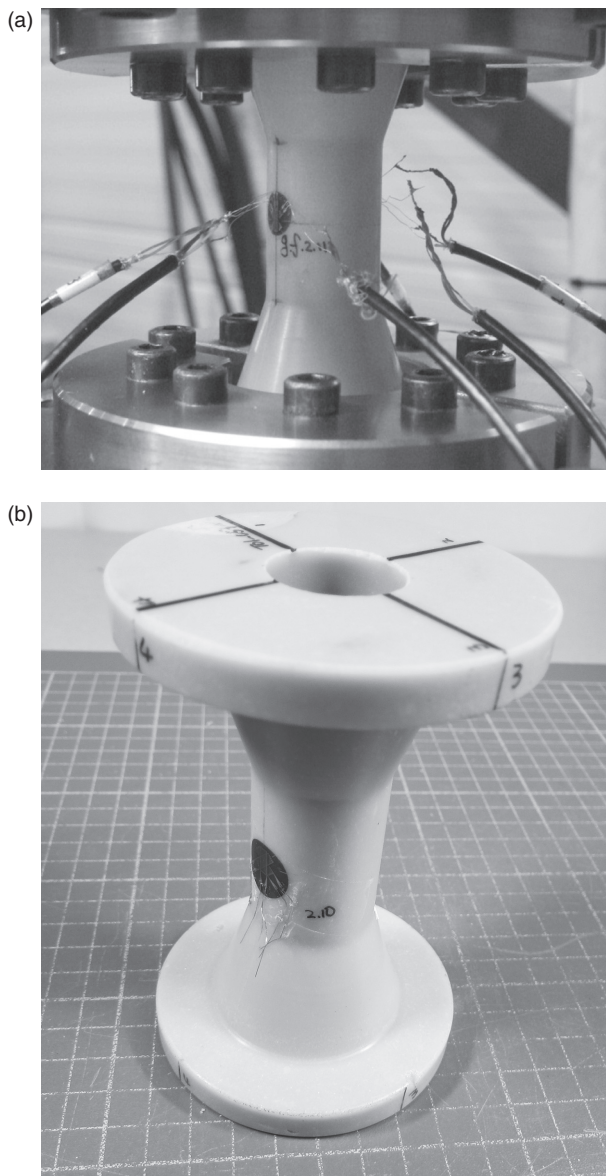
A bondline can be defined as the structure including – but not limited to – the adhesive between two structurally bonded parts. The performance of the adhesive connection depends largely on the behaviour of adherends, which is why the definition of a bondline is broader than the adhesive bonding paste in itself. This makes testing of a bondline different from the characterisation of an adhesive. In a bondline test, the applied loads and boundary conditions must be representative for the realistic structure. That is part of the reason why bondline research for the most part is included in subcomponent research, although characterisation of the bonding paste adhesive itself is also being carried out (Fig. 6.22).

6.5.6 Leading- and trailing-edge reinforcement

As rotor blades increase in size, classical scaling rules dictate that the normal internal stresses that are most affected by the upscaling are the gravity-



6.21 Bonding paste material, a glass-filled epoxy, before and after resin burn-off.



6.22 Bi-axial (tension-torsion) fatigue test set-up for full-adhesive tubular bonding paste specimen. (b) Specimen before mounting in test fixture; (a) test set-up showing specimen in test fixture in dedicated 250 kN/4kNm tension-torsion test frame.

induced blade bending stresses. These are roughly proportional to the blade length. These gravity-induced loads are carried by partial reinforcement of the blade leading- and trailing-edges, typically using laminate strips or tapes

similar to the spar cap material, over a shorter spanwise length than the central spar caps themselves. Typically, the total trailing/leading edge reinforcement will be quite limited in mass, ca. 5% of the mass of the spar caps.

6.6 Future trends

Several trends can be identified in the current and future blade materials market.

6.6.1 Significance of material models for blade tests

New blade designs are subjected to static and fatigue tests. While static tests are used to validate the ability of the design to withstand extreme loads, the ability of the blade to withstand the design fatigue load histogram is verified in accelerated fatigue tests. ‘Accelerated’ means that the test loads are scaled up from the design loads, so that a damage state equivalent to the (variable amplitude) design life of ca. 20 years is achieved within a practical test duration, i.e. 1–5 million (constant amplitude) fatigue cycles.

These fatigue tests have proven valuable in identifying the critical areas in a blade design, as well as in finding the cause of unexpected damaged encountered in the field.

Accurate fatigue characterisation of the materials is not only vital for a sound blade design, but is also key to the derivation of test loads. Generally the design load spectrum is translated to a constant amplitude test load. Therefore both the shape of the CLD and the slope of the S-N curves have an impact on the test loads, which highlights the importance of good material characterisation. As a blade is a hybrid structure, different material characteristics (different S-N slopes) inevitably mean that not all parts are tested equally and some parts are overloaded or underloaded.

An interesting aspect is that, should an incorrect slope parameter for a material be derived in the materials test programme for a blade, this is not tested for in the blade fatigue test. For instance, a too flat slope for the S-N curve will result in allowable stress assumptions for the blade design that are too high, when extrapolating to high cycle counts. In the blade fatigue test, however, the same slope parameter will cause the test loads to be scaled up correspondingly (in this case lower than for the correct S-N slope). The blade is therefore only tested against the assumed fatigue characteristics – proof that the accuracy of the blade test is determined by the accuracy of the material model.

Blade fatigue tests are limited by the test method chosen. Various methods exist, such as single-axis (near) resonance, dual-axis forced displacement and dual-axis (near) resonance. Each method has its particular advantages and disadvantages related to energy consumption, speed and realism. Every

simplification in the test loading (e.g. testing at $R = -1$ in resonance tests) will increase the dependence on the accuracy of the material models to design a suitable test. Furthermore validation of a part and of the construction details of the blade not only requires a suitable test method, but also requires that representative data for all materials in these components are available. More on blade test methods can be found in Chapter 14.

6.6.2 Probabilistic modelling

Probabilistic modelling has in recent years become a more and more relevant research topic, applying reliability methods, which are more common in civil engineering, to wind turbine design. Recently, extensive efforts have been spent on probabilistic modelling of blades. This is highly relevant in view of the scatter in static and fatigue data, which is not dealt with properly at present, and for optimal calibration of materials factors (see e.g. References 22 and 23).

6.6.3 Structural health monitoring

The eventual use of structural health monitoring will be to make rotor blades ‘smart’, in the sense that operation can be based on the instantaneous condition and anticipated wind loading. Blades are currently among the least condition-monitored wind turbine components, due to their size, the prevalence of local damage and the lack of understanding of the effects of defects.

6.6.4 Sustainability

As part of their focus on providing a ‘green’ product, wind turbine blade manufacturers are compelled to study the life cycle of blades and the use of natural fibres and bio-resins, and to develop techniques for meaningful end-of-life solutions. It can be expected that this industry will have significant spin-offs in other industries where conventional materials are being replaced or augmented with composites in large quantities. In civil engineering there are already some studies comparing concrete and steel (small) bridges with composite alternatives (e.g. Reference 24).

6.6.5 Testing

The amount of industrial material testing has grown exponentially in the past years. One could say that, two decades ago, blades were designed on the basis of ten static tensile tests on a UD laminate, and a few assumptions.

Currently it is not uncommon for suppliers to be asked to meet strict material specifications that must be verified by several hundreds of static and fatigue tests of various types, and up to hundreds of millions of cycles in total. Several reasons can be identified for this increase in material testing: the need for the limits of material performance to be investigated more closely; the fact that blade and turbine manufacturers avoid relying completely on a single set of suppliers; and the fact that new materials and processing methods are being developed at a higher rate.

6.6.6 Reaching the limits

Manufacturers have become aware of both the limits to material structural performance and the limits to existing knowledge of material behaviour.

If a blade is designed as a loadbearing cantilever beam with aerodynamic shells, the structural performance required of these shells is limited. As blade designs get leaner, more of the blade components are designed to perform to their limits, and components and materials such as bondlines and sandwiches acquire an emphasised structural function.

For cases where the material or structural limits are still unclear, testing of coupons, but more relevantly subcomponents and blades, is a cost-effective way of identifying issues that cannot be detected from material models that are limited in their description of possible failure modes and damage progression. Structural testing helps ascertain the material limits and guides the material modelling process.

In some cases manufacturers are more aware of how to describe material limits. Take for example the case of lamina(te) failure criteria. First-ply failure criteria are the most rudimentary of criteria and require limited experimental verification. Nowadays, designers are reluctant to use them, as they are conservative in most loading modes of the composite and in most applications of composites in wind turbine blades. With the advancements in material modelling, one could expect that the verification required would be less experimental (i.e. where more confidence is put in the model). This is not entirely the case. Take, for instance, the Puck description of lamina failure, a multi-parameter model that requires significant number of coupon tests of various types, all above average in experimental complexity. Nowadays, where the Germanischer Lloyd (GL) guidelines recommend the use of the Puck criterion for inter fibre failure,²⁵ this entails an additional experimental burden with regards to proving the viability of the design.

The role of the certification bodies in the progression of structural limits is evident. The certifier requires at least a nominally conservative design approach to warrant operational robustness, but the designer is given a free rein to, and sometimes invited to, explore more complex and competitive methods.

6.6.7 Redundancy of supply

Blade manufacturers face the task of producing blades with manufacturing lead times of a day, in order to meet the market demand. Basing production on single-source supply of materials in such a situation is not strategic.

This means, that for each of the materials in the blade, multiple suppliers are sought. Their materials can be qualified either by the blade manufacturer or by the suppliers themselves; as the investment in materials increases, it can be attractive for both parties to have the qualification performed by independent laboratories through the suppliers. Consequently, the amount of testing performed in-house and externally by suppliers is subject to growth. The experience of the aerospace industry, where independent test laboratories can have as many as several hundreds of fatigue machines, seems to suggest that the end of the growth curve may not yet be in sight.

6.6.8 Automated production

Automated production offers the potential that the amount of testing can be reduced in the long run. This is due to both the lower scatter that can be expected in the performance data as a result of better control of production, and the more accurate reproducibility of material average properties.

6.6.9 Repair

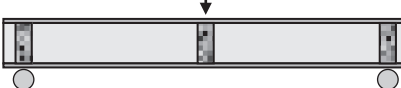
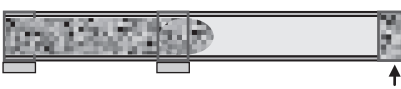
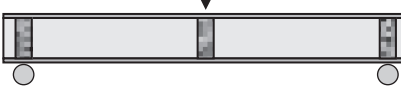
As wind turbines increase in size, larger investment implies that methods for structural health monitoring, load alleviation through advanced load prediction, control and smart structures, should become more economically viable. The same is true for repair, both on installed blades as well as post-manufacturing.

6.6.10 Subcomponent research

In recent years, a methodology that is already widespread in aerospace engineering has started to emerge in wind turbine testing: the use of subcomponents for structural validation. In the testing pyramid (coupon level material verification at the bottom, full-scale structural validation at the top), sub-component tests are one level above the coupon level.

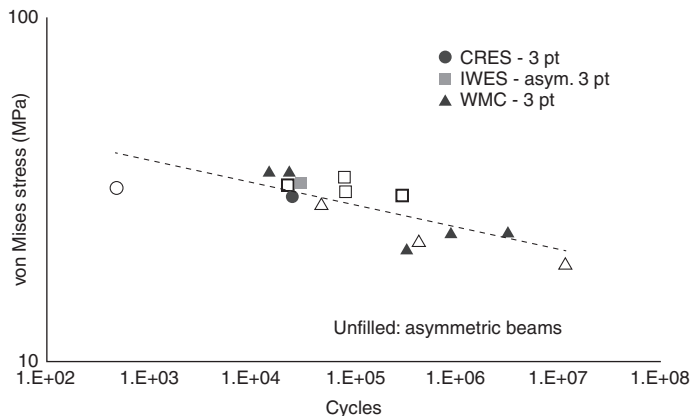
Mandell *et al.* performed subcomponent tests on wind turbine structures as early as 1996.^{26,27} The UPWIND project was the first project where the field of subcomponent research was explored both numerically and experimentally.^{28–33} In this project, the subcomponent approach was used by various

Table 6.1 Test types and number of tests for I-beam subcomponents

Partner	Tests type	Reference
CRES/UP		29
IWES		30,31
STFC		32
VUB		33
		
WMC		34

laboratories to quantify adhesive bondline behaviour through experiments and experiment modelling, leading to various test configurations and associated numerical validations of failure and damage loads as well as qualification. In the project, 40 I-beams of 1 m length, divided into two sets of 20 each (a symmetric and asymmetric cross-sections design), were distributed to the various laboratories listed in Table 6.1. A comparison of the results is shown in Fig. 6.23.

There are two main approaches: the manufacturing and testing of dedicated subcomponents, and the research into generic subcomponents. Most likely, the two approaches will converge leading to the development of sub-components that are sufficiently dedicated to describe one or a few failure modes in a blade detail, but sufficiently generic to be able to compose an ‘atlas’ of possible blade details which can be investigated through standardised specimens that are limited in size and required loads, so that they can be tested in a standard test laboratory.



6.23 von Mises stress S-N lines of different beam subcomponent test configurations.³⁴

Finally, a current topic in wind turbine blade design is that of ‘Smart’ blades: blades equipped with actuators combined with an intelligent control algorithm, which aim to mitigate fatigue loads and optimise energy production. Most of today’s research on this topic is concerned with the aeroelastic and control implications of this technology, and several conceptual designs of actuators are under consideration. As the technology enters the implementation phase, the details of the actuators, including their own fatigue characteristics, and how they are attached to the (locally modified) blade structure (e.g. via ribs manufactured of thermoplastic composite, see Reference ¹), will have to be validated in more detail with an emphasis on structural properties. Here also, an important role for subcomponent evaluation will exist.

6.7 Conclusion

Rotor blades are fatigue- and cost-driven structures. Past emphasis was on describing material behaviour, while current interest lies in understanding of the fatigue mechanisms and the interaction between structure and material. The high technical requirements for wind turbine blade structures will continue to drive the development of material and structural models, as well as of composite materials themselves.

6.8 Sources of further information and advice

Brøndsted, Povl, Holmes, John W., Sørensen, Bent F. Wind rotor blade materials technology. *European Sustainable Energy Review*, issue: 2, pages: 36–41, 2008.

- Brøndsted, Povl, Lilholt, Hans, Lystrup, Aa. Composite materials for wind power turbine blades. *Annual Review of Materials Research*, vol: 35, pages: 505–538, 2005.
- Hayman, B., Wedel-Heinen, J., Brøndsted, Povl. Materials challenges in present and future wind energy. *MRS Bulletin* (ISSN: 0883-7694), vol: 33, issue: 4, pages: 343–353, 2008.
- <http://www.coe.montana.edu/composites/Overview.htm>
- http://energy.sandia.gov/?page_id=2916
- <https://www.upwind.eu>
- <https://www.wmc.eu/optimatblades.php>
- Mandell J.F., Samborsky D.D., ‘DOE/MSU Composite Material Fatigue Database: test methods, materials, and analysis’, Sandia National Laboratories/Montana State University, Sandia National Laboratory report: SAND97-3002, (online via www.sandia.gov/wind, database regularly updated, last update 31 March 2011).
- Sørensen Bent F, John W. Holmes, Povl Brøndsted, Kim Branner. Blade materials, testing methods and structural design. In *Wind Power Generation and Design*, Ed Wei Tong. WIT Press Southampton, Boston. 2010. ISBN: 978-1-84564-205-1.
- Vassilopoulos, A.P., *Fatigue Life Prediction of Composites and Composite Structures*, Woodhead Publishing, 2010, ISBN 978-1-84569-525-5 (book), ISBN 978-1-84569-979-6 (ebook).

6.9 References

1. Joncas, S. (2010), ‘Thermoplastic Composite Wind turbine blades’, dissertation, Delft University of Technology, 2010, ISBN 978-2-921145-73-2
2. Jaquemette, Klaus-Peter, presentation on VDI Konferenz – Rotoren und Rotorblätter von Windenergieanlagen, Hamburg, 12–13 April 2011.
3. Bortolotti, P. ‘Glass-carbon hybrid materials for wind turbine rotor blades’, MsC report, WMC-2012-026, 5 April 2012.
4. van Wingerde, A., van Delft, D., Molenveld, K., Bos, H., Bulder, B., de Bonte, H., ‘Bladeco eindrapport’, Bladeco Final Report, no. BLDPV1-05, May 2002.
5. Nijssen, R.P.L., de Winkel, G.D., Peeringa, J.M., ‘WMC5MW laminate lay-out of reference blade for WP3’, UPWIND report, 22 May 2007.
6. Nijssen, R.P.L., Brøndsted, P., ‘Fatigue performance of composites used in wind turbine blades’, Proc. of the 32nd Risø International Symposium on Materials Science: Composite Materials for structural performance: towards higher limits’, Ed. S. Faester, D. Juul Jensen, B. Ralph, B.F. Sørensen, Risø National Laboratory for Sustainable Energy, Technical University of Denmark, 2011, pp. 127–141.
7. van Delft, D.R.V., van Leeuwen, J.L., Noordhoek, C., Stolle, P., ‘Fatigue Testing of a Full Scale Steel Rotor Blade of the WPS-30 Wind turbine’, Journal of Wind Engineering and Industrial Aerodynamics 27, Amsterdam, 1988.
8. Nijssen, R., ‘Fatigue life prediction and strength degradation of wind turbine rotor blade composites’, dissertation, Delft University of Technology, 2006, ISBN: 978-90-9021221-0.
9. Pasipoularidis, V., ‘Residual strength and life prediction of composites after fatigue’, dissertation, University of Patras, 2008.

10. Wahl, N.K., 'Spectrum Fatigue Lifetime and Residual Strength for Fiberglass Laminates', dissertation, Montana State University, Department of Mechanical Engineering, 2001.
11. Post, N., 'Reliability based design methodology incorporating residual strength prediction of structural fiber reinforced polymer composites under stochastic variable amplitude fatigue loading', dissertation Virginia Polytechnic Institute and State University, 18 March 2008.
12. van Leeuwen, H., van Delft, D., Heijdra, J., Braam, H., Jørgensen, E.R., Lekou, D. and Vionis, P., 'Comparing fatigue strength from full scale blade tests with coupon-based predictions', *Journal of Solar Energy Engineering*, Vol. 124, no. 4, 2002, pp. 404–411.
13. van Delft, D.R.V., Rink, H.D., Joosse, P.A. and Bach, P.W., 'Fatigue behavior of fiberglass wind turbine blade material at the very high cycle range', Proc. EWEA Conference and Exhibition, 1994, pp. 379–384.
14. Samborsky, D.D., 'Fatigue of E-glass fiber reinforced composite materials and substructures', M.Sc. report, Montana State University, Bozeman, MT, December 1999.
15. Qian, C., Nijssen, R.P.L., Samborsky, D.D., Kassapoglou, C., Gürdal, Z. and Zhang, G.Q. (2010), 'Tensile fatigue behavior of single fibers and fiber bundles', Proc. 14th European Conference on Composite Materials, Budapest, 2010.
16. van Wingerde, A.M., van Delft, D.R.V., Janssen, L.G.J., Philippidis, T., Brøndsted, P., Dutton, G., Kensche, C., Jacobsen, T., Lekou, D., Van Hemelrijck, D., 'OPTIMAT BLADES: Results and Perspectives', Proc. European Wind Energy Conference, Athens, 27 February–2 March 2006.
17. de Jonge, J.B., 'The analysis of load-time histories by means of counting methods', in F. Liard (ed.), *Helicopter Fatigue Design Guide*, AGAARD-AG-292, November 1983.
18. Nijssen, R.P.L., 'Phenomenological fatigue analysis and modelling', in Vassilopoulos, A.P. (ed.), *Fatigue Life Prediction of Composites and Composite Structures*, Woodhead Publishing Ltd., ISBN 978-1-84569-525-5, 2010.
19. Qian, C., 'Multi-scale modelling of fatigue of wind turbine rotor blade composites', Dissertation, WMC and Delft University of Technology, 22 April 2013, ISBN: 978-94-6203-337-5.
20. van Wingerde, A.M., 'Evaluation on the effect of thick laminates', OPTIMAT report # OB_TG4_R013, Rev. 000, May 2005.
21. Cormier, L., Nijssen, R.P.L., Raijmakers, S., 'Temperature and frequency effects on the fatigue properties of unidirectional glass fiber-epoxy composites', AIAA SDM Conference, April 2012.
22. Toft, H. S., Sørensen, J.D., Branner, K., Berring, P., 'Reliability-based calibration of partial safety factors for wind turbine blades', Proc. European Wind Energy Conference, 14–17 March 2011.
23. Bacharoudis, K.C., Lekou, D.J., Philippidis, T.P., 'Structural reliability analysis of rotor blades in ultimate loading', Proc. European Wind Energy Conference, 14–17 March 2011.
24. Danhof, W., 'The future belongs to bridges of polymer composites' (in Dutch), July 2009, accessed via <http://www.startgreen.nl/documents/FiberCore-ArtikelLCABruggen.pdf>.

25. Germanischer Lloyd, Hamburg, Rules and Guidelines, Industrial Services, 'Guideline for the Certification of Wind Turbines', Edition 2010 (paragraph 5.5.3.1)
26. Mandell, J.F., Creed, R.F., Jr., Pan, Qiong, R., Combs, D.W. and Shrinivas, M., 'Fatigue of fiberglass generic materials and substructures', SED-Vol. **15**, Wind Energy, 1994, pp. 7.
27. Samborsky, D.D., 'Fatigue of E-glass fiber reinforced composite materials and substructures', M.Sc. report, Montana State University, Bozeman, MT, December 1999.
28. Presentation on I-beam testing on 11th progress meeting WP3, Bremerhaven, Germany, 15–17 December 2011, presentation by Denja Lekou – CRES and Theodore Philippidis – UP.
29. Post, N., Sayer, F. and van Wingerde, A., 'Beam test report – Static and fatigue component test results from Fraunhofer IWES', UpWind document 3–10-WP-0197, November 2010.
30. Antoniou, A., and Sayer, F., 'Test report: Henkel – Upwind Beam1', UpWind document 3–10+PU-0174, 19 March 2010.
31. Dutton, G., 'I-beam fatigue test report – Including thermoelastic stress analysis', STFC-2010-UPWIND-001, UpWind document CPS-07-PU-0075, 15 November 2010.
32. Zarouchas, D., Makris, A., and van Hemelrijck, D., 'I-Beam Test Report – Four point bending experiments and numerical simulations', UpWind document 3–10-PU-0253, November 2010.
33. Nijssen, R.P.L., Westphal, T. and Stammes, E., 'Beam test report- Tests performed at WMC', WMC-2009–32-Rev04, 22 March 2011.
34. Stammes, E. and Sayer, F., 'BEAM TEST REPORT Comparison and evaluation of beams tested within WP3', WMC-2011–14, 17 June 2011.

Effects of resin and reinforcement variations on fatigue resistance of wind turbine blades

J. F. MANDELL, D. D. SAMBORSKY and
D. A. MILLER, Montana State University, USA

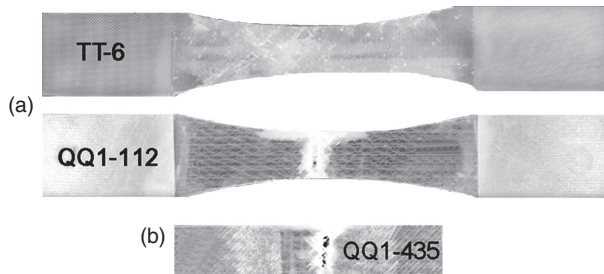
DOI: 10.1533/9780857097286.2.210

Abstract: This chapter explores the influence of resin and reinforcing fabric variations on the fatigue sensitivity for a wide range of typical blade laminates reported recently in the SNL/MSU/DOE database. Test results are presented for static and fatigue property variations with resin type, reinforcing fabric construction and weight, fiber content and laminate construction. Critical resin/fabric interactions and damage mechanisms are identified. The effects of resin and fiber type are also explored for material transitions at ply drops, where ply delamination is the dominant damage.

Key words: wind turbine blade composites, fatigue, reinforcing fabric construction, resins, ply drops.

7.1 Introduction

Wind turbine blades are constructed of a variety of laminate types in different structural elements, often including unidirectional (UD) material in spars and several forms of multidirectional (MD) reinforcement such as biaxial and triaxial fabrics in skins and webs. Each can have significant fatigue sensitivity depending on the component fibers and resin and type and direction of loading (Sokrieh and Lessard, 2003; Mandell *et al.*, 2010). Typical failed fatigue test coupons for MD glass/epoxy laminates are shown in Fig. 7.1. In addition to in-plane fatigue loads, special attention is required in areas of high stress gradients at material transitions, such as ply drops used in thickness tapering, adhesive joints and flaws of various types. This chapter provides a summary of recent results from the MSU/Sandia National Laboratories (SNL) blade material fatigue program, available in the SNL/MSU/DOE Fatigue of Composite Materials Database (Mandell and Samborsky, 2011). The database, updated annually, contains results for over 350 laminates and adhesives under a variety of loading and environmental conditions.



7.1 Typical failed fatigue coupons of multidirectional laminates in tensile fatigue (a) and reversed loading (b) (Mandell *et al.*, 2010).

The first section gives a general overview of fatigue trends for glass and carbon fiber laminates over a range of loading conditions, identifying major areas of concern for fatigue resistance. The main body of the chapter explores the performance of major types of resin-infused glass fiber laminates under tensile fatigue loading, with a focus on resin and fabric structure interactions. Comparisons are given for various levels of structure, from simple aligned strands (AS) and UD fabrics to MD laminates, identifying critical details of structure for particular resin types. Lists of resins and fabrics are included in Tables 7.1a and 7.1b, with further details available in the database (Mandell and Samborsky, 2011). The final section describes the results of two major studies of damage progression at ply drops, including prepreg glass and carbon fiber laminates and resin-infused laminates, the latter with a variety of resins, providing a wide range of delamination resistance.

7.2 Effects of loading conditions for glass and carbon laminates

Broad characterization studies for several blade laminate systems with glass and carbon fibers, involving extensive data generation, have been reported in the literature in the last decade. Fatigue tests run under load control at varying maximum load and for differing R-value, where R is the ratio of minimum to maximum load, result in typical stress or strain vs cycles to failure (S-N) data sets, usually curve fit to a power law:

$$S = A N^B \quad [7.1]$$

or,

$$N = C S^b \quad [7.2]$$

where S is the maximum stress or strain, N is the cycles to failure, A and C are constants, and B and b are fatigue exponents, with $B = 1/b$. The form and notation in Equation [7.1] is used to represent data in this chapter. The fatigue exponent may also be represented as n , where:

$$n = -\frac{1}{B} \quad [7.3]$$

While the power law model is generally preferred, exponential and three-parameter models have also been used for blade materials; the power law representation has been shown to provide a good fit to S-N data for small strands to 10^{10} cycles. The fits given here are for mean lifetime, but various confidence levels are typically represented for design purposes (Nijssen, 2006; Mandell *et al.*, 2010, p. 58).

This sub-chapter includes discussion of several laminates which are described in greater detail in Mandell *et al.* (2010), and referenced by their designation in the database (Mandell and Samborsky, 2011). Resin descriptions can be found in Table 7.1a and reinforcing fabric descriptions in Table 7.1b. Details for laminates composed of single fabric types (UD, Biax or Triax) are given in figure captions. The laminates listed with database designations are multidirectional laminates (MD) described as follows (all are glass fiber, resin infusion processed except for the prepreg processed hybrid laminate P2B):

QQ1: fabrics B and L, epoxy resin EP-2, $V_f = 0.53, ((\pm 45)/0_2)$ s.

QQ2: fabrics B and L, epoxy EP-2, $V_f = 0.52, (\pm 45/0/\pm 45)$ s.

QQ4: fabrics C and M, epoxy EP-2, V_f varied as shown, $(\pm 45/0/\pm 45/0/\pm 45)$.

TT: fabrics D and M, epoxies EP-3 and EP-1 and polyester UP-1, V_f varied as given, $(\pm 45/0/\pm 45/0/\pm 45)$.

TT1A: fabrics D and L, epoxy EP-2, V_f varied as given, $(\pm 45/0/\pm 45/0/\pm 45)$.

DD: fabrics A and K, polyester UP-2, V_f varied as given, $(0/\pm 45/0)$ s.

P2B: Newport epoxy prepgres NCT-307-D1-34-600 (carbon, 0°) and NB-307-D1-7781-497A (± 45 , glass), $V_f = 0.55, (\pm 45/0_4)$ s.

S-N data and power law curve fits for an MD glass fiber/epoxy laminate designated QQ1 are given in Fig. 7.2a for six R-values including tension-tension (0.1 and 0.5), compression-compression (10) and reversed tension-compression (-0.5, -1.0 and -2.0). The nonlinearity of the data trends at low cycles results in a poor fit of Equation [7.1] in this range; while three parameters are necessary to obtain a good fit at both low and high cycles

Table 7.1a Infusion resins and post-cure conditions

Name	Type	Resin	Post-cure temperature(°C)
EP-1	Epoxy	Hexion MGS RIMR 135/MGS RIMH 1366	80
EP-1(b)	Epoxy	Hexion MGS RIMR 135/MGS RIMH 1366	35 and 70
EP-2	Epoxy	Vantico TDT 177–155	70
EP-3	Epoxy	SP Systems Prime 20LV	80
EP-4	Epoxy	Huntsman Araldite LY1564/XB3485	60 and 82
EP-5	Epoxy	Hexion MGS RIM 135/MGS RIMH 137	40 and 80
EP-6	Epoxy	Jeffco 1401	60 and 82
EP-7	Epoxy	DOW un-toughened epoxy	90
EP-8	Epoxy	DOW toughened epoxy	90
UP-1	Polyester	U-Pica/HexionTR-1 with 1.5% MEKP	90
UP-2	Polyester	CoRezyn 63-AX-051 with 1% MEKP	65
UP-5	Polyester	Reichhold Polylite X4626–31	25 and 70
VE-1	Vinyl ester	Ashland Derakane Momentum 411 with 0.1% CoNap, 1% MEKP and 0.02 phr 2,4-Pentanedione	100
VE-2	Vinyl ester	Ashland Derakane 8084 with 0.3% CoNap and 1.5% MEKP	90
VE-4	Vinyl ester	Reichhold Dion X4486–14	25 and 70
VE-5	Vinyl ester	Reichhold Dion X4235–91	35 and 70
VE-6	Vinyl ester	Reichhold Dion X4627–39	25 and 70

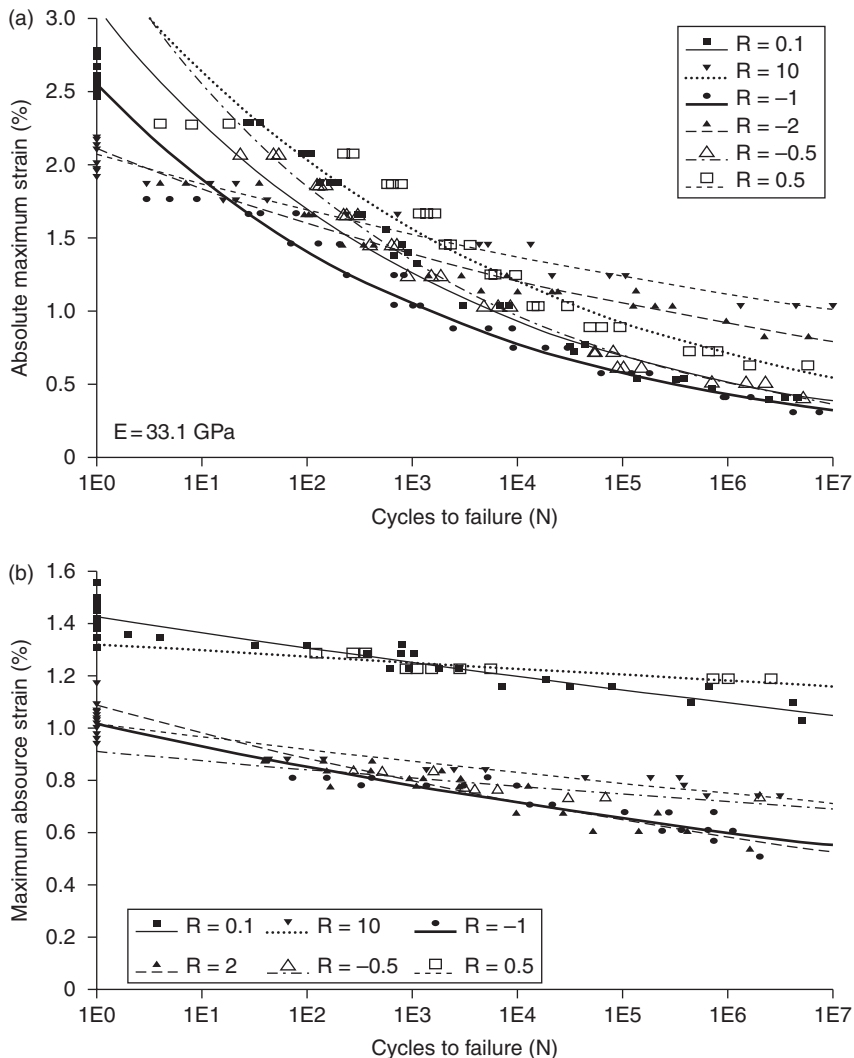
(Mandell *et al.*, 2010, p. 57), most studies use the power law fit and do not include low cycle data. For glass fiber systems the S-N data sets are significantly less steep for more compressive R-values, while reversed loading, -1 and -0.5 and tension, 0.1, give the steepest trends and lowest maximum strain at equivalent cycles. Although widely used, the UD glass fabric B in the MD laminates represented in Fig. 7.2a shows particularly high fatigue sensitivity, yielding low high-cycle strains for R-values between 0.1 and -1.0. Similar data sets for other glass fiber MD laminates with epoxy (Nijssen, 2006) and polyester (Mandell *et al.*, 2003a) resins show less steep trends and higher strains in this range of R-value; the polyester system represented significantly lower fiber content laminates, which improves the strain levels, as discussed later. Figure 7.2b gives corresponding S-N data at various R-values for the hybrid carbon UD/glass biax, prepreg laminate, designated P2B, where the S-N trends are much less steep than for glass at corresponding R-values, particularly 0.1 and -1.

Table 7.1b Fabric specifications (from manufacturers or measured)

Fabric I.D.	Manuf.	Designation	Areal Wt. (g/m ²)	Component Strands, Warp Dir.(wt.%)				
				0°	±45°	90°	Mat	Stitch
A	Knytex	D155	527	0	0	99	0	1
B	Saertex	U14EU920– 00940-T1300–100000	955	91	0	8	0	1
C	Saertex	S15EU980– 01660-T1300–088000	1682	97	0	2	0	1
D	Vectorply	E-LT-5500	1875	92	0	6	0	2
H	PPG-Devold	L1200/G50-E07	1261	91	0	3	4	1
I	OCV	1000UD	985	96	0	2	0	2
J	OCV	1200UD	1150	95	0	4	0	1
K	OCV	1322UD	1450	95	0	4	0	1
L	Saertex	VU-90079–00830–01270– 000000	831	0	97	2	0	1
M	Fiber Glass Ind.	SX-1708	857	0	68	0	30	2
T	PPG-Devold	DB810-E05-A	809	0.2	99	0	0	1
U	OCV	OC1800 triax	1885	50	50	0	0	
V	Saertex	U32EY490–00790–2540	800	49	50	0	0	1
W	Saertex	U32EY480–01170-T2565	1200	48	51	0	0	1

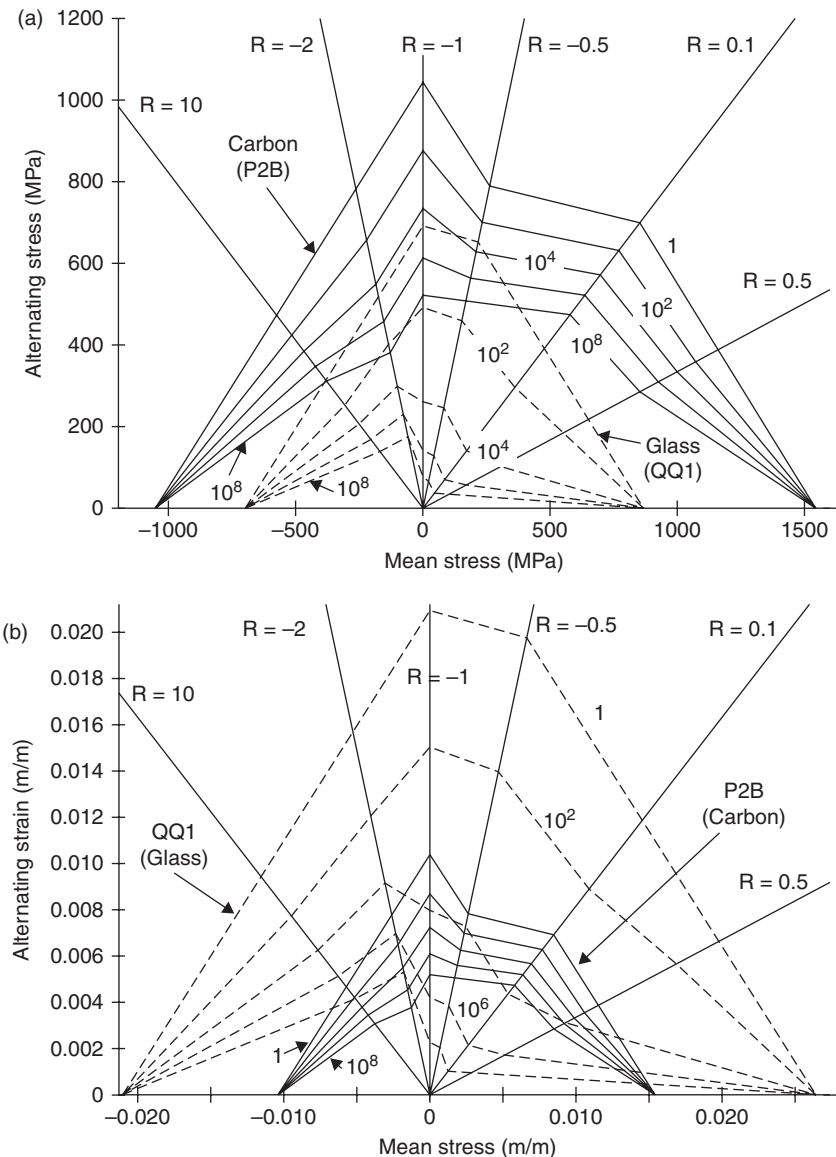
Data sets like those in Fig. 7.2a and 7.2b can be represented for convenience as constant life diagrams (CLDs), lines of constant lifetime on stress or strain amplitude vs mean value plots, as described in detail by Nijssen (2006). S-N trends at particular R-values then plot as straight lines emanating from the origin. CLDs based on stress and strain are given in Figs. 7.3a and 7.3b, comparing the infused MD glass/epoxy laminate in Fig. 7.2a, QQ1, with the prepreg hybrid carbon glass laminate in Fig. 7.2b, P2B. The stress based plot in (a) demonstrates the greater strength and less-steep S-N trends for carbon. The strain plot (b) demonstrates the generally superior strain capacity of laminates with glass UD plies. However, the strains at high cycles for glass fall significantly below those for carbon in the R-value range –1 to 0.1 for this particular glass MD laminate. Data requirements for CLDs have been identified as five or six S-N data sets by both Nijssen (2006) and Sutherland and Mandell (2005).

The trends in Fig. 7.3 demonstrate the critical in-plane properties for the two material types: low compression strains for carbon UD plies, and low reversed loading and tensile fatigue resistance at high cycles for glass UD plies. It is primarily the tensile part of the reversed loading response which is most degrading for the glass, as compression trends are similar to carbon. Carbon shows relatively low steepness S-N trends at all R-values, but low static and fatigue failure strain levels in compression

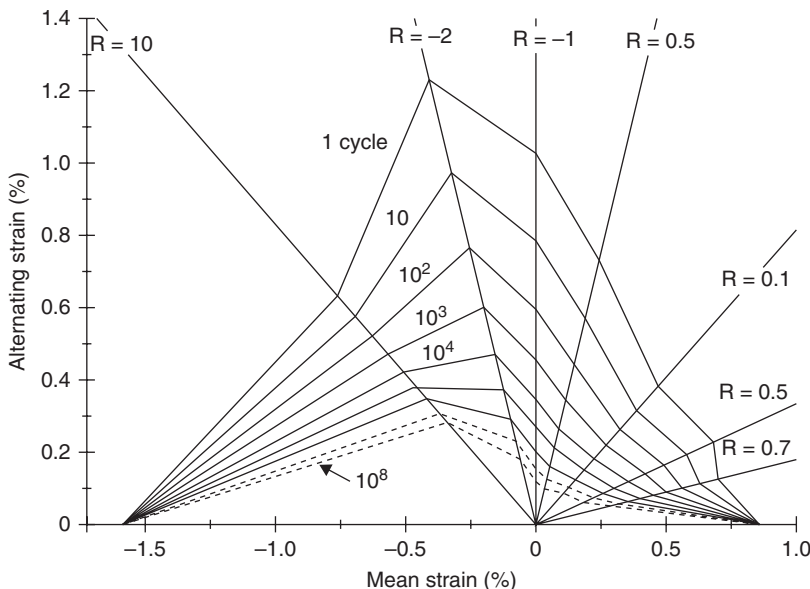


7.2 Effect of loading conditions (R-value) on fatigue strain vs lifetime for (a) glass/epoxy laminate QQ1 and (b) hybrid glass ($\pm 45^\circ$)/carbon (UD) laminate P2B, axial direction (Mandell *et al.*, 2010).

(Mandell *et al.*, 2008). Compressive strength and fatigue resistance are primarily affected by waviness, either within fabrics or on a larger scale as in spar caps or skin wrinkles. Well-constructed carbon infusion fabrics like the MMWK fabric (a Saertex triaxial fabric with carbon fiber 0° strands and glass fiber $\pm 45^\circ$ strands) in Mandell *et al.* (2010, p. 82) and Griffin (2009) can have compressive strain capability equal to or exceeding typical carbon prepreg. (The great advantage of carbon laminates is



7.3 Fatigue constant life diagrams (lines of constant cycles, 1, 10², 10⁴, 10⁶, 10⁸ to failure) as a function of mean and alternating stress (a) and strain (b) comparing prepreg carbon/epoxy P2B and infused glass/epoxy QQ1 laminates derived from S-N data sets at labeled R-values (Mandell *et al.*, 2010).



7.4 Transverse direction strain constant life diagram for laminate QQ1 (Mandell *et al.*, 2010).

their approximately three times axial (UD) stiffness advantage over glass laminates, a critical blade design driver.)

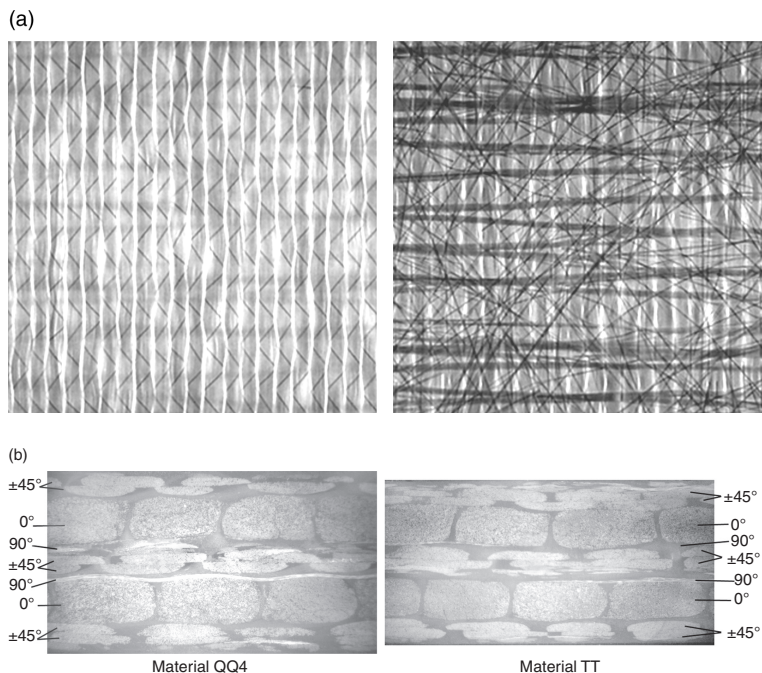
Resin dominated cracking is also fatigue sensitive, including transverse and shear properties and interlaminar strength and crack resistance. S-N data and CLDs are reported for the transverse direction by Mandell *et al.* (2008) for the MD glass (Fig. 7.4) and carbon materials in Fig. 7.3, but tested in the transverse direction. The peaks of the CLD in Fig. 7.4 are shifted significantly toward compression R-values compared with the axial load direction CLD. Maximum transverse failure strains for tensile dominated R-values are in the 0.1–0.2% range at high cycles for UD glass/epoxy laminates (Samborsky *et al.*, 2012).

7.3 Tensile fatigue trends with laminate construction and fiber content for glass fiber laminates

This section, together with Section 7.4, explores the fatigue sensitivity of glass fiber laminates for tensile dominated R-values, represented by $R = 0.1$. The fatigue sensitivity for typical MD laminates is summarized in terms of fiber content as well as fabric and resin effects. Trends are broken out in terms of resin effects at various levels of structure, including aligned strand UD, UD stitched fabrics, biax fabrics and MD laminates.

7.3.1 Materials

Standard laminates (without the addition of features like ply drops) discussed in this section include the following reinforcement structures, in order of complexity: (1) simple unidirectional (UD) aligned strand (AS) structures, typified by preprints, infused rods and dry wound and infused panels; (2) UD stitched fabrics where primary strands at 0° are aligned and stitched to a backing including transverse strands and/or mat (Fig. 7.5a); (3) ‘biax’ fabrics including primary strands at $\pm 45^\circ$, often including backing; (4) multi-directional (MD) laminates reinforced with ‘triax’ fabrics having layers at 0° and $\pm 45^\circ$; and (5) MD laminates with combinations of UD and biax fabrics (see cross-sections in Fig. 7.5b). The laminates were vacuum infused with various commercial epoxy (EP), polyester (UP) or vinyl ester (VE) resins with low viscosity, developed for this process; other resins are also discussed. Laminates were either fabricated at Montana State University (MSU) or supplied by industry partners. A more detailed description of the fabrication process may be found in Mandell *et al.* (2010, p. 32); material designations



7.5 (a) Front and back views of UD fabric PPG-Devold L1200/G30-E07 (Mandell *et al.*, 2010); (b) cross-sections of laminates with high density unidirectional fabrics, QQ4 (fabrics C and M) and TT (fabrics D and M) (Mandell *et al.*, 2010).

are consistent with Mandell and Samborsky (2011 and updates), where particular resins and fabrics are defined in more detail.

Details of experimental methods can be found in Samborsky and Mandell (2012) and Mandell *et al.* (2002, 2010). Typical test coupon geometries were as follows: tensile UD and biax laminate tests, as well as all tests with a compression component, used straight-sided coupons, while waisted (dog-bone) shapes (Fig. 7.1) were used for MD laminates in tension, to provide improved failure modes and locations; thickness tapered coupons were used for selected AS laminate tensile fatigue tests for the same reason (Samborsky *et al.*, 2012). Fatigue tests were run under load control at frequencies in the range of 1–5 Hz, keeping surface heating to a few °C maximum with surface cooling by forced air flow, and also keeping the load rate approximately constant (Sims, 2003). The testing and coupon conditioning environment was laboratory air, approximately 20% RH and 20°C, unless noted. Reported strains were measured in the first few test cycles by extensometer, or determined from a look-up table established from typical specimen static stress-strain curves; strains were not monitored throughout the tests except in special cases as noted. Where given, compression strains were taken from static compression stress-strain tests with strain gages, not measured in fatigue tests, due to the short gage length. Compression and reversed loading fatigue tests were conducted on servo-hydraulic machines with specialized restraints on rotation and lateral piston movement (Mandell *et al.*, 2010, p. 41). Full details for individual tests can be found in the current installment of the SNL/MSU/DOE Fatigue of Composite Materials Database, updated annually (Mandell and Samborsky, 2011).

7.3.2 Fatigue parameters for different laminate types

Fatigue S-N data for composites are commonly represented as stress, or stress normalized by static strength (Sims, 2005), or strain (Samborsky *et al.*, 2010) vs cycles to failure. Normalizing the stress by the static strength has the effect of reducing discrepancies caused by variations in fiber content and fraction of 0° plies in MD laminates. The use of strain has a similar effect without normalization. Strain curve fits (Equation [7.1]) can differ from stress fits in terms of exponents, and reflect the nonlinearity of stress-strain response at higher stresses, particularly for biax and MD laminates. Strain is often impossible to monitor over the entire coupon lifetime due to instrumentation failure. Strain data presented in the figures correspond to the initial strain measured with an extensometer at the beginning of a test (or from a look-up table), and do not represent the accumulation of strain over the coupon lifetime. While the initial strain is meaningful for materials such as UD laminates, for which strain changes during the lifetime are not

great, it is not meaningful for materials such as biax laminates, which may accumulate several times the initial strain over the lifetime.

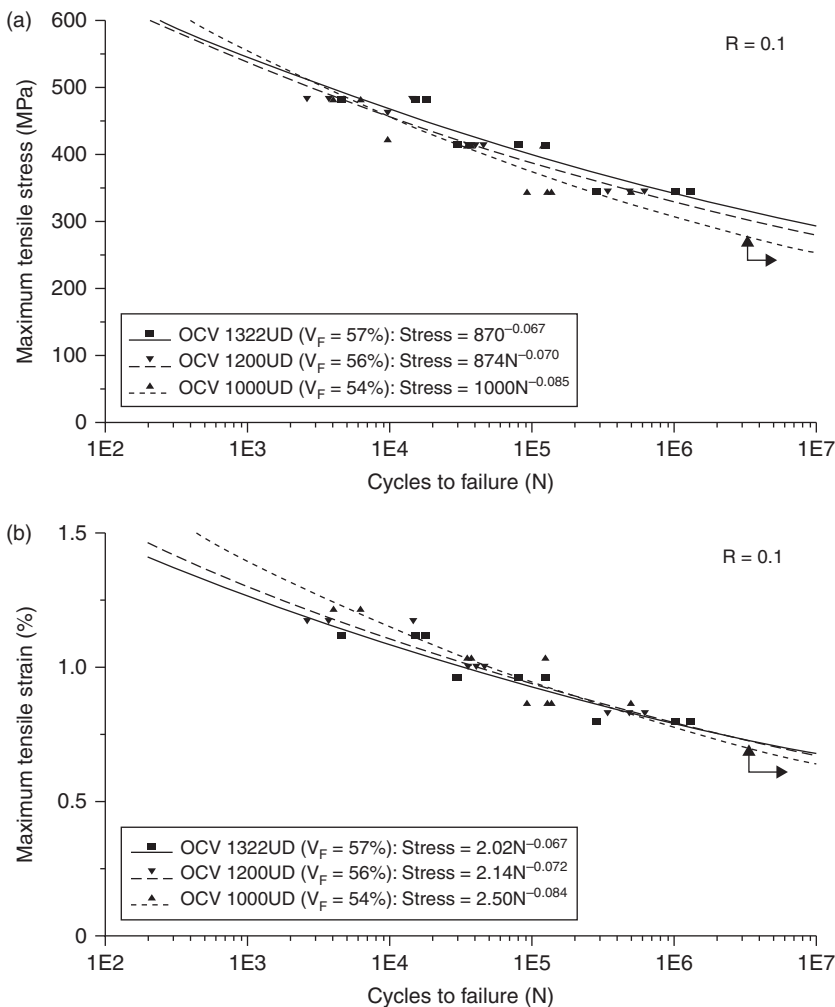
Typical stress and strain based S-N data sets are given in Fig. 7.6 for UD fabric laminates and Fig. 7.7 for MD triax fabric laminates, all with epoxy EP1 resin. These figures illustrate the effects of laminate structure on typical fatigue trends as well as the effects of fabric weight. The three UD fabrics represented in Fig. 7.6 give very similar fatigue trends on a strain basis, while the intermediate weight fabric laminate shows slightly lower stresses due to its lower fiber content. The fatigue exponents (B , Equation [7.1]) are in the range -0.067 to -0.064 for both stress and strain plots, and the coefficients, A (Equation [7.1]) are close to the static strength. Another useful measure of fatigue resistance is the maximum initial strain associated with a lifetime of one million cycles; this parameter is useful as single property representing fatigue resistance which does not have the ambiguity of an exponent (which can be misleading in the absence of the coefficient, A (Samborsky *et al.*, 2010)). From the curve fits in Fig. 7.6, the million cycle strain ranges from 0.78% to 0.80%.

MD laminates such as the three typical triax materials (varying in fabric weight) in Fig. 7.7 fail by a progressive process of matrix cracking in the $\pm 45^\circ$ plies eventually followed by fiber failure in the 0° plies (Mandell *et al.*, 2010, p. 68). The fatigue exponents, B , now range from -0.126 to -0.146 for stress and -0.155 to -0.159 for strain, representing much steeper S-N curves than for UD laminates; the coefficients, A , are also much higher than the static strength. Million cycle strain values range from 0.61% to 0.70%. Thus, for the triax laminates the S-N curves are steeper and the million cycle strains moderately lower than for the UD laminates. The exponents and million cycle strains for the fabrics in Figs 7.6 and 7.7 are typical for these types of laminates with epoxy resins.

Laminates based on other resins such as polyesters may behave in a more fatigue sensitive manner. Figure 7.8 compares the strain S-N data sets for laminates based on an epoxy and a polyester resin, with the same reinforcing fabrics and lay-up. This figure illustrates the effect of resin type as well as demonstrating the million cycle strain characterization. While the fit exponents, B , fall in a similar range, the million cycle strains differ by a factor of two, and better depict the difference in fatigue resistance of the two laminates.

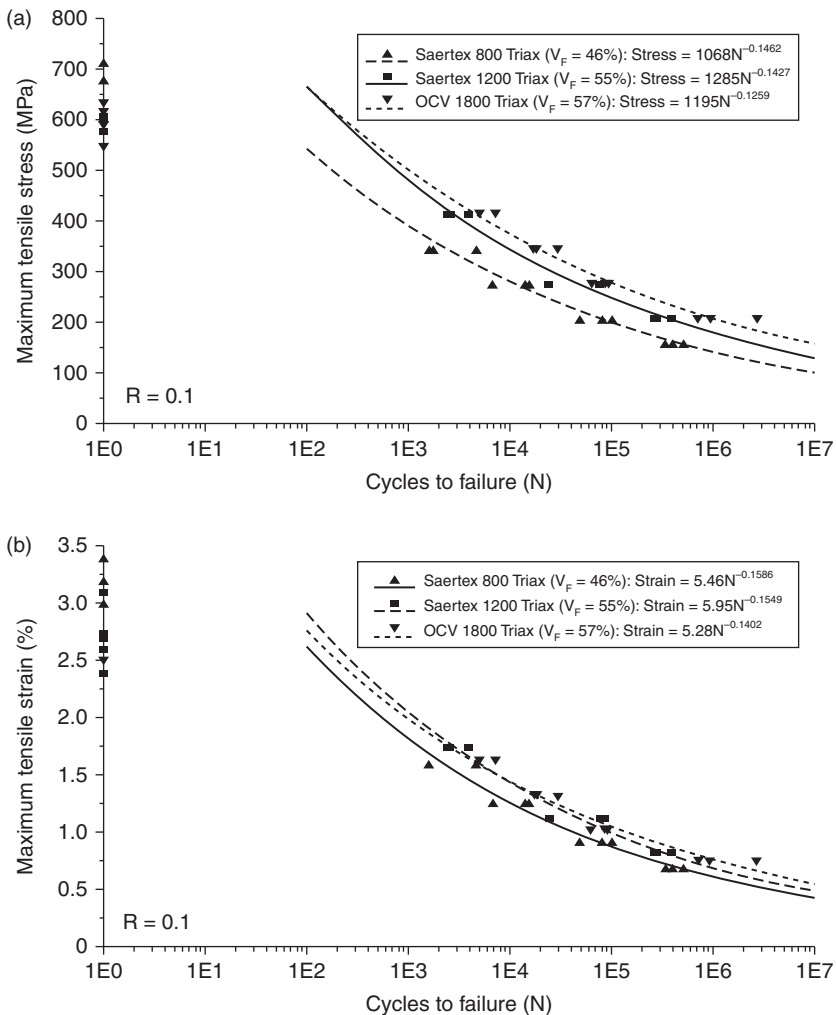
7.3.3 Effects of fiber content

S-N trends for tensile fatigue over a broad range of glass fiber contents have been reported for several glass fabrics with various epoxy resins (Mandell *et al.*, 2005, p. 78, 2008), and for impregnated glass strands (Mandell *et al.*,



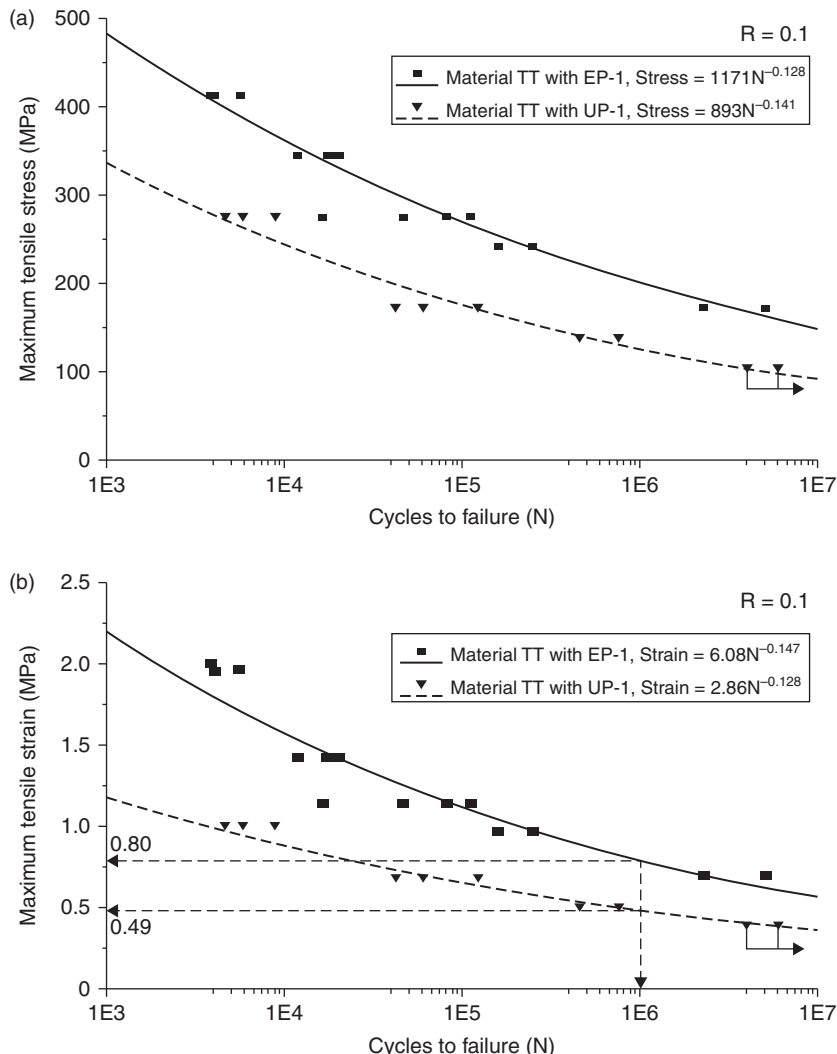
7.6 Stress (a) and strain (b) vs cycles for UD laminates with three different weight OCV™ technical fabrics, EP1 epoxy, $R = 0.1$ (Samborsky *et al.*, 2012).

2002, p. 156). Trends of the million cycle tensile fatigue strain with fiber content for MD laminates constructed with several UD fabrics are given in Fig. 7.9. The broad fiber content variation was achieved by infusing between hard molds with controlled spacing, compared with the standard process having a hard mold on one side and a vacuum bag on the other (Mandell *et al.*, 2010, p. 32). The MD laminates based on 955 g/m² UD fabric B, QQ1, show a sharp transition to reduced fatigue resistance above 40–45% fiber by volume, similar to (DD-series) polyester resin laminates with a 527 g/m²



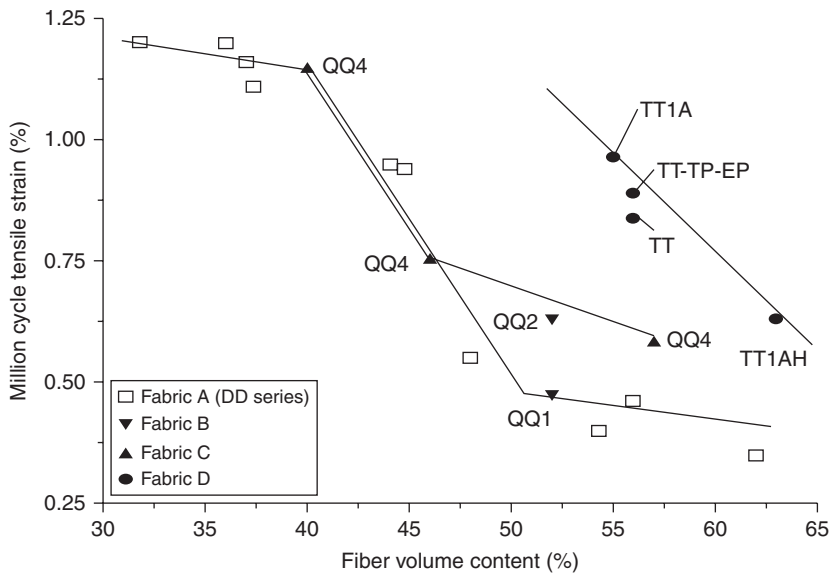
7.7 Stress (a) and strain (b) vs cycles to fail for laminates with three different weight triax fabrics, epoxy EP1, $R = 0.1$ (Samborsky *et al.*, 2012).

UD fabric. In contrast, the TT-series laminates, based on an 1875 g/m^2 UD fabric, show reduced fatigue resistance only above 55–60% fiber. Compared with the QQ1 laminate, the TT-series laminates show much more extensive biax ply cracking and delamination prior to UD ply failure (Fig. 7.1). The QQ4-series laminates, based on a heavier 1682 g/m^2 fabric, but otherwise similar to QQ1, also showed a reduced strain in the same range as QQ1, but the strain was increased to the range of the TT laminates when 50%

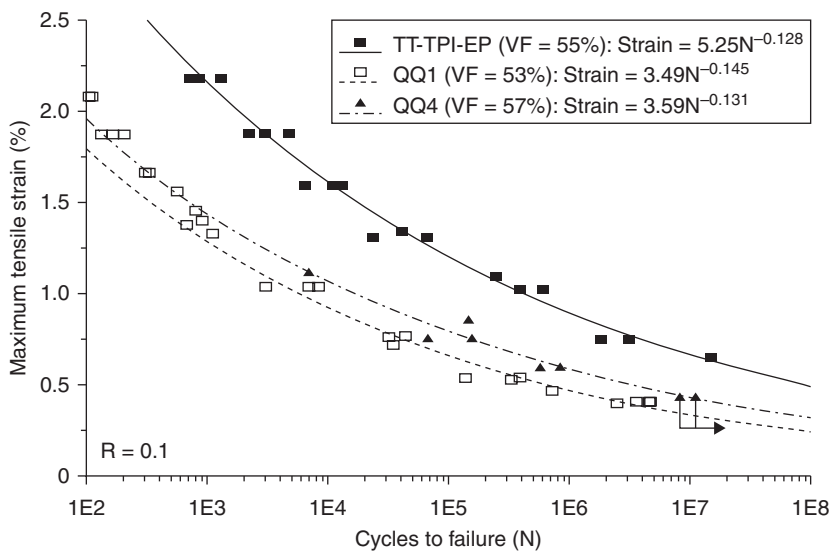


7.8 Stress (a) and strain (b) vs log cycles data illustrating the million cycle strain characterization for MD, TT laminates containing fabrics D and M, TT-EP-1 (epoxy, $V_f = 52\%$), TT-UP-1 (polyester, $V_f = 52\%$), $R = 0.1$ (Mandell *et al.*, 2010).

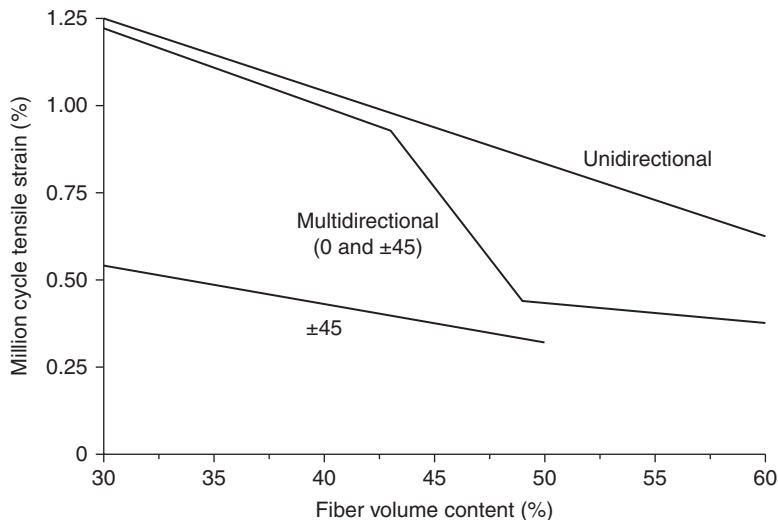
fiber volume laminates were infused with a hard mold on one side only; this molding change did not affect laminate QQ1 (Mandell *et al.*, 2010, p. 80). Figure 7.10 compares the QQ1 and QQ4 laminates with the TT laminate in the fiber content range typical of current blades, showing the greatly improved performance of fabric D in the TT material (the epoxy resins are similar, EP2 and EP4).



7.9 Million cycle strain vs fiber volume content for various laminates showing transitions to reduced fatigue resistance as a function of 0° fabric, $R = 0.1$ (Mandell *et al.*, 2010).



7.10 Effect of fabric on MD glass/epoxy laminates at similar fiber content, laminates based on UD fabrics B (QQ1), C (QQ4) and D (TT-TPI-EP) (Mandell *et al.*, 2010).



7.11 Fatigue trends vs fiber volume content for unidirectional, multidirectional and biax laminates based on early low density weft unidirectional fabrics D155 and D092, biax fabrics DB120 and DB240, with polyester resin UP-2 (Samborsky *et al.*, 2010).

The million cycle strain trend with fiber content is compared in Fig. 7.11 for early MD, UD and biax laminates with polyester resin UP-2. The unidirectional laminate million cycle fatigue strain gradually decreases with increasing fiber content; the biax strain also decreases gradually with fiber content, but in a much lower strain range. (These are initial strains, which, as for all biax laminates, are not representative of failure strains.) For the multidirectional laminates, the million cycle strain follows the unidirectional laminate strain at lower fiber content, then transitions to near the biax strain above about 45% fiber volume (plotted as DD-series in Fig. 7.9). The DD-series laminates are about 70% unidirectional material, 30% biax; at higher fiber contents the multidirectional laminates fail when the biax plies crack significantly in a local area, at the relatively low fatigue cracking strain capability of these biax materials. At low fiber contents the multidirectional laminates are able to withstand failure of the biax plies, eventually failing near the independent unidirectional ply strain condition. The UD fabric in this series is fabric A, a weft UD fabric with no backing material.

The fiber contents for the low fabric density materials in Fig. 7.11, when molded at low pressure (10 kPa), are around 35–40% by volume. The higher density UD fabrics such as B, D and H (Figs 7.4 and 7.5), typically used for infusion processing with a mold on one side, naturally reach a fiber volume content of around 50–60% at low mold pressure, e.g. 10 kPa (Samborsky

et al., 2008a). Figure 7.11 indicates that MD laminate failure strains in the higher fiber content range for naturally lower density fabrics with the polyester resin follow the biax ply initial strain. The S-N trends in Fig. 7.12 for infused MD laminates with high density fabrics D and M (the better performing TT materials in Fig. 7.9) indicate that this same trend is observed for the polyester resin, but the epoxy resin laminates survive for about a decade of cycles after the biax initial strain is reached. Damage such as resin cracking in MD fatigue coupons at failure is more localized for the polyester, but global damage to the biax layers is evident with the epoxy before coupon separation (Fig. 7.1, Samborsky *et al.*, 2010). The poorer-performing epoxy resin laminates, QQ1 in Fig. 7.9, show localized damage and low failure strains at higher fiber content, similar to the polyester resin laminates.

The results discussed in this section indicate a trend of increasing tensile fatigue sensitivity with increasing fiber content for glass laminates. Different UD fabrics and resin types shift the trend lines for, say, million cycle strains, into higher or lower fiber content ranges (Fig. 7.9). As described in Section 7.4.3, even very high fiber content laminates can have excellent fatigue resistance in terms of million cycle strain if the reinforcement structure is sufficiently refined, as for aligned strand laminates.

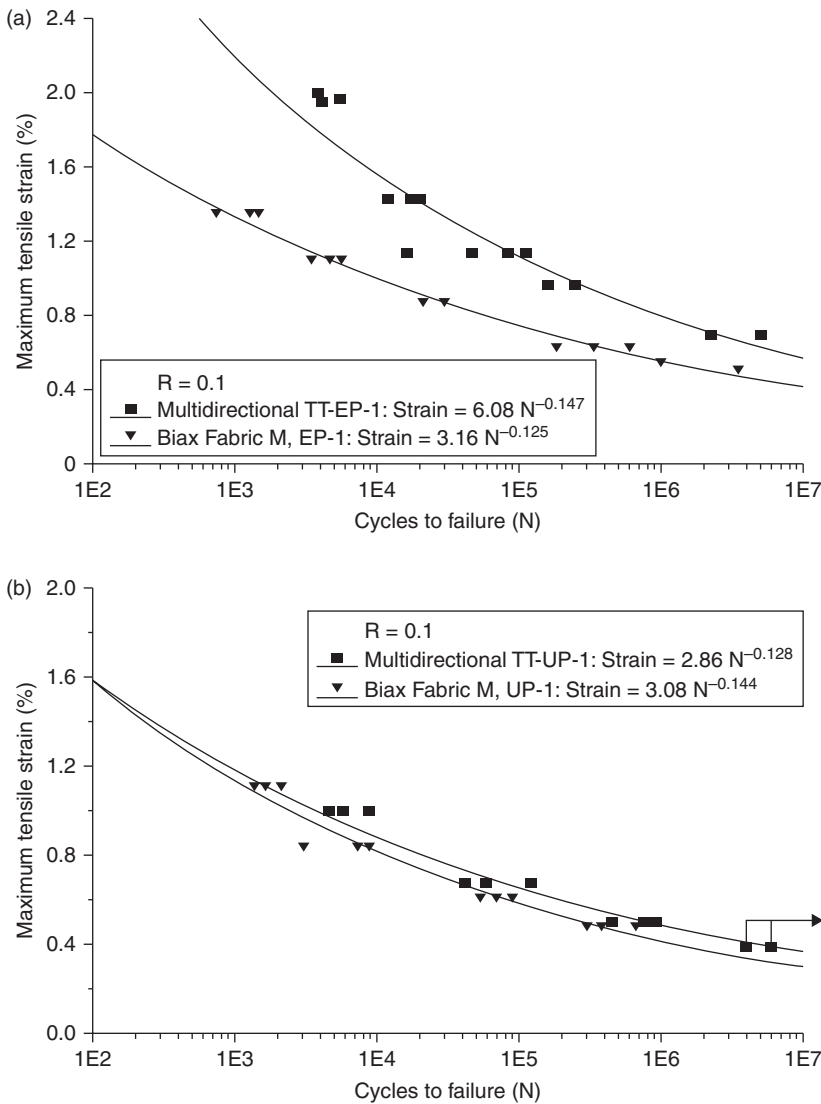
7.4 Effects of resin and fabric structure on tensile fatigue resistance

This section presents a detailed exploration of the effects of various resins and fabric structures on the tensile fatigue performance of laminates.

7.4.1 Effects of resin on multidirectional (MD) laminates

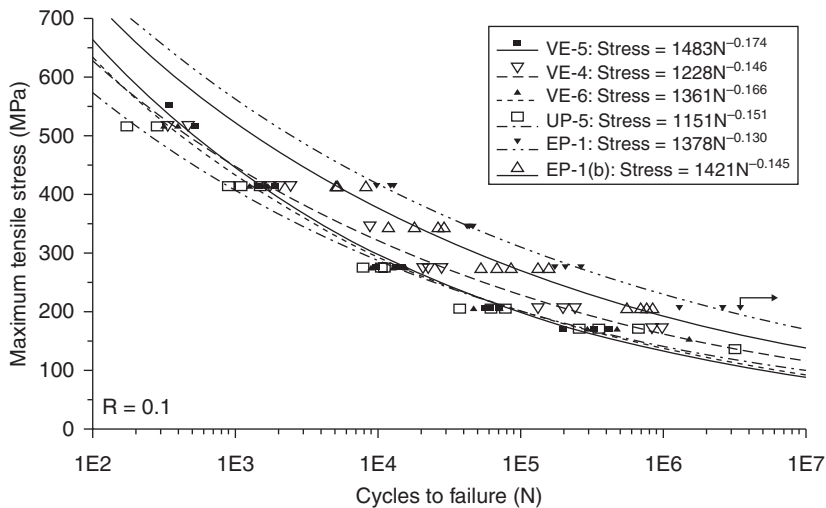
The previous section indicates that tensile fatigue resistance is significantly impacted by interactions between resin, fabric and fiber content; this section explores these interactions in detail.

Tests of laminates with current styles of glass reinforcement for infusion (Fig. 7.5), at fiber volume contents in the 50–60% range, show a marked ordering of fatigue resistance according to resin type, with epoxy superior to polyester, and vinyl esters bridging the range between the two. Results for a series of MD laminates with the same reinforcing fabrics but five different resins are given in Fig. 7.13, and million cycle initial strains for a broader range of laminates are given in Fig. 7.14. The left side of Fig. 7.14 relates to the early DD-series laminates with UD fabric A having no backing material and processed between two hard molds, discussed earlier (Fig. 7.11). These laminates showed no effect of the type of resin on the tensile or compressive

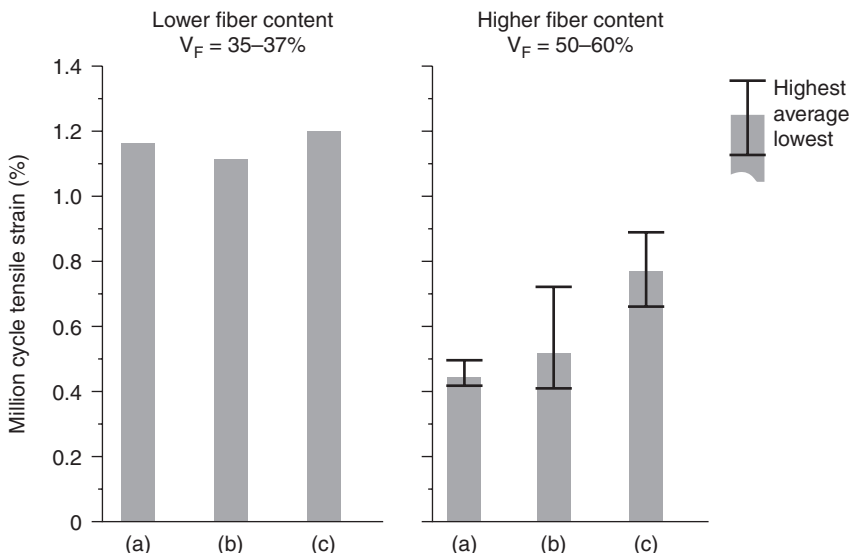


7.12 Comparison of biax and MD laminate strain-cycles data for epoxy (a) and polyester (b) resins (Mandell *et al.*, 2010).

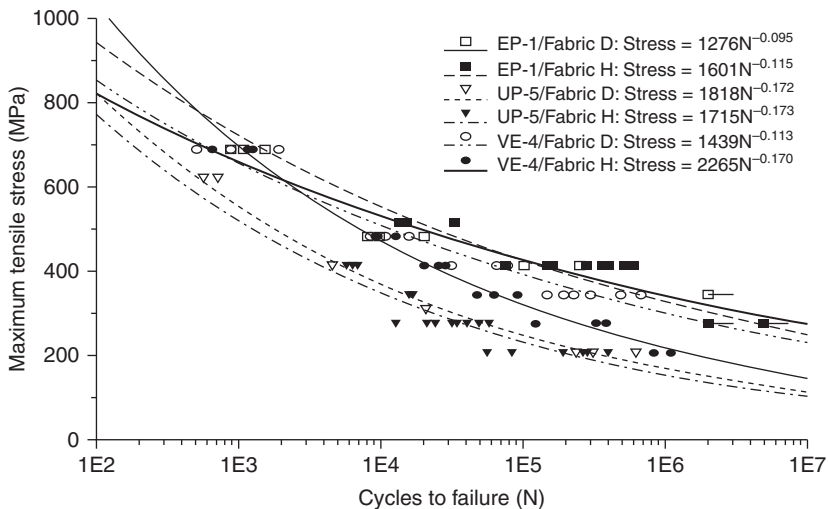
fatigue resistance (Mandell and Samborsky, 1997, p. 30), consistent with results in the early European database FACT (DeSmet and Bach, 1994). The laminates on the right side of Fig. 7.14 are based on UD fabrics D and H, and include the results for TT-series laminates in Figs 7.8, 7.9, 7.10 and 7.12. Epoxy resin laminates QQ1 and QQ4 (Figs 7.9 and 7.10) would fall into the polyester range if included, but were molded with two-sided molds;



7.13 S-N datasets for MD laminates, fabrics H and T, comparing five resins (EP-1 cured at 80°C, EP-1b cured at 70°C) (Samborsky *et al.*, 2012).



7.14 Comparison of (a) polyester, (b) vinyl ester and (c) epoxy resin laminates at low (fabric A, left) and higher (fabrics D, G and H, right) fiber contents (Samborsky *et al.*, 2010).



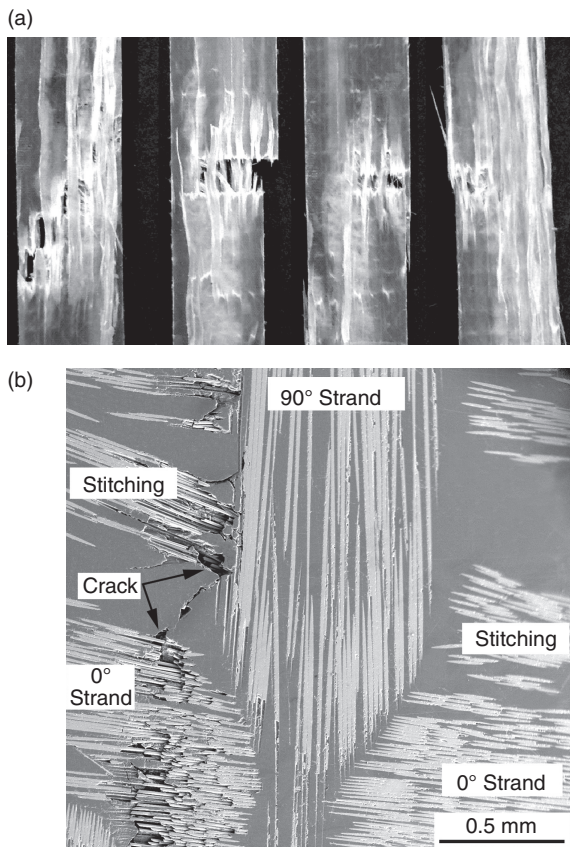
7.15 Comparison of UD fabric laminate S-N results for epoxy, vinyl ester and polyester resins with fabrics H and D (Samborsky *et al.*, 2012).

as noted earlier, QQ4 infused with a one-sided mold falls within the epoxy range in Fig. 7.14, but infused QQ1 still falls close to the polyester.

7.4.2 Effects of resin on unidirectional (UD) fabric laminates

Laminates with the same resins and UD fabric H as in Fig. 7.13 were also tested as two-ply UD laminates. Figure 7.15 gives S-N trends for three of the resins, EP-1, VE-4 and UP-5, with both Fabric H and D. Fabric D is based on heavier, 4400 Tex roving, compared with fabric H, 2400 Tex roving, both with PPG Hybon 2026 size. The epoxy performs well with both fabrics, while the vinyl ester approaches the epoxy performance only with fabric D. The polyester performs relatively poorly with both fabrics.

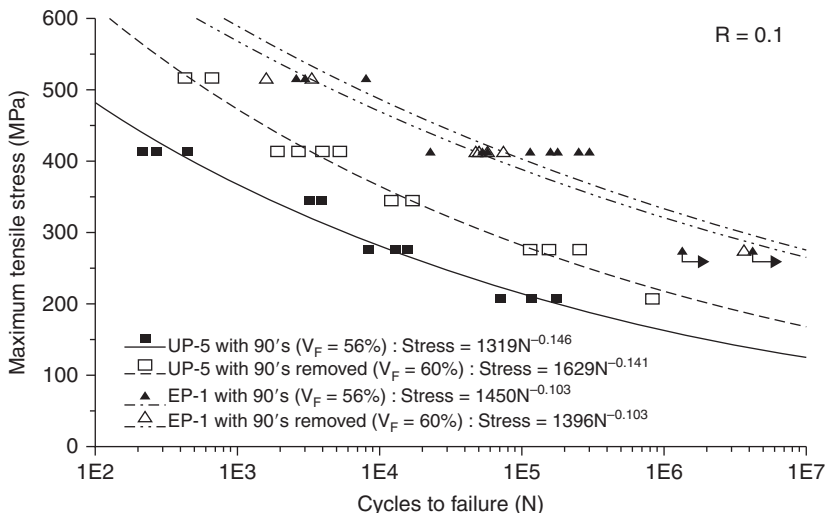
The UD laminate tests with fabric H (see Fig. 7.5) and the polyester and vinyl ester resins showed a clear failure pattern of cracking associated with the fabric transverse strand locations (Fig. 7.16). Failures of this type were rare with the epoxy. To explore the effect of the transverse backing strands further, the strands were carefully removed from the fabric in the gage section prior to infusion, leaving the mat strands intact; the resulting laminates were good quality. The effect of removing the transverse fabric strands on the tensile fatigue performance is shown in Fig. 7.17. The polyester laminate is significantly improved by removing the transverse strands, while the epoxy laminate is unaffected.



7.16 (a) Failed coupons of UP5/fabric showing cracking associated with transverse fabric backing strands, and (b) micrograph of cracking along transverse strand and stitching, with failed 0° strand (Samborsky *et al.*, 2012).

7.4.3 Effects of resin on UD aligned strand (AS) laminates compared to UD fabric laminates

A fundamental question in evaluating the performance of UD fabrics with various resins relates to the performance in the absence of any fabric related structure. To explore this issue, a series of infused, dry wound aligned strand UD laminates were specially prepared and supplied by industry (see Section 7.10). The tensile fatigue performance of the AS structured UD laminates is compared, in Fig. 7.18, with the UD fabric H laminates. Both laminate types contain the same UD rovings, PPG 2400 Tex with Hybon 2026 finish. The fabric data for the epoxy resin are typical of data for other fabrics of similar construction (see Figs 7.6 and

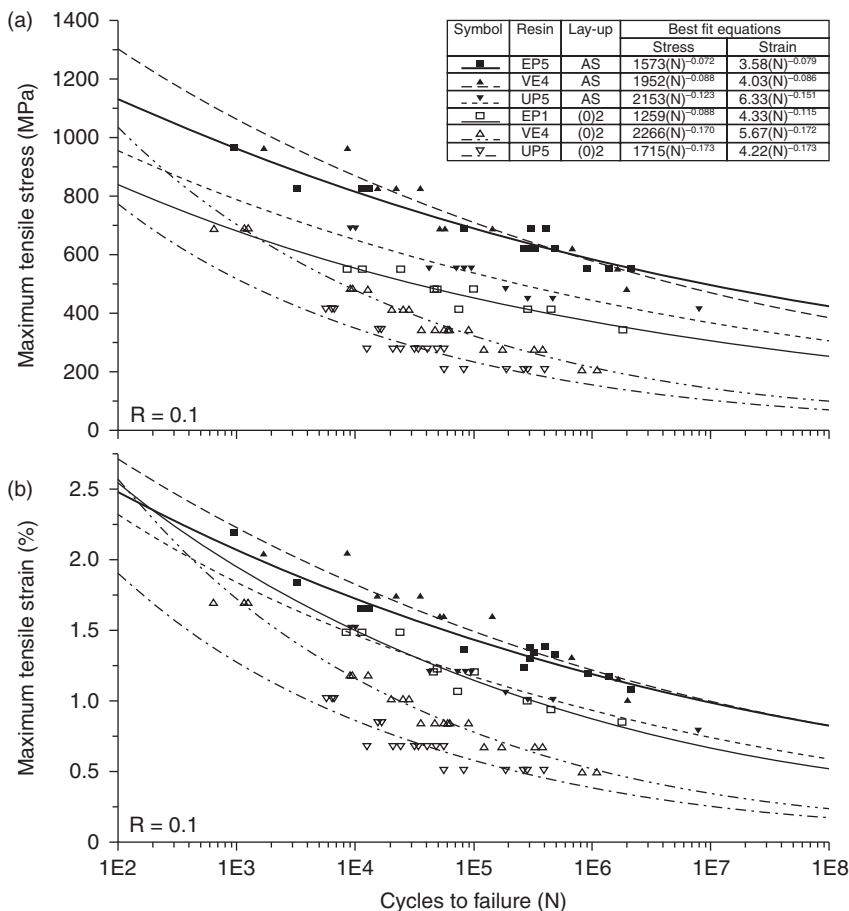


7.17 Effect of removing transverse backing strands on fabric data from Fig. 7.13 (Samborsky *et al.*, 2012).

7.16). (Note that epoxies EP1 (fabric) and EP5 (AS) differ only slightly; both have RIMR 135 resin, but the EP1 hardener is RIMH 1366 while the EP5 hardener is very similar, RIMH137; post-cure temperatures were also slightly different.) The data in Fig. 7.18 establish that laminates with only aligned strand for reinforcement significantly outperform laminates containing typical fabric, with all three resins. The high fiber contents for the AS laminates provide superior strength and modulus combined with the best tensile fatigue resistance in terms of million cycle strain known with glass fibers, exceeding reported fatigue strains for prepreg laminates (Mandell *et al.*, 2002, p. 155). The vinyl ester VE4 performs as well as the epoxy with the AS structure, while the polyester shows reduced fatigue resistance compared with epoxy; the polyester AS laminates still perform significantly better than the fabric laminates.

Improvements shown with the AS laminates are due in part to overall fiber content differences, as fiber packing is improved for AS laminates. A second factor is the difference in fiber content in the axial, 0° direction, as the transverse and mat backing strands do not contribute significantly to strength properties in the axial (load) direction. Table 7.2 gives the overall and 0° direction fiber contents. The substantial differences between 0° fabric V_f and AS V_f help to explain the observed property differences.

A simple definition of fabric efficiency which reflects the actual laminate properties is the ratio P_F/P_{AS} , where P_F is the property of the fabric laminate and P_{AS} is the property of the AS laminates without the fabric structure. In



7.18 Comparison of (a) stress and (b) strain fatigue trends for aligned strand (AS) and fabric (O_2) based laminates for epoxy (EP1 and EP5), vinyl ester (VE4) and polyester (UP5) (Samborsky *et al.*, 2012).

Table 7.2, the ratio for the $0^\circ V_f$ ranges from 0.76 to 0.83 for different resins. The modulus ratios are slightly higher, reflecting the backing contribution to increasing the modulus relative to pure resin. The UTS and fatigue parameters fall below the ratio for $0^\circ V_f$ indicating more than proportional decrease for these fabric properties with fiber content, particularly for the UP and VE resins.

Clearer relationships emerge if the fabric efficiency is adjusted for the $0^\circ V_f$ difference by considering the parameter (P_F/P_{AS}) ($AS\ V_f/Fabric\ 0^\circ V_f$) in the bottom section of Table 7.2. The adjusted efficiency indicates fabric properties relative to expectations from AS laminates assuming

Table 7.2 Fabric efficiency: translation of aligned strand (AS) structure properties into UD fabric H laminates for different resins

Resin	EP1/EP5 ^a	VE4	UP5
Fiber Volume Fraction, V_f			
AS Laminates	0.64	0.66	0.68
Fabric Laminates	0.58	0.55	0.58
0° V_f , Fabric Laminates	0.53	0.50	0.53
0° Direction Fabric Efficiency: P_f/P_{AS}			
0° V_f	0.83	0.76	0.78
Modulus, E	0.88	0.85	0.81
UTS	0.73	0.68	0.62
10 ⁶ cycle stress	0.64	0.37	0.40
10 ⁶ cycle strain	0.73	0.43	0.49
P_f/P_{AS} Adjusted for 0° V_f; (P_f/P_{AS}) (AS V_f/Fabric 0° V_f)			
Modulus, E	1.06	1.12	1.04
UTS	0.88	0.89	0.79
10 ⁶ cycle stress	0.77	0.49	0.51
10 ⁶ cycle strain	0.88	0.49	0.63

^aEP1 for fabric laminates, EP5 for AS laminates.

Fabric laminate properties/AS laminate properties and values adjusted for 0° fiber content; PPG 2400 Tex rovings with Hybon 2026 finish.

Source: Samborsky *et al.*, 2012.

proportional changes with 0° V_f . The fabric laminate modulus now shows a value greater than 1.0 due to the small contribution of the backing strands. The UTS is 79–89% of the expected proportional change, probably due to relatively poor strand alignment in the fabric as can be seen in Fig. 7.5a. The fatigue ratios for the epoxy are close to the UTS ratio, about as good as could be expected. However, the fatigue ratios for the UP and VE resins fall well below the UTS ratio, showing particular sensitivity to fabric structure for these resins, apparently related to the transverse strands.

The results in Table 7.2 and Fig. 7.18 relate specifically to Fabric H (see Table 7.1b). As discussed earlier (see Fig. 7.15), UD laminate fatigue data have also been obtained for the heavier Fabric D, which only contains transverse strands in the backing (no mat), and also has 4400 Tex warp strands (AS laminate data are not yet available with these strands). Figure 7.15 indicated similar fatigue trends for both fabrics for EP and UP resins, with higher performance for the epoxy. The VE resin approaches the epoxy performance at higher cycles for the Fabric D laminates, as it does for AS laminates in Fig. 7.18. Thus, the VE resin may perform on par with epoxy for some fabric structures or strands, but not others.

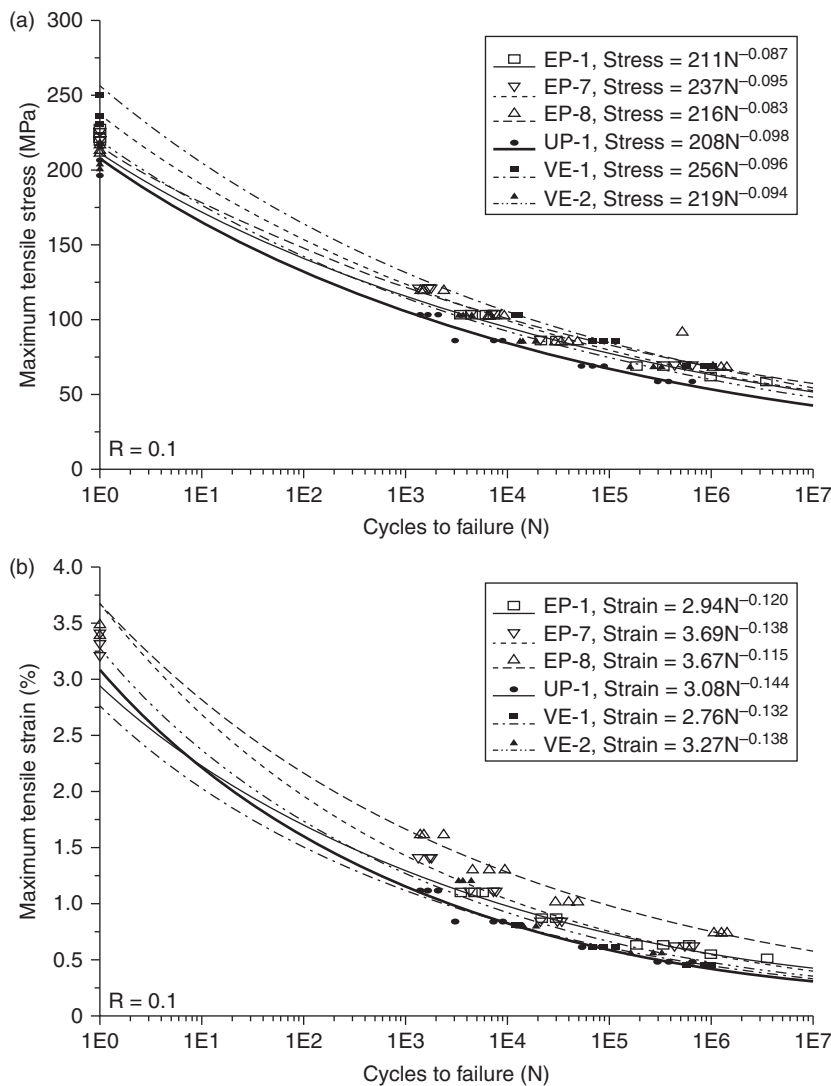
7.4.4 Effects of resin on biax laminates

Laminates constructed from biax and triax fabrics are commonly used in blade skins, spars and root build-up areas and as components in MD laminates. Biax laminates vary considerably in backing, including no backing, warp or weft backing strands and mat. The backing can significantly affect biax laminate properties in axial (0°) and transverse directions. A variety of static and fatigue results for typical blade biax fabrics at several R-values, tested in different directions have been reported by Mandell *et al.* (2010, p. 87). The effects of the resin on the tensile fatigue of biax laminates containing mat backing, fabric M, is explored in Fig. 7.19. Compared to the relative performance of MD laminates in Fig. 7.13, there is considerably reduced sensitivity to the resin for this particular biax fabric; only the toughened epoxy resin EP-8 provides significant improvement. Biax laminate stress-strain curves are significantly nonlinear (Mandell *et al.*, 2010, p. 67), and their strain S-N fatigue exponents are significantly higher than for stress (Mandell *et al.*, 2010, p. 88). The initial strain values given in Fig. 7.19 (bottom) are of questionable significance due to the significant strain accumulation over the lifetime, as discussed in Section 7.3.2. Since damage in MD laminates typically occurs first in the biax layers, biax fatigue strains are important in practice, and depend on both the fabric structure (and fiber sizing) and the resin.

7.4.5 Effects of fabric weight and structure on epoxy resin MD laminates

UD laminate data for five different UD fabrics with different weights, backing, strands and fiber finish, all with epoxy EP1 resin, as in Figs 7.6 and 7.15, as well as data for MD laminates using fabrics D and H, also all with epoxy EP1 resin, as in Figs 7.8 and 7.13, show similar fatigue performance, with similar million cycle fatigue failure strains (Mandell *et al.*, 2010, p. 80; Samborsky *et al.*, 2012). This suggests that epoxy resins such as EP1 are not strongly sensitive to the fabric structures in infusion molding. (Fabric B in MD material QQ1 appears to be an exception (see Fig. 7.10); this fabric appeared similar to others, but was the earliest fabric obtained for these studies, a single roll, *circa* 2000).

A more controlled and systematic study was carried out in cooperation with Devold AMT AS (see acknowledgements) to explore the issue of the consistency of performance of UD glass fabrics with an epoxy resin over a broad range of stitched fabric constructions. Ten stitched fabrics with differences in weight, backing structure and stitching, all with 2400 Tex PPG Hybon 2026 sized rovings, were specially prepared by Devold. Most were



7.19 Comparison of (a) stress and (b) strain S-N data sets for biax laminates with six resin systems (fabric M) (Mandell *et al.*, 2010).

tested in fatigue at a single maximum stress level, while four were tested at several stress levels. All laminates were MD structure with the UD fabrics listed in Table 7.3, combined with a Devold 800 g/m² biax fabric. All laminate configurations were ($\pm 45^\circ/0^\circ$)s except for the heaviest, L2400, which used a single 0° layer due to its doubled areal mass relative to the standard L1200. Fiber volume contents were 54–61%.

Table 7.3 Fatigue results for ten MD laminates supplied by Devold with varied UD fabrics, epoxy EP5, R = 0.1

Material (UD Fabric)	Tensile Modulus, E _T (GPa)	Ultimate Strain (%)	Ultimate Tensile Stress (UTS) (MPa)	Normalized Maximum. Stress, 414/UTS	Log Cycles to Failure at a Maximum Stress of 414 MPa	COV (%)
L1200	35.7	2.8	891	0.465	4.77	2.7
L1400	38.6	2.8	896	0.462	4.91	4.3
L2400	35.8	2.9	920	0.450	4.80	3.2
LT1200	35.2	2.8	818	0.506	4.36	0.80
TLT1200	36.3	2.5	857	0.483	4.74	0.74
LT1200_G50	36.8	2.8	809	0.512	4.35	3.9
L1400_T	36.8	2.8	770	0.538	4.88	5.9
L1400_TCU	40.9	2.8	779	0.531	4.53	4.0
L1400_TCS	37.4	2.7	760	0.545	4.74	2.7
L1400_BTW	38.3	3.1	946	0.437	4.89	2.5

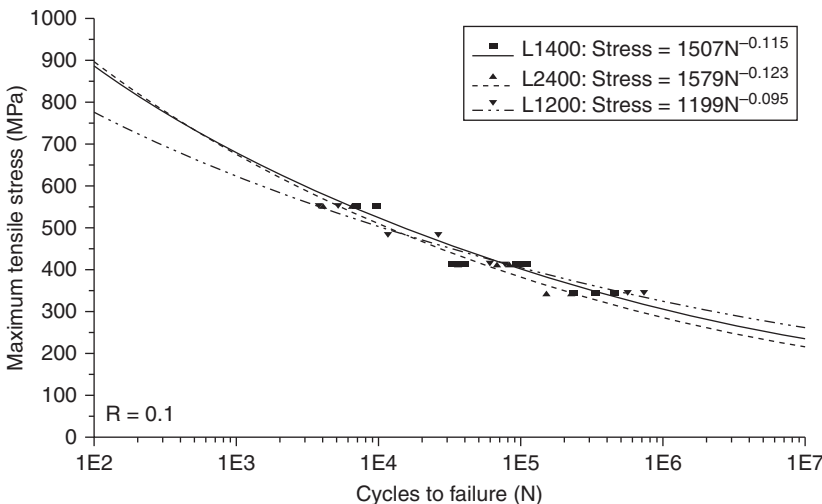
Source: Samborsky *et al.*, 2012.

Test results for the ten fabric variations are given in Table 7.3. The first three fabrics, L1200, L1400 and L2400 vary only in fabric weight. L1400 has more closely spaced yarns while L2400 has larger yarns. More complete data for different stress levels are given in Fig. 7.20. The effect of fabric weight is not great, with only a possibility of slightly lower cycles for the heaviest fabric at the lowest stress. The next three fabrics varied in backing structure: weft yarn on lower side (LT), weft yarn top and bottom (TLT) and weft yarn plus chopped strand (LT1200_G50). The bottom four fabrics varied in stitching details: tricot (T), un-symmetric tricot chain (UTC), symmetric tricot chain (STC) and stitch in-between roving (BTW). The log cycles to failure at the same maximum stress (R = 0.1) as in Table 7.3 were not significantly affected by any of these variations for this epoxy resin.

Thus, laminates with an overall total of fourteen different UD fabrics demonstrate that tensile fatigue resistance is not strongly affected by fabric details for a broad range of fabric weights, backing, stitching and strands/fibers/finishes for similar epoxy resins EP1 and EP5. Consistent results among several polyester resins with different fabrics have also been reported by Mandell *et al.* (2010, p. 80) (but at a lower performance level than for epoxies).

7.5 Delamination and material transitions

Composite structures in general are expected to experience significant thickness-direction stresses leading to delamination failures (Gilchrist, 2005). Various studies of substructural elements (Vizzini and Lee, 1995;

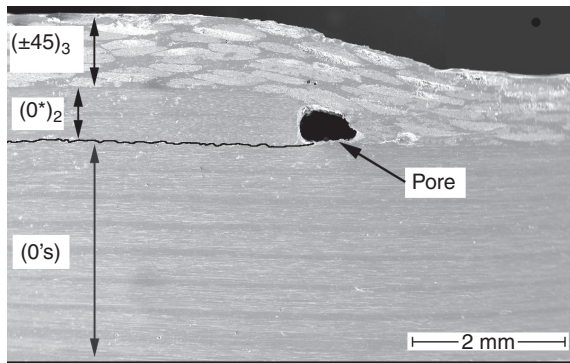


7.20 Stress vs cycles for MD laminates fabricated with three different weight UD fabrics from Table 7.3, epoxy EP5, $R = 0.1$ (Samborsky *et al.*, 2012).

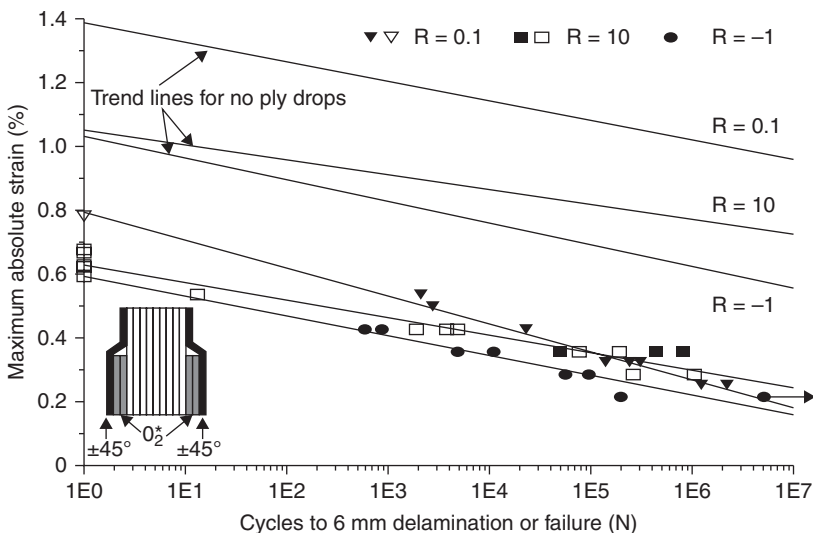
Mandell *et al.*, 1998, 2003b) and details like ply drops (Murri *et al.*, 1991; Mandell *et al.*, 2002, p. 121; Samborsky *et al.*, 2008b) and adhesive joints (Samborsky *et al.*, 2011) have confirmed the importance of delamination under fatigue loading for typical wind blade materials. Delamination resistance, particularly in opening mode, has long been understood to be dominated by the resin toughness (Hunston *et al.*, 1987), something which has been demonstrated for blade laminate infusion resins (Mandell *et al.*, 2000; Agastra *et al.*, 2009).

7.5.1 Ply drops in carbon and glass prepreg laminates

The improved fatigue resistance of carbon over glass in the axial direction (see Figs 7.2 and 7.3) is not observed for resin dominated properties like delamination resistance at material transitions. Ply drops are material transitions used in laminate thickness tapering, where individual or multiple plies are terminated. Figures 7.21–7.23 are from an experimental and finite element study of crack extension at ply drops of various thickness and position in carbon and glass prepreg laminates by Wilson (2006) and Mandell *et al.* (2010, p. 101). The stress concentration associated with the ply drop can result in delamination crack growth at much lower strains than for similar laminates without ply drops, particularly at associated pores, as in Fig. 7.21; special treatments such as ply edge chamfering (Wilson, 2006) and pinking (Griffin, 2009) can improve the performance. As indicated in Fig. 7.22,

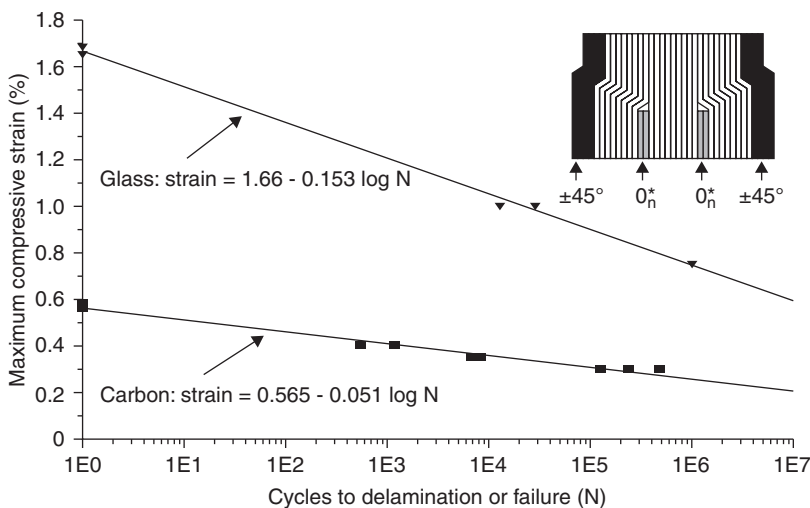


7.21 Photograph of delamination crack growing from pore ahead of double ply drop, carbon 0° plies, glass biax plies, compression fatigue (crack path enhanced) (Mandell *et al.*, 2010).



7.22 Maximum absolute strain versus cycles to failure for a $(\pm 45/0^*_2/0^*/0^*_2/\pm 45)$ laminate, $R = 0.1, 10$ and -1 , (contains ply drops for the 0^*_2 plies; 0° plies are carbon, $\pm 45^\circ$ plies are glass) (Mandell *et al.*, 2010).

Ply drops can greatly reduce the strains for significant damage growth under all R-values for the normally fatigue-resistant carbon fiber laminates. Figure 7.23 illustrates the much lower fatigue strains that can produce delamination where carbon plies are dropped, when compared with glass plies, both prepregs having the same resin (total dropped thickness 0.6 mm). The greater modulus of carbon UD plies results in increased strain energy



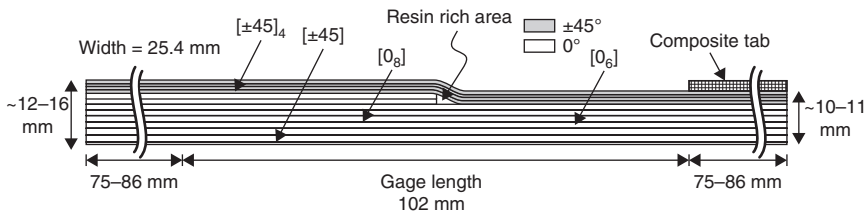
7.23 Maximum compressive strain versus cycles to delaminate with two double internal ply drops for thick laminates with carbon and glass 0° plies, $\pm 45^\circ$ plies are glass, $[(\pm 45^\circ)_3/0_9/0_2^*/0_9/0_2^*/0_9/(\pm 45^\circ)_3]$ (Mandell *et al.*, 2010).

available for delamination at the same axial strain level, predicted by finite element analysis (FEA) crack analysis or strength of materials approximation; the strain energy release rates associated with delamination cracks are generally proportional to the thickness of dropped material at a particular location (Mandell *et al.*, 2010, p. 101). The measured values for critical strain energy release rates, G_{Ic} and G_{IIc} , were slightly higher for the glass, possibly due to a lower V_f for the glass prepreg, which tends to raise G_{Ic} (Mandell *et al.*, 2010, p. 100).

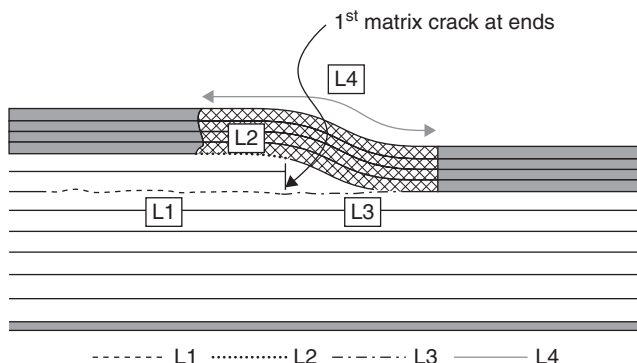
7.5.2 Infused complex structured coupons with ply drops

The concept in this study was based on a complex structured mini-substructure coupon test for infused laminates (Fig. 7.24), representative of thickness tapered blade structure with ply drops (Aggrastra *et al.*, 2009; Mandell *et al.*, 2010, p. 114; Samborsky *et al.*, 2010). The test allows convenient comparison of different resin types, fabrics and ply drop geometric details, under tension, compression and reversed loading, in terms of both damage growth characteristics and strain knockdowns.

The complex structured coupon provides a basis for comparing infused blade material and lay-up parameters for a case which is more representative of a real blade structure than are plain laminate tests. The sequence of damage initiation and growth illustrated in Fig. 7.25 depends on both in-plane properties of the fabric layers and interlaminar properties, the latter

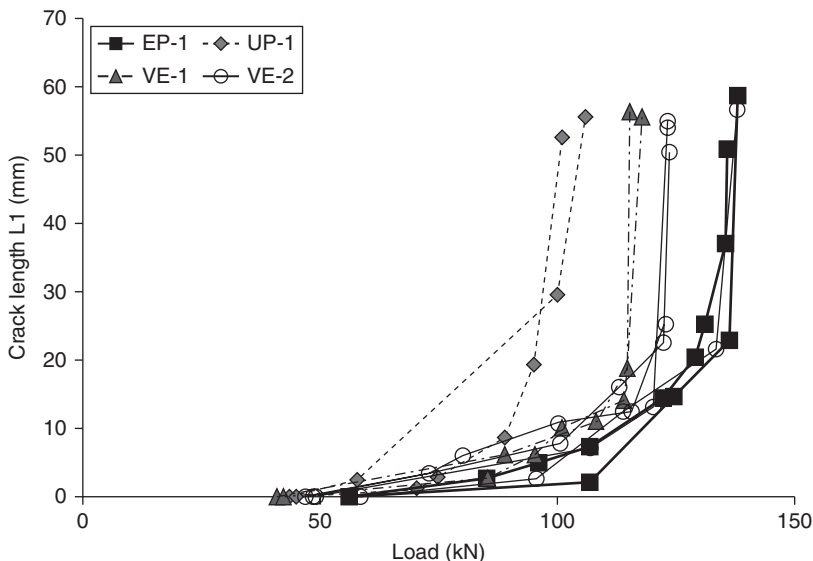


7.24 Complex coupon schematic for infused laminate ply drop study (Mandell *et al.*, 2010).

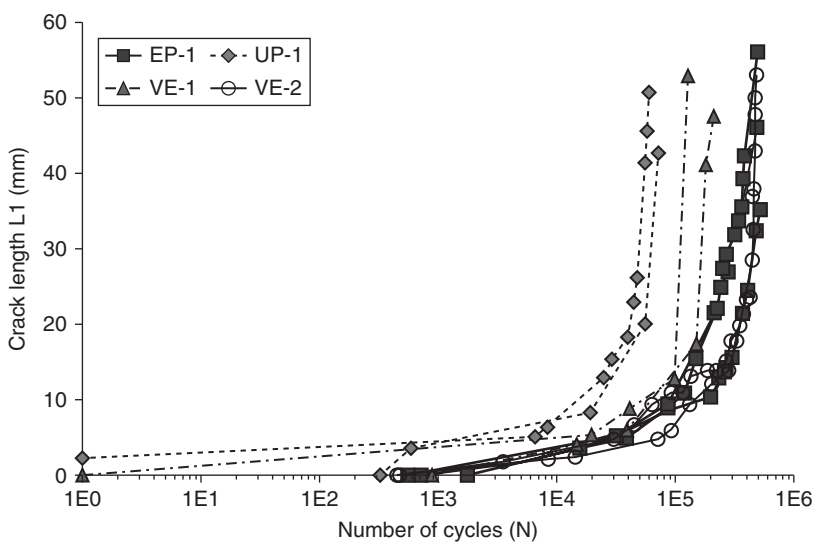


7.25 Schematic of various damage components and extents for complex coupon (Mandell *et al.*, 2010).

dominated by the resin. The test coupon geometry, designed by FEA, shows only minor effects of non-symmetry, which allows for increased thickness coupons more representative of blades. Table 7.4 gives the pure modes I and II critical strain energy release rate values for five resins which have been investigated; the VE-2 is a toughened vinyl ester (Table 7.1), and polydicyclopentadiene (pDCPD) is a new thermoset resin with a particularly high toughness, as well as low viscosity and density (Edgecombe *et al.*, 2010). Delamination growth from the ply drops is given in Figs 7.26 (static) and 7.27 (fatigue) for the top four listed resins in Table 7.4. The results indicate improved performance for the epoxy EP-1 relative to vinyl ester VE-1 or polyester UP-1; the toughened vinyl ester VE-2 performed on a par with epoxy. The resin effects are consistent with the delamination resistance G_{Ic} and G_{IIc} in Table 7.4. A variety of other test results are given by Mandell *et al.* (2010, p. 114) for the effects of the thickness of dropped material, fatigue load and R-value, and fabric type. Results for million cycle strains as a function of ply drop thickness are given in the next section.



7.26 Static data for delamination growth vs applied load for various resins, complex coupon with two plies dropped, fabrics D and M (Mandell *et al.*, 2010).



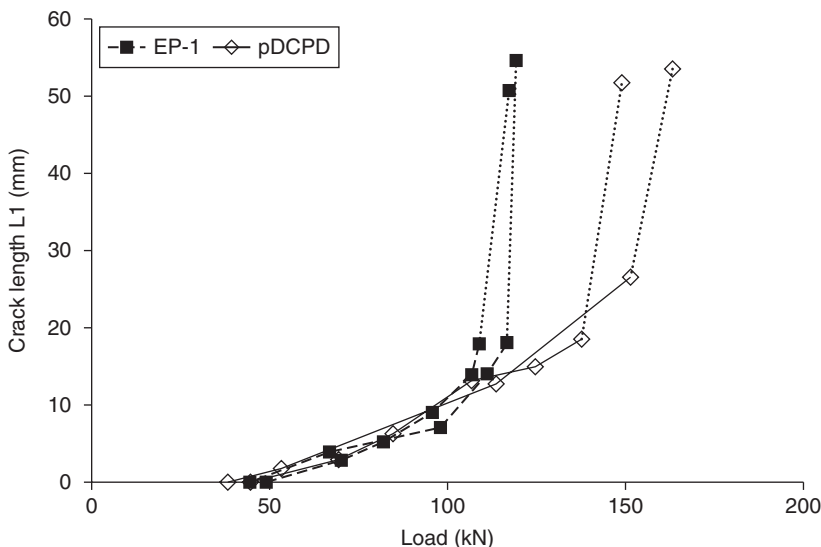
7.27 Delamination growth in fatigue for various resins, complex coupon with two plies dropped, fabrics D and M, R = 0.1, 44.5 kN applied maximum load (Mandell *et al.*, 2010).

Table 7.4 Pure mode delamination test results with unidirectional laminates, 090 fabric D

Resin	0–0 Interface (090/900//090/900)				90–90 Interface (900/090//900/090)			
	V_f (%)	Initial G_{IC} (J/m ²)	V_f (%)	Initial G_{IIC} (J/m ²)	V_f (%)	Initial G_{IC} (J/m ²)	V_f (%)	Initial G_{IIC} (J/m ²)
EP-1	60	303 (40)	60	3446 (201)	62	321 (38)	61	1887 (97)
UP-1	60	166 (17)	60	1662 (200)	62	175 (27)	62	928 (353)
VE-1	64	252 (24)	63	2592 (130)	64	223 (13)	63	1653 (124)
VE-2	61	433 (53)	61	2998 (313)	61	272 (33)	61	1689 (349)
pDCPD	64	1560(241)	64	2728 (305)	—	—	—	—

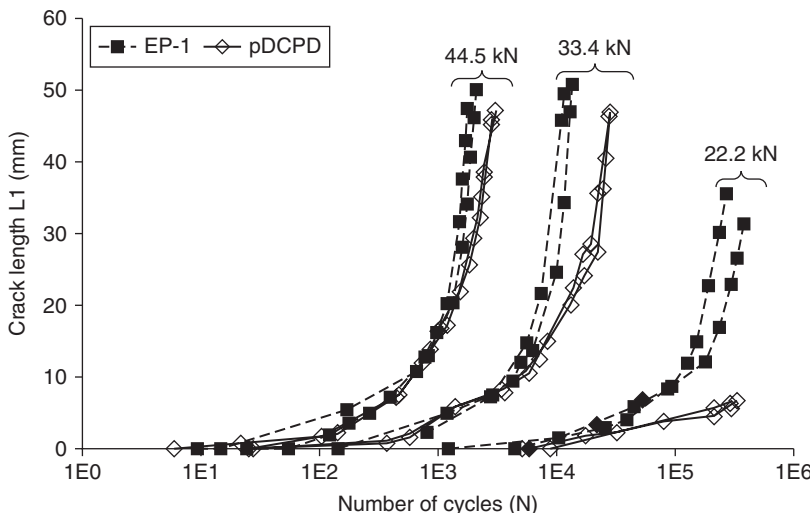
Note: // indicates crack position, numbers in parentheses are standard deviations for 3–5 tests.

Source: Mandell *et al.*, 2010.



7.28 Comparison of epoxy and pDCPD resins under static loading, two plies dropped, fabrics L and D (Mandell *et al.*, 2010).

Figures 7.28 and 7.29 compare the pDCPD resin, which has a very high G_{IC} value, with Epoxy EP-1. These figures indicate improved performance for pDCPD relative to epoxy under static loading and higher cycle fatigue, the latter shown for reversed loading. The major delamination, L_1 in Figure 7.25, is predominantly Mode II for initiation and shorter cracks, but Mode I for longer cracks, consistent with the improved performance of pDCPD, having higher G_{IC} , at longer crack lengths (Agastra *et al.*, 2009). Table 7.5 compares the near-threshold strains under reversed loading for epoxy, polyester and pDCPD. These results give an indication of the damage



7.29 Epoxy and pDCPD under reversed loading fatigue loading, $R = -1$, at various maximum load levels, fabrics L and D (Mandell *et al.*, 2010).

Table 7.5 Near-threshold results (5-mm delamination length L_1 in 10^6 cycles), $R = -1$, two plies dropped at one position

Resin	Max. force (kN) and thin side average strain (%)	Force change from epoxy	Observed damage
Epoxy EP-1	19 (0.18%)	–	L_1 , L_2 , crack at ply ends
Polyester UP-1	14 (0.13%)	-26%	L_1 , L_2 , biax cracking, crack at ply ends
pDCPD	22 (0.21%)	+16%	L_1 , crack at ply ends

Source: Mandell *et al.*, 2010.

growth thresholds for the polyester (-26%) and pDCPD (+16%) relative to the baseline epoxy.

7.6 Comparison of fatigue trends for blade materials

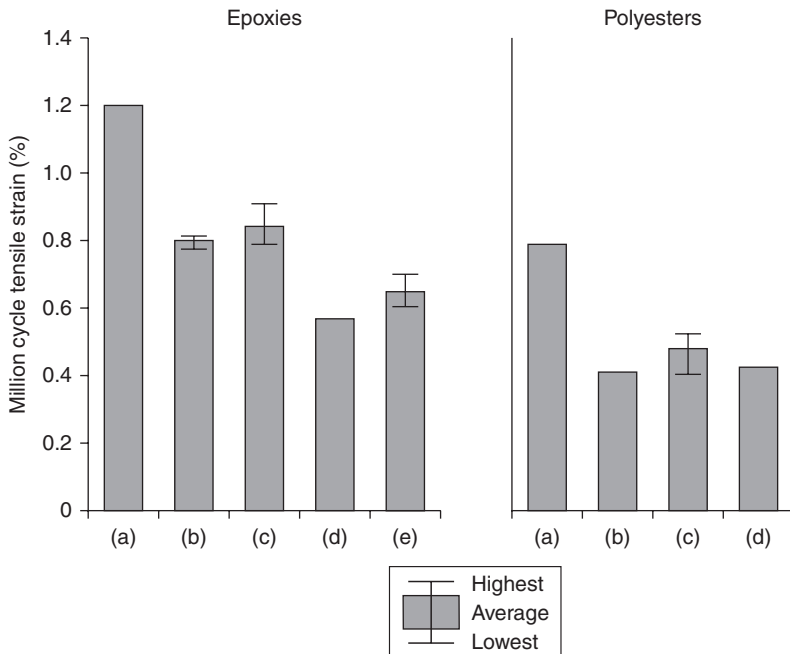
Table 7.6 and Fig. 7.30 compare fatigue data trends. Included in Table 7.6 are laminates of increasing complexity: UD aligned strand, UD fabric and MD laminates, all based on the same strands and resins. Additional laminate trends are given for UD fabric in the transverse direction, biax fabrics, triax fabrics, structured coupons containing ply drops, where ply delamination is the dominant damage, and lap shear adhesive joints. Blades are constructed from most or all of these materials. Adjacent materials in a blade must withstand similar strains. Comparison of fatigue exponents B

Table 7.6 Tensile strength and fatigue ($R = 0.1$) trends for various blade materials

Material form	Resin	UTS (MPa)	A/UTS	B	n	10^6 Cycle Strain (%)
UD Aligned Strand Laminates, PPG 2400 Tex, Hybon 2026 Finish						
AS	EP-5	1369	1.149	-0.072	13.9	1.20
AS	VE-4	1340	1.457	-0.088	11.4	1.23
AS	UP-5	1382	1.558	-0.123	8.13	0.79
UD Fabric H Laminates (contain PPG 2400 Tex Strands)						
(0) ₂ Fabric H	EP-1	995	1.265	-0.088	11.4	0.88
(0) ₂ Fabric H	VE-4	912	2.485	-0.170	5.88	0.53
(0) ₂ Fabric H	UP-5	884	1.940	-0.173	5.78	0.39
MD Laminates, UD Fabric H and Biax FabricT						
[$(\pm 45)_2/(0)_2$]s	EP-1	704	1.957	-0.130	7.69	0.79
[$(\pm 45)_2/(0)_2$]s	VE-4	628	1.955	-0.146	6.85	0.53
[$(\pm 45)_2/(0)_2$]s	UP-5	663	1.736	-0.151	6.62	0.42
Transverse Direction Fabric H UD Laminates						
(0) ₆ Fabric H	EP-5	52.4 ^a	1.857	-0.114	8.77	0.124
Biax Fabric M (± 45 /mat) Laminates						
($\pm 45/m$) ₃ Fabric M	EP-1	224	1.004	-0.092	10.9	0.53
($\pm 45/m$) ₃ Fabric M	VE-1	239	1.000	-0.090	11.1	0.44
($\pm 45/m$) ₃ Fabric M	UP-1	208	0.972	-0.098	10.2	0.41
Triax Fabric W						
($\pm 45/0$ s) Fabric W	EP-1	585	2.20	-0.143	6.99	0.70
Delamination at thick ply drops, MD Laminates						
1 ply drop, Fabric D	EP-1	—	—	—	—	0.55
2 ply drop, Fabric D	EP-1	—	—	-0.120	8.3	0.39
4 ply drop, Fabric D	EP-1	—	—	-0.099	10.1	0.35
1 ply drop, Fabric D	UP-1	—	—	—	—	0.39
Thick Adhesive Lap Shear Joints						
Hexion Adhesive EP135G3/EKH1376G	—	13.9 ^b	1.63	-0.109	9.17	—
3M W1100	—	13.8 ^b	2.11	-0.135	7.41	—
Neat Resin and Adhesive						
Epoxy EP-1 Resin	—	41.0 ^c	2.02	-0.081	12.3	0.77
Adhesive EP135G3/ EKH1376G	—	44.5 ^c	1.29	-0.044	22.7	0.79

^aFirst cracking stress^bApparent lap shear strength for 3.25 mm thick adhesive, 25 mm overlap length, 5 mm thick UD Fabric D/EP-1 adherends.^c0.2% offset yield stress.Sources: Mandell and Samborsky, 2010; Samborsky *et al.*, 2012.

and n (see Equations [7.1] and [7.3]), and the million cycle fatigue strain, gives some indication of the most fatigue critical areas of blades. The curve fit in Equation [7.1] is normalized as a function of the static tensile strength, UTS (determined at the standard test rate of 0.0254 mm/s), by including A/



7.30 Comparison of typical polyester and epoxy resin laminate million cycle fatigue strains with the same fabrics. (a) aligned strand, (b) unidirectional fabric, (c) multidirectional laminate, (d) double bias fabric and (e) triaxial fabric. (Samborsky *et al.*, 2012).

UTS, which does not affect the exponent. These properties must be viewed in the context of actual blade stress distributions and the potential presence of flaws.

As the laminate complexity increases from AS to UD fabric to MD, the fatigue S-N curves steepen, reflected in the exponents B and n , and the million cycle strain decreases. This trend is particularly strong for the VE and UP resins. Transverse direction and biax (Fig. 7.19) exponents indicate relatively flat S-N behavior compared to some UD and MD laminates, but the million cycle initial fatigue strain is lower, particularly in the transverse direction. Neat epoxy EP-1 fatigue properties are generally consistent with laminate properties, with the million cycle strain higher than values for the transverse and biax fabric values, and similar to the fiber dominated laminate range. Ply drop delamination million cycle strains are close to the biax laminate initial strain values for a single drop of the 1.3 mm thick fabric D with EP-1 and UP-1 resins, but multiple drops at the same position result in very low damage strains (Samborsky *et al.*, 2012). Triax constructions (Fig. 7.7) have steeper S-N exponents, in the range of other MD laminates, representing a two-stage failure process in some cases, between the biax

Table 7.7 Comparison of typical database properties for polyester resin compared with epoxy resin laminates

Property	Ratio UP/EP
Axial (UD) tensile modulus	1.0
Axial (MD) tensile modulus	1.0
Axial (UD) static tensile strength	0.90
Axial (MD) static tensile strength	0.95
Transverse (UD) static tensile cracking strain	0.42
Axial (UD) 10^6 cycle strain ($R = 0.1$)	0.51
Axial (MD) 10^6 cycle strain ($R = 0.1$)	0.53
Axial (Biax) 10^6 cycle strain ($R = 0.1$)	0.77
Interlaminar G_{lc} (0–0 interface), Table 7.4	0.55
Interlaminar G_{llc} (0–0 interface), Table 7.4	0.48
Ply drop delamination, threshold fatigue strain ($R = -1$), Table 7.5	0.74

Note: $V_f = 0.5\text{--}0.6$, UD Fabrics D and H, Biax Fabrics M and T.

Source: Samborsky *et al.*, 2012.

and UD layers (Mandell *et al.*, 2010, p. 68). The epoxy based adhesive joint fatigue S-N trend is relatively flat for the more brittle EP135 adhesive, similar in exponent to the resin dominated transverse and biax trends for epoxy resin, and in the same range as for the UD laminates. The neat adhesive response is even less fatigue sensitive. Adhesive joint S-N curves are more fatigue sensitive for reversed loading (Sears *et al.*, 2010).

Figure 7.30 illustrates the effect of structure on the million cycle fatigue strain, showing the clear improvement with aligned strand reinforcement for both epoxies and polyesters. Epoxy performance with UD fabrics in UD and MD laminates is similar, exceeding that with the triax and, particularly, biax reinforcements. The polyesters fall significantly below the epoxies for each case except the biax. UD fabric, MD and triax strains fall in a similar range for the polyesters. Table 7.7 provides additional comparisons of laminate properties for epoxy based and polyester based laminates, indicating similar stiffness (modulus) and static axial strength values, the primary blade design drivers, but significantly reduced off-axis, fatigue, delamination and ply drop damage values for polyesters.

7.7 Conclusion

This chapter has summarized recent results from the Sandia National Laboratories/Department of Energy sponsored MSU study of fatigue in wind turbine blade materials, now in its twenty-third year. Intensive testing of particular glass and carbon laminates over a range of loading conditions identified the critical conditions for glass fiber dominated laminates as the R-value range -1 to 0.1 , where fatigue failure maximum strains fall to relatively low levels at high cycles, actual strains depending on the resin

and fabric. Carbon fiber dominated laminates are less fatigue sensitive than glass at all R-values, but failure strains are relatively low in compression, and are sensitive to fiber waviness in the overall laminate and within the fabric structure. While carbon prepreg tends to produce the straightest fibers and best compression properties, specialized carbon fabrics for infused laminates can achieve similar or higher compressive strains (Griffin, 2009; Mandell *et al.*, 2010, p. 82). Carbon fiber laminates are also prone to delamination in detail areas like ply drops at low strains, so material transition areas should be refined, with low thickness taper rates.

The tensile fatigue performance of glass fiber laminates is resin sensitive and can also be sensitive to reinforcing fabric details for many resins, less so for the tested epoxies. Transitions to sharply reduced fatigue resistance with increasing fiber content occur with some fabrics and resins, but excellent fatigue resistance is found with aligned strand reinforcement in the 64–68% fiber by volume range for several resins. Performance with the baseline EP-1 and EP-5 epoxy was similar for a broad range of commercial and specially prepared UD fabrics; aligned strand laminates with no fabric structure performed better than fabric laminates, but mostly due to their higher 0° fiber content in the case of these epoxy resins. At the other extreme, polyesters perform poorly relative to epoxy in UD fabric dominated laminates, and are sensitive to fabric details like transverse backing strands. Vinyl esters fall between polyesters and epoxies in fatigue performance, many falling closer to the polyester range, but some are equal to epoxy for aligned strand and certain UD fabric laminates. Fatigue in off-axis directions also tends to favor epoxies, but biax fabric laminates show reduced resin sensitivity compared to UD fabrics. Triax fabrics tested recently with epoxy fail at only slightly lower strains than UD fabrics, an improvement from early triax fabrics with polyester resins (Mandell and Samborsky, 1997).

Structural detail areas such as ply drops (Mandell *et al.*, 2010), adhesive joints and core close-outs and flaws (Mandell *et al.*, 2002) can fail in fatigue, primarily by delamination, at significantly lower strains than the corresponding values for standard laminates with the same resin. Resin toughness in opening and shearing modes is critical; epoxies again outperform most vinyl esters, with polyesters showing the poorest delamination resistance. The best performance was found with pDCPD, a new, very tough resin which imparts a high opening mode delamination resistance.

7.8 Future trends

Considerable opportunities remain in the evolution of blade materials. Combined with manufacturing developments, tougher, stronger, stiffer more processable resins with good bonding qualities could reduce the sensitivity to flaws and structural details, provide improved off-axis properties, and

improve structural reliability. Higher performance glass or carbon fibers can improve both stiffness and fatigue resistance, where cost-effective. Infusion fabrics need to be optimized for higher performance fibers, particularly carbon, where fiber waviness is most detrimental.

Improved efficiency and reliability could also be realized by improved testing methodologies and commitment. Basic characterization appears to be lagging in the areas of off-axis (including 3-D) laminate properties, adhesives and core materials. Basic properties are needed as well as validation of failure criteria. Multi-material, multiaxial material transition areas are difficult to test and predict, and appear to require increased commitment to substructure scale testing and model validation. One challenge is to develop testing approaches which capture critical structure failure modes at reasonable expense, to allow a wide range of materials to be included in a test program. Increasingly, with the focus on offshore and hydrokinetic applications, environmental effects must be included with substructure testing. Finally, blade reliability improvements require that realistic manufacturing flaws receive greater attention.

7.9 Sources of further information and advice

Traditional sources of information on wind turbine blade materials have been wind conferences and sessions and contractor reports from Sandia in the U.S. and Optimat and Upwind in Europe. In the U.S., wind sessions have been focused on the conferences of the American Institute of Aeronautics and Astronautics (AIAA) (the Aerospace Sciences Meeting and Exhibit, the Wind Energy Symposium and, recently, the AIAA/ASME/ASCE/AHS/ASC Structures, Structural Dynamics and Materials (SDM) conference), and the conferences of the Society for the Advancement of Material and Process Engineering (SAMPE), with some technical information and much commercial information from materials suppliers at the American Wind Energy Association's Windpower conference. Increasingly, as wind blade materials technology expands and matures, more useful information is available in the many polymers, composites and mechanics journals and conferences.

Property information can be found in the main public databases, available (often with associated reports) on web sites: the SNL/MSU/DOE Database is available on Sandia's Wind Energy website and on the MSU site, www.coe.montana.edu/composites/. The large European database OptiDAT is available on www.wmc.eu/optimat_blades.

7.10 Acknowledgments

The authors wish to acknowledge the continued support over many years from Sandia National Laboratories and the U.S. Department of Energy. We have greatly appreciated the many industry interactions evident throughout

this work. Particular note is made of two contributions which are central to the findings presented here. Aligned strand laminates with various resins were specially prepared by Reichhold (Dr. Stephen Brooks) and PPG Industries, Inc (Mr. Sandeep Vennam). A series of laminates with specially prepared, systematically varied fabrics were supplied by Devold AMT AS (Dr. Roman Hillermeier, now with Momentive).

7.11 References

- Agastra, P, Samborsky, D D and Mandell, J F (2009), 'Fatigue Resistance of Fiberglass Laminates at Thick Material Transitions', AIAA SDM Conf., Palm Springs, CA, paper AIAA-2009-2411.
- DeSmet, B J and Bach, P W (1994) 'Database FACT: Fatigue of Composites for Wind Turbines', ECN-C 94-045, ECN, Petten, The Netherlands.
- Edgecombe, B D, Cruce, C, Stephen, T, McCarthy, T, Mandell, J F, Samborsky, D D, Agastra, P and Wetzel, K K (2010) 'Effects of a new, high-toughness infusion resin on the fatigue performance and defect-tolerance of glass composite laminates', *AWEA Windpower Conference*, Dallas, Texas, May 23–26, 2010.
- Gilchrist, M D (2005), 'The fatigue performance of composite structural components', in Harris B *Fatigue in Composites*, Abington, Cambridge, England, Woodhead Publishing Limited, Ch 22.
- Griffin, D (2009) 'Blade System Design Study Part II: Final Project Report (GEC)', Contractor Report SAND2009-0686, Sandia National Laboratories, Albuquerque, NM.
- Hunston, D L, Moulton, R J, Johnson, N J and Bascom, W D (1987), 'Matrix Resin Effects in Composite Delamination: Mode I fracture Aspects', Toughened Composites, ASTM STP 937, Norman J. Johnson, Ed., American Society for Testing and Materials, Philadelphia, pp. 74–94.
- Mandell, J F and Samborsky, D D (1997), 'DOE/MSU Composite Material Fatigue Database: Test Methods, Materials, and Analysis', Contractor Report SAND97-3002, Sandia National Laboratories, Albuquerque, NM.
- Mandell, J F, Samborsky, D D, Combs, D F, Scott, M E and Cairns, D S (1998), 'Fatigue of Composite Material Beam Elements Representative of Wind Turbine Blade Substructure', Report NREL/SR-500-24374, National Renewable Energy Laboratory, Golden, Co.
- Mandell, J F, Samborsky, D D, Li, M, Orozco, R and Cairns, D S (2000), 'Selection of fiberglass matrix resins for increased toughness and environmental resistance in wind turbine blades', Proc. 2000 ASME Wind Energy Symposium, ASME/AIAA, New York, pp. 354–366.
- Mandell, J F, Samborsky, D D and Cairns, D S (2002) 'Fatigue of Composite Materials and Substructures for Wind Turbine Blade', Contractor Report SAND2002-0771, Sandia National Laboratories, Albuquerque, NM.
- Mandell, J F, Samborsky, D D, Wahl, N F and Sutherland, H J (2003a), 'Testing and Analysis of Low Cost Composite Materials Under Spectrum Loading and High Cycle Fatigue Conditions', ICCM-14, SME/ASC, Paper 1811.
- Mandell, J F, Cairns, D S, Samborsky, D D, Morehead, R B and Haugen, D J (2003b), 'Prediction of Delamination in Wind Blade Structural Details', *J. Sol. Energy Eng.*, **125**, paper 009304.

- Mandell, J F, Samborsky, D D and Agastra, P (2008), 'Composite Materials Fatigue Issues in Wind Turbine Blade Construction', Proc. SAMPE 2008, Long Beach, CA, paper L238.
- Mandell, J F, Samborsky, D D, Agastra, P, Sears, A T and Wilson, T J (2010), 'Analysis of SNL/MSU/DOE Fatigue Database Trends for Wind Turbine Blade Materials', Sandia Contractor Report SAND2010-7052.
- Mandell, J F and Samborsky, D D (2011), 'DOE/MSU Fatigue of Composite Materials Database', 2011 update, Sandia National laboratories, Albuquerque, NM. (www.sandia.gov/wind/other/973002upd0309.pdf).
- Murri, G B, Salpekar, S A and O'Brien, T K (1991), 'Fatigue Delamination Onset Prediction in Unidirectional Tapered Laminates', Composite Materials: Fatigue and Fracture (Third Volume), ASTM STP 1110, T.K. O'Brian, Ed., American Society for Testing and Materials, Philadelphia, pp. 312–339.
- Nijssen, R P L (2006), 'Fatigue Life Prediction and Strength Degradation of Wind Turbine Rotor Blade Composites', Contractor Report SAND2006-7810P, Sandia National Laboratories, Albuquerque, NM.
- Samborsky, D D, Agastra, P and Mandell, J F (2008a), 'Effects of Glass Fabric and Laminate Construction on the Fatigue of Resin Infused Blade Materials', Proc. 2008 ASME Wind Energy Symposium, ASME/AIAA, Reno, NV, Paper AIAA-2008-1346.
- Samborsky, D D, Wilson, T W, Agastra, P and Mandell, J F (2008b), 'Delamination at thick ply drops in carbon fiber laminates under fatigue loading', *J. Sol. Energy Eng.*, **130**, paper 031001.
- Samborsky, D D, Agastra, P and Mandell, J F (2010), 'Fatigue Trends for Wind Blade Infusion Resins and Fabrics', 2010 AIAA SDM, Wind Energy Session, Orlando, AIAA-2010-2820.
- Samborsky, D D, Sears, A T, Agastra, P and Mandell, J F (2011), 'Mixed Mode Static and Fatigue Crack Growth in Wind Blade Paste Adhesives', 2011 AIAA SDM conf., Denver, paper AIAA-2011-1755.
- Samborsky, D D, Mandell, J F and Miller, D (2012), 'The SNL/MSU/DOE Fatigue of Composite Materials Database: Recent Trends', 2012 AIAA SDM conf., Honolulu, AIAA-2012-1573.
- Sears, AT, Samborsky, D D, Agastra, P and Mandell, J F (2010) 'Fatigue Results and Analysis for Thick Adhesive Notched Lap Shear Test', 2010 AIAA SDM conf., Orlando, AIAA-2010-2821.
- Shokrieh, M M and Lessard, L B (2003) 'Fatigue under multiaxial stress systems', in Harris B *Fatigue in Composites*, Abington, Cambridge, England, Woodhead Publishing Limited, Ch 3.
- Sims, G D (2003), 'Fatigue test methods, problems and standards', in Harris B *Fatigue in Composites*, Abington Cambridge, England, Woodhead Publishing Limited, Ch 2.
- Sutherland, H J and Mandell, J F (2005), 'Optimized Goodman Diagram for the analysis of fiberglass composites used in wind turbine blades', *ASME J. Solar Energy Eng.*, **127**, 563–569.
- Vizzini, A J and Lee, S W (1995), 'Damage analysis of composite tapered beams', *J. Am. Helicopter Soc.*, **40** (2), 43–49.
- Wilson, T J (2006), 'Modeling of In-Plane and Interlaminar Fatigue Behavior of Glass and Carbon Fiber Composite Materials', MS Thesis, Department of Mechanical Engineering, Montana State University, Bozeman, MT, USA.

Fatigue life prediction of wind turbine blade composite materials

A. P. VASSILOPOULOS, École Polytechnique Fédérale de Lausanne (EPFL), Switzerland

DOI: 10.1533/9780857097286.2.251

Abstract: Fatigue life prediction of wind turbine rotor blades is a very challenging task, as blade failure is led by different failure types that act synergistically. Inherent defects like wrinkles, fiber misalignments and voids, that can be introduced during fabrication, can constitute potential damage initiation points and rapidly develop to failure mechanisms like matrix cracking, transverse-ply cracking, interface cracking, debonding, fiber breakage, etc. Different methods have been established to address this problem, some based on phenomenological and others on actual damage mechanics modeling. This chapter aims to provide an overview of fatigue life modeling and prediction methodologies for the composite materials and structural composite elements that compose a wind turbine rotor blade under complex loading conditions.

Key words: fatigue life prediction, phenomenological fatigue modeling, residual strength, residual stiffness, fracture.

8.1 Introduction

The scientific community long ago identified fatigue as a critical loading pattern and it is now recognizing that the majority of structural failures in both composite and conventional structures occur due to fatigue and fatigue-related mechanisms (Vassilopoulos, 2010). In any case, it was not until the twentieth century that fiber-reinforced polymer (FRP) composite materials were used as critical elements in emerging applications for which failure can mean anything from interrupted operation to catastrophic collapse with subsequent fatal accidents involving operators and users.

Numerous structures of this kind can be found in different applications: in the aerospace sector, where significant parts of commercial and fighter airplanes are made of advanced composite materials; in the automotive industry, where composite racing car chassis, ceramic brakes, etc., are common today; in the wind industry, where wind turbine rotors with diameters of more than 100 m are now constructed using fiber-reinforced composite

materials; and even in the civil engineering domain, where composites are being increasingly used for foot and vehicular bridges and conceptual composite house designs have begun to be seen.

All of the above-mentioned structures encounter different loading profiles during their operational life and must therefore be designed to sustain all conceivable loading conditions, from ultimate static loads to time-dependent loads. Wind turbine rotor blades will probably be required to sustain 10^9 fatigue cycles during the 25 years of their expected operational life, while a normal short-span vehicular bridge can sustain 10^7 – 10^8 fatigue cycles over a period of 50–70 years. Although most of these cycles are of low amplitude, they cause damage that is accumulated in the material and degrades its properties. Therefore, the fatigue of composite materials and structural elements cannot be neglected and must be seriously taken into account in design processes in order to yield durable structures.

There is a long list of reasons why fatigue is critical for the life assessment of wind turbine rotor blades and other composite structural components (Vassilopoulos and Keller, 2011):

- Composites are used for critical structural components in emerging structures that must bear significant fatigue loads (significantly greater compared to the dead loads) during operation, such as airplanes, wind turbine rotor blades, leisure boats, foot and vehicular bridges. This development has changed the common perception concerning the sensitivity of each structure to fatigue.
- An understanding of the fatigue behavior of a wind turbine rotor blade is also valuable for the improvement of product development practices. Product development practice up to now has been based on an iterative process whereby a prototype rotor blade is built and tested against real, or realistic, loading patterns. However, this process is costly and time-consuming. The ability to simulate the fatigue behavior of the material, the blade structural component and/or the wind turbine rotor blade reduces the cost and allows the development of a wider range of products without the need for increasing the number of physical prototypes.
- The durability of composite structures is also an important factor. The danger of evaluating durability on the basis of static strength calculations is that the durability impact of cyclic loads is likely to be disregarded. The introduction of fatigue life prediction methodologies into durability simulation procedures allows the assessment of durability performance early in the product development process and the establishment of clear recommendations for guiding major design choices.

During the last 30 years, numerous experimental programs have been conducted for the characterization of the fatigue behavior of several structural

FRP composite materials for wind turbine rotor blades (de Smet and Bach, 1994; Philippidis and Vassilopoulos, 2002; Nijssen, 2006; Mandell and Samborsky, 2011). As technology developed and new test frames and measuring devices were invented, it became more and more straightforward to conduct complex fatigue experiments and measure properties and characteristics, something which some years earlier would not have been possible. As a result, almost all failure modes of FRP composites and rotor blades made from them have been identified and many theoretical models have been established for modeling and eventually predicting the fatigue life of several different material systems and design configurations.

Wind turbine rotor blades are very complex structures comprising different composite laminates and numerous adhesively bonded connections between similar and between different materials. Fatigue analysis of a wind turbine rotor blade necessitates the analysis of the independent structural components and their connections. The use of properly designed adhesively bonded joints is beneficial for the structural behavior of the blades for several reasons (Holmes *et al.*, 2007). The adhesive can play a very beneficial role as its compliance allows for dimensional mismatches to be accommodated (e.g. from thermal expansion) and reduces stress concentrations at locations where elastic modulus mismatch is present. In addition, selection of less rigid adhesive layers in appropriately calculated thicknesses introduces ductility to the inherently brittle FRP blades improving their overall structural integrity. However, existence of joints increases the complexity of the fatigue analysis.

Fatigue life prediction of wind turbine rotor blades is very challenging as blade failure is led by different failure types that act synergistically. Inherent defects such as wrinkles, fiber misalignments and voids, introduced during fabrication, can constitute potential damage initiation points and rapidly develop into failure mechanisms such as matrix cracking, transverse-ply cracking, interface cracking, debonding, fiber breakage, etc. These failure mechanisms occur sometimes independently and sometimes interactively, and are sources of microbuckling, translaminar crack growth and delaminations (Brøndsted *et al.*, 2005) that can yield catastrophic failure. A combination of different (conceptually and practically – in terms of need for input data) methods is needed for the assessment of the effect of each one of the failure mechanisms if a reliable fatigue lifetime prediction of a modern wind turbine rotor blade is to be achieved. Understanding the fatigue behavior of the rotor blade allows the timely identification of problems, and provides an early alert to fatigue failure that might have catastrophic consequences.

Nevertheless, it is impossible to experimentally investigate the fatigue behavior of any material or structure under all possible loading conditions. Because of this, standard experiments are performed in laboratories and appropriate models are established in order to simulate as far as possible

the fatigue behavior of the examined materials and structural components. The objective of all these efforts is the development of a reliable methodology for the prediction of the fatigue life of wind turbine rotor blades under realistic loading conditions.

The implementation of a numerical procedure for the fatigue analysis and the fatigue life prediction involves a number of distinct calculation modules, related to life prediction. Some of these are purely conjectural or of a semi-empirical nature, e.g. the failure criteria, while others rely heavily on experimental data, e.g. S-N curves and constant life diagrams (CLD). The basic steps of such processes are the material characterization and the modeling of the exhibited material behavior. The most common way of representing the fatigue data of composite materials and structural components is based on phenomenological modeling concepts. Phenomenological or empirical design relies on the derivation of reliable S-N curves (plots of lifetime vs the applied cyclic stress), able to accurately simulate the exhibited fatigue behavior of the material of interest. Empirical fatigue prediction theories are then established using the derived S-N curves as input data.

The literature comprises a vast number of publications on the aforementioned topics, dealing with the modeling and the eventual prediction of the examined material's fatigue life based on empirical or micromechanical modeling. Mathematical models have been developed in order to describe fatigue damage analytically, and conclusively predict the fatigue lifetime of composite materials. For the different materials studied, measurable material characteristics have been selected, based on previous experience of fatigue life prediction for metallic materials, to form the fatigue damage metric. Material damage has then been measured based on the degradation of that quantity or the propagation of the crack(s) (when fatigue modeling is based on fracture mechanics) with loading cycles. Different approaches have been adopted, based on different damage metrics for measuring fatigue damage accumulation. The aim of such studies has been to establish a process requiring a minimum of experimental data, while reliably predicting the condition of the material.

For composite laminates, the S-N curves are usually derived under given loading conditions in order to model the constant amplitude fatigue behavior of the examined materials. The significant effect of the stress ratio, $R = \sigma_{\min}/\sigma_{\max}$, on fatigue life has been reported in the literature and extensively investigated to establish theoretical models (e.g. Beheshty and Harris, 1998; Kawai and Koizumi, 2007; Vassilopoulos *et al.*, 2010a, 2010b) for the subsequent prediction of fatigue life under more complicated loading conditions such as block and variable amplitude loading. The effect of other parameters on the fatigue life prediction, e.g. cyclic counting method (Nijssen, 2006; Vassilopoulos, 2006), S-N curve and constant life diagram formulations (Nijssen, 2006; Vassilopoulos *et al.*, 2008; Vassilopoulos *et al.*, 2010b; Sarfaraz

et al., 2012), fatigue failure criteria (Philippidis and Vassilopoulos, 1999; Quaresimin *et al.*, 2010; Vassilopoulos *et al.*, 2010c) and damage accumulation rules (Vassilopoulos, 2006), has been assessed in previous publications.

When the design is based on micromechanical modeling approaches based on the identification of defects (a crack or cracks) that develop inside the material and the way they propagate under given fatigue loading spectra, the matrix crack density, delaminations, or cracks in structural joints are normally conceived as being acceptable damage metrics. Extensive research efforts have been devoted to the investigation of fatigue crack growth under Mode I (Hojo *et al.*, 2006; Shivakumar *et al.*, 2006; Shahverdi *et al.*, 2011), Mode II (Tanaka and Tanaka, 1997; Argüelles *et al.*, 2010) and mixed-mode (Zhang *et al.*, 2009; Naghipoura *et al.*, 2011) fracture of composite joints under fatigue loading. Instead of the S-N curves, fatigue crack growth (FCG) curves are used to represent the fatigue behavior and also provide information concerning the developed damage in terms of a crack or cracks that propagate during fatigue loading. Additional information can be gained from S-N curves derived from the fracture mechanics data. In such cases methods for the determination of damage tolerant design allowables can be established (Zhang *et al.*, 2010a).

This chapter aims to provide an overview of fatigue life modeling and prediction methodologies for the composite materials and structural composite elements that compose a wind turbine rotor blade under complex loading conditions.

8.2 Macroscopic failure theories

This is the broadest group of theoretical models for the modeling and prediction of the fatigue behavior of composite materials. Mainly because of the simplicity of the necessary measurements during fatigue loading, this type of modeling was adopted far more rapidly than the others. August Wöhler, as far back as the 1850s, conceived the idea of representing cyclic stress against the number of cycles to failure in order to quantify the results of his experimental program. The only input required with regard to experimental data consists of pairs of number of cycles up to failure and the corresponding alternating stress or strain parameter. The S-N or ε -N curve of the material is then determined under the applied loading condition. However, another half century went by before the introduction of the first mathematical model to describe this relationship. In 1910, Basquin stated that the lifetime of the material increases as a power law when the external load amplitude decreases. The value of the exponent, which denotes the slope of the S-N curve, is related to the examined material. It is now documented that for composite materials this exponent ranges between 7 and 25, being higher (less steep curve) for unidirectional carbon and lower

(steeper curve) for multidirectional glass fiber composites. Although laws of this kind are empirical, and do not have any direct physical meaning, they can stimulate the accumulation of the microscopic damage of the examined material which they finally describe (Kun *et al.*, 2008).

The choice of a particular (and appropriate) fatigue theory for composite materials is based on the material's behavior under the given loading pattern and the experience of the user. For uniaxial loading, the established S-N curves for metals were initially adopted for composites as well. Traditionally, the S-N data are fitted by a semi-logarithmic or logarithmic equation. Other types of S-N curve formulations are usually employed to take into account the statistical nature of fatigue data (e.g. Sendeckyj, 1981; Whitney, 1981). Recently, artificial intelligence methods and soft computational techniques have been introduced for the fatigue life modeling of composite materials. Artificial neural networks (Vassilopoulos *et al.*, 2007), adaptive neuro-fuzzy inference systems (Vassilopoulos and Bedi, 2008) and genetic programming (Vassilopoulos *et al.*, 2008) have proved to be very powerful tools for modeling the non-linear behavior of composite laminates subjected to cyclic, constant amplitude, loading. They can be used to model the fatigue life of several composite material systems, and compare favorably with other modeling techniques. Finding the appropriate S-N curve type for the examined material is not simple, since there is no rule governing this selection process. The best S-N curve type is simply the one that can best fit the available fatigue data.

A common S-N behavior of FRP laminates has been described by Sendeckyj's wear-out model (Sendeckyj, 1981) as a power curve that flattens at high cyclic stress levels. In another work by Salkind (1972) this change of slope at the LCF regime is attributed to the sensitivity of FRP composites to high strain ranges that occur under high stress levels. A comparative study by Mandell (1990) on short fiber-reinforced composites showed that the S-N data for chopped glass strand polyester laminates follow a different trend. The behavior can be effectively simulated by a linear curve in the semi-logarithmic scale, although in the high-cycle fatigue (HCF) regime the presence of run-outs causes a decrease in the slope of the S-N curve. Detailed analysis of fatigue data using computational tools, such as genetic programming (e.g. Vassilopoulos *et al.*, 2008), has shown that a multi-slope curve better fits the fatigue behavior of typical composite laminates.

A review of articles on the fatigue behavior of composite materials shows that the mechanism of fatigue failure can alter with changes in the cyclic stress level (Mandell *et al.*, 1983; Bakis *et al.*, 1990; Miyano *et al.*, 1997; Aymerich and Found, 2000; Philippidis and Vassilopoulos, 2001) explaining the variation in the S-N curve slope. Different fatigue behavior was identified at high and low stress levels for an injection-molded polysulfone matrix composite reinforced by short glass and carbon fibers (Mandel

et al., 1983). The experimental results showed a significant change in the S-N curves at around 10^3 – 10^5 cycles. Different fatigue responses under high and low stress levels was also reported (Bakis *et al.*, 1990; Aymerich and Found, 2000) for carbon/polyether ether ketone (PEEK) laminates where the dominant failure changed from fiber to matrix damage when the cyclic load level was decreased. Investigation of the fatigue behavior of glass/polyester $[0/(\pm 45)_2/0]_T$ composite laminates (Philippidis and Vassilopoulos, 2001) showed a significant difference in the stiffness degradation at failure (it was found to be higher for lower stress levels), although no difference was identified in the fracture surfaces. Miyano *et al.* (1997) reported different failure modes under low and high stress levels in conically-shaped FRP joint systems, proved by observation of the fracture surfaces and a lower slope of the S-N curve at high stress levels.

8.2.1 S-N curve formulations

With this variety of behaviors exhibited by composite materials, the selection of the fatigue model, which is established by fitting a mathematical equation to the experimental data, becomes of paramount importance for any fatigue analysis. The fatigue model reflects the behavior of the experimental data in theoretical equations that are subsequently used during design calculations. A number of different types of fatigue models (or types of S-N curves) have been presented in the literature, with the most ‘famous’ being the empirical exponential (Lin-Log) and power (Log-Log) relationships. According to these models, the logarithm of the loading cycles is linearly dependent on the cyclic stress parameter, or its logarithm. The exponential and power fatigue models are commonly used for the interpretation of composite material fatigue data because they are straightforward, not based on any assumptions, and easily applied, even on limited databases, in order to derive a reliable estimate of fatigue life. The estimation of the model parameters is based on linear regression analysis that can be performed by simple hand calculations. Fatigue models determined in this way do not take different stress ratios or frequencies into account, i.e. different model parameters should be determined for different loading conditions. Moreover, they do not take into account any of the failure mechanisms that develop during the failure process. Other more sophisticated fatigue formulations that do take the influence of stress ratio and/or frequency into account have been reported (Adam *et al.*, 1989; Epaarachchi and Clausen, 2003). A unified fatigue function that permits the representation of fatigue data under different loading conditions (different R -ratios) in a single two-parameter fatigue curve was proposed by Adam *et al.* (1989). In another work by Epaarachchi and Clausen (2003), an empirical model that takes into account the influence of

the stress ratio and loading frequency was presented and validated against experimental data for different glass fiber-reinforced composites. Although these models seem promising, their empirical nature is a disadvantage as their predictive ability is strongly affected by the selection of a number of parameters that must be estimated or even, in some cases, assumed.

Usually, fatigue data for preliminary design purposes are gathered from fatigue cycle regimes ranging between 10^3 and 10^7 . However, depending on the application, high- or low-cycle fatigue regimes can be of interest. Additional data are needed in such cases to avoid the danger of poor modeling due to extrapolation into unknown spaces. Although for the high-cycle fatigue (HCF) regime long-term and time-consuming fatigue data must be acquired, the situation seems easier for low-cycle fatigue (LCF) where static strength data can apparently be used in combination with the fatigue data. However, when the static strength data are considered in the analysis, other problems arise (Sarfaraz *et al.*, 2012).

Experimental evidence has shown that the commonly used models are not appropriate for fitting material behavior from the LCF to the HCF region (see, for example, Sarkani *et al.*, 1999; Harik *et al.*, 2002). Sarkani *et al.* (1999) reported a deviation between the power S-N curve and the experimental data points obtained for bonded and bolted FRP joints. Similar experimental evidence is provided by Harik *et al.* (2002) for glass fiber reinforced polymer (GFRP) laminates. Bilinear models, in the logarithmic and semi-logarithmic scales, were introduced in both works to separately fit the material fatigue behavior in different (LCF and HCF) regions. The disadvantage of these approaches is that, given the need for fatigue data in all regions for the fitting of model parameters, they are effectively unable to extrapolate any result, since they are merely fitting procedures. In addition to this, the resulting S-N curve equations are not continuous since different model parameters are estimated for low-cycle and high-cycle fatigue, and the selection of the data subsets corresponding to each group has to be performed based on the experience of the user, which makes the curves impractical for integration into design methodologies.

Other models, able to derive multi-slope S-N curves, are available. However, they require more data in all the examined life regions, since they, too, are merely fitting equations that simulate material behavior by adjusting a number of fitting parameters. Mu *et al.* (2011) proposed a multi-slope model comprising three parameters for modeling the fatigue behavior of composite materials. However, the model is based purely on the fitting of a logistic function to the experimental data and therefore its results cannot be extrapolated outside the range of existing experimental data.

Methods based on damage mechanics, therefore having a physical background, also exist. A typical example is the wear-out model adopted by Sendeckyj (1981). The wear-out model for composite materials was initially

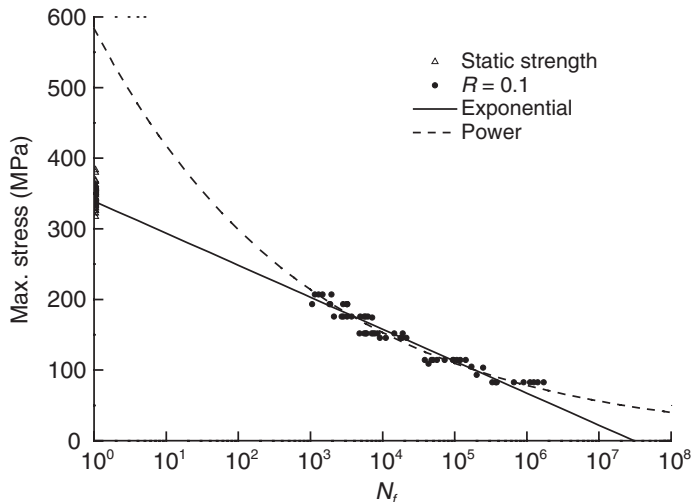
introduced by Halpin *et al.* (1973) and was based on metal crack growth concepts. However, owing to objections to the dominant crack assumption for composites, the model has been reviewed and modified by a number of authors who consider residual strength to be the damage metric. The form of the wear-out model adopted by Sendeckyj is based on the 'Strength Life Equal Rank Assumption' or SLERA, introduced by Hahn and Kim (1975), which states that a specimen of a certain rank in the static strength probability distribution has the same rank in the fatigue life distribution. In other words, application of the wear-out model is valid as long as no competing failure modes are observed during fatigue life, or even between the fatigue and static loading.

Methods for the S-N curve modeling of composite materials (also appropriate for the derivation of S-N curves) that take into account the probabilistic nature of the fatigue properties of composite materials have been established to permit the derivation of S-N curves with a given statistical significance from limited data sets (e.g. Sendeckyj, 1981; Whitney 1981). These statistical methods, presented in detail in Vassilopoulos and Keller (2011), are also based on a deterministic S-N equation for representation of the fatigue data; however a more complicated process, compared to the simple regression analysis, is followed for the estimation of model parameters, which in one of the models presented (wear-out) leads to a multi-slope S-N curve.

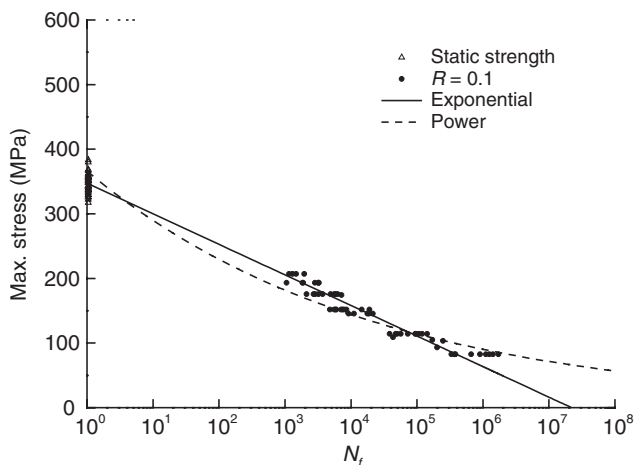
The wear-out model (Sendeckyj, 1981) is capable of deriving multi-slope reliability-based S-N curves that fit quite accurately the available static strength and fatigue data. However, it has the drawback of the quite complicated optimization process required in order to estimate the model parameters. A detailed analysis reveals several other disadvantages, including the sensitivity of the model parameter estimation to the exhibited scatter of the fatigue data and the difficulty the model has in extrapolating the life modeling to the LCF region when no available data (static strength or LCF fatigue data) exist (Sarfaraz *et al.*, 2012).

The disadvantages of the common S-N formulations are summarized and demonstrated by modeling the fatigue behavior of a wide variety of composite material systems (Figs 8.1 and 8.2). An alternative S-N formulation is established, based on the commonly used exponential and power S-N fatigue models, in order to resolve the shortcomings of the common models and appropriately simulate the fatigue life of several composite materials and composite structural elements from the LCF to the HCF region. The modeling ability of the proposed new formulation is evaluated by comparison of the derived S-N curves with the fatigue data and resulting curves from the existing fatigue models.

Comparison between the S-N curves derived from the power and the exponential fatigue models shows that the performance of the exponential



8.1 Comparison of exponential and power curves for [0/+45/90/-45/0]_s E-glass/vinylester laminate fatigue data (Post, 2008) (excluding static data).



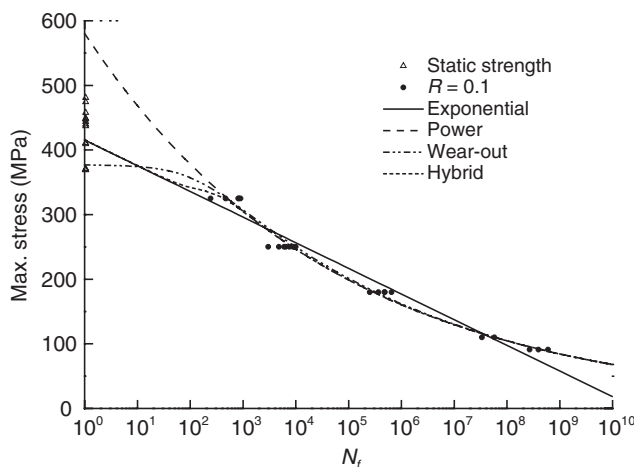
8.2 Comparison of exponential and power curves for [0/+45/90/-45/0]_s E-glass/vinylester laminate fatigue data (Post, 2008) (including static data).

model is superior to that of the power model in the LCF region, while the power model is more accurate in the HCF region. In the LCF region, the power model curve almost always overestimates the fatigue strength of the material. On the other hand, the exponential fatigue model underestimates

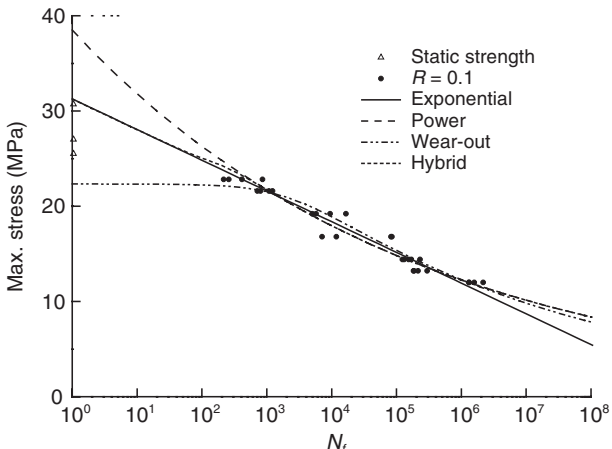
the lifetime for large numbers of cycles and occasionally estimates finite life as being at zero stress level. This behavior is shown in Fig. 8.1 for the typical constant amplitude fatigue data of composite materials, in this case E-glass/polyester laminates (Post, 2008).

The aforementioned low accuracy of the power model in the LCF region can be improved by including the static strength data when deriving the power S-N curve, considering them as fatigue data. However, the simultaneous treatment of static and fatigue data may result in an incorrect slope which affects the entire range of the lifetime, as shown in Fig. 8.2. New models have been developed (e.g. Mu *et al.*, 2011; Sarfaraz *et al.*, 2012) which aim to retain the advantages of the existing ones, but at the same time improve their weaknesses in order to effectively model the fatigue life of composite materials in the LCF and the HCF regions.

Typical cases of fatigue databases for glass fiber-reinforced laminates with different matrix resins and stacking sequences that contain adequate constant amplitude fatigue data can be found in the literature (Sarfaraz *et al.*, 2012). Two of them have been selected and are examined here. The first database comprises data from constant amplitude fatigue loading applied to $[(\pm 45)_8/0_7]_S$ E-glass/polyester laminates under tension-tension ($R = 0.1$) loading (see Fig. 8.3), retrieved from the FACT (part of Optidat) database (Nijssen, 2006). The data set includes fatigue data points corresponding to a life of only a few cycles right up to a life of more than 100 million cycles. A newly introduced (Sarfaraz *et al.*, 2012) hybrid model is fairly accurate across the entire range of cycles, while the power and wear-out models fail to accurately simulate fatigue life in the LCF region



8.3 Comparison of hybrid model with other S-N curves for $[(\pm 45)_8/0_7]_S$ E-glass/polyester laminate fatigue data (Nijssen, 2006).



8.4 Comparison of hybrid model with other S-N curves for double-lap joints (Sarfaraz *et al.*, 2011).

and the exponential model provides only a rough averaging of the experimental data in this case.

The new hybrid formulation can also be applied (and compared to existing modeling techniques) to the modeling of the fatigue behavior of pultruded FRP adhesively bonded joints. An extended database has been created recently (Sarfaraz *et al.*, 2011) and contains tension-tension, compression-compression and tension-compression constant amplitude fatigue data and static strength values obtained under high strain rates, similar to those for the fatigue loading. The data set selected for the demonstration of fatigue model applicability relates to the tension-tension fatigue results ($R = 0.1$). The resulting S-N curves according to the different fatigue models are shown in Fig. 8.4. All of the above-mentioned disadvantages of common existing models are clearly apparent in Fig. 8.4. The power model overestimates the life in the LCF region, the exponential model underestimates the life at the HCF region, while the wear-out model fails to converge with the static strength data and is unable to extrapolate any prediction to the LCF region. The hybrid fatigue model produces the most accurate S-N formulation across the entire lifetime (Sarfaraz *et al.*, 2012).

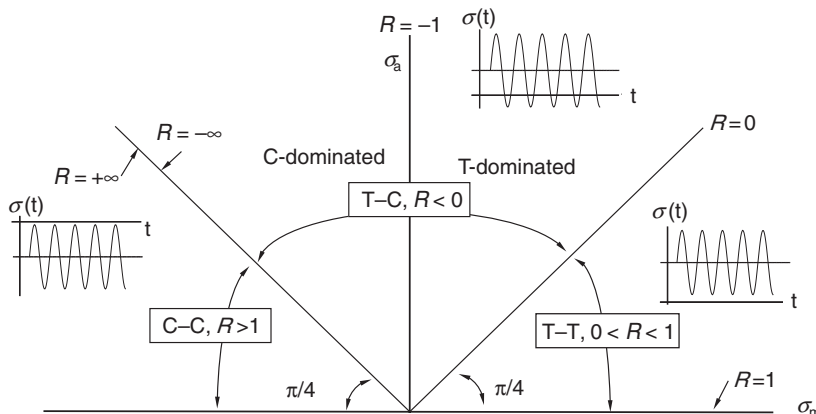
8.2.2 Constant life diagrams

The discussion so far has mainly concerned the modeling of the constant amplitude fatigue behavior of composite materials. However, for materials used in structures that operate in the open air the loading patterns are

usually of a stochastic nature and can be simulated by a time series of irregular amplitude and mean values. Regardless of the method used for modeling, the established model in terms of the mathematical expression can be used to interpolate or extrapolate the fatigue behavior for different numbers of fatigue cycles. However, the situation is not so simple for the modeling of the behavior of a composite material when it is loaded under different loading patterns, e.g. tension-tension (T-T), tension-compression (T-C) or compression-compression (C-C) fatigue, a very common situation for wind turbine rotor blade materials. The effect of the different mean stress levels of the various loading cases is very critical for the fatigue life of any composite material. It is not easy to interpolate between different loading domains in order to model the behavior of the material under new loadings and so constant life diagrams (CLD) were established to address this problem. Depending on the CLD formulation, the interpolation between known material behaviors can be linear or non-linear. However, the accuracy of a CLD can only be evaluated based on comparisons with available fatigue data for the examined material.

Constant life diagrams reflect the combined effect of mean stress and material anisotropy on the fatigue life of the examined composite material. Furthermore, they offer a predictive tool for the estimation of the fatigue life of the material under loading patterns for which no experimental data exist. The main parameters that define a CLD are the mean cyclic stress, σ_m , the cyclic stress amplitude, σ_a , and the *R*-ratio defined as the ratio between the minimum and maximum cyclic stress, $R = \sigma_{\min}/\sigma_{\max}$. A typical CLD annotation is presented in Fig. 8.5.

As shown, the positive ($\sigma_m - \sigma_a$) half-plane is divided into three sectors, the central one comprising combined tensile and compressive loading. The



8.5 Annotation for $\sigma_m - \sigma_a$ plane (Philippidis and Vassilopoulos, 2002a).

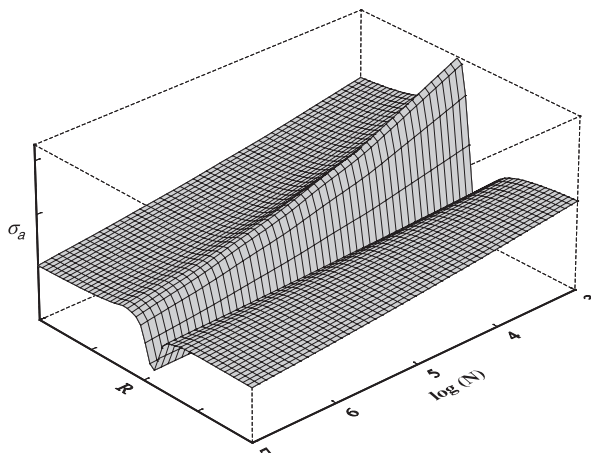
tension–tension (T–T) sector is bounded by the radial lines, representing the S-N curves at $R = 1$ and $R = 0$, the former corresponding to static fatigue and the latter to tensile cycling with $\sigma_{\min} = 0$. S-N curves belonging to this sector have positive R -values less than unity. Similar comments regarding the two remaining sectors can be derived from the annotations shown in Fig. 8.5. Every radial line with $0 < R < 1$, i.e. in the T–T sector, has a corresponding symmetric line with respect to the σ_a -axis, which lies in the compression–compression (C–C) sector and whose R -value is the inverse of the tensile R -value, e.g. $R = 0.1$ and $R = 10$.

Radial lines emanating from the origin are expressed by:

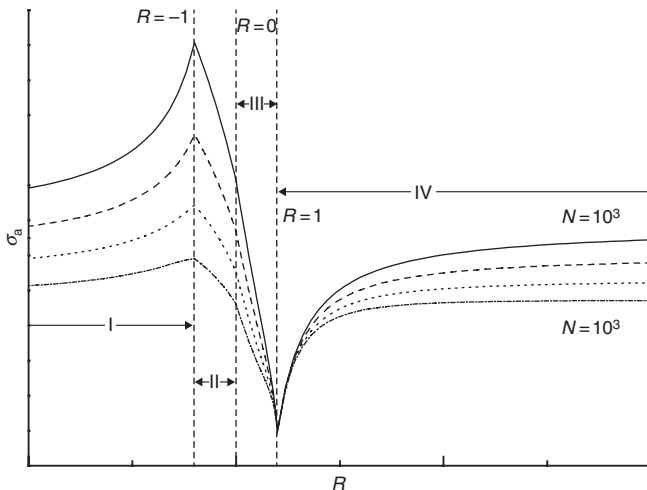
$$\sigma_a = \left(\frac{1-R}{1+R} \right) \sigma_m \quad [8.1]$$

and represent single S-N curves. Data on these lines belong to the S-N curve for that particular stress ratio. Constant life diagrams are formed by joining data points corresponding to the same numbers of cycles on consecutive radial lines.

However, there is no rational explanation for the selection of the two aforementioned stress parameters. Any other combination of σ_a – σ_m – R can just as well be used for the derivation of a constant life diagram. A plot of stress amplitude against stress ratio for different numbers of loading cycles is presented in Fig. 8.6.



8.6 Representation of the relationship between fatigue parameters σ_a – R – $\log(N)$.



8.7 Representation of constant life diagram on $R-\sigma_a$ plane.

The surface in Fig. 8.6 also represents the fatigue failure locus of the examined material. Any loading combination above the surface causes failure. A projection of this surface on the $R-\sigma_a$ plane can be considered as a constant life diagram (Fig. 8.7).

In Fig. 8.7, the x-axis represents the R -ratio and ranges from $-\infty$ to $+\infty$. The y-axis represents the stress amplitude and has positive values. S-N curves for any stress ratio, R , are represented by vertical lines. The above-mentioned diagram can be divided into four distinct regions, each corresponding to different loading conditions: Part I for compression–tension (C–T) loading under $-\infty \leq R \leq -1$, Part II for tension–compression (T–C) loading under $-1 \leq R \leq 0$, Part III corresponding to T–T loading under $0 \leq R \leq 1$ and Part IV for C–C loading under $1 \leq R \leq +\infty$. The behavior of each of the aforementioned parts can be described by simple phenomenological equations and model parameters can be estimated by using appropriate boundary conditions for each part of the diagram and known values of σ_a , σ_m and R , as described by Vassilopoulos *et al.* (2010a).

Although from a theoretical point of view the above representation of the CLD is rational, it reveals a deficiency, since it cannot accurately model the fatigue behavior of the examined material for loadings in the regions of the T–T (e.g. $R = 0.95$) and C–C (e.g. $R = 1.05$) sectors close to the horizontal axis, which represent loading under very low stress amplitude and high mean values with a culmination for zero stress amplitude ($R = 1$).

The classic CLD formulations require that the constant life lines converge to the ultimate tensile stress (UTS) and the ultimate compressive stress (UCS), regardless of the number of loading cycles. However, this is

an arbitrary simplification brought about by the lack of information about the fatigue behavior of the material when no amplitude is applied. In fact, this type of loading cannot be considered fatigue loading, but rather creep of the material (constant static load over a short or long period). Although modifications to take the time-dependent material strength into account have been introduced, their integration into CLD formulations requires the adoption of additional assumptions (Awerbuch and Hahn, 1981; Sutherland and Mandell, 2005).

In several papers found in the literature (Gathercole *et al.*, 1994; Behesty and Harris, 1998; Mandel *et al.*, 2003; Sutherland and Mandel, 2005; Kawai and Koizumi, 2007; Vassilopoulos *et al.*, 2010b) it has been proved that, although the classic linear Goodman diagram is the most commonly used, particularly for metals, it is not suitable for composite materials, mainly because of the variation in the tensile and compressive strengths that they exhibit. The damage mechanisms under tension are different from those under compression. In tension, the composite material properties are generally governed by the fibers, while in compression the properties are mainly determined by the matrix and matrix–fiber interaction. Therefore, straight lines connecting the ultimate tensile stress (UTS) and the ultimate compressive stress (UCS) with points on the $R = -1$ line for different numbers of cycles are not capable of describing the actual fatigue behavior of composite materials. A typical constant life diagram (CLD) for composite materials is thus usually shifted to the right-hand side and the highest point is located away from the line corresponding to zero mean stress, $\sigma_m = 0$.

Several CLD models have been presented in the literature in order to deal with the aforementioned characteristics of composite materials. A comprehensive evaluation of the fatigue life predicting ability of the most commonly used and the most recent models is presented in Vassilopoulos *et al.* (2010b). Since the introduction of the constant life diagram concept by Gerber and Goodman back in the nineteenth century (Gerber, 1874; Goodman, 1899), all methods have two common features: they represent the fatigue data on the σ_m – σ_a plane and their formulation is based on the fitting of available fatigue data for specified R-ratios or the interpolation between them. The same concept has been followed for the derivation of CLDs for composite materials.

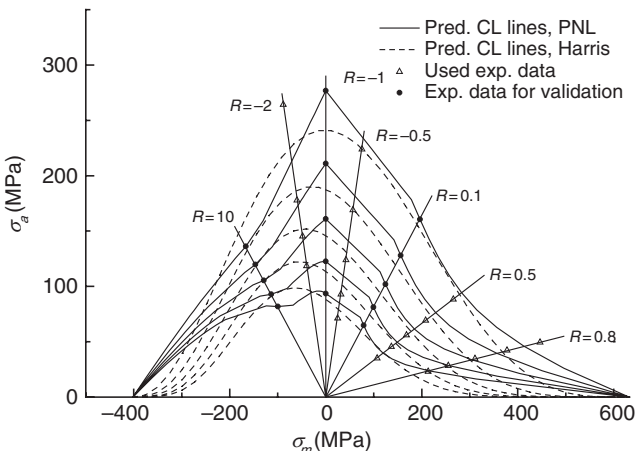
Starting from the basic idea of the symmetric and linear Goodman diagram and the non-linear Gerber equation, different modifications were proposed to address the peculiarities of the behavior of composite materials. A linear model representing a modified Goodman diagram was presented by Passipoularidis and Philippidis (2009). The model is based on a single experimentally derived S-N curve and linear interpolation for the estimation of any others. More sophisticated models, although still based on the linear interpolation between known S-N curve values and static strength

data, were presented and analytical expressions for the theoretical derivation of any desired S-N curve were developed (Philippidis and Vassilopoulos, 2002a; Philippidis and Vassilopoulos, 2004). In the proposed models, a minimum amount of experimental data was used, while simultaneously accommodating the particular characteristics of composites.

An alternative semi-empirical formulation was proposed in a series of papers by Harris's group (Gathercole *et al.*, 1994; Behesty *et al.*, 1998; Harris, 2003). The solution was based on fitting the entire set of experimental data with a non-linear equation to form a continuous bell-shaped line from the ultimate tensile stress to the ultimate compressive stress of the examined material. The drawback of this idea was the need to adjust a number of parameters based on experience and existing fatigue data. Kawai (2007) and Kawai and Koizumi (2007) proposed the so-called anisomorphic CLD that can be derived by using only one 'critical' S-N curve. The critical R -ratio is equal to the ratio of the ultimate compressive over the ultimate tensile stress of the examined material. The obvious drawback of this model is the need for experimental data for this specific S-N curve and therefore, theoretically, it cannot be applied to existing fatigue databases. However, the minimum amount of data required is an advantage of the proposed methodology. Based on the Gerber line, another formulation of the CLD was proposed by Boerstra (2007). This offers a simple method for the lifetime prediction of laminated structures subjected to fatigue loads with continuously varying mean stress, and dispenses with any classification of fatigue data according to R -values. The disadvantage of this method is the complicated optimization process, with five variables that must be followed in order to derive the CLD model.

A new model was recently proposed by Kassapoglou (2007, 2010) based on the assumption that the probability of failure during any fatigue cycle is constant and equal to the probability of failure under static loading. Following this assumption, S-N curves under any loading pattern can be derived by using only tensile and compressive static strength data. However, this restricted use of static data disregards the different damage mechanisms that develop during fatigue loading and in many cases leads to erroneous results (Awerbuch and Hahn, 1981).

A novel constant life diagram formulation was introduced by Vassilopoulos *et al.* (2010a). The model was established on the basis of the relationship between the stress ratio (R) and the stress amplitude (σ_a). Simple phenomenological equations were derived from this relationship without the need for any assumptions. The model parameters can be estimated based on a limited number of fatigue data. The validity of the proposed CLD formulation was evaluated by comparing predicted and experimental results for a wide range of composite materials. This new formulation, designated the 'Piecewise Non-Linear' (PNL) model, compares well with the existing ones,



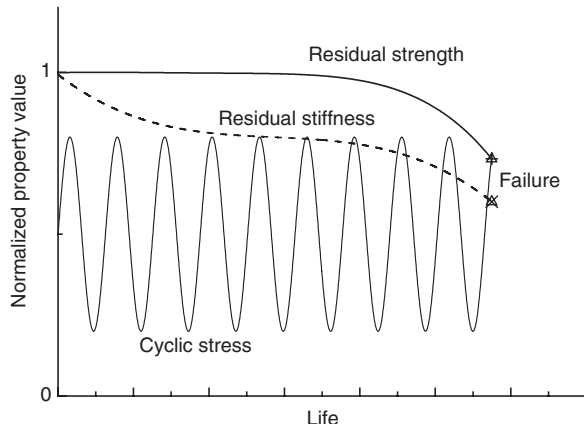
8.8 PNL compared to Harris bell-shaped diagram for $[90/0/\pm 45/0]_s$ E-glass/polyester material; $N = 10^3 - 10^7$ (Vassilopoulos *et al.*, 2010a). CL lines: constant life lines.

being more accurate in some of the studied cases for a wide range of glass and carbon fiber composite materials (Vassilopoulos *et al.*, 2010a).

A performance comparison of two of the most accurate CLD models for composite materials according to Vassilopoulos *et al.* (2010b) is presented in Fig. 8.8. Comparison of the resultant diagrams according to the PNL and the Harris bell-shaped model are presented for a $[90/0/\pm 45/0]_s$ E-glass/polyester material (Mandell and Samborsky, 2011). As demonstrated in this figure, the PNL model is highly accurate for the examined material, while the Harris CLD fails to represent material behavior under low-amplitude fatigue, i.e. when approaching the stress ratio $R = 1$. The influence of the constant life diagram formulation on the prediction of the fatigue life of composite materials was extensively studied by Vassilopoulos *et al.* (2010b).

8.3 Strength and stiffness degradation fatigue theories

Strength and stiffness degradation fatigue theories have been introduced in order to model and predict the fatigue life of composite materials by taking into account the actual damage state, expressed by a representative damage metric of the material status. The damage metric is usually the residual strength or the residual stiffness. Failure occurs when one of these metrics decreases to such an extent that a certain limit is reached. Residual strength theories assume that failure occurs when the residual strength of the material reaches the maximum applied cyclic stress level, see Fig. 8.9. On the other hand, stiffness degradation theories are not linked to the macroscopic

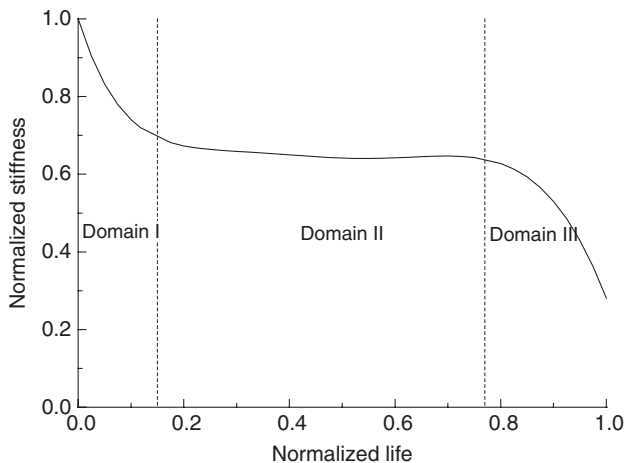


8.9 Degradation of composite strength and stiffness during constant amplitude fatigue loading.

failure (rupture) of the examined material but rather to the prediction of its behavior in terms of stiffness degradation. Failure can be determined in various ways, e.g. when a predetermined critical stiffness degradation level is reached (see e.g. Fig 8.9); or when stiffness degrades to a minimum stiffness designated by the design process in order to meet operational requirements for deformations; or even as a measure of the actual cyclic strains – e.g. failure occurs when the cyclic strain reaches the maximum static strain (Hwang and Hahn, 1986; Zhang *et al.*, 2008).

Methods that are able to assess the development of the remaining strength and stiffness degradation of a material or a structural component during fatigue life are valuable for damage tolerant design considerations. In situations like this, the effect of local failure and the stiffness degradation caused by the failure must be investigated to ensure structural integrity under the given (acceptable) damage. Life prediction schemes for composite laminates have been developed based on these concepts (Eliopoulos and Philippidis, 2011). A set of appropriate stiffness degradation rules can be applied in order to characterize a ply-drop condition in a ply-to-laminate life prediction process. In addition, this effective medium description requires the gradual strength and stiffness degradation assessment due to cyclic loading. It is obvious that important experimental effort is necessary for the parameter estimation of such a hybrid (strength and stiffness degradation) modeling process.

A wide variety of composite materials exhibit a stiffness degradation trend that can be simulated by a curve like the one schematically shown in Fig. 8.10. The three regions designated in this figure were firstly distinguished by Schulte for the tension–tension fatigue of cross-ply carbon/epoxy laminates (van Paepengem, 2010).



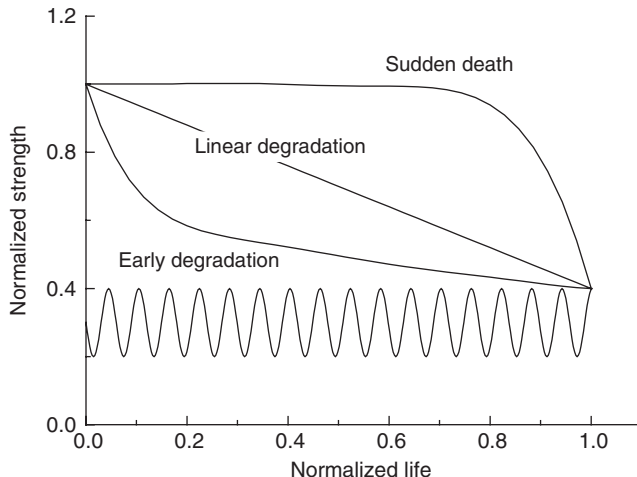
8.10 Schematic representation of a typical stiffness degradation curve for composite materials.

In the initial region, and up to around 10% of fatigue life, the material exhibits a sudden stiffness reduction (compared to region II). In the intermediate region, the material's stiffness degrades at a constant and moderate rate. Finally, significant deterioration of the material can be observed close to the end of the fatigue life. A third region with a steeply descending slope simulates this phenomenon.

Experimental evidence (e.g. Nijssen, 2006) has shown that typical composite materials used in wind turbine rotor blades exhibit strength degradation trends similar to those presented in Fig. 8.11 (Vassilopoulos and Nijssen, 2010). A wide range of materials exhibit the behavior that was described as ‘sudden death’ by Chou and Croman (1979) as their strength remains practically unchanged until very close to failure, when it decreases rapidly (Nijssen, 2006). Early or linear strength degradation, frequently a combination of more than one trend, can be observed experimentally (Shokrieh and Lessard, 1997).

Mechanistic or phenomenological models have been developed since the early seventies in order to describe this behavior. As defined by Philippidis and Passipoularidis (2007), mechanistic models are those that qualitatively take into account the progression of damage in composite materials, considering the different micromechanical damage modes that appear in the material after failure. On the other hand, phenomenological models characterize residual strength in terms of macroscopically observable properties such as strength and/or stiffness.

As regards this topic, the main objective of the research community is to model the stiffness and strength degradation for any selected



8.11 Schematic representation of typical types of strength degradation behavior.

composite material for different structural applications. The ability to quantify strength reduction at any point during realistic loading applied to the structure constitutes the major advantage of strength and stiffness degradation methods for life prediction. Wind turbine rotor blades are not designed according to a site-specific load description, but rather a ‘wind class’, a site category describing the typical expected loading. This implies that any rotor blade can be over- or under-designed for a more specific site or when site conditions deviate from the excepted loading. Recording blade loads during operation, and predicting blade residual strength, can provide an estimate of the blade’s structural reserves and serve as a monitoring technique for early identification of problems that allows the scheduling of maintenance and repair processes (Vassilopoulos and Nijssen, 2010).

Both residual strength and residual stiffness methods have advantages and disadvantages. As mentioned by Passipoularidis and Philippidis (2009b), residual strength prediction has been the subject of numerous investigations during recent decades for several good reasons. In the first place, modeling the loss of strength of a material after cyclic loading can be a powerful tool in the development of life prediction schemes, especially when dealing with variable amplitude or spectrum loading, since it offers a meaningful physical alternative to empirical damage accumulation rules such as the Palmgren–Miner rule. In addition, knowledge of the residual strength of composite structures that are designed and certified against an envelope of extreme static loads, as well as of cyclic loading, enables the designer to certify the

capacity of the structures to bear the design load during their operational life. Finally, according to state-of-the-art design practices, large safety factors take into account loss of strength. Reliable prediction of static strength degradation would help to reduce such safety factors and ultimately achieve full use of the composite material.

Residual strength fatigue theories can be successfully used in predicting the fatigue life of composite materials by means of a progressive damage modeling process, for example, Passipoularidis and Philippidis (2007). However they do have some disadvantages. Residual stiffness fatigue theories were developed to overcome some of these disadvantages:

- The remaining fatigue life cannot be assessed by non-destructive evaluation since the theories are based on a damage metric that necessitates the failure of the material in order to derive it.
- Residual strength degradation is not a sensitive measure of damage accumulation as it changes very slowly until close to failure, when it decreases rapidly. Chou and Croman described this behavior as ‘sudden death’ (Chou and Croman, 1979). On the other hand, stiffness exhibits greater changes during fatigue life.
- Extensive experimental characterization is needed for each laminate and material system in order to establish a comprehensive database for residual strength.

In 2002 a stiffness degradation model was introduced by van Paepegem and Degrieck (2002a, 2002b, 2002c) in order to demonstrate qualitatively that cumulative damage rules are not needed when applying residual stiffness models, in terms of damage growth rate equations, to the problem of variable amplitude loading.

Residual stiffness fatigue theories can also be implemented in order to derive fatigue design curves that do not correspond to failure but to a certain percentage of stiffness degradation. This concept was introduced by Salkind (1972), when he suggested drawing a family of S-N curves, being contours of a specified percentage of stiffness loss, to represent fatigue data. The same concept was adopted later (Philippidis and Vassilopoulos, 2000) in connection with the statistical analysis of fatigue data to develop the so-called stiffness controlled curves (Sc-N).

However, while stiffness can be easily and continuously monitored, stiffness changes as a function of fatigue loading cannot be easily predicted (Sendekyj, 1981), since this involves the accurate modeling of the damage accumulation process. A rational assessment of the advantages and the disadvantages of strength (or stiffness) degradation theories vs the existing phenomenological theories can be found in the work of Vassilopoulos and Nijssen (2010).

8.4 Fracture mechanics fatigue theories

Use of the crack that initiates and propagates in the material during fatigue loading as the damage metric has been proven very valuable in the case of metal fatigue, where one crack is created and its propagation controls the material's behavior. However it is questionable whether the same concept can be used for composite materials, for which failure is a result of different interacting phenomena (matrix cracking, delaminations, fiber cracking, etc) that act synergistically causing failure. Nevertheless, failure of adhesively bonded composite joints is controlled by a dominant crack which, if monitored during fatigue life, can be an acceptable damage metric (Bloyer *et al.*, 1998). Adhesively bonded joints are currently used in many locations in a wind turbine rotor blade. The advances made in polymers during recent decades enable structural adhesives to meet a wide range of structural requirements.

Single-lap joints and double-lap joints are the two main types of structural joints found in many structural applications. During the loading of a structural joint, a crack or cracks initiate naturally and propagate along the weakest path within the joint. This uncontrollable phenomenon led scientists to focus on the investigation of fracture mechanics joints, i.e. the concept of pre-cracked joints: pure Mode I crack propagation (e.g. double cantilever beam (DCB)) or Mode II fracture (e.g. end-notched flexure (ENF) or end-loaded split (ELS) beam) (Ashcroft *et al.*, 2001; Blackman *et al.*, 2003; Hadavinia *et al.*, 2003). Fracture mechanics data, such as the crack length, a , the crack propagation rate, da/dN , and the strain energy release rate, G_{\max} , corresponding to a fatigue cycle under a specific applied load P_{\max} , can thus be derived.

When structural joints are used instead of fracture joints, the situation becomes more complicated as the failure mode is not pure Mode I or Mode II failure but a mixed-mode failure. The proportion of each failure mode depends on the material, joint geometry, type of loading and environmental conditions. The strain energy release rate calculated for this mixed-mode failure is designated the total strain energy release rate (Mall *et al.*, 1987) and is assumed to be equal to the sum of G_I and G_{II} , $G_{\text{tot}} = G_I + G_{II}$. Moreover, the crack initiates naturally and propagates in an uncontrollable way in a structural joint without a pre-crack.

Fracture mechanics theory has been used to study the fatigue behavior of structural joints by a number of researchers. Analytical solutions and, more frequently, numerical methods have been used to model the fatigue life of the examined joint configurations.

8.4.1 Manipulation of fracture mechanics data

Two categories of fracture mechanics data can be distinguished: the first contains data that can be directly measured and recorded, such as crack

length under specific load for a certain number of loading cycles; the second contains data to be calculated using the recorded data, such as crack propagation rate, system compliance and its fluctuations during fatigue life, and strain energy release rate as a function of crack length and/or crack propagation rate.

If the crack length can be measured during loading, the life of the examined structure can be modeled directly by integration of the crack propagation rate between two different crack lengths:

$$N - N_i = \int_{N_i}^N dN = \int_{a_i}^a \frac{1}{(d\alpha/dN)} da \quad [8.2]$$

where N_i denotes number of cycles for crack initiation, and a_i denotes initial crack length. $N - N_i$ corresponds to the number of cycles for crack propagation between crack lengths a_i and a . The application of Equation [8.2] is straightforward, since only a method for the calculation of the crack propagation rate, $d\alpha/dN$, has to be selected (Zhang *et al.*, 2010a).

This application is directly linked to the specific experimental data and does not take into account the materials and/or geometry of the structural element. Based on fracture mechanics data, however, predictive methods can be developed that combine the experimental evidence obtained from one type of structural element and analytical or numerical solutions for other types of structural elements, made from the same materials, in order to predict the strength or fatigue life of the latter (Curley *et al.*, 1998). One parameter that is often used for this purpose is the strain energy release rate, G . For an isotropic or anisotropic plate of constant thickness, B , and a crack with length, a , the strain energy release rate is a function of the applied load, P , and the rate of compliance change, dC/da :

$$G = \frac{P^2}{2B} \frac{dC}{da} \quad [8.3]$$

In the case of cyclic loading, the maximum value of the strain energy release rate during one fatigue cycle can be deduced accordingly:

$$G_{\max} = \frac{P_{\max}^2}{2B} \frac{dC}{da} \quad [8.4]$$

where P_{\max} is the maximum cyclic load during the fatigue cycle.

The FCG curves are plots of the stress intensity factor, SIF or K , (Paris and Gomez, 1961; Andersons *et al.*, 2004) or the strain energy release rate, SERR or G , (Wilkins *et al.*, 1982; Russell and Street, 1988; Martin and Murri, 1990) versus the crack propagation rate, $d\alpha/dN$, usually on logarithmic axes. Although the stress intensity factor is mainly used for the derivation of FCG curves for metals/alloys, the strain energy release rate is preferred for composite materials, since for the calculation of G there is no need to directly calculate the local stress field close to the crack tip, which is difficult, if not impossible, for composite laminates (Rans *et al.*, 2011). FCG curves show three regions: the subcritical region, during which the crack propagates very slowly under low G values and can occasionally indicate a fatigue threshold; the second region, during which a stable crack growth is observed; and the unstable region, during which a small increase in G causes significant increase in the crack propagation rate.

Paris *et al.* (1961) observed that along the second region, the relationship between the crack propagation rate, $d\alpha/dN$, and the stress intensity factor range, ΔK , or the maximum stress intensity factor, K_{\max} , follows a power law equation. This observation was initially validated by Mode I experimental data on two aluminum alloys, 2024-T3 and 7075-T6 from three independent sources. The Paris law has also been extensively employed for the modeling of the fatigue crack propagation of composite materials under pure Mode I (Wilkins *et al.*, 1982; Bathias and Laksimi, 1985; Mall and Johnson, 1986; Mall *et al.*, 1989; O'Brien, 1990; Hojo *et al.*, 1994; Shrivakumar *et al.*, 2006), (mixed) Mode I/II (Wilkins *et al.*, 1982; Johnson and Mall, 1985; Mall and Johnson, 1986; Gustafson and Hojo, 1987; Mall *et al.*, 1989; Kenane *et al.*, 2011), pure Mode II (Allegri *et al.*, 2011), and for adhesively bonded structural joints (Mall and Johnson, 1986; Curley *et al.*, 2000; Jia and Davalos, 2004).

The major, linear, part of the relationship can be fitted by the following equation:

$$\frac{da}{dN} = D(G_{\max})^m \quad [8.5]$$

where D and m are empirical constants for the given loading ratio, frequency of testing and environment (Bathias and Laksimi, 1985). In previous studies (Sendeckyj, 1991; Andersons *et al.*, 2004), D and m were considered as material constants that do not depend on joint configuration. This assumption allowed their estimation from standardized DCB tests (Bathias and Laksimi, 1985; Mall and Johnson, 1986; Andersons *et al.*, 2004) and the subsequent application of the same values to estimate life for more complex joint configurations. Despite the fact that this argument seems rational, it was not supported by experimental evidence. As shown by Andersons *et al.* (2004),

the adoption of this assumption led to an over-prediction of the fatigue life of carbon fiber composite joints bonded with an epoxy adhesive.

Martin and Muri (1990) introduced a phenomenological equation that is able to model the FCG behavior along the entire range of applied G , from the first to the third region. The derived model is called the ‘total fatigue life model’ and expresses the crack growth rate as a function of the maximum cyclic strain energy release rate, G_{\max} , the strain energy release rate threshold, G_{th} , and the critical strain energy release rate, G_c . Shivakumar *et al.* (2006) used the total fatigue life model for characterizing the crack growth rate in glass/vinylester delaminated composite panels subjected to Mode I cyclic loading.

Equivalently to Equation [8.5] the following equation can be used according to the total life fatigue model:

$$\frac{da}{dN} = D(G_{\max})^m \frac{\left(1 - (G_{\text{th}}/G_{\max})^{Q_1}\right)}{\left(1 - (G_{\max}/G_c)^{Q_2}\right)} \quad [8.6]$$

where, D , m , Q_1 and Q_2 are empirical model parameters dependent on material and loading conditions. Equation [8.6] can be applied between the limits set by the threshold and the critical value of the strain energy release rate, $G_{\text{th}} \leq G_{\max} \leq G_c$. As G_{\max} approaches G_{th} , da/dN tends to become minimum, and as G_{\max} approaches G_c , da/dN tends asymptotically to infinity.

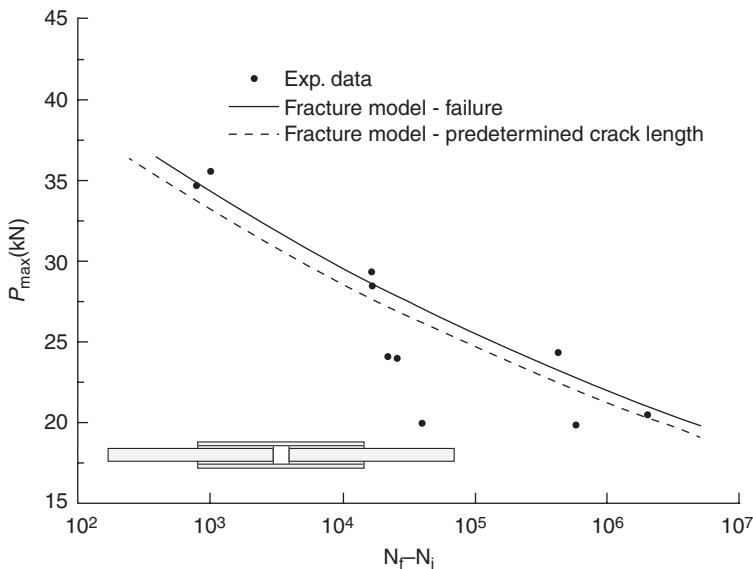
By substituting da/dN with its equivalent from Equation [8.5] or Equation [8.6], Equation [8.2] becomes:

$$N - N_i = \int_{a_i}^a \frac{1}{D(G_{\max})^m} da \quad [8.7]$$

or

$$N - N_i = \int_{a_i}^a \frac{1}{D(G_{\max})^m \frac{\left(1 - (G_{\text{th}}/G_{\max})^{Q_1}\right)}{\left(1 - (G_{\max}/G_c)^{Q_2}\right)}} da \quad [8.8]$$

Depending on the values of G_{\max} and the corresponding limits of the integration (corresponding to failure or a predetermined crack length), Equation [8.7] or Equation [8.8] can be used for the derivation of conservative or non-conservative design allowables in line with a damage tolerant design



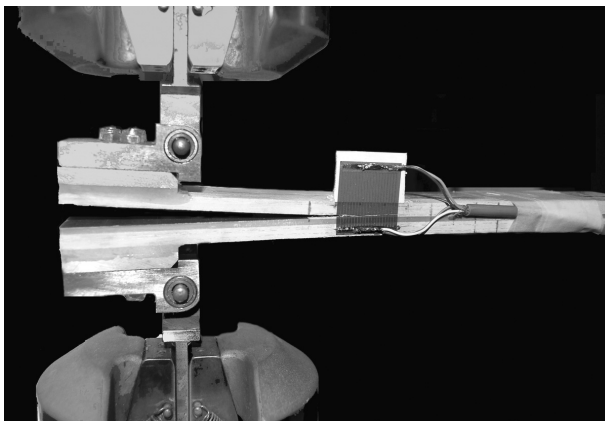
8.12 S-N curves for DLJs obtained from fracture model (Zhang *et al.*, 2010a).

philosophy (e.g. estimation of the number of cycles required to attain a specific crack length under a specific applied load). Predicted S-N curves for double-lap joints (DLJs), according to the fracture model, are shown in Fig. 8.12 (Zhang *et al.*, 2010a).

The process for the derivation of the FCG curve (and the consecutive estimation of the parameters D , m , Q_1 and Q_2) is similar for fracture mechanics and structural joints as long as the strain energy release rate and the corresponding crack propagation rate values are derived. Experimental results from adhesively bonded pultruded GFRP double cantilever beams (DCB) (see Fig. 8.13) will be used in the following paragraphs for the simulation of the FCG curve derivation (Shahverdi *et al.*, 2012a).

Standard methods for the SERR calculation are based on Equation [8.4], the difference between them basically being the way in which the derivative dC/da is obtained. A thorough analysis of the applicability of several methods for the calculation of the SERR to similar composite joints is presented by Zhang *et al.* (2010b). Their analysis shows that for similar pultruded GFRP DCB joints, all methods give similar results with the exception of simple beam theory.

The relationship between specimen compliance and crack length is required in order to estimate the SERR. The compliance of the specimen, C , defined as the ratio of the maximum displacement over the maximum load (δ_{max}/P_{max}), can be calculated at each number of cycles directly from



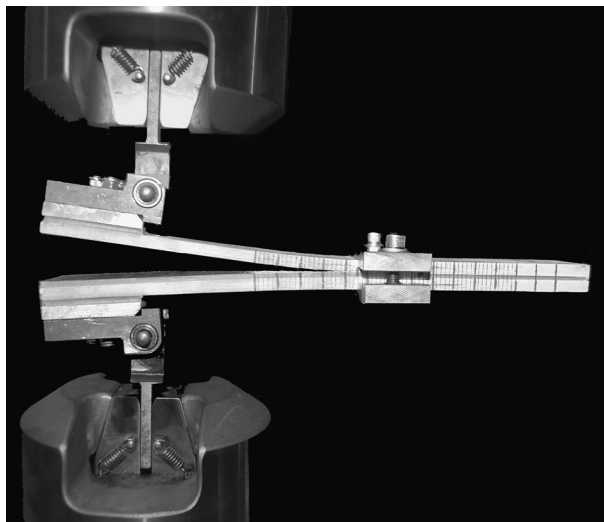
8.13 Crack gage at the crack tip (Shahverdi *et al.*, 2012a).

the recorded data. However, derivation of the crack length during fatigue loading is not an easy task. Direct methods – crack gages and visual observation – and also indirect methods, e.g. the dynamic compliance calibration introduced by Costa *et al.* (2009), exist for this purpose.

One of the most commonly used methods is based on the visual crack observation. According to this method, the fatigue experiment is interrupted at a predetermined number of cycles, and the joint is opened until a displacement equal to the maximum cyclic displacement is reached. An optical microscope is used to record the crack length. The process is repeated several times to establish a relationship between joint compliance, C , and crack length, a . This is the simplest method for determining the relationship between crack length and compliance. The disadvantage of this method is the scatter caused by the interruptions of the experiment (Shivakumar *et al.*, 2006).

The relationship between crack length and compliance can also be determined during fatigue loading, without any interruption, by using crack gages (Shahverdi *et al.*, 2012a). The crack gages, shown in Fig. 8.13, include 20 parallel wires with a pitch of 1.15 mm placed perpendicular to the adhesive layer. As the crack propagates, the wires are progressively cut and the electrical resistance of the gage increases. The high cost is the main drawback of this method, especially if it has to cover the total length of the specimen, i.e. use several gages along its length.

Another method for determining the relationship between crack length and compliance is based on a dynamic compliance calibration (Costa *et al.*, 2009). According to this method, the fatigue experiment is terminated without the recording of any crack length measurements. The specimen is then clamped by a mechanical fixture, see Fig. 8.14, that can be moved along the

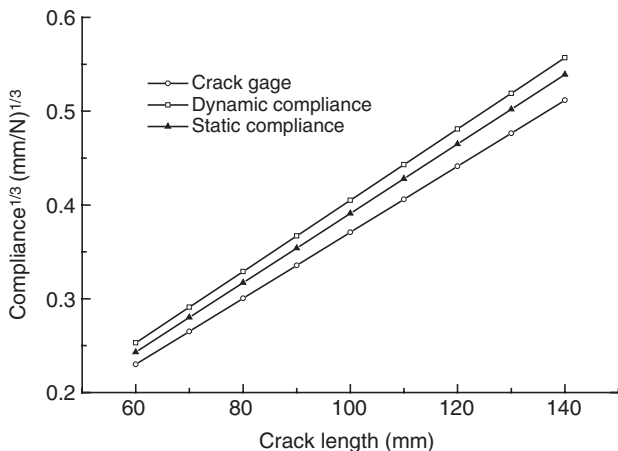


8.14 Clamping at crack tip, dynamic compliance method (Shahverdi et al., 2012a).

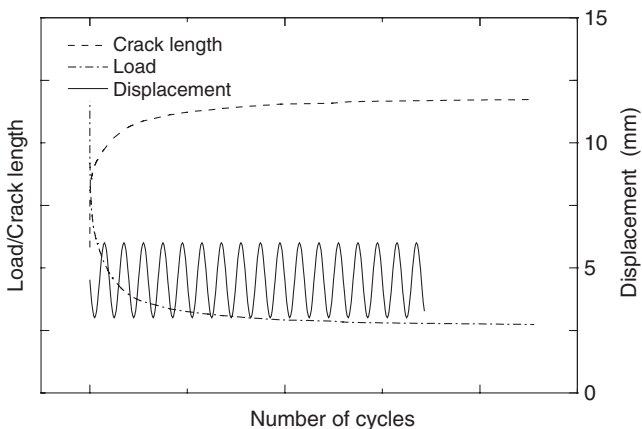
specimen to simulate different crack lengths reached during fatigue loading. For each selected crack length, a fatigue block of around 1000 cycles with maximum and minimum displacements equal to those in the real fatigue experiment is applied and the displacement and load are recorded to estimate the compliance of the joint. The drawback of this method is that it cannot capture the effect of the fiber bridging on the compliance, since the measurements are performed on the cracked specimen, when the bridging fibers are already broken.

The average compliance of the same type of specimens examined under quasi-static loading can be used when the examined joints exhibit the same behavior under static and fatigue loading. In this method, the effect of fiber bridging on the compliance of the examined joints is included, but only partially correlated to the applied fatigue loading conditions, as different fiber bridging effects are seen under different *R*-ratios. Another disadvantage is the scatter of the compliance measurements of the quasi-static experimental results, which is considerable and makes the adoption of a single compliance for all cases very difficult.

The comparison between the results obtained using the three methods, crack gages, dynamic compliance calibration and average static compliance, is shown in Fig. 8.15, where the compliance vs the crack length is given. As expected, the compliance calculated using crack gages is lower than that calculated by the dynamic compliance method that does not consider the fiber bridging occurring during crack opening. The difference between the



8.15 Comparison of the average compliance vs crack length relationship for different methods (Shahverdi *et al.*, 2012a).



8.16 Schematic illustration of load and crack growth during fatigue life.

average static compliance and the dynamic compliance is due to the scatter of the experimental data in both methods and also the effect of the fiber bridging.

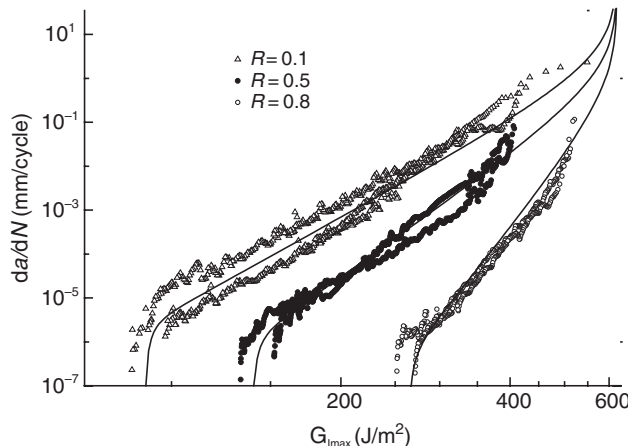
The variation of the maximum applied load during a displacement controlled fatigue test, and the corresponding crack length increase are shown in Fig. 8.16. The maximum load decreases rapidly at the beginning and then follows a smoother decreasing trend until reaching a plateau value, corresponding to the fatigue threshold. Consequently, crack length increases rapidly at the beginning of the experiment when the maximum load is high and at a reduced rate as the load decreases.

Calculation of the crack growth rate (da/dN), which is necessary for the FCG derivation, can be performed in two different ways: the secant method and the incremental polynomial fitting methods as prescribed in the ASTM standard, ASTM E647-08. According to the secant or point-to-point method, the crack propagation rate can be determined by calculating the slope of a straight line connecting two contiguous data points on the a - N curve. The incremental polynomial method fits a second-order polynomial to sets of a specified number of successive data points, usually 3, 5, 7 or 9. The slope of the determined equation at any point corresponds to the crack propagation rate.

As reported in the literature (Ashcroft and Shaw, 2002; Zhang *et al.*, 2010; Shahverdi *et al.*, 2012a) the secant method shows high sensitivity to scatter, while increasing the number of points in the polynomial method effectively decreases this sensitivity without changing the actual trend of experimental data. In general, the crack propagation rate continuously decreases with increasing crack length. However the rate of this decrease is not constant, being higher at the beginning, and at the end of the experiment, close to the fatigue threshold, and more moderate for the major part of the fatigue loading.

Typical FCG curves showing the variation of the crack growth rate (da/dN) as a function of the strain energy release rate (G_{Imax}) throughout fatigue life are presented in Fig. 8.17. As shown, G_{Imax} decreases with an increasing number of cycles (from right to left) and this reduction is more pronounced for lower R -ratio values.

Experimental evidence has proved that, independent of the examined material or joint, FCG curves show similar trends. However, contradictory



8.17 Crack growth rate versus G_{Imax} , solid lines are plots of model results (Shahverdi *et al.*, 2012b).

results were found in the literature concerning the effect of the R -ratio on the FCG curves. Nevertheless, most of the published experimental data are limited to the second region of the FCG curve (e.g. Wilkins *et al.*, 1982; Mall and Johnson, 1986; Zhang *et al.*, 2010a) since it is very time-consuming to estimate the fatigue threshold, and difficult to monitor the fast region close to G_c . The majority of publications on the subject, (e.g. Martin and Murri, 1990; O'Brien, 1990; Shahverdi *et al.*, 2012a) report that higher R -ratios result in steeper FCG curves, independent of the strain energy release rate parameter (G_{\max} , or ΔG) that is used for the derivation of the curves. However, there are other experimental results showing FCG curves for different R -ratios that are parallel to each other (e.g. Hojo *et al.*, 1994; Jia and Davalos, 2004).

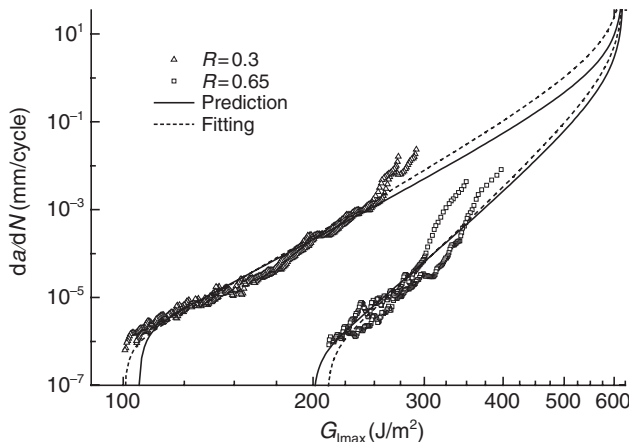
Independent of the exhibited behavior, the crack propagation under constant amplitude (CA) loading at any R -ratio has been modeled using the Paris law model. Several models can be found in the literature for the simulation of the crack propagation along the second region of the FCG curve (e.g. Walker, 1970; Hojo *et al.*, 1994; Andersons *et al.*, 2004; Jia and Davalos, 2004a, 2004b), incorporating the effect of the R -ratio so that all data could be condensed to a single master curve. Nevertheless, despite the fact that there are plenty of research works on the fatigue crack growth rate in composite material, there is no study in which the effect of the R -ratio on the total fatigue life has been modeled.

An empirical fatigue crack growth formulation for the modeling of constant amplitude Mode I fatigue behavior of adhesively-bonded pultruded glass fiber-reinforced polymer DCB joints under different R -ratios has recently been introduced (Shahverdi *et al.*, 2012b). The model was established using existing experimental data and was validated through comparisons to new fatigue/fracture experimental results. It was shown by Shahverdi *et al.* (2012b) that, if the model parameters are estimated accurately, the model can be used for the derivation of reliable FCG curves for several unknown loading conditions. Therefore it can assist the development of methodologies for the fatigue life prediction of the examined joints under realistic loading conditions.

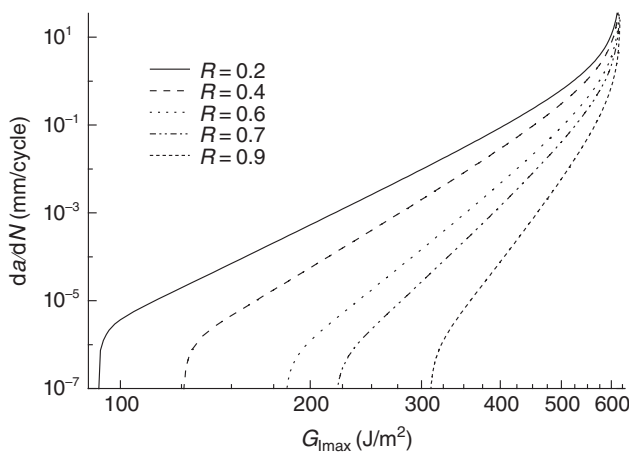
The predicted FCG curves for R -ratios equal to 0.3 and 0.65 are plotted in Fig. 8.18 by solid lines. Two experimentally derived FCG curves per loading case, and the fitted lines (dashed lines, according to Equation [8.8]) are also given for comparison. As shown, the predicted FCG curves are validated by the experimental data and fitted lines.

This new total life fatigue model can be used for the derivation of other FCG curves, under different R -ratios, as long as the baseline fatigue data exist and allow derivation of the relationships between the model parameters and the R -ratio used.

Theoretical FCG curves for different R -ratios are shown in Fig. 8.19. Such curves can be used for crack length estimation under block and variable



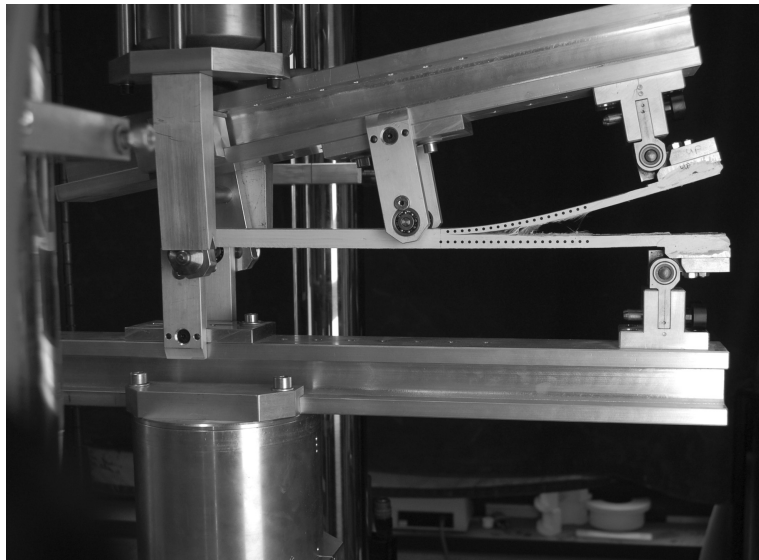
8.18 Modeling validation by comparison of experimental results and modeling $R = 0.3$ and $R = 0.65$ (Shahverdi *et al.*, 2012b).



8.19 Predicted FCG curves at various R -ratios (Shahverdi *et al.*, 2012b).

loading conditions characteristic of the way real stress fields develop in wind turbine rotor blades.

Although this particular modeling process seems to lead to quite accurate life prediction results, there is still a lot of work that must be done in order to deal with real loading conditions and the actual fracture behavior of adhesively bonded structural components in wind turbine rotor blades. Connections of rotor blade components (e.g. between the flange of the spar beam and the aerodynamic shell) result in asymmetric joints of non-standardized dimensions and configurations, with adherends that are generally



8.20 Mixed-mode bending experimental setup.

composed of different materials. Mixed-mode fracture conditions develop in such cases and more complicated modeling and predicting schemes are necessary for the prediction of the behavior of the examined joints during the lifespan of the rotor blade.

To this end, mixed-mode experiments (usually using the mixed-mode bending (MMB) specimen configuration, see Fig. 8.20) have been conducted (Reeder, 1993) to investigate the Mode I/Mode II fracture behavior of given adhesively bonded joints with the aim of developing mixed mode fracture failure criteria that can assess the complex fracture under realistic conditions. It has been shown that the development of such criteria, based solely on experimental input from Mode I and Mode II fracture joints and numerical modeling of the areas exhibiting mixed-mode fracture, enable the reliable assessment of the examined structural element condition and provide valuable information about the structural integrity of the entire structure.

8.5 Case study: Phenomenological fatigue life prediction

Several conceptually different approaches to the problem of the fatigue life prediction of materials and structural elements of wind turbine rotor blades were presented in the previous sections. The application of the classic (phenomenological) fatigue life prediction methodology that leads to the

calculation of the Miner's damage coefficient is presented in this section by way of demonstration of the process that must be followed.

The classic fatigue life prediction methodology can be considered an articulated method, since a number of subproblems must be solved sequentially to produce the final result. Five basic steps can be identified in this method:

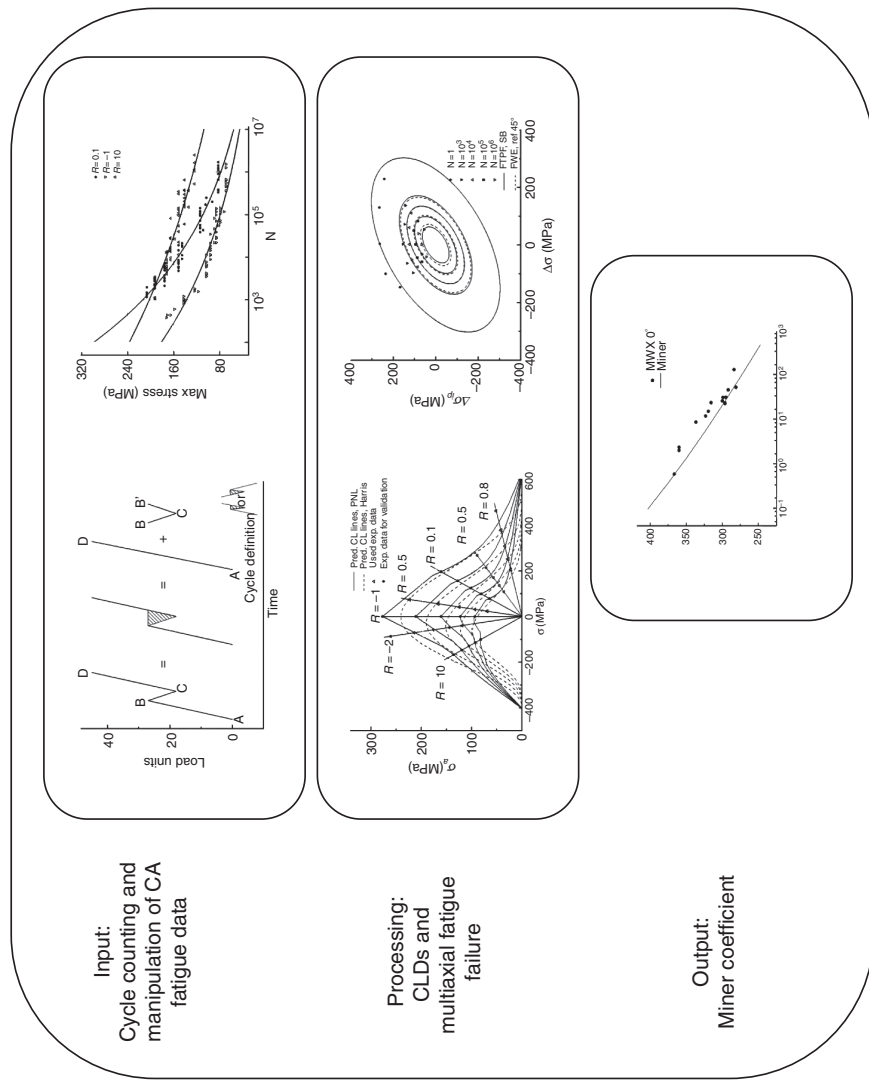
1. Cycle counting
2. Modeling of the experimental constant amplitude fatigue behavior
3. Interpretation of fatigue behavior for assessment of the mean stress effect
4. Adoption of the fatigue failure criterion
5. Damage summation.

The first two tasks, as described in the list above, concern mainly interpretation of the applied loading spectrum and modeling of the constant amplitude fatigue behavior of the material. Modeling constant amplitude fatigue behavior involves determination of the S-N curves (plot of cyclic stress vs life, typically by grouping data at a single R -value ($R = \sigma_{\min}/\sigma_{\max}$)). (Incidentally, depending on the R -value, an S-N curve can be constructed from data obtained at varying mean and amplitude.) Modeling of the fatigue behavior for the assessment of the mean stress effect results in the construction of the constant life diagram (CLD), described by the third task in the above list. These two processes can be treated as separate steps, but are related in the sense that the CLD is constructed from the available S-N curves, and new S-N curves could be extracted from this CLD. However, the third task (as well as the fourth – the fatigue failure criterion) yields new results predicting the fatigue life of the examined material or structural element under new, 'unseen during modeling' loading conditions. The last task, concerning the damage summation, is the purely predicting module of this type of methodology, where the final damage index emerges.

A graphical representation of a classic life prediction methodology is presented in Fig. 8.21. The necessary input for the application of such a methodology is the applied loading spectrum and the static and constant amplitude fatigue data of the material under consideration. As regards to the cycle counting, appropriate methods are used to summarize (often lengthy) irregular load time series by providing the number of occurrences of cycles of various sizes. On the other hand, the available constant amplitude fatigue data are treated accordingly aiming to the derivation of reliable S-N curves of the material. The models (with the estimated, during this first stage, model parameters) are used as input to the next stages of the methodology.

The effect of the mean stress on the constant amplitude fatigue life of the material is assessed using constant life diagrams. Constant life diagrams also

8.21 Graphical representation of phenomenological life prediction scheme.



offer a predicting tool for estimating the fatigue life of the material under loading patterns for which no experimental data exist. When appropriate modeling has been achieved, the determination of the fatigue life of a composite material is the next step. This task is relatively simple when uniaxial loading is applied to a material and a uniaxial stress state develops as a result. In this case, the fatigue life can be estimated by means of reliable S-N curves and the assistance of the constant life diagrams. However, when complex stress states develop due to the application of either multiaxial fatigue loading patterns or uniaxial loading patterns that produce complex stress states along the material's principal system, e.g. off-axis fatigue of unidirectional laminates, a multiaxial fatigue failure criterion must be introduced to take all the stress components present into account.

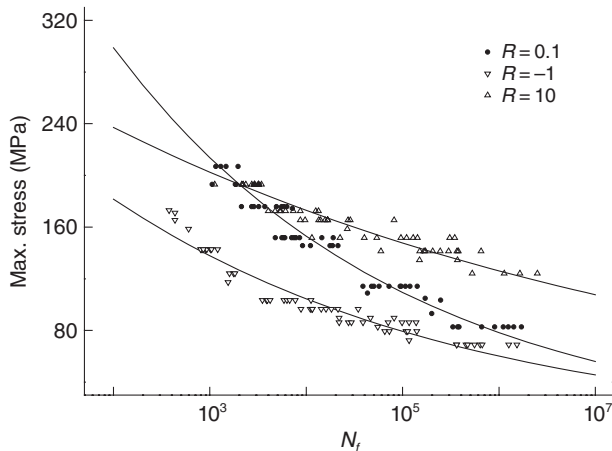
The last module in the life prediction algorithm is the accumulation of damage, which is carried out according to the linear Palmgren–Miner rule. The number of operating cycles, n , of each bin, derived from rainflow counting, is divided by the allowable number of cycles, N_f , (derived directly using the S-N curve equation when a uniaxial fatigue stress state develops, or, by the solution of the fatigue failure criterion for N_f when multiaxial fatigue stress fields are present) to form a partial damage coefficient. The summation of all partial damage coefficients and comparison with unity indicate whether the material will survive the application of the variable amplitude loading under examination.

A recent database released by Virginia Tech (Post, 2008) containing experimental data from axial loading on pseudo-quasi-isotropic glass/vinyl ester specimens fabricated using the vacuum-assisted resin transfer molding (VARTM) technique will be used here for the demonstration of the case study method.

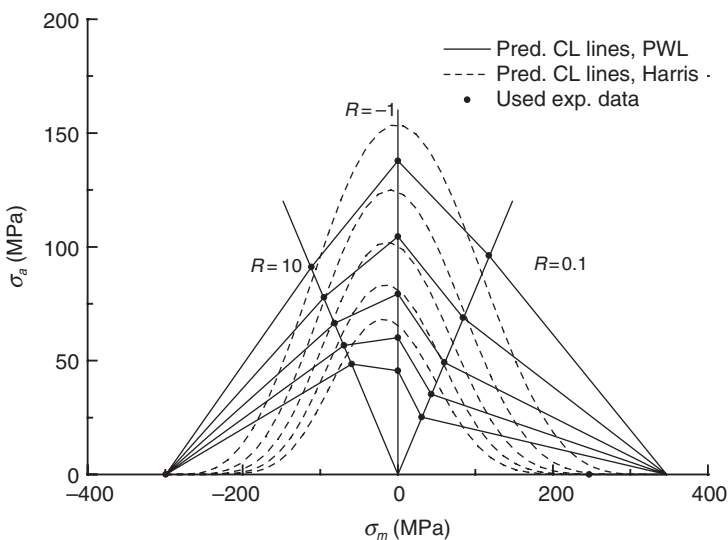
The ultimate tensile stresses (UTS) and the ultimate compressive stresses (UCS) of the material were derived experimentally. The values are UTS = 346.81 ± 15.77 MPa, UCS = 299.20 ± 13.24 MPa. The constant amplitude fatigue data under 3 R -ratios ($R = 10, -1$ and 0.1) are presented in Fig. 8.22. S-N curves of different types can be fitted to simulate the exhibited fatigue behavior. Additional fatigue data under a fatigue spectrum (A Rayleigh spectrum (RAY-0.95 in Post, 2008) with the majority of the cycles having an R -ratio around $R = -1$) are also available and will be used for the evaluation of the predicting accuracy of the method.

Treatment of the constant amplitude fatigue data and the static strength data according to given models yields the constant life diagrams presented in Fig. 8.23.

The selected loading condition is uniaxial and therefore there is no need to use a multiaxial fatigue failure criterion for the evaluation of the fatigue life. Fatigue life predictions according to different life prediction schemes



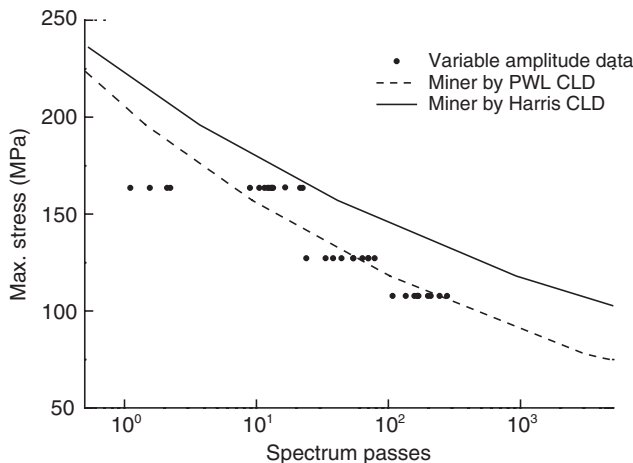
8.22 Constant amplitude fatigue behavior and S-N curves under $R = 10$, -1 and 0.1 .



8.23 Constant life diagrams for the examined material.

(selection of different cycle counting algorithms, constant life diagrams, etc.) are presented in Fig. 8.24.

As shown in Fig. 8.24, differences can result when different methods are employed for the solution of each one of the steps of the phenomenological life prediction methodology. In this case it can be seen that the selection of the Harris CLD (which is less conservative around $R = -1$) yields less



8.24 Lifetime prediction based on different schemes.

conservative fatigue life predictions. Nevertheless, as there is a direct connection between the chosen solutions for each step of the methodology (e.g. the decision concerning the S-N curve type also affects the shape of the constant life diagram and subsequently the lifetime calculation), it is difficult to quantify and get a clear idea of the criticality of each step.

8.6 Future trends

The major objective of any life prediction methodology is the accurate estimation of the fatigue life of a structural component and consequently of an entire engineering structure. Whether based on an empirical model or on damage and fracture mechanics concepts, the process of accurate fatigue life prediction comprises several different steps, each one of which requires careful treatment to avoid introducing additional uncertainties into the full process.

A classic life prediction methodology can be considered as an articulated method, since a number of different subproblems (cycle counting, S-N modeling, CLD formulations, fatigue failure criterion for multiaxial stress states, damage summation) must be solved sequentially to produce the final result (Vassilopoulos and Nijssen, 2010). As shown in the previous section, the overall accuracy of the process depends on the accuracy of each one of the methods employed for the modeling and/or the prediction of the exhibited fatigue behavior (see, for example, Passipoularidis and Philippidis 2009a; Vassilopoulos *et al.*, 2010c; Vassilopoulos and Keller, 2011, for assessment of the effect of different methods on the life prediction results). On the other hand, progressive fatigue life prediction schemes (e.g. Eliopoulos and

Philippidis, 2011) necessitate the accurate modeling and/or prediction of the S-N behavior together with the strength and stiffness degradation modeling during the fatigue life.

An additional uncertainty is introduced due to the actual stochastic nature of the loads, the material properties, etc., which are usually considered deterministic in the available fatigue failure prediction methodologies. The physical uncertainty around aspects of the process such as the fatigue strength (e.g. Lekou and Philippidis, 2008; Lekou *et al.*, 2011) and the applied loads, as well as the model uncertainty around the tools used (S-N curve, CLD formulations, Miner's rule, etc.) must be assessed in order to increase the reliability of any life prediction scheme (Toft and Sorensen, 2011a). Adoption of probabilistic/stochastic methods for reliability testing of blades in both ultimate and fatigue limit states can lead to a direct reliability-based blade design process (Toft and Sorensen, 2011b).

The majority of composite blades contain adhesive joints. This joining technique has been used for a long time in automotive and aerospace applications, offering many advantages compared to riveting and bolting, such as considerable mass saving, cheaper fabrication, improved aerodynamics and the avoidance of holes that act as areas of stress concentration and potential moisture ingress along cut fibers. Despite the similarities, there are also fundamental differences between aerospace and wind turbine rotor blade constructions in terms of the manufacturing process, material architecture, dimensions of components and operational conditions. Nevertheless, what is certain is that, for a wind turbine blade, joints are the most likely locations for failure initiation and, since their function is to transfer loads from one part of the structure to another, their structural integrity is of high importance for the viability of the entire blade. Additional efforts must be put into the development of reliable methods for modeling the behavior and the eventual life prediction of the structural joints in a wind turbine rotor blade. The task of developing mixed-mode failure criteria that take into account asymmetric joint configurations between different adherends is very challenging and will surely preoccupy wind engineers for some time to come.

Wind turbine rotor blades are long and/or slender structures susceptible to buckling and other instabilities. Therefore, efforts should also be devoted to the investigation of the stability behavior of the blades and blade components, e.g. the spar beam, under cyclic loads. It is known that the common models for the assessment of the wrinkling loads of sandwich structures under multiaxial stress states lead to considerably conservative design solutions (Manshadi *et al.*, 2011a, 2011b, 2012) that hinder the design optimization of the entire structure. Methods for the estimation of wrinkling loads under biaxial cyclic loading conditions such as the one derived by Manshadi *et al.* (2012) for quasi-static compression–tension loading will be valuable in design and life assessment processes.

Methods for the fatigue life prediction of composite laminates, composite sandwich structures and the joints between them are very likely to be developed in the coming years. Assessment of the results of each method and the establishment of relevant progressive damage modeling tools for the entire structure, based on damage tolerant concepts, would ensure reliable fatigue life prediction of wind turbine rotor blades.

8.7 References

- Adam T., Fernando G., Dickson R. F., Reiter H. and Harris B. (1989), 'Fatigue life prediction for hybrid composites', *Int J Fatigue*, **11**(4), 233–237.
- Allegri G., Jones M. I., Wisnom M. R. and Hallett S. R. (2011), 'A new semi-empirical model for stress ratio effect on mode II fatigue delamination growth', *Compos Part A Appl-S*, **42**(7), 733–740.
- Andersons J., Hojo M. and Ochiai S. (2004), 'Empirical model for stress ratio effect on fatigue delamination growth rate in composite laminates', *Int J Fatigue*, **26**(6), 597–604.
- Argüelles A., Viña J., Canteli A. F. and Bonhomme J. (2010), 'Fatigue delamination, initiation, and growth, under mode I and II of fracture in a carbon-fiber epoxy composite', *Polymer Compos*, **31**(4), 700–706.
- Ashcroft A. I. and Shaw S. J. (2002), 'Mode I fracture of epoxy bonded composite joints: 2 fatigue loading', *Int J Adhes Adhes*, **22**(2), 151–167.
- Ashcroft A. I., Hughes D. J. and Shaw S. J. (2001), 'Mode I fracture of epoxy bonded composite joints: 1. Quasi-static loading', *Int J Adhes Adhes*, **21**(2), 87–99.
- Aymerich F. and Found M. S. (2000), 'Response of notched carbon/peek and carbon/epoxy laminates subjected to tension fatigue loading', *Fatigue Fract Eng M*, **23**(8), 675–683.
- Awerbuch J. and Hahn H. T. (1981), 'Off-axis fatigue of graphite/epoxy composite'. In: Lauraitis N. K. (Ed.), *Fatigue of Fibrous Composite Materials*, ASTM STP, **723**, 243–273.
- Bakis C. E., Simonds R.A., Vick L. W. and Stinchcomb W. W. (1990), 'Matrix toughness, long-term behavior, and damage tolerance of notched graphite fiber-reinforced composite materials'. In: Garbo S. P. (Ed.), *Composite Materials: Testing and Design*, ASTM STP, **1059**, 349–370.
- Bathias C. and Laksimi A. (1985), 'Delamination threshold and loading effect in fiber glass epoxy composite'. In: Johnson W. S. (Ed.), *Delamination and Debonding of Materials*, ASTM STP, **876**, Philadelphia, 217–237.
- Beheshty M. H. and Harris B. (1998), 'A constant life model of fatigue behavior for carbon fiber composites: the effect of impact damage', *Compos Sci Technol*, **58**(1), 9–18.
- Blackman B. R. K., Hadavinia H., Kinloch A. J., Paraschi M. and Williams J. G. (2003), 'The calculation of adhesive fracture energies in mode I: revisiting the tapered double cantilever beam (TDCB) test', *Eng Fract Mech*, **70**(2), 233–248.
- Bloyer D. R., Rao K. T. V. and Ritchie R. O. (1998), 'Fracture toughness and R-curve behavior of laminated brittle-matrix composites', *Metall Mater Trans A*, **29**(10), 2483–2496.
- Boerstra G. K. (2007), 'The multislope model: a new description for the fatigue strength of glass reinforced plastic', *Int J Fatigue*, **29**, 1571–1576.

- Brøndsted P., Lilholt H. and Lystrup A. (2005), 'Composite materials for wind power turbine blades' *Annu Rev Mater Res*, **35**, 505–538.
- Chou P. C. and Croman R. (1979), 'Degradation and sudden death models of fatigue of graphite/epoxy composites': In Tsai S. W. (Ed.), *Composite Materials: Testing and Design (5th Conference)*, ASTM STP, **674**, 431–454.
- Costa J., Mahdi S., Vicens J., Blanco N. and Rodriguez-Bellido A. (2009), 'Fatigue behavior of adhesive films and laminated resins in bonded joints for repair purposes': In: *Proceedings of the ICCM 17 Conference*, 27–31 July, Edinburgh, UK.
- Curley A. J., Hadavinia H., Kinloch A. J. and Taylor A. C. (2000), 'Predicting the service life of adhesively-bonded joints': *Int J Fract*, **103**(1), 41–69.
- Curley A. J., Jethwa J. K., Kinloch A. J. and Taylor A. C. (1998), 'The fatigue and durability behaviour of automotive adhesives. Part III: predicting the service life': *J Adhesion*, **66**(11), 39–59.
- de Smet B. J. and Bach P. W. (1994), 'DATABASE FACT, fatigue of composites for wind turbines': In: *3rd IEA-Symposium on Wind Turbine Fatigue*, 21–22 April, The Netherlands: ECN Petten.
- Eliopoulos E. N. and Philippidis, T. P. (2011), 'A progressive damage simulation algorithm for GFRP composites under cyclic loading. Part I: Material constitutive model': *Compos Sci Technol*, **71**(5), 742–749.
- Epaarachchi J. A. and Clausen P. D. (2003), 'An empirical model for fatigue behavior prediction of glass fibre-reinforced plastic composites for various stress ratios and test frequencies': *Compos Part A-Appl S*, **34**(4), 313–326.
- Gathercole N., Reiter H., Adam T. and Harris B. (1994), 'Life prediction for fatigue of T800/5245 carbon fiber composites: I. constant amplitude loading': *Int J Fatigue*, **16**(8), 523–532.
- Gerber W. Z. (1874), 'Bestimmung der zulässigen spannungen in eisen-construktionen (Calculation of the allowable stresses in iron structures)': *Z Bayer Archit Ing-Ver*, **6**(6), 101–110.
- Goodman J. (1899), *Mechanics Applied to Engineering*, Longman Green, Harlow, UK.
- Gustafson C. G. and Hojo M. (1987), 'Delamination fatigue crack growth in unidirectional graphite/epoxy laminates': *J Reinf Plast Compos*, **6**(1), 36–52.
- Hadavinia H., Kinloch A. J., Little M. S. G. and Taylor A. C. (2003), 'The prediction of crack growth in bonded joints under cyclic-fatigue loading. I. Experimental studies': *Int J Adhes Adhes*, **23**(6), 449–461.
- Hahn H. T. and Kim R. Y. (1975), 'Proof testing of composite materials': *J Compos Mater*, **9**(3), 297–311.
- Halpin J. C., Jerina K. L. and Johnson T. A. (1973), 'Characterization of composites for the purpose of reliability evaluation': In: Whitney J. M. (Ed.), *Analysis of the Test Methods for High Modulus Fibers and Composites*, ASTM STP, **521**, 5–64.
- Harik V. M., Klinger J. R. and Bogetti T. A. (2002), 'Low-cycle fatigue of unidirectional composites: Bi-linear S-N curves': *Int J Fatigue*, **24**(2–4), 455–462.
- Harris B. (2003), 'A parametric constant-life model for prediction of the fatigue lives of fiber-reinforced plastics': In: Harris, B. (Ed.), *Fatigue in Composites*, Woodhead Publishing Limited, Cambridge, 546–568.
- Hojo M., Matsuda S., Tanaka M., Ochiai S. and Murakami A. (2006), 'Mode I delamination fatigue properties of interlayer-toughened CF/Epoxy laminates': *Compos Sci Technol*, **66**(5), 665–675

- Hojo M., Ochiai S., Gustafson C. G. and Tanaka K. (1994), 'Effect of matrix resin on delamination fatigue crack growth in CFRP laminates', *Eng Fract Mech*, **49**(1), 35–47.
- Holmes J. W., Sorensen B. F. and Brondsted P. (2007), 'Reliability of wind turbine blades: An overview of materials testing', *Wind Power Shanghai*, Shanghai, China, 1–3 November.
- Hwang W. and Han K. S. (1986), 'Fatigue of composites – fatigue modulus concept and life prediction', *J Compos Mater*, **20**(2), 154–165.
- Jia J. and Davalos J. F. (2004a), 'Study of load ratio for Mode-I fatigue fracture of wood–FRP bonded interfaces', *J Compos Mater*, **38**(14), 1211–1230.
- Jia J. and Davalos J. F. (2004b), 'Loading variable effects on Mode-I fatigue of wood–FRP composite bonded interface', *Compos Sci Technol*, **64**(1), 99–107.
- Johnson W. S. and Mall S. (1985), 'A fracture mechanics approach for designing adhesively bonded joints? In Johnson W. S. (Ed.), *Delamination and Debonding of Materials, ASTM STP*, **876**, Philadelphia, 189–199.
- Kassapoglou C. (2007), 'Fatigue life prediction of composite structures under constant amplitude loading', *J Compos Mater*, **41**(22), 2737–2754.
- Kassapoglou C. (2010), 'Fatigue of composite materials under spectrum loading', *Compos Part A-Appl Sci*, **41**(5), 663–669.
- Kawai M. (2007), 'A method for identifying asymmetric dissimilar constant fatigue life diagrams for CFRP laminates', *Key Eng Mater*, **334–335**, 61–64.
- Kawai M. and Koizumi M. (2007), 'Nonlinear constant fatigue life diagrams for carbon/epoxy laminates at room temperature', *Compos Part A – Appl S*, **38**(11), 2342–2353.
- Kenane M., Azari Z., Benmedakhene S. and Benzeggagh M. L. (2011), 'Experimental development of fatigue delamination threshold criterion', *Compos Part B–Eng*, **42**(3), 367–375.
- Kun F., Carmona H. A., Andrade J. S. Jr. and Herrmann, H. J. (2008), 'Universality behind Basquin's Law of Fatigue', *Phys Rev Lett*, **100**(9), 094301-1 to 094301-4.
- Lekou D. J. and Philippidis T.P. (2008), 'Mechanical property variability in FRP laminates and its effect on failure prediction', *Compos Part B – Engineering*, **39**(7–8), 1247–1256.
- Lekou D. J., Assimakopoulou T. T. and Philippidis T.P. (2011), 'Estimation of the uncertainty in measurement of composite material mechanical properties during static testing', *Strain*, **47**(5), 430–438.
- Mall S. and Johnson W. S. (1986), 'Characterization of Mode I and mixed-mode failure of adhesive bonds between composite adherends', In: Whitney J. M. (Ed.), *Composite Materials: Testing and Design (Seventh Conference)*, *ASTM STP*, **893**, Philadelphia, 322–334.
- Mall S., Ramamurthy G. and Rezaizdeh M. A. (1987), 'Stress ratio effect on cyclic debonding in adhesively bonded composite joints', *Compos Struct*, **8**(1), 31–45.
- Mall S., Yun K. T. and Kochhar N. K. (1989), 'Characterization of matrix toughness effect on cyclic delamination growth in graphite fiber composites', In: Lagace P. A. (Ed.), *Composite Materials: Fatigue and Fracture, Second Volume, ASTM STP*, **1012**, Philadelphia, 296–310.
- Mandell J. F. (1990), 'Fatigue behavior of short fiber composite materials', In: Reifsnider, K. L. (Ed.), *Fatigue of Composite Materials*, Elsevier, Amsterdam, 1990.

- Mandell J. F., McGarry F. J., Huang D. D. and Li C. G. (1983), 'Some effects of matrix and interface properties on the fatigue of short fiber-reinforced thermoplastics', *Polym Composite*, **4**(1), 32–39.
- Mandell J. F., Samborsky D. D., Wang L. and Wahl N. K. (2003), 'New fatigue data for wind turbine blade materials', *Journal of Solar Energy Engineering, Transactions of the ASME*, **125**(4), 506–514.
- Mandell J. F. and Samborsky D. D. (2011), 'SNL/MSU/DOE Composite Material Fatigue Database: Test Methods Material and Analysis', Sandia National Laboratories/Montana State University, version 20.0, available at: <http://www.coe.montana.edu/composites/>
- Martin R. H. and Murri G. M. (1990), 'Characterization of mode I and mode II delamination growth and thresholds in AS4/PEEK composites', In: Garbo S. P. (Ed.), *Composite Materials: Testing and Design, ASTM STP*, **1059**, Philadelphia, 251–270.
- Manshadi B. D., Vassilopoulos A. P. and Keller T. (2011a), 'Shear buckling resistance of GFRP plate girders', *J Compos Construct*, **15**(3), 431–440.
- Manshadi B. D., Vassilopoulos A. P. and Keller T. (2011b), 'Contribution to shear wrinkling of GFRP webs in cell-core sandwiches', *J Compos Construct*, **15**(5), 833–840.
- Manshadi B. D., Vassilopoulos A. P., de Castro, J. and Keller T. (2012), 'Instability of thin-walled GFRP webs in cell core sandwiches under combined bending and shear loads', *Thin-walled Struct*, **53**, 200–210, doi:10.1016/j.tws.2011.12.021
- Miyano Y., Nakada M. and Muki R. (1997), 'Prediction of fatigue life of a conical shaped joint system for reinforced plastics under arbitrary frequency, load ratio and temperature', *Mech Time-Depend Mat*, **1**(2), 143–159.
- Mu P., Wan X. and Zhao M. (2011), 'A new S-N curve model of fiber reinforced plastic composite', *Key Eng Mat*, **462–463**, 484–488.
- Naghipoura P., Bartscha M. and Voggenreitera H. (2011), 'Simulation and experimental validation of mixed mode delamination in multidirectional CF/PEEK laminates under fatigue loading', *Int J Solids Struct*, **48**(6), 1070–1081.
- Nijssen R. P. L. (2006), 'OptiDAT – fatigue of wind turbine materials database', available at: http://www.kc-wmc.nl/optimat_blades/index.htm
- Nijssen R. P. L. (2006), 'Fatigue life prediction and strength degradation of wind turbine rotor blade composites' PhD Thesis, TU Delft, ISBN 013:978-90-9021221-0.
- O'Brien T. K. (1990), 'Towards a damage tolerance philosophy for composite materials and structures', In: Garbo S. P. (Ed.), *Composite Materials: Testing and Design. ASTM STP*, **1059**, 7–33.
- Paris P. C., Gomez M. P. and Anderson W. E. (1961), 'A rational analytic theory of fatigue', *Trend Eng*, **13**, 9–14.
- Passipoularidis V. A. and Philippidis T. P. (2007), 'Residual strength after fatigue in composites: Theory vs. experiment', *Int J Fatigue*, **29**(12), 2104–2116.
- Passipoularidis V. A. and Philippidis T. P. (2009a), 'A study of factors affecting life prediction of composites under spectrum loading', *Int J Fatigue*, **31**(3), 408–417.
- Passipoularidis V. A. and Philippidis T. P. (2009b), 'Strength degradation due to fatigue in fiber dominated glass/epoxy composites: A statistical approach', *Journal Compos Mater*, **43**(9), 997–1013.
- Philippidis T. P. and Vassilopoulos A. P. (1999), 'Fatigue strength prediction under multiaxial stress', *J Compos Mater*, **33**(17), 1578–1599.

- Philippidis T. P. and Vassilopoulos A. P. (2000), 'Fatigue design allowables of GRP laminates based on stiffness degradation measurements', *Compos Sci Technol*, **60**(15), 2819–2828.
- Philippidis T. P. and Vassilopoulos A. P. (2001), 'Stiffness reduction of composite laminates under combined cyclic stresses', *Adv Compos Lett*, **10**(3), 113–124.
- Philippidis T. P. and Vassilopoulos A. P. (2002), 'Complex stress state effect on fatigue life of GRP laminates. Part I, experimental', *Int J Fatigue*, **24**(8), 813–823.
- Philippidis T. P. and Vassilopoulos A. P. (2004), 'Life prediction methodology for GFRP laminates under spectrum loading', *Compos Part A-Appl S*, **35**(6), 657–666.
- Post N. L. (2008), 'Reliability based design methodology incorporating residual strength prediction of structural fiber reinforced polymer composites under stochastic variable amplitude fatigue loading', Virginia Polytechnic Institute and State University, PhD thesis.
- Quaresimin M., Susmel L. and Talerja R. (2010), 'Fatigue behavior and life assessment of composite laminates under multiaxial loadings', *Int J Fatigue*, **32**(1), 2–16.
- Rans C. D., Alderliesten R. C. and Benedictus R. (2011), 'Misinterpreting the results: how similitude can improve our understanding of fatigue delamination growth', *Compos Sci Technol*, **71**(2), 230–238.
- Reeder J. R. (1993), 'A Bilinear Failure criterion for mixed-mode delamination', In: Camponeschi E. T. Jr. (Ed.), *Composite Materials Testing and Design, ASTM STP*, **1206**, Philadelphia, 303–322.
- Russell A. J. and Street K. N. (1988), 'A constant ΔG test for measuring Mode I interlaminar fatigue crack growth rates', In: Whitcomb J. D. (Ed.), *Composite Materials Testing and Design (eighth conference), ASTM STP*, **972**, Philadelphia, 259–277.
- Salkind M. J. (1972), 'Fatigue of composites', In: Corten H. T. (Ed.), *Composite Materials: Testing and Design (second conference), ASTM STP*, **497**, 143–169.
- Sarfraz R., Vassilopoulos A. P. and Keller T. (2011), 'Experimental investigation of the fatigue behavior of adhesively-bonded pultruded GFRP joints under different load ratios', *Int J Fatigue*, **33**(11), 1451–1460.
- Sarfraz R., Vassilopoulos A. P. and Keller T. (2012), 'A hybrid S-N formulation for fatigue life modeling of composite materials and structures', *Comp A-Appl Sci*, **43**(2), 445–453.
- Sarkani S., Michaelov G., Kihl D. P. and Beach J. E. (1999), 'Stochastic fatigue damage accumulation of FRP laminates and joints', *J Struct Eng*, **125**(12), 1423–1431.
- Sendeckyj G. P. (1981), 'Fitting models to composite materials fatigue data', In: Chamis, C. C. (Ed.), *Test Methods and Design Allowables for Fibrous Composites, ASTM STP*, **734**, 245–260.
- Shahverdi M., Vassilopoulos A. P. and Keller T. (2012a), 'Experimental investigation of R-ratio effects on fatigue crack growth of adhesively-bonded pultruded GFRP DCB joints under CA loading', *Compos A – Appl Sci*, **43**(10), 1689–1697.
- Shahverdi M., Vassilopoulos A. P. and Keller T. (2012b), 'A total fatigue life model for the prediction of the fatigue crack growth of adhesively-bonded pultruded GFRP DCB joints under CA loading', *Compos A-Appl Sci*, **43**(10), 1783–1790.
- Shivakumar K., Chen H., Abali F., Le D. and Davis C. (2006), 'A total fatigue life model for mode I delaminated composite laminates', *Int J Fatigue*, **28**(1), 33–42.

- Shokrieh, M. M. and Lessard, L. B. (1997), 'Multiaxial fatigue behaviour of unidirectional plies based on uniaxial fatigue experiments—II. Experimental evaluation', *Int J Fatigue*, **19**(3), 209–217.
- Sutherland H. J. and Mandell J. F. (2005), 'Optimized constant life diagram for the analysis of fiberglass composites used in wind turbine blades', *J Sol Energ-T ASME*, **127**(4), 563–569.
- Tanaka K. and Tanaka H. (1997), 'Stress-ratio effect on mode II propagation of inter-laminar fatigue cracks in graphite/epoxy composites', *Compos Mater: Fatigue Fract ASTM Spec Tech Publ*, **1285**, 126–142.
- Toft H. S. and Sorensen J. D. (2011a), 'Probabilistic fatigue design of composite material for wind turbine blades', In: Faber, Köhler, and Nishijima (Ed.), *Applications of Statistics and Probability in Civil Engineering*, Taylor and Francis, London.
- Toft H. S. and Sorensen J. D. (2011a), 'Reliability-based design of wind turbine blades', *Struct Saf*, **33**(1), 333–342.
- van Paepegem W. and Degrieck J. (2002a), 'A new coupled approach of residual stiffness and strength for fatigue of fibre-reinforced composites', *Int J Fatigue*, **24**(7), 747–762.
- van Paepegem W. and Degrieck J. (2002b), 'Coupled residual stiffness and strength model for fatigue of fibre-reinforced composite materials', *Compos Sci Technol*, **62**(5), 687–696.
- van Paepegem W. and Degrieck J. (2002c), 'Calculation of damage-dependent directional failure indices from the Tsai–Wu static failure criterion', *Compos Sci Technol*, **63**(2), 305–310.
- van Paepegem W. (2010), 'Fatigue damage modeling of composite materials with the phenomenological residual stiffness approach', In: Vassilopoulos A. P. (Ed.), *Fatigue life prediction of composites and composite structures*, Woodhead Publishing Ltd, Cambridge, 102–138.
- Vassilopoulos A. P. (2006), 'A new software framework for fatigue life prediction of composite materials under irregular loading', *Adv Compos Lett*, **15**(1), 23–29.
- Vassilopoulos A. P., Georgopoulos E. F. and Dionyssopoulos V. (2007), 'Artificial neural networks in spectrum fatigue life prediction of composite materials', *Int J Fatigue*, **29**(1), 20–29.
- Vassilopoulos A. P. and Bedi R. (2008) 'Adaptive Neuro–Fuzzy Inference System in modeling fatigue life of multidirectional composite laminates', *Compos Mater Sci*, **43**(4), 1086–1093.
- Vassilopoulos A. P., Georgopoulos E. F. and Keller T. (2008), 'Comparison of genetic programming with conventional methods for fatigue life modeling of FRP composite materials', *Int J Fatigue*, **30**(9), 1634–1645.
- Vassilopoulos A. P. (2010), 'Introduction to fatigue life prediction of composite materials and structures: past, present and future prospects', In: Vassilopoulos A. P. (Ed.), *Fatigue life prediction of composites and composite structures*, Woodhead Publishing Limited, Cambridge, 1–44.
- Vassilopoulos A. P., Manshadi B. D. and Keller T. (2010a), 'Piecewise non-linear constant life diagram formulation for FRP composite materials', *Int J Fatigue*, **32**(10), 1731–1738.
- Vassilopoulos A. P., Manshadi B. D. and Keller T. (2010b), 'Influence of the constant life diagram formulation on the fatigue life prediction of composite materials', *Int J Fatigue*, **32**(4), 659–669.

- Vassilopoulos A. P., Sarfaraz R., Manshadi B. D. and Keller T. (2010c), 'A Computational tool for the life prediction of GFRP laminates under irregular complex stress states: Influence of the fatigue failure criterion', *Comput Mater Sci*, **49**(3), 483–491.
- Vassilopoulos A. P. and Nijssen R. P. L. (2010), 'Fatigue life prediction of composite materials under realistic loading conditions (variable amplitude loading)', In: Vassilopoulos A. P. (Ed.), *Fatigue life prediction of composites and composite structures*, Woodhead Publishing Limited, Cambridge, 293–333.
- Vassilopoulos A. P. and Keller T. (2011), *Fatigue of Fiber-Reinforced Composites*, Springer-Verlag London Limited., London, Dordrecht, Heidelberg, New York.
- Walker K. (1970), 'The effect of stress ratio during crack propagation and fatigue for 2024-T3 and 7075-T6 aluminium', In: Rosenfeld M. S. (Ed.), *Effects of Environment and Complex Load History on Fatigue Life, ASTM STP*, **462**, American Society for Testing Materials, Philadelphia, 1–14.
- Whitney J. M. (1981), 'Fatigue characterization of composite materials', In: Lauraitis K. N. (Ed.), *Fatigue of Fibrous Composite Materials, ASTM STP*, **723**, 133–151.
- Wilkins D. J., Eisenmann J. R., Camin R. A., Margolis W. S. and Benson R. A. (1982), 'Characterizing delamination growth in graphite/epoxy', In: Reifsneider K. L. (Ed.), *Damage in Composite Materials, ASTM STP*, **775**, American Society for Testing and Materials, Philadelphia, 168–182.
- Zhang Y., Vassilopoulos A. P. and Keller T. (2008), 'Stiffness degradation and fatigue life prediction of adhesively-bonded joints for fiber-reinforced polymer composites', *Int J Fatigue*, **30**(10–11), 1813–1820.
- Zhang Y., Vassilopoulos A. P. and Keller T. (2009), 'Environmental effects on fatigue behavior of adhesively-bonded pultruded structure joints', *Compos Sci Technol*, **69**(7–8), 1022–1028.
- Zhang Y., Vassilopoulos A. P. and Keller T. (2010a), 'Fracture of adhesively-bonded pultruded GFRP joints under constant amplitude fatigue loading', *Int J Fatigue*, **32**(7), 979–987.
- Zhang Y., Vassilopoulos A. P. and Keller T. (2010b), 'Mode I and II fracture behavior of adhesively-bonded pultruded composite joints', *Eng Fract Mech*, **77**(1), 128–143.

Micromechanical modelling of wind turbine blade materials

L. MISHNAEVSKY Jr., Technical University of Denmark, Denmark

DOI: 10.1533/9780857097286.2.298

Abstract: An overview of the micromechanics of materials methods and approaches that can be used for the modelling of wind turbine blade composites is given in this chapter. Using the various modelling methods reviewed here, the strength, stiffness and lifetime of composite materials can be predicted and the suitability of different groups of materials for applications in wind turbine blades can be analysed. The effects of interface and matrix properties, fibre clustering and nanoreinforcement on the strength and lifetime of composites are studied in a number of simulations, and some examples of the analysis of microstructural effects on the strength and fatigue life of composites are provided.

Key words: micromechanics, composites, wind turbine blades, microstructures, computational modelling, fibre clustering, kinking, microstructure–property relationships, 3-D modelling, nanoreinforcement, statistical effects.

9.1 Introduction

The efficiency and practical usability of wind energy technology depends on the reliability and the longevity of wind turbines (Brøndsted *et al.*, 2005). The repair and the maintenance of wind turbines are generally expensive and time-consuming. But how can one predict, and increase, the lifetime of wind turbine blades? These structures are subject to complex, multiaxial, cyclic loading and their failure processes are controlled by microscale degradation of the materials. Experimental testing of the many different materials under a variety of service conditions would require huge effort and expense. The solution to this problem lies in the application of numerical experiments in which various materials which are used, or have the potential to be used, for wind energy applications are tested in computational models. The computational models should include realistic microscale structures of the materials, realistic deformation and damage mechanisms and realistic

loading conditions. This approach, in which the mechanical behaviour and the strength of materials is studied as a function of their microstructures on the basis of numerical models, is realized in the framework of computational micro- and meso-mechanics of materials (Mishnaevsky Jr., 2007; Schmauder and Mishnaevsky Jr., 2008).

In this chapter, an overview is given of the methods and approaches of micromechanics of materials that can be used for the modelling of wind turbine blade composites. Various materials modelling methods and the results of several simulations are discussed.

The computational modelling of wind turbine blade materials is carried out at several scale levels: macrolevel (or structural scale level, concentrating on adhesive joints, skin, web, etc), mesolevel (or laminate scale level) and microlevel (fibre–matrix scale level). In some cases, nanoreinforcement is introduced into the fibre sizing or matrix, thus requiring an additional level of analysis, nanolevel. Currently, the computational analysis of wind turbine blades at the structural level seldom includes the local properties and complex structures of composites; rather, these materials are considered as homogeneous. Thus, this direction lies, in fact, outside of the micro-mechanical (microstructure-based modelling) field.

At the mesolevel, the laminates and sandwiches of the blade shells are considered multilayered materials, with laminae (plies) being anisotropic fibre-reinforced composites. Such multilayered structures can fail along weak interfaces. Delamination of laminates, debonding between the skin and the core in sandwich structures and failure of adhesive joints are examples of such failure mechanisms. The delamination failure, e.g. buckling-driven delamination or fatigue delamination, are modelled using fracture mechanics based models. In fracture mechanics, the energy-based and stress-based criteria of crack formation and growth are used to predict the failure conditions of materials and structures (Sørensen, 2010). Delamination typically represents a mixed-mode fracture process, i.e. fracture under combined shear and tensile local stresses. In order to determine delamination conditions, local stress distribution, energy release rate (i.e. the energy dissipated during fracture per unit of newly created fracture surface area) and other parameters are calculated. In numerical studies, the cohesive zone model is often used, in which the material separation due to the crack growth is described using the traction–separation law, which links the tractions to the separation of the faces of the new surface at the front of the crack (Sørensen and Kirkegaard, 2006).

At the fibre–matrix level (microlevel), the main damage mechanisms include fibre cracking, cracking and void growth in the matrix, and interface debonding. A short overview of the modelling methods of these processes is given below.

9.2 Analytical models of the mechanical behaviour, strength and damage of fibre-reinforced composites: an overview

This section discusses analytical models of the mechanical behaviour, strength and damage of fibre-reinforced polymer composites subjected to tensile and compressive loading.

9.2.1 Tensile loading

The strength of fibre-reinforced composites is determined by the microscale cracking, debonding and interaction between the elements and phases of the composite. In order to model these processes, several analytical methods have been developed, among them shear lag based models, the fibre bundle model and its generalizations, fracture mechanics based models and continuum damage mechanics based models (Mishnaevsky Jr., 2007).

The **shear lag model**, developed by Cox in 1952, is one of the most often-used approaches in the theoretical analysis of the strength and damage of fibre-reinforced composites. In this model, the force balance in the fibre is considered on the basis of the assumption that the load transfer from fibre to matrix occurs only via shear stresses. Hedgepeth (1961) was first to apply the shear lag model to a multifibre system. He studied the stress distribution around broken fibres in 2-D unidirectional composites with infinite fibre arrays. Since then, a number of techniques and approaches based on this model have been developed, among them the 3-D elastic multifibre shear lag model, which includes the case of the elasto-plastic matrix (Hedgepeth and van Dyke, 1967); the break influence superposition (BIS) technique, developed by Sastry and Phoenix (1993) to analyse the effects of multiple fibre breaks and their interaction on the stress distribution and strength of composites; the quadratic influence superposition (QIS) technique by Beyerlein and Phoenix (1996), which enables analysis of the deformation and damage of elastic fibres in an elastic-plastic matrix, taking into account interface debonding; the 3-D shear lag model, in which matrix displacements are interpolated from the fibre displacements (Landis *et al.*, 1999); and Green's function model (GFM) (Ibnabdeljalil and Curtin, 1997a, 1997b; Xia *et al.*, 2001), which enables analysis of the interaction between multiple breaks in fibres. The models based on the shear lag approach enable the study of the redistribution of stresses from failed to intact fibres and the analysis of the stress distribution and damage accumulation in materials, taking into account the multiple breaks in the fibres and the effects of fibre–matrix debonding and

fibre–matrix interfacial friction (Ibnabdeljalil and Curtin, 1997a, 1997b; Zhou and Wagner, 1999).

In the **fibre bundle model**, the damage evolution in a bundle of fibres after one or several fibres have failed is modelled using statistical models of fibre strength and different load-sharing rules. This model, developed initially by Daniels (1945), considers a bundle of fibres with identical elastic properties under uniform tensile stress. When a fibre breaks, the load from the broken fibre is distributed equally over all the remaining fibres (global load sharing (GLS)). As noted by Zhou and Wagner (1999), the GLS model is applicable only to a loose fibre bundle, with no matrix between the fibres; in the case of fibres which are bound together by a matrix, other load-sharing models should be used. For the qualitative description of the load redistribution after the fibre failure, stress concentration factor (SCF) was introduced as a ratio between the local stress in an intact fibre (which is equal to the overload at the fiber related with the fiber break, and applied stress) and the applied stress (Zhou and Wagner, 1999). Harlow and Phoenix (1978) proposed the local load sharing (LLS) model, in which the extra load, from the failed fibre(s), is transferred to the two nearest neighbours of the fibre(s). Gücer and Gurland (1962) developed a model for ‘dispersed fracture’ as a chain of elements, each of them considered a fibre bundle. Recently, a number of generalizations of the classical fibre bundle model have been suggested, which take into account the roles of the matrix and interfaces, the non-linear behaviour of the fibres and the matrix, and the real micromechanisms of composite failure. Among these, one can mention in particular the continuous damage fibre bundle model (CDFBM), as well as versions of this model which consider creep rupture, fibre plasticity, and interfacial failure (Kun *et al.*, 2000; Raischel *et al.*, 2006).

For off-axis or transverse loading, the problem of material toughening by crack bridging fibres gains importance. In the cracked composite with bridging fibres, the fibre–matrix bonding (frictional bonding or chemical bonding) determines the fracture resistance of the composite. The classical **fracture mechanics based model of matrix cracking** was developed by Aveston, Cooper and Kelly in 1971. Assuming that the fibres are held in the matrix only by frictional stresses, Aveston and his colleagues carried out an analysis of the energy changes in a composite due to matrix cracking. On the basis of this energy analysis, they obtained the conditions for matrix cracking in composites. Marshall, Cox and Evans (1985) and Marshall and Cox (1987) used a stress intensity approach to determine the matrix cracking stress in composites. In this approach, the bridging fibres were represented by the traction forces connecting the fibres through the crack. The matrix cracking stress was determined by equating the composite stress intensity factor, defined through the distribution of closure pressure on the crack

surface, to the critical matrix stress intensity factor. Budiansky, Hutchinson and Evans (1986) considered the propagation of steady-state matrix cracks in composites, and generalized some results of the Aveston–Cooper–Kelly theory, including the results for the initial matrix stresses, taking into account the frictional energy and the potential energy changes due to the crack extension. They determined the matrix cracking stress for composites with unbonded (frictionally constrained and slipping) and initially bonded, debonding fibres.

In several works, continuum models of a bridged matrix crack are used (e.g. McCartney, 1987). In these models, the effect of fibres on the crack faces is smoothed over the crack length and modelled by the continuous distribution of tractions, which act on the crack faces. The relationships between the crack bridging stresses and the crack opening displacement (bridging laws) are used to describe the effect of fibres on the crack propagation.

A number of models of degradation of fibre-reinforced composites are based on the methods of **continuum damage mechanics (CDM)** (Hild *et al.*, 1994, 1996; Burr *et al.*, 1997; Megnisi *et al.*, 2004). In continuum damage mechanics, the influence of many microcracks on the material behaviour is modelled as a tensor characterizing the reduced effective areas of a material. The advantages of the CDM approach for the modelling of fibre-reinforced composites include rather simple definitions of damage variables in the unidirectional materials, and, consequently, the straightforwardness of its application.

In the framework of analytical micromechanics of materials, the relationships between the volume content, shape and orientation of any reinforcement and the mechanical properties of materials are established using the variational principles of mechanics of materials and other continuum mechanics methods. These relationships allow the effect of the material structure, the reinforcement geometry and the distribution of the elastic properties of the composites to be studied. They range from the simplest rule-of-mixtures formula to the variational principles for non-linear elasticity of materials (Hashin and Shtrikman ,1962a, 1962b, 1963), to complex composite cylinder assemblage (Hashin and Rosen, 1964), self-consistent models (Mori and Tanaka, 1973; Christensen and Lo, 1979), transformation field analysis (TFA) (Dvorak, 1992) and the method of cells (MOC) (Aboudi, 1989, 1999).

Generally, analytical models permit analysis of the interaction between the main damage modes in composites in cases of simple regular microstructures with elastic phases and simple loading conditions. It is difficult to extend these methods to complex effects, such as non-linear material behaviour, evolving microstructures, etc.

9.2.2 Compressive loading

The compressive strength of composites is often considerably lower than their tensile strength (compressive strength is about 60–80% of tensile strength for glass fibre-reinforced composites, and about 40–70% of tensile strength for carbon fibre-reinforced composites).

The failure mechanisms of unidirectional composites under compressive loading differ greatly from those under tensile loading. In many composites, kinking is the dominant compression failure mechanism (Moran and Shih, 1998).

A series of investigations into the first stage of the kinking mechanism, incipient kinking (microbuckling of fibres, caused by imperfections of microstructures and matrix shears), has been carried out with the use of the analytical methods of theories of elasticity and, later, plasticity. Sadowsky *et al.* (1967) considered a long fibre in an infinitely large volume of elastic matrix under compression for the case of low volume content of fibres. Taking into account equilibrium equations, they derived a formula for the critical compressive force which led to the fibre buckling. Rosen (1964) and Schuerch (1966) considered buckling of fibres due to elastic instabilities, and recognized two buckling modes: the shear (in-phase) and extension (out-of-phase) modes. In their models, fibres and matrix were considered as layers, rather than cylinders embedded into a medium. The in-phase failure takes place at high concentrations of stiff fibres, while the out-of-phase mechanism is observed at low concentrations. Using the elastic microbuckling analysis, Rosen and Schuerch derived formulas for composite failure stress for these failure modes.

Budiansky and Fleck (1993) considered the compressive kinking of elastic fibres, taking into account the plastic strain hardening in the matrix, as well as combined compression and shear loading. They derived analytical formulas for kinking stress as a function of the parameters of the Ramberg–Osgood constitutive law for the matrix, and studied the effects of these parameters, kink band inclinations, etc., on the kinking stress.

A number of further models for the buckling and kinking stresses have been proposed, which take into account additional aspects of the fibre kinking, e.g. a model of stress evolution and waviness effects in carbon fibre composite based on the classical beam theory (Effendi *et al.*, 1995), a model of the kink band formation based on Rice's theory of the localization of plastic deformation (Christoffersen and Jensen, 1996; Jensen, 1999), a unit cell model of a composite as a 2-D periodic array of imperfect fibres with sinusoidal imperfections (Kiryakides *et al.*, 1995), and a Timoshenko shear deformation beam model of microbuckling by Niu and Talreja (2000).

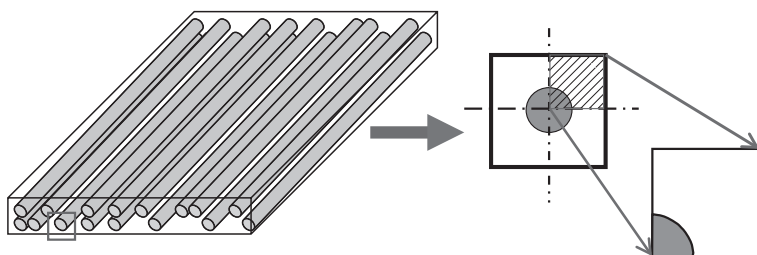
The later stages of kinking, the propagation and broadening of kink bands, have been modelled with the use of fracture mechanics methods, e.g. a cohesive zone model of microbuckle growth (Soutis *et al.*, 1991); a model of microbuckle propagation in carbon fibre-epoxy composites as mode II (for in-plane microbuckles) and mode I (out-of-plane microbuckles) cracking by Sutcliffe and Fleck (1994), and a size effect model by Bažant and colleagues (1999). In some works, micromechanical (finite element) models of microbuckling were used (Sutcliffe *et al.*, 1966; Sutcliffe and Fleck, 1997; Hsu *et al.*, 1999).

9.3 Unit cell modelling of fibre-reinforced composites

The analytical estimation of the mechanical properties of composites is a non-trivial problem even in the case of linear-elastic components and relatively simple microstructures. Therefore, the generalization of the analytical estimations and bounds to complex microstructures and non-linear phase behaviour presents an even bigger challenge for specialists. In such complex cases, the interrelationships between microstructures and the strength and other properties of composites can be analysed with the use of discretized numerical models, which incorporate discrete, real or generic microstructures of materials.

For the analysis of the microstructure–property relationships of wind turbine blade materials, considering in particular complex loading and initial and evolving microstructures (e.g. damage), numerical micromechanical methods are applied. Most often, the problems are solved using the finite element method, in which the solutions of integral and differential equations describing the material deformation and microstructure evolution are obtained on the basis of discretization of the considered bodies and discrete approximations of the equations. Böhm (1998) classified the theoretical approaches to the analysis of discrete microstructures as follows:

- Periodic microfield approach (PMA) or unit cell (UC) methods: assuming the periodic phase arrangement, analysis is performed on a repeating unit cell in the microstructure.
- Embedded cell approach: a material is represented as a cut-out (unit cell) with a real microstructure and embedded into a region of the material with averaged properties.
- ‘Windowing’ approach: microstructure samples, chosen using ‘mesoscale test windows’ and randomly placed in a heterogeneous material, are subjected to homogeneous boundary conditions; by averaging the results for several ‘windows’, bounds for the overall behaviour of the material can be obtained (Nemat-Nasser and Hori, 1993).
- Modelling of the full microstructure of a sample.



9.1 Plane strain unit cell model of a fibre-reinforced composite.
(Source: Reprinted from Mishnaevsky Jr., 2007, with kind permission of John Wiley and Sons.)

Of these approaches, unit cell methods are the most widely used in the micromechanics of materials. In fact, fibre-reinforced composites (FRC) subjected to transverse loading constitute the simplest subject materials for the numerical unit cell analysis of the mechanical behaviour of materials. The statistical periodicity of the fibre arrangement is apparent, and the problem is simply reduced to the 2-D version (see Fig. 9.1). The most widely used 2-D unit cells for unidirectional fibre-reinforced composites are designed on the basis of the assumed square or hexagonal arrangement of fibres. When designing unit cells, the symmetries of the model geometry should be taken into account to determine the minimized, but representative, unit cells.

However, in real cases, fibres are not arranged on an ideal square lattice, but are arranged randomly. In order to include this in the models, different versions of the unit cell model have been suggested, such as the off-centre fibre unit cell (perturbing periodic array) for composites with non-strict regularity of the fibre arrangement (Böhm and Rammerstorfer, 1993).

Unit cell models of materials can also be used to analyse damage initiation and evolution in materials. Unit cells with damaged elements, such as broken or debonded inclusion (Michel, 1993; Mozhev and Kozhevnikova, 1996, 1997), have been used to analyse the effect of microcracks on the mechanical behaviour of composites.

The analysis of the interaction between reinforcing inclusions in materials under loading is possible in the framework of multi-inclusion unit cells (see Segurado *et al.*, 2003; Mishnaevsky Jr., 2004; etc). In these models, an assumption as to the regular arrangement of groups of fibres or particles, rather than the regular arrangement of single reinforcing elements, is made. This version of the unit cell approach allows the simulation of more realistic distributions of particles or fibres than the traditional single element unit cell models do. In the works mentioned above, González and LLorca (2006) developed a multiscale 3-D FE model of fracture in composites.

Some boundary effects can be observed in unit cells, due to the fact that the load is applied to the cell (periodic element) instead of the whole sample. In order to exclude boundary effects in the vicinity of the loading points of the cells, and to take into account the interaction between the cut-out of microstructure and the rest of the material, the embedded cell approach is used. In this approach, a unit cell is embedded into a volume of the material with effective properties. The properties of the embedding can be determined experimentally, or by using the homogenization methods (averaging, self-consistent procedures). Axelsen (1995) and Axelsen and Pyrz (1995) developed a unit cell model of a fibre-reinforced composite that consists of a sample area (with different types of random distributions of fibres) and a boundary area. The boundary area interacts with the sample area, and its size is determined on the basis of 'zone of influence' calculations.

On the basis of the above review, it can be concluded that the main approaches used in the analysis of the strength and damage of fibre-reinforced composites are based on the shear lag model and the fibre bundle model, as well as unit cell models. When analysing the strength, damage and fracture of fibre-reinforced composites a number of challenges have to be overcome, among them the problem of the correct representation of the load transfer and redistribution between fibres and matrix, the need to take into account the interaction between multiple fibre cracks, matrix, and interface cracks, and the difficulty in correctly modelling the interface bonding mechanisms and their effects on the composite behaviour.

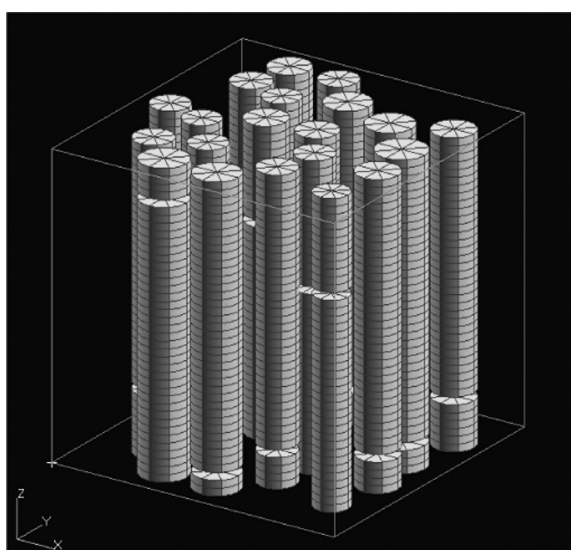
9.4 Three-dimensional modelling of composite degradation under tensile loading

One of the ways to analyse and predict the performance of materials for use in wind turbines is to carry out the 'virtual testing' of different microstructures, using micro- and meso-mechanical models of the materials. The concept of optimal choice of materials on the basis of the numerical testing of microstructures can be realized if a series of numerical experiments for different materials and microstructures can be carried out automatically, quickly and in a systematic way. This can be done, provided the labour costs for the numerical experiments, a significant part of which are the costs of the generation of micromechanical models, are kept very low.

To solve this problem a series of programs has been developed, which should automate the process of generating 3-D microstructural models of materials. After a 3-D microstructural model of a material with a complex microstructure has been generated, the numerical testing of the microstructure is carried out with the use of commercial finite element software.

One such program code, 'Meso3DFiber' (Mishnaevsky Jr. and Brøndsted, 2009b), written in Compaq Visual Fortran, generates a command file for the

commercial software MSC/PATRAN. The parameters of the model (volume content and number of fibres, probabilistic/constant distributions of fibre radii, availability of interphase, etc.) are introduced interactively. The fibres in the unit cells are placed randomly in X and Y directions, using the random number generator. The command file is played with PATRAN, and a 3-D microstructural (unit cell) model of the composite with pre-defined parameters is generated. In order to model the fibre cracking, damageable layers are introduced in several sections of fibres. The random arrangement of the potential failure planes in this case reflects the statistical variability of the fibre properties. These layers have the same mechanical properties as the fibres (except that they are damageable). A similar concept was used to simulate the interface cracking of composites. The interface was represented as a ‘third (interphase) material layer’ between the homogeneous fibre and matrix materials. The damage evolution in the damageable layers, placed in random sections of fibres as well as in the matrix and interphase layers, was modelled using the finite element weakening method (Mishnaevsky Jr., 2007), in which the stiffness of finite elements is reduced if a stress or a damage parameter in the element, or a nodal point, exceeds some critical level. This approach has been realized in the ABAQUS subroutine User Defined Field. Figure 9.2 shows an example of the FE models generated in simulations with 20 fibres and layers of potential fracturing removed. Another program capable of generating unit cells in simulations with a high volume



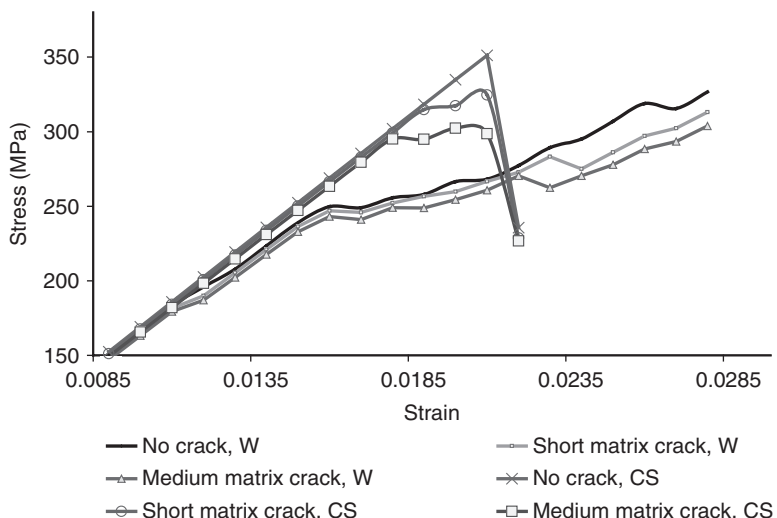
9.2 An example of a 3-D FE micromechanical model. (*Source:* Reprinted from Mishnaevsky Jr. and Brøndsted, 2009b, with kind permission of Elsevier.)

content of fibres and up to hundreds of fibres was developed by Qing and Mishnaevsky Jr. (2009a).

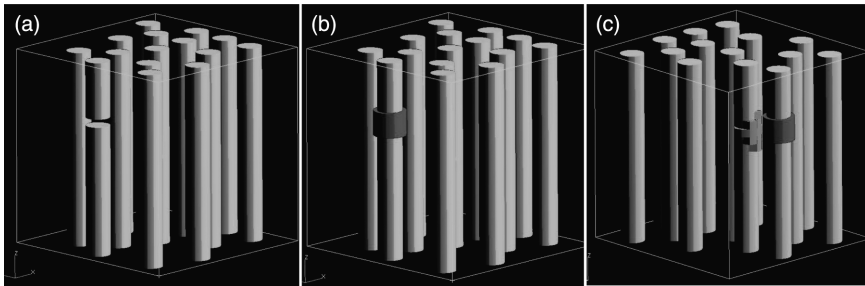
A number of three-dimensional multifibre unit cells were generated automatically using these programs and subjected to a uniaxial tensile displacement loading along the axis of fibres. In one series of simulations, using ABAQUS/Standard, the stress-strain curves and the damage-strain curves were obtained as output results, as well as the stress and strain and damaged element distributions in the unit cells. The properties of the phases used in these simulations are given in Mishnaevsky Jr. and Brøndsted (2009b).

In order to analyse the effects of the variability of fibre properties on the damage in composites, the deformation and damage in unit cells with fibres of randomly distributed (Weibull) strengths and in unit cells with fibres of constant strength, assuming a very strong fibre-matrix interface bonding, were also simulated. The parameters of the Weibull distribution of fibre strengths were $\sigma_0 = 1649$ MPa and $m = 3.09$. For the case of the constant fibre strength, the strength value was calculated as a mean value of the Weibull distribution, using the formula: $\sigma_{av} = \sigma_0 \Gamma(1 + 1/m) = 1474$ MPa.

The stress-strain curves are shown in Fig. 9.3. On the basis of the simulations it was concluded that homogeneous fibres lead to a stronger composite at pre-critical loads. However, fibres with randomly distributed strengths lead to higher strength composites at post-critical loads, i.e. after the fibre cracking has begun.



9.3 Stress-strain curves of the unit cells with random (Weibull: W) and constant fibre strengths (CS). (Source: Reprinted from Mishnaevsky Jr. and Brøndsted, 2009b, with kind permission of Elsevier.)

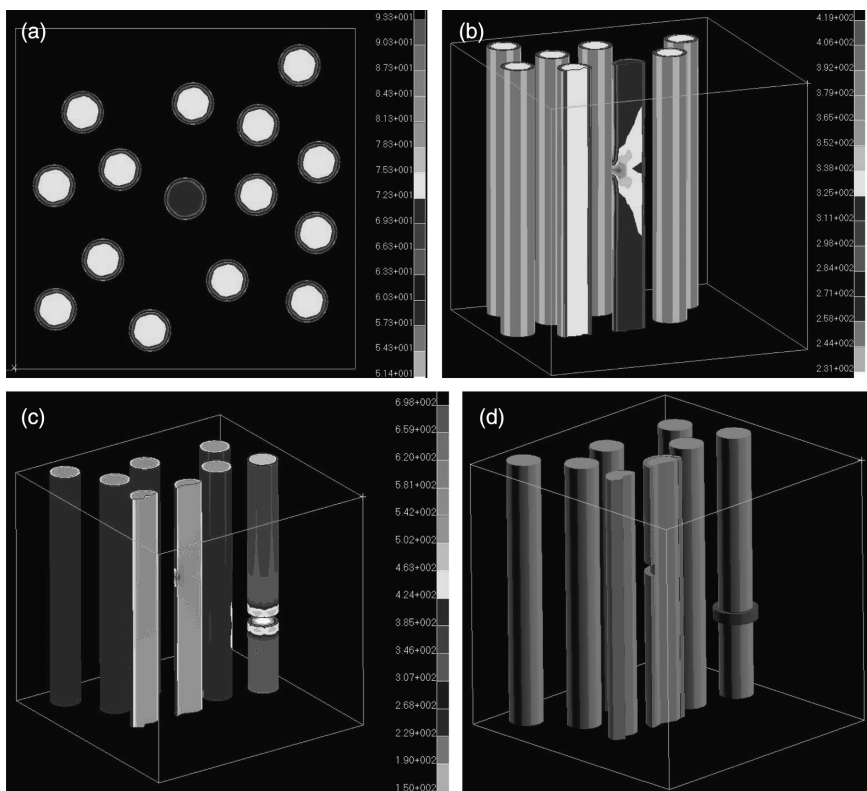


9.4 Damage evolution in a composite with damageable interface and fibres, and strong matrix: (a) Fibre cracking, $\varepsilon = 7\text{e}^{-3}$, ε – applied strain, (b) Interface damage near the fibre crack, $\varepsilon = 7.2\text{e}^{-3}$, (c) Interface damage near the neighbouring fibre, $\varepsilon = 9.4\ldots 9.8\text{e}^{-3}$. (Source: Reprinted from Mishnaevsky Jr. and Brøndsted, 2009b, with kind permission of Elsevier.)

Figure 9.4 shows the damage evolution in the composite with strong matrix, and damageable interfaces and fibers. One can see that the interface crack forms near the fiber cracks, and is triggered by fiber cracking. Using the developed model, one can analyse the effect of the damaged interface on fibre cracking in the composite. A half-circular interface microcrack was introduced into an interface layer in a unit cell model with 15 fibres (Fig. 9.5). The unit cell with the microdamaged interface was subjected to tensile loading. The critical stress in the interface was assumed to be 770 MPa. Some results from the simulation are shown in Fig. 9.5. It is of interest that the damaged interface leads to a slightly lower stress level in the corresponding fibre: while the stresses in the vicinity of the interface crack are rather high, the far-field stresses in the fibre are lower than those in the fibres with undamaged interfaces. As a result, it is not the fibre with the damaged interface that fails first, but another fibre. Further, it can be seen from Figure 9.5 that the fibre crack (which took place not in the fibre with the damaged interface, but in another fibre) leads to the interface damage just around the fibre crack.

The interaction between all three damage modes (matrix cracks, interface damage and fibre fracture) in composites can now be considered. Figure 9.6 shows the results of simulations in a unit cell with 20 fibres, analysing damage formation in the fibres, interface and matrix. The damage evolution begins with formation of a crack in a fibre and (in another, rather distant, site) in the matrix ($\varepsilon = 0.01$). Then the interface crack forms close to the fibre crack, and the large matrix crack is formed ($\varepsilon = 0.015$). Figure 9.7 shows the damage–strain curves for this case.

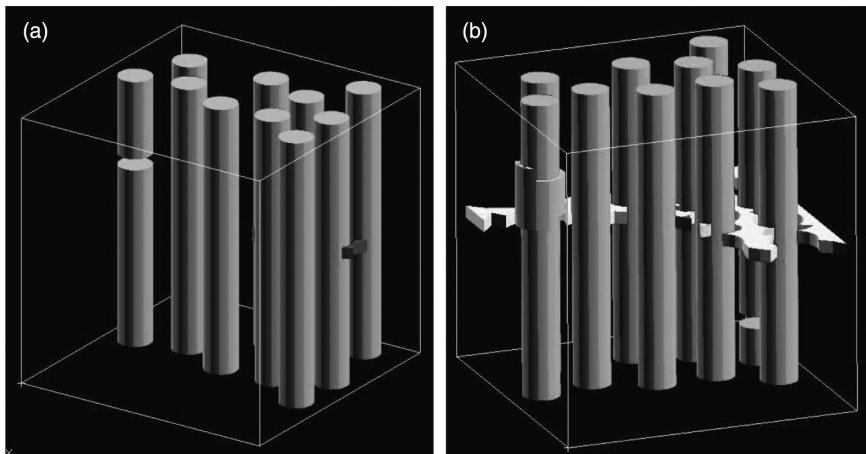
It is of interest that in this case, in which all three damage mechanisms are possible, the competition between the matrix cracking and the interface debonding can be observed. In the area in which the interface is damaged, no matrix crack forms; conversely, in the area in which the long matrix



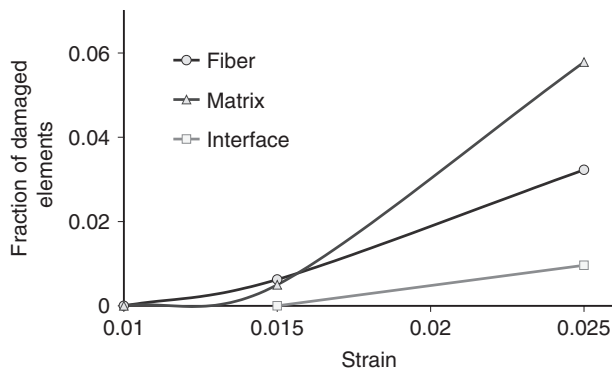
9.5 Stress distribution in the unit cell with microdamaged interface: the Mises stress distribution in a horizontal section of the cell (a), in a vertical section of the fibres with intact and damaged interface layers before (b) and after (c) first fibre cracking, and the formation of interface cracks in the unit cell (d). (Source: Reprinted from Mishnaevsky Jr. and Brøndsted, 2009b, with kind permission of Elsevier.)

crack is formed, the fibre cracking does not lead to the interface damage. One can conclude that local weak places in composite interfaces can be rather beneficial for the strength and toughness of the composite: they can prevent matrix failure (by channelling the fracture energy into interface defects), and can even delay fibre failure. Practically, this means that a heterogeneous interface (an interface with both weak and strong regions) can prevent matrix failure and therefore ensure the integrity of the material.

In this section it has been demonstrated that micromechanical models can be used to identify the microstructural features responsible for damage mechanisms and modes in composites, and to analyse possible sources of improvement for composite materials that are currently used or that could be used in the manufacture of wind turbine blades.



9.6 Competition of damage modes: (a) one failed fibre and a few microcracks in the matrix, $\varepsilon = 0.01$, and (b) two fibres have failed, the interface crack is formed in the vicinity of a fibre crack and the matrix crack is formed ($\varepsilon = 0.015$). (Source: Reprinted from Mishnaevsky Jr. and Brøndsted, 2009b, with kind permission of Elsevier.)



9.7 Damage-strain curves for the case of three acting damage mechanisms. (Source: Reprinted from Mishnaevsky Jr. and Brøndsted, 2009b, with kind permission of Elsevier)

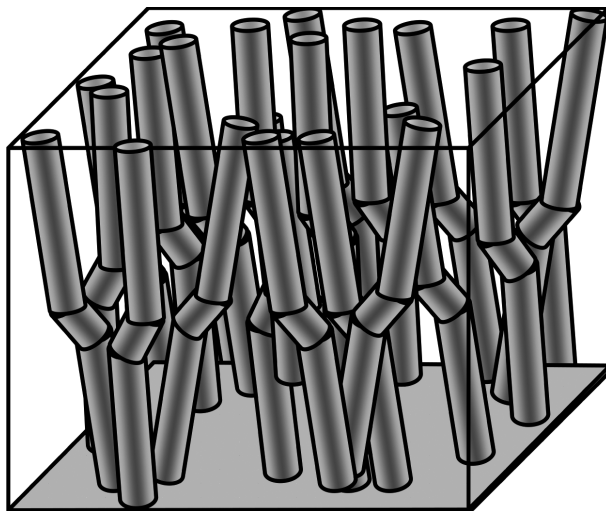
9.5 Carbon fibre-reinforced composites: statistical and compressive loading effects

A very promising alternative to glass fibre composites are carbon fibre-reinforced composites, which have much higher tensile strength and stiffness. However, the compressive strength of carbon composites is significantly lower than their tensile strength. While, under both tensile and compressive

loading, glass fibre composites often fail by cracking, carbon fibre composites demonstrate an additional damage mechanism under compressive loading, namely fibre kinking.

This section investigates the effect of microstructures and the statistical distribution of microstructural parameters of composites on the damage and the compressive and fatigue strength of carbon fibre-reinforced composites under compressive and cyclic loading. It does so by presenting a recently developed computational model of compressive loading of a fibre-reinforced composite with randomly distributed and randomly misaligned fibres. A series of computational experiments in which this model has been used to analyse the effect of microstructures on the compressive and fatigue strength of the composite is discussed.

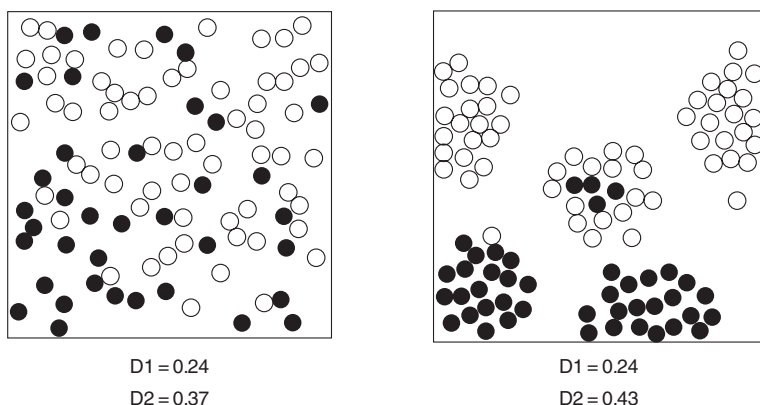
The model is based on the Monte-Carlo method and the Budiansky–Fleck fibre kinking condition (Mishnaevsky Jr. and Brøndsted, 2009b). According to the model, the fibres are randomly arranged in the cell, using the RSA (random sequential absorption) algorithm (Mishnaevsky Jr., 2007). The misalignment angles are assigned to each fibre, using random normal number generator (with truncated Gaussian probability distribution, from -3° to 3°) (Mishnaevsky Jr. and Brøndsted, 2009c). Then, the unit cells are subjected to axial loading (or repeated loadings). For each fibre, the kinking condition is checked, according to the Budiansky–Fleck kinking condition. If one or several fibres kink, the stress is redistributed over the remaining fibres, according to the power load sharing law, thus increasing the load on the remaining fibres, and the likelihood of their kinking. A schema of the multi-fibre unit cell with random misalignments is given in Fig. 9.8.



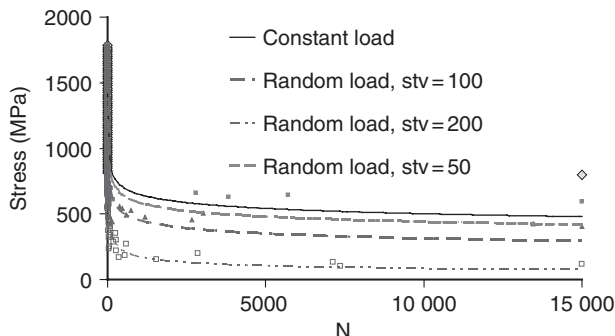
9.8 A schema of the multifibre unit cell with random misalignments.

Two scenarios are considered for the load redistribution after the fibre kinking, depending on the ‘rate’ of the load redistribution: ‘quick’ loading (when the fibres are loaded, and fail independently, and the load redistribution takes place only at the next loading), and ‘slow’ loading (where, after a fibre has failed, the stress on the remaining fibres increases instantly according to the ‘effective stress concept’ and ‘load sharing rule’, and so on for all the fibres, which fail one after another). In the first case (‘quick’ loading), the j -th fibre does not ‘know’ that the i -th fibre has failed until the next cycle of loading. Only in the next cycle is the load redistributed over the remaining fibres. In the latter case, the fibres kink one after another, depending on the misalignment of each fibre. Thus the ‘slow’ loading leads to autocatalytic fibre kinking, caused not by the increase of applied load, but rather by the load redistribution after the fibre begins to kink.

This model can be applied in order, among other things, to analyse the effect of fibre clustering on the compressive strength of composites. This was done in another experiment, in which a clustered fibre arrangement was generated automatically, using the algorithm described by Mishnaevsky Jr. and Brøndsted (2009c). In order to make the clustering effect more visible, the composite was considered to have 20% volume content of fibres. The unit cell models with random and clustered arrangements of fibres were subjected to loadings (‘quick’ loading scheme). In the simulations, it was observed that the fibre clustering had no effect on the damage at the first ‘quick’ loading. However, at the second ‘quick’ loading, the composites with clustered fibre arrangements demonstrated sufficiently higher damage. Figure 9.9 shows the distributions of failed fibres in the case of clustered and



9.9 Distribution of failed fibres in the case of clustered and random homogeneous fibre arrangements. The case of 100 fibres, 5 clusters, volume content (vc) = 20%. D1, D2 = fraction of kinked fibers at first and second loadings. (Source: Reprinted from Mishnaevsky Jr. and Brøndsted, 2009c, with kind permission of Elsevier.)

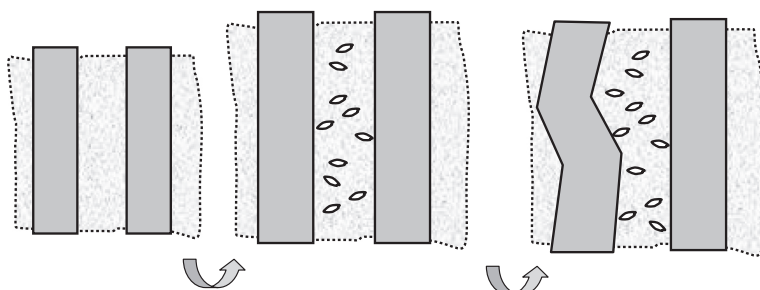


9.10 Random compressive loading: S-N curves for the case of constant stress in each cycle, and for the cases of random loadings with standard deviations of 50, 100 and 200 MPa. (Source: Reprinted from Mishnaevsky Jr. and Brøndsted, 2009c, with kind permission of Elsevier.)

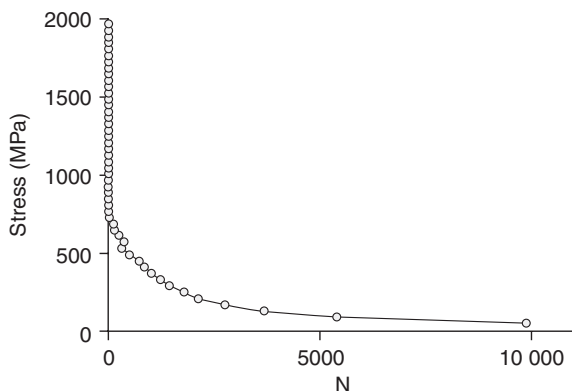
random homogeneous fibre arrangements, for the $N = 100$ (5 clusters), after the second loading cycle. One can see that the clustered fibre arrangement leads to the quicker failure of the composite, due to the effect of the load redistribution. While there might be no difference between the clustered and homogeneous fibre arrangements where the material is not pre-damaged, the clustered arrangement leads to the much quicker failure of fibres at the second loading (or if the material is pre-damaged). For instance, at the compressive stress 1500 MPa, the damage in the composite with clustered fibres is 32.5% higher than in the composite with homogeneously arranged fibres.

A further experiment analysed the effect of cyclic random loading variations on the damage evolution in and the fatigue life of the composite. The unit cells were subjected to cyclic loading, which was random Gaussian value in each loading. Three levels of the standard deviation of the normal distribution of loads (stresses) in each cycle of the loading were considered: 50, 100 and 200 MPa. Figure 9.10 shows the S-N curves (given as trend lines obtained for a number of points) for the three levels of stress variation, and for the case of the constant stress. One can see that the random loading variations lead to the shortening of the fatigue life of the composite. For instance, the stresses at which the lifetime of the composite exceeds 15 000 cycles are 797 MPa for the case of constant stress in each cycle and 594, 406 and 117 MPa for the cases of the random loadings with standard deviations of 50, 100 and 200 MPa, respectively. Thus, even small elements of random loading lead to rather large reductions of the lifetime.

The model can be further generalized to include damage mechanisms other than progressive fibre kinking, for example the assumption that progressive



9.11 Schema: Degradation of the composite matrix leading to the reduction of shear modulus of the matrix and to the fibre kinking. (Source: Reprinted from Mishnaevsky Jr. and Brøndsted, 2009c, with kind permission of Elsevier.)



9.12 Example S-N curves of composite. (Source: Reprinted from Mishnaevsky Jr. and Brøndsted, 2009c, with kind permission of Elsevier.)

damage in the matrix and/or on the fibre–matrix interface is responsible for the slow degradation of the composite properties during undercritical loadings. Figure 9.11 shows the model schematically. In this case, the nanoscale degradation of polymer matrix due to cyclic loading leads to the reduction of the shear modulus of matrix, and, ultimately, to fibre kinking according to the Budiansky–Fleck condition (for the fibres which do not kink according to the condition as long as the matrix is intact). Figure 9.12 shows a typical S-N curve for this case. The simulations were carried out up to 10 000 cycles.

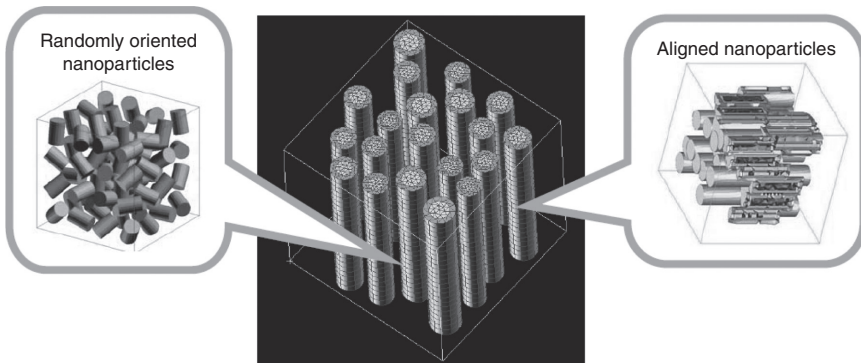
Thus, the use of this computational model of compressive loading of fibre-reinforced composite with randomly distributed misalignments in the experiments and simulations described in this section has demonstrated that

the clustered fibre arrangement in composites leads to the lower failure strength of fibres. For instance, at the compressive stress 1500 MPa, the damage in a composite with clustered fibres is 32.5% higher than in a composite with homogeneously arranged fibres. It has also demonstrated that random loading variations lead to the shortening of the fatigue life of composites.

9.6 Hierarchical composites with nanoengineered matrix

It is known that adding small amounts of nanoparticle reinforcement can lead to the drastic, qualitative improvement of the strength and stiffness of polymers. While nanoparticle reinforced materials were expensive up until a few years ago, prices have now started to fall, and their widespread use can be expected in the near future. And so the question arises: are composites with nanoparticle reinforced components likely to become the wind energy materials of the future? In order to analyse the effect on the strength of composites of nanoparticle distribution in the matrix and in the interface, a computational multiscale model has been developed, which includes the fibre–matrix interaction at the higher scale level (microllevel) and the nanoclay/epoxy–matrix interaction at the nanolevel.

For the simulations at microllevel, the computational unit cell model of the composite consisted of cylindrical fibres, surrounded by interphase/sizing layers and embedded in the matrix. The 3-D unit cells with 20 fibres were generated using the automatic software Meso3DFibre (Wang *et al.*, 2011). The effect of nanoparticle reinforcement (nanoclay) was introduced into the microllevel model via the constitutive laws and the stress–damage curves obtained from the lower level model. The 3-D micromechanical models of a polymer reinforced with nanoclay particles of different shapes were generated using the program code ‘Nanocomp3D’ written in ABAQUS Python Development Environment. The unit cells included nanoparticles of different shapes and orientations, surrounded by multilayered effective interfaces. The term ‘effective interface’ as used here means the interface/interphase layer between the matrix and a particle, reflecting the modified structure of the polymer near the nanoparticles (Odegard *et al.*, 2005). The generalized effective interface model (GEIM), developed by Wang *et al.* (2011), considers the effective interface which consists of several (e.g. two) sublayers, with different properties, and with the stronger layers typically being the outer layers. The effective interface layers (or some of their sublayers) are allowed to overlap, reflecting the fact that the peculiar properties of these regions are caused by modified local atomistic structures, molecular structures or diffusion processes, and do not represent separate phases.



9.13 Multiparticle unit cell of nanoparticle-reinforced composite with effective interface model (Wang *et al.*, 2010).

The overlapping of effective interfaces or sublayers of the effective interfaces was realized using Boolean operations in ABAQUS. Figure 9.13 shows several examples of the 3-D unit cells of nanoclay-reinforced epoxy considered in the simulations. The mechanical properties of the phases are given in Wang *et al.* (2011) with the strengths of the effective interfaces estimated on the basis of Chen *et al.* (2010).

Using the nanolevel model, the tensile stress–strain curves and stress–damage curves for the different shapes and arrangements of the nanoparticles were determined. These data were used as input parameters (material law) in the upper level model, realized as ABAQUS Subroutine User Defined Field. Several cases were considered: spherical nanoparticles in interface layers and in the matrix, horizontally aligned (i.e. normally to the microscale fibre axes) cylindrical nanoparticles in interface layers, randomly oriented nanoparticles in interface layers and in the matrix, etc. In the comparison of hierarchical microstructures with different nanoreinforcement types in the fibre sizing, it was observed that while the horizontal cylinders give a few per cent higher stiffness to the nanoreinforced material, they have a lower failure strain than the round nanoparticles. At the microlevel, this means that the availability of nanoreinforcement and its shape and orientation can potentially change the overall mechanisms of composite failure: from interface debonding controlled (horizontal cylindrical nanoparticles) to fibre controlled (round nanoparticles).

9.7 Conclusions and future trends

This chapter has looked at the ideas, methods and concepts of micromechanical modelling of materials for wind turbine blades. Using the variety of modelling methods reviewed here, one can predict the strength, stiffness

and lifetime of materials, optimizing their microstructures with a view to their improved usability for wind turbines, or comparing the suitability of different groups of materials for wind turbine blade applications.

Some examples of the analysis of microstructural effects on the strength and fatigue life of composites have been shown. The simulations discussed have demonstrated that fibres with constant strengths produce a stronger composite at the pre-critical load, while fibres with randomly distributed strengths lead to a stronger composite at post-critical loads. Competition between matrix cracking and interface debonding was also observed in the described simulations: in the areas with intensive interface cracking, both fibre fracture and matrix cracking are delayed. Conversely, in the area where a long matrix crack is formed, fibre cracking does not lead to interface damage. It has been shown that a clustered fibre arrangement leads to the failure of fibres under lower load. The availability of nanoreinforcement in fibre sizings, and its shape and orientation, can potentially change the overall mechanisms of composite failure: from interface debonding controlled (horizontal cylindrical nanoparticles) to fibre controlled (round nanoparticles).

Nevertheless a lot of challenges still have to be overcome before computational models lead to the design of lightweight, strong and durable materials for wind turbine blades. These challenges include the following:

- **Random effects and defects.** The microstructures of composites are random and contain various defects and shape deviations which can greatly influence the mechanical properties, strength and lifetime of wind turbine blade materials. Even small deviations and irregularities (such as 1 degree misalignment of fibres, clustering of fibres or resin rich regions) can have a very strong effect on the compressive strength and the fatigue lifetime. However, such random effects are difficult to include in the continuum mechanical models of composites, and they require separate analysis.
- **Fatigue effects.** The mechanisms of material deformation and degradation under cyclic loadings are different from those under static loading. For instance, the interface shear effects play a much bigger role under cyclic loading than under static loading. In particular, the material degradation under tension-compression cyclic loading is a rather complex process. The direct transfer of static models onto the cyclic loading case and the modelling of evolving structures require huge computational resources. That is why phenomenological models are now the main tools used for fatigue analysis in composites. Furthermore, the real loading conditions include random multiaxial fatigue, which is also difficult to model in the framework of continuum mechanics damage and fatigue concepts.

- **Moisture and temperature, time dependency and combined effects.** In real service conditions, wind turbine blade materials are subject to varying temperatures and varying moisture conditions, in addition to the cyclic loadings due to rotational and turbulence effects and the extreme loads due to strong winds. These effects interact in different ways. Temperature effects and moisture can enhance damage growth, especially interface debonding and delamination. The damage evolution in composites is also rate dependent (viscous flow in polymer resins, dynamic loading effects under strong wind). To date, the computational modelling of the combined, multifactorial effects, able to take into account the microstructure of materials, has proved a considerable challenge for the micromechanics of wind turbine blade materials.
- **Nanoscale and multiscale effects.** Degradation and damage in wind turbine blade materials are determined by microscale and nanoscale properties. Small additions of nanoreinforcements can drastically change the strength and fatigue properties of composites. However, in order to simulate the nanoscale effects influenced by atomistic and other small scale factors, continuum mechanics and micromechanics methods need to be supported and combined with other, physically-based, methods, such as atomistic and molecular dynamics simulations. Further, the processes of materials degradation are multiscale, and therefore require multiscale methods in order to take into account, say, the interaction between defects on the fibre–matrix scale and the strength of laminates on the ply scale.

Future developments in the micromechanics of wind turbine blade materials should lead to models which are able to cover all of these complex effects – multiaxial random cyclic loading, nanoscale and multiscale effects, thermal and environmental aspects – as well as take into account manufacturing defects and other imperfections of the materials.

9.8 Sources of further information and advice

The ideas, concepts and methods of the mechanics and strength of fibre-reinforced composites have been summarized and explained in several books that are listed in Section 9.10 below: Christensen (1979), Aboudi (1991), Jones (1998), Daniel and Ishai (2005), Malick (2007), Barbero (finite element modelling of composites) (2007). The ideas and methods of the micromechanics of composites and other heterogeneous materials are presented by Buryachenko (mathematical theory) (2007), Mishnaevsky Jr. (2007), Li and Wang (2008), and Schmauder and Mishnaevsky Jr. (2008). However, the computational micromechanics of wind turbine blade composites that considers, not ‘spheric horses in vacuum’ but rather real materials, with local

defects and heterogeneities and subject to random multiaxial cyclic loadings amplified by thermal and environmental effects, is a developing branch of micromechanics. The newest results and developments can be found in composites and computational mechanics journals such as *Composite Science and Technology* and *Computational Materials Science*.

9.9 Acknowledgements

The author gratefully acknowledges the financial support of the Danish Council for Strategic Research through the Sino-Danish collaborative project 'High reliability of large wind turbines via computational micromechanics based enhancement of materials performances' (Ref. no. 10-094539), of the European Community through the 'UpWind' project, and also of the Sino-Danish Committee of Scientific and Technological Collaboration through the '3D Virtual Testing of composites for wind energy applications' project. Furthermore, the author is grateful to the Danish Council for Strategic Research for its support through the Danish Centre for Composite Structures and Materials for Wind Turbines (DCCSM) (contract number 09-067212).

9.10 References

- Aboudi, J. (1989), Micromechanical analysis of composites by the method of cells. *Applied Mechanics Reviews*, **42**, pp. 193–221.
- Aboudi, J. (1991), *Mechanics of Composite Materials*, Elsevier, Amsterdam.
- Aveston, J., Cooper, G.A. and Kelly, A. (1971), Single and multiple fracture, In: *The Properties of Fibre Composites*, IPC Science and Technology Press, Surrey, pp. 15–26.
- Axelsen, M.S. and Pyrz, R. (1995), Microstructural influence on the fracture toughness in transversely loaded unidirectional composites, Proc. 10th Int Conf Composite Materials, Whistler, Canada 1995, Eds. A.Poursartir *et al*, pp. 471–478.
- Axelsen, M.S. (1995), Quantitative description of morphology and microdamages of composite materials, PhD Thesis, Aalborg University.
- Barbero, E. (2007), *Finite Element Analysis of Composite Materials*, CRC Press, New York.
- Beyerlein, I.J. and Phoenix, S. L. (1996), Stress concentrations around multiple fiber breaks in an elastic matrix with local yielding or debonding using quadratic influence superposition. *Journal of the Mechanics and Physics of Solids*, **44**(12), pp. 1997–2039.
- Böhm, H.J. (1998), *A Short Introduction to Basic Aspects of Continuum Micromechanics*, TU Wien, Vienna, pp. 102.
- Böhm, H.J. and Rammerstorfer, F.G. (1993), Micromechanical models for investigating fibre arrangements in MMC's, Proc Int. Seminar Micromechanics of Materials (MECAMAT), Moret-sur-Loigne, France, pp. 383–394.

- Brøndsted, P., Lilholt, H. and Lystrup, A. (2005), Composite materials for wind power turbine blades. *Annual Review Materials Research*, **35**, pp. 505–538.
- Budiansky, B. and Fleck, N.A. (1993), Compressive failure of fibre composites. *Journal of the Mechanics and Physics of Solids*, **41**(1), pp. 183–211.
- Budiansky, B., Hutchinson, J.W. and Evans, A.G. (1986), Matrix fracture in fiber-reinforced ceramics, *Journal of Mechanics and Physics of Solids*, **34**(2), pp. 167–189.
- Budiansky, B. and Fleck, N.A. (1994), Compressive kinking of fibre composites: a topical review. *Applied Mechanics Reviews*, **47**(6), Part 2, pp. S246–S250.
- Burr, A., Hild, F. and Leckie, F. (1997), Continuum description of damage in ceramic-matrix composites. *European Journal of Mechanics A/Solids*, **16**, pp. 53–78.
- Buryachenko, V.A. (2007), *Micromechanics of Heterogeneous Materials*, Springer, Heidelberg.
- Chen, J.K., Wang, G.T., Yu Z.Z., Huang, Z.P. and Mai, Y.W. (2010), Critical particle size for interfacial debonding in polymer/nanoparticle composites. *Composites Science and Technology*, **70**(5), pp. 861–872.
- Cox, H.L. (1952), The elasticity and strength of paper and other fibrous materials. *British Journal of Applied Physics*, **3**, pp. 73–79.
- Christensen, R. M. (1979), *Mechanics of Composite Materials*, Wiley-Interscience, New York.
- Christensen, R.M. and Lo, K.H. (1979), Solution for effective shear properties in three-phase sphere and cylinder models. *Journal of the Mechanics and Physics of Solids*, **27**, pp. 315–330.
- Christoffersen J. and Jensen H.M. (1996), Kink band analysis accounting for the micro-structure of fiber reinforced materials. *Mechanics of Materials*, **24**, pp. 305–315.
- Daniels, H.E. (1945), The statistical theory of the strength of bundles of threads, *Proc. Royal Soc. London*, **183**(A995), pp. 405–435.
- Daniel I.M. and Ishai O. (2005), *Engineering Mechanics of Composite Materials*, Oxford University Press, Oxford.
- Dvorak, G. (1992), Transformation fields analysis of inelastic composite materials, *Proc. Royal Soc. London*, **A437**, pp. 311–327.
- Gonzalez, C. and LLorca, J. (2006), Multiscale modeling of fracture in fiber-reinforced composites. *Acta Materialia*, **54**, pp. 4171–4181.
- Gücer, D.E. and Gurland, J. (1962), Comparison of the statistics of two fracture modes. *Journal of the Mechanics and Physics of Solids*, **10**, pp. 365–373.
- Harlow, D.G. and Phoenix, S.L. (1978), Chain-of-Bundles Probability Model for Strength of Fibrous Materials .1. Analysis and Conjectures. *Journal of Composite Materials*, **12**, pp. 195–214.
- Hashin, Z. and Rosen, B.W. (1964), The elastic moduli of fibre-reinforced materials. *Journal of Applied Mechanics*, **31**, pp. 223–232.
- Hashin, Z. and Shtrikman, S. (1962a), On some variational principles in anisotropic and nonhomogeneous elasticity. *Journal of the Mechanics and Physics of Solids*, **10**, pp. 335–342.
- Hashin, Z. and Shtrikman, S. (1962b), A variational approach to the theory of the elastic behaviour of polycrystals. *Journal of the Mechanics and Physics of Solids*, **10**, pp. 343–352.
- Hashin, Z. and Shtrikman, S. (1963), A variational approach to the theory of the elastic behaviour of multiphase materials. *Journal of the Mechanics and Physics of Solids*, **11**, pp. 127–140.

- Hedgepeth, J.M. (1961), *Stress Concentrations in Filamentary Structures*, NASA TND-882, Langley Research Center.
- Hedgepeth, J.M. and van Dyke, P. (1967), Local stress concentrations in imperfect filamentary composite materials. *Journal of Composite Materials*, **1**, pp. 294–309.
- Hild F., Burr A. and Leckie, F.A. (1994), Fiber breakage and fiber pull-out of fiber-reinforced ceramic-matrix composites. *European journal of mechanics. A. Solids*, **13**(6), pp. 731–749.
- Hild, F., Burr A. and Leckie, F.A. (1996), Matrix cracking and debonding of ceramic-matrix composites, *International Journal of Solids and Structures*, **33**(8), pp. 1209–1220.
- Hsu, S.-Y., Vogler, T.J. and Kyriakides, S. (1999), On the axial propagation of kink bands in fiber composites. Part II: Analysis, *International Journal of Solids Structure*, **36**, pp. 575–595.
- Ibnabdeljalil, M. and Curtin, W.A. (1997a), Strength and reliability of fiber-reinforced composites: Localized load-sharing and associated size effects. *International Journal of Solids and Structures*, **34**(21), pp. 2649–2668.
- Ibnabdeljalil, M. and Curtin, W.A. (1997b), Strength and reliability of notched fiber-reinforced composites, *Acta Materialia*, **45**(9), pp. 3641–3652.
- Jensen, H.M. (1999), Analysis of compressive failure of layered materials by kink band broadening. *International Journal of Solids and Structures*, **36**, pp. 3427–3441.
- Jones, R.M. (1998), *Mechanics of Composite Materials*, Taylor and Francis, Philadelphia.
- Kun, F., Zapperi, S. and Herrmann, H.J. (2000), Damage in fiber bundle models. *European Physical Journal*, **B17**, pp. 269–279.
- Landis, C.M. and McMeeking, R.M. (1999), A shear-lag model for a broken fiber embedded in a composite with a ductile matrix. *Composites Science and Technology*, **59**(3), pp. 447–457.
- Landis, C.M., McGlockton, M.A. and McMeeking, R.M. (1999), An improved shear lag model for broken fibers in composites. *Journal of Composite Materials*, **33**, pp. 667–680.
- Li, S.F. and Wang, G. (2008), *Introduction to Micromechanics and Nanomechanics*, World Scientific, Singapore.
- Mallick, P.K. (2007), *Fiber-Reinforced Composites: Materials, Manufacturing, and Design*, CRC Press, Boca Raton, Florida.
- Marshall, D.B., Cox, B.N. and Evans, A.G. (1985), The mechanics of matrix cracking in brittle-matrix fiber composites. *Acta Metallurgica*, **33**, pp. 2013–2021.
- Marshall, D.B. and Cox, B.N. (1987), Tensile properties of brittle matrix composites: influence of fiber strength. *Acta Metallurgica et Materialia*, **35**, pp. 2607–2619.
- Marshall, D.B. and Cox, B.N. (1987), Tensile properties of brittle matrix composites: influence of fiber strength. *Acta Metallurgica*, **35**, pp. 2607–2619.
- McCartney, L.N. (1987), Mechanics of matrix cracking in brittle-matrix fiber-reinforced composites, *Proc. R. Soc. London, A*, **409**, pp. 329–350.
- Michel, J.C. (1993), A numerical study of the effects of particle cracking and particle debonding on matrix void growth in Al-SiC composites, Proc. International Seminar Micromechanics of Materials (MECAMAT), Moret-sur-Loingne, Editions Euroelles, Paris, pp. 395–405.

- Mishnaevsky Jr. L. (2004), Three-dimensional numerical testing of microstructures of particle reinforced composites. *Acta Materialia*, **52**(14), pp. 4177–4188.
- Mishnaevsky Jr. L. (2007), *Computational Mesomechanics of Composites*, Wiley, Chichester, UK, 280 pp.
- Mishnaevsky Jr. L. and Brøndsted, P. (2009a), Micromechanical modeling of damage and fracture of unidirectional fiber reinforced composites: A review. *Computer Materials Science*, **44**(4), pp. 1351–1359.
- Mishnaevsky Jr. L. and Brøndsted, P. (2009b), Micromechanisms of damage in unidirectional fiber reinforced composites: 3D computational analysis. *Composites Science and Technology*, **69**(7–8), pp. 1036–1044.
- Mishnaevsky Jr. L. and Brøndsted, P. (2009c), Statistical modelling of compression and fatigue damage of unidirectional fiber reinforced composites. *Composites Science and Technology*, **69**(3–4), pp. 477–484.
- Mishnaevsky Jr. L., Freere, P., Sinha, R., Acharya, P., Shrestha, R. and Manandhar, P. (2011), Small wind turbines with timber blades for developing countries: Materials choice, development, installation and experiences, *Renewable Energy*, **36**, pp. 2128–2138.
- Mishnaevsky Jr. L., Brøndsted, P., Nijssen, R.P.L., Lekou D.J. and Philippidis T. P. (2011), Materials of large wind turbine blades: Recent results in testing and modelling. *Wind Energy*, **15**(1), pp. 83–97.
- Moran, P.M. and Shih, C.F. (1998), Kink band formation and band broadening in ductile matrix fiber composites: experiments and analysis. *Int. J. Solids Struct.*, **35**, pp. 1709–1722.
- Mori, T. and Tanaka, K. (1973), Average stress in matrix and average elastic energy of materials with misfitting inclusions. *Acta Metallurgica et Materialia*, **21**, pp. 571–574.
- Mozhev, V.V. and Kozhevnikova, L.L. (1996), Unit cell evolution in structurally damageable particulate-filled elastomeric composites under simple extension. *Journal of Adhesion*, **55**, pp. 209–219.
- Mozhev, V.V. and Kozhevnikova, L.L. (1997), Highly predictive structural cell for particulate polymeric composites. *Journal of Adhesion*, **62**, pp. 169–186.
- Nemat-Nasser, S. and Hori, M. (1993), *Micromechanics: Overall Properties of Heterogeneous Materials*, North-Holland, London.
- Niu, K. and Talreja, R. (2000), Modeling of compressive failure in fiber-reinforced composites. *International Journal of Solids and Structures*, **37**(17), pp. 2405–2428.
- Odegard G. M., Clancy T.C. and Gates T.S. (2005), Modeling of the mechanical properties of nanoparticle/polymer composites. *Polymer*, **46**(2), 553–562.
- Qing H. and Mishnaevsky Jr. L. (2009b), Unidirectional high fiber content composites: Automatic 3D FE model generation and damage simulation, *Computational Materials Science*, **47**(2), pp. 548–555.
- Qing H. and Mishnaevsky Jr. L. (2009c), Moisture-related mechanical properties of softwood: 3D micromechanical modeling. *Computational Materials Science*, **46**(2), pp. 310–320.
- Raischel, F., Kun, F. and Herrmann, H.J. (2006), Failure process of a bundle of plastic fibers, *Physical Review E*, **73**, pp. 066101–066112.
- Rosen, B.W. (1964), Tensile failure of fibrous composites. *AIAA (The American Institute of Aeronautics and Astronautics) Journal*, **2**, pp. 1985–1991.

- Sadowsky, M.A., Pu, S.L. and Hussain, M.A. (1967), Buckling of microfibers, *Journal of Applied Mechanics*, **34**, pp. 1011–1016.
- Sastry, A.M. and Phoenix, S.L. (1993), Load redistribution near non-aligned fibre breaks in a two-dimensional unidirectional composite using break-influence superposition, *Journal of Materials Science Letters*, **12**(20), pp. 1596–1599.
- Schmauder S. and Mishnaevsky Jr. L. (2008), *Micromechanics and Nanosimulation of Metals and Composites*, Springer, Heidelberg, pp. 420.
- Schuerch, H. (1966), Prediction of compressive strength in uniaxial boron fiber-metal matrix composite materials, *AIAA (The American Institute of Aeronautics and Astronautics) Journal*, **4**(1), pp. 102–106.
- Segurado, J. and LLorca, J. (2002), A numerical approximation to the elastic properties of sphere-reinforced composites. *Journal of Mechanics and Physics of Solids*, **50**, pp. 2107–2121.
- Soutis, C., Fleck, N.A. and Smith, P.A. (1991), Failure prediction technique for compression loaded carbon fibre-epoxy laminate with open holes. *Journal of Composite Materials*, **25**(11), pp. 1476–1498.
- Sutcliffe, M.P.F. and Fleck, N.A. (1994), Microbuckle propagation in carbon fibre – epoxy composites. *Acta Metallurgica et Materialia*, **42**(7), pp. 2219–2231.
- Sutcliffe, M.P.F., Fleck, N.A. and Xin, X.J. (1996), Prediction of compressive toughness for fibre composites. *Proc. Royal Soc.*, **452**, 2443–2465.
- Sutcliffe, M.P.F. and Fleck, N.A. (1997), Microbuckle propagation in fibre composites. *Acta Metallurgica et Materialia*, **45**, 921–932.
- Sørensen, B.F. and Kirkegaard, P. (2006), Determination of mixed mode cohesive laws. *Engineering Fracture Mechanics*, **73**, 2642–2661.
- Sørensen, B. F. (2010), Cohesive laws for assessment of materials failure: Theory, experimental methods and application, Dr. Thesis, Risø DTU, Roskilde.
- Wang H. W., Zhou H.W., Mishnaevsky Jr. L., Brøndsted, P. and Wang L.N. (2009), Single fibre and multifibre unit cell analysis of strength and cracking of unidirectional composites. *Computational Materials Science*, **46**(4), pp. 810–820.
- Wang H.W., Zhou, H.W., Peng R.D. and Mishnaevsky Jr. L. (2011), Nanoreinforced polymer composites: 3D FEM modeling with effective interface concept. *Composites Science and Technology*, **71**(7), pp. 980–988.
- Xia, Z., Curtin, W.A. and Peters, P.W.M. (2001), Multiscale modeling of failure in metal matrix composites. *Acta Materialia*, **49**(2), pp. 273–287.
- Zhou, H.W., Mishnaevsky Jr. L., Brøndsted, P., Tan, J. and Gui, L. (2010), SEM in situ laboratory investigations on damage growth in GFRP composite under three-point bending tests. *Chinese Science Bulletin*, **55**(12), 1199–1208.
- Zhou, X.-F. and Wagner, H.D. (1999), Stress concentrations caused by fiber failure in two-dimensional composites. *Composites Science and Technology*, **59**, pp. 1063–1071.

Probabilistic design of wind turbine blades

D. J. LEKOU, Centre for Renewable Energy Sources and Saving (CRES), Greece

DOI: 10.1533/9780857097286.2.325

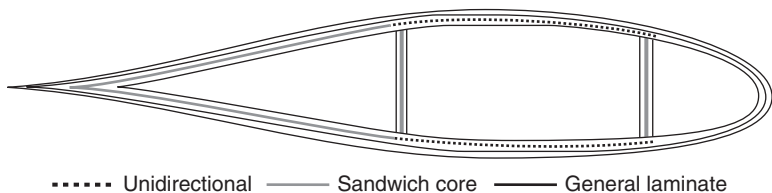
Abstract: The chapter discusses the topic of probabilistic analysis of wind turbine blades. First, structural analysis models, the definition of ‘failure’ and the treatment of random variables will be explored, focusing on the challenges involved in a probabilistic design depending on the choices made during each step. Next, the various probabilistic methods (Monte Carlo method, first-order reliability method, Edgeworth expansion method, response surface method) will be described. Issues arising out of the use of composite material structures, in applications such as wind turbine blades, as well as other aspects relating to wind energy applications will be highlighted, and techniques will be discussed through examples.

Key words: probabilistic design, wind turbine blades, composite material structures, structural reliability methods, aeroelastic tools.

10.1 Introduction

Wind turbine blades are composite material structures designed for safe life (as opposed to being designed according to the fail-safe design philosophy). The operational life of the blades, so as to ensure sustainability of wind energy systems in terms of cost, is 20–30 years. The loading imposed on blades during their operational life is synthesized from various deterministic and stochastic cases that are determined by large variations in load caused by the irregularity of wind speed and direction, fluctuations in turbulence intensity and the effects of site terrain.

Modern wind turbine blades have cross-sections that are usually thin- to thick-walled, multicellular, non-symmetrical heterogeneous constructions of multilayered composite laminates. The typical blade cross-section shown in Fig. 10.1 depicts the location of the unidirectional layers (UD) in the spar caps (which carry the axial loading), the sandwich core (structural foam which prevents local buckling) and the laminates composed of bidirectional layers (which take the shear loading developed on the section). The layout of the materials and the number and the position of shear webs are design



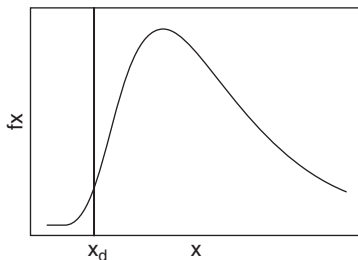
10.1 Typical cross-section of blade.

features and so, if required, additional unidirectional layers with fibres running along the blade length can be placed near the trailing and the leading edges of the section. The same is true for sandwich cores near the leading edge when buckling is anticipated.

For the design of wind turbine blades, international standard IEC 61400–1:2005 is followed. This standard provides a minimum set of specifications regarding wind turbine blade design. More detailed recommendations for the design of blades exist in the form of guidelines from certification bodies, such as GL (Germanischer Lloyd, 2010) and DNV (DNV-DS-J102, 2010), and these are usually followed during structural blade design for items not covered by IEC 61400–1.

A traditional structural analysis, which covers safety assessment in fulfilment of a particular design standard as is commonly required in the case of wind turbine blades, involves a simplified procedure for verifying that the probability of failure of the structure is acceptably small. In such design codes, all problem variables are given only one characteristic value and safety factors are applied to these. The design procedure in such a case consists of three main steps: first, assume that the blade is a beam, second take into account the external loads applied during operation, and last design every section so that no failure will occur. Failure is tested so that every laminate on the section can carry the stress resultants without failure (and of course, checking each laminate means checking each lamina (layer) forming it). The (single) characteristic values for loads and structural properties (e.g. material properties and geometrical properties) are determined as specific quantiles of the respective statistical distributions of the parameters of the problem (see Fig. 10.2).

Structural reliability methods go one step further, using more information, which is incorporated in the statistical distributions such as those shown in Fig. 10.2, so that a more accurate probability of failure is estimated. A reliability analysis is performed following the same steps as above, the only difference being that each parameter of the problem is characterized, not by a single value, but by statistical measures, namely, the parameters of its distribution function (or by the moments of the distribution, i.e. its average and standard deviation, etc.).



10.2 Definition of characteristic values.

In general therefore, for the application of a structural reliability analysis, four steps should be followed (Christensen *et al.*, 1996):

1. Definition of failure model;
2. Definition of design model;
3. Definition of structural reliability estimation model;
4. Estimation of failure probability.

In the first step the failure mode is determined, i.e. the various failure processes of the structure are identified and the basic variables and the failure criteria are set. In the second step the structure is described using the deterministic approach and the design parameters, together with the design functions, are incorporated in the model. In the reliability model, boundary conditions are included and the limit state functions are determined based on the deterministic problem and the statistical distributions of the basic variables of the problem. Based on this, a probabilistic method is then selected for the estimation of the structural reliability.

This chapter will look in closer detail at these steps in the context of the challenges of using probabilistic analysis as a tool to improve the structural design and assess the structural reliability of wind turbine blades. The structural analysis models for wind turbine blades that are used in the numerical simulations, the failure definition used to characterize the acceptable and non-acceptable state of the structure, and the parameters or input variables that are incorporated in the problem and whose variability (or randomness) contributes significantly to the final reliability estimation, will be covered. The focus will be on how the challenges inherent in the probabilistic design of composite material wind turbine blades depend on the choices made during each step of the stochastic simulation.

In the chapter, alternative probabilistic methods, namely the Monte Carlo simulation method, the first-order reliability method, the response surface method and the Edgeworth expansion technique, will also be presented. The various techniques will be addressed through a short review of examples of

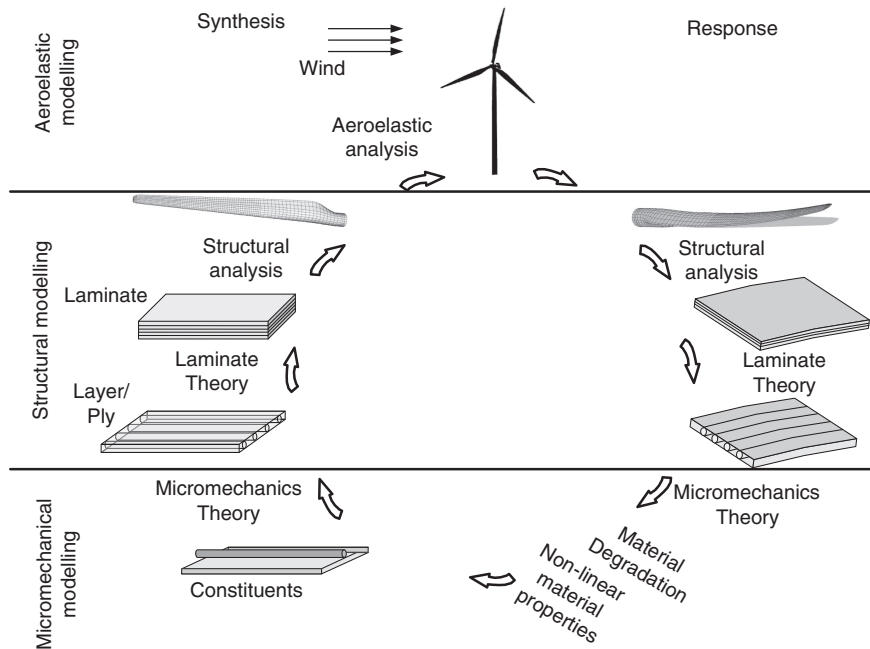
applications that have been selected to show the effects of failure definition, selection of input variables and different choices of methods. Central to the discussions will be an appraisal of the advantages and disadvantages of using stochastic methodologies during the design of the blade. Possible future developments that would increase the range of probabilistic applications for wind turbine blades will also be discussed.

10.1.1 Overview of probabilistic design

The use of probabilistic analysis in the design of wind turbine blades is a relatively new approach, with the first publications appearing during 1999 (see e.g. Braam *et al.*, 1999). The recent works draw together the multidisciplinary advances that had taken place independently during the preceding 50 or 60 years, and embrace issues such as composite materials, their properties and the testing methods applied to them, as well as their modelling and behaviour prediction; wind turbine blades per se, and matters relevant to their testing and modelling; and, finally, probabilistic methods of structural reliability analysis.

A theoretical complete simulation cycle for the structural design of blades, resembling the computational simulation of Chamis (1997), is shown in Fig. 10.3. Supposedly, starting from the microlevel of the composite material constituents – the fibres and the matrix – and using micromechanical models to take into account their probabilistic material properties, one arrives, by simulation, at the properties on the ply level (a ply being a layer in the lamination sequence). On the next level, using classical lamination theory and information on the material layout and the geometric properties of the blade, the blade model is created and analysed. This structural analysis produces information that is required for the aeroelastic modelling of the blade, and of the wind turbine as a system, in which the external loading is introduced through modelling of the wind inflow. Using the output of the aeroelastic analysis the response of the overall structure is predicted, and, again, structural analysis is necessary to decompose the resulting information in order to estimate the response to loading of the individual laminates, and, through laminate theory, the individual plies. Again theoretically, and using micromechanical theory, predicting the stresses acting on and the response of the fibre and the matrix is the next step in the simulation cycle. From there, information on material degradation is fed into the new simulation cycle, and this is repeated until all loads have been analysed. The left side of the cycle as presented can be seen as the synthesis part of the simulation cycle, with the right side representing the analysis part of the cycle.

However, current practice, even in the deterministic approach, far from resembles this theoretical simulation cycle. The micromechanics level is not

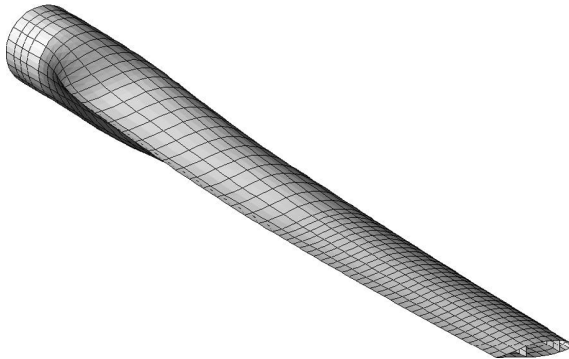


10.3 Full simulation cycle for the structural design of wind turbine blades.

addressed at all, due to reasons that will be explained later in the chapter. Synthesis and analysis of the blade during the design process start and end on the ply level. Current state-of-the-art aeroelastic tools, such as Bladed and Focus (Brood *et al.*, 2010), used for the prediction of loading on the rotor blades but also for the assessment of the whole wind turbine, model the blades using a beam finite element formulation, specially adapted for more accurate predictions of the wind turbine response (see e.g. Jonkman and Bull, 2005; Riziotis *et al.*, 2010). Therefore, information regarding the loading and the response is given in terms of the beam model, and then this information has to be interpreted to allow it to be fed into the structural model of the blade for the purposes of further analysis.

10.2 Structural analysis models

In order to perform a detailed structural design of the blade that examines the internal stress distribution within the blade, a 3-D finite element (FE) model of the blade is necessary (Veers *et al.*, 2003). Such a model comprises thousands of composite shell elements, and typically uses commercial finite element analysis



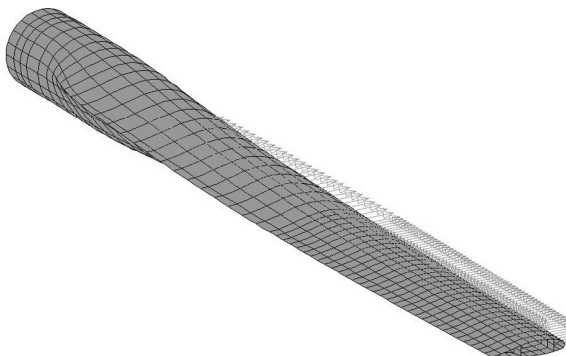
10.4 FE model of a blade.

codes (see e.g. Philippidis *et al.*, 1994; Kong *et al.*, 2005). Elements suitable for modelling thick, layered anisotropic shells are used. In some cases, solid (or brick) elements in combination with shell elements are employed to refine the analysis of the blade (see e.g. Jensen, 2008). An example of such a blade model is shown in Fig. 10.4. The tip of the blade is cut off to allow the modelling of the internal structure to be seen. Modelling usually assumes a rigid connection to the hub by restraining the nodes on the root of the blade.

The level of modelling that is required for the accurate and effective prediction of the response of wind turbine blades to a wide range of wind and operational conditions is still the subject of investigation, especially as regards the local stresses that play a significant role in damage initiation (see e.g. Pardo and Branner, 2005). The details of the various models that make up the full range available falls beyond the scope of this chapter, and so the reader is referred to more focused work, for example the review of Veers *et al.* (2003) or that of Chen *et al.* (2010). However, some of the implications for the blade design simulation cycle and the practice of structural modelling using finite element models that arise from the discussion above do need to be explored here, and in particular load modelling.

Actual mechanical loading on the blade is introduced as a pressure load distributed on the outer shell surface, or through gravitational and centrifugal forces distributed over the length of the blade. As already mentioned, estimations of the blade loading are performed using aeroelastic simulation codes. The relevant output of such simulation codes is a time series of stress resultants for specific sections along the blade length.

Hence, the aeroelastic simulation results have to be converted to allow their application as external loading in the 3-D finite element model of the blade. To this end, a suitable equivalent system is required, which it has been shown can be achieved by modifying the methodology used for the evaluation of the blade strength on the basis of load component distribution during

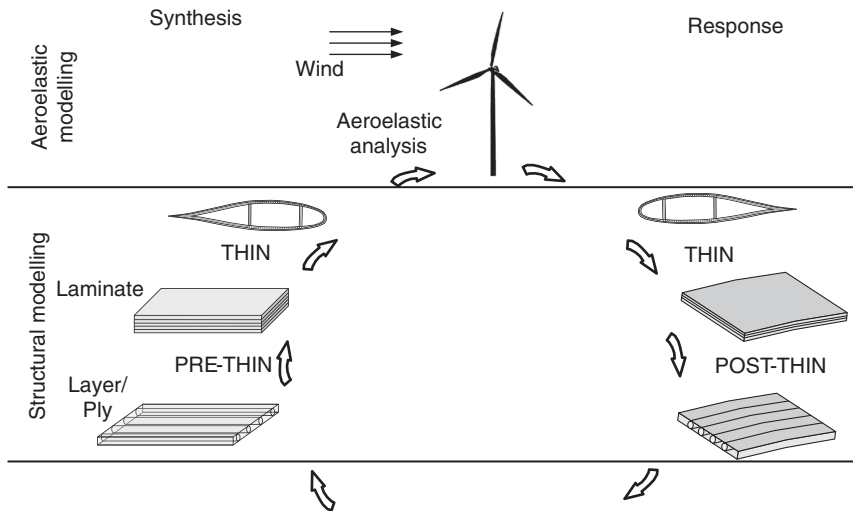


10.5 FE model of a blade with loading condition.

blade testing (IEC/TS 61400–23:2001) (see e.g. Bacharoudis and Philippidis, 2010). An image of the distributed load in the flap and lead lag directions for the blade finite element model is shown in Fig. 10.5. Last sentence of paragraph was changed by production. Please, change back to the original, or accept proposed editing. Nevertheless, the problem remains that application of the concentrated forces on the 3-D shell elements could result in fictitious stress concentrations near the application points or, without adjustment for the torsion value produced, introduction of torsion not predicted by the aeroelastic simulation.

Three-dimensional finite element models, although necessary for the final blade designs, are too costly (Veers *et al.*, 2003) and too detailed (Malcolm and Laird, 2003) for direct use in a system of aeroelastic analysis. At the same time, the size of the blades for multi-MW turbines requires blade designers to consider the structure of the blade earlier in the design process (Veers *et al.*, 2003); therefore, a closer, more effective interaction between the codes performing aeroelastic analysis for the wind turbine system and the tools used for blade structural design is crucial. With the advances in numerical computation capacity, tools based on the deterministic design approach are constantly being developed and improved, for example Focus 6 (Brood *et al.*, 2010).

Nevertheless, due to the increased computational effort required for probabilistic analysis, numerical models that enable detailed calculations on a ply-by-ply basis, simplifying the structural details and therefore reducing the computation effort, are still attractive. Such models include sectional analysis approaches that take advantage of modern aeroelastic codes, but also accurately represent the mechanical properties of the full three-dimensional blade in the one-dimensional beam element of the load estimation using aeroelastic codes. They are also able to perform the necessary detailed strength, stiffness and/or stability assessments after stress resultants for each section have been calculated (see e.g. THIN-PROBEAM described in Philippidis *et al.*, 1996).



10.6 Simulation cycle using THIN and PRE- and POST-THIN modules.

Regardless of whether the structural analysis is conducted using a 3-D finite element model of the blade or a sectional analysis, the procedure for the application of the state-of-the-art tools in a full simulation cycle including aeroelastic analysis tools is as set out in Fig. 10.6. Without loss of generality, the description is based on THIN, with the relevant modules for pre-processing and post-processing, PRE-THIN and POST-THIN, as described in Philippidis *et al.* (1996) for the deterministic approach, and in Lekou and Philippidis (2009) for the probabilistic assessment.

Following Lekou and Philippidis (2009), PRE-THIN is the module in which, using the detailed input for the material properties and the information on the lamination sequences used at each location on the section, the effective properties of each laminate are calculated using the classical lamination theory (CLT) approach. The effective properties calculated for each laminate are used as input to be fed into the main calculation module, THIN. Using the basic processor, THIN, which is based on thin wall beam theory, and taking into account the inhomogeneity and elastic anisotropy of the cross-sectional elements (Philippidis *et al.*, 1996), the effective cross-sectional properties are estimated. These might then be used with aeroelastic tools to model the overall wind turbine system, simulate its behaviour and calculate stress resultants in each blade section. In this procedure, differences are observed between the various available tools. For example, in Malcolm and Laird (2003) a similar methodology is presented using the complete 3-D finite element model of the blade.

The resultant internal axial and shear forces and bending and torsional moments for each selected section are subsequently provided by the

aeroelastic simulation code (for each load case). These are used as input to THIN, to perform the detailed analysis of the section, or to the relevant structural analysis tool, for example Focus 6 (Brood *et al.*, 2010). Then, the stress resultants in the walls of each element composing the inhomogeneous section are post-processed (e.g. POST-THIN module) to estimate the in-plane stress components of each ply in the laminated walls of the inhomogeneous section. Once stress fields for each ply have been obtained, strength assessments are then performed at this elementary level of the blade section.

10.3 Failure definition

According to ISO 2394, during structural design the behaviour of the whole structure or a part of it should be described in terms of a group of limit states, which must not be exceeded if the structure is to satisfy the design specifications. The word ‘failure’ is therefore used according to the general meaning of the word, and describes the inability of the structure to satisfy a specific criterion of a limit state, which could in some cases equate to the global failure of the structure.

For the design of the blade a number of performance constraints are set. Exceeding any of the response limits could be defined as failure, i.e. a non-acceptable condition in the stochastic analysis. For example, to prevent blades hitting the tower, they should not exceed a predefined maximum deformation, usually set at the tip, under any load condition. This condition is connected with the stiffness of the blade and the load conditions during its life, but it could also be the result of progressive failure (leading to stiffness degradation). In addition, the blade should not exceed specific limits set for the natural frequencies of vibrations. This is actually a dynamic response problem under random loading, connected with operational, loading, stiffness and mass parameters. Global and local buckling of the blade is also prohibited, although for local buckling the requirements are more relaxed if the analysis includes strength assessment of the blade for this condition – buckling is stiffness and load related. And finally, there is the strength constraint posed by design rules and standards. This involves both the strength under ultimate loads, and failure due to fatigue loads.

Focus in this chapter is on the latter constraint, i.e. the strength of the blade, which requires special treatment due to the various failure modes observed in composite material structures. To accurately predict failure of the blade, a point-to-point assessment of the strength at any location on the blade is necessary. Such an assessment must use methods of analysis suitable for multilayered composite components and must take into account not only the developed axial normal stresses, i.e. along the blade length, but also the complex in-plane stress field in the principal coordinate system of each ply, together with the associated anisotropy in strength.

10.3.1 Lamina failure probability

In the case of composite material structures, and in particular wind turbine rotor blades, in order to model the failure of the structural element under in-plane static stress condition, the engineer faces a multitude of options regarding the expression of failure, each of which inevitably has a different degree of accuracy. Of the various theories that have been developed over the years, some have found wide acceptance and application in the design of structural elements, while others are not yet experimentally proven, or require a better appreciation of the underlying problem. Even when following the results and recommendations of the World-Wide Failure Exercise (Soden *et al.*, 2004) the designer is advised to implement two theories together to arrive at optimum results regarding failure prediction of unidirectional composite material plies (laminae) under combined loading (Soden *et al.*, 2004), while for the prediction of final strength of multidirectional laminates it was found that none of the 19 theoretical approaches considered in the failure exercise could claim great accuracy (Soden *et al.*, 2004).

In general, the models for predicting the failure of a composite material layer can be divided into (Gibson, 1994):

- micromechanical models, i.e. models that are used for the failure prediction of the layer starting at the fibre–matrix level; and
- macromechanical models, i.e. models that are usually based on the failure description of the medium without getting into details of the fracture at the fibre–matrix level.

The failure phenomena that are developed at the microscopic level are rather complex, which in turn leads to models of equal complexity and of disputable accuracy that are therefore difficult to apply during the design of a structure (Hashin, 1980; Soden *et al.*, 2004). Especially for structural reliability assessments, the difficulties in obtaining experimentally the required statistical information for a micromechanics approach (Sriramula and Chryssanthopoulos, 2009) lead to lack of confidence in the variability predictions at the macroscopic level.

In Orifici *et al.* (2008), the various methodologies for the modelling of composite materials incorporating failure are reviewed. The review discusses not only the various failure criteria but also modelling considerations for specific failure modes, including delamination, as well as damage modelling and damage progression modelling.

For wind turbine blade design specifically, the relevant design guidelines, GL (Germanischer Lloyd, 2010) and DNV-DS-J102 (2010), propose the use of failure criteria at the layer level, differentiating, for composite materials,

between matrix and fibre failure. A recommended failure criterion, which allows the failure mode to be identified, is the Puck criterion (Puck, 1969, 1996; Puck and Schuermann, 1998). Under the Puck criterion for the investigation of the failure of a layer in in-plane stress condition, separate limit state equations for each failure mode have to be checked simultaneously. For the deterministic analysis this can be easily solved. But in a probabilistic analysis, for each failure condition the result will be the probability of failure for each mode. Thus in order to estimate the failure probability of the lamina, a special analysis has to be conducted that considers the various failure modes and their correlation (if any). Furthermore, full usage of the Puck criterion gives the potential for predicting damage evolution, by degradation of the material properties whenever the failure condition for a specific mode is satisfied, especially as regards to inter-fibre failure through the development of matrix cracks.

A compromise at this stage of development of the probabilistic methodologies for the structural design of wind turbine blades is to apply a phenomenological failure criterion, which combines elements from the micromechanical failure analysis in a single function (mathematical expression) and has an acceptable level of experimental verification. An example of such a criterion, which can be written in the form of a failure polynomial tensor (Wu, 1973), is the failure criterion derived by Tsai and Wu (1971) in its general form.

10.3.2 Lamine failure probability

A lamine can be modelled as a system of many components (layers), each one of which is characterized by its own failure function as previously described. Failure of the lamine may in turn be characterized, either by failure of the first ply (FPF), or by total failure, i.e. the successive failure of all layers in the lamine up to the failure of the last ply (LPF). When the lamine is designed so that at the limit state the FPF condition is not exceeded, the aim is to avoid any development of microcracks in the material. Alternatively, when the design is performed so that at the limit state the LPF condition is not exceeded, then the scope is to exploit the material in the best possible way and, therefore, optimize the use of the lamine.

Both design guidelines for wind turbine blades (Germanischer Lloyd, 2010; DNV-DS-J102, 2010) do not allow degradation if fibre failure is predicted, while DNV-DS-J102 suggests further analysis of failure sequences if, however, the failure identified is demonstrated to be non-critical. Thus, a progressive failure analysis for failure sequences involving non-critical inter-fibre failures could be performed. In this case, from a statistical point of view, the composite lamine should be treated as a series system

of parallel subsystems. In other words, each failure sequence represents a parallel system of its basic failure events (i.e. all components in the failure sequence should fail) and the entire laminate failure is the union of the failure sequences (Liu and Mahadevan, 2000).

In deterministic design that uses failure propagation analysis only one failure path is determined; in a probabilistic analysis, however, this approach results in a number of possible failure sequences. The number of possible failure sequences then becomes enormous, even for laminates with less than ten layers (Papazoglou and Sanoudos, 1991). Therefore, the selection of the most relevant failure sequences is required (Papazoglou and Sanoudos, 1991; Liu and Mahadevan, 2000). Furthermore, for the LPF prediction, failure propagation analysis is incorporated; this entails much discussion concerning the appropriate failure criterion and degradation methodology for the prediction of multiaxial laminates (see e.g. Soden *et al.*, 2004). While the most common way of determining the degradation methodology is to verify the assumptions with experimental results, the process of choosing a methodology can lead to greater uncertainty in the reliability estimation.

On the other hand, the FPF approach leads to a conservative estimate of the ultimate failure strength of the laminate. Then again, with the use of a failure criterion such as that developed by Tsai and Wu the damaging effect of matrix cracks on the lamina strength is hidden. Thus, it is assumed that treating the laminate system as a series system will result in a conservative, yet safe approach to the design of composite material blades (Lekou and Philippidis, 2009).

Assuming a series system, the limits for the failure probability of the laminate are (Ang and Tang, 1984):

$$\max_i P_{f_i} \leq P_F \leq 1 - \prod_{i=1}^k (1 - P_{f_i}) \quad [10.1]$$

where P_{f_i} denotes the probability of failure of layer i and P_F the probability of failure of the laminate having k layers.

The range between the upper and the lower limit depends on the number of layers in the laminate and the relative values of their probabilities. For example, if there is a dominant layer failure, the reliability of the system will depend on the probability of failure of this layer, and in some cases it would be appropriate to estimate the probability of failure of the laminate only by the probability of failure of the dominant layer. In such a case, the limits will cover a narrow range. In general, however, the limits will be rather wide, especially if the number of independent failure modes is large. In the case of composite materials, the independent modes of failure are equal to the

number of layers in the laminate if each layer is characterized by its own failure function (as described in the previous section).

If a narrower estimation of the failure probability limits for the laminate is sought, the correlation coefficient between the failures of the layers should be determined. However the correlation coefficient is difficult to estimate, since the degree of correlation of the layer properties in a laminate depends, for example, on the manufacturing procedure of the laminate, the spatial distribution of the fabric properties and the lamination sequence. In particular, for similar layers it can be assumed that the more standardized the manufacturing procedure is, the more positive the correlation of the layer properties will be. Therefore, if the failures of the layers in the laminate are positively correlated, the probability of failure of the laminate is given by:

$$P_F = \max_i P_{f_i} \quad [10.2]$$

If, on the other hand, the failures of the layers can be assumed to be uncorrelated, implying lack of relationship (and therefore correlation) between the material properties of each layer in the lamination sequence, then the more conservative limit of Equation [10.1] should be used instead.

During testing for the determination of the composite material strength properties, specimens of more than one layer are used, depending on the layer thickness. These are then subject to uniaxial loading until the separation of the coupon or until no load increase can be sustained by the specimen. In this case, nevertheless, while a laminate is actually being tested, it is assumed that the laminate properties coincide with the properties of the individual layer. In other words, it is assumed that the properties of all the layers in the lamination sequence are equal. Yet behind this assumption lies the hypothesis that the material properties of the individual layers are fully positively correlated.

10.3.3 Failure probability of the blade section

At the next level of failure analysis the meaning of ‘blade section failure’ should be defined, especially since the subject of the analysis is the failure of a composite material rotor blade, i.e. a multicellular thin-walled heterogeneous section made of fibre-reinforced laminates. Similar to the line of thinking followed for the laminate, the section of the blade is considered as a series system. In other words, failure of any of the elements in the blade section is assumed to result in failure of the section. Moreover, the failures of the elements in the section are assumed to be positively correlated.

Therefore, it is assumed that the failure probability of the section can be approximated by the maximum failure probability estimated in any element (laminated substructure) of the section, supposing that the section is a series system and that a positive correlation exists in the behaviour of the elements in the sequence. This is well supported by the fact that for similar elements a more standardized manufacturing procedure results in a more positive correlation of the element properties.

However, this assumption neglects differences between elements in a section, which depend on the manufacturing method for the whole blade. These might include differences in the section elements of the main spar and in those close to the leading edge or close to the trailing edge of the blade, as well as differences between sandwich constructions and laminates. Particularly in sections on the transition area between the aerodynamic part of the blade and the cylindrical root of the blade, parts close to the leading and trailing edge might be prone to material defects, due to the high curvatures involved.

10.4 Random variables

In a probabilistic design, the uncertainty and variability of all parameters affecting the output of the failure probability should be taken into account. These parameters form the basic variables of the system under investigation, and include but are not limited to the mechanical material properties, the geometry of the structure, the ambient conditions during operation (temperature, relative humidity) and the external loading conditions. The combination of the geometry and the material properties defines the resistance of the structure or the strength of the system. The variables describing the characteristics of the resistance/strength are called the design variables. Some of them (if not all) have a stochastic nature.

Definition of the basic variables means, therefore, the selection of the probability density functions and the estimation of the statistical parameters of the distributions whenever the variables are characterized as stochastic, whether this is the result of a natural variation or the result of the incomplete knowledge we have of them. Both uncertainty sources, i.e. those of the external parameters and those of the internal parameters are grouped into a vector of basic variables. The variations in those variables may be time-dependent. In this chapter, however, the analysis is limited to those states where the uncertainties can be defined independent of time.

The focus in this chapter is on the material properties and the applied loads. The external geometry of the blade is assumed to be controlled during manufacturing, especially since it plays an important role in the aerodynamic performance of the blade as part of the functioning wind turbine. It is true that variability in the internal geometric parameters of the blade is

observed, but this is not treated here. The thickness of the layer and the fibre orientation, which are in essence geometric parameters, are considered as material properties and discussed in the relevant section.

10.4.1 Material properties

According to Germanischer Lloyd (2010) and DNV-DS-J102 (2010), the material properties to be used in the design of a blade should be determined (through experiments) at the layer level. Current methodologies developed for the probabilistic design of blades therefore consider the material properties at the ply level as the necessary input parameters.

Composite materials exhibit inherent variability of mechanical properties mainly due to their inhomogeneous nature and the methods used in their manufacture. Previous studies, for example Lekou and Philippidis (2008) and Lekou and Philippidis (2006), have underlined the importance of incorporating not only the variability in strength properties, but also the variability in elastic material properties in the probabilistic analysis of composite material structures.

For the statistical characterization of the variability in the material parameters experimental databases are used, which contain information not only for the strength properties of the orthotropic media but also for the relevant elastic properties (see e.g. Philippidis *et al.*, 2006, 2010; Lekou and Philippidis, 2008; Philippidis *et al.*, 2010). For the characterization of the random variables, the experimental data should be statistically analysed. This analysis includes estimation of descriptive statistics for the different samples, calculation of empirical distributions, and parameter estimation of statistical model distributions (Weibull, Lognormal, Normal, etc.), using methods such as the method of moments or the maximum likelihood. Hypothesis testing follows the analysis using statistical tests such as Kolmogorov–Smirnov and Anderson–Darling to assess the goodness of fit to the corresponding empirical distribution.

The material properties at the layer level are usually assumed to be uncorrelated random variables. The origin of this assumption is twofold. First, if these were correlated, it would mean that the engineering assumptions regarding the response of the layer would be inconsistent, since the five strength properties and the four elastic properties of the orthotropic medium are considered as independent and experiments are required for their determination. Second, if they were assumed to be correlated, then assumptions as to their correlation should be made. Without experimental verification, however, the uncertainty of the final results would be increased.

Obviously the spatial distribution of the material properties of a wind turbine blade should be taken into consideration when employing probabilistic

methodologies. This has to be done at two levels: at the ply level, since the manufacturing process of composite materials results in differences in material properties over an area, as well as at the level of the blade, due to the non-uniform structure of the blade. However, the discussion on the length of the correlation and the distributions used to represent the stochastic field, even for a single ply, is ongoing (see e.g. Charmpis *et al.*, 2007), since there are no experimental verifications for the properties.

The thickness of the layer could also be treated as a stochastic variable; but care should be taken, since the thickness of the layer depends on the fibre volume fraction, which in turn affects the properties of the layer. Therefore the material (layer) properties, especially those driven by the matrix properties, are correlated to the thickness of the layer. To overcome this, during the design of the blades, the nominal thickness of the plies is usually used and material properties are scaled to this.

A further point is that, although the determination of the material properties at the ply level through experiments is thought to be a straightforward procedure, this is not actually the case, especially for properties in compression and shear (see e.g. Broendsted *et al.*, 2005; MIL-HDBK-17-1F, 2002).

Addressing the issue of experimental material property determination from a probabilistic point of view, an interesting approach that seems to be a first step towards multiscale reliability evaluation of composites is reported in Shaw *et al.* (2012). In that work, estimation of material properties characteristics, including variability at macroscale, is performed using microscale properties. The results are validated through experimental comparisons.

Finally, the statistical evaluation of the material properties requires the separation of the inherent variability of the material from the experimental measurement uncertainty. To achieve this, some recommend tests on different batches of material (see e.g. HDBK-17-1F, 2002); others propose the linking of macromechanical properties with micromechanical rules (see e.g. Rollet *et al.*, 2009); others again (see e.g. Lekou *et al.*, 2011) suggest the evaluation of measurement uncertainty for these experiments – something which is of particular importance for fatigue properties, where uncertainties are incorporated in the model used for the description of material behaviour under cyclic loading.

10.4.2 Loads

A major task in estimating wind turbine blade reliability is the stochastic modelling of the loading. Substantial research efforts have been directed towards methods for improving load prediction through more efficient representation of the stochastic wind conditions (wind speed, turbulence, etc.) and so for the extreme wind loads (see e.g. Fitzwater and Winterstein, 2001;

Veers and Butterfield, 2001; Peeringa, 2003; Moriarty *et al.*, 2004). Results from this research have been incorporated in the latest edition of the wind turbine design standards, IEC 61400–1 (2005).

As mentioned previously, the loads that are used in the design of a wind turbine and, therefore, a wind turbine blade, are the results of dynamic aeroelastic simulations. The loads are delivered in the form of time series, covering all load cases and conditions prescribed in IEC 61400–1 (2005). Modern aeroelastic analysis tools, for example Bladed, deliver these time series for wind turbine blades as sectional stress resultants, incorporating the effects of aerodynamic, gravitational and inertial loads acting on the blade. Multiple simulations are prescribed in IEC 61400–1 for each loading case, in order to incorporate the variability of wind inflow conditions and also uncertainties arising from the operation of the wind turbine, such as when wind inflow direction and rotor orientation are not the same.

Where ultimate strength analysis or buckling analysis are being performed, the loads can be modelled (using the time series simulation results) by the distribution of the extreme maximum values within a given reference period as simple random variables, making the problem a time invariant reliability problem. Such a procedure is described in Annex F of IEC 61400–1 (2005).

However, as discussed in, for example, Genz *et al.* (2006) and Freudenreich and Argyriadis (2008), the description of the method for load extrapolation given in IEC 61400–1 (2005) was considered to provide insufficient guidance, potentially leading to high uncertainties in results, depending on interpretations, choices of approach and distribution, numbers of simulations and user experience. An amendment to IEC 61400–1 was eventually issued (IEC 61400–1 A1/CDV: 2008).

This amendment (IEC 61400–1 A1/CDV, 2008) also covers the issue of contemporaneous loads, a subject of importance in the design of wind turbine blades, whether a deterministic or a probabilistic approach is used. In the case of deterministic design, there are defined methods for taking into account the contemporaneous nature of load components in each blade section. For a probabilistic approach, however, this has to be extended to take into account the statistical correlation of the sectional load components. The correlation among the six components of the stress resultants (three force and three moment related) at each section of the blade should also be investigated. This was part of a study (Bacharoudis *et al.*, 2011) where it was shown that, for the case under consideration, the axial component had very little correlation with the rest of the load components, while flap, edge and torsion were found to be correlated to varying degrees. This correlation should be taken into account in a reliability analysis, and the relevant information should be fed into structural analysis codes for the estimation of the reliability of the blade.

In the case of structural simulation codes, such as THIN (Lekou and Philippidis, 2009), where a sectional analysis of the blade is performed, this procedure is straightforward. However, if 3-D shell models are used for the stress analysis, a method should be developed for the stochastic representation of the load boundary conditions set on the FE model.

Since the loading of the blade is available in the form of stress resultants for specific sections along the blade length, obtained through aeroelastic simulations of the beam model, these stress resultants have to be properly converted in order to be applied as external loading on the 3-D finite element model of the blade. To this end, an equivalent system is required, which can be realized by modifying the methodology used for the evaluation of the blade strength on the basis of load component distribution during blade testing (see IEC/TS 61400–23, 2001).

Again, as in the case of load components on a blade section, a closer look at the correlation among the loads, this time along the length of the blade, is considered necessary. Thus, following the determination of the statistical distributions for the concentrated loads along the blade length, an evaluation of the correlation between these forces should be performed.

10.5 Probabilistic methods and models

Having accepted the division of structural behaviour into a ‘failure state’ and a ‘safe state’ (or a state of no failure) we can now have a closer look at the methods which can be used for the estimation of the probability of each state. A reliability estimation method is a method for the estimation of the reliability of the structure (i.e. the survival probability) or its complement, the failure probability, P_F .

A general review of probabilistic design methodologies, specifically for composite structures, is found in Gary and Riskalla (1997) and in the more recent work by Chiachio *et al.* (2012). It can be seen that the methodologies differ in terms of their position on the life of the structure (e.g. design, certification, operation), their analysis objectives, their mathematical approach, etc. The progress made in these probabilistic tools, combined with increases in computational power, have resulted in the development of general purpose software for the reliability assessment of structures. Pellissetti and Schueller (2006) review the available software, highlighting the need for the specialized reliability assessment software to work together with finite element analysis software. It is also noted that there are still limitations on the number of random variables that such tools can handle, as well as some limitations on the estimation of very low probability of failures.

Pellissetti and Schueller (2006) conclude that the commercially available software applications for the structural reliability assessment are still difficult to incorporate into the structural design process, where many iterations

are required before the final design. In the following, a short description will be given for each of the widely used probabilistic methods.

10.5.1 Monte Carlo simulation method

The Monte Carlo simulation method is based on the iterative solution of the deterministic problem by generating for every repetition a probable value for each stochastic variable of the problem. Due to its simplicity, the method is valuable for use in the verification of newly developed methods for the prediction of reliability, despite the high numerical effort involved. In a problem involving stochastic variables that follow a specific probability distribution, the Monte Carlo (MC) method comprises the following steps:

- Sample generation for each basic stochastic variable according to the corresponding probability distribution of each variable.
- For each value of the samples, solution of the deterministic problem and determination of the structural response.
- Formation of the response sample using the results of all deterministic iterations.
- Statistical analysis of the response sample.

For a structural reliability assessment under a strength constraint the analysis is simplified, since it is enough to check at each repetition whether the structural element has failed or not. Thus, the probability of failure of the element (where the strength constraint has been defined) is given by:

$$P_{f_i} = \frac{n_{f_i}}{n_{\text{tot}}} \quad [10.3]$$

where n_{f_i} is the number of iterations during simulation where the limit condition function took values indicating failure of the element i , and n_{tot} is the total number of iterations. A rule of thumb for the number of iterations required for the failure probability of the simulated structural system to be deemed accurately predicted is $100/P_F$ where P_F is the expected probability of failure (Bjerager, 1991).

Since a sample of values (responses) produced as a result of the MC simulation is similar to a sample of experimental observations, the method could be regarded as a sampling method, with the results, therefore, being subject to statistical uncertainties. The first step of the MC simulation, i.e. the procedure by which series of numbers are generated, involves the use of a pseudo-random number generator. For accurate results, the algorithms of

random number generators should be verified through statistical tests (Press *et al.*, 1994). Furthermore, the specific algorithm for the generation of the various random variables used in simulation should be tested, together with the pseudo-number generator employed, regardless of the number of tests that the generator passes (Knuth, 1998). This is because, in practical applications, it is rare to need a sample for only one variable. Therefore the samples of a generator are usually split into subgroups, so as to form samples for more than one variable. This procedure, however, results in the alteration of the behaviour of the generator sample regarding randomness (Knuth, 1998). Therefore, statistical tests, such as the tests described in Knuth (1998) and Rubinstein (1981), should also be performed on the subset of random samples.

10.5.2 Edgeworth expansion method

According to the Edgeworth expansion method, an unknown cumulative distribution function of variable x can be approximated by use of a series expansion of the Normal distribution, $\Phi(x)$ in terms of the central moments of x . This is given by (Cramer, 1971):

$$\begin{aligned} F(x) &= \Phi(x) \\ &- \frac{1}{3!} \frac{\mu_3}{\mu_2^{3/2}} \Phi^{(3)}(x) \\ &+ \frac{1}{4!} \left(\frac{\mu_4}{\mu_2^2} - 3 \right) \Phi^{(4)}(x) + \frac{10}{6!} \left(\frac{\mu_3}{\mu_2^{3/2}} \right)^2 \Phi^{(6)}(x) + \dots \end{aligned} \quad [10.4]$$

where, $\Phi^{(n)}(x)$ is the n -th derivative of the normal CDF and μ_i are the central moments of the failure function. Each line of Equation [10.4] represents one term of the series, i.e. the first three terms are shown. Although the approach is asymptotic, according to Cramer (1971) it is not advisable to use terms containing higher moments than the third, or fourth, since these are difficult to obtain by use of small sample sizes. Even though the third- and fourth-order central moments are sensitive to observed outliers, the method should be used with care, especially if a small sample size has been used (less than 200 observations) (Hahn and Shapiro, 1994). In any case, the key aim is to approximate the unknown cumulative distribution function with as few terms as possible. The probability of survival, or reliability, is given by $P_f = F(0) = P(G \leq 0)$ if the failure condition is denoted by G and failure is assumed for $G \leq 0$.

For the estimation of the failure function, the method of moments can be used (Hahn and Shapiro, 1994), with evaluation of derivatives at the mean values of the basic variables. The Edgeworth expansion method is thus formulated in terms of the moments of the failure function, which in turn

are calculated using the moments of the individual strength and elasticity properties, the applied loads, etc., depending on which problem variables are assumed to be stochastic. Therefore the Edgeworth expansion method does not require the definition of a specific statistical distribution of the basic variables, but rather of their statistical moments, which could also be attained experimentally, without the need to fit them in an empirical distribution (e.g. Normal or Weibull distribution). For the final step, the correlations between input variables can be handled through the estimation of the system moments.

10.5.3 First-order reliability method

The first-order reliability method (FORM) has been widely used in structural reliability estimation applications. The method involves Taylor expansion of the failure function, i.e. the linearization of the limit state equation, not performed around the mean value of the function, but at a point that is called the ‘most probable failure point’. The selection of an appropriate linearization point is an important consideration (Ang and Tang, 1984), and actually leads to an iterative solving procedure.

Based on the underlying theory and adopting the method proposed by Hasofer and Lind, the following is a summary of the selection procedure. The process starts with the transformation of the non-normal variables to standard normal variables with zero mean and unit variance (Madsen *et al.*, 1986), using the Rosenblatt transformation (see also Ang and Tang, 1984). The target is to find the most probable failure point, i.e. the point on the failure locus that defines the minimum distance of the limit state surface from the origin in the space of the reduced variables (Shinozuka, 1983). The shortest distance between the failure surface and the origin in the space of the reduced variables is called the reliability index β .

The point on the failure surface that has the minimum distance from the origin can be found by using, for example, the method of Lagrange multipliers (Ang and Tang, 1984), following an iterative procedure. Given that β is now available, the failure probability of the system can be approximated by:

$$P_f = \Phi(-\beta) \quad [10.5]$$

where $\Phi(-\beta)$ is the cumulative distribution of the standard normal variate (Madsen *et al.*, 1986).

For linear failure functions this solution is exact. For non-linear failure functions, as in the case of the failure function of a composite material

layer, the exact calculation of the failure probability or the reliability generally involves mathematical and computational difficulties. Following the reviews by, for example, Eamon *et al.* (2005) and Schueller *et al.* (2004), of various structural reliability methods and their accuracy and effectiveness in solving problems based on the number of random variables and the linearity (or not) of the failure function, FORM can be seen to have limitations for non-linear failure functions having a large number of random variables.

Several algorithms have been proposed for the approximation of the most probable failure point and the β index (see e.g. Ang and Tang, 1984; Madsen *et al.*, 1986). In a comparison between five algorithms that can be used for the approximation of the most probable failure point (Liu and Der Kiureghian, 1991), the general conclusion is that the decision as to which is the most effective algorithm depends on the failure function of interest. Similarly, in Wang and Grandhi (1994) a new search algorithm is proposed for the estimation of the β index, and its application is compared with other widely used algorithms. An iterative algorithm already applied for composite laminates is described in Madsen *et al.* (1986). However, when a limit state function is not unimodal, that is, if there is more than one local minimum, it is not certain that the global minimum will be obtained. In fact the failure function as described in the previous section is multimodal (Miki *et al.*, 1990), and therefore the search algorithm might need modifications. Still, there is no guarantee that the algorithm will converge in all cases, and it is likely that when it is being applied it will produce, for the basic variables, values that are outside of their natural limits (Madsen *et al.*, 1986).

10.5.4 Response surface method

Response surface method (RSM) has a long history and nowadays has many applications in the field of engineering and in structural reliability; it is especially used in combination with finite element models. A probabilistic assessment using commercial finite element software would require solution of the (deterministic) problem through application of Monte Carlo simulations on the basic variables. For cases of 3-D wind turbine blade models, the computational time for a direct Monte Carlo simulation becomes prohibitive. To overcome this problem, an approximation of the actual limit state equation is derived through an estimate of the response surface for the finite element model. Monte Carlo simulation is then used on the response function to estimate the reliability.

For the approximation of the true input–output function, second-order polynomial models are typically used in the form:

$$y = b_0 + \sum_{j=1}^k b_j X_j + \sum_{j=1}^k \sum_{i=1}^k b_{ij} X_i X_j \quad [10.6]$$

where b_0 , b_j and b_{ij} are the regression coefficients with $i, j = 1, 2, \dots, k$ and X_i are the k input variables. For some applications, cross-terms of the quadratic polynomial may be omitted.

The first step for the determination of the regression coefficients is to produce the ‘reference’ output, through selection of the values of the input variables. The procedure is called ‘design of experiment’ (DoE) and provides the appropriate sample points that are used for a limited number (few hundreds) of experiments, i.e. solving repetitions (e.g. finite elements) to fit the regression models. The selection of the proper DoE method depends on many factors which fall out with the scope of the present chapter. However, two methods are commonly used (Reh *et al.*, 2006): the central composite design and the Box–Behnken design. Since the latter has some limitation regarding the number of variables that can be supported, central composite design is more suitable for applications such as probabilistic analysis of composite blades. For the central composite design (Reh *et al.*, 2006) a fractional factorial design is used, since the number of simulations for the full factorial design grows by 2^n , with n being the number of basic variables. This is composed of two axis points per input variable, the factorial points at the corners of the hypercube and one centre point (see e.g. Rajashekhar and Ellingwood, 1993).

Following DoE, simulations are performed and the regression analysis, usually least squares fitting, is implemented to estimate the unknown coefficients of the approximation models. Statistical tests are commonly used afterwards, to validate the regression models. However, since the ‘experiments’ performed in the process of estimating the coefficients of the response surface are actually deterministic computer ‘experiments’, which lack random error, only residual plots and the coefficient of determination can be helpful for validation of the regression model (Simpson *et al.*, 1997; Myers and Montgomery, 2002).

Finally, after the definition of the regression models, the Monte Carlo method needs to be implemented for a significant number of simulations, depending on the expected probability of failure. It should be remembered that the lower the probability of failure the higher the number of simulations. The only difference at this stage between the response surface method combined with Monte Carlo simulation (RSM/MC) and the direct Monte Carlo method is that the stresses or strains are calculated through the regression models instead of through solving the complete finite element or sectional model of the blade, respectively; in this way, the speed of the procedure is increased by a factor of at least four.

10.6 Application examples and discussion of techniques

The application of probability methods in the field of wind turbines, and especially for design of wind turbine blades, is a relatively new development. The need for probabilistic models for both loads and mechanical material properties has become more evident in recent years, as efforts are made to reduce the cost of the structures while maintaining the required reliability. Earlier works addressed the problem of failure of the blade root section due to bending moments developed against fatigue (see e.g. Braam *et al.*, 1999; Veldkamp, 2000), as well as against ultimate loading (see e.g. Ronold and Larsen, 2000). In Ronold and Larsen (2000) the first-order reliability method (see e.g. Madsen *et al.*, 1986) was used for the estimation of reliability in all cases, through the implementation of the commercially available code PROBAN (Tvædt, 2006), while the commercially available code STRUREL (Gollwitzer *et al.*, 2006) has been implemented in FAROW (Winterstein and Veers, 2000), a more general tool for fatigue calculations and reliability estimations of wind turbine components, which focuses on modelling the interaction between the environment, the load response to the environment and the cumulative damage process underlying the lifetime calculation. The applications presented in these earlier works (see e.g. Braam *et al.*, 1999; Ronold and Larsen, 2000; Veldkamp, 2000) were limited to estimating the reliability of the root section of the blade, which is usually symmetrically built, taking into account only the developed stress in the axial direction due to bending in the flap direction, and only the strength in the respective direction of the laminate. However, the root section is not always the critical section of a blade, which is designed for optimized material use throughout the blade length.

Tools developed especially for the probabilistic strength analysis of composite material blades were presented in Lekou and Philippidis (2009) and Bacharoudis *et al.* (2011), with the analysis being based on a sectional model of the blade. Common to these tools is the fact that the probability estimations are conducted by performing a ply-by-ply analysis using the quadratic version of the failure tensor polynomial (Tsai and Wu, 1971), taking into account the heterogeneous configuration of the blade. These studies also considered the effects of the stochastic nature of the anisotropic material properties (both in terms of elasticity and strength), as well as of the loads, on the reliability estimation for the layer and therefore, by extension, for the laminate, the blade section and the overall blade. The response surface method combined with Monte Carlo simulation (RSM/MC) and the Edgeworth expansion technique were assessed and compared with direct Monte Carlo simulation results.

It can be seen that the RSM/MC results predictions are accurate even at very low probabilities of failure at the ply level, while the Edgeworth

expansion results, although following the trend, lack accuracy. This is compensated for by the computational time required for a simulation, with the Edgeworth Expansion method requiring 10 s, the RSM/MC method, 3 h and the direct Monte Carlo method, 13 h – all on the same ordinary PC; with model size and computer characteristics varying greatly, interest lies in the relative time costs. The previously mentioned computational time differences are so, even though, because of the desire to save computational time (finite element simulations) in Bacharoudis *et al.*, 2011, the RSM method has not been used in its classical form as for example in Bucher and Bourgund (1990) and Rajashekhar and Ellingwood (1993), but rather for the derivation of approximate models for the in-plane strains ($\varepsilon_x, \varepsilon_y, \varepsilon_s$) developed at any ply of any element in the blade, since an analytic expression of the state function is available.

On the other hand, the possibility of linking structural design tools to aeroelastic simulation codes was shown in Lekou and Philippidis (2009) and Bacharoudis *et al.* (2011). In the former, the statistical parameters of the elastic properties of the section were presented as an output of the developed tool, which could be directly used in aeroelastic simulations should the variability of the blade's elasticity be taken into account. In the latter, the loads on the section were the output of aeroelastic simulation runs, although a statistical assessment was conducted prior to structural simulation to attain the parameters for the extreme load distribution.

Probabilistic assessment of the blade using three-dimensional finite element models was considered in Bacharoudis and Philippidis (2010), where results were presented using a full 3-D finite element shell model produced by the commercial code ANSYS. Reliability of an actual blade under extreme loading was investigated and, for the purposes of the probabilistic analysis, a procedure to convert the bending moment distribution, obtained from the aeroelastic beam model, to an equivalent system of concentrated forces acting on the 3-D shell finite element blade model, was developed. Additionally, the correlation between loads on the blade sections was investigated, with results revealing that, for the same load component at various sections, such a correlation does exist; however, the magnitude of correlation varies between positions of sections and simulation cases. For the analysis, the response surface method combined with Monte Carlo was employed. Due to ANSYS code limitations on the number of variables that can be dealt with, a special procedure was developed which involved taking ANSYS simulations results and performing a further analysis procedure with a different code outside the ANSYS environment. RSM was performed on the ply strains as described above, and, apart from that, only the results of the upper and lower layer in each lamination configuration were estimated directly through the ANSYS tool. Then, further analysis for the other plies in the sequence was performed through an external FORTRAN routine,

including the required regression analysis, presenting the failure probability of all elements of the full finite element blade model as derived from the results for all the plies in each lamination sequence. Thus, only part of the DoE was completed using the commercial code, indicating the limitations of commercial reliability finite element tools for direct use as a structural design tool for wind turbine blades. The work of Bacharoudis and Philippidis (2010) was recently extended, in Bacharoudis and Philippidis (2012), to the investigation of the elastic stability of the blade as the limit state function, with similar conclusions being reached.

Analysis using a three-dimensional finite element blade model was also performed in Toft *et al.* (2011b), where post-buckling response was investigated through a non-linear finite element analysis. Response surface method was combined with Monte Carlo and first-order reliability method (FORM). The reliability of the blade was estimated for the second layer of each element on the central line of the main spar cap. Elastic and strength properties of the material ply were assumed to be stochastic and the quadratic failure criterion used was applied on the ply level. In Toft *et al.* (2011b), as in Lekou and Philippidis (2009), the issue of modelling biaxial and triaxial plies using data from unidirectional plies was raised. Variability and uncertainty of the imposed loading was taken into account in Toft *et al.* (2011b), yet the load was scaled up to the level of the first ply level observed. Results of the study show that FORM underestimated the probability of failure, and this is attributed to the nonlinearity of the response surface. However, FORM was used to identify the sensitivity of the solution to other uncertainties included in the model, such as the uncertainty of the failure criterion employed, which is shown to be important.

Aiming at reducing the number of calls to the high complexity finite element model required as part of the classical response surface method, the model correction factor method is employed in Dimitrov *et al.* (2013). In this method, a simplified analytical model, for example a beam model, replaces the detailed finite element model. In order, however, for the beam model to correctly capture the structural behaviour, it is calibrated to the complex finite element model in a probabilistic sense. The application is performed on a symmetric with respect to the chord line aerofoil-shaped cross-section of constant thickness and uniform throughout the whole blade length. Maximum deflection and strength criteria are checked as limit functions, employing the multimodal Hashin criterion (Hashin, 1980) for the latter. Issues regarding the level of computational effort required, as well as difficulties observed in cases using the strength criterion, are covered in the discussion.

In Toft *et al.* (2011a), the reliability of a blade component is investigated under the assumption of the presence of defects (delaminations) and the use of non-destructive inspection methods for the detection of such defects.

In the example presented a generic blade model is used, where all the components are assumed identical. The maximum strain criterion is used as the failure condition and a methodology is presented to take into account the effect of defects on the probability of failure of the component through a degradation factor. Furthermore, the subject of having a series system of parallel systems is discussed, through the generic blade model. The method presented could be used as a starting point for reliability-based inspection planning; but, to enable actual application for wind turbine blades, several issues, such as the effectiveness of inspection methods and damage growth models, have to be improved.

A methodology for estimating the structural reliability of the blade against fatigue failure is presented in Toft and Soerensen (2011), in this case with an oversimplified model for the load-carrying capacity of the wind turbine blade, comprising a single failure mode and equivalent stress definition from the out-of-plane cycle loading on the blade. Furthermore, the model includes two parts: damage from small stress cycles and damage from large stress cycles. The study contains information on uncertainty at various levels of the blade design, ranging from coupon tests and the suitability of failure criteria, to loading uncertainties, but focusing, nevertheless, on issues around the required number of tests and the uncertainty of failure models.

Evidently the probabilistic design of wind turbine blades is a multidisciplinary and multilevel problem, comprising multiple failure modes and failure sequences. In the pursuit of a sound and comprehensive structural reliability estimation, information on all levels is being assimilated, collected from detailed analysis, as, for example, in Bacharoudis *et al.* (2011), and incorporated in more complete models, as in Toft and Soerensen (2011).

10.7 Challenges and future trends

From the above, it is obvious that much is still needed in order to arrive at a comprehensive probabilistic design tool for composite wind turbine blades that encompasses the full simulation circle from the micromechanics level to the level of the complete wind turbine. The versatility of constituent material combinations, internal structural design solutions and manufacturing methods, in combination with the randomness of loading conditions and difficulties in inspection on turbines throughout their operational lives, renders the reliance on partial safety factors ineffective. This is even more the case given that optimization of material use, as well as increasing operational reliability, is at the centre of the drive to reduce wind energy costs.

A practical step towards building an all-inclusive probabilistic wind turbine design tool would be the expeditious integration of probabilistic tools for wind turbine blade design and aeroelastic tools. The first actions towards facilitating such a connection have already been completed, as discussed

in previous sections, with tools such as those developed by Lekou and Philippidis (2009) and Bacharoudis *et al.* (2011). At the very least, the realization of an aeroelastic analysis that took into account the variability of the blade elasticity parameters would shed light on the effect of these parameters on the loads of the wind turbine.

Improvement of the recently developed methodologies will probably be sought through implementation of superior composite material models. Up to now, probabilistic applications for wind turbine blades have been limited to the use of the Tsai and Wu failure criterion for ultimate strength assessments and uniaxial failure modes for fatigue cases: employing the recommended Puck failure criterion (Puck, 1996) would be the natural way forward for ultimate load cases, as in the case presented in Dimitrov *et al.* (2013). For the fatigue cases, it might be premature to expect the direct adaptation of approaches for the probabilistic fatigue estimation of composite laminates as e.g. in Liu and Mahadevan (2005) for use in the field of blade design, owing to high computation costs and missing input parameters for material properties. In this regard, confidence should first be built in fatigue failure models for composite materials, both at the ply level and at the structure level by, ensuring the validation of these models as, for example, in Passipoularidis *et al.* (2011).

From a different perspective, that of detailed analysis of the blade structure, methodologies such as the one recently presented in Kimiaeifar *et al.* (2012) are also likely to be adopted in the full simulation cycle. The work of Kimiaeifar *et al.* (2012) focuses on the probabilistic analysis of adhesive bonded scarf joints, employing a Monte Carlo simulation of a three-dimensional analysis model in ANSYS. Since blades encompass adhesive bonded joints, it is expected that efforts will also be directed this way, in parallel perhaps with the developments in deterministic design.

At this phase of development of the relevant probabilistic tools, the greatest challenge is probably the verification of methods in order to increase confidence in the simulation results. Traditionally, the comparison of results from the developed stochastic methods is performed against Monte Carlo simulation data. But in the first place, Monte Carlo simulation is too expensive for use in the complete design cycle, and in the second place, the alternative probabilistic method and the Monte Carlo simulation both share the same modelling assumption. It would be necessary therefore, to validate the methodologies through experimental data. However these data are hard to collect, either due to the cost of performing the necessary statistically important tests or due to lack of relevant historic operational data.

In the future, for very large wind turbines and hence for their blades, it is expected that the direct use of probabilistic methods by designers and manufacturers will be required as an indispensable tool for providing a cost-effective product, not only in terms of capital costs, but also with a view to

operational costs. The trend becomes clearer if one considers the statistical character of the recently introduced guidance for design load estimations in the main design standard for wind turbines, IEC 61400–1:2005, the requirement for accredited laboratories to report uncertainties in experimental data under ISO/IEC 17025:2005, as well as recent scientific publications dealing with the reliability assessment of wind turbines and blades.

10.8 Sources of further information and advice

In order to perform a probabilistic analysis of the reliability of wind turbine blades knowledge of various fields needs to be combined. This include issues such as composite materials, their properties and the testing methods applied to them, as well as their modelling and behaviour prediction; wind turbine blades per se; and finally structural probabilistic analysis methodologies. This book covers the state-of-the-art in the subject of design of wind turbine rotor blades, as well as in the subject of composite materials as applied in these blades, including their properties, testing and modelling. Therefore, for these topics, the interested reader is referred to the relevant chapters of the book.

Regarding probabilistic analysis methodologies in general, a lot of work has been done in the framework of civil engineering structures (see e.g. Ditlevsen and Madsen, 1996), with the work in the field continuously being improved and updated within the framework of the Joint Committee on Structural Safety (www.jcss.byg.dtu.dk). With respect to probabilistic methods specifically for analysis of composite material structures, much of the developments in the field of aircraft structures are summarized and reviewed in reports of the US Department of Transportation (see e.g. Shiao, 2001; Ushakov *et al.*, 2002), while advances regarding aerospace structures and other composite structures are available through relevant NASA reports (see e.g. Chamis, 2007). Chiachio *et al.* (2012) recently reviewed the methods and current developments in the reliability of composite structures.

The majority of recent developments in probabilistic analysis specifically relating to wind turbine blades have been achieved within the framework of an EU-funded project, UPWIND, Grant No. SES6–019945 (www.upwind.eu), within work packages WP3 (see e.g. Lekou and Philippidis, 2009; Bacharoudis and Philippidis, 2010; Bacharoudis *et al.*, 2011), or within the framework of the Danish national projects at Aalborg University (see e.g. Toft and Soerensen, 2011; Toft *et al.*, 2011a, 2011b). The work of Philippidis and co-authors is based on probabilistic methodologies for composite materials and focuses on better estimation of the probability of failure initiation in the composite material layers, while the work of Soerensen and co-authors, originating from civil engineering approaches, encompasses, using less detailed analysis models, a more comprehensive list of the uncertainties

that abound in the prediction of the response of wind turbine blades, which can be used for calibration of partial safety factors.

10.9 References

- Ang AH-S, Tang WH. (1984), *Probability concepts in engineering planning and design, Vol. II: Decision, risk and reliability*, John Wiley & Sons.
- Bacharoudis KC, Lekou DJ, Philippidis TP. (2011), Structural reliability analysis of rotor blades in ultimate loading, in Avia Aranda F, *Scientific Proceedings of European Wind Energy Association Conference EWEA2011*, Brussels, Belgium, pp. 129–135.
- Bacharoudis KC, Philippidis TP. (2010), Structural reliability analysis of a composite rotor blade in ultimate loading, in Voutsinas S, Chaviaropoulos T, *Proceeding of the European Academy of Wind Energy 3rd Conference: 'The Science of Making Torque from Wind' TORQUE 2010*, Heraklion, Greece, pp. 811–828.
- Bacharoudis KC, Philippidis TP. (2012), A probabilistic approach for strength and stability evaluation of wind turbine rotor blades in ultimate loading, *Structural Safety*, **40**, 31–38.
- Bjerager P. (1991), Methods for structural reliability computations, in Casciati F and Roberts JB, *Reliability Problems; General Principles and Applications in Mechanics of Solids and Structures*, Courses and Lectures, No. 317, chapter 3, Springer Verlag, pp. 89–135.
- Braam H, Christensen CJ, Ronold KO, Thogersen ML. (1999), ‘PRODETO, a computer code for probabilistic fatigue design’, in Petersen EL, Jenssen PH, Rave K, Helm P, Ehmann H, *Proceedings of European Wind Energy Conference 1999: 'Wind Energy for the Next Millennium'*, London, James & James Science Publishers, pp. 195–198.
- Broendsted P, Lilholt H, Lystrup A. (2005), Composite materials for wind power turbine blades, *Annual Review of Material Research*, **35**, 505–538.
- Brood RRH, Numan R, De Ruiter MJ, De Winkel GD. (2010), Focus 6 – Integrated modular wind turbine design tool, Presented in *Sandia Blade Workshop 2010*, <http://windpower.sandia.gov/2010BladeWorkshop/PDFs/2-2-E-2-Numan.pdf>
- Bucher CG, Bourgund U. (1990), A fast and efficient response surface approach for structural reliability problems, *Structural Safety*, **7**, 57–66.
- Charmpis DC, Schueller GI, Pellissett MF. (2007), The need for linking micromechanics of materials with stochastic finite elements: A challenge for material science, *Computational Materials Science*, **41**, 27–37.
- Chamis CC. (1997), Probabilistic Composite Design, Hooper SJ, *Composite Materials: Testing and Design*, ASTM STP 1242, American Society of Testing and Materials, 23–42.
- Chamis CC. (2007), Probabilistic methods for structural reliability and risk, NASA technical memorandum, NASA/TM-2007-214703.
- Chen H, Yu W, Capellaro M. (2010), A critical assessment of computer tools for calculating composite wind turbine blade properties, *Wind Energy*, **13**(6), 497–516.
- Cheng PW, Bierbooms WAAM. (2001), Distribution of extreme gust loads of wind turbines, *Journal of Wind Engineering and industrial Aerodynamics*, **89**, 309–324.

- Chiachio M, Chiachio J, Rus G. (2012), Reliability of composites – A selective review and survey of current development, *Composites: Part B*, **43**, 902–913.
- Christensen CJ, Joergensen E, Ronold KO, Wedel-Heinen J, van den Horn B, Rademakers L. (1996), European Wind Turbine Standards, Part 2: Calibration of Safety Factors, Final Report JOU2-CT93-0387, EUR 16898 EN.
- Cramer H. (1971), *Mathematical Methods of Statistics*, Princeton University Press, Princeton.
- Dimitrov N, Frijs-Hansen P, Berggreen C. (2013), Reliability analysis of a composite wind turbine blade section using the model correction factor method: Numerical study and validation, *Applied Composite Materials*, **20**(1), 17–39, DOI 10.1007/s10443-011-9246-3.
- Ditlevsen O, Madsen HO. (1996), *Structural reliability methods*, John Wiley and Sons.
- DNV-DS-J102. (2010), *Design and Manufacture of Wind Turbine Blades, Offshore and Onshore Wind Turbines*.
- Eamon CD, Thompson M, Liu Z. (2005), Evaluation of accuracy and efficiency of some simulation and sampling methods in structural reliability analysis, *Structural Safety*, **27**(4), 356–392.
- Fiessler B, Neumann H-J, Rackwitz R. (1979), Quadratic limit states in structural reliability, *Journal of Engineering Mechanics Division*, **105**(EM4), 661–676.
- Fitzwater LM, Winterstein SR. (2001), Predicting design wind turbine loads from limited data: Comparing random process and random peak models, *Journal of Solar Energy Engineering*, **123**(4), 364–372.
- Freudenreich K, Argyriadis K. (2008), Wind turbine load level based on extrapolation and simplified methods, *Wind Energy*, **11**, 589–600.
- Gary PM, Riskalla MG. (1997), *Development of Probabilistic Design Methodology of Composite Structures*, DOT/FAA/AR-95/17.
- Genz R, Nielsen KB, Madsen PH. (2006), An investigation of load extrapolation according to IEC 61400-1 Ed.3, European Wind Energy Conference 2006, [<http://proceedings.ewea.org/ewec2006/> (last accessed: 14.08.2013)].
- Germanischer Lloyd Industrial Services GmbH. (2010), Rules and Guidelines, IV Industrial Services, Part 1 Guideline for the Certification of Wind Turbines.
- Gibson RF. (1994), *Principles of composite material mechanics*, McGraw-Hill, Inc., Singapore.
- Gollwitzer S, Kirchgaessner B, Fischer R, Rackwitz R. (2006), PERMAS-RA/STRUREL system of programs for probabilistic reliability analysis, *Structural Safety*, **28**(1–2), 108–129.
- Hahn GJ, Shapiro SS. (1994), *Statistical Models in Engineering*, John Wiley & Sons, Inc., New York.
- Hashin Z. (1980), Failure criteria for unidirectional fiber composites, *Journal of Applied Mechanics*, **47**, 329–334.
- Hodges DH, Yu W. (2007), A rigorous, engineer-friendly approach for modelling realistic, composite rotor blades, *Wind Energy*, **10**, 179–193.
- Hoffman O. (1967), The brittle strength of orthotropic materials, *Journal of Composite Materials*, **1**, 200–206.
- IEC 61400-1:2005, Wind Turbines – Part 1: Design Requirements, 3rd Edition.
- IEC 61400-1 A1/CDV: 2008, Amendment 1 to IEC 61400-1 Ed.3: Wind Turbines Part 1: Design Requirements, Committee draft for voting, 88/339CDV.

- IEC/TS 61400–23:2001, Wind turbine generator systems – Part 23: Full-scale structural testing of rotor blades, 1st edition.
- ISO 2394:1986, General Principles on reliability for structures, 2nd edition.
- ISO/IEC 17025:2005, General requirements for the competence of testing and calibration laboratories.
- Jensen FM. (2008), Ultimate strength of a large wind turbine blade, PhD Thesis, Risøe, Risoe-Phd-34, Roskilde, Denmark.
- Jonkman JM, Buhl ML Jr. (2005), *Fast User's Guide*, NREL Technical Report NREL/EL-500-38230, Golden, Colorado, USA, National Renewable Energy Laboratory (NREL).
- Kimiaeifar A, Toft H, Lund E, Thomsen OT, Soerensen JD. (2012), Reliability analysis of adhesive bonded scarf joints, *Engineering Structures*, **35**, 281–287.
- Knuth DE. (1998), *The Art of Computer Programming, Vol. 2, Seminumerical Algorithms*, Addison Wesley Longman, 3rd Ed., USA.
- Kong C, Bang J, Sugiyama Y. (2005), 'Structural investigation of composite wind turbine blade considering various load cases and fatigue life', *Energy*, **30**, 2101–2114.
- Lekou DJ, Philippidis TP. (2006), Influence of mechanical property variability on failure prediction of FRP laminates, in Lilholt H, Madsen B, Andersen TL, Mikkelsen LP, Thygesen A, *Proceedings of the 27th Risø International Symposium on Materials Science; Polymer Composite Materials for Wind Power Turbines*, Roskilde, Denmark, 197–204.
- Lekou DJ, Assimakopoulou TT, Philippidis TP. (2011), Estimation of the uncertainty in measurement of composite material mechanical properties during static testing, *Strain*, **47**(5), 430–438, DOI: 10.1111/j.1475–1305.2009.00705.x.
- Lekou DJ, Philippidis TP. (2008), Mechanical Property variability and its Effect on Failure Prediction, *Composites Part B: Engineering*, **39**, 1247–1256.
- Lekou DJ, Philippidis TP. (2009), PRE- and POST-THIN: A tool for the probabilistic design and analysis of composite rotor blade strength, *Wind Energy*, **12**(7), 676–691.
- Liu P-L, Der Kiureghian A. (1991), Optimization algorithms for structural reliability, *Structural Safety*, **9**, 161–177.
- Liu Y, Mahadevan S. (2000), Ultimate strength failure probability estimation of composite structures, *Journal of Reinforced Plastics and Composites*, **19**, 403–426.
- Liu Y, Mahadevan S. (2005), Probabilistic fatigue life predictions of multidirectional composite laminates, *Composite Structures*, **69**, 11–19.
- Madsen HO, Krenk S, Lind NC. (1986), *Methods of structural safety*, Prentice-Hall Inc.
- Malcolm DJ, Laird DL. (2003), Modeling of blades as equivalent beams for aeroelastic analysis, *41st Aerospace Sciences Meeting and Exhibit*, AIAA-2003-870, Reno, Nevada.
- Malcolm DJ, Laird DL. (2007), Extraction of equivalent beam properties from blade models, *Wind Energy*, **10**, 135–157.
- MIL-HDBK-17-1F. (2002), *Composite materials handbook; Volume 1: Polymer Matrix Composites – Guidelines for characterization of structural materials*, Department of Defense Handbook, USA.
- Miki M, Murutsu Y, Tanaka T, Shao S. (1990), Reliability of unidirectional fibrous composites, *AIAA Journal*, **28**(11), 1980–1986.

- Moriarty PJ, Holley WE, Butterfield SP. (2004), *Extrapolation of extreme and fatigue loads using probabilistic methods*, NREL Technical report NREL/TP-500-34421, Golden, Colorado, USA, National Renewable Energy Laboratory (NREL).
- Myers RH, Montgomery DC. (2002), *Response Surface Methodology: Process and Product Optimization Using Designed Experiments*, New York, John Wiley.
- Orifici AC, Herszberg I, Thomson RS. (2008), Review of methodologies for composite material modeling incorporating failure, *Composite Structures*, **86**, 194–210.
- Papazoglou VJ, Sanoudos JV. (1991), Introducing structural reliability concepts into laminate analysis, in Paipetis SA and Philippidis TP, *Advanced Composites in Emerging Technologies*, AMATEC, Patras, Greece, 559–573.
- Pardo DR, Branner K. (2005), Finite element analysis of the cross-section of wind turbine blades; a comparison between shell and 2D-solid models, *Wind Engineering*, **29**(1), 25–32.
- Passipoularidis VA, Philippidis TP, Broendsted P. (2011), Fatigue life prediction in composites using progressive damage modeling under block and spectrum loading, *International Journal of Fatigue*, **33**, 132–144.
- Peeringa JM. (2003), *Extrapolation of extreme responses of a multi megawatt wind turbine*, ECN Report, ECN-C – 03-131, Petten, The Netherlands, Energy Research Centre of The Netherlands (ECN).
- Pellissetti MF, Schueller GI. (2006), On general purpose software in structural reliability – An overview, *Structural Safety*, **28**(1–2), 3–16.
- Philippidis TP, Eliopoulos EN, Bacharoudis K, Masmanidis I, Assimakopoulou TT. (2010), *Test Results of In-Plane Mechanical Properties for Modeling Complex Stress States*, UPWIND Deliverable D.3.3.6, University of Patras, Patras, Greece, [<http://www.upwind.eu/publications/3-rotor-structure-and-materials.aspx> (last accessed 14.08.2013)].
- Philippidis TP, Lekou DJ, Bacharoudis C. (2006), *Assessment of failure probability under uni-axial and multi-axial static and fatigue load*, OPTIMAT BLADES report, OB_TG2_R035_rev.000, University of Patras, Patras, Greece, [www.wmc.eu/public_docs/index.htm (last accessed 14.08.2013)].
- Philippidis TP, Roupakias GS, Vionis P. (1994), Assessment of composite rotor blade structural modelling efficiency through comparison of FEM numerical results and experimental data, Tsipouridis JL, Proceedings of European Wind Energy Conference EWEC 94, 155–160.
- Philippidis TP, Vassilopoulos AP, Katopis KG, Voutsinas SG. (1996), THIN/PROBEAM: A software for fatigue design and analysis of composite rotor blades, *Wind Engineering*, **20**(5), 349–362.
- Press WH, Teukolsky SA, Vetterling WT, Flannery BP. (1994), *Numerical recipes in Fortran – The art of scientific computing*, 2nd Ed. Cambridge University Press.
- Puck A. (1969), Festigkeitsberechnung an Glasfaser/Kunststoff – Laminaten bei zusammengesetzter Beanspruchung; Bruchhypothesen und Schichtenweise Bruchanalyse, *Kunststoffe*, **59**(11), 780–787.
- Puck A. (1996), *Festigkeitsanalyse von Faser-Matrix-Laminaten; Modelle für die Praxis*, Carl Hanser Verlag.
- Puck A, Schuermann H. (1998), Failure analysis of FRP laminates by means of physically based phenomenological models, *Composites Science and Technology*, **58**, 1045–1067.

- Rajashekhar MR, Ellingwood BR. (1993), A new look at the response surface approach for reliability analysis, *Structural safety*, **12**, 205–220.
- Reh S, Beley J-D, Mukherjee S, Khor EH. (2006), Probabilistic finite element analysis using ANSYS, *Structural Safety*, **28**, 17–43.
- Riziotis VA, Voutsinas SG, Manolas DI, Politis ES, Chavariopoulos PK. (2010), Aeroelastic analysis of pre-curved rotor blades, European wind energy conference EWECC2010, Scientific Track.
- Riziotis VA, Voutsinas SG, Politis ES, Chavariopoulos PK. (2004), Aeroelastic stability of wind turbines: The problem, the methods, the issues, *Wind Energy*, **7**, 373–392.
- Robinson DG. (1998), *A survey of probabilistic Methods used in reliability, risk and uncertainty analysis: Analytical Techniques I*, Sandia Report, SAND98-1189, Sandia National Laboratories, California, USA.
- Rollet Y, Bonnet M, Carrere N, Leroy F-H, Maire J-F. (2009), Improving the reliability of material databases using multiscale approaches, *Composites Science and Technology*, **69**, 73–80.
- Ronold KO, Larsen GC. (2000), Reliability-based design of wind-turbine rotor blades against failure in ultimate loading, *Engineering Structures*, **22**, 565–574.
- Rubinstein ARY. (1981), *Simulation and the Monte Carlo Method*, Wiley, USA.
- Schueller GI, Pradlwarter HJ, Koutsourelakis PS. (2004), A critical appraisal of reliability estimation procedures for high dimensions, *Probabilistic Engineering Mechanics*, **19**, 463–474.
- Shaw A, Sriramula S, Gosling PD, Chryssanthopoulos MK. (2010), A critical reliability evaluation of fibre reinforced composite materials based on probabilistic micro and macro-mechanical analysis, *Composites: Part B*, **41**, 446–453.
- Shiao M. (2001), Evaluation of the probabilistic design methodology and computer code for composite structures, Report of the U.S. Department of Transportation – Federal Aviation Administration, DOT/FAA/AR-99/12.
- Shinozuka M. (1983), Basic analysis of structural safety, *Journal of Structural Engineering*, **109**(3), 721–740.
- Simpson TW, Peplinski JD, Koch PN, Allen JK. (1997), On the use of statistics in design and the implications for deterministic computer experiments, in *Proceedings of DET'97, 1997 ASME Design Engineering Technical Conferences*, Sacramento, California, 1997.
- Soden PD, Kaddour AS, Hinton MJ. (2004), Recommendations for designers and researchers resulting from the world-wide failure exercise, *Composites Science and Technology*, **64**, 589–604.
- Toft HS, Branner K, Berring P, Soerensen JD. (2011a), Defect distribution and reliability assessment of wind turbine blades, *Engineering Structures*, **33**, 171–180.
- Toft HS, Soerensen JD. (2011), Reliability-based design of wind turbine blades, *Structural Safety*, **33**, 333–342.
- Toft HS, Soerensen JD, Branner K, Berring P. (2011b), Reliability-based calibration of partial safety factors for wind turbine blades, in Avia Aranda F, *Scientific Proceedings of European Wind Energy Association Conference EWEA2011*, Brussels, Belgium, 124–128.
- Tsai SW, Wu EM. (1971), A general theory of strength for anisotropic materials, *Journal of Composite Materials*, **5**, 58–80.
- Tvedt L. (2006), Proban – probabilistic analysis, *Structural Safety*, **28**(1–2), 150–163.

- Ushakov A, Stewart A, Mishulin I, Pankov A. (2002), Probabilistic design of damage tolerant composite aircraft structures, Report of the U.S. Department of Transportation – Federal Aviation Administration, DOT/FAA/AR-01/55.
- Veers PS, Butterfield S. (2001), Extreme load estimation for wind turbines: Issues and opportunities for improved practice, *2001 ASME Wind Energy Symposium*, AIAA/ASME, AIAA 2001-0044 [<http://windpower.sandia.gov/asme/AIAA-2001-0044.pdf> (last accessed: 14.08.2013)].
- Veers PS, Ashwill TD, Sutherland HJ, Laird DL, Lobitz DW, Griffin DA, Mandell JF, Musial WD, Jackson K, Zuteck M, Miravete A, Tsai SW, Richmond JL. (2003), Trends in the design, manufacture and evaluation of wind turbine blades, *Wind Energy*, **6**, 245–259.
- Veldkamp D. (2006), *Chances in Wind Energy: A probabilistic approach to wind turbine fatigue design*, PhD Thesis, DUWIND Delft University Wind Energy Research Institute, Delft, The Netherlands.
- Wang L, Grandhi RV. (1994), Efficient safety index calculation for structural reliability analysis, *Computers and Structures*, **52**(1), 103–111.
- Winterstein SR, Veers PS. (2000), *Theory manual for FAROW Version 1.1: A numerical analysis of the fatigue and reliability of wind turbine components*, Sandia Report, SAND94-2459.
- Wu EM. (1973), Phenomenological anisotropic failure criterion, in Sendeckyj GP, *Composite Materials Vol. 2, Mechanics of Composite Materials*, Academic Press, N. York, 353–431.

Biobased composites: materials, properties and potential applications as wind turbine blade materials

B. MADSEN, P. BRØNDSTED and T. LØGSTRUP ANDERSEN,
Technical University of Denmark, Denmark

DOI: 10.1533/9780857097286.3.363

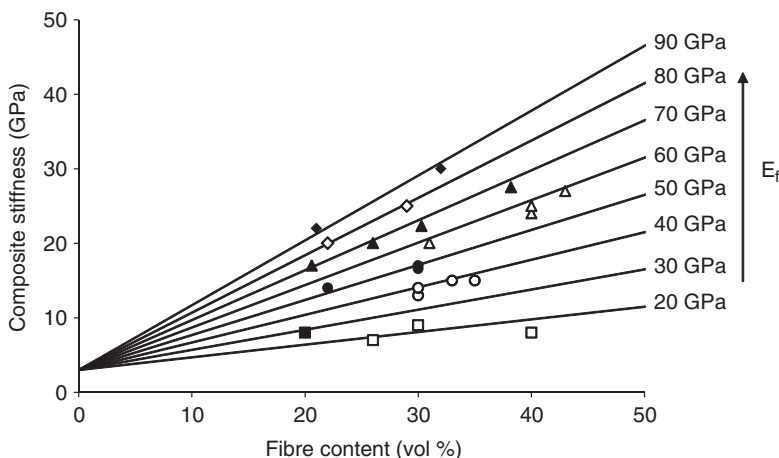
Abstract: This chapter about biobased composites starts by presenting the most promising types of cellulose fibres; their properties, processing and preforms for composites, together with an introduction to biobased matrix materials. The chapter then presents the typical mechanical properties of biobased composites, based on examples of composites with different fibre/matrix combinations, followed by a case study of the stiffness and specific stiffness of cellulose fibre composites vs glass fibre composites using micromechanical model calculations. Finally, the chapter presents some of the special considerations to be addressed in the development and application of biobased composites.

Key words: biobased composites, cellulose fibres and bioresin, composite preforms, tensile properties, micromechanical models.

11.1 Introduction

Biobased composites are a new class of materials with an attractive combination of good technical performance and low environmental impact (Mohanty *et al.*, 2005; Pickering, 2008; Müssig, 2010; CELC, 2012). The fibres that show the most promising potential for composite reinforcement in structural applications are cellulose fibres derived from plants, such as flax and hemp grown in Europe, and jute and bamboo grown in Asia. The fibres extracted from these plants are relatively long, making it possible to make preforms with controlled fibre orientations for composites; they also have a high cellulose content – in the form of aligned crystalline microfibrils, giving them good mechanical properties – and a low density.

During the last two decades, a large number of scientific studies have reported on the performance of biobased composites (see recent reviews by Hill and Hughes, 2010; Zini and Scandola, 2011; Faruk *et al.*, 2012; Shahzad, 2012). Most focus has been on composites with a random in-plane fibre orientation, because of their large-scale industrial use for semi-structural panels in the automotive industry (Karus *et al.*, 2002; Müssig, 2010). However, a

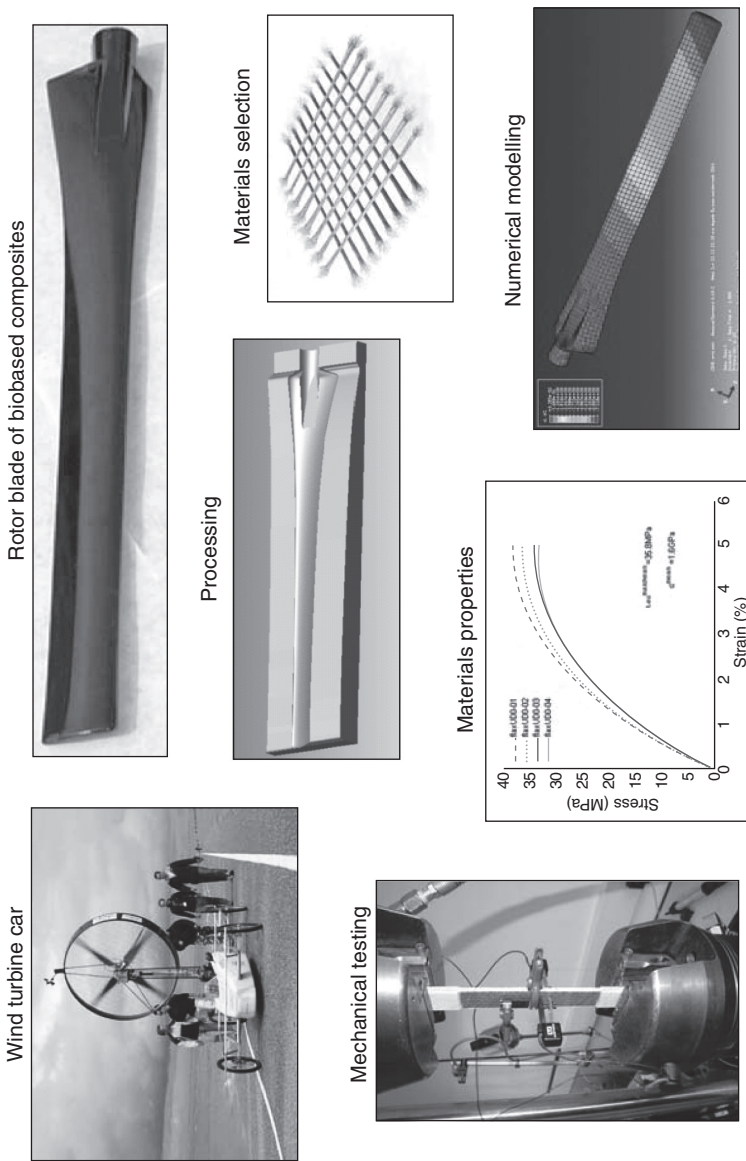


11.1 Data from literature on stiffness of unidirectional biobased composites. Lines are rules-of-mixtures model predictions with variable fibre stiffness from 20 to 90 GPa (Mehmood and Madsen, 2012).

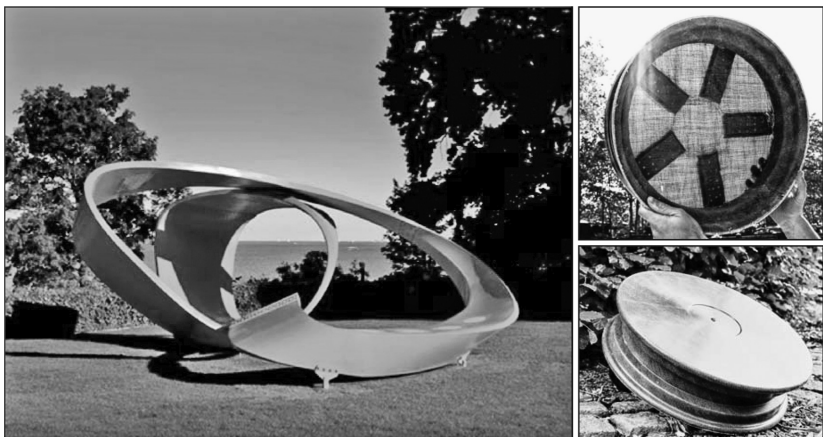
range of studies have reported on the performance of biobased composites with unidirectional fibres in terms of their fibre content and their ability to utilize the good properties of the fibres (e.g. Roe and Ansell, 1985; Hepworth *et al.*, 2000; Oksman, 2001; Van de Weyenberg *et al.*, 2003; Thygesen *et al.*, 2007; Madsen *et al.*, 2009; Mehmood and Madsen, 2012; Shah *et al.*, 2012). Based on experimental results from a selection of studies, Fig. 11.1 shows the stiffness of unidirectional biobased composites as a function of fibre content. The results are grouped according to the estimated effective stiffness of the fibres, with values from 20 to 90 GPa, and lines represent the rule-of-mixtures model predictions. The figure illustrates well *the span of reinforcement efficiencies of cellulose fibres*, depending on the quality of the fibres, and it also demonstrates the possibility of having cellulose fibres with stiffnesses as high as 80–90 GPa, the benchmark stiffnesses of glass fibres.

The good technical performance of biobased composites with controlled fibre orientations has made it reasonable to consider these composites for structural applications, such as the rotor blades of wind turbines. Recently, in the context of research and development projects, a number of demonstrators have been created to highlight the potential of biobased composites:

- Small-scale rotor blade to be used for a wind turbine car: EU 7th Framework Programme project, WOODY (2009–2012) (Fig. 11.2).
- Sculpture shown at the special exhibition ‘Green architecture for the future’, Louisiana Museum of Modern Arts, Denmark: joint venture of 20 companies coordinated by 3XN Architects, Denmark; winner of the JEC innovation award 2010; (Fig. 11.3, left).



11.2 Development of prototype small-scale rotor blades using biobased composites. (Source: Modified from Pignatti and Bottoli, 2011.)



11.3 Demonstrators of biobased composites: (left) Sculpture developed by a joint venture of 20 companies coordinated by 3XN Architects, Denmark; (right) Wheel rim developed within the EU 7th Framework Programme project NATEX. (*Source:* Modified from Møller *et al.*, 2012.)

- Wheel rim; EU 7th Framework Programme project, NATEX (2008–2012) (Fig. 11.3, right).

11.2 Biobased fibres and matrix materials

Here follows a presentation of the most promising types of biobased fibres; their properties, processing and preforms for composites, together with an introduction to biobased matrix materials.

11.2.1 Biobased fibres

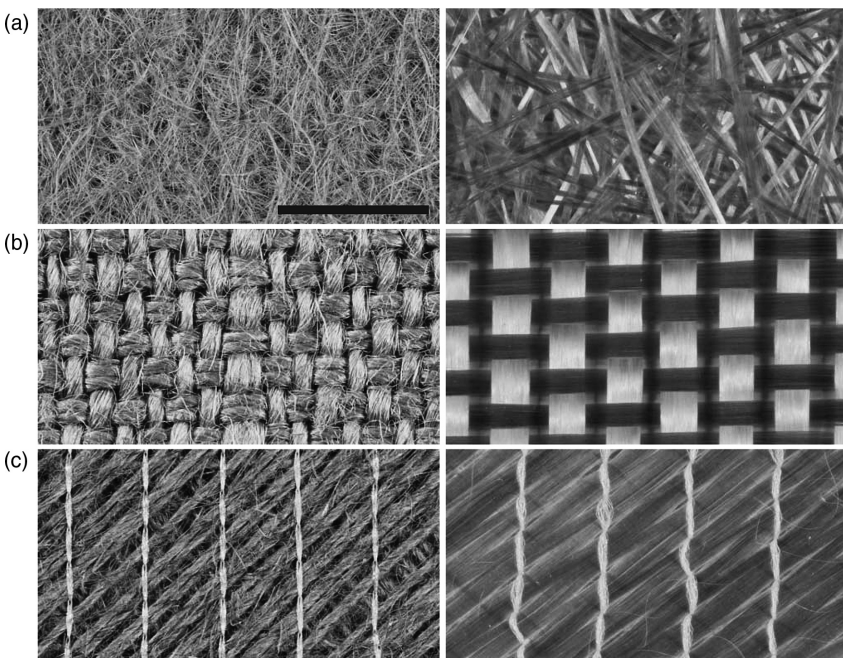
The technical requirements for fibres in high performance composites are low density, good mechanical properties and availability in composite preforms with well-defined aligned fibre orientations. A selection of biobased fibres with the potential to fulfil these requirements is presented in Table 11.1: flax, hemp, jute and bamboo. The table shows the properties of these fibres, together with those of glass and carbon fibres, the two synthetic fibres conventionally used for high performance composites. The table shows that the biobased fibres have: (i) a density of about 1.5 g/cm^3 , lower than that for glass and carbon fibres, (ii) a stiffness in the range 20–90 GPa, which, for the best quality biobased fibres, is comparable to that of glass fibres, and (iii) a strength in the range 200–900 MPa, which, however, is inferior to that of both glass and carbon fibres.

As shown in Table 11.1, the composite preforms that are available for biobased fibres are similar to those for synthetic fibres. Pictures of the various preforms are shown in Fig. 11.4. Non-woven mats have been commercially

Table 11.1 Properties of a selection of biobased fibres with the potential to be used for structural composite applications, and typical values for two synthetic fibres

Fibre type	Main chemical component	Density (g/cm ³)	Stiffness (GPa)	Strength (MPa)	Composite preforms available
Biobased fibres					Non-woven mats, woven fabrics, non-crimp fabrics
Flax	Cellulose, in a matrix of	1.5	50–90	500–900	
Hemp	hemicellulose	1.5	30–60	300–800	
Jute	and lignin	1.4	20–55	200–500	
Bamboo		1.4	27–40	500–575	
Synthetic fibres					Non-woven mats, woven fabrics, non-crimp fabrics
Glass	Silicon oxide	2.6	70–87	2500–4700	
Carbon	Graphite	1.8	240–830	3500–4400	

Source: Lilholt and Lawther, 2000; Oksman, 2001; Bunsel and Renard, 2005; Abdul Khalil *et al.*, 2012.



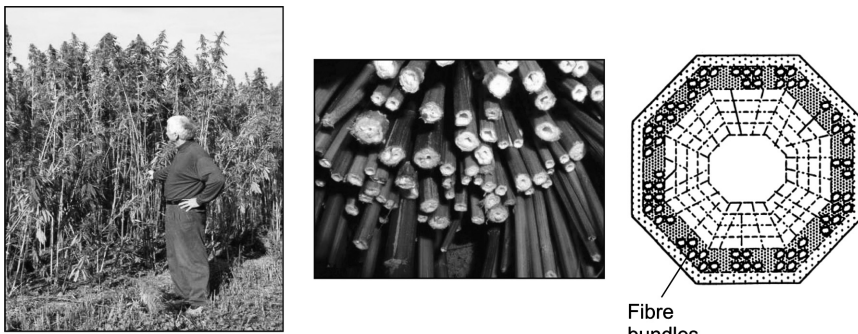
11.4 Composite preforms with cellulose fibres (left column) and glass fibres (right column): (a) non-woven mat of jute fibres and chopped strand mat of glass fibres, (b) plain weave of jute fibres and glass fibres, and (c) non-crimp fabric (biaxial, ±45°) of flax fibres and glass fibres. Scale bar is 10 mm.

available for biobased fibres for some time, and these are successfully used for semi-structural automotive panels. The planar fibre orientation in the non-woven mats is nominally 2-D random, but they can show a preferred fibre orientation in the machine direction. When the fibres are spun into a yarn, two composite preforms with well-defined aligned fibre orientations can be made: woven fabrics and non-crimp fabrics. Woven fabrics can be made using different textile weaving patterns, such as plain, twill and satin weave, with the yarns being interlaced in the two main planar directions. Non-crimp fabrics consist of yarns that are not held together by being woven into each other, but are instead stitched together. This means that the yarns are fully stretched, i.e. they have no crimp, since they do not have to go over and under each other, which gives the fibres an improved reinforcement efficiency. Recently, a number of European companies have begun production of non-crimp fabrics made from flax fibres; for the first time, therefore, preforms of biobased fibres that are specifically tailored for high performance composites are now commercially available.

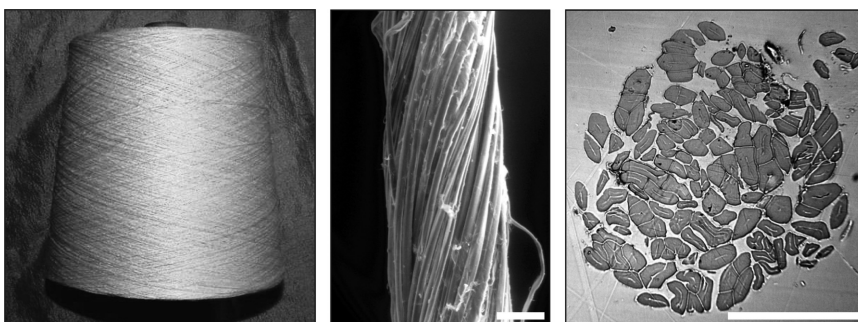
The main chemical component of biobased fibres is cellulose, which is found in the form of partly crystalline microfibrils embedded in a matrix of hemicellulose and lignin polymers. The cell walls of the fibres are furthermore arranged in a multi-layered configuration differing by the angle of the cellulose microfibrils to the longitudinal axis of the fibres (Siau, 1995; Thygesen *et al.*, 2005). Thus, cellulose fibres have a highly complex chemistry and microstructure. This is not surprising, since the fibres originate from living organisms with a long evolutionary history that have evolved to meet a number of specific mechanical requirements, in addition to other functional requirements. In contrast, the synthetic glass and carbon fibres are monolithic and have a much more simple microstructure.

The natural origin of biobased fibres necessarily implies a different processing method than the one used for synthetic fibres, which is typically performed under strictly controlled conditions, e.g. the melt extrusion of glass fibre rovings. Using the bast fibres hemp, flax and jute as an example, the following is a brief description of the processing steps, from the extraction of the fibres from the plants to the spinning of the yarns.

- *Fibre extraction.* In the plants, the fibres are situated in bundles at the periphery of the stem, hence the name ‘bast fibres’. After the end of the growing season, the plants are harvested (Fig. 11.5) and the fibres are separated from the plant stems by two processes: retting and mechanical extraction. The initial retting process aims to degrade the stem tissue that interconnects the fibre bundles, and this is done by storing the stems in the field or in water tanks where the stems are decomposed by microbial organisms. After retting, the fibres are extracted from the stems by a mechanical process in which the core of the stems is broken into small extractable parts (Müssig, 2010).

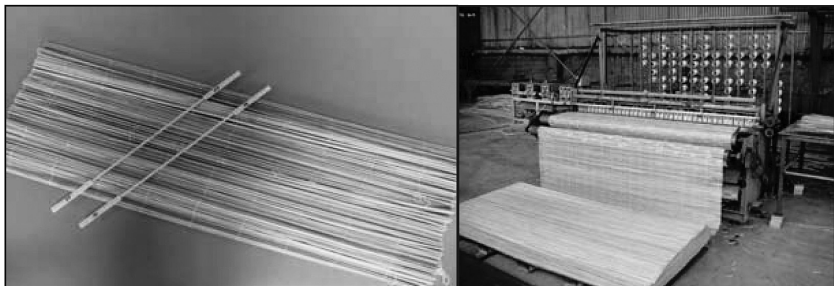


11.5 Bast fibres: (left) field of hemp plants, (middle) harvested hemp stems, (right) schematic view of cross-section of a stem showing the bundles of fibres in the periphery of the stem.



11.6 Bast fibre yarn: (left) bobbin with flax yarn, (middle) outside view of hemp yarn, scanning electron microscope, (right) cross-sectional view of hemp yarn, optical microscope. Scale bars are 100 µm.

- *Yarn spinning.* To enable the extracted fibres (with lengths of 2–50 mm) to be spun into a continuous yarn (Fig. 11.6, left), the textile processes of carding, combing and drafting are applied to improve the separation of fibre bundles into single fibres, to remove some of the shortest fibres, and to align the fibres. A range of different spinning techniques exists, with ring spinning being the most widely used. During spinning, the assembly of aligned fibres is twisted so that the fibres take up a helical configuration (Fig. 11.6, middle) where the twisting angle of the fibres is decreased from the outer surface to the interior of the yarn (Klein, 1998). The cross-sectional view of a yarn (Fig. 11.6, right) shows that some fibres are well separated into single fibres, while some fibres are situated in bundles consisting of a few single fibres bonded together. The twisted configuration of the fibres in the yarn cannot, however, be identified from the cross-sectional view due to the non-circular shapes of the fibres.



11.7 Bamboo preforms for composites: (left) strips, (right) curtain.

A special class of biobased fibres is bamboo. Bamboo belongs to the grass family and has an extremely high growth rate taking the structural strength into account. Many bamboo species reach full height of up to 30–40 m in less than 6 months, and harden and reach maturity in 3–5 years. When harvested, bamboo re-grows and is self-fertilizing, which simplifies the management of forests. From an environmental viewpoint, bamboo forests represent a very important source of carbon mitigation, with a carbon sequestration capacity in the biomass similar to or exceeding that of timber forests.

Jiang (2002) presents a comprehensive review of bamboo utilization, forest management, mechanical properties, chemical analysis and microstructure. Bamboo has been used as structural materials for thousands of years. It is used as timber in a variety of structural applications including housing, tooling, laminated bamboo flooring, laminated beams and wall panels for buildings. Bamboo can be used as harvested in full culms; it can be processed by machining fibre strands, or strips taken parallel to the culm length (Fig. 11.7, left); or it can be extracted as individual bamboo fibres and used for textiles. The mechanical properties of the fibres are very much dependent upon the species and are also influenced by local climatic conditions during growth. Compared with intact bamboo strips (e.g. for the manufacture of curtains, Fig. 11.7, right), the extraction of fibres or fibre bundles from a bamboo culm requires additional processing steps (and, accordingly, energy/chemical consumption) which results in higher costs.

11.2.2 Biobased matrix materials

Similar to conventional polymer matrices for composites, biobased matrix materials can be divided into the two fundamentally different polymer groups of thermoplastics and thermosettings. Thermoplastic polymers are characterized by a reversible melting/solidifying process controlled by heating/cooling, while thermosetting resins are characterized by an irreversible chemical reaction (cross-linking) during heating. What the two polymer groups have in

common is that they can only be considered suitable matrix materials for composites if their viscosity is low enough to efficiently wet out and impregnate the individual reinforcement fibres during the manufacturing process.

Because their viscosity is mainly controlled by temperature, thermoplastic polymers require a considerable heat input during the manufacturing process. For polylactic acid (PLA), a biobased thermoplastic polymer, the lower limit process temperature is 190°C. PLA from NatureWorks® was introduced to the market in 2001, being the first fully mature, commercially available biopolymer. Design and development of PLA was initially driven by the environmental need for a sustainable and degradable polymer especially for packaging of food and other consumer goods. PLA is regarded as being virtually CO₂-neutral, due to its being made from annually renewable resources, typically corn, and as having good mechanical properties compared with related thermoplastics polymers, like polypropylene. The use of thermoplastic matrix materials (both conventional and biobased) for commercial manufacturing of wind turbine blades had not been established successfully as at the end of 2012.

For thermosetting resins, it is in many cases possible to obtain, during the initial phase of the cross-linking process, a sufficiently low viscosity to allow efficient fibre impregnation at room temperature. Pre-curing of the resin ensures the required mechanical stability of the composite component to allow demoulding. Subsequently, the component can be post-cured at elevated temperatures to approach full cross-linking of the resin. Envirez®, one of the first biobased thermosetting resins, was introduced to the market by Ashland Composite Polymers in 2003, when John Deere began using this bioresin for side-body panels. Typically, bioresins are characterized by being only partly based on renewable resources. The above-mentioned Envirez® resin is 12–25% biobased. The development of 100% biobased resins with similar performance and processing requirements as the conventional petroleum based resins (e.g. epoxy and polyester) is ongoing.

11.3 Biobased composites

This section discusses examples of partly and fully biobased composites, with special emphasis on their processing and mechanical properties.

11.3.1 Glass fibre/bioresin composites

A study has been performed of the mechanical properties of unidirectional glass fibre composites with different matrices – two partly biobased resins and a conventional petroleum based resin (Andersen, 2011). Specifications for the glass fibre fabric were: L1200/G50-E07 (Devold AMT), area weight 1250 g/m² of which 1150 g/m² was oriented in the 0° direction. Specifications

Table 11.2 Mechanical properties of unidirectional glass fibre composites made using biobased and conventional resin matrices (Andersen, 2011)

Composites	Resin bio-content (wt. %)	Fibre	Stiffness		Strength	
		content	(GPa)		(MPa)	
		(vol-%)	0°	90°	0°	90°
Glass/Polylite 4729	57	54	41	11	773	53
Glass/SuperSap 1100	53	53	40	10	821	44
Glass/Polylite 413–575	0	51	39	12	782	49

for the resins were: Polylite 4729, 57% biobased polyester (Reichhold); SuperSap 1100, 53% biobased epoxy (Entropy Research); Polylite 413–575, 0% biobased conventional polyester (Reichhold). Composite plates were manufactured by vacuum-assisted resin infusion moulding, performed at room temperature, and the plates were post-cured for 18 h at 60°C after demoulding. The mechanical properties of the composites are shown in Table 11.2.

The results in Table 11.2 for tensile stiffness and strength in the axial and transverse direction of the composites show no clear difference between the biobased and the conventional resins. The study therefore demonstrates the good potential of bioresins as a direct replacement for conventional resins in composites for structural applications, although more studies are needed to document their full mechanical performance, e.g. in compression, shear and fatigue.

11.3.2 Bamboo fibre/epoxy composites

Several methods of utilizing bamboo fibre strips in a similar way to the use of glass and carbon fibre rovings as reinforcement in polymer based composites have been brought to market. Among these are bamboo/poplar/epoxy composites introduced by the International Centre for Bamboo and Rattan in China (Holmes *et al.*, 2009). These composites are built-up using bamboo curtains as unidirectional fabrics (see Fig. 11.7). The curtains are stacked in layers using poplar veneer as an absorbing film. The stacked bamboo/poplar assemblies are soaked in the resin (epoxy) and consolidated by hot pressing. Alternatively, the composites can be manufactured by vacuum-assisted resin infusion moulding. The composite plates show excellent mechanical properties and the stiffness/density ratio (i.e. specific stiffness) is in line with that of unidirectional glass/epoxy composites (Table 11.3). In July 2010, it was announced from China that the first rotor blade (40 m) made with bamboo composites had passed the static blade test (Fig. 11.8).

Table 11.3 Mechanical properties of bamboo/poplar/epoxy and glass/epoxy composites (Holmes *et al.*, 2009)

Composites	Density (g/cm ³)	Stiffness (GPa)		Strength (MPa)		Spec. stiffness (GPa/g cm ⁻³)	
		Tension	Comp.	Tension	Comp.	Tension	Comp.
Bamboo/ poplar/ epoxy	0.9	21	22	180	113	25	26
Glass/epoxy	1.9	40	40	800	113	21	21



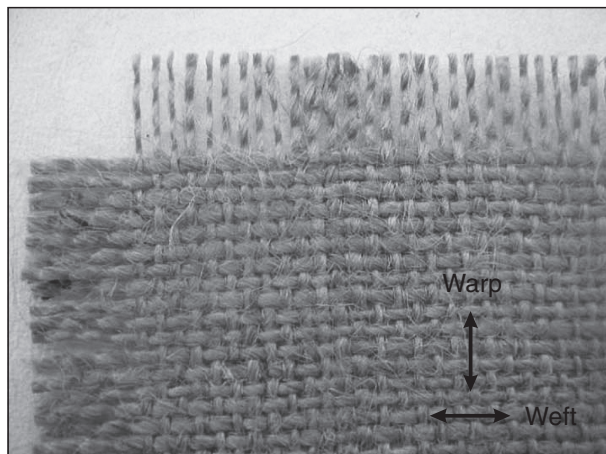
2010年7月，用竹基纤维复合材料研制的世界首片1.5MW竹制风电桨叶片顺利通过静载测试

11.8 Rotor blade (40 m) made using bamboo composites under static test.

11.3.3 Jute fibre/bioresin composites

Investigations have been carried out into the properties of fully biobased composites consisting of jute fibres in a bioresin matrix (Andersen, 2011). The fibre preform was a plain weave jute fibre fabric (Juteväv 100/16, Nevotex) with an area weight of 380 g/cm³ (dried) and with a warp/weft yarn weight ratio of 30/70. A picture of the fabric is shown in Fig. 11.9. Four different types of resins were used: Epobiox, 70% biobased epoxy (Amroy Europe Oy); Polylite 4729, 57% biobased polyester (Reichhold); SuperSap 1100, 53% biobased epoxy (Entropy Research); Epikote 135/137, 0% biobased conventional epoxy (Hexion). Composite plates were manufactured by vacuum-assisted resin infusion moulding, performed at room temperature, and the plates were post-cured for 18 h at 60°C after demoulding. The mechanical properties of the composites, tested in the weft direction, are shown in Table 11.4.

The results in Table 11.4 for tensile properties in the weft direction of the composites show a grand mean stiffness and strength of 7.7 GPa and 80 MPa, respectively, with no clear difference between the biobased and the conventional resin composites, as was also seen above for the glass fibre/bioresin



11.9 Plain weave jute fibre fabric with a warp/weft yarn weight ratio of 30/70.

Table 11.4 Mechanical properties of plain weave jute fibre composites made using biobased and conventional resin matrices

Composites	Resin bio-content (wt. %)	Fibre content (vol-%)	Stiffness (GPa) weft direct.	Strength (MP) weft direct.
Jute/Epobiox	70	30	7.5	81
Jute/Polylite 4729	57	33	7.8	72
Jute/SuperSap 1100	53	32	7.6	82
Jute/Epikote 135/137	0	30	8.0	84

Source: Andersen, 2011.

composites (Table 11.2). By using the combined rule-of-mixtures model (see below, Equation [11.1]), the effective stiffness of the jute fibres can be calculated to be about 25 GPa, which, however, is much lower than the stiffness of glass fibres. The reinforcement efficiency of these jute fibres is therefore at the lower end of the span of reinforcement efficiencies of between 20 and 90 GPa typically seen for cellulose fibres (see Fig. 11.1).

The quality and performance of cellulose fibres is inevitably linked to their cost. Further studies are needed to investigate the cost–performance relations of biobased composites.

11.4 Case study: Comparison between cellulose and glass fibre composites

Using well-established micromechanical models for the properties of composites, a case study can be made comparing cellulose fibre composites with

glass fibre composites. In this case study, stiffness (E) and stiffness per weight (i.e. the specific stiffness) (E/ρ) are used as the central mechanical properties for the comparison between the two composites. These two properties can be predicted by the combined rule-of-mixtures model for the stiffness of composites (Bunsell and Renard, 2005) and the standard equation for the density of multiphase materials:

$$E_c = \eta_0 \eta_l V_f E_f + V_m E_m \quad [11.1]$$

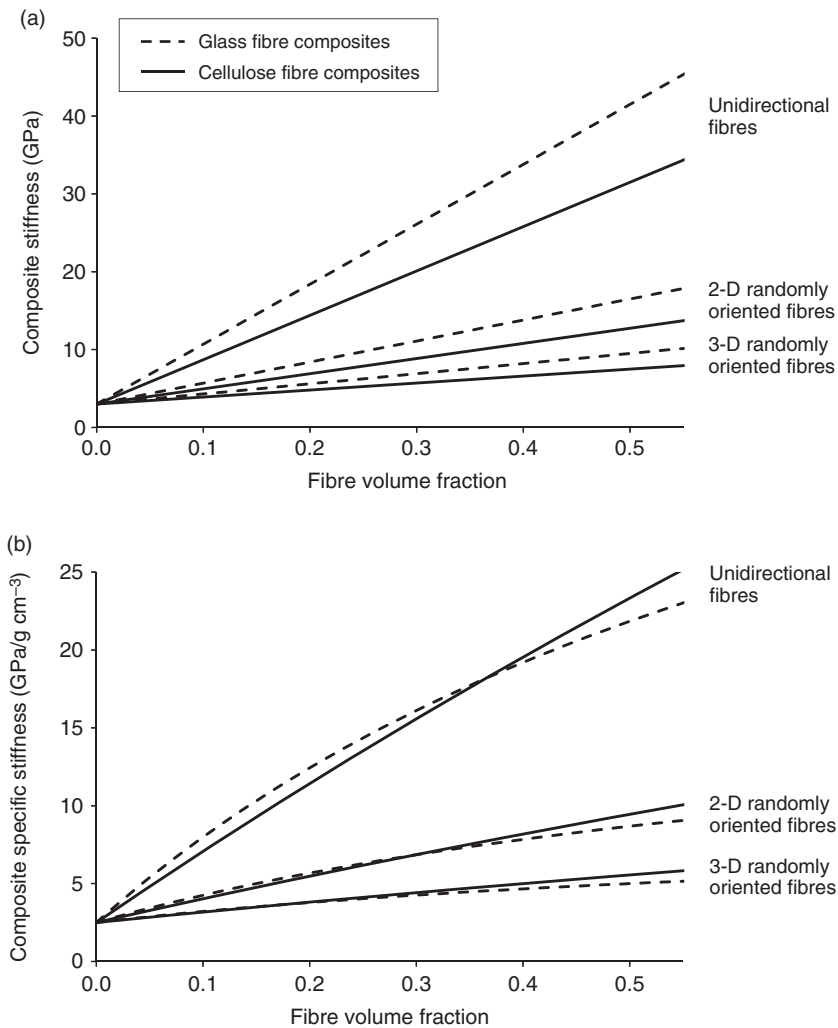
$$\rho_c = V_f \rho_f + V_m \rho_m \quad [11.2]$$

where V is the volume fraction, η_l is the fibre length factor, η_0 is the fibre orientation factor, and the subscripts c, f, m , and p are composites, fibres, matrix and porosity, respectively. The fibre volume fraction (V_f) is used as the variable parameter in the comparison between the two composites. The applied values for the constant materials parameters are: $E_m = 3$ GPa (reflecting a typical thermosetting polymer); $E_{f\text{cell}} = 60$ GPa; $E_{f\text{glass}} = 80$ GPa; $V_m = 1 - V_f$ (assuming no porosity in the composites); $\eta_l = 1$ (due to an aspect ratio of the fibres above 50 (see Madsen *et al.*, 2009)); $\rho_m = 1.2$ g/cm³; $\rho_{f\text{cell}} = 1.5$ g/cm³; $\rho_{f\text{glass}} = 2.6$ g/cm³. To predict the properties of composites with different fibre orientations, η_0 is set equal to 1, 3/8 and 1/5, reflecting the situation of unidirectional fibres, 2-D randomly oriented fibres and 3-D randomly oriented fibres, respectively (Krenchel, 1964).

Due to the anisotropic nature of cellulose fibres, the modelling approach of using a single elastic constant, E_f , for the fibre stiffness in non-unidirectional composites is not fully correct. More correctly, the model calculations should take into account the difference in axial and transverse properties of the cellulose fibres. However, for reasons of simplicity, a single elastic constant is used to reflect the reinforcement efficiency of the fibres.

The resulting model predictions for the comparison of E_c and E_c/ρ_c for cellulose and glass fibre composites with three different fibre orientations are shown in Fig. 11.10.

The model predictions show the *optimal performance* of composites with no porosity, perfectly oriented fibres and perfect fibre/matrix interface bonding. It should be noted that the limited packing ability of fibre assemblies (in general, for all fibre types) constrains the maximum obtainable fibre volume fraction in composites (Madsen *et al.*, 2007b). For composites with a non-unidirectional fibre orientation, a fibre volume fraction above 0.50 might not be realistic. Some studies have indicated that the packing ability of cellulose fibre assemblies is lower than for glass fibre assemblies (Madsen and Lilholt, 2002) leading to lower maximum obtainable fibre volume fractions in cellulose fibre composites. Nonetheless, the model predictions shown in



11.10 Model predictions for comparison of stiffness (a) and specific stiffness (b) as function of fibre volume fraction for cellulose fibre composites and glass fibre composites, with different fibre orientations. See chapter text for more details.

Fig. 11.10 are useful guidelines for the comparison between the two types of composites.

In Fig. 11.10a, for composites with a fibre volume fraction of 0.50, the stiffness values for the cellulose and glass fibre composites with the three fibre orientations are 32 vs 42 GPa, 13 vs 17 GPa and 8 vs 10 GPa, respectively. Thus, as also clearly shown by the curves in the figure, the stiffness of glass fibre composites is greater than the stiffness of cellulose fibre composites,

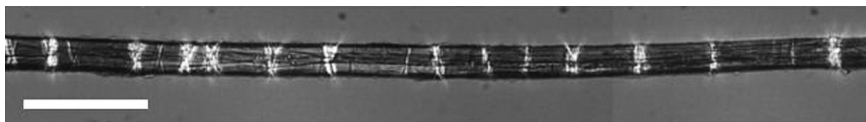
but the difference is reduced when the alignment of the fibres is lowered, i.e. going from unidirectional oriented fibres to 2-D and 3-D randomly oriented fibres. This explains the current success of cellulose fibre composites in replacing glass fibre composites in automotive semi-structural panels, where non-woven mats with a 2-D random orientation are used. It should be pointed out that this development is also driven by the lower cost of non-woven mats made from cellulose fibres.

The greater stiffness of the glass fibre composites is solely due to the larger $E_{f\text{glass}}$ on 80 GPa vs $E_{f\text{cell}}$ on 60 GPa, the latter value representing a typical value for commercially available high-quality cellulose fibres (Madsen *et al.*, 2007a, 2009). However, as indicated in Fig. 11.1, even higher quality cellulose fibres can be obtained with stiffness values up to 90 GPa. This was the case for the flax fibres used in the study by Oksman (2001) in which a novel biotechnical process using enzymes and microbial cultures was applied for the extraction of fibres from the plants. The future development and commercialization of processing techniques (both agricultural and textile) for cellulose fibres is therefore likely to result in these composites comparing more favourably with the glass fibre composites.

The lower density of cellulose fibres compared to glass fibres (1.5 vs 2.6 g/cm³) is advantageous with respect to the weight-based specific stiffness of the composites (E_c/ρ_c). These model predictions are shown in Fig. 11.10b. The specific stiffness of the cellulose and glass fibre composites are similar with values of 23.3 vs 21.8 GPa/g cm⁻³, 9.4 vs 8.7 GPa/g cm⁻³ and 5.6 vs 5.0 GPa/g cm⁻³ for the three fibre orientations, respectively, for composites with a V_f of 0.50. It can be seen from the model lines in the figure that a low V_f in the composites will favour the higher stiffness of the glass fibres, and a high V_f will favour the lower density of the cellulose fibres, with respect to the calculated specific stiffness. Thus, as also shown by the model lines, a threshold V_f exists above which the specific stiffness of the cellulose fibre composites is greater than that of the glass fibre composites. The threshold V_f is about 0.37, 0.30 and 0.19 for the three fibre orientations. These values serve as valuable guidelines for when to expect a weight-based benefit from cellulose fibre composites.

11.5 Special considerations in the development and application of biobased composites

Due to there being a new class of composite materials, biobased composites are faced with a number of key issues that still need to be addressed. This was also the situation with the past development of other classes of composites, such as glass and carbon fibre composites, which are now well-established materials. The following is an introduction to some of these special considerations.



11.11 Polarized optical microscope image of a flax fibre with defects.
Scale bar is 100 µm (Mehmood and Madsen, 2012).

11.5.1 Fibre defects

Using knowledge of the molecular structure of crystalline cellulose and the density and energy of the chemical bonds involved, the theoretical maximum strength of cellulose fibres can be calculated to a high value of 15 000 MPa (Lilholt and Lawther, 2000). However, as shown above in Table 11.1, the practical obtainable strength of cellulose fibres is rather low, being in the range 200–900 MPa. Strength is often said to be the key property of cellulose fibres that needs to be improved. Observations of cellulose fibres with the microscope reveal that the fibres contain a number of structural irregularities distributed along their lengths (Fig. 11.11), which probably act as defects capable of lowering the strength of the fibres. Accordingly, the topic of defects in cellulose fibres has become an important one (see review by Hughes, 2012). In a recent study, the number of processing steps performed to extract the fibres from the plants was shown to be correlated to the measured strength of the fibres; the fewer the processing steps, the higher the strength (Thygesen *et al.*, 2011). This offers some hope for the development of cellulose fibres with higher strength through refinements of the fibre processing techniques.

11.5.2 Variability in fibre properties

It is often stated that the large variability in the properties of cellulose fibres is one of the major limitations in the use of these fibres for composites. The uncertainty about the reasons for the variability, and how it influences the mechanical properties of the composites, leads to the fact that cellulose fibre composites are often employed only in semi-structural composite applications. The variability in the properties of cellulose fibres is caused by four main factors:

- Plant anatomy, i.e. the internal organization of the plant structure.
- Growth conditions.
- Fibre processing conditions.
- Experimental characterization methods.

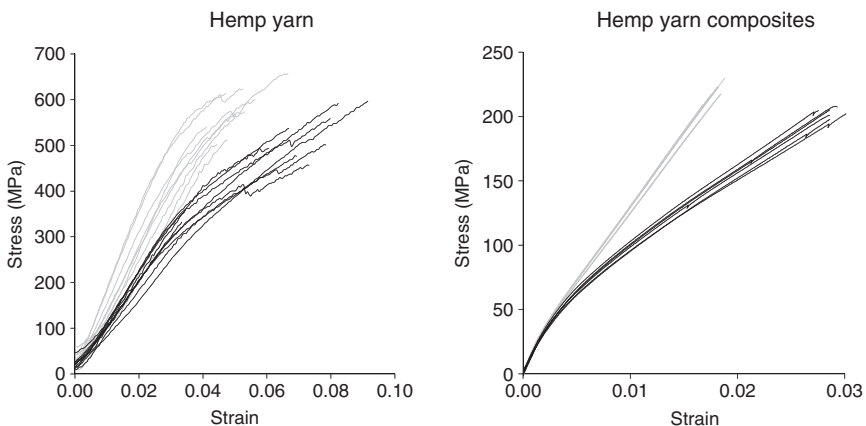
The first three factors cause *true variability* in fibre properties. They lead to variability *between batches* of fibres, e.g. because of the inevitable changes in growth conditions from year to year (or from field to field); they also lead to variability *within batches* of fibres, e.g. because of the inherent spread of differently matured fibres from different plants, and because of the non-uniform processing conditions when the fibres are extracted from the plants. In contrast, the fourth factor causes *artificial variability* in fibre properties due to measuring errors introduced by inaccurate experimental characterization methods, and thereby significantly contributes to the total observed variability of the fibres (Aslan *et al.*, 2011; Thomason *et al.*, 2011).

Figure 11.12 shows an example of the variability in properties between and within batches of cellulose fibres. Shown are stress–strain curves for two different batches of textile hemp yarn of the same nominal quality, but purchased at an interval of two years. From a textile point of view, the two batches are probably considered identical since they show overlapping strength values in the same range of 450–650 MPa. Strength is the key mechanical property of textile yarns. However, from an engineering point of view, the difference in stress–strain behaviour of the two hemp yarn batches is more critical. This is demonstrated by the resulting different properties of unidirectional composites made from the two batches of hemp yarn, namely stiffnesses of 20.1 ± 0.6 GPa and 17.6 ± 0.7 GPa, and strengths of 221 ± 5 MPa and 205 ± 5 MPa, respectively (Madsen *et al.*, 2007a). Thus, the composite reinforcement efficiency of the fibres between batches is not identical.

Figure 11.12 also shows that the relative large spread of stress–strain curves for the neat hemp yarn within each of the two batches is reduced in the composites, which show almost identical stress–strain curves. It is typically observed that test specimens cut from the same composite plate show low variability in properties with coefficient of variation of less than 5% for tensile stiffness and strength (Madsen *et al.*, 2007a). In any case, duplicate composite plates with identical properties can be made when the process conditions are well controlled (Mehmood and Madsen, 2012). In general, therefore, the large variability in properties of the fibres within batches is levelled out in the composites leading to an acceptable low variability in properties of the composites.

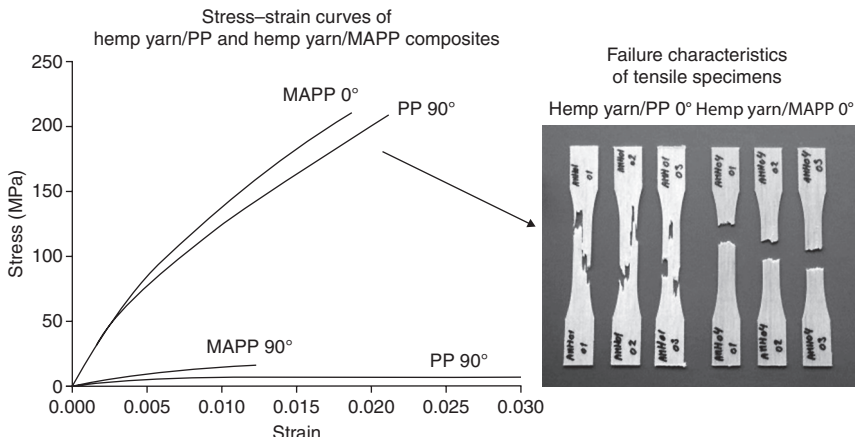
11.5.3 Interface properties

Due to the complex and non-uniform surface chemistry of cellulose fibres, chemical and physical treatments to control the properties of the fibre/matrix interface are challenging. Even so, a range of methods, based on wood fibre composites, have been shown to enhance the compatibility between



11.12 Stress–strain curves of two batches of textile hemp yarn of equal nominal quality: (a) neat hemp yarn, and (b) composites of unidirectional hemp yarn in a thermoplastic matrix (Madsen *et al.*, 2007a.)

wood fibres and polymer matrices (Lu *et al.*, 2000), and these methods have proved to be applicable to plant fibre composites as well (Zafeiropoulos *et al.*, 2002). Typically, the fibres are treated chemically or physically to reduce their polarity (which, as a positive side effect, also lowers the moisture sensitivity of the fibres). Acetylation is an example of a well-studied method (Khalil *et al.*, 2001). In this method, the polar hydroxyl groups (OH) at the fibre surface are covalently bonded with the non-polar acetyl groups (CH_3CO) of acetic anhydride by an esterification reaction. This approach establishes a more intimate contact between fibres and matrix, and promotes interatomic fibre/matrix adhesion by van der Waals forces. Coupling agents can be used to create stronger covalent bonds between fibres and matrix (Lu *et al.*, 2000). A commonly applied coupling agent is maleic anhydride (MA). The compatibilization process includes two steps: (i) MA is reacted with the thermoplastic matrix polymer (e.g. polypropylene, PP) to form a reaction product (e.g. MAPP) consisting of anhydride units located along the polymer carbohydrate chains, and (ii) MA is reacted with the hydroxyl groups at the fibre surface to form intermolecular covalent and hydrogen bonds (Myers *et al.*, 1991). Figure 11.13 shows the results from a study of unidirectional hemp/PP composites where MA was used as coupling agent (Madsen *et al.*, 2001). In the transverse direction (90°), stiffness and strength of the composites is clearly improved by the use of MAPP. In the axial direction (0°), the stress–strain behaviour of the composites is almost identical, but the fracture characteristic is changed from a ductile fracture mode with splitting cracks moving along the fibres, to a more brittle fracture mode with one crack moving transverse to the fibres.



11.13 Stress–strain curves and failure characteristics of unidirectional hemp yarn/PP composites with and without a MA coupling agent.
(Source: Modified from Madsen *et al.*, 2001.)

11.5.4 Other issues

Among the other key issues of biobased composites that still need to be addressed are:

- *Moisture related properties.* The moisture sorption of cellulose fibres is larger than for synthetic fibres. For the bast fibre types hemp, flax and jute, the equilibrium moisture content at 65% RH is in the range 8–10% (Hill *et al.*, 2009). Changes in the surrounding humidity lead to changes in moisture content, which in turn lead to changes in dimensions and properties of the fibres. In the composites, the fibres are embedded in a polymer matrix which serves to lower the rate of moisture diffusion. In a study of unidirectional hemp yarn composites in a thermoplastic matrix, the dimensional changes in the transverse directions were found to be 1.1%, with practically zero dimensional change in the axial direction, when the surrounding humidity was changed from 65% to 85% RH (Madsen *et al.*, 2012). The moisture related properties of biobased composites have been addressed in a large number of studies (e.g. George *et al.*, 1998; Alvarez *et al.*, 2004; Wang *et al.*, 2006; Akil *et al.*, 2009; Almgren *et al.*, 2009; Chen *et al.*, 2009), and the work is ongoing.
- *Packing ability of fibres.* Cellulose fibres show lower packing ability than synthetic fibres (Madsen and Lilholt, 2002), probably due to their less uniform cross-sectional shapes, rougher surface topology and higher degree of fibre misalignment. This typically leads to lower fibre volume content in biobased composites than in synthetic fibre composites for

the same manufacturing conditions. The packing ability, or compaction behaviour, of cellulose fibre assemblies has been addressed only in a limited way, and is yet to be fully understood.

- *Processing of composites.* Biobased composites can in principle be processed using the same manufacturing techniques as for synthetic fibre composites, but some modifications of techniques and adjustments of conditions are required. The high moisture content of the fibres, even at room conditions, means that in some cases drying of the fibre preform materials is required before manufacturing begins. Such a process step is standard in some industries, for instance during manufacturing of furniture with wood veneer, and is relatively easy to establish. The existence of a maximum process temperature of about 200°C, to prevent the onset of thermal degradation of the fibres, is an example of constrained manufacturing conditions, but one which is mainly relevant for composites with thermoplastic matrices.
- *Porosity in composites.* Biobased composites typically contain a greater porosity (or void) content than synthetic fibre composites. This is caused by a number of factors related to the cellulose fibres: (i) the existence of luminal cavities in the fibres, (ii) the complex fibre-surface chemistry, which complicates fibre/matrix compatibilization, and (iii) the heterogeneous form and dimensions of the fibres, which restrict matrix impregnation. A direct way of maximising the performance of biobased composites would be to lower the porosity content. Nevertheless, the topic of porosity in biobased composites has only been addressed to a limited extent in the literature (Madsen *et al.*, 2007b, 2009).
- *Full specifications of composite mechanical performance.* Until now, most studies of biobased composites have reported on basic mechanical properties in tension and bending, while specifications of more complex mechanical properties, e.g. compression, shear and multiaxial stress-strain behaviour, both in static tests and in fatigue tests, have been considered in only a few studies (e.g. Towo and Ansell, 2008; Liang *et al.*, 2012; Shah *et al.*, 2012).

11.6 Sources of further information and advice

Reviews in scientific journals

Abdul Khalil HPS, Bhat IUH, Jawaid M, Zaidon A, Hermawan D, Hadi YS. (2012). Bamboo fibre reinforced biocomposites: A review. *Materials and Design*. **42**: 353–368.

Faruk O, Bledzki AK, Fink H, Sain M. (2012). Biocomposites reinforced with natural fibers: 2000–2010. *Progress in Polymer Science*. **37**: 1552–1596.

- Hill C, Hughes M. (2010). Natural fibre reinforced composites – Opportunities and challenges. *Journal of Biobased Materials and Bioenergy*. **4**: 148–158.
- Mohanty AK, Misra M, Hinrichsen G. (2001). Biofibres, biodegradable polymers and biocomposites: An overview. *Macromolecular Materials and Engineering*. **276/277**: 1–24.
- Shahzad A. (2012). Hemp fiber and its composites – A review. *Journal of Composite Materials*. **46**: 973–986.
- Wambua P, Ivens J, Verpoest I. (2003). Natural fibres: Can they replace glass in fibre reinforced plastics? *Composites Science and Technology*. **63**: 1259–1264.
- Zini E, Scandola M. (2011). Green composites: An overview. *Polymer Composites*. **32**: 1905–1915.

Text books

- Bledzki AK, Sperber VE, Faruk O. (2002). Natural and wood fibre reinforcement in polymers. *Rapra Review Reports*. Vol. **13**. No. 8.144 pages.
- CELC European Scientific Committee. (2012). Flax and hemp fibres: a natural solution for the composite industry. Editors F. Reux and I. Verpoest. JEC Composites Group and the European Hemp and Flax Confederation. Paris, France. 214 pages.
- Jiang ZH. (2007). *Bamboo and Rattan in the World*. China Forestry Publishing House, Beijing, China. 360 pages.
- Lilholt H, Lawther JM. (2000). Natural organic fibers. In *Comprehensive Composite Materials* (6 vols). Editors A. Kelly and C. Zweben. Elsevier Science. Vol. **1**, Chap. 10, pp. 303–325.
- Mohanty AK, Misra M, Drzal LT. (2005). *Natural Fibers, Biopolymers, and Biocomposites*. CPR Press, Taylor & Francis Group, USA. 855 pages.
- Müssig J. (2010). *Industrial Applications of Natural Fibres – Structure Properties and Technical Applications*. John Wiley & Sons, United Kingdom. 523 pages.
- Pickering KL. (2008). *Properties and Performance of Natural-fibre Composites*. Woodhead Publishing Limited, Cambridge, England. 543 pages.

11.7 References

- Abdul Khalil HPS, Bhat IUH, Jawaid M, Zaidon A, Hermawan D, Hadi YS. (2012). Bamboo fibre reinforced biocomposites: A review. *Materials and Design*. **42**: 353–368.
- Akil HM, Cheng LW, Ishak ZAM, Bakar AA, Rahman MAA. (2009). Water absorption study on pultruded jute fibre reinforced unsaturated polyester composites. *Composites Science and Technology*. **69**: 1942–1948.
- Almgren KM, Gamstedt EK, Berthold F, Lindström M. (2009). Moisture uptake and hygroexpansion of wood fiber composite materials with polylactide and polypropylene matrix. *Polymer Composites*. **30**: 1809–1816.
- Alvarez VA, Fraga AN, Vázquez A. (2004). Effects of the moisture and fiber content on the mechanical properties of biodegradable polymer-sisal fiber composites. *Journal of Applied Polymer Science*. **91**: 4007–4016.
- Andersen TL. (2011). Bio/bio-kompositter. National project funded by Regional Growth Forum Zealand, Denmark. Project Report. Risø-I-3094 (DA).

- Aslan M, Chinga-Carrasco G, Sørensen BF, Madsen B. (2011). Strength variability of single flax fibres. *Journal of Materials Science*. **46**: 6344–6354.
- Bunnell AR, Renard J. (2005). *Fundamentals of Fibre Reinforced Composite Materials*. Institute of Physics Publishing Ltd, London, United Kingdom.
- CELC European Scientific Committee. (2012). Flax and hemp fibres: a natural solution for the composite industry. In *JEC Composites Group and the European Hemp and Flax Confederation*. Eds. F. Reux and I. Verpoest. Paris, France.
- Chen H, Miao M, Ding X. (2009). Influence of moisture absorption on the interfacial strength of bamboo/vinyl ester composites. *Composites Part A*. **40**: 2013–2019.
- Faruk O, Bledzki AK, Fink H, Sain M. (2012). Biocomposites reinforced with natural fibers: 2000–2010. *Progress in Polymer Science*. **37**: 1552–1596.
- George J, Bhagawan SS, Thomas S. (1998). Effects of environment on the properties of low-density polyethylene composites reinforced with pineapple-leaf fibre. *Composites Science and Technology*. **58**: 1471–1485.
- Hepworth DG, Hobson RN, Bruce DM, Farrent JW. (2000). The use of unretted hemp fiber in composite manufacture. *Composites Part A*. **31**: 1279–1283.
- Hill C, Hughes M. (2010). Natural fibre reinforced composites – opportunities and challenges. *Journal of Biobased Materials and Bioenergy*. **4**: 148–158.
- Hill CAS, Norton A, Newman G. (2009). The water vapor sorption behavior of natural fibers. *Journal of Applied Polymer Science*. **112**: 1524–1537.
- Holmes JW, Brøndsted P, Sørensen BF, Jiang Z, Chen ZX. (2009). Development of a bamboo-based composite as a sustainable green material for wind turbine blades. *Wind Engineering*. **33**: 197–210.
- Hughes M. (2012). Defects in natural fibres: their origin, characteristics and implications for natural fibre-reinforced composites. *Journal of Materials Science*. **47**: 599–609.
- Jiang ZH. (2002). *Bamboo and Rattan in the World*. Liaoning Science and Technology Publishing House.
- Karus M, Kaup M, Ortmann S. (2002). Use of natural fibers in the German and Austrian automotive industry. Market survey 2002: Status, analysis and trends. Nova-Institute GmbH, Hürth, Germany.
- Khalil HPSA, Ismail H, Rozman HD, Ahmad MN. (2001). The effect of acetylation on interfacial shear strength between plant fibres and various matrices. *European Polymer Journal*. **37**: 1037–1045.
- Klein W. (1998). *The Technology of Short-staple Spinning*. 2nd edition. The Textile Institute, Manchester, United Kingdom.
- Krenchel H. Fibre reinforcement. Akademisk forlag. Copenhagen, Denmark, 1964. p. 16–22.
- Liang S, Gning PB, Guillaumat L. (2012). A comparative study of fatigue behaviour of flax/epoxy and glass/epoxy composites. *Composites Science and Technology*. **72**: 535–543.
- Lilholt H, Lawther JM. (2000). Natural organic fibers. In *Comprehensive Composite Materials* (6 vols). Eds. A. Kelly and C. Zweben. Elsevier Science. Vol. **1**, chap. 10, p. 303–325.
- Lu JZ, Wu Q, McNabb HS. (2000). Chemical coupling in wood fiber and polymer composites: A review of coupling agents and treatments. *Wood and Fiber Science*. **32**: 88–104.
- Madsen B, Andersen TL, Plackett D, Lilholt H. (2001). Evaluation of properties of unidirectional hemp/polypropylene composites – influence of fiber content and

- fiber/matrix interface variables. In the Proceedings of the 6th International Conference on Woodfiber-Plastic Composites. Madison, USA.
- Madsen B, Hoffmeyer P, Lilholt H. (2007a). Hemp yarn reinforced composites – II. Tensile properties. *Composites Part A*. **38**: 2204–2215.
- Madsen B, Hoffmeyer P, Lilholt H. (2012). Hemp yarn reinforced composites – III. Moisture content and dimensional changes. *Composites Part A*. **43**: 2151–2160.
- Madsen B, Lilholt H. (2002). Compaction of plant fibre assemblies. In the Proceedings of Sustainable Natural and Polymeric Composites – Science and Technology. 23rd Risø International Symposium on Materials Science. September 2002. Risø, Denmark.
- Madsen B, Thygesen A, Lilholt H. (2007b). Plant fibre composites – porosity and volumetric interaction. *Composites Science and Technology*. **67**: 1584–1600.
- Madsen B, Thygesen A, Lilholt H. (2009). Plant fibre composites – porosity and stiffness. *Composites Science and Technology*. **69**: 1057–1069.
- Mehmood S, Madsen B. (2012). Properties and performance of flax yarn/thermo-plastic polyester composites. *Journal of Reinforced Plastics and Composites*. **31**: 62–73.
- Mohanty AK, Misra M, Drzal LT. (2005). *Natural Fibers, Biopolymers, and Biocomposites*. CPR Press, Taylor & Francis Group, USA.
- Møller M, Skovgaard F, Okholm A. (2012). Characterization, dimensioning and manufacturing of bio-composites. Student project report. Department of Wind Energy, Technical University of Denmark.
- Müssig J. (2010). *Industrial Applications of Natural Fibres – Structure Properties and Technical Applications*. John Wiley & Sons, United Kingdom.
- Myers GE, Chahyadi IS, Coberly CA, Ermer DS. (1991). Wood flour/polypropylene composites: Influence of maleated polypropylene and process and composition variables on mechanical properties. *International Journal of Polymeric Materials*. **15**: 21–44.
- Oksman K. (2001). High quality flax fibre composites manufactured by the resin transfer moulding process. *Journal of Reinforced Plastics and Composites*. **20**: 621–627.
- Pickering KL. (2008). *Properties and Performance of Natural-fibre Composites*. Woodhead Publishing Limited, Cambridge, England.
- Pignatti L, Bottoli F. (2011). Design and processing of structural components in biocomposite materials – Case study: Rotor blade for wind turbine cars. Master thesis report. Department of Wind Energy, Technical University of Denmark.
- Roe PJ, Ansell MP. (1985). Jute-reinforced polyester composites. *Journal of Materials Science*. **20**: 4015–4020.
- Shah D, Schubel PJ, Clifford MJ, License P. (2012). Fatigue characterisation of plant fibre composites for small-scale wind turbine blade applications. In 5th Innovative Composites Summit – JEC Asia 2012, Singapore.
- Shah DU, Schubel PJ, Clifford MJ, Licence P. (2012). The tensile behavior of off-axis loaded plant fiber composites: An insight on the nonlinear stress-strain response. *Polymer Composites*. **33**: 1494–1504.
- Shahzad A. (2012). Hemp fiber and its composites – a review. *Journal of Composite Materials*. **46**: 973–986.

- Siau JF. (1995). Wood: Influence of moisture on physical properties. Department of Wood Science and Forest Products, Virginia Polytechnic Institute and State University, USA.
- Thomason JL, Carruthers J, Kelly J, Johnson G. (2011). Fibre cross-section determination and variability in sisal and flax and its effects on fibre performance characterisation. *Composites Science and Technology*. **71**: 1008–1015.
- Thygesen A, Madsen B, Bjerre AB, Lilholt H. (2011) Cellulosic fibres: Effect of processing on fibre bundle strength. *Journal of Natural Fibres*. **8**: 161–175.
- Thygesen A, Oddershede J, Lilholt H, Thomsen AB, Ståhl K. (2005). On the determination of crystallinity and cellulose content in plant fibers. *Cellulose*. **12**: 563–576.
- Thygesen A, Thomsen AB, Daniel G, Lilholt H. (2007). Comparison of composites made from fungal defibrated hemp with composites of traditional hemp yarn. *Industrial Crops and Products*. **25**: 147–159.
- Towo AN, Ansell MP. (2008). Fatigue evaluation and dynamic mechanical thermal analysis of sisal fibre-thermosetting resin composites. *Composites Science and Technology*. **68**: 925–932.
- Van de Weyenberg I, Ivens J, De Coster A, Kino B, Baetens E, Verpoest I. (2003). Influence of processing and chemical treatment of flax fibers on their composites. *Composites Science and Technology*. **63**: 1241–1246.
- Wang W, Sain M, Cooper PA. (2006). Study of moisture absorption in natural fibre plastic composites. *Composites Science and Technology*. **66**: 379–386.
- Zafeiropoulos NE, Williams DR, Baillie CA, Matthews FL. (2002). Engineering and characterisation of the interface in flax fibre/polypropylene composite materials. Part I. Development and investigation of surface treatments. *Composites Part A*. **33**: 1083–1093.
- Zini E, Scandola M. (2011). Green composites: an overview. *Polymer Composites*. **32**: 1905–1915.

Surface protection and coatings for wind turbine rotor blades

B. KJÆRSIDE STORM, Aalborg University, Denmark

DOI: 10.1533/9780857097286.3.387

Abstract: This chapter discusses surface layer protection for wind turbine rotor blades. The surface protection and coating can be a gelcoat or a paint and can be made of unsaturated polyester, epoxy, polyurethane or acrylic. As wind turbines are often erected in harsh climates, the blade surface will be exposed to conditions that cause erosion and wear. There are tests to measure resistance against these attacks, and the surface is designed to minimize damage to the blade caused by the environment. By using existing standards for surface layers for offshore use and for helicopters, it has been found that a combination of accelerated tests for UV degradation, chemical attack and wear give a complete picture of the performance of surface layers.

Key words: rotor blades, protection, surface layers, test for surface performance, surface protection lifetime, lightning protection.

12.1 Introduction

The main advantage of current protection technology is that it offers a variety of ways of manufacturing successful surfaces for wind turbine rotor blades. Choices must be made between the different technologies and materials available. For instance, one decision that must be made is whether a soft or a hard surface will be used. In some cases, a soft surface will provide superior wear resistance, particularly at the beginning of the life of the wind turbine rotor blade. This is because hard particles can be absorbed by the soft surface, making it become harder. However, the surface needs to be reasonably thick in order for this to happen, and the materials that give a soft surface do not necessarily provide adequate chemical protection and may be degraded more quickly by UV light than the harder surface.

Thus, there will always be a choice to be made between considerations such as performance, environmental challenges, and the materials and technologies that are available, and one must decide which consideration should take priority. However, there will always be limitations; for example, a surface that offers protection from sunlight will not normally offer strong wear

resistance. Unfortunately, this is not a problem that will diminish in the future, since new wind turbines are larger and therefore have larger rotor blades, which will need more protection.

When deciding which consideration to favour, it is important to consider the conditions to which the wind turbine rotor blade will be subject. The surfaces of wind turbine rotor blades are exposed to various types of adverse conditions including:

- temperature (from -50°C to 70°C);
- UV radiation from sunlight;
- chemical attack (from various chemicals);
- blood from insects;
- faeces from birds;
- lightning and other mechanical attack;
- ice;
- water attack;
- hailstorms;
- rain erosion;
- salinity in the air;
- wear from sand and other small particles.

The weather will cause damage as the temperature changes from frost to thaw, whilst blistering of the surface of the blade can be caused by wear from sand and salt, water diffusion and chemical attack from the surroundings. Wear will cause the strength of the surface layer to decrease, and will affect the adhesion between the laminate and the surface layer.

Rotor blades need to be protected as much as possible against these different attacks. It is not possible to protect blades from all of these threats, but they should be manufactured so that the surface layer – the gelcoat or the paint – provides as much protection as possible. Gelcoat is made as the top layer when a rotor blade is produced: it is added to the mould, and then the fibres, the foam and the resin are added. Paint, if it is to be used, is added after the rotor blade has been produced, with the thickness of a paint layer normally being much less than that of a gelcoat layer. The surface should not be too glossy, since it will reflect sunlight, and it should not be too rough, since this will lead to inefficiency.

Research has been carried out in an attempt to find a way to protect the surface layers of wind turbine rotor blades. The difference in the environments in which rotor blades operate makes it difficult to develop ways of protecting the surfaces: some turbines are placed in deserts, some in arctic climates, some in offshore wind farms, etc., and they all need different protection. It may be possible to develop specialist surface layers that can be applied in each different environment. However, this would not be the best

solution, as it would mean a specialized surface layer having to be made for each application.

It is possible to learn from old wind turbines, which in some cases have been exposed to a harsh environment for around twenty years. Examinations of old rotor blades have been carried out for this purpose. However, it can be very difficult to find out what the surface layer was like when the rotor blade was produced since the production of turbine rotor blades in previous decades was not controlled to the extent that it is today. Furthermore, there will always be some uncertainty about the thickness of the layer: though it is possible to measure how much gelcoat or paint there is in total on the surface, the thickness may not be equal across the surface. When investigating the attack from the surroundings, it is useful to compare the used rotor blade with an unused one. However, unused blades are difficult to find because most rotor blades are produced for use.

This chapter will examine existing protection technologies for the surface layer of wind turbine rotor blades, looking in detail at the protection used against ice, lightning and air traffic. Performance testing and accelerated testing of surface coatings will also be discussed.

12.2 Fundamentals of surface protection for wind turbine blades

Wind turbine rotor blades are protected on the surface by gelcoat or paint. The surface protection is necessary because there will always be pinholes in the composite – the laminate – of which the rotor blades are made. In reality, it is desirable to have a surface layer without pinholes, but because of contractions, curing, practical treatment and other circumstances, a laminate – and a surface – will not be without pinholes. By adding more layers, the risk of having pinholes in the surface will decrease. The gelcoat or the paint may also have pinholes, but if the layer is made correctly, the risk of having pinholes will be negligible.

Both paints and gelcoats can be made from different types of polymers. In most cases, the laminate will be made from glass- or carbon-fibre reinforced polymers. The matrices can be of different types, but in most cases they will be unsaturated polyesters, epoxies or, occasionally, polyurethanes or vinyl esters. A matrix can also be made from thermoplastics, but only gelcoats and paints for the thermoset matrices will be discussed here.

If the surface layer is a gelcoat, it will be made from a polymer that is compatible with the laminate. If the surface layer is paint, the paint should be able to wet the surface of the laminate. The compatibility, or the wetting ability, is necessary in order to give adequate adhesion of the surface layer to the laminate. If the adhesion is poor, the surface layer can work

loose from the laminate. Without the surface layer, the laminate can easily be destroyed by environmental influences.

12.2.1 Adhesion of surface coatings

The Hansen Solubility Parameters (HSPs) are a useful tool when investigating whether the adhesion in the interface between gelcoat and laminate and between paint and laminate is satisfactory. The HSP expresses the secondary bond energy of a chemical substance; the secondary bond energy is the energy that holds molecules together to form materials or liquids.

The one-dimensional solubility parameter is defined as:

$$\delta_{\text{tot}}^2 = \frac{\Delta E_{\text{vap}}}{V_1}$$

where δ_{tot} is the total solubility parameter, ΔE_{vap} is the heat of evaporation and V_1 is the molar volume.

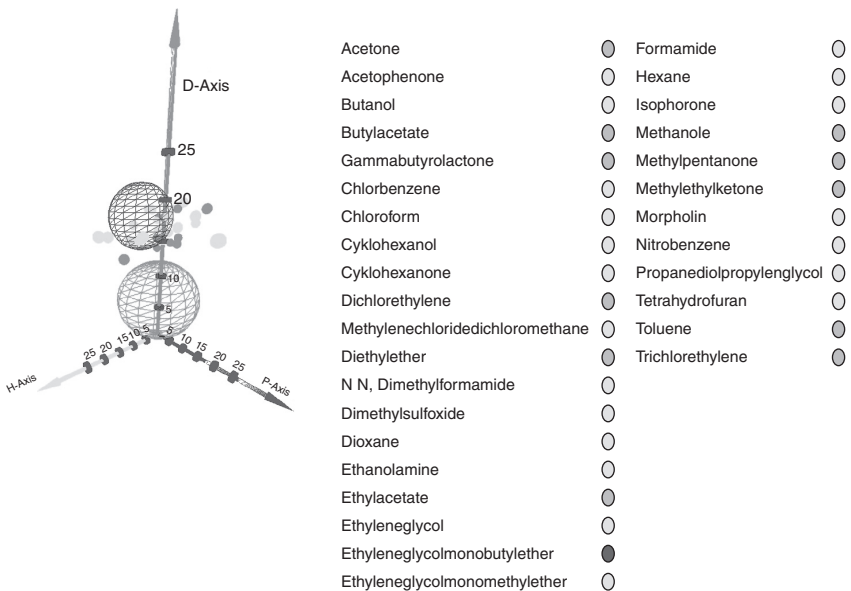
The total solubility parameter can be divided up by the three-dimensional solubility parameter, HSP:

$$\delta_{\text{tot}}^2 = \delta_d^2 + \delta_p^2 + \delta_h^2$$

where δ_d is the contribution from the dispersion forces, δ_p is the contribution from the polar forces and δ_h is the contribution from the hydrogen forces.

The solubility parameter for the laminate, the gelcoat and the paint is expressed as the three contributions from the secondary bond energy and an action radius. This is because the HSP can be plotted in a three-dimensional coordinate system, with the three different secondary bond energies as the three axes, where the unit of the axis for the dispersion forces is double that of the other two axes. When plotted using the coordinate system, the HSP will cover a sphere with the secondary bond energy as the centre and the action radius, R_0 , as the radius of the sphere. Figure 12.1 shows how the HSP can be set up in a three-dimensional coordinate system. The solubility area will appear as a sphere in the coordinate system. The centre of the sphere is the HSP for the material/solvent and the radius of the sphere is the action radius, R_a .

Using the HSP, the compatibility between two materials can be represented as the Relative Energy Density, the RED number, which is defined as:



12.1 HSP for two different materials. The D-Axis has double unit compared with the two other axes. In this way the solubility area can be represented as a sphere in the coordinate system. To the right, the solvents used for determining the HSP in this particular case are shown.

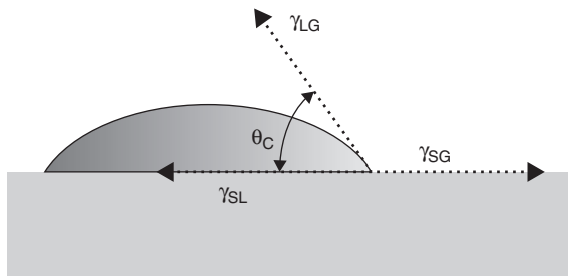
$$\text{RED} = \frac{R_a}{R_0}$$

where R_a is the distance between the radii of the spheres for the two materials, and R_0 is the radius of the material with which the other material must be compatible.

R_a is calculated as:

$$R_a^2 = 4(\delta_{d1} - \delta_{d2})^2 + (\delta_{p1} - \delta_{p2})^2 + (\delta_{h1} - \delta_{h2})^2$$

If $\text{RED} \leq 1$, compatibility between the two materials is highly likely. If $\text{RED} \geq 1$, the two materials will not be compatible and there cannot be wetting between the two materials. If there is strong adhesion in the interface of the gelcoat/laminate system and in that of the laminate/paint system, the RED number for the systems will be less than 1, and the spheres for the two systems will cover or touch each other.¹



12.2 Contact angle for measurement of surface tension. γ_{LG} , γ_{SG} and γ_{SL} : surface tension and the interface forces between the liquid, gas (LG), solid, liquid (SL) and solid gas (SG).

To achieve effective wetting, the surface tension of the surface to be wetted should be higher than the surface tension of the medium that will wet it. For example, if the gelcoat is to be wetted by the resin in the laminate, the surface tension of the resin should be lower than the surface tension of the gelcoat.

The surface tension of a medium or a material depends on the secondary bond energy, and there are correlations between the surface tension and the solubility parameters. The correlations depend on which functional groups are present in the materials. An example of a correlation is:

$$\gamma = 0.0688V^{1/3} \left[\delta_D^2 + k(\delta_P^2 + \delta_H^2) \right]$$

where γ is the surface tension, V is the molar volume and k is a constant depending on the functional groups.¹ The constant (0.0688) depends on the functional groups present in the material, and in this case it is an alcohol group.

In order to achieve a good wetting, the contact angle between the two media must be less than 90°, but ideally as low as possible: the lower the contact angle, the better the wetting of the surface. Figure 12.2 shows an example of wetting of a surface, in which the contact angle is suitably low.

The surface tension of laminates made by epoxy or unsaturated polyester is approximately 40 dyn/cm or 40 mN/m. The surface tension of the gelcoat needs to be higher than that in order to achieve a good wetting of the gelcoat, and, as a result, a good adhesion between the laminate and the gelcoat. If the surface layer is to be painted, the surface of the laminate needs to have a higher surface tension than the paint. If the surface layer to which the paint is to be applied has been contaminated or contains lubricants or waxes with a lower surface tension – between 16 and 31 dyn/cm – it is very difficult to achieve good adhesion, because of the lack of wetting. The low surface tension of materials such as waxes is due to a lack of polarity in the secondary bonds between the molecules. In these cases, it is necessary to polish the surface before painting it in order for there to be strong adhesion.

12.2.2 Selection criteria for coatings

The decision as to whether the surface of a wind turbine rotor blade will be gelcoat or paint is made during the construction of the blade. The manufacturer faces the decision as to whether the surface should be so hard and strong that it can resist all types of mechanical attack, especially wear attack from different type of particles, or if the surface shall be soft and tough, so that hard particles will be absorbed by the surface and in that way create a harder surface. There is also a decision to be made on how resistant a surface needs to be, because the resistance will in many cases depend on the thickness of the layer.

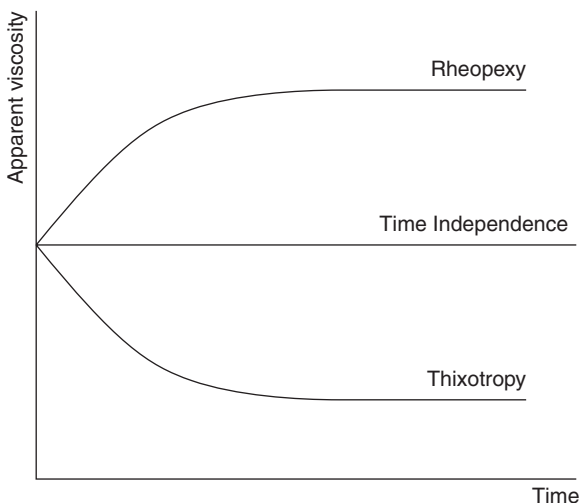
The thickness of the layer will in turn depend on the type of gelcoat/paint used and the application method (i.e. either painting the surface or using a gelcoat on the surface). For some old rotor blades, it is assumed that the thickness of the gelcoat has been about 300 μ . Today, the layer of gelcoat will be up to 800 μ , but there can be large differences depending on the materials used to make the gelcoat. Paints are added to blade surfaces in lower quantities than gelcoats. One of the reasons for using paints and not gelcoats is that they provide thinner layers of protection. The thinner the surface layer, the better the chemical and mechanical resistance. With paint, the protection layer will normally be less than 200 μ . The manufacturer's choice of gelcoat or paint will depend on the way that production has been set up. In the case of reparation, it will normally be a paint which is added to the surface.

Gelcoats and paints can be made from various types of polymers, with different additives depending on the desired properties of the surface layer. The viscosity of both gelcoats and paints needs to be controlled so that they will remain on the surface. A highly viscous gelcoat or paint will, in most cases, display thixotropic behaviour, and so will stay on the surface. The viscosity should be at a level that is low enough to allow the coating material to be applied to the surface and yet high enough to ensure it remains there until the curing can start. The curing should not start until the gelcoat or paint has spread evenly across the surface. Figure 12.3 shows a schematic diagram of the thixotropic behaviour of a material.

The most commonly used types of polymers for gelcoats and paints are unsaturated polyester, epoxy, acrylate and polyurethane. The differences in the properties of these polymers will be examined below.

12.2.3 Particular coating materials

Gelcoats and paints are thermosets: they cross-link during the curing process. The cross-linking contributes to the chemical resistance and wear resistance of the surface.



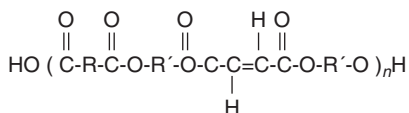
12.3 Thixotropic behaviour of a fluid. The thixotropic behaviour is a time-dependent behaviour, where the viscosity will decrease over time, when a force is added to the fluid.

Unsaturated polyesters

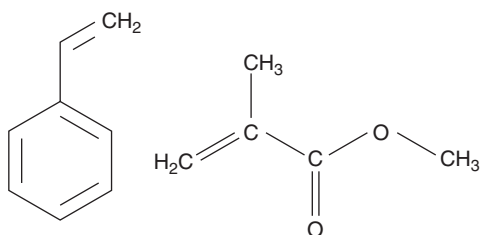
Unsaturated polyesters are a group of thermosets that are cured by cross-linking using a free-radical polymerization process. The unsaturated polyester gelcoat, like unsaturated polyester for resins, consists of an unsaturated acid, a saturated acid and a bi-functional alcohol. The unsaturated acid is maleic acid or fumaric acid. The saturated acid can be phthalic acid or aliphatic acid. The bi-functional alcohol can be a glycol or an aromatic alcohol. In Fig. 12.4, a general chemical formula for unsaturated polyester is shown. The unsaturated polyester is dissolved in styrene or in a combination of styrene and methyl-methacrylate (MMA). Both styrene and MMA, which are shown in Fig. 12.5, contain a double bond over which the cross-linking/curing will take place. Because of the health and safety problems associated with the use of styrene, other solvents containing double bonds are likely to be developed for use in the future. Whilst the curing system will change when styrene substitutes become available, the process will remain a free-radical curing process, since the solvent used will still have a double bond as the active group.

The cross-linking is initiated by a peroxide, often methyl-ethyl-ketone-peroxide (MEKP), which starts the free-radical polymerization process. If the process is to continue over several temperature intervals, the initiator needs to contain more than one peroxide.

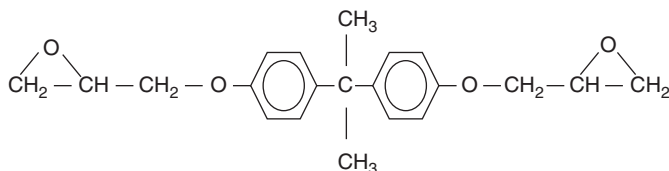
Styrene is used as the cross-linking agent, as a solvent to dissolve the unsaturated polyester, and as a means to control the viscosity of the gelcoat. MMA is also a cross-linker and contributes to the UV protection of the surface, as the ester group in the side group gives UV protection.



12.4 Unsaturated polyester. The unsaturated polyester is made from an unsaturated acid, maleic acid, a saturated acid, often an aromatic acid, and a glycol, often propylene glycol. The cross-linking will take place over the double bond coming from the maleic acid.



12.5 Styrene to the left and methylmethacrylate to the right. Both monomers can be used as cross-linkers for unsaturated polyester.

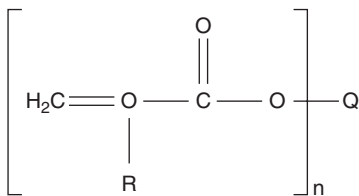


12.6 Epoxy made from Bisphenol A. The cross-linking of the epoxy resin will take place with reaction over the epoxide group with an amine, an anhydride or an alcohol.

Epoxies

Epoxies are a group of thermosets that contain an epoxy group in the pre-polymer. In Fig. 12.6, the epoxy group can be seen. Epoxy is a widely used thermoset for resins and paint because it has properties such as chemical and wear resistance. Epoxies are widely used as matrices in rotor blades, and when the laminate is made of epoxy, the gelcoat will often be made of epoxy as well because it will provide good wetting and the laminate and the surface will be compatible.

Epoxies, like polyesters, can be made from many different materials. Epoxies are most often made from DGEBA(DiGlycidyl Ether of Bisphenol A) and cross-linked by a diamine or an anhydride. Diamines and anhydrides can have many different chemical compositions and can therefore form many different types of epoxies. Epoxies can also be aliphatic instead of being made of Bisphenol A. An aliphatic epoxy will be softer and tougher than an



12.7 A schematic figure of an acrylate. The cross-linking and the reaction will take place over the double bond.

aromatic epoxy and can be used as a component of a gelcoat or a paint, if the surface is tough and is designed for use at very low temperatures.

Epoxies have the advantage of having a lower water uptake than polyesters and they exhibit less shrinking under curing than polyester. A disadvantage of epoxies for use as surface protection is that epoxy gelcoats and paints have lower UV resistance than other materials.

Acrylates

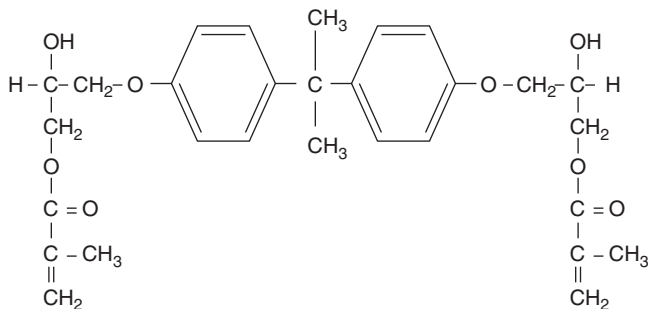
Acrylates of different types can be used as surface protection. Acrylates cure by cross-linking over a double bond; the curing happens very quickly, which can be a great advantage. Acrylates generally have high UV resistance. Acrylates can be made with a hard surface, but there are also softer acrylates. An example of the formula of an acrylate is given in Fig. 12.7.

Vinylesters

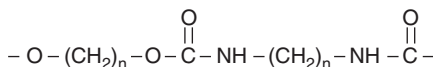
Vinylesters are a combination of an epoxy and of an unsaturated polyester. Curing takes place via a polyester curing system. Like the other coating materials described here, they can be used as gelcoats, but they are used less often due to their high price. Because of their chemical structure, vinylesters are placed in a side chain with the ester group. A general formula for vinylesters is shown in Fig. 12.8.

Polyurethanes

Like the other thermosets, polyurethanes are made from many different materials. In Fig. 12.9, a general chemical formula of polyurethane is given. Polyurethane as a gelcoat or a paint will give a surface that is tougher than any of the above-mentioned types of surface protection. Polyurethane surfaces are used because small and sharp particles can be taken up by the surface and therefore do not cause wear. Polyurethanes are generally more UV resistant than other coating materials, especially epoxies. They can come in the form of a tape which is used for protection of the front edge of the rotor



12.8 A vinylester. The backbone is made from Bisphenol A, and the cross-linking will be similar to the cross-linking for an unsaturated polyester over the double bond.



12.9 Schematic figure of polyurethane.

Table 12.1 Advantages and disadvantages of materials used as gelcoats and paints to provide surface protection for wind turbine rotor blades

Material	Advantages	Disadvantages
Unsaturated polyester	Cheap. Can cure up at room temperature. Difficult to control the curing process.	Low chemical resistance, but this depends on the formulation. Long curing time to full curing.
Epoxy	Good chemical resistance. Hard surface can be obtained.	Curing has to be carried out at elevated temperature. Long curing time.
Acrylate	Short curing time. Cures up at room temperature. UV resistant.	Brittleness can be introduced in the surface. Low chemical resistance. Needs energy to cure, e.g. from IR or UV radiation.
Polyurethane	Short curing time. Can cure at room temperature. Tough surface, which can give good wear resistance because of uptake of sharp particles by the surface.	Tough surfaces. Low wear resistance.

blade. It is often called ‘helicopter tape’, because it is developed to protect the front edges of helicopter rotor blades.

The advantages and disadvantages of each of the above-mentioned materials when used as a gelcoat or a paint are set out in Table 12.1.

12.3 Protection from blade icing, lightning and air traffic

Blade icing and lightning are two phenomena which can spoil or even destroy the rotor blades. Blade icing can further lower the production of the turbine. To be struck by lightning will normally cause damage of the rotor blade, and for that reason the blades are protected against lightning. Air traffic protection is made for protecting the air traffic more than to protect the rotor blades.

12.3.1 Wind turbine blade icing

Icing of rotor blades is a problem in areas with a cold climate. There are many different types of icing, because the type of ice and its structure depends on factors such as temperature, wind speed, humidity, etc.

In-cloud icing happens when cooled water droplets hit the surface of the rotor blade at a temperature below 0°C. The droplets freeze upon impact, because the temperature of the droplets can be down to -30°C. The structure of the in-cloud ice depends on the size of the droplets, the temperature, the wind speed and other parameters.

Thin layers of ice with needles and flakes are called 'rime'. Whether the rime is soft or hard depends on the thickness of the layer and of the density of the ice. The temperature must be below 0°C in order for rime to form on the surface.

The term 'glaze' is used to describe the situation that occurs when a portion of droplets does not freeze immediately, but runs back on to the surface and freezes later. The density of glaze is higher than that of rime and its adhesion to the surface of the blade is strong.³

Different types of precipitation can cause icing. When rain falls at temperatures below 0°C, it is called freezing rain. The density of ice caused by freezing rain is high and its adhesion to the surface of the rotor blades is strong. Wet snow turns to liquid when the air temperature is between -3°C and 0°C. It sticks to the surface but is easy to remove if this is done before it freezes.

Many different techniques have been tested for de-icing or prevention of icing of blade surfaces. When blades were shorter and wind turbines were mainly placed onshore and in accessible environments, de-icing did not pose a major problem because the ice could be removed mechanically. Today, most turbines are placed in environments that are not easily accessible, and therefore other methods for de-icing need to be developed.

Active methods for de-icing include heating by electricity provided by thermo electrical foils or heating provided by microwaves.⁵ All heating systems require energy, and microwave systems use less energy than other heating systems. Systems with active heating elements can be almost 100% efficient.^{3,4}

There are also some passive methods for providing heat for de-icing and some that can prevent icing. Hydrophobic foils with low surface tension

can be used to prevent icing, but are only effective in certain circumstances. Hydrophobic foils are typically made of fluorocarbons or silicon, both of which have a low surface tension and non-stick properties. The lower the surface tension of the foil, the less the ice will adhere to the surface. Warm air blowing over the surface of the blades can also reduce icing, but with large blades this can be difficult in practice.

The best solution to icing is a combination of hydrophobic foils and heating.

12.3.2 Lightning protection

Wind turbines are already large appliances, but future turbines will be even bigger. Lightning tends to hit the highest parts of the turbine, and therefore lightning protection is necessary to avoid damage to the blades and hence the turbine.

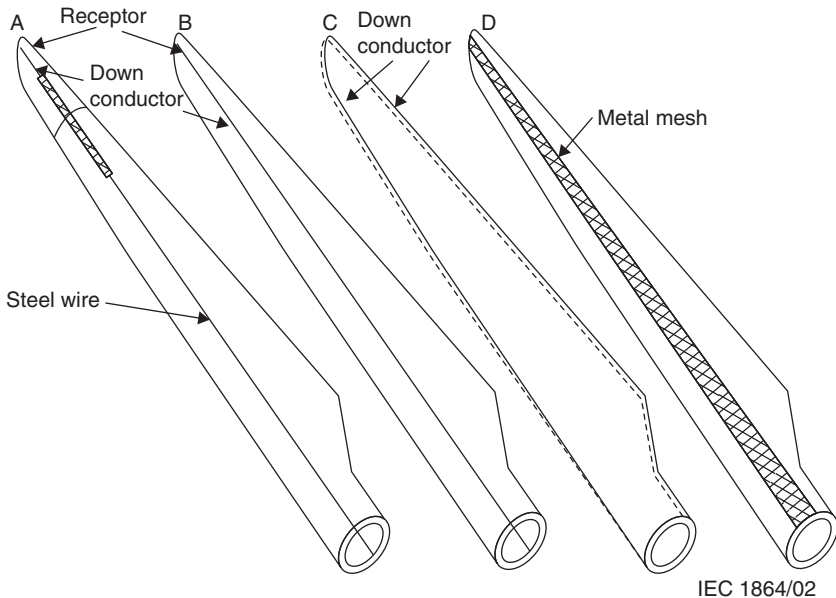
Protection of wind turbine rotor blades against lightning is described in IEC 61400–24⁸: all lightning protection systems must follow these regulations. All wind turbines need to have a lightning protection system (LPS). The lightning protection level (LPL) is generally recommended to be LPL1, which is the highest level of protection.

Lightning is an atmospheric discharge of current. The lightning parameters are peak current, flash charge, specific energy and average steepness. The value of the lightning current varies from very low up to 250 kA. The average peak current is calculated to be about 30 kA. According to IEC 61400–24, wind turbine blades are protected at LPL1 level if there is a 99% probability that lightning current parameters will be within the range 3 kA – 200 kA, and the protection system is adequate to withstand that range of current.

Lightning can be classified as upward initiated or downward initiated. Downward initiated lightning is commonly known as cloud-to-ground lightning, and upward initiated lightning is known as ground-to-cloud lightning.^{9,10} Downward lightning is the most common form of lightning strike (90% of all flashes are downward lightning), but taller wind turbines experience increasing amounts of upward lightning: when lightning strikes structures that are more than 100 m tall, 80% of the flashes are upward flashes.

The lightning strike points on a wind turbine can be the blades, the tower or the nacelle, and the anemometer may also be struck. The rotor blades are the highest point of a wind turbine, and since cloud-to-ground lightning will often strike the highest point, rotor blades must be protected. Good lightning protection in the rotor blades can protect against the worst effects of lightning strikes.

There are many different forms of LPS, and each manufacturer has their own solution. Some lightning protection concepts for large modern rotor blades can be seen in Fig. 12.10.¹⁰ All methods of protection have a down conductor, which conducts the current from the lightning to the ground. A receptor is often placed in the tip. The down conductor can be a wire or a



12.10 Lightning protection concepts for large modern wind turbine rotor blades.

mesh made of copper, steel or another metal with good electrical conductivity. Most conductors are made of copper because it is highly conductive.

12.3.3 Protection from air traffic

In order to ensure the safety of air traffic, it is necessary to light the rotor blades of some wind turbines. Many rotor blades have signs in different colours, often in the form of luminous stripes on the blades; white turbines with white rotor blades are highly visible. Synchronized flashing lights, however, are best for large constructions and wind farms.

12.4 Performance testing of protection layers: an introduction

The surface of the rotor blades are exposed to various types of adverse conditions. It would be pleasant if the blades were well protected against all conditions, but in reality it is not possible because the variation in conditions is enormous and the synergy between the variations is difficult to foresee. Therefore it is necessary for the manufacturer of the blades to make decision about how to handle the testing of the protection layers against the adverse conditions.

12.4.1 Performance testing considerations

There are many different methods that can be employed to test the surfaces of wind turbine rotor blades. The operators of wind turbines are looking for tests that can guarantee that a surface will be unaffected by weathering and wear throughout the lifetime of the wind turbine. The manufacturer of the wind turbine prefers quick tests that ensure that the wind turbine will deliver the service that has been promised to customers. The main difficulties for the manufacturer are working to short time limits and deciding which test should be used in order to ascertain how the surface will behave under different conditions.

It is preferable to test the subject or test specimen in the natural environment so as to measure its degradation in these environments. However, in reality this is not a practical way of estimating the lifetime of the material, especially if the subject is to be used in different types of climate, as is the case with rotor blades. Therefore the tests for estimating the lifetime of the material are carried out in an artificial environment. It is good practice to compare the laboratory tests with accelerated tests, but comparing the real atmosphere with an artificial atmosphere is difficult. As a result, predictions of the lifetime of surface protection can never be certain.

Large plants have been designed for outdoor testing and for measuring UV radiation: there is one such plant in Florida. The tests carried out and the artificial climate used for the test will depend on the subject and the planned location for the wind turbine. For a turbine that is to be placed in a desert, it is necessary to test for UV degradation and sandblasting. For an offshore turbine, there should be tests for humidity, UV radiation and the influence of salinity.

Polymers that are designed for outdoor use are influenced and degraded by sunlight, rain, hailstorms, salinity in the atmosphere and chemicals. In a test situation, these factors can be judged either individually or simultaneously, depending on the purpose of the test. Under natural circumstances, the different factors can cause a synergistic effect.

The best way to measure the influence of a particular condition is to place the subject in its proposed environment, but in practice this method is too time-consuming.

In this introduction to performance testing of surface protection it may be useful at this point to examine what happens when a polymer system degrades.

12.4.2 Degradation of polymers

Degradation is an unwanted change in the properties of a polymer. The change can be physical or chemical. Issues can include degradation of the backbone of the polymer, changes in side chains or sidegroups,

cross-linking, or loss of materials. Degradation of additives or loss of additives can also affect the system and cause degradation.

Weathering

During the process of weathering, energy is transferred to the surface and the rotor blade by radiation from sunlight. The energy in the radiation depends on the relative angle between the sunrays and the surface and the wavelength of the sunrays. The combination of oxygen in the atmosphere and humidity can induce chemical degradation. Erosion and wear from sand particles and the like can also attack and damage the surface.

Sunlight

Sunlight is the visible part of the electromagnetic radiation from the sun and it contains light of different wavelengths. The energy content of some parts of sunlight is so high that it can break the primary bonds – the covalent bonds – in the gelcoat or paint on the surface of a rotor blade. When the bonds have been destroyed, the surface layer begins to degrade. Sunlight is divided into ultraviolet (UV) radiation, visible light and infrared light. Most of the radiation from sunlight is visible.² When the wavelength is shorter, the energy content in the radiation is greater. UV radiation has the shortest wave lengths and these wavelengths are further classified as UVA, UVB, or UVC, with UVA being the longest of the three. Only UVA radiation, which has a wavelength ranging from 380 and 400 nm, is relevant to this chapter, since UVB and UVC radiation are absorbed in the atmosphere.

Oxygen and humidity

Polymers react with oxygen and with water, and therefore oxygen and humidity influence polymer surfaces. Water can be taken up by the structures of the materials, and in many cases the polymers in the matrix material and the gelcoats or paints can take up water, because of the hydrogen bonds in the molecules which come from the oxygen and nitrogen content of the polymers. As already mentioned, the blade surface is influenced by UV radiation, which causes free radicals to form in the structure. Oxygen can react with the free radical that is formed, which results in a new chemical formula. If the structure is an open structure, water can go into the structure. If the polymers do not cross-link as much as expected, water can attack the structures of the gelcoat and the laminate. The risk of degradation is then higher, as the adhesion between the laminate and the gelcoat or paint will deteriorate. Degradation caused by a combination of UV radiation and oxygen is called thermo-oxidative degradation. It is the starting point for chemical degradation of the surface and of the adhesion between the surface

protection layer and the laminate underneath. Degradation of appliances in the open air will usually be thermo-oxidative degradation.

Degradation mechanisms

Degradation of a polymer system can take place as a result of a break in the polymer backbone, depolymerisation, cross-linking, changes in the covalent bond system or changes in a side chain. The seriousness of the problem lies not in the type of change that takes place, but in the type of polymer that is affected.

Cross-linking is often possible in thermosets, which are used in most surface protection layers. Cross-linking can take place using the energy of functional groups. In a thermoset system there will be functional groups, which can react. In an unsaturated polyester system there will be unreacted double bonds, which can cross-link using energy from sunlight. The low energy in the covalent π -bond (compared to the energy in the σ -bond) will cause cross-linking if there are double bonds in the surface. Cross-linking in the system provides greater strength and hardness, but it will also result in less flexibility and will therefore give a more brittle material. Cracks may appear in the surface because of volume contraction of the total system. If humidity attacks the polymer system, a depolymerisation may take place. In most cases, this will cause voids in the structure, which will cause more water to be taken up by the structure.

In a polymer system, the bond energy depends on the covalent bonds in the backbone of the polymer: it depends on the elements between which the bond has been created and the bond length between the atoms in the molecule. Table 12.2 shows an overview of some bond energies. The lower the bond energy in a polymer system, the greater the risk of degradation of the system. From Table 12.2, it can be seen that the bond energy in polymers is so low that the bonds will be attacked by UV radiation from sunlight.

The oxidation rate depends on the structure of the molecules. Double bonds will oxidize more easily than an ester group: due to the structure of the molecule, ester groups can be stabilized by degradation, especially if the ester group is placed as a side chain. For example, this happens when MMA is used as a cross-linker in a gelcoat for an unsaturated polyester, as there will be a group that is naturally protected against degradation caused by UV radiation.

12.4.3 Measuring the degradation of polymer systems

Different methods can be used to measure how much a polymer system has changed as a result of weathering.

One method involves measuring the colour change and change in gloss caused by degradation.¹³ Most rotor blades are white or grey, and colour

Table 12.2 Bond energies and bond length of some covalent bond²

Type of bond	Typical bond length (nM)	Typical average bond energy (kJ/mol)
C – C	0.154	347
C = C	0.134	615
C – H	0.120	414
C – O	0.143	352
C = O	0.123	715
C – N	0.147	293
C ≡ N	0.116	890
C – Si	0.187	288
C – S	0.181	260
C – Cl	0.177	331
S – S	0.204	213
N – H	0.101	390
S – H	0.135	339
O – H	0.960	465
O – O	0.148	138

changes are easily seen with these colours. The colour is often the first sign of degradation. Measuring the colour change does not show what has happened, but it is an indication that degradation is taking place.

An explanation of the effects of degradation in the polymer system can be attained by taking Fourier transform infrared spectroscopy (FTIR) measurements before and after the reaction in the system has been affected. Attenuated total reflexion IR (ATR-IR) can be used in most situations. If degradation has taken place, the new functional groups will cause a peak: there will be changes in the peaks where there has been degradation. If the polymer system has double bonds, the concentration of double bonds will noticeably decrease. More changes can be seen using near infrared spectroscopy (NIR) than when using normal IR.

Chromatography methods and mass spectrophotometry can be used to determine the molecular weight before and after a system has been influenced, but these methods can only be used with materials that can be dissolved.

Another way of measuring degradation is by examining the physical, mechanical and chemical properties of the surface before and after degradation. The strength and stiffness of the surface will often change with degradation, and if cross-linking has taken place, the subject or test specimen will often be more brittle but stronger. By both examining the mechanical properties and using IR, an indication can be given as to which chemical has affected the polymer.

In the artificial environment, the lifetime of polymers used as surface protection can be determined from changes in the physical, mechanical and

chemical properties of the surface. This can then be used to calculate an estimate of the lifetime of the surface in the natural environment by using an accelerator factor. The acceleration factor depends on the cause of degradation and the type of artificial environment that has been used.

12.4.4 Accelerated testing: an introduction

UV tests and xenon light tests

There are many different methods for accelerating tests in the laboratory. UV tests or xenon light tests with different wavelengths are often used when predicting the lifetime of surface protections and these are tests that can be accelerated. By increasing the temperature, the reaction time can be reduced. The relation between reaction time and temperature can be estimated using the Arrhenius equation:

$$k = A \frac{E_a^{-E}}{RT}$$

In the Arrhenius equation, k is the rate constant for the reaction, E_a is the activation energy, T is the temperature in Kelvin, R is the gas constant and A is the collision frequency factor.

UV tests can be performed using different wavelengths. UVA radiation is widely used as it makes up most of the UV radiation on the surface of the earth. UVA radiation alone does not show what happens to a surface in a natural environment, but it can to a certain degree show what will happen under the influence of sunlight. UVB radiation (which is mostly absorbed by the atmosphere) causes rapid degradation, but, in most cases, results from UVB radiation tests cannot be used to predict degradation from sunlight, because of its fast degradation rate, and also because of other differences between it and UVA.

By using xenon lights, a distribution of wavelengths that are more like the distribution of sunlight can be attained. The xenon light source can cover the UV area, the visible light area and the IR radiation area. The visible light and the IR radiation do not contain enough energy to break the covalent bonds in a polymer system, and therefore a xenon source will cause less degradation than a UVA source.

Ozone

The influence of ozone, humidity and elevated temperature can be examined using an ozone cabinet. Special double bonds and rubbers can be degraded by the influence of ozone. It is normal to replicate the influence over 72 h

with an ozone concentration of 50 ppm. It is possible to make a mechanical influence at the same time. For the testing of rotor blades the methods are of limited use, but the ozone cabinet is a useful method for testing the adhesive bonding between two shells or parts.

Combined influences

Combined influences are tests in which the test specimens can be influenced by multiple influences and/or by influences that alternate in a cycle. The combined test will normally be a UVA test combined with oxygen tests, humidity tests, elevated temperature tests, salt spray tests, ice and frost tests, etc. The test specimens can be placed in an automatic cycle, or they can be moved from influence to influence in a planned cycle. The schedule and the different influences can be set up in such a way that they are similar to the subject's natural environment. Combined tests often give the best results.

12.5 Accelerated testing of the surface coatings of wind turbine blades in practice

It would be nice if all protection layers of the rotor blades could be tested by exactly the same conditions it would be exposed to while working. But that is not possible, because it is first of all too time-consuming and furthermore the conditions to which the rotor blades can be exposed to can be really difficult to foresee. Therefore, it is desirable to find methods for accelerated testing so that the life time of surface coatings can be compared and foreseen as precise as possible.

12.5.1 Standards

There are no general standards for the testing of the surface protection of rotor blades. The standards for testing helicopter blades are useful guidelines, but helicopter rotor blades are examined after a certain number of hours in the air, whilst wind turbine rotor blades need to be protected in a way that ensures they can operate for years without maintenance.

The standards for both offshore constructions and the paints and varnishes used on them can be used as guidelines when creating a set of test parameters for the surface protection of wind turbine rotor blades.

Various other standards can also be used as guidelines, including the Norsok Standard M-501, 'Surface preparation and protective coating', which is a standard developed by the Norwegian petroleum industry, and the European standard ISO 20340 'Paints and varnishes – Performance and requirements for protective paint systems for offshore and related structures'^{14,15} ISO 4628 'Paints and varnishes – Evaluation of degradation of coatings' and

'Designation of quantity and size of defects, and of intensity of uniform changes in appearance'¹⁶ can be used to create a programme that tests the influence of the different parameters that can attack the surface. Parts 4628–2, 4628–4 and 4628–5 are especially useful for wind turbine rotor blades.^{17–19}

The standards for offshore painted steel structures are more relevant than the standards for helicopter blades when standardizing protection for wind turbine rotor blades, because wind turbines are similar to offshore installations for the petroleum industry. Offshore structures used in the petroleum industry are divided into four zones based on the environment that each structure is exposed to (ISO 20340).¹⁴ One zone corresponds to the area exposed to atmospheric category C5-M, and the other three zones correspond to category Im2, which are the underwater zone, the tidal zone and the splash zone.¹⁴

All four zones are relevant for wind turbine towers, but only the zone corresponding to atmospheric category C5-M is regarded as relevant to rotor blades (see Reference 20 for ISO 12944–2:2000). Both category C5-M and Im2 are categories that describe a harsh environment. The categories are both designed for steel constructions, but most of the parameters can be applied to composites and structures with surface protection. C5-M and Im2 define corrosiveness based on the mass or thickness lost by standard specimens, and they also describe typical atmospheric environments.

This section will now conclude by describing a selection of useful tests that have been proved to be able to highlight the ability of different surfaces to withstand harsh atmospheres. These are modified from tests for paints and varnishes in offshore (marine) atmospheres, taking into consideration that the standard tests have been designed for metals, in particular painted steel.

12.5.2 Selected test methods

Norsok test

The Norsok test exposes the material to a cycle of different atmospheres. The test includes various forms of simulated weathering, starting with a salt spray chamber and followed by a UVA chamber or a xenon light chamber. The temperature can be elevated in the UVA chamber/xenon light chamber to increase the rate of any degradation. A xenon light chamber is better than a UVA chamber because the sunlight spectrum is more like the spectrum of xenon light than that of UVA light.

The test normally takes place at an elevated temperature over 32 weeks, and afterwards the surfaces of the test pieces are examined according to standards ISO 4628, 2, 4 and 5 for blistering, cracking and flaking, and according to standard ISO 12944–2 for adhesion to the laminate. It is a time-consuming test, but the results are comparable to the degradation of rotor blades in a marine atmosphere.

Wear test

The Norsok test does not examine wear resistance, and none of the ISO standards for paints and varnishes for offshore use require a wear test.

It is important to test the wear resistance of a surface because it is difficult to judge wear in advance. The tip and the first-third of the blade are the parts that are most at risk of wear. Under extreme weather conditions, particles can hit the blades at more than 300 km/h. The higher the wind turbine tower is, the finer the sand particles in the air will be.²¹

Hailstorm and rain erosion are not included in the Norsok test, but both should be tested. The combination of a water flow test and a wear test can illustrate and foresee the degradation caused by rain erosion. The resistance of the material to wear as a result of hailstorms can be tested by using ice particles as the medium instead of sand or corundum, since the sharp edges of ice particles cause wear on the surface. A material with a soft surface offers flexibility and wear resistance.

Humidity test

The Norsok test and most other combined tests include humidity as a part of the test. Once the test specimen has taken up as much water as possible, it is frozen and then allowed to thaw again; this imitates weathering in cold environments. After this test, the specimen is checked for blistering. Blisters form when frozen water and liquid water interact because the volume of the frozen water increases. A strong material will not blister extensively.

Chemical attack

Wind turbine rotor blades can be exposed to different types of ‘chemicals’; they can be contaminated by dirt, faeces from birds, blood from insects, oil, salt deposits, contaminated rain, etc. None of the combined tests takes these exposures into consideration. Suitable tests do exist, however, as part of the programme ‘Lifetime of wind turbine blades’.²² Test chemicals include carbon black, which imitates smoke and deposits from smoke, diluted sulphuric acid to imitate acid rain, oil to imitate dirt and other types of grease, and artificial sea water. None of these chemicals acting alone will attack the gelcoat or paint or cause any damage to them, but in combination they have a destructive effect.

Results of tests

Since the tests are not mechanical they do not give direct results, but they need to be judged according to standard ISO 4628.^{16–19} Blistering, cracking

and flaking can occur after the tests, and this can be used to judge the surface gelcoat or paint. The adhesion between the laminate and the gelcoat can also be examined although test specimens need to be prepared separately for this purpose, which involves bonding a fixture for a mechanical (peel/tension) test to the gelcoat or including an opening in the gelcoat to allow it to be peeled from the laminate.

12.6 Conclusions, challenges and future trends

It is not possible to foresee all the conditions to which the wind turbines blades will be subjected to in the future. Therefore, it is necessary to give some qualified recommendations. In the future, the wind turbine blades will definitely be longer. The turbines will be placed in more harsh climates and in more impracticable places than they are placed today. All these aspects will be a challenge for making exactly the right surface protection of the rotor blades.

12.6.1 Advantages and limitations of different protection technologies

When manufacturing protection for wind turbine rotor blades, the different materials available offer many advantages. However, these must be balanced against the limitations, and there are decisions to be made; these include the choice between a hard and a soft surface, and between a gelcoat or a paint.

A hard surface can be achieved by using a gelcoat made of epoxy with a high hardness or unsaturated polyester with a high hardness. For a thermoset to have a high hardness, there needs to be a high level of cross-linking, since this results in low flexibility and more shrinkage. A soft surface can be produced by using a softer polyurethane as the paint or gelcoat, or by applying a polyurethane tape to the tip especially on the leading edge and the third part of the rotor blade, thus giving better protection.

Different materials can be used to minimize different types of damage from the environment. To reduce water absorption by the surface, the coating should be epoxy rather than polyester. To achieve a low hydrolysis rate, vinylester should be chosen rather than unsaturated polyester. UV protection is increased if the cross-linker is a methylmethacrylate rather than styrene, but this does not offer the best working environment since MMA is allergenic. Additionally, a surface is easier to de-ice if it has a low surface tension, but a material with a low surface tension is more at risk of attack by components that cause wear and rain erosion.

The process of weighing up the advantages and limitations of different surface materials also extends to the challenge of achieving a strong enough adhesion between the surface and the laminate whilst trying to protect the

surface against weathering. When the adhesion between the surface and the laminate is not strong enough, the material may split open, leaving it exposed to weathering.

12.6.2 Challenges and future trends

In the future, wind turbines will be larger and they will be placed in harsher climates, e.g. offshore, in deserts, in cold areas or on top of mountains. These locations will enable increased performance, and the noise from the turbines will not be disruptive. However, there is more wear and chemical attack on the surface when the turbine is located in an extreme climate. In addition, because they will be situated in less accessible, inhospitable areas, maintenance will be difficult and therefore the strength and durability of the surface protection will become critical to performance.

However, small turbines will also be on the market in the future. These will be installed onshore and in an environment with limited variation in the weather conditions. Nevertheless, their rotor blades will require surface protection, and there is no reason why the solutions that have been developed whilst manufacturing large wind turbines with rotor blades that are more than 60 m long cannot also be applied to small-scale wind turbines.

New materials

New materials for surface protection will be developed to meet these future challenges. New types of paints and aerofoils may offer better protection, and they will be developed and tested for the harsher climate situation. For example, protective paints are being developed: one potential product is based on imides, and another contains fluorocarbons in the surface to protect against icing. New materials are widely used for aircrafts, and the materials and technologies that are developed for aircraft can be transferred to wind turbine rotor blades. Foils are widely developed, especially for helicopter rotor blades. With more and larger wind turbines, foils may be developed specifically for wind turbines. Foils that protect against icing are one of the focusses in the development of new materials.

Protection of the surroundings

In the future, it is likely that there will be more restrictions and regulations of the surroundings in both the onshore and the offshore environments. Already, many problems with wind turbine farms have come to light and many people are against having a wind farm nearby. This has resulted in new requirements for the surfaces of rotor blades, relating to the gloss, the radar cross-section and the lightning protection.

Some of these requirements are easily solved and the solutions are known. Radar cross-section protection involves regulations regarding lighting or luminous stripes on the rotor blades. The gloss on the blades can be reduced by using a less glossy paint/gelcoat, although this will result in reduced performance. Solving the aero-acoustic problem is a challenge because so many parameters are involved in creating the noise from rotor blades.

Working environment

The working environment is a challenge in the surface protection technology for rotor blades and some problems have come to light. These are problems that must be solved at the manufacturing stage.

For some of the materials and technologies that are involved in making surface protection, the problem is with volatile organic components/solvents (VOCs), because the resins used for the surface protection are organic. New technologies can solve that problem, but for cleaning tools, etc., VOCs or surfactants are still necessary. Surfactants cause problems in the waste water, whilst the VOCs cause pollution in the air. Some other materials are epoxy-based or acrylic-based and these can cause problems with allergies.

Protective clothing, gloves and masks are therefore essential for workers involved in manufacturing the surface of the blades. The challenge here is that it is necessary to make the technology safe for the working environment, but without reducing its performance and the technical properties of the final product.

Test methods

To ensure that wind turbine rotor blades can be used for a long time without damage, more test methods and modelling need to be developed. Today, many methods relating to the dynamical properties of the blades are being developed and used. Models have been developed as solutions to some electrical and mechanical issues relating to the blade surfaces, e.g. lightning protection and surface aero-acoustics phenomena. However, no models have been developed for wear or chemical resistance of the rotor blades, or for icing of the blades.

12.7 References

1. Hansen, Charles: *Hansen Solubility Parameters: A Users Handbook*. 2nd edition. CRC Press. 2007.
2. Rodriguez, Ferdinand: *Principles of Polymer Systems*. 4th Edition. Washington, Taylor & Francis. 1996.
3. Olivier Parent and Adrian Ilinca: Anti-icing and de-icing techniques for wind turbines: Critical review. *Cold Regions Science and Technology*, Volume **65**, Issue 1, pp 88–96, January 2011.

4. Kaj Olsen, Flemming Møller Larsen, Peter Graubau, J. E. Jespersen: Wind Turbine Blade with a system for deicing and lightning protection. US Patent US 6,612,810 B1. September 2003.
5. Jesper Måansson: Why de-icing of Wind Turbine Blades? LM Windpower. Presentation at Global Wind. Chicago, 28–30 March 2004.
6. Purves, W. K., Orians, G. H., Heller, H. C. R.: *Life: The Science of Biology*. 4th Edition. Sinauer Associates. 2008.
7. Kirk McMichaels: Organic Chemistry Pages, California State Universities, 2007. <http://chemistry2.csudh.edu/rpendarvis/Polymer.html> (accessed 1 July 2011).
8. International Electrotechnical Commission: IEC 61400–24 Wind turbines – Part 24: Lightning Protection, 2010–06.
9. Vidyadhar Peesapati and Ian Cotton: Lightning Protection of Wind Turbines – A Comparison of Real Lightning Strikes Data and Finite Element Lightning Attachment Analysis. Supergen V Wind Energy Theme. 2010.
10. Sebastian G.M. Krämer. Fernando Puente Leon, Bastian Lewke, Yaru Mendez Hernandez: Lightning Impact Classification on Wind Turbine Blades using a Fiber Optic Measurement System. Proceedings of Windpower, Los Angeles, CA, 3–6 June 2007.
11. ‘Bekendtgørelse omstøj fra vindmøller (Statutory Order on Noise from wind turbines)’, nr. 1284, Miljøministeriet, 15 December 2011.
12. Michael S. Selig and Brian D. McGranahan: Wind Tunnel Aerodynamic Tests of six Airfoils for use on Small Wind Turbines. Subcontractor Report. NREL/SR-500-34515. National Renewable Energy Laboratory. October 2004.
13. DS/EN ISO 2813: ‘Paints and varnishes – Determination of specular gloss of non-metallic paint films at 20°C, 60°C and 85°C’, 1st edition. 15 March 2000.
14. ISO 20340: Paints and varnishes – Performance requirements for protective paint and systems for offshore and related structures. 2009.
15. Norsok Standard M-501: Surface preparation and protective coating. Rev. 5 June 2004.
16. ISO 4628:2003: ‘Paints and varnishes – Evaluation of degradation of coatings’ – ‘Designation of quantity and size of defects, and of intensity of uniform changes in appearance’. 2003.
17. ISO 4628–2: ‘Assessment of degree of blistering’. 2003.
18. ISO 4628–4: ‘Assessment of degree of cracking’. 2003.
19. ISO 4628–5: ‘Assessment of degree of flaking’. 2003.
20. ISO 12944–2:2000: ‘Paints and varnishes – corrosion protection of steel structures by protective paint systems’ – Part 2: ‘Classification of environments’. 2001.
21. Birgit Kjærside Storm, Milosz Gwisdalski, Danny Kedochim: Wear Test of Composites. *Academic Journal of Manufacturing Engineering*, Volume 8, Issue 4, pp. 91–96, 2010.
22. Susanne Damgaard, Nanna Svendsen, Bent F. Sørensen, Birgit Kjærside Storm, Bente Nedergaard Christensen, Allan Cordes: Energistyrelsen Vindenergi. Forskning af materialeteknologi til overfladebelægning af vindmøllelevinger og udvikling af testmetoder for levetid til belægninger. Journalnr.1363/03–007. February 2006.
23. ISO 4624:2002 (identically with ASTM D4541): ‘Paints and varnishes: Pull-off test for adhesion’. 2002.

Design, manufacture and testing of small wind turbine blades

P. D. CLAUSEN and F. REYNAL, University of Newcastle,
Australia and D. H. WOOD, University of Calgary, Canada

DOI: 10.1533/9780857097286.3.413

Abstract: Small wind turbine blades share a number of features with large blades, but have some important differences. The two main differences are their much higher rotational speed, which causes more fatigue cycles and higher yaw moments, and their operation at low Reynolds number, which means that thick aerofoil sections cannot be used near the root. This chapter discusses the design challenges arising from these differences, the materials commonly used for blade manufacture, and the fatigue testing of small blades. The use of timber is highlighted for very small blades, and fibre-reinforced composite manufacture of larger ones is discussed in terms of sustainability, conformity of manufactured shape, and fatigue behaviour.

Key words: small blades, timber, composites, gyroscopic loads, fatigue, testing.

13.1 Introduction

This section describes the main features of small wind turbine blades in comparison to the blades typically used on large wind turbines. The main differences are that small blades experience higher centrifugal loading and more fatigue cycles, and require thin airfoil sections near the hub.

13.1.1 Background

Wind turbines of all sizes are designed and certified to the standards issued by the International Electrotechnical Commission, IEC. The standard applicable to small wind turbines, IEC 61400–2, defines a small (horizontal axis) wind turbine as having a rotor swept area less than 200 m². This corresponds to a blade radius, R , less than 8 m and a rated power output below about 50 kW. Small turbines are becoming more popular,¹ and are developing rapidly in

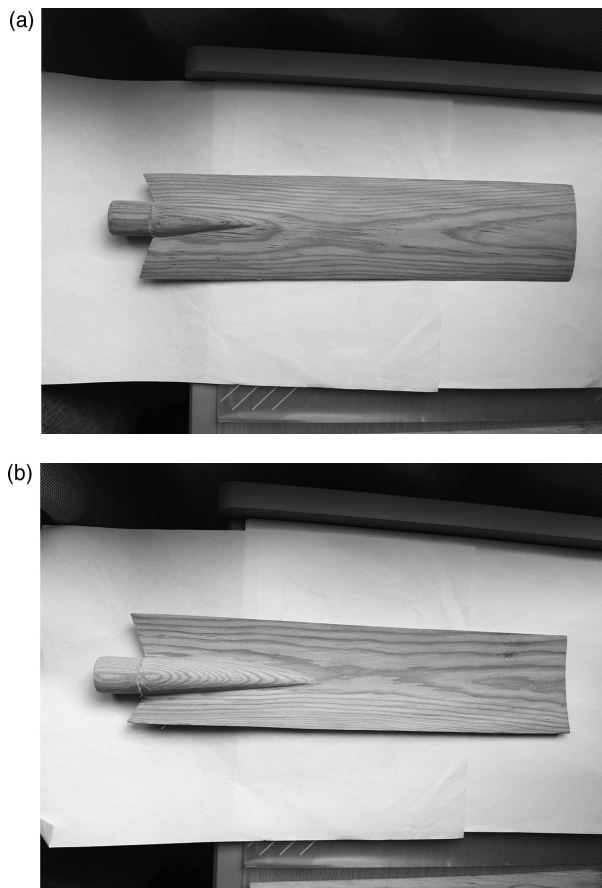
¹ For example, <http://www.smartplanet.com/blog/smart-takes/small-wind-turbine-market-to-double-by-2013-study-says/2747>

technological maturity. IEC 61400–2 is currently under revision and the result is likely to be a technology-defining document. Nevertheless, there is a much wider range of small than of large turbine types partly due to their range of applications, and partly to a relative lack of maturity of the technology in general. Many building installations, for example, use vertical axis wind turbines (VAWTs). These are excluded from IEC 61400–2 and will not be considered extensively here. Even among small horizontal axis wind turbines (HAWTs) there is a wide variation in number of blades, and several commercially successful ones have downwind rotors. It is generally believed that small turbines have poorer reliability and require more maintenance than large ones, and our knowledge of several key aspects of blade behaviour is deficient.

13.1.2 Small versus large blades

The tips of many large blades are designed to minimize the noise produced along with the trailing vortices. Most power is produced in the outer 20–30% of the blade, while the blade thickness increases substantially, reaching typically 25–30% of the chord, towards the circular attachment near the hub. Power is generated by the outer part of small blades as well, but tip noise is usually negligible. The next big difference from large blades is the lack of pitch adjustment. Blades of all sizes rely on aerodynamic torque for starting, but the starting torque on small blades comes mainly from the hub region, Clifton-Smith *et al.* (2010). There the angles of attack are high and Reynolds numbers are low, which means that thin aerofoils are required to avoid poor performance caused by separation mechanisms that are absent at higher Reynolds numbers. Since blade centrifugal stresses scale as R^{-1} , e.g. Wood (2011), the structural design of the hub region of small blades has particular challenges.

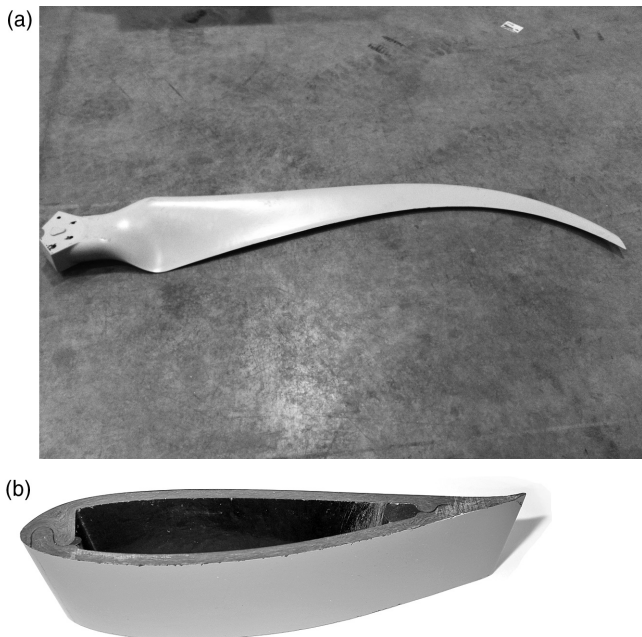
Blade materials also vary more in small turbines than large ones. Blades shorter than about 1.5 m can be made wholly from timber as shown in Fig. 13.1. These blades were hand-carved and have large variations in mass and inertia, J . The limitation on length of solid timber blades is the cost of knot-free blanks, (Peterson and Clausen, 2004; Sinha *et al.*, 2010). There are complications; it is best, for example, to use timber quarter-sawn from well-seasoned logs (the main cuts being in the radial direction after the log has been quartered), which is not standard practice. It can also be difficult to reproduce accurately the three-dimensional shape of a well-designed blade; however, considerable progress has been made in developing a cheap copying router by Astle *et al.* (2013). Most water-pumping windmills, which fall under the IEC definition of small wind turbines, have metal blades, frequently rolled from galvanized steel sheet. Their slow rotation means that typical blade stresses are low. Counteracting this is the high inertia of multi-bladed rotors which can cause high gyroscopic loads during yaw.



13.1 8 cm chord, 30 cm long timber blades for a 50 W turbine. Photos from KAPEG, Nepal. (a) Photo shows downwind view, (b) photo shows upwind view.

Windmills are the least-studied variety of small turbine and will not be mentioned again.

Most small wind turbine blades are made from composites. Some, such as the well-established Bergey range use pultruded blades with constant chord and twist. The current market-leading Southwest Windpower Skystream has hollow carbon-fibre composite blades, Fig. 13.2. In other blades, the thin laminate surfaces are kept apart by a shear web or equivalent, as on large blades, because the downwind surface is nearly always in compression during operation and so there is a real possibility of blade buckling. The required properties of the composite materials are largely independent of blade size, so that resins developed for large blades are suitable for small ones. The current edition of



13.2 (a) The Skystream blade and (b) cross-section.

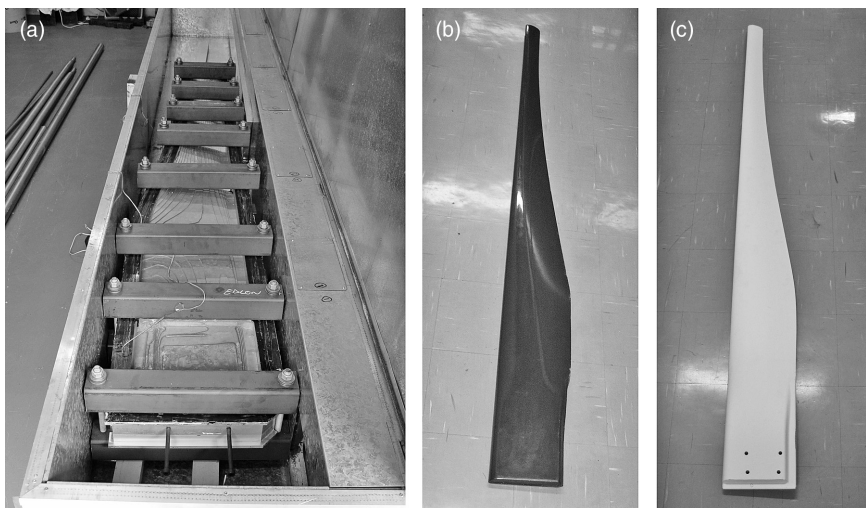
the well-known Germanischer Lloyd Guidelines (GL, 2010) is the first to provide specific advice and requirements for small blade materials and testing. As for large blades, there is considerable activity in searching for ‘green’ materials and manufacturing methods. Some of these will be described.

13.1.3 Scope and layout

The rest of this chapter is organized as follows. Section 13.2 discusses the structural and manufacturing requirements of small blades. The following section summarizes the main materials used at present. Section 13.4 covers static and fatigue testing, and quality control. Some installation and operation issues are considered in Section 13.5, and our views of the challenges and future trends for small wind turbines are contained in Section 13.6.

13.2 Requirements for small wind turbine blades

Small blades experience higher centrifugal stresses and gyroscopic loads but lower load variations due to wind shear and gravity. Their mounting and control is simplified by the absence of pitch adjustment but the need to have thin aerofoils near the hub makes the structural design of this region particularly



13.3 (a) A 5 kW blade mould going in the oven and (b) a 2.5 m blade. The blade is attached through four boltholes drilled in the rectangular attachment section at the bottom (c).

challenging. Blade flexing is less critical as small blades tend to be mounted further from the tower as a fraction of blade radius. Nevertheless, the IEC 61400–2 requirement that (stationary) blade deflection under the extreme wind load is less than the distance from the blades to the tower divided by the appropriate ‘partial load factor’, either 1.35 or 3.0, is often a considerable challenge in the absence of centrifugal stiffening by rotation.

The basic shape of all blades should be driven largely by the aerodynamic requirement of maximizing the lift:drag ratio (LDR) of the individual blade elements, which are aerofoil sections. Specific features include the curving in the plane of rotation of the downwind blades on the Skystream presumably to minimize blade-tower interaction. All the blades designed by the authors are upwind ones having straight leading edges to facilitate closed-mould manufacture. An example is shown in Fig. 13.3.

Choosing the right aerofoil is critical for small blades that operate in Reynolds number, Re , ranges where the LDR varies significantly with Re . Fortunately a few excellent aerofoils are available, Giguere and Selig (1997, 1998) and Kogaki *et al.* (2002), designed specifically for high LDR at low Re . As for large blades, the workhorse of aerodynamic design is traditional blade element theory (BET). It is almost trivially easy to design a blade to maximize power extraction for a hypothetical steady wind, see e.g. Chapters 5 and 7 of Wood (2011), but harder to extend the optimization to include, for example, starting performance and noise minimization. Techniques for numerical multi-dimensional optimization are described in Wood (2011)

and Clifton-Smith *et al.* (2011) to which the reader is referred for details. Here we note only a rule-of-thumb deduced from many real and conceptual designs: optimizing any one objective function usually gives worst case behaviour for at least one other. For example, a blade designed purely for maximum power extraction in a steady wind will typically have poor starting performance and a high sound power level. It is always necessary to trade-off a small fraction of power extraction efficiency to lower noise or reduce starting time by a much larger fraction.

These design outcomes are the chord and pitch distribution along the blade. As implied above, the choice of aerofoil profile is usually made beforehand or the designer restricts attention to a small range of candidates, dictated partly by the scarcity of aerofoils that perform well at low Re . Often the same profile is used for the entire small blade, but a few geometric liberties are still possible. For example, BET makes no restriction on the location of the blade element along the design chord line so that using, say, a linear indentation of the leading edge as on large blades, or having a straight leading edge, should have no impact on aerodynamic performance. There are usually practical restrictions on the maximum chord so that the optimal (for steady power extraction) chord distribution (inversely proportional to radius) is never followed. Only a small amount of power is ‘lost’ by deviating from the ideal towards the hub.

Small blades are usually bolted to a holder or disc using the holes visible in the hub end in Figs 13.2 and 13.3. If the blade has a foam core, this has to be protected from water ingress through the bolt holes. In turn, the holder or disk is attached to the input shaft of the gearbox or generator. This simple arrangement is cheap, but care is required in assessing the loads on the shaft, principally due to the gyroscopic moments during yaw, for example Wood (2009, 2011).

Fatigue issues also differentiate small wind blades because of their much faster angular velocities and operation in more turbulent wind. The latter is caused by location close to the load (homestead, village, etc.) and, therefore, to buildings, trees, and the like. Small blades experience up to two orders of magnitude more fatigue cycles than their larger counterparts over a nominal 20-year lifetime. Small turbines compete with mature power generation technologies like diesel engine generator sets and photovoltaics, so must be manufactured as cheaply as possible.

13.3 Materials and manufacture

It has been noted that small blades are made from a wider range of materials using a wider range of manufacturing methods, than large blades. This section describes the most common materials and methods of manufacture.

13.3.1 Timber

Timber-laminate composites have long been used in large blades, see e.g. Sutherland (2000), but now have been replaced by glass fibre and carbon-fibre composites. Furthermore for larger blades, the weight of solid timber exceeds that of well-designed laminate. As previously stated, timber is an ideal material for short blades when it is possible to obtain clear blanks.

The fatigue properties are well known for a number of North American and European timbers for use as laminates in large blades (Tsai and Ansell, 1990). More recently, Peterson and Clausen (2004) determined the S-N curve for two Australian plantation grown timbers – hoop pine and *Pinus radiata* (native to North America) – and Astle *et al.* (2013) determined the fatigue properties of two north American timbers – Douglas fir and Sitka spruce. Using their data and a blade fatigue spectrum based on Epaarachchi and Clausen (2003), Peterson and Clausen (2004) concluded that a 1 m long blade constructed from *Pinus radiata* had a fatigue life of over 190 years compared with those constructed from Hoop pine, which had a fatigue life in excess of 20 000 years.

The soft and porous timbers suitable for small blades are susceptible to degradation due to exposure to the sun and erosion from dust particles in the air. Sinha *et al.* (2010) tested a range of blade coating materials primarily for use in Nepal and found that enamel paint with a primer undercoat offered excellent surface protection.

Timber blades can be manufactured using a number of processes. These include, in order of decreasing sophistication:

- special-purpose computer numerically controlled (CNC) routers;
- copying from a master in a copying machine; and
- hand carving.

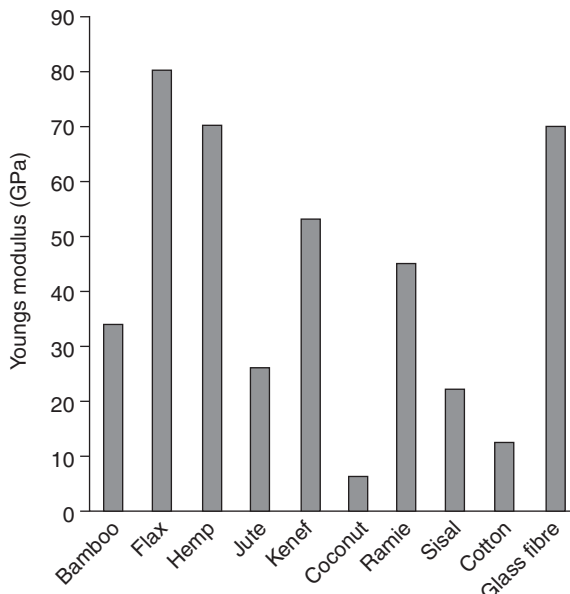
Accurate and durable CNC routers are expensive even for small blades. Copying machines are much cheaper, but a commercial unit designed for gun stocks and related items was found inadequate for blades where the tip chord is of the order of 5 cm (Astle *et al.*, 2013). Accuracy problems are exacerbated by the dominance of the tip region in producing power. Hand carving is the cheapest alternative, but Clausen *et al.* (2009) showed significant errors in the blade pitch of hand-carved blades, which resulted in poor performance. Furthermore, measurements of three blades including that in Fig. 13.1 showed a 100% variation in the inertia, J . More work is needed to improve the manufacture of small timber blades.

13.3.2 Fibre-reinforced composites

Most small blades are made from fibre-reinforced composites. High performance requires significant variation in chord and pitch along the blade, which

precludes pultruded profiles. The type of composite used within the blade structure and its orientation is readily designed with the aid of finite element modelling using, say, the simple load model of the IEC 61400–2, e.g. Bechly and Clausen (1997), Sharma and Wetzel (2010), and Wood (2011). Generally the resins and reinforcements used for large blades are also suitable for small ones (GL, 2010). Manufacturing techniques generally depend on the required quantity of blades. Resin transfer moulding is an appropriate technique for a large production run. Closed and clamped small blade moulds can be put into an oven for curing at elevated temperatures (Fig. 13.3a). This will ensure a blade with a glass transition temperature in excess of 65 °C, the minimum allowed by GL (2010). Wood (2011) gives examples of blade manufacture by vacuum infusion which is more suitable for small batches as it has a low set-up cost but a high labour component. Sharma and Wetzel (2010) describe the manufacture of 3.2 m long blades by vacuum-assisted resin transfer moulding and their subsequent static and fatigue testing. Injection-moulding is used for the volume production of smaller composite blades because the high initial tooling cost is countered by low production costs.

In recent years, research into bamboo-based and other composites shows promise for a ‘green’ composite suitable for use in blades of all sizes (Holmes *et al.*, 2009). These composites offer higher strength and stiffness over birch constructed laminates (Holmes, *et al.*, 2009), with quick-growing



13.4 Young's modulus of several composite materials. (Source: From Frohnnapfel *et al.*, 2010.)

bamboo addressing some issues related to sustainability. Frohnnapfel *et al.* (2010) discuss the strength of green fibres and methods for making small blades with them. Figure 13.4 shows the Young's modulus of some natural fibres in comparison with common glass fibre; flax and hemp have excellent material properties.

13.4 Blade testing

This section discusses balancing the rotor and the use of static and fatigue testing to determine the fatigue life of a blade. Some quality control and installation issues are then described.

13.4.1 Static testing

Applying static loads in the flapwise direction to a blade cantilevered from its attachment block is a quick and accurate method of checking the overall stiffness of the blade. It is also required by IEC 61400–2. Measurement of the deflection along the length of the blade can yield a large amount of additional information, such as the quality of the fibreglass lay or the variability of a timber constructed blade. Measurement of the centre of mass for a batch of blades is important for subsequent balancing. It also gives insight into how the mass is distributed within the blade. For composite blades, variations in the centre of mass could indicate resin-rich regions which may affect the mechanical properties of the composite, especially those associated with fatigue strength and life. For a timber blade, a change in the centre of mass usually results from variations in density along the blade provided there is no variation in shape between blades. Many timber species also exhibit large variations in density between samples.

If it is assumed that the turbine rotor contains equi-spaced blades whose centres of mass lie in the plane of rotation, the eccentricity of the rotor centre of mass depends only on the mass and centre of mass of the individual blades. Determining these properties allows matching of blade sets to minimize or eliminate the need to adjust for rotor balance. In our experience, a batch of blades whose mass and centre of mass have standard deviations of less than 1% usually do not need further balancing.

13.4.2 Small blade fatigue

A recent and important survey of the complex subject of (large) blade fatigue is given by Veers (2011). As previously stated, small blades experience significantly more fatigue cycles than larger ones and, along with different operational conditions such as free yaw, the operational loading



13.5 Fatigue test rig in operation at the University of Newcastle testing a 2.5 m long blade. A static test rig can be seen on the right.

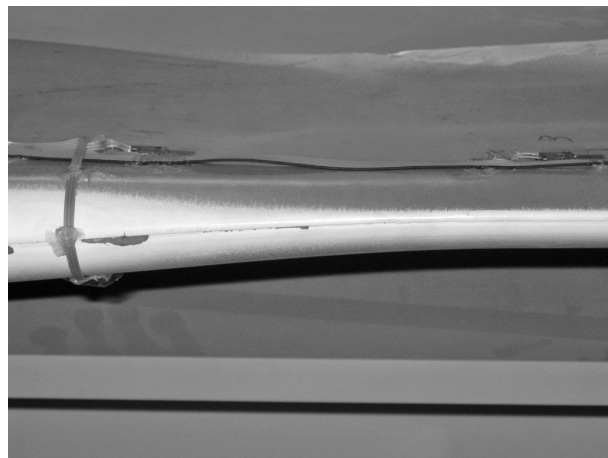
for small wind turbines is sufficiently different to invalidate the accelerated blade fatigue routines developed for large blades (Bechly and Clausen, 1999). Before developing an appropriate fatigue routine for small turbines, the loading on an operating blade must be known for a broad range of wind and operating conditions. The remaining key issues in developing fatigue tests for small blades are:

- Blade flapping dominates the lead-lag loads and gravity can be ignored.
- Wind shear is much less important for small blades.
- Fatigue testing machines must apply loads at higher frequency which usually precludes the use of hydraulics. Figure 13.5 shows the electric-motor-driven fatigue test rig used over many years at the University of Newcastle. The photograph also shows a static test rig.
- The limited knowledge about small blade fatigue means that there are aspects of the standards that may be deficient. For example, the work of Wilson *et al.* (2008) shows that yaw rates can exceed the nominal limits in the IEC 61400–2, suggesting the standards are not conservative enough.

In developing fatigue tests, it is necessary to estimate the load spectrum over a typical blade lifetime, say 20 years, at a ‘typical’ site. This was done by Epaarachchi and Clausen (2006) using Australian Bureau of Meteorology wind data and blade response data from an operating turbine, Bechly and Clausen (1999). It is worth noting that this turbine was operating in low

turbulence flow and loading cycles from the turbine responding to gusts and highly turbulent flows were not included. Load cycles were ‘rainflow counted’, Veers (2011), with cycles binned for R values between 0 and 0.9, where R is the ratio of minimum cyclic wind speed/maximum cyclic wind speed, over the operating wind speed of the turbine. The wind cycles were converted into blade stress cycles via finite element model predictions. The fatigue characteristics of the material used in the critical root section of the blade are generally experimentally determined to generate an S-N curve (cycles required for the sample to fail for a range of cyclic stresses) for the material. A fatigue routine was then developed from the blade stress cycles and S-N data after excluding cycles that resulted in negligible damage to the blade. Undertaking this fatigue test routine for a blade design life of 20 years at a test rate of 3 Hz would take some 6 months of dedicated testing. To reduce the testing time without unduly compromising the test routine, the damage accumulated over all R values for a given blade stress level is determined for one R value (Owen and Howe, 1972), with Miner’s rule used to calculate the equivalent number of cycles. Fatigue testing undertaken by the authors has reduced 20 years of fatigue spectrum to around one month of dedicated testing.

Post *et al.* (2008) have reviewed a broad range of damage accumulation models for composite materials. Unpublished work by the authors suggests that the very simple Palmgren-Miner model (Miner’s rule) is the most conservative, with a model proposed by Owen and Howe (1972) giving predictions closest to the experimental results. However Veers (2011) justifies the use of Miner’s rule on the grounds that the effects it cannot model, such as



13.6 Leading edge damage to a vacuum-infused 2.5 m long blade after an accelerated fatigue test to the equivalent of 20 years.

those caused by a specific sequence of loads or the state of the composite, are hard to determine accurately and impossible to predict. This rule is also recommended by IEC 61400–2.

An equivalent 20-year test of the vacuum-infused version of the blades in Fig. 13.3 using the test rig of Fig. 13.5 showed negligible property deterioration. Fatigue life predictions based on the fatigue test routine previously discussed and experimentally determined material fatigue properties suggest that the fatigue life of this blade is effectively infinite. After the equivalent of 20 years, there was some damage along the leading edge (Fig. 13.6), which was probably caused by the rigidity of the loading arm connection which did not allow the blade to flex naturally. It is worth noting that strain gauges were attached to the blade, see Fig. 13.6, to continually monitor material stiffness degradation throughout the testing routine. It was found that several of the strain gauges failed during testing, presumably due to fatigue, with no noticeable reduction in blade stiffness as determined from the surviving gauges.

13.4.3 Quality control

The three issues considered are:

1. ensuring the structural integrity by sample or non-destructive testing;
2. the conformity of the blade shape to the original design; and
3. limits on imbalance in forming the rotor.

It is worthwhile at this point to briefly review the requirements of IEC 61400–2 and GL (2010) for the safe design and structural integrity of small blades. The IEC safety assessment is based on assigning ‘load factors’ to the calculations of the imposed loads, such as the blade root bending moment, and ‘material factors’ to the computed stresses to account for the level of knowledge about the blade materials. Wood (2011) describes typical load calculations according to the IEC ‘Simple Load Model’. Here we concentrate on the materials and their safety factors shown in Table 13.1. The IEC standard requires a blade static test but not a fatigue test.

Table 13.1 Partial safety factors for material characterization from IEC 61400–2

Condition	Full characterization	Minimal characterization
Fatigue strength	1.25	10.0
Ultimate strength	1.1	3.0

To use the full characterization factors, i.e. the lower safety factors, the material properties must have been estimated with 95% probability at a 95% confidence level. The other requirements are:

- the properties have been obtained from materials and configurations representative of the final structure;
- the test samples come from the same process as the final product;
- static and fatigue testing have been done with appropriate load spectrum and rate effects;
- environmental effects, such as ultraviolet degradation, have been included; and
- any appropriate geometry effects, such as fibreglass orientation in composite blades, have been adequately accounted for.

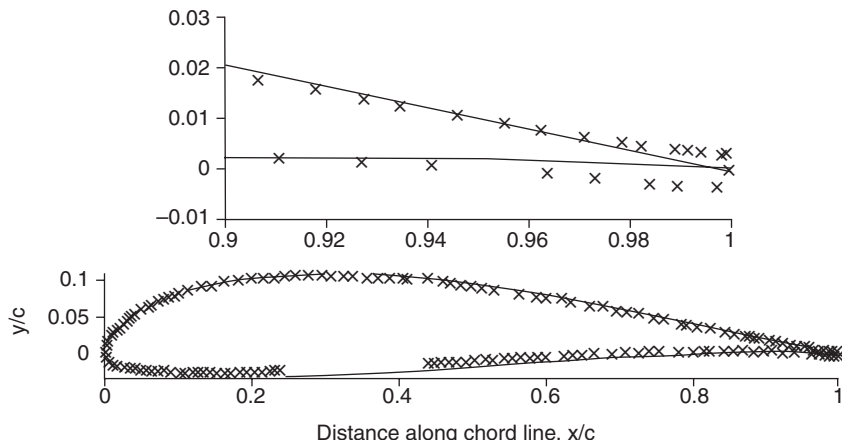
From GL (2010):

- the environmental degradation of composite fibres ‘shall be considered by a material degradation factor of 1.35. This factor can be reduced if representative tests show lower degradation effects’;
- temperatures above room temperature attract a material degradation factor of 1.1 unless coupon tests at the highest operational temperature justify a value of 1.0; and
- corrosion is to be excluded by adequate protection for the life of the turbine.

Many of the remaining issues relating to material quality and quality maintenance are covered in Chapter 3 of GL (2010).

Material testing involves making individual samples of the composite – the ‘coupons’ – or cutting them from a blade. Coupons should be the same thickness as the actual blade section, with the coupon dimensions of 150 mm \times 25 mm and of a ‘dog-bone’ shape with a minimum width of 10 mm to localize the failure. The coupons are then tested to determine Young’s modulus of elasticity as in Fig. 13.4 or fatigue tested at a number of positive R values (for a given load cycle $R \equiv$ maximum stress/minimum stress). Testing is normally not done at R values close to unity as excessively long test time is required, especially for the lower stress levels. Obviously coupons are much easier to test than whole blades and, among other things, can give information on the variability of blade material properties.

There is surprisingly little information available on the conformity of the shape of blades of any size. Kramkowski *et al.* (1997) measured the surface of 20 m long blades and Wood (2011) gives some measured profiles for the blades in Fig. 13.3. An example is shown in Fig. 13.7. The actual blade is too thin, possibly as a result of vacuuming the two blade halves together

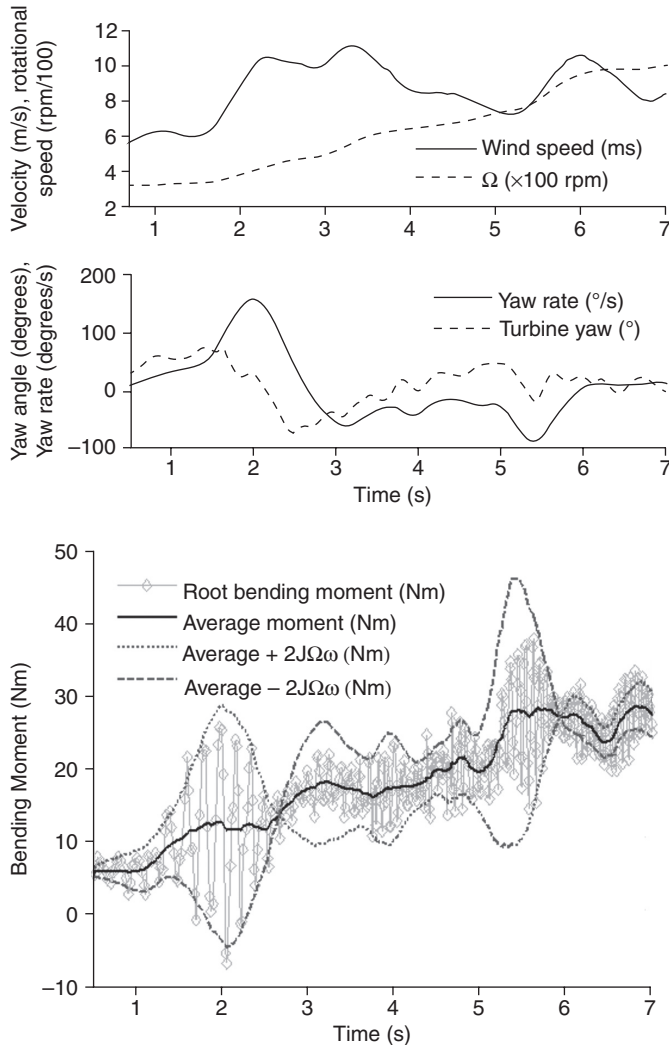


13.7 Measured blade section from the power producing section of the Aerogenesis 2.5 m long blade. Bottom graph shows whole section. The top graph highlights the trailing edge. (*Source:* Data from Rachel Wong.) The gap in the lower surface data is due to mounting of blade section for measurement. (*Source:* From Wood, 2011.)

when they were glued, and it can be seen that the trailing edge is too thick which is a typical problem for vacuum infusion. Trailing edge thickness can be a significant problem for small blades if it causes excessive noise from vortex shedding. Aerofoil trailing edge ‘thickness’ is usually quoted in terms of the chord length and so the values required to guarantee no trailing edge noise from small blades usually translate into razor-thin edges. Fortunately, the calculations of Clifton-Smith (2010) suggest that realistic trailing edge thicknesses of 1 mm or higher are unlikely to lead to significant extra noise.

13.5 Installation and operation

Most small blades are bolted to the blade holder, so they are easy to fit on-site and their light weight and small size presents no problems in transport. The towers of small wind turbines, however, are normally hinged for raising and lowering and the blades can easily be damaged in either process. (The section shown in Fig. 13.2 was taken from a blade broken during lowering.) There is no simple way of protecting the blades during raising and lowering because the centre of mass of most small turbines is on the blade side of the tower so the blades will always be closer to the ground than all other components except the nosecone. Proper care and a control system that ensures that the blades are either stationary or very close to it during lowering or raising, are the best means of protection.



13.8 Blade root bending moment measured on a 1.94 m diameter three-bladed turbine. (Source: From Wilson *et al.* 2008.)

The higher number of fatigue cycles of small blades when compared to large ones has already been noted. Another consequence of their higher angular velocity and the free-yaw behaviour of most small turbines, is their exposure to high gyroscopic moments. Figure 13.8 shows strain-gauge measurements of the root bending moment on a 1.94 m diameter three-bladed turbine. The blades were deliberately made weak and flexible to allow easy determination of the moment from a row of strain gauges mounted along the blade (Wilson *et al.*, 2008). The electrical connections for the gauges were



13.9 Lightning damage at the trailing edge near the tip of a Westwind 20 kW wind turbine blade at the CSIRO Energy Centre, Newcastle.
(Source: Photo courtesy of Phil May, Solartec Renewables.)

enclosed within the blade to avoid aerodynamic interference. It is clear that the cyclic loads are activated by the yaw rate, ω , and they are bounded by $\pm 2J\Omega\omega$ centred on the ‘average’ moment caused largely by the blade thrust, where Ω is the angular velocity. The bounds are the magnitude of the gyroscopic moment which is often the largest load on a small blade. The frequency of the gyroscopic moment is set by Ω as can be appreciated from comparing the oscillations around 2 s with those centred on 5.5 s. One of the few ways to minimize gyroscopic loads is to minimize J which also improves starting behaviour (Wood, 2011). Low-inertia blades, however, are more susceptible to gusts and require a responsive control system to ensure safety.

The IEC standards for large blades mandate lightning protection, usually in the form of embedded conducting strips, but there is no similar requirement for small blades. Lightning usually strikes in the tip region (Fig. 13.9) and causes significant imbalance by removing blade material. On the other hand, the tip region is not critical structurally and can be repaired easily provided the repaired blades are well balanced. The damaged blade shown in Fig. 13.9 was repaired at the University of Newcastle and returned to service.

13.6 Challenges and future trends

Perhaps the two biggest challenges facing small wind over the last few years are the reductions in many jurisdictions of the ‘feed-in tariffs’ that have done much to stimulate the industry, and the continuing rapid reduction in the cost of photovoltaics, PV. This cost reduction has been driven by lower costs as production volume has risen, and does not have a lot to do with the

rapid advances in developing new types of PV materials. It is hard to see how small wind turbines in the 1–10 kW range will be able to compete in many cases, but there are several niche areas that are worth pursuing:

- Remote power systems use a multiplicity of resources (usually solar and wind), which can add to system reliability and reduce time without power.
- For building mounting, the installation cost of PV is driven by the wind loads and can be a large percentage of the total project cost, so it makes sense to place small turbines in windy areas and PV in calmer ones.
- Most developing countries do not make their own PV whereas it is possible for a large proportion of a small wind turbine to be built locally. This can stimulate the renewable energy industry and reduce imports.
- Little attention has been paid to the higher power (larger) small wind turbines. It should be possible to design and build a 50 kW wind turbine using small turbine technology to reduce costs and gain major improvements of scale, such as significantly increased generator efficiency (typically 70% for a 1 kW generator and 95% for a 50 kW one). Unfortunately most large small wind turbines on the market are, in effect, small large ones with complications such as hydraulic yaw drives that are expensive and unnecessary. The advantage over PV comes from the space requirements. It can take 25–35 m² of PV modules to generate an average of 1 kW of power so there is a point where the vertical area required by wind turbines becomes a natural advantage over ground or roof area.

The next major challenge has already been mentioned: life cycle and sustainability issues of blade materials. Here small blades will benefit from the worldwide effort investigating thermosetting and bio-resins, and green composites. Small blades offer a natural test bed for these developments as they are easier to make and to test and to modify if necessary. Combined with increasingly sophisticated multi-dimensional optimization methods that consider variables such as power extraction, noise, starting performance, and structure, for example, Wood (2011), it is likely that blade design will continue to be refined significantly. To ultimately make small blades at prices comparable to large blades, about \$10 per kg, remains the biggest challenge.

13.7 Acknowledgements

The development of blade manufacturing at the University of Newcastle was supported by the Asia-Pacific Partnership for Clean Development and subsequently by the Australian Research Council. D. H. Wood's work

at the University of Calgary was supported by the National Science and Engineering Research Council, the ENMAX Corporation and the Schulich Endowment.

13.8 References

- Astle, C., Burge, I., Chen, M., Herrler, T., Kwan, L., Zibin, N., Wood, D. (2013) Timber for Small Wind Turbine Blades, *Energy for Sustainable Development* (to appear).
- Bechly, M.E., Clausen, P.D. (1997) Structural design of a composite wind turbine blade using finite element analysis, *Computers and Structures*, **63**, pp 639–646.
- Bechly, M.E., Clausen, P.D. (1999) Some dynamic strain measurements from the blade of a small wind turbine, *Wind Engineering*, **23**, pp 15–22.
- Clausen, P. D., Freere, P., Peterson, P., Wilson, S. V. R., Wood, D. H. (2009). The shape and performance of hand-carved small wind turbine blades, *Wind Engineering*, **33**, pp 299–304.
- Clifton-Smith, M. (2010) Aerodynamic noise reduction for small wind turbine rotors, *Wind Engineering*, **34**, pp 403–420.
- Clifton-Smith, M., Wood, D. H., Wright, A. D. (2011) Optimising design and construction for wind energy systems in low wind environments. In *Wind Energy Systems: Optimising Design and Construction for Safe and Reliable Operation*, Sørensen J.D., Sørensen J.N. (eds), Woodhead Publ, pp 370–391.
- Epaarachchi, J. A., Clausen, P. D. (2003) An empirical model for fatigue behaviour prediction of glass fibre-reinforced plastic composites for various stress ratios and test frequencies, *Composites Part A: Applied Science and Manufacturing*, **34**, pp 313–326.
- Epaarachchi, J. A., Clausen, P. D. (2006) The development of a fatigue loading spectrum for small wind turbine blades, *Journal of Wind Engineering and Industrial Aerodynamics*, **94**, pp 207–223.
- Frohnnapfel, P., Muggenhamer, M., Schlägl, C., Drechsler, K. (2010) Natural fibre composites for innovative small scale wind turbine blades, *Intl Workshop Small Scale Wind Energy for Developing Countries*, Pokhara, Nepal, 15–17 November. <http://www.kapeg.com.np/home/workshop/2010-international-workshop-on-small-scale-wind-energy-for-developing-countries/workshop-information> (select ‘Presentation videos’ from ‘2010 Workshop Pokhara’).
- Giguere, P., Selig, M. S. (1997) Low Reynolds number airfoils for small horizontal axis wind turbines, *Wind Engineering*, **21**, pp 367–380.
- Giguere, P., Selig, M. S. (1998) New airfoils for small horizontal axis wind turbines, *Journal of Solar Energy Engineering*, **120**, pp 108–114.
- GL (2010) Guidelines for the certification of wind turbines, Germanischer Lloyd. https://www.gl-group.com/wind_guidelines/wind_guidelines.php?lang=en
- Holmes, J. W., Brøndsted, P., Sørensen, B. F., Jiang, Z., Sun, Z., Chen, X. (2009) Development of a bamboo composite as a sustainable green material for wind turbine blades, *Wind Engineering*, **33**, pp 197–210.
- IEC 61400–2 ed2.0 (2006–03) Wind Turbines. Part 2 – design requirements for small turbines.
- Kogaki, T., Matsumiya, H., Iida, M., Inaba, T., Yoshimizu, N., Kieda, K. (2002) Development and experimental verification of an airfoil for small wind turbines.

Proceedings of 2002 Global Windpower Conference and Exhibition. 2–5 April, Paris, France.

- Kramkowski, T., Foussekis, D., Chaviaropoulos, T., Ronsten, G. (1997) Harmonisation and improvement of rotor blade quality control, DEWI Final Report. <http://www.dewi.de/dewi/fileadmin/pdf/publications/Publikations/JOR3-CT95-0082.pdf>
- Owen, M. J., Howe, R. (1972) The accumulation of damage in glass-reinforced plastic under tensile and fatigue loading, *Applied Physics*, **5**, pp 1637–1639.
- Peterson, P., Clausen, P. D. (2004) Timber for high efficiency small wind turbine blades, *Wind Engineering*, **28**, pp 87–96.
- Post, N. L., Case, J. J., Lesko, J. J. (2008) Modeling the variable amplitude fatigue of composite materials: A review and evaluation of the state of the art for spectrum loading, *International Journal of Fatigue*, **30**, pp 2064–2086.
- Sharma, S., Wetzel, K. K. (2010) Process development issues of glass-carbon hybrid-reinforced polymer composite wind turbine blades, *Journal of Composite Materials*, **44**, pp 437–456.
- Sinha, R., Acharya, P., Freere, P., Sharma, R., Ghimire, P., Mishnaevsky, L. (2010) Selection of Nepalese timber for small wind turbine blade construction, *Wind Engineering*, **34**, pp 263–276.
- Sutherland, H. J. (2000) A summary of the fatigue properties of wind turbine materials, *Wind Energy*, **3**, pp 1–34.
- Tsai, K. T., Ansell, M. P. (1990). The fatigue properties of wood in flexure, *Journal of Materials Science*, **25**, pp 865–878.
- Veers, P.S. (2011) Fatigue loading of wind turbines: Optimising design and construction for safe and reliable operation. In Sørensen JD, Sørensen JN (eds), *Wind Energy Systems-Optimising Design and Construction for Safe and Reliable Operation*, Woodhead Publ, pp 370–391.
- Wilson, S. V. R., Clausen, P. D., Wood, D. H. (2008) Gyroscopic moments on small wind turbines blades at high yaw rates, *Trans IE Aust, Australian Journal of Mechanical Engineering*, **5**, 1–9.
- Wood, D. H. (2009) Using the IEC Simple Load Model for small wind turbines, *Wind Engineering*, **33**, pp 139–154.
- Wood, D. H. (2011) *Small Wind Turbines: Analysis, Design, and Application*, Springer, UK.

Wind turbine blade structural performance testing

J. J. HEIJDRA, M. S. BORST and D. R. V. VAN DELFT,
Knowledge Centre WMC, The Netherlands

DOI: 10.1533/9780857097286.3.432

Abstract: International safety and design standards for structural performance analysis require full-scale testing of each wind turbine blade prototype and of blades that have undergone major design changes. The purpose of blade testing is to demonstrate that the blade design and production are such that the blade possesses the intended strength and service life. Full-scale testing can be seen as final design verification that also checks the assumptions used in the design. In this chapter, aspects of full-scale blade testing are considered in the practical context of the blade test laboratory. An overview is given of the tests which make up the complete test program, the loads used for each and the equipment and instrumentation used.

Key words: full-scale testing, certification, static testing, fatigue testing, test load, design load, single-axial test, multi-axial test.

14.1 Introduction

The blades are generally regarded as the most critical structural parts of a wind turbine. Therefore safety standards require full-scale tests of each prototype and of blades that have undergone a major design change. The purpose of these blade tests is to demonstrate that the design and production of the blade are such that the blade possesses the planned strength and service life.

The requirements for full-scale blade testing are contained in international standards such as IEC-61400-23 and the *Guideline for the Certification of Wind Turbines, Edition 2010* from Germanischer Lloyd Industrial services GmbH, Renewables Certification (GL).

In general, full-scale testing is seen as a final design verification that also checks the assumptions used in the design. Examples of such assumptions are that the calculated stresses and strains are accurate or at least conservatively estimated and that the strength and the fatigue resistance of the materials used are accurately known, or conservatively estimated. Another

assumption is that production has been carried out in accordance with the design. What is not tested is the validity of the design loads, the scatter of the results and the possible changes in the production or the design.

In this chapter, aspects of full-scale blade testing are considered in the practical context of the blade test laboratory. An overview is given of the tests which make up the complete test program, the test loads used for each and the equipment and instrumentation used. Practical issues such as the clamping of the blade in the laboratory and how the load is applied to the blades are touched on.

Full-scale testing of a prototype is compulsory for proper certification of a wind turbine. If a turbine is to be certified according to IEC-61400-23, the complete test program – static test, fatigue test and post-fatigue static test – is required. For certification according to GL (2010), only the static test is compulsory and the necessity for a fatigue test has to be decided in each individual case.

14.2 Test program

A complete test program consists of the following tests and measurements:

- Measurement of the weight and the lengthwise position of the center of gravity.
- Measurement of the natural frequencies of the blade.
- Static test.
- Fatigue test.
- Static test after fatigue.

The weight and the position of the center of gravity are important for validation of the model used for determining the test loads. Comparison of measured values with model data is required.

The measurement of the natural frequencies normally encompasses the first and second flap frequencies and the first and second edge frequencies. Sometimes the first torsional frequency is of interest. The measured frequencies are used for validation of the blade model. Modal testing, which entails measuring not only the natural frequencies but also the corresponding mode shapes, can be carried out instead of a simple natural frequency test.

Although for blade certification purposes a fatigue test is not always required, recent testing experience has shown that a lot can be learnt by doing this test. The new IEC standard even requires a post-fatigue static test. Performing this test as part of the complete program can help predict whether the blade can continue to withstand extreme loads, even after the type of damage it can be expected to incur during 20 years of operation.

14.3 Types of tests

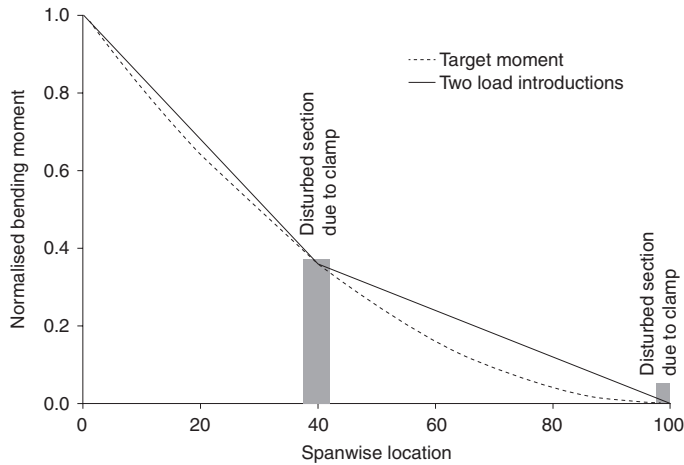
In order to prove that the blade fulfils its design criteria, several tests are performed.

14.3.1 Static tests

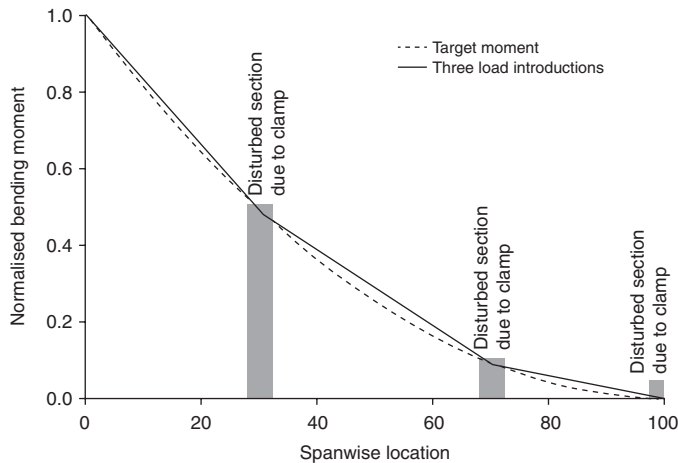
Static tests are performed to demonstrate that the blade can withstand the extreme design loads. The bending moment distribution in several directions along the blade span is defined from the design load cases. During the test, these bending moment curves are simulated by application of load at discrete locations. The static test not only gives information on the ability of the blade to withstand the loads, but, depending on test instrumentation, also provides valuable information on blade structural properties, deflections and strains.

Static tests generally involve pulling on the blade by means of winches, cranes or hydraulic actuators. For small blades, methods include stacking mass such as sandbags or metal ingots on the blade, or hanging water-filled oil drums from the blade. However, testing with dead load carries the risk of catastrophic failure since the load cannot be easily reduced when the blade starts to show signs of failure. In addition, the mass needs to be very carefully applied since the dynamic effects from the increasing load can easily lead to overload. When the load is applied by cranes or actuators, for each load case the blade is loaded simultaneously and in the same direction at several spanwise positions. The load can be applied vertically downward, in which case gravity will contribute to the test load, but horizontal load application or vertical upward pulling can also be used. In all cases the additional load component due to gravity has to be accounted for.

The number of load application points is not strictly defined. It may depend on, amongst other things, the shape of the target moment distribution along the blade, the allowable loads locally on the blade (shear loads also need to be considered), costs, or preferences of the test designer. Account must be taken of the fact that, due to the presence of the load introduction clamps, the blade is locally not properly loaded and the sections bearing the clamps will not be regarded as correctly tested for certification purposes. Therefore no critical structural sections, such as ends of shear webs, large cross-sectional transitions or other features that could introduce stress concentrations in the undisturbed blade, should be covered by the clamps. A simplified example of how a target moment curve can be approximated when two load introduction locations are used, and also when three are used, is shown in Figs 14.1 and 14.2. The overloads are clearly larger with the two load introductions than with the three.



14.1 Two point bending moment curve.



14.2 Three point bending moment curve.

14.3.2 Fatigue tests

For the current generation of blades, two different fatigue test methods are commonly used. In the first and much simpler method, the blade is cantilevered horizontally or at a small angle from a rigid test stand and excited in its first resonance mode. Since the blade motion is in one direction, this test is called a ‘single-axial’ fatigue test. The test frequency is (very close to) the natural frequency of the blade, including the mass of the excitation system.

The flapwise natural frequency is lower than that of the lead-lag. Typical figures for the natural frequencies of blades with a length of around 60 m are 0.7 Hz flapwise and 1.1 Hz lead-lag (Kooijman *et al.*, 2003).

The test is performed sequentially: once in the flapwise direction, followed by once in the lead-lag direction. Masses are sometimes added on one or more sections of the blade to change the distribution of the test bending moment along the span of the blade. The excitation is provided by rotating eccentric mass, or by hydraulic actuators between the blade and a fixed point, or by oscillating masses fixed to the blade and driven by hydraulic actuators.

In a flapwise fatigue test the main focus is on the spar caps, while in a lead-lag fatigue test the trailing and leading edges of the blade are the critical parts being tested.

In the second type of test the blade is loaded in flapwise and lead-lag direction simultaneously. This type of testing is referred to as ‘multi-axial’ testing (IEC, 2003). Normally this test is performed at or near the first flap natural frequency, and the lead-lag motion is forced to follow in the same frequency with a pre-described phase angle. In this case the blade tip describes an elliptical path in space, instead of a linear path as is the case with the single-axial tests. In this combined flap and lead-lag testing a much larger part of the blade circumference is properly tested. However, one drawback of this method is that either in some cases the tip section of the blade in lead-lag direction (the trailing and leading edges) is not well tested. Or is that higher overloads have to be accepted on the inboard section in order to reach a sufficiently high load on the outboard section. Another possible method is to excite both flap and lead-lag in their own first natural frequency, in which case the displacement is a complex figure (‘Lissajous’) whose shape depends on the ratio between flap and lead-lag test frequency.

A control system can be implemented using theoretical quantities such as a prescribed tip displacement or a prescribed strain. A more precise method is to establish the relation between local bending moment at a certain cross section and the strains measured locally, and then control the test moment distribution in the blade based on these calibrated strain gauges.

14.3.3 Ultimate tests

Occasionally test customers want to know the ultimate strength of a blade. A static test to failure is then performed. Normally this test is done on a blade that has undergone the complete test program as described above. It is obvious that only a single load direction can be tested to failure, and often this is a load case where buckling determines the maximum load. Depending on the setup and blade orientation, this can be spar cap buckling

or leading edge buckling. Debonding and subsequent buckling of the trailing edge might also be a realistic scenario. The test is almost identical in setup to a normal static test, with the difference that the test is not stopped at the onset of failure. The load case is applied using the same clamps fixed at the same locations; however sometimes a clamp is removed if it appears to be in a critical location that is prone to failure.

The failure mode of a blade in such a load case can be really catastrophic. Precautions have to be taken to guarantee the safety of all personnel involved in the test. In addition, the equipment used may suffer damage from the sudden release of energy at the moment of failure. Another consideration after such a catastrophic failure is that, even after release of the applied forces, a large amount of elastic energy can still be present in the blade, and that extreme caution must therefore be applied when dismantling the test.

14.4 Test loads

The loads that have to be applied in the tests, must give the assurance that the blade can withstand its design loads. The multitude of loads on a turbine in 20 years of operating has to be translated into a few manageable test loads.

14.4.1 Static test

The test load is defined as the actual load reached during the test. The target load is the load that should be reached in order to properly test a blade. This means that the test load must be equal to or higher than the target load for all areas of the blade that must be tested. Target loads are based on the entire envelope of the design loads. The design loads from this envelope have to be multiplied by test load factors, which are established by the certifying bodies. Test load factors are necessary in order to account for the fact that only one blade out of a large population is tested, and also for the fact that testing generally takes place under environmental (e.g. temperature) conditions that are much more benign than the actual operating conditions for the blade.

For the static test, as a practical minimum, four load cases are considered, although sometimes critical combinations can require additional load cases. In GL (2010), positive and negative flap and lead-lag are specified as essential load cases. In practice, four or five loadcases that combine flap and lead-lag loads, can better cover the envelope of all operational loadcases.

As a rule only the flapwise and the lead-lag moments and shear forces are applied as test loads. The radial load, mainly originating from gravity and centrifugal forces, causes low stresses. Torsion is generally not considered,

unless it is determined that torsion loads are critical for the design, in which case representative torsion should be applied.

14.4.2 Fatigue test

The fatigue load on a wind turbine blade may consist of a couple of hundred million cycles with a high variability. Ideally, the test load should be equal to this operating load. In practice, however, it is only feasible to test for a couple of months. Since test frequencies are generally around 0.5–1 Hz and since, after it is set up and tuned to achieve the desired targets, the test has to be interrupted regularly for inspections and calibrations, the number of cycles has to be reduced to only a few million cycles. A reduction can be achieved by omitting non-damaging cycles from the operating load, but this still leaves an unacceptably high number of cycles. In order to further reduce the number of fatigue cycles, the amplitude of the load cycles has to be increased. With increasing load, however, a nonlinear response, such as buckling or deformation of the cross section, may occur in the structure. Therefore any increase in fatigue load amplitude has a practical upper limit.

Therefore, while fatigue load can be increased by increasing the amplitude of the lower cycles of the operating load, the result is that the load more and more resembles a constant amplitude load. This is why most fatigue tests on larger blades are currently performed as constant amplitude tests at or near the first resonance frequency of the blade.

In this way, the complex combination of the varying loading patterns that occur during the lifetime of the blade is greatly simplified, giving a constant amplitude load for a largely reduced number of cycles. In practice, however, the result is that not all parts of a blade can be properly tested.

For each part of the blade that has to be tested (leading edge, trailing edge, spar caps, shearweb, panels, etc.) it has to be shown that the damage due to the fatigue test load is equal to or higher than the damage due to the target load. In order to determine the damage due to a load system, the load has to be translated into strain or stress. From these strain or stress cycles the damage can be calculated using an appropriate method of cycle counting and an appropriate fatigue formulation. One criterion used to determine the need to test a certain section of a blade is the reserve against fatigue failure in that area. This determination should be made in accordance with the certifying body.

The reserve against fatigue failure can be expressed by the fatigue strain factor (FSF). This is the factor by which the load has to be multiplied to obtain damage equal to unity. Since the determination of the damage is a nonlinear process, the FSF has to be determined iteratively. For areas for which this factor is high, a large reserve against fatigue damage exists and

hence the need for testing this area is less urgent. If this factor is close to unity, the area is critical with respect to fatigue and testing is required.

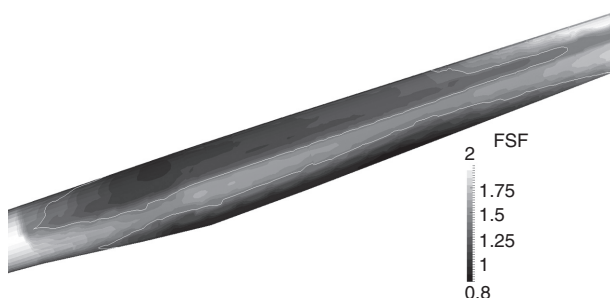
In order for a given area to be properly tested, the damage due to the test load must be equal or higher than the damage due to the target load. This means that the FSF for the fatigue test load must be equal to or lower than the FSF for the fatigue target load.

The ratio between the FSF for the target load and the FSF for the test load can be defined as the relative FSF (rFSF):

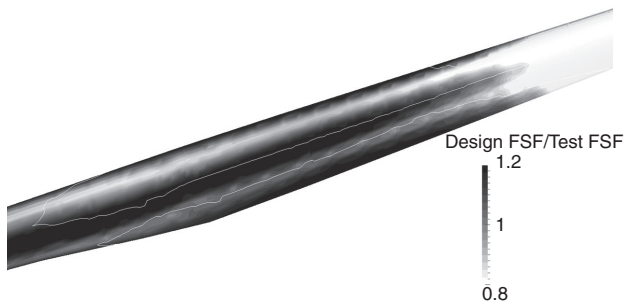
$$rFSF = \frac{FSF_{target}}{FSF_{test}} \quad [14.1]$$

At all locations where the rFSF is bigger than unity the blade is properly tested.

By way of example, the test load evaluation for a generic 62.5 m blade is given for two test methods (Figs 14.3–14.5). The examples given only deal with the stresses in the blade's longitudinal direction, and so possible critical details and stresses in other directions are not considered. The position of the load introduction and the magnitude and phase (for the multi-axial test) of the flap and edge load are optimized to get a minimum error between the FSF for the target load and the FSF for the test load in the inboard part of the blade. In the first method, the test load evaluation is given for a sequential single-axial test where the blade is sequentially loaded in pure flap and pure lead-lag direction. On the 62.5 m blade, strains are computed for every 2 m of rotor diameter and for 56 locations distributed over the circumference of the chord for each spanwise location. From the resulting time series of strains in all these locations, together with the occurrences table and the fatigue life formulation, the damage and FSFs are determined. The damage in each material is calculated, and for overlapping materials with a different



14.3 Design FSF.



14.4 rFSF and critical areas, sequential single-axial test.



14.5 rFSF and critical area, multi-axial test.

fatigue formulation the minimum FSF is considered. All computations are performed on the complete load set specified by IEC guidelines using the FOCUS6 integrated wind turbine design tool.

The damage in the blade after 20 years of service has been determined. The FSFs are presented as contour plots in Fig. 14.3.

In this example, it has been arbitrarily decided to consider areas with an FSF lower than 1.4 as critical. The white line over the contour in Fig.14.3 connects the points where the FSF equals 1.4. The areas of the blade where the FSF has a value lower than 1.4 should therefore be tested. Areas where computation might underestimate stresses should also be considered, for example areas of high stress concentration in the bolted root connection, in the bonded joints of leading edge (LE) and trailing edge (TE), and in the area between the root and the largest chord.

Sequential single-axial, single location

At a single location two separate periodically varying loads are applied successively in the main directions. The load in this example is applied at blade length $L = 38.6$ m. The load due to acceleration of the blade mass is

neglected. The number of test cycles for each test load is fixed at 1 million cycles. Figure 14.4 shows the ratio between test and design FSF. In the graph, the critical areas from Fig. 14.3 are also indicated with a white contour line. The graph also shows the extent of the critical area tested, and the fact that locally in the critical area the blade is more than 24% overloaded. This example concerns only a single load introduction point and does not take into account inertia effects. These effects can be taken into consideration by ensuring a more realistic load distribution.

Multi-axial, single location

The second example is from a bi-axial test where, at a single location, a flap load and a lead-lag load are applied with a phase offset of about 90° so that the load introduction point describes an ellipsoidal trajectory in space. The load in this example is applied at blade length $L = 39.4$ m. The rFSF contours are given, together with the aforementioned critical area, in Fig. 14.5.

It can be seen that for this type of test method a much bigger part of the critical area is tested, while the overload in this area is limited to 14%.

In these examples, and with the arbitrarily chosen FSF value of 1.4 to define the critical area, it appears that, for both types of test, parts of the critical area are not satisfactorily tested. However it can also be seen that, for fatigue testing, combined loading (multi-axial testing) results in a considerably bigger part of the blade being properly tested.

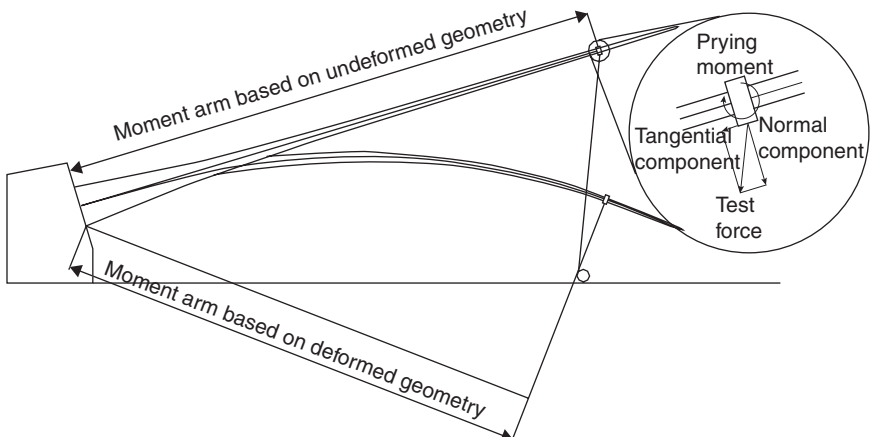
14.5 Test details

For the execution of a blade test lots of small detail matters have to be accounted for. Some practical points regarding loading and instrumentation are mentioned in this sub-section.

14.5.1 Load introduction

The load is generally introduced to the blade using load clamps that are shaped to the local profile. Alternatively, bonded pads are used for load introduction. It must be noted that the load clamps may locally stiffen the blade and therefore the part of the blade close to the load clamps may be considered not properly tested. It also may be necessary to reinforce the blade locally at the positions of the clamps. Parts of the blade are considered critical, e.g. the root area where the cross section shape and properties change strongly in spanwise direction, or sections where there is a low calculated reserve against buckling. The clamp position, and hence the reinforcement if needed should not be in these critical areas.

The deformation of a wind turbine blade under the test load is large. When a blade is loaded by means of winches or actuators with their attachment



14.6 Effects on load due to blade deformation.

points fixed, this can result in the direction of the force varying with magnitude. Certainly in flapwise tests, the direction relative to the blade axis and the moment arm relative to the blade root can significantly vary. This effect is sketched in Fig. 14.6.

When the load vector is not perpendicular to the elastic axis, slip may occur between the saddle and the blade. Moreover, when the load application point is not on the elastic axis, an additional moment is applied which may result in high local prying forces. This effect is sketched in the inset in Fig. 14.6.

14.5.2 Blade root clamping

It is advisable when testing a rotor blade to test it together with its mounting structure, such as a pitch bearing. In such a case, the mounting bolts and the blade root in the vicinity of these mounting bolts have the correct load applied to them, and the test is therefore able to give information on the behavior of these bolts. When the mounting bolts are fitted with strain gauges or other measurement instruments, the loads in the bolts are known. For pre-stressed tension bolts, the bolt factor, which is the ratio between the actual change in bolt load due to the test load and the hypothetical change in bolt load if only the net area of all the bolts had to carry the loads, can be determined. This ratio is essential for the calculations of the fatigue life of the tension bolts.

An advantage of including the pitch bearing in the test is that this may give the test center an easy way of rotating the blade between different load cases. However attention should be paid to proper clamping of the

rotational degree of freedom during each test. Sometimes for fatigue testing the bearing is replaced by a fixed mounting ring. This is usually because the fatigue load at the root is not representative of the real-life fatigue load in the (steel) bearing material. Using a fixed mounting ring reduces the need for a clamping mechanism to prevent rotation and there is no risk of failure of the balls in the bearing.

14.5.3 Instrumentation

This section describes the quantities measured during a blade structural performance test, focussing on some of the instrumentation used.

Applied force

Since the purpose of a test is to prove that the blade can withstand the target load, measurement of the forces that are applied is critical. Correctly calibrated load cells are installed at the load introduction clamps to measure the locally applied force.

Strains

The design of the blade is based on the allowable stress or strain values of the materials used. It is therefore important to measure strains at relevant points on the blade. Strains can be measured in various ways, for example using electrical or optical strain gauges and Digital Image Correlation (DIC) systems. In general, the strains on the main load-carrying parts, such as the girder in the upper and lower shell and the leading and trailing edges, must be measured at sufficient locations along the length of the blade. Strains on other critical parts of the blade, such as panels where buckling is critical in the design calculations, can also be measured. During the static test, at intermediate load levels, the strains can be plotted against the bending moment, the root bending moment or the local bending moment, whichever is available. Nonlinearity in the resulting graphs may indicate the onset of buckling and may warn off catastrophic events at higher loads. Measurement of the shear strains in the web at the blade root may provide additional information about the blade behavior. During a fatigue test, these strain measurements can reveal possible damage in the bond line between the web and the shell.

Displacements

The stiffness of the blade is important because of the need for adequate clearance between the blade tip and the tower: for larger blades this stiffness

may even become the driving design value. Displacement measurements are therefore essential to enable comparison between the deflections of the blade in the model and in the test. Normally the displacements will be measured at the location of the load introductions, and/or at the blade tip. It is important to be aware that during a static test a blade shows large deflections, and that, due to the twist and the unequal stiffness in flap and lead-lag direction, the deformation of the blade may not be in the direction of the applied load. The large displacements occurring during blade tests can easily be measured with the aid of draw-wire displacement transducers, where a thin flexible steel cable is wound around a drum that is coupled to a potentiometer or an encoder. The change in length of the steel cable is translated to rotation of the drum, and this rotation is then changed into an electrical signal. Since these wire displacement transducers only measure the change in length between their fixed point and the wire attachment point, for two-dimensional (2D) or three-dimensional (3D) displacements it may be necessary to connect 2 or 3 transducers with different fixed points to the moving point on a blade and use triangulation to derive the displacements. Optical (laser) equipment is also available for measuring displacements. Of course, for this type of transducer, the alignment in case of 2D or 3D displacement is not always obvious.

The finite stiffness of the frame to which the blade is mounted can also contribute to displacements of the blade under the test load. If this contribution is not expected to be negligible, measurements of the displacement of this root mounting frame can be used to correct the displacements at the load introduction points for rigid body rotations of the blade due to root frame flexibility. For these small displacements, small linear variable differential transformers (LVDTs) or contactless laser sensors can be used.

Accelerations

For a modal test (Avitabile, 2001), displacements or accelerations have to be measured on at least 6–8 positions on the blade. If torsion modes are to be measured in addition to flat and edge modes, each section requires three transducers. For ease of installation accelerometers are often used, alongside an excitation device such as a shaker or impact hammer, in order to measure the mode shapes.

Environmental conditions

Since environmental conditions during the test may have an influence on the behavior of the materials, the temperature and relative humidity of the test location must be recorded. Some standards require a correction to the test load if the temperature during the test is below a certain reference value.

Electrical conductivity of lightning protection system

New guidelines recommend including the measurement of the electrical resistance of the lightning protection system in the test. This may be done using an ohmmeter, which is to be installed in such a way that the lightning protection system is part of the electrical circuit that is being measured.

14.6 Conclusion

The size of wind turbine rotor blades continues to increase. Moreover, Asia and South America are becoming bigger players in the global wind turbine rotor blade market. New blade test facilities are being developed on these continents, and existing facilities are expanding to meet the demand for testing larger blades and larger volumes of blades. It is evident that there is an increasing demand for the full blade structural performance testing program, including the post-fatigue static test.

14.7 References

- Avitabile, P., *Experimental Modal Analysis, A Simple Non-Mathematical Presentation*. Sound and Vibration, January 2001.
- FOCUS6 Integrated Wind Turbine Design Suite. <http://www.wmc.eu/focus6.php> (Accessed 12 March 2013).
- Germanischer Lloyd. *Guidelines for the Certification of Wind Turbines*, 2010.
- IEC 61400–23 *Wind Turbine Generator Systems Part 23: Full-scale Structural Testing of Rotor Blades*.
- Kooijman, H. J. T., Lindenburg, C., Winkelaar, D. and Van der Hooft, E. L. *Aero-elastic Modelling of the DOWEC 6MW Pre-design in PHATAS*, ECN-CX – 01–135, 2003.

- ABAQUS subroutine User Defined Field, 307
accelerated fatigue tests, 201
accelerometers, 53
acrylates, 396
actuation loads, 44–6
 schematic diagram, 44, 45
actuator disc method, 62
actuator line method, 62
adhesive bondline
 failure, 14
 trailing edge shells with
 out-of-plane deformations, 15
adhesive joints, 290
aerodynamic conversion, 36
aerodynamic damping, 157–8, 165
aerodynamic design
 wind turbine rotors, 59–108
 blade element momentum (BEM),
 63–72
 design parameters, 72–8, 78–86
 design process, 86–102
 future trends, 102–3
 overview, 59–63
 aerodynamic loads, 36–9, 178
 blade cross-section and aerodynamic
 forces, 36
 lift/drag/momentum coefficients of an
 aerofoil, 37
 load cases according to IEC
 61400–1, 38
aerodynamic shell, 181–2
 cost, 182–3
 estimated blade material cost
 breakdown, based on 61 m
 blade, 183
 skin, 181–2
 sandwich test set-up in three-point
 bending, 182
- aeroelastic design
 aeroelasticity, 150–5, 155–62
 blade design, 162–7
 aerofoils, 166–7
 analysis, 164–6
 resonance avoidance, 162–3
 structural pitch angle, 164
 challenges and future trends,
 170–1
 complete turbine design, 167–70
 backward and forward whirling mode,
 169
 two-bladed vibrating turbine,
 168
 wind turbine blades, 150–71
aeroelastic tailoring, 55
aeroelasticity, 151–5, 155–62
 airfoil up and down movement,
 152
 eigenmodes of a uniform beam,
 154
 mass and spring system, 152, 154
 wind turbine blade instabilities,
 156–62
 aerofoil aerodynamic damping,
 157
 classical flutter on an aerofoil,
 161
 flapwise deformation, 160
 non-dimensional values for
 damping, 159
 stall flutter on an aerofoil,
 160
 wind turbine blade modes, 155–6
aerofoils, 166–7
airfoils, 89–94
 centrifugal and Coriolis forces,
 133–40
 3-D correction models, 134–6

- 3-D correction models
 - applications, 137–40
- characteristics at high angles of attack, 128–33
 - deep stall angle variation, 130
 - measured aerodynamic performance, 131
 - measured lift curve, 129
 - measured pressure distributions, 129
- C_l _{design, blade} distribution, 93
- C_C _d_{design, blade} distribution, 94
- computational methods, 110–16
- 2D airfoil characteristics for FFA-W3–241, 92
- 2D airfoil characteristics for FFA-W3–301, 92
- 2D airfoil characteristics for NACA 632415, 90
- 2D airfoil characteristics for NACA 633418, 91
- 2D airfoil characteristics for NACA 634421, 91
- α _{design, blade} distribution, 94
- design data, 140–5
 - available airfoils, 141–3
 - establishing the data, 143–5
 - measured and predicted
 - performance, 144
 - wind turbines with a design lift
 - coefficient with maximum relative thickness of 18%, 142
 - wind turbines with a design lift
 - coefficient with maximum relative thickness of 21%, 142
 - wind turbines with a design lift
 - coefficient with maximum relative thickness of 25%, 142
- design parameters, 110
- desired characteristics, 116–20
 - blades velocity and forces, 116–19, 117
 - inboard airfoils, 119–20
 - outboard airfoils, 119
- future trends, 145–6
- performance, 75–8
 - characteristic measurement, 76
 - local power loss, 77
- roughness and Reynolds number effect, 120–4
- testing, 124–8
 - low-speed wind tunnel., 126
 - pressure orifices, 127
 - setup and equipment, 127–8
 - test setup using a balance system, 128
- wind turbine blade characteristics, 109–49
- Anderson-Darling, 339
- anhydrides, 395
- anisomorphic CLD, 267
- anisotropy, 263
- annual energy production (AEP), 98
- ANSYS, 349
- Arrhenius equation, 405
- artificial variability, 379
- attenuated total reflexion IR (ATR-IR), 404
- axial velocity, 68–9
- bamboo, 370
- bast fibres, 368
- bending force, 118
- Bernoulli's equation, 64–6
- bias laminates
 - effects of resin, 234
 - S-N data sets vs. six resin systems, 235
- biobased composites
 - biobased fibres and matrix materials, 366–71
 - bamboo preforms for composites, 370
 - bast fibre yarn, 369
 - bast fibres, 369
 - biobased fibres, 366–70
 - biobased matrix materials, 370–1
 - composite preforms with cellulose fibres and glass fibres, 367
 - properties of selection of biobased fibres, 367
- comparison between cellulose and glass fibre composites, 374–7
- model predictions for comparison of stiffness, 376
- examples, processing and mechanical properties, 371–4
 - bamboo fibre/epoxy composites, 372–3

- biobased composites (*cont.*)
- glass fibre/bioresin composites, 371–2
 - jute fibre/bioresin composites, 373–4
 - mechanical properties of bamboo/
poplar/epoxy and glass/epoxy
composites, 373
 - mechanical properties of plain weave
jute fibre composites,
374
 - mechanical properties of
unidirectional glass fibre
composites, 372
 - plain weave jute fibre fabric with
warp/weft yarn weight ratio of
30/70, 374
 - rotor blade made using bamboo
composites under static test,
373
 - special considerations in development
and application, 377–82
 - fibre defects, 378
 - interface properties, 379–81
 - other issues, 381–2
 - polarised optical microscope image
of flax fibre with defects, 378
 - stress-strain curves and failure
characteristics of unidirectional
hemp yarn/PP composites,
381
 - stress-strain curves of two batches of
textile hemp yarn of equal nominal
quality, 380
 - variability in fibre properties, 378–9
- wind turbine blade materials,
- 363–82
 - demonstration of biobased
composites, 366
 - development of prototype small-
scale rotor blades using biobased
composites, 365
 - stiffness of unidirection biobased
composites, 364
- blade element momentum (BEM), 61–2,
63–72
- blade element momentum theory,
68–72
- division of a wind turbine rotor into
annular elements, 68
- formulation symbols, 69
- one-dimensional momentum theory,
63–7
- blade element momentum theory, 68–72
- blade fatigue tests, 201–2
- blade loads
- design verification testing, 50–4
 - calibration of global bending
moment, 53–4
 - instrumentation, 52–3
 - load measurements, 51
 - process, 50–2
 - fatigue, 46–9
 - future trends, 54–6
 - design options, 55
 - material issues, 56
 - operation strategies, 55–6
- generation, 35–46
- actuation loads, 44–6
 - aerodynamic loads, 36–8
 - blade mass *vs.* rotor diameter,
41
 - Campbell plot, 42
 - edgewise vibration, 43
 - inertia, gravitational and gyroscopic
loads, 39–44
 - rotor plane blade root bending
moments, 40
 - tower effect, 39
 - wind turbine control, 35
- types, 30–4
- deflection and deformation,
33–5
 - global, 30–2
 - strain and stress, 32–3
- wind turbine blades, 29–56
- blade passing frequency, 162
- blade root bending, 43
- blade section failure, 337
- bondlines, 199
- bi-axial tension-torsion fatigue test
set-up for full-adhesive tubular
bonding paste, 200
 - bonding paste material, glass-filled
epoxy before and after resin,
199
- Boolean operations, 317
- Box-Behnken design, 347
- Brazier load, 11
- break influence superposition (BIS)
technique, 300
- buckling, 12–13, 35

- ‘back to back’ strain measurements, 12
- trailing edge, 12
- buckling-driven delamination, 14–17
 - buckling mode map, 16
 - flat UD solid element panels reduced compressive strength, 17
- Budiansky-Fleck fibre kinking condition, 312
- Campbell plot, 41
- carbon fibre-reinforced composites
 - statistical and compressive loading effects, 311–16
 - degradation of composite matrix leading to reduction of shear modulus, 315
 - distribution of failed fibres in case of clustered and random homogenous fibre, 313
 - example S-N curves of composite, 315
 - random compressive loading, 314
 - schema of multifibre unit cell with random misalignments, 312
- carbon laminates, 211–17
- cellulose, 368
- central composite design, 347
- centrifugal forces, 133–40
- centrifugal stiffening, 163
- chemical attack, 408
- chromatography, 404
- classic life prediction methodology, 289–90
- classical beam theory, 303
- classical flutter, 161
- classical lamination theory (CLT), 328, 332
- cloud-to-ground lightning, 399
- combined flap and lead-lag testing, 436
- Compaq Visual Fortran, 306–7
- composite wind turbine blades
 - blade structure and components, 177–83
 - rotor blade structural components, 178
- fatigue as design driver, 175–206
 - fundamentals, 183–91
 - materials in blades, 176–7
- research and modelling, 191–201
- future trends, 201–6
 - automated production, 204
 - probabilistic modelling, 202
 - reaching the limits, 203
 - redundancy of supply, 204
 - repair, 204
- significance of material models for
 - blade tests, 201–2
 - structural health monitoring, 202
 - subcomponent research, 204–6
 - sustainability, 202
 - testing, 202–3
- compression-compression (C-C) fatigue, 263
- compressive loading, 303–4
- computational fluid dynamics (CFD), 61–2, 111–15
 - airfoil contour investigation, 113
 - boundaries conditions, 114
 - computing, 114
 - inspection results, 115
 - mesh generation, 113
 - mesh inspection, 113–14
 - turbulence model, 114
- constant life diagram (CLD), 187, 214, 262–8
- annotation, 263
- PNL compared to Harris bell-shaped diagram, 268
- representation of relationship between fatigue parameters, 264, 265
- constant rotational rotor speed, 81
- contactless laser sensors, 444
- continuous damage fibre bundle model (CDFFBM), 301
- continuum damage mechanics (CDM), 302
- Coriolis forces, 133–40
- 3-D correction models, 134–6
 - applications, 137–40
 - corrected airfoil characteristics, 138, 139
 - measured 3-D data, computed
 - mechanical power and thrust force for NREL rotor, 140
- NREL/NASA Ames rotor data, 137
- cost, 182–3
- crack growth rate, 281
- cross-linking, 403

- cross-sectional shear distortion
 crushing pressure from the longitudinal bending, 13
 transverse shear distortion, 13
- cryogenic tunnel, 125
- cyclic loading, 39
- damage-strain curves, 308
- deflection, 33–4
 buckling, 34
 schematic diagram, 34
- deformation, 33–4
 buckling, 34
- delamination
 material transitions, 236–43
 infused complex structured coupons with ply drops, 239–43
 ply drops in carbon and glass prepreg laminates, 237–9
- design constraints, 84–5, 88–9
 blades thickness distribution, 89
- design driver
 fatigue for composite wind turbine blades, 175–206
 blade structure and components, 177–83
 fundamentals, 183–91
 future trends, 201–6
 materials in blades, 176–7
 research and modelling, 191–201
- design of experiment (DoE), 347
- diamines, 395
- digital image correlation (DIC), 443
- diglycidyl ether of bisphenol A (DGEBA), 395
- displacement controlled tests, 190–1
- DNV-DS-J102, 334, 335, 339
- double cantilever beam (DCB), 273
- double-lap joints, 273
- downward lightning, 399
- drag coefficient, 75, 131–3
- drag force, 117
- dynamic blade test, 52
- dynamic compliance calibration, 278–9
- edgewise mode, 158
- edgewise stall-induced vibrations, 42–3
- Edgeworth expansion, 327, 344–5, 348
- eigenmode, 153–4
- embedded cell approach, 304
- empirical fatigue modelling, 191–2
 constant amplitude tensile fatigue data of spar cap material, 192
- End-Loaded Split (ELS), 273
- End-Notched Flexure (ENF), 273
- Envirez, 371
- Epikote 135/137, 373
- Epobiox, 373
- epoxies, 395–6
- epoxy resin MD laminates
 effects of fabric weight and structure, 234–6
 fatigue results for ten MD laminates supplied by Devold, 236
 stress vs. cycles for MD laminates fabricated with 3 different weight UD fabrics, 237
- European standard ISO 20340, 406
- exponential model, 262
- extreme coherent gust with direction change (ECD), 37
- extreme conditions, 198
 specimens tested at room temperature –40°C vs. +60°C, 198
- extreme direction change (EDC), 37
- extreme operating gust (EOG), 37
- extreme turbulence model (ETM), 39
- extreme wind shear (EWS), 39
- extreme wind speed model (EWM), 37–39
- fabric efficiency, 231–2
- FACT database, 227, 261
- failure of the first ply (FPF), 335, 336
- failure of the last ply (LPF), 335, 336
- FAROW, 348
- fatigue
 design driver for composite wind turbine blades, 175–206
 blade structure and components, 177–83
 fundamentals, 183–91
 future trends, 201–6
 materials in blades, 176–7
 research and modelling, 191–201
- root transition area, 14
- wind turbine blade fundamentals, 183–91
 contribution of each load cycle to fatigue damage, 186
 fatigue modelling, 187–91

- need for design optimisation, 186–7
 number of load cycles, 184–5
 significance of fatigue loading on
 blades, 183–4
 variability of cycles, 185–6
 fatigue damage, 186
 fatigue effects, 318
 fatigue life prediction
 wind turbine blade composite materials,
 251–91
 case study on phenomenological
 fatigue life prediction, 284–9
 fracture mechanics fatigue theories,
 273–84
 future trends, 289–91
 macroscopic failure theories, 255–68
 strength and stiffness degradation
 fatigue theories, 268–72
 fatigue loading, 47–9
 capture matrix for normal power
 production, 49
 normalised cumulative flapwise blade
 load spectra, 50
 rainflow method, 48
 significance on blades, 183–4
 fatigue loading in applications of
 structural composites, 185
 rotor blade tests at Delt University
 of Technology in 1984, 184
 fatigue modelling, 187–91, 257–8
 fatigue cycle and definitions, 188
 schematic of Constant Life Diagram
 (CLD), 189
 strain controlled S-N curves for skin
 material, 190
 fatigue parameters
 different laminate types, 219–20
 stress and strain *vs.* cycles for UD
 laminates with three different
 weight OCV fabrics, 221
 stress and strain *vs.* cycles to fail
 for laminates with three different
 weight triax fabrics, 222
 stress and strain *vs.* log cycles data,
 223
 fatigue resistance
 resin and reinforcement variations
 effects of wind turbine blades,
 210–48
 delamination and material
 transitions, 236–43
 fabric structure on tensile fatigue
 resistance, 226–36
 fatigue trends comparison for blade
 materials, 243–6
 future trends, 247–8
 loading conditions effects for glass
 and carbon laminates, 211–17
 tensile fatigue trends with laminate
 construction and fibre content for
 glass fibre, 217–26
 typical failed fatigue coupons of
 multidirectional laminates, 211
 fatigue strain factor (FSF), 438
 fatigue test, 435–6
 test loads, 438–41
 multi-axial, single location, 441
 sequential single-axial, single
 location, 440–1
 fatigue trends
 comparison for blade materials, 243–6
 database properties for polyester
 resin *vs.* epoxy resin laminates,
 246
 tensile strength and fatigue trends for
 various blade materials,
 244
 typical polyester and epoxy resin
 laminate million cycle fatigue
 strains *vs.* same fabrics, 245
 fibre bundle model, 301
 fibre content effects, 220–6
 biax *vs.* MD laminate strain-cycles data
 for epoxy, polyester and resins, 227
 effect of fabric on MD glass/epoxy
 laminates at similar fibre content,
 224
 fatigue trends *vs.* fibre volume content
 for unidirectional, multidirectional
 and biax,
 225
 million cycle strain *vs.* fibre volume
 content, 224
 fibre extraction, 368
 fibre-reinforced composites, 419–21
 analytical models of mechanical
 behaviour, strength and damage,
 300–4
 compressive loading, 303–4
 tensile loading, 300–2
 unit cell modelling, 304–6
 plane strain unit cell model, 305

- fibre volume fraction, 375
finite element analysis (FEA), 22
finite element models, 304
finite element weakening, 307
first-order reliability method (FORM), 327, 345–6, 350
fixed blades, 81
flap mode, 156, 157–8
flapwise fatigue test, 436
FOCUS 6, 331
FORTRAN routine, 349
Fourier transform infrared spectroscopy (FTIR), 404
fracture mechanics based model, 301–2
fracture mechanics fatigue theories, 273–84
manipulation of fracture mechanics data, 273–84
average compliance *vs.* crack length relationship, 280
clamping at crack tip, dynamic compliance method, 279
crack gage at the crack tip, 278
crack growth rate *vs.* solid lines are plots of model results, 281
mixedmode bending experimental set-up, 284
modelling validation by comparison of experimental results and modelling, 283
predicted FCG curves at various r-ratios, 283
S-N curves for DLJs obtained from fracture model, 277
schematic illustration of load an crack growth during fatigue life, 280
full-scale testing, 18
Gaussian value, 314
gelcoat, 388
Germanischer Lloyd Guidelines, 416
generalised effective interface model (GEIM), 316
generator size, 79–80, 87–8
generator torque, 79
Gerber equation, 266
Germanischer Lloyd, 339
glass laminates, 211–17
glaze, 398
global bending moment, 53–4
global load sharing (GLS), 301
global loads, 30–2
gravity, shear, aerodynamic center and pitch axis of blades, 31
upscaling history for the size of wind turbines, 32
Goodman diagram, 191, 266
gravitational loads, 39–44
gravity load, 178
Green's function model (GFM), 300
ground-to-cloud lightning, 399
Guideline for the Certification of Wind Turbines, Edition 2010(I), 432
gyroscopic loads, 39–44
hand lay-up, 177
Hansen Solubility Parameters (HSP), 390
hierarchical composites
nanoengineered matrix, 316–17
multiparticle unit cell of nanoparticle-reinforced composite with interface model, 317
high-cycle fatigue (HCF), 258
homogenisation methods, 306
horizontal axis wind turbines (HAWT), 59, 60, 414
humidity test, 408
IEC 61400–1:2005, 326
IEC 61400–2, 413, 421
IEC-61400–23, 432, 433
IEC 61400–24, 399
IEC 61400–1 (2005), 341
IEC 61400–1 A1/CCDV (2008), 341
IKEA bolt connection, 180
in-field blade test, 52
inboard airfoils, 119–20
flatback airfoil, 120
inertia, 39–44
inflow angle, 75
infused complex structured coupons, 239–43
International Electrotechnical Commission (IEC), 413
ISO 2394, 333
ISO 4628, 406, 407, 409
ISO 20340, 406
ISO 12944–2, 408

- kinking mechanism, 303
 Kolmogorov-Smirnov, 339
- L1200/G50-E07, 371
 layer-scale laminate modelling, 193
 leading-edge reinforcement, 199–201
 lift, 89–94
 lift coefficient, 75, 131–2
 lift force, 117
 lift–drag ratio, 75, 417
 lightning, 399
 lightning protection level (LPL), 399
 lightning protection system (LPS), 399
 linear variable differential transformers (LVDTs), 444
 load bearing components, 179–81
 root and blade joint connections, 180–1
 Ikea bolt connections test specimen, 180
 load-carrying box girder, 4
 load controlled test, 189
 load cycle, 47, 184–5
 contribution to fatigue damage, 186
 strain based ultra-high cycle fatigue data from laminate and strands, 186
 loading conditions
 effects for glass and carbon laminates, 211–17
 effect on fatigue strain *vs.* lifetime for glass/epoxy and hybrid glass laminate, 215
 fabric specifications, 214
 fatigue constant life diagrams for blade, 216
 infusion resins and post-cure conditions, 213
 transverse direction strain constant life diagram for laminate QQ1, 217
 local load sharing (LLS) model, 301
 local power coefficient, 76–7
 logarithmic equation, 256
 low cycle fatigue (LCF), 47, 258
- macromechanical models, 334
 macroscopic failure theories, 255–68
- constant life diagrams, 262–8
 S-N curve formulations, 257–62
 exponential *vs.* power curves for E-glass/vinyl ester laminate, excluding static data, 260
 exponential *vs.* power curves for E-glass/vinyl ester laminate, including static data, 260
 hybrid model *vs.* other S-N curves for double-lap joints, 262
 hybrid model *vs.* other S-N curves for E-glass/polyester laminate fatigue data, 261
- maleic anhydride (MA), 380
 mass spectrophotometry, 404
 matrix cracking, 301–2
 mechanistic models, 270
 Meso3DFibre, 306–7
 meteorology and site, 31
 method of cells (MOC), 302
 method of Lagrange multipliers, 345
 methyl-ethyl-ketone-peroxide (MEKP), 394
 methylmethacrylate (MMA), 394
 micromechanical modelling, 192–6
 fatigue behaviour of fibre bundles, neat resin and composite, 193
 fibre tows, variation in fibre diameter, 196
 hierarchical approach, 194
 single-fibre fragmentation test, 194
 UD composites, tow bundles and variation in fibre content, 196
 UD non-woven fabric, 195
 wind turbine blade materials, 298–319
 analytical models of mechanical behaviour, strength and damage of fibre-reinforced composites, 300–4
 carbon fibre-reinforced composites statistical and compressive loading effects, 311–16
 future trends, 317–19
 hierarchical composites with nanoengineered matrix, 316–17
 three-dimensional modelling of composite degradation under tensile loading, 306–11
 unit cell modelling of fibre-reinforced composites, 304–6
- micromechanical models, 334

- million cycle strain trend, 225
 Miner's rule, 423
 mixed-mode bending (MMB), 284
 moisture, 319
 moment coefficient, 136
 Monte Carlo simulation, 312, 327, 343–4,
 348
 most probable failure point, 345
 MSC/PATRAN software, 307
 multi-scale approach, 21
 multidirectional laminates, 211
 effects of resin, 226–9
 polyester, vinyl ester and epoxy resin
 laminates at low *vs.* higher fibre
 contents, 228
 S-N datasets for MD laminates, 228
 multiscale effects, 319
 multi-axial testing, 436
- NACA standard roughness,
 121
 Nanocomp3D, 316
 nanoengineered matrix, 316–17
 nanolevel model, 317
 nanoscale effects, 319
 NASA standard roughness, 122
 NatureWorks, 371
 Navier–Stokes codes;
 see computational fluid dynamics
 (CFD)
 normal turbulence model (NTM), 37
 normal wind profile model (NWP),
 37
 Norsok Standard M-501, 406
 Norsok test, 407
 numerical modelling, 192
- one-dimensional momentum theory, 63–7,
 70
 flow around ideal wind turbine rotor, 64
 power and thrust coefficient, 67
 one-dimensional solubility parameter, 390
 OPTIMAT BLADES project,
 187
 outboard airfoils, 119
- paint, 388
 Palmgren–Miner rule, 287, 423
 panel codes, 111
 vs. Navier–Stokes codes, 115–16
 computational details, 116
- computational speed, 115
 measurement comparison, 116
 preparation time, 115–16
 Paris law, 275
 periodic microfield approach (PMA), 304
 phenomenological fatigue life prediction
 case study, 284–9
 constant amplitude fatigue behaviour
 and S-N curves,
 288
 constant life diagrams for examined
 material, 288
 lifetime prediction based on different
 schemes, 289
 schematic representation, 286
 phenomenological fatigue modelling,
 191–2
 phenomenological models, 270
 Piecewise Non-Linear (PNL) model,
 267–8
Pinus radiata, 419
 pitch control, 55, 81
 pitch regulation variable speed
 (PRVS), 82–3, 86
 pitchable blades, 81
 ply drops
 carbon and glass prepreg laminates,
 237–9
 image of delamination crack growing
 from pore ahead of double ply
 drop, 238
 maximum absolute strain *vs.* cycles to
 failure, 238
 maximum compressive strain *vs.*
 cycles to delaminate with double
 internal ply drops, 239
 infused complex structured coupons,
 239–43
 complex coupon schematic for
 infused laminate ply drop study,
 240
 delamination growth in fatigue for
 various resins, complex coupon,
 241
 epoxy *vs.* pDCPD under reversed
 loading fatigue loading,
 243
 near-threshold results,
 243
 pure mode delamination test results
 with unidirectional laminates, 242

- schematic of various damage components and extents for complex coupons, 240
- static data for delamination growth vs. applied load, 241
- polylactic acid (PLA), 371
- Polylite 4729, 373
- Polylite 413–575, 372
- polyurethanes, 396–7
- POST-THIN, 333
- power coefficient, 72–3
- power law model, 212
- PRE-THIN, 332
- pressure tunnel, 125
- probabilistic design
- application examples and discussion of techniques, 348–51
 - failure definition, 333–8
 - failure probability of the blade section, 337–8
 - lamina failure probability, 334–5
 - laminate failure probability, 335–7
- future trends, 351–3
- probabilistic methods and models, 342–7
- Edgeworth expansion method, 344–5
 - first-order reliability method, 345–6
 - Monte Carlo simulation method, 343–4
 - response surface method, 346–7
- random variables, 338–42
- loads, 340–2
 - material properties, 339–40
- structural analysis models, 329–33
- FE model of a blade, 330
 - FE model of a blade with loading condition, 331
 - simulation cycle using THIN and THIN modules, 332
- wind turbine blades, 325–53
- definition of characteristic values, 327
 - full simulation cycle for structural design of wind turbine blades, 329
 - overview, 328–9
 - typical cross-section of blade, 326
- probabilistic modelling, 202
- Puck criterion, 335
- quadratic influence superposition (QIS) technique, 300
- rainflow counting, 47
- Ramberg-Osgood constitutive law, 303
- random defects, 318
- random effects, 318
- random sequential absorption (RSA) algorithm, 312
- rated power, 80
- rated wind speed, 80
- reinforcement variations
- resin effects on fatigue resistance of wind turbine blades, 210–48
 - delamination and material transitions, 236–43
 - fabric structure on tensile fatigue resistance, 226–36
 - fatigue trends comparison for blade materials, 243–6
 - future trends, 247–8
 - loading conditions effects for glass and carbon laminates, 211–17
 - tensile fatigue trends with laminate construction and fibre content for glass fibre, 217–26
- Relative Energy Density (RED) number, 390–1
- relative FSF, 439
- reliability estimation method, 342
- representative volume element (RVE), 193
- residual stiffness, 271–2
- residual strength, 271–2
- resin, 176–7
- effects on UD aligned strand (AS) laminates vs. UD fabric laminates, 230–3
 - fabric efficiency, 233
 - fatigue trends vs fabric based laminates for epoxy, vinyl ester and polyester, 232
- fabric structure on tensile fatigue resistance, 226–36
- effects of fabric weight and structure on epoxy resin MD laminates, 234–6
- effects on biax laminates, 234
- effects on multidirectional (MD) laminates, 226–9
- effects on unidirectional (UD) fabric laminates, 229–30

- resin (*cont.*)
- reinforcement variations effects on
 - fatigue resistance of wind turbine blades, 210–48
 - delamination and material transitions, 236–43
 - fatigue trends comparison for blade materials, 243–6
 - future trends, 247–8
 - loading conditions effects for glass and carbon laminates, 211–17
 - tensile fatigue trends with laminate construction and fibre content for glass fibre, 217–26
- resonance, 41–2, 155
- avoidance, 162–3
 - Campbell diagram, 163
- response surface method (RSM), 346–7
- response surface method with Monte Carlo simulation (RSM/MC), 347, 348
- Revolutions Per Minute (RPM), 184
- Reynolds number, 100–1, 122–4, 124–5
- aerodynamic performance of airfoil NACA 64₃–418, 124
- RFOIL, 111, 144
- predicted and measured characteristics, 112
 - predicted transition location, 112
- Rice's theory, 303
- rime, 398
- Rosenblatt transformation, 345
- rotor blades, 178
- rotor control, 80–3, 88
- pitch regulated variable speed (PRVS), 83
 - stall regulation principle, 82
- rotor disc, 66
- rotor plane, 65
- rotor size, 79–80, 87–8
- roughness, 121–2
- contamination by insect debris, 121
- NACA standard, 122
- S-N curve formulations, 256, 257–62
- semi-logarithmic equation, 256
- shear lag model, 300
- simple beam theory, 277
- single-axial fatigue test, 435
- single-fibre
- fragmentation test, 194
 - properties, 176
- single-lap joints, 273
- sizing, 177
- skin, 181–2
- small blade fatigue, 421–4
- small wind turbine blades
- blade testing, 421–6
 - fatigue test rig, 422
 - leading edge damage to vacuum-infused 2.5 m long blade, 423
 - measured blade section from power producing section of Aerogenesis 2.5 m long blade, 426
 - partial safety factors for material characterisation form IEC 61400–2, 424
 - quality control, 424–6
 - small blade fatigue, 421–4
 - static testing, 421
- challenges and future trends, 428–9
- design, manufacture and testing, 413–29
- 8 cm chord, 30 cm long timber for a 50 W turbine, 415
 - background, 413–14
 - scope and layout, 416
 - the Skystream blade, 416
 - small *vs.* large blades, 414–16
- installation and operation, 426–8
- blade root bending moment
 - measured on 1.94 m diameter three-bladed turbine, 427
 - lightning damage at trailing edge near the tip of Westwind 20 kW wind turbine blade, 428
- materials and manufacture, 418–21
- fibre-reinforced composites, 419–21
 - timber, 419
 - Young's modulus of several composite materials, 420
- requirements, 416–18
- AA 5 kW blade mould and 2.5 m blade, 417
- Smart blades, 206
- Southwest Windpower Skystream, 415
- spar cap, 179–80
- stall control, 81
- stall flutter, 159
- stall induced vibration, 158

- static blade test, 52
 static compression stress-strain tests, 219
 static test, 421, 434–5
 test loads, 437–8
 steeper curve, 256
 stiffness degradation fatigue theories,
 268–72
 degradation of composite strength and
 stiffness, 269
 schematic representation of typical
 stiffness degradation curve, 270
 schematic representation of typical
 types of strength degradation
 behaviour, 271
 strength degradation fatigue theories,
 268–72
**Strength Life Equal Rank Assumption
 (SLERA), 259**
 stress concentration factor (SCF), 301
 stress-strain curves, 308
 structural health monitoring, 202
 structural performance testing, 432–45
 instrumentation, 443–5
 accelerations, 444
 applied force, 443
 displacements, 443–4
 electrical conductivity of lightning
 protection system, 445
 environmental conditions, 444
 strains, 443
 test details, 441–5
 blade root clamping, 442–3
 effects on load due to blade
 deformation, 442
 load introduction, 441–2
 test loads, 437–41
 design FSF, 439
 fatigue test, 438–41
 rFSF and critical area, multi-axial
 test, 440
 rFSF and critical areas, sequential
 single-axial test, 440
 static test, 437–8
 test program, 433
 types of tests, 434–7
 fatigue tests, 435–6
 static tests, 434–5
 three point bending moment curve,
 435
 two point bending moment curve,
 435
 ultimate tests, 436–7
 structural pitch angle, 164
STRUREL, 348
 styrene, 394
 subcomponent research, 204–6
 test types and number of tests for
 I-beam subcomponents, 205
 von Mises stress S-N lines of different
 beam subcomponent test
 configurations, 206
 subcomponent test, 21
SuperSap 1100, 372, 373
 surface protection and coatings
 accelerated testing, 405–6
 combined influences, 406
 ozone, 406
 UV tests and xenon light tests,
 405–6
 accelerated testing of the surface
 coatings, 406–9
 standards, 406–7
 challenges and future trends, 409–11
 advantages and limitations of
 different protection technologies,
 409–10
 new materials, 410
 protection of the surroundings,
 410–11
 test methods, 411
 working environment, 411
 degradation of polymers, 401–3
 bond energies and bond length of
 some covalent bond, 404
 degradation mechanisms, 403–4
 oxygen and humidity, 402–3
 sunlight, 402
 weathering, 402
 fundamentals of surface protection for
 wind turbine blades, 389–98
 adhesion of surface coatings, 390–2
 contact angle for measurement of
 surface tension, 392
 HSP for two different materials,
 391
 selection criteria for coatings, 393
 particular coating materials, 393–8
 acrylate schematic figure, 396
 acrylates, 396
 advantages and disadvantages of
 materials used as gelcoats and
 paints, 397

- surface protection and coatings (*cont.*)
 epoxies, 395–6
 epoxy made from Bisphenol A, 395
 polyurethane schematic figure, 397
 polyurethanes, 396–7
 styrene and methylmethacrylate structures, 395
 thixotropic behaviour of a fluid, 394
 unsaturated polyester structure, 395
 unsaturated polyesters, 394
 vinylester structure, 397
 vinylesters, 396
- performance testing of protection layers, 400–6
 measuring the degradation of polymer systems, 403–5
 performance testing considerations, 401
- protection from blade icing, lightning and air traffic, 398–400
 lightning protection, 399–400
 lightning protection concepts for large modern wind turbine rotor blades, 400
 protection from air traffic, 400
 wind turbine blade icing, 398–9
- selected test methods, 407–9
 chemical attack, 408
 humidity test, 408
 Norsok test, 407
 results of tests, 408–9
 wear test, 408
- wind turbine rotor blades, 387–411
- tangential force coefficient, 136
 tangential velocity, 68–9, 71
 target load, 437
 Taylor expansion of the failure function, 345
 temperature, 319
 tensile fatigue trends
 laminate construction and fibre content for glass fibre, 217–26
 fatigue parameters for different laminate types, 219–20
 fibre content effects, 220–6
 materials, 218–19
 front and back view of UD fabric PPG and cross-sections of laminates, 218
- tensile loading, 300–2
 tension-compression (T-C) fatigue, 263
 tension-tension (T-T) fatigue, 263
 test load, 437
 thermoplastic polymers, 370–1
 thermosetting resins, 371
 thick laminates, 196–7
 test specimens, test set-up and results for thick laminate test specimens, 197
 waviness in cross-section of thick laminate, 197
- THIN, 332, 342
- thin wall beam theory, 332
- three-dimensional modelling
 composite degradation under tensile loading, 306–11
 competition of damage models, 311
 damage evolution in composite with damageable interface fibres and strong matrix, 309
 damage-strain curves for the case of three acting damage mechanisms, 311
 example of 3-D FE micromechanical model, 307
 stress distribution in unit cell with microdamaged interface, 310
 stress-strain curves of unit cells with random and constant fibre strengths, 308
- thrust coefficient, 71–2
- timber, 419
- time dependency, 319
- tip speed ratio (TSR), 74, 78–9, 94
 vs. power coefficient, 79
- torque force, 117
- torsion mode, 156
- total fatigue life model, 276
- total solubility parameter, 390
- trailing-edge reinforcement, 199–201
- transformation field analysis (TFA), 302
- true variability, 379
- ultimate compressive stress (UCS), 265
 ultimate loading, 46–7

- ultimate tensile strength, 188
- ultimate tensile stress, 265
- ultimate tests, 436–7
- Ultra High Cycle project, 186
- unidirectional aligned strand (AS)
 - laminates, 230–3
 - unidirectional fabric laminates, 230–3
 - effects of resin, 229–30
 - effect of removing transverse backing strands on fabric data, 231
 - failed coupons of UP5/fabrics and image of cracking along transverse strand and stitching, 230
 - UD fabric laminates S-N results for epoxy, vinyl ester and polyester vs fabrics H and D, 229
- unit cell modelling, 304–6
- unsaturated polyesters, 394
- upward lightning, 399
- vacuum-assisted resin transfer moulding (VARTM), 287
- variable amplitude, 185
- variable rotational rotor speed, 81
- Vassilopoulos, 256
- vertical axis wind turbines (VAWT), 59, 414
- Vestas Wind Systems, 5
- vinylesters, 396
- virtual testing, 306
- vortex generators, 55
- wake rake, 127
- wear-out model, 259
- wear test, 408
- web failure, 17–18
 - modes observed in full-scale test, 18
 - skin debonding failure, 19
 - trailing edge failure, 17
- Weibull strengths, 308
- wind climate, 87
- wind direction, 32
- wind field, 31, 37
- wind speed, 31, 36
 - vector, 31
- wind turbine blades
 - aeroelastic design, 150–71
 - aeroelasticity, 151–5, 155–62
 - blade design, 162–7
- challenges and future trends, 170–1
- complete turbine design, 167–70
- airfoils characteristics, 109–49
 - centrifugal and Coriolis forces, 133–40
 - computational methods, 110–16
 - contamination and Reynolds number effect, 120–4
- design data, 140–5
- design parameters, 110
- desired characteristics, 116–20
- future trends, 145–6
- high angles of attack, 128–33
- testing, 124–8
- biobased composites as materials, 363–82
- biobased composites, 371–4
- biobased fibres and matrix materials, 366–71
 - comparison between cellulose and glass fibre composites, 374–7
- special considerations in development and application, 377–82
- challenges and future trends, 18–25
 - assembled box girder with cap reinforcement, 24
 - box girder manufacturing, 24
 - full-scale testing, 20
 - manufacturing, 23–5
 - multi-scale approach, 22
 - new design philosophy using internal members, 23
 - testing approach, 18–23
- design, 3–25
- design evaluation, 95, 97–102
 - angle of attack as a function of radius, 100
 - lift coefficient as a function of radius, 101
 - local mechanical power and thrust coefficient as a function of rotor radius, 100
 - mechanical power and thrust as a function of wind speed, 98
 - power and thrust coefficient as a function of tip speed ratio, 99

- wind turbine blades (*cont.*)
- Reynolds number as a function of radius, 102
 - rotational speed and pitch as a function of wind speed, 99
 - design principles and failure mechanisms, 6–18
 - aerodynamic and gravity loads applied to the FE model, 10
 - anchor plates in full-scale tests, 11
 - crushing pressure, 9
 - interlaminar shear failure of load-carrying cap laminate, 11
 - load application to the blade structure, 10
 - safety margins, 8
 - effects of resin and reinforcement variations on fatigue resistance, 210–48
 - delamination and material transitions, 236–43
 - fabric structure on tensile fatigue resistance, 226–36
 - fatigue trends comparison for blade materials, 243–6
 - future trends, 247–8
 - loading conditions effects for glass and carbon laminates, 211–17
 - tensile fatigue trends with laminate construction and fibre content for glass fibre, 217–26
 - fatigue life prediction of composite materials, 251–91
 - case study on phenomenological fatigue life prediction, 284–9
 - fracture mechanics fatigue theories, 273–84
 - future trends, 289–91
 - macroscopic failure theories, 255–68
 - strength and stiffness degradation fatigue theories, 268–72
 - loads, 29–56
 - design verification testing, 50–4
 - fatigue, 46–9
 - future trends, 54–6
 - generation, 35–46
 - types, 30–4
 - materials micromechanical modelling, 298–319
 - analytical models of mechanical behaviour, strength and damage of fibre-reinforced composites, 300–4
 - carbon fibre-reinforced composites
 - statistical and compressive loading effects, 311–16
 - future trends, 317–19
 - hierarchical composites with nanoengineered matrix, 316–17
 - three-dimensional modelling of composite degradation under tensile loading, 306–11
 - unit cell modelling of fibre-reinforced composites, 304–6
 - one point design, 95
 - chord distribution, 97
 - entities used in the blade design process, 96
 - relative thickness distribution, 97
 - twist distribution, 97
 - overview, 3–6
 - LM Wind, SSP Technology design and Vestas box girder, 7
 - load-carrying box girder, 6
 - one shear web, 5
 - ribs/bulkheads, 7
 - two shear web, 5
 - weight vs. length, 4
 - probabilistic design, 325–53
 - application examples and discussion of techniques, 348–51
 - failure definition, 333–8
 - future trends, 351–3
 - probabilistic methods and models, 342–7
 - random variables, 338–42
 - structural analysis models, 329–33
 - structural performance testing, 432–45
 - test details, 441–5
 - test loads, 437–41
 - test program, 433
 - types of tests, 434–7
 - wind turbine rotor blades, 290
 - surface protection and coatings, 387–411
 - accelerated testing of the surface coatings, 406–9

- fundamentals of surface protection
for wind turbine blades,
389–98
- future trends, 409–11
- performance testing of protection
layers, 401–6
- protection from blade icing, lightning
and air traffic,
398–400
- wind turbine rotors
- aerodynamic design, 59–108
 - blade element momentum (BEM),
63–72
 - design parameters, 72–8, 78–86
 - airfoil performance, 75–8
 - chord distribution, 74
 - design constraints, 84–5
 - design evaluation, 86
 - number of blades, 85
 - rotor control, 80–3
 - rotor/generator size, 79–80
 - tip speed ratio, 78–9
 - design process, 86–102
- blade design evaluation, 95, 97–102
- blade one point design, 95
- design constraints, 88–9
- lift and airfoils, 89–94
- number of blades, 89
- rotor control, 88
- rotor/generator size,
87–8
- tip speed ratio, 94
- wind climate, 87
- future trends, 102–3
- overview, 59–63
 - HAWT and VAWT, 60
 - models and elements, 63
 - state-of-the-art design, 61–3
- windowing approach, 304
- wing section theory, 69
- XFOIL, 111, 144
- yarn spinning, 369
- zone of influence, 306